

Understanding the tensile properties of concrete

Edited by Jaap Weerheijm

Understanding the tensile properties of concrete

Related titles:

Understanding the rheology of concrete
(ISBN 978-0-85709-028-7)

Eco-efficient concrete
(ISBN 978-0-85709-424-7)

Nanotechnology in eco-efficient construction
(ISBN 978-0-85709-544-2)

Details of these books and a complete list of titles from Woodhead Publishing can be obtained by:

- visiting our web site at www.woodheadpublishing.com
- contacting Customer Services (e-mail: sales@woodheadpublishing.com; fax: +44 (0) 1223 832819; tel.: +44 (0) 1223 499140 ext. 130; address: Woodhead Publishing Limited, 80, High Street, Sawston, Cambridge CB22 3HJ, UK)
- in North America, contacting our US office (e-mail: usmarketing@woodheadpublishing.com; tel.: (215) 928 9112; address: Woodhead Publishing, 1518 Walnut Street, Suite 1100, Philadelphia, PA 19102-3406, USA)

If you would like e-versions of our content, please visit our online platform: www.woodheadpublishingonline.com. Please recommend it to your librarian so that everyone in your institution can benefit from the wealth of content on the site.

We are always happy to receive suggestions for new books from potential editors. To enquire about contributing to our Civil and structural engineering series, please send your name, contact address and details of the topic/s you are interested in to gwen.jones@woodheadpublishing.com. We look forward to hearing from you.

The team responsible for publishing this book:

Commissioning Editor: Jess Rowley
Publications Coordinator: Adam Davies
Project Editor: Diana Paulding
Editorial and Production Manager: Mary Campbell
Production Editor: Richard Fairclough
Project Manager: Newgen Knowledge Works Pvt Ltd
Copy-editor: Newgen Knowledge Works Pvt Ltd
Proofreader: Newgen Knowledge Works Pvt Ltd
Cover Designer: Terry Callanan

Woodhead Publishing Series in Civil and Structural Engineering:
Number 48

Understanding the tensile properties of concrete

Edited by
Jaap Weerheijm



Oxford Cambridge Philadelphia New Delhi

© Woodhead Publishing Limited, 2013

www.EngineeringBooksPDF.com

Published by Woodhead Publishing Limited,
80 High Street, Sawston, Cambridge CB22 3HJ, UK
www.woodheadpublishing.com
www.woodheadpublishingonline.com

Woodhead Publishing, 1518 Walnut Street, Suite 1100, Philadelphia,
PA 19102-3406, USA

Woodhead Publishing India Private Limited, 303, Vardaan House, 7/28 Ansari Road,
Daryaganj, New Delhi – 110002, India
www.woodheadpublishingindia.com

First published 2013, Woodhead Publishing Limited
© Woodhead Publishing Limited, 2013. Note: the publisher has made every effort to ensure that permission for copyright material has been obtained by authors wishing to use such material. The authors and the publisher will be glad to hear from any copyright holder it has not been possible to contact.
The authors have asserted their moral rights.

This book contains information obtained from authentic and highly regarded sources. Reprinted material is quoted with permission, and sources are indicated. Reasonable efforts have been made to publish reliable data and information, but the authors and the publisher cannot assume responsibility for the validity of all materials. Neither the authors nor the publisher, nor anyone else associated with this publication, shall be liable for any loss, damage or liability directly or indirectly caused or alleged to be caused by this book.

Neither this book nor any part may be reproduced or transmitted in any form or by any means, electronic or mechanical, including photocopying, microfilming and recording, or by any information storage or retrieval system, without permission in writing from Woodhead Publishing Limited.

The consent of Woodhead Publishing Limited does not extend to copying for general distribution, for promotion, for creating new works, or for resale. Specific permission must be obtained in writing from Woodhead Publishing Limited for such copying.

Trademark notice: Product or corporate names may be trademarks or registered trademarks, and are used only for identification and explanation, without intent to infringe.

British Library Cataloguing in Publication Data
A catalogue record for this book is available from the British Library.

Library of Congress Control Number: 2013938655

ISBN 978-0-85709-045-4 (print)
ISBN 978-0-85709-753-8 (online)
ISSN 2052-4714 Woodhead Publishing Series in Civil and Structural Engineering (print)
ISSN 2052-4722 Woodhead Publishing Series in Civil and Structural Engineering (online)

The publisher's policy is to use permanent paper from mills that operate a sustainable forestry policy, and which has been manufactured from pulp which is processed using acid-free and elemental chlorine-free practices. Furthermore, the publisher ensures that the text paper and cover board used have met acceptable environmental accreditation standards.

Typeset by Newgen Knowledge Works Pvt Ltd, India
Printed by Lightning Source

Contents

	<i>Contributor contact details</i>	<i>xi</i>
	<i>Woodhead Publishing Series in Civil and Structural Engineering</i>	<i>xv</i>
	<i>Preface</i>	<i>xix</i>
1	Introduction to concrete: a resilient material system	1
	J. WEERHEIJM and K. VAN BREUGEL, TNO and Delft University of Technology, The Netherlands	
1.1	Introduction	1
1.2	Concrete structure at the micro-scale: the cement matrix	4
1.3	Concrete structure at the meso-scale: bond cement matrix and aggregates	8
1.4	Concrete structure and mechanical properties	11
1.5	References	14
Part I	Concrete in static tensile loading	17
2	Factors affecting the tensile properties of concrete	19
	H. W. REINHARDT, University of Stuttgart, Germany	
2.1	Introduction	19
2.2	Effect of composition	20
2.3	Effect of curing and moisture	23
2.4	Effect of temperature	25
2.5	Influence of specimen size	27
2.6	Effect of age	30
2.7	Effect of load duration	31
2.8	Effect of cyclic loading	34
2.9	Effect of type of loading	38
2.10	Crack development at the meso-scale	44

vi	Contents	
2.11	The relationship between tensile strength and compressive strength	46
2.12	The practical implications of laboratory tests	47
2.13	References	49
3	Modelling the effect of material composition on the tensile properties of concrete	52
	Ł. SKARŻYŃSKI and J. TEJCHMAN, Gdańsk University of Technology, Poland	
3.1	Introduction	52
3.2	Modelling damage in concrete	54
3.3	Behaviour of concrete beams under three-point bending conditions	56
3.4	Behaviour of concrete elements under uniaxial tension	69
3.5	Conclusions	86
3.6	Acknowledgements	94
3.7	References	94
4	Modelling moisture transport in intact and fractured concrete	98
	P. MOONEN and J. CARMELIET, ETH Zürich and Empa Dübendorf, Switzerland	
4.1	Introduction	98
4.2	Modelling moisture transport in intact concrete	100
4.3	Modelling moisture transport in degraded concrete	110
4.4	Interaction between moisture transport and material behaviour	112
4.5	Case study: application of outside render to masonry walls	113
4.6	Summary and future trends	117
4.7	References	118
Part II	Concrete in dynamic tensile loading	123
5	Modelling the response of concrete structures to dynamic loading	125
	W. RIEDEL, Ernst Mach Institut, Germany and P. FORQUIN, University of Lorraine, France	
5.1	Introduction: dynamic loading regimes affecting concrete structures	125

5.2	Earthquake loading and impact deflection: inertia effects	127
5.3	Blast response: rate-dependent strength	127
5.4	Projectile impact loading: compressibility and high triaxial stresses	128
5.5	Contact detonations and explosive formed projectiles (EFPs): shock and release properties	131
5.6	Concluding remarks	133
5.7	References	135
 6	 Dynamic test devices for analyzing the tensile properties of concrete	 137
	P. FORQUIN, University of Lorraine, France, W. RIEDEL, Ernst Mach Institut, Germany and J. WEERHEIJM, TNO and Delft University of Technology, The Netherlands	
6.1	Introduction	137
6.2	Different experimental methods to characterize the tensile response of concrete	138
6.3	Characterizing the tensile strength and fracture energy of concrete at intermediate loading rates ($\dot{\sigma} \leq 100$ GPa/s or $\dot{\epsilon} \leq 2$ /s)	139
6.4	Characterizing the tensile strength and fracture energy of concrete at high loading rates ($100 \text{ GPa/s} \leq \dot{\sigma} \leq 1000 \text{ GPa/s}$ or $20/\text{s} \leq \dot{\epsilon} \leq 200/\text{s}$)	147
6.5	Characterizing the tensile strength of concrete at very high loading rates ($\dot{\sigma} \geq 10^5$ GPa/s or $\dot{\epsilon} \geq 2000/\text{s}$)	171
6.6	Edge-on impact tests performed on concrete	176
6.7	Conclusions	177
6.8	References	178
 7	 Response mechanisms of concrete under impulsive tensile loading	 181
	J. WEERHEIJM, TNO and Delft University of Technology, The Netherlands and P. FORQUIN, University of Lorraine, France	
7.1	Introduction: concrete response mechanisms under impulsive tensile loading	181
7.2	The effect of cracking rates on the tensile strength of concrete	183
7.3	The effect of cracking rates on the fracture process under moderate and high loading regimes	203

viii	Contents	
7.4	Conclusions	214
7.5	References	215
8	Modelling the dynamic response of concrete with mesoscopic heterogeneity	218
	Y. LU, University of Edinburgh, UK	
8.1	Introduction	218
8.2	The mesoscopic structure of concrete and computational considerations	220
8.3	Types of mesoscale model and their applications in the dynamic analysis of concrete	224
8.4	A comprehensive mesoscale continuum model for the dynamic analysis of concrete	231
8.5	A pseudo-3D (sandwich) mesoscale model for the dynamic analysis of concrete in compression	242
8.6	Mesoscale modelling of the tensile behaviour of concrete in dynamic splitting (Brazilian) tension	248
8.7	Modelling of heterogeneity in concrete with stochastic material properties	254
8.8	Modelling of spalling and fragmentation in concrete structures with a stochastic material property distribution	259
8.9	Conclusions	261
8.10	Acknowledgements	262
8.11	References	262
9	Mesosopic modeling of concrete under different moisture conditions and loading rates	268
	R. R. PEDERSEN, Aalborg University, Denmark, A. SIMONE and L. J. SLUYS, Delft University of Technology, The Netherlands	
9.1	Introduction	268
9.2	Constitutive modeling of concrete	270
9.3	Mesosopic modeling of concrete	274
9.4	The Split Hopkinson Bar test	278
9.5	Modified Split Hopkinson Bar test	284
9.6	Summary and conclusions	288
9.7	Acknowledgements	289
9.8	References	289
9.9	Appendix A: computation of the homogenized material tensor for different saturation levels	293

10	Modelling the response of concrete structures from strain rate effects to shock induced loading	295
	J. OZBOLT, University of Stuttgart, Germany and W. RIEDEL, Ernst Mach Institut, Germany	
10.1	Introduction to the modelling of loading-rate effects on concrete	295
10.2	Measuring the strain-rate dependent strength of concrete	301
10.3	Modelling shock-induced tensile loading of concrete structures	320
10.4	Summary	332
10.5	References	334
11	Understanding the dynamic response of concrete to loading: practical examples	338
	N. GEBBEKEN, University of the Bundeswehr München, Germany and T. KRAUTHAMMER, University of Florida, USA	
11.1	Introduction	338
11.2	Impact, penetration and perforation	339
11.3	Contact detonation	342
11.4	Blast	345
11.5	Residual load-bearing capacity of damaged structural elements	348
11.6	Behaviour of reinforced-concrete beams under localized static and impact loads	352
11.7	Project examples: improving blast resistance	358
11.8	Conclusions	363
11.9	Acknowledgements	363
11.10	References	363
	<i>Index</i>	365

Contributor contact details

(* = main contact)

Editor

Dr Jaap Weerheijm
TNO Defence Security and Safety
Delft University of Technology
Stevinweg 1
2628 CN Delft
The Netherlands

Email: j.weerheijm@tudelft.nl

Chapter 1

Dr Jaap Weerheijm*
TNO Defence Security and Safety
Delft University of Technology
Stevinweg 1
2628 CN Delft
The Netherlands

Email: j.weerheijm@tudelft.nl

Professor Klaas van Breugel
Delft University of Technology
Stevinweg 1
2628 CN Delft
The Netherlands

Chapter 2

Professor Hans W. Reinhardt
Department of Construction
Materials
University of Stuttgart
Pfaffenwaldring 4
70569 Stuttgart, Germany
Email: reinhardt@iwb.uni-stuttgart.de

Chapter 3

Dr Ł. Skarżyński and Professor
J. Tejchman*
Faculty of Civil and Environmental
Engineering
Gdańsk University of Technology,
Poland
80–233 Gdańsk-Wrzeszcz,
Narutowicza 11/12

Email: lskarzyn@pg.gda.pl;
tejchmk@pg.gda.pl

Chapter 4

Dr Peter Moonen* and Professor
J. Carmeliet
Empa, Swiss Federal Laboratories
for Materials Science and
Technology

Department of Civil and
Mechanical Engineering
Überlandstrasse 129
8600 Dübendorf, Switzerland

Email: peter.moonen@empa.ch

ETH Zürich
Department of Architecture
Wolfgang-Pauli-Strasse 15
8093 Zürich Hönggerberg
Switzerland

Email: moonen@arch.ethz.ch

Chapter 5

Professor Werner Riedel*
Dept. Safety Technology and
Protective Structures
Fraunhofer Institute for High-
Speed Dynamics, Ernst Mach
Institut

Am Klingenberg 1
79588 Efringen-Kirchen
Germany

Email: werner.riedel@emi.
fraunhofer.de

Professor Pascal Forquin
Université de Lorraine
Bat.C, Ile du Saulcy
57045 Metz cedex 1
France

Email: pascal.forquin@univ-
lorraine.fr

Chapter 6

Professor Pascal Forquin*
Université de Lorraine
Bat.C, Ile du Saulcy
57045 Metz cedex 1

France

Email: pascal.forquin@univ-
lorraine.fr

Professor Werner Riedel
Dept. Safety Technology and
Protective Structures
Fraunhofer Institute for High-
Speed Dynamics, Ernst-Mach-
Institut

Am Klingenberg 1
79588 Efringen-Kirchen

Email: werner.riedel@emi.
fraunhofer.de

Dr Jaap Weerheijm
TNO Defence Security and Safety
Delft University of Technology
Stevinweg 1
2628 CN Delft
The Netherlands

Email: j.weerheijm@tudelft.nl

Chapter 7

Dr Jaap Weerheijm*
TNO Defence Security and Safety
Delft University of Technology
Stevinweg 1
2628 CN Delft
The Netherlands

Email: j.weerheijm@tudelft.nl

Professor Pascal Forquin
Université de Lorraine
Bat.C, Ile du Saulcy
57045 Metz cedex 1
France

Email: pascal.forquin@univlorraine.
fr

Chapter 8

Professor Yong Lu
Institute for Infrastructure and
Environment
School of Engineering
University of Edinburgh
William Rankine Building
The King's Buildings
Edinburgh, EH9 3JL, UK
Email: yong.lu@ed.ac.uk

Chapter 9

Dr Ronnie R. Pedersen
Department of Civil Engineering
Aalborg University Niels Bohrs
Vej 8
6700 Esbjerg
Denmark
Dr Angelo Simone and Professor
Bert Sluys*
Faculty of Civil Engineering and
Geosciences
Delft University of Technology
P.O. Box 5048, 2600 GA Delft
The Netherlands
Email: l.j.sluys@tudelft.nl

Chapter 10

Professor Joško Ožbolt*
Institute of Construction Materials
University of Stuttgart
Pfaffenwaldring 4
70569 Stuttgart, Germany
Email: ozbolt@iwb.uni-stuttgart.de

Professor Werner Riedel
Dept. Safety Technology and
Protective Structures
Fraunhofer Institute for High-
Speed Dynamics, Ernst Mach
Institut
Am Klingenberg 1
79588 Efringen-Kirchen
Germany
Email: werner.riedel@emi.
fraunhofer.de

Chapter 11

Professor Norbert Gebbeken*
University of the Bundeswehr
München
85577 Neubiberg, Germany
AJG Consulting Engineers
81925 München, Germany
Email: norbert.gebbeken@unibw.de
Professor T. Krauthammer
University of Florida
Gainesville, FL 32611, USA

Woodhead Publishing Series in Civil and Structural Engineering

- 1 **Finite element techniques in structural mechanics**
C. T. F. Ross
- 2 **Finite element programs in structural engineering and continuum mechanics**
C. T. F. Ross
- 3 **Macro-engineering**
F. P. Davidson, E. G. Frankl and C. L. Meador
- 4 **Macro-engineering and the earth**
U. W. Kitzinger and E. G. Frankel
- 5 **Strengthening of reinforced concrete structures**
Edited by L. C. Hollaway and M. Leeming
- 6 **Analysis of engineering structures**
B. Bedenik and C. B. Besant
- 7 **Mechanics of solids**
C. T. F. Ross
- 8 **Plasticity for engineers**
C. R. Calladine
- 9 **Elastic beams and frames**
J. D. Renton
- 10 **Introduction to structures**
W. R. Spillers
- 11 **Applied elasticity**
J. D. Renton
- 12 **Durability of engineering structures**
J. Bijen
- 13 **Advanced polymer composites for structural applications in construction**
Edited by L. C. Hollaway

- 14 **Corrosion in reinforced concrete structures**
Edited by H. Böhni
- 15 **The deformation and processing of structural materials**
Edited by Z. X. Guo
- 16 **Inspection and monitoring techniques for bridges and civil structures**
Edited by G. Fu
- 17 **Advanced civil infrastructure materials**
Edited by H. Wu
- 18 **Analysis and design of plated structures Volume 1: Stability**
Edited by E. Shanmugam and C. M. Wang
- 19 **Analysis and design of plated structures Volume 2: Dynamics**
Edited by E. Shanmugam and C. M. Wang
- 20 **Multiscale materials modelling**
Edited by Z. X. Guo
- 21 **Durability of concrete and cement composites**
Edited by C. L. Page and M. M. Page
- 22 **Durability of composites for civil structural applications**
Edited by V. M. Karbhari
- 23 **Design and optimization of metal structures**
J. Farkas and K. Jarmai
- 24 **Developments in the formulation and reinforcement of concrete**
Edited by S. Mindess
- 25 **Strengthening and rehabilitation of civil infrastructures using fibre-reinforced polymer (FRP) composites**
Edited by L. C. Hollaway and J. C. Teng
- 26 **Condition assessment of aged structures**
Edited by J. K. Paik and R. M. Melchers
- 27 **Sustainability of construction materials**
J. Khatib
- 28 **Structural dynamics of earthquake engineering**
S. Rajasekaran
- 29 **Geopolymers: Structures, processing, properties and industrial applications**
Edited by J. L. Provis and J. S. J. van Deventer
- 30 **Structural health monitoring of civil infrastructure systems**
Edited by V. M. Karbhari and F. Ansari
- 31 **Architectural glass to resist seismic and extreme climatic events**
Edited by R. A. Behr
- 32 **Failure, distress and repair of concrete structures**
Edited by N. Delatte
- 33 **Blast protection of civil infrastructures and vehicles using composites**
Edited by N. Uddin

- 34 **Non-destructive evaluation of reinforced concrete structures Volume 1: Deterioration processes**
Edited by C. Maierhofer, H.-W. Reinhardt and G. Dobmann
- 35 **Non-destructive evaluation of reinforced concrete structures Volume 2: Non-destructive testing methods**
Edited by C. Maierhofer, H.-W. Reinhardt and G. Dobmann
- 36 **Service life estimation and extension of civil engineering structures**
Edited by V. M. Karbhari and L. S. Lee
- 37 **Building decorative materials**
Edited by Y. Li and S. Ren
- 38 **Building materials in civil engineering**
Edited by H. Zhang
- 39 **Polymer modified bitumen**
Edited by T. McNally
- 40 **Understanding the rheology of concrete**
Edited by N. Roussel
- 41 **Toxicity of building materials**
Edited by F. Pacheco-Torgal, S. Jalali and A. Fucic
- 42 **Eco-efficient concrete**
Edited by F. Pacheco-Torgal, S. Jalali, J. Labrincha and V. M. John
- 43 **Nanotechnology in eco-efficient construction**
Edited by F. Pacheco-Torgal, M. V. Diamanti, A. Nazari and C.-G. Granqvist
- 44 **Handbook of seismic risk analysis and management of civil infrastructure systems**
Edited by F. Tesfamariam and K. Goda
- 45 **Developments in fiber-reinforced polymer (FRP) composites for civil engineering**
Edited by N. Uddin
- 46 **Advanced fibre-reinforced polymer (FRP) composites for structural applications**
Edited by J. Bai
- 47 **Handbook of recycled concrete and demolition waste**
Edited by F. Pacheco-Torgal, V. W. Y. Tam, J. A. Labrincha, Y. Ding and J. de Brito
- 48 **Understanding the tensile properties of concrete**
Edited by J. Weerheijm
- 49 **Eco-efficient construction and building materials**
Edited by F. Pacheco-Torgal, J. Labrincha, G. Baldo and A. de Magalhaes

Concrete is one of the oldest building materials, and is still in use because of its special properties. It is also a versatile material, which has evolved using new production techniques, new additives and new mixtures, providing properties tuned to the requirements of the application.

The response of concrete under tensile loading is crucial for most applications, because concrete is much weaker in tension than in compression. Understanding the response mechanisms of concrete under tensile conditions is key to understanding and using concrete in structural applications. This is the reason why tensile behaviour has been studied so extensively and so many books have been written on this subject. Experimental and computational techniques to analyse and understand the properties and behaviour of materials have developed considerably in the last decade. However, even with these developments, specific features of the response of concrete under dynamic tensile loading are still not well known. It is for this reason that I invited leading experts to share their knowledge and provide a state-of-the-art overview on the behaviour of concrete under tensile loading, with a special focus on dynamics. The result is this book, which is divided into two parts: Part I deals with static response, and Part II with dynamic response.

The book begins with an introduction to concrete, which is described at different length scales to give a general background of the response mechanisms and properties that are presented and discussed in the following chapters. Part I on static response begins with a summary chapter (Chapter 2) on the most important parameters that affect the tensile response of concrete. This provides an overview of the complex response mechanisms involved, and shows that curing, water saturation level, and moisture transport have clear effects on concrete response. Chapter 3 shows how multi-scale modelling is used to relate concrete composition to tensile properties. Multi-scale modelling is a powerful technique that is used to understand and analyse the response of the heterogeneous concrete. It is also relatively new and still at the academic level for discrete fracture processes. The part on the static response ends with Chapter 4 on moisture transport through the pore structure and cracks in concrete.

Part II on dynamic response begins with an introduction (Chapter 5) to the different regimes of dynamic loading, ranging from the low frequency loading by wind or earthquakes, up to the extreme dynamic conditions due to explosions and ballistic impacts. Concrete exhibits a pronounced rate dependency, especially in tension. This introduction provides a reference for the observed loading rate and relates it to the structural loading conditions. The next chapter (Chapter 6) reviews dynamic testing techniques and devices that deal with the various regimes of dynamic loading. Structural and material response is always integrated in dynamic tests. Inertia effects play a role at all scale levels and the problem of how to distinguish the true material response from the structural response is yet to be solved. There is no unique answer, as it depends on the level of detail used to model the structure and material.

Chapters 7–10 highlight the dynamic behaviour of concrete from different viewpoints. First, the fundamental response mechanisms are discussed in Chapter 7, based on the heterogeneity of concrete using the static response as a reference. Chapter 8 provides a broad review of the numerical modelling options to treat concrete as a mesoscopic heterogeneous material. The next chapter (Chapter 9) presents the numerical mesoscopic analysis of dynamic tensile tests at different rates and different moisture levels. The issue of structural inertia at material level in detailed numerical modelling is discussed in Chapter 10. The mechanisms that drive cracking and damage growth are analysed using advanced numerical modelling. The last part of this chapter makes a link to the introductory chapter, dealing with the high tensile rates that only occur after shock conditions due to explosions or impact. The book ends with a chapter (Chapter 11) of practical examples of how this ‘detailed knowledge’ is used by engineers.

I would like to thank all the authors for their time, kind cooperation and their valuable contributions. I also want to thank Woodhead for giving us the opportunity to compile and publish this book on concrete. Last, but not least, I wish to thank my wife Christien for giving me the time and encouraging me to undertake the book.

*Jaap Weerheijm
Delft, October 2012*

Introduction to concrete: a resilient material system

J. WEERHEIJM and K. VAN BREUGEL,
TNO and Delft University of Technology, The Netherlands

DOI: 10.1533/9780857097538.1

Abstract: The strength of concrete is its heterogeneous composition. It is a system that is formed by the chemical process of hydration, producing crystalline and amorphous reaction products interlocking and binding the aggregates together. The material grows in time, resulting in a resilient system that is sufficiently strong to carry loads but can also respond to environmental conditions. Crack initiation and crack growth at the various scale levels govern the mechanical tensile response of the heterogeneous concrete material. Therefore, the fracture mechanics principles of strength and energy criteria help in understanding and modelling the response mechanisms. The internal stress conditions and defect distributions are at (i) meso-level, governed by the aggregate grading, mortar and bonding (ITZ) properties, and at (ii) micro-level, defining the mortar properties (aggregates–cement matrix, ITZ and capillary pore system). The structure at micro/nano-level (cement matrix and micro-pore system) gives the sub-scale condition for the mortar. In this chapter we will describe the concrete system and the material structure from the material science point of view at the microscopic and mesoscopic levels, respectively. It provides general background information for the chapters that follow.

Key words: cement clinker, hydration process, porosity, micro-cracking, interface transition zone (ITZ), meso-scale, material testing.

1.1 Introduction

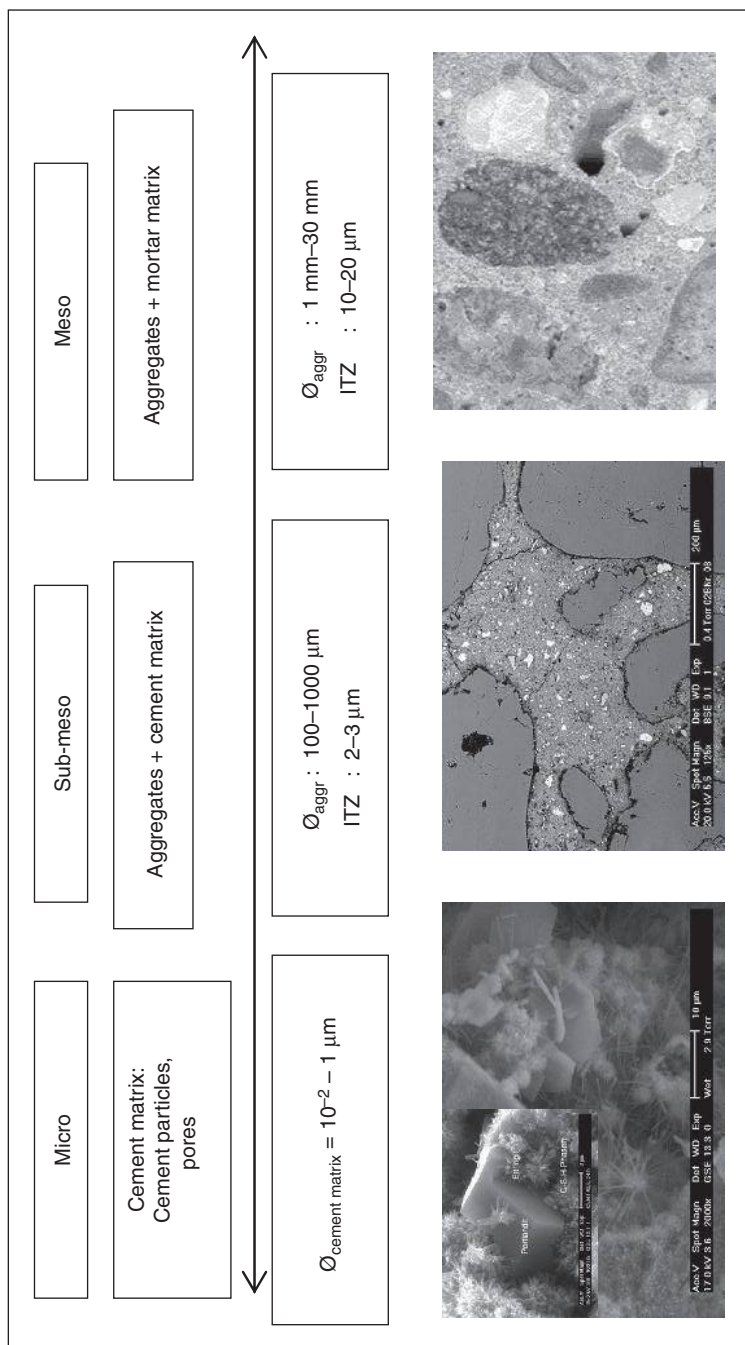
Concrete is the most widely used material in construction, found in houses, skyscrapers, bridges, dams, roads, pipes, silos, nuclear-waste containers, etc. It is a versatile material which can be moulded to almost any shape, and its properties can be modified and controlled by varying its composition and using additives. Egyptian pyramids and Roman aqueducts are often mentioned as the precursors of modern concrete technology. The application and development of modern cement-based materials dates back to the nineteenth century. Nowadays, high performance concretes are produced by the

use of additives and control of the hardening process, thus making possible new structural applications such as the 830 m high Burj Khalifa Tower in Dubai.

The strength of concrete is due to its heterogeneous composition. The system is formed by the chemical process of hydration, producing crystalline and amorphous reaction products which interlock and bind the aggregates together. The material develops over time, as the Latin word ‘concretum’ (growing together) suggests, resulting in a resilient system with sufficient strength to carry loads but which is also capable of responding dynamically to environmental conditions. The pore system, moisture distribution and chemical residuals play an important role in the ability of concrete to respond to changing conditions.

In practical design applications, only the overall behaviour, i.e. the macroscopic properties of concrete, are considered, and most experiments produce data on its macroscopic response. The dependency of the macroscopic behaviour on parameters such as aggregate grading and shape, moisture content, load duration and specimen size and shape, has also been studied and quantified (see Chapters 2, 6 and 7). Since it is now understood that the behaviour of concrete is governed by its heterogeneity, research is increasingly being redirected towards studying the response of concrete at smaller scales. Experimental techniques and computational modelling are now focusing on the meso-scale, even down to the nano-, molecular and atomic scales.¹ The current state of mesoscopic modelling of concrete in static and dynamic loading conditions and the knowledge gained from these analyses is reviewed in Chapters 3, 8 and 9.

This introductory chapter aims to provide general background information for the chapters that follow. As will be seen, crack initiation and crack growth at the various scale levels govern the mechanical tensile response of the heterogeneous concrete material. Therefore, the fracture mechanics principles of strength and energy criteria aid in understanding and modelling of the response mechanisms. The internal stress conditions and defect distributions are at (i) meso-level, governed by the aggregate grading, mortar and bonding ITZ properties, and at (ii) micro-level, defined by the mortar properties (aggregates–cement matrix, ITZ and capillary pore system). The structure at the micro/nano-level (cement matrix and micro-pore system) gives the subscale condition for the mortar. The different length scales, with the corresponding characteristic defect sizes, are summarised in Fig. 1.1. In the remainder of this chapter, the concrete system is described from the material science point of view at the microscopic and mesoscopic levels, respectively. No mechanical response aspects are addressed, as these are presented in other chapters.



1.1 Three geometrical scales of concrete: micro, sub-meso and meso-scale (MicroLab DUT).

1.2 Concrete structure at the micro-scale: the cement matrix

The binder in concrete is cement. The cement matrix is formed during the hydration process and binds the aggregates together. The cement fraction, about 300 kg/m³ concrete, is limited but dominates most concrete properties. Cement is produced in many varieties, but the most common is Portland cement (and its modified versions). The basic elements in the production of Portland cement are limestone (CaCO₃), silica (SiO₂), alumina (Al₂O₃), iron oxide (Fe₂O₃) and other substances in minor quantities. To produce cement clinker, the raw materials are mixed, ground and burned in a rotary kiln at about 1450°C. The constituents react to form new minerals. The four major minerals in cement clinker are tricalcium silicate (C₃S)^{*}, dicalcium silicate (C₂S)^{**}, tricalcium aluminate (C₃A)[†] and tetracalcium aluminoferrite (C₄AF)[‡]. In normal cement, the weight percentages of these minerals are about: 45–65% C₃S, 30–10% C₂S, 15–5% C₃A and 5–12% C₄AF. Although these are the principal minerals, other constituents may have a considerable effect on the hydration process, the properties of the cement matrix, and heat production. These aspects are not discussed in this chapter, but information may be found in Taylor's 'Cement chemistry',² and also in excellent summary given by van Mier.³

The minerals in the clinker begin to react when water is added. This series of chemical reactions is called the hydration process, and consists of various phases. It starts immediately, and the dominant reactions occur on the first day. However, the chemical reactions continue for months, or even years, slowing down gradually. In engineering practice, the hydration process is often supposed to be 'finished' after around 28 days when the representative strength is reached. It is presented schematically in Fig. 1.2 according to Locher.⁴

The three main products formed during hydration are (i) ettringite[§] (AFt), (ii) calcium silicate hydrates^{§§} (CSH), and (iii) calcium hydroxide[¶] (CH). It is interesting to observe the manner in which the hydration process develops, giving the boundary conditions for practical applications.

Ettringite is formed from the reaction of the alumina-phase and gypsum.⁵ The latter product is added to the cement in order to avoid false set. This reaction is very fast and is followed by a period of low reactivity, which is

^{*} C₃S = 3CaO.SiO₂

^{**} C₂S = 2CaO.SiO₂

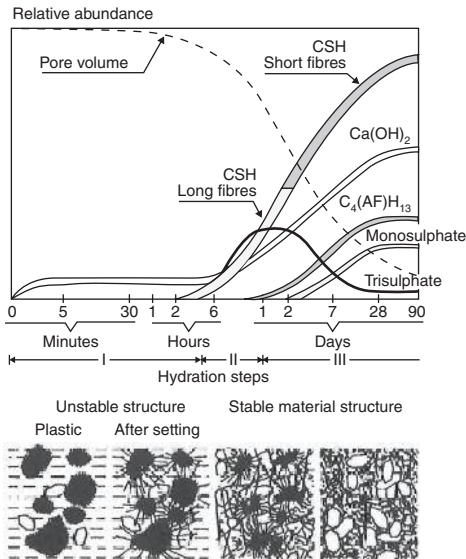
[†] C₃A = 3CaO.Al₂O₃

[‡] C₄AF = 4CaO.Al₂O₃.Fe₂O₃

[§] The chemical formula for ettringite is (CaO)₃(Al₂O₃)(CaSO₄)₃.32H₂O

^{§§} CSH = C₃S₂H₃ with C = CaO, S = SiO₂ and H = H₂O

[¶] CH = Ca(OH)₂

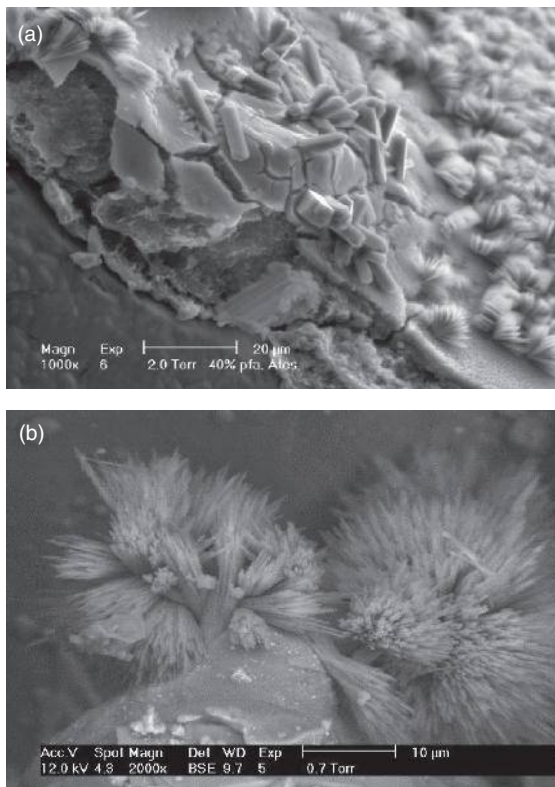


1.2 Scheme of the hydration process according to Locher.⁴ (Top) The development of the individual components and (bottom) schematic sketches of the material structure at 4 corresponding stages in time.

known as the dormant phase. The role of ettringite in the dormant stage is still the subject of debate.

This dormant period, i.e. the period in which the concrete can be transported and poured, is followed by the acceleration phase, during which a large quantity of CSH and CH crystals are formed, resulting in stiffening and hardening of the concrete. As indicated in the Locher-scheme, long CSH needles are initially formed, followed by shorter, stronger needles which produce a more dense structure. The structures of these crystals are illustrated in the scanning electron microscopy (SEM) images given in Fig. 1.3. Stutzman⁶ discusses the hydration products and the use of SEM technique.

The formation of CH is accompanied by an increase in the pH of the pore water up to values in the order of 12 to 13. This alkaline environment provides reinforcement against corrosion. Another aspect that should be noted is heat production in the exothermic hydration reactions. The expansion of material causes internal stresses, depending on the stiffness of the hardening material. In practice, the heat production and potential initial defects are significant issues. The dimensions of the cast structure or specimen and the curing conditions obviously affect the initial damage level. In addition to the curing conditions, heat production and timing can be controlled by the composition of the cement clinker and its additives. Special expertise is needed to control and direct the whole hardening process of cement and

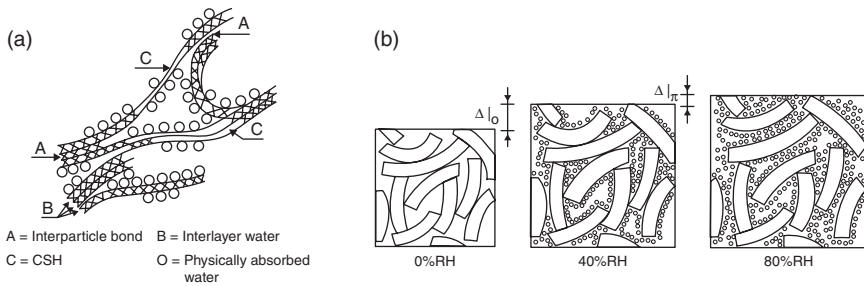


1.3 Typical examples of microstructure of cement-based materials, illustrating (a) crystalline and (b) amorphous features (Courtesy of MicroLab, M.R. de Rooij).

concrete. More information may be found in the literature, e.g. Mindess and Young⁷ and van Breugel,⁸ who studied the evolution of heat production and its effect on the properties of hardened cement.

The final structure of the cement matrix is a complex 3D-framework of needles, shells and plates formed by the hydration products at the scale of 10^{-7} – 10^{-5} m. The internal free surface of the cement is greatly increased by the formation of crystals. It grows from about $0.3 \text{ m}^2/\text{g}$ of the initial clinker to $200 \text{ m}^2/\text{g}$ after full hydration. (This free surface is available to bind water physically.)

The strength of the cement matrix is mainly due to the strong CSH ‘chains’, which have a geometry of fibres and/or rolled blades. The strength of the CSH fibres is obtained primarily from the strong ion-binding between the molecules, resulting in dense crystals. The secondary bonding is due to van der Waals forces between the solid surfaces, and becomes weaker with increasing intermediate distance. When water is available, it can penetrate



1.4 Model for hardened cement paste after Feldman and Sereda (a) and Wittmann (b).

between the CSH crystals, thus increasing the distance between the CSH surfaces. The secondary bonding is lost and the matrix strength reduced. Several models have been developed to represent the interaction mechanisms between the CSH particles and the absorbed, physically bonded water. Well-known models are (i) Powers (1958),⁹ (ii) Feldmann and Sereda (1968),¹⁰ and (iii) Wittmann (1977).¹¹ The model of Feldmann and Sereda is illustrated in Fig. 1.4a. They distinguish between the ‘interlayer water’ between the rolled-up blades of the CSH particles, and the physically absorbed water mentioned above. The loss of the secondary bonds and the volume change with increasing relative humidity (RH) is given by Wittmann and is illustrated in Fig. 1.4b. More recently, Jennings¹² has proposed ‘globules’ as the basic building blocks of CSH gel. The basic unit of CSH is a colloidal particle (globule) having a radius of the order of 1.5 nm. These globules condense to form low density CSH clusters with pores which are emptied of water only at a relative humidity below 20%. The globules probably form first and then condense to form a low density structure during a period of between 10 and 24 hours. At later stages, collections of low density CSH clusters aggregate to form a higher density microstructure.

During the hydration process, it is evident that, whatever the type of cement, the amount of water dominates the final structure and properties of the cement matrix and is quantified by the water cement (mass) ratio (w/c ratio). It was observed that during the hydration process a certain amount of water is chemically bonded to the hydration products, while some is physically bonded by adhesion to free surfaces. The latter evaporates at temperatures beyond 105°C, while the chemically bonded water can only be de-bonded beyond 1000°C. About 40 weight% water is needed for the full hydration process, i.e. 25% chemically and 15% physically bonded water. The volume of the reaction product is less than the sum of the volumes of the water and the cement from which it is formed. This chemical shrinkage is equal to about 25% of the volume of the chemically bound water and manifests itself by the

formation of pores. When the w/c is more than 0.4, the surplus water is not bonded and the result is a system of capillary pores. However, when the w/c is less than 0.4, not all the cement is hydrated and the cores of the cement clinker do not react. Because no free water remains, the porosity of the final product decreases significantly. Low w/c values are used for the development of high-strength concretes. The application of super-plasticisers, which reduce the surface tension in the cement paste, compensates for the resultant low workability.

Ultra-fine fillers, such as silica fume, are added to further reduce porosity in the cement matrix. Silica fume is a hydraulic powder with an average particle size of about 0.05–0.1 μm , which produces a very dense and strong cement matrix.

From the above summary of cement matrix chemistry, it is obvious that this is a complex and fascinating process, which can be influenced in several ways. Current practice offers many possibilities making use of special chemicals and controls to improve the production process and curing conditions.

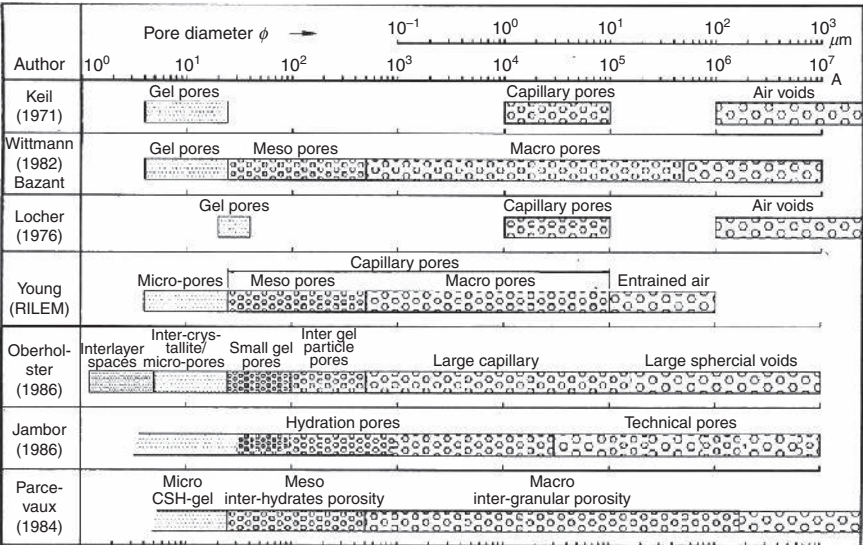
In the following chapters, the mechanical response of concrete is discussed, taking fracture mechanic principles as the main theme. The complex structure of hardened cement will receive only general consideration, but the heterogeneity, size and distribution of initial defects will be covered in detail. Having regard to this, and to the dominant effect of water, the characteristics of the pore system are given in Table 1.1 and Fig. 1.5, according to the overviews of Haynes (1973)¹³ and van Breugel (1997),⁸ respectively. These overviews show that the definitions and nomenclature used by researchers are not unanimous. However, the numbers give the dimension range for pores and voids in hardened cement. Figure 1.6 gives a characteristic quantitative example of pore distribution in mortar using pressurisation depressurisation cycling mercury intrusion porosimetry.

1.3 Concrete structure at the meso-scale: bond cement matrix and aggregates

The backbone of concrete is formed by the aggregate skeleton, which is capable of carrying high compressive loads. This skeleton is held together by the cement matrix. Therefore, the bond between the aggregates and the matrix has the dominant effect on the final properties of the concrete. The bonding zone is the weakest link in normal concrete. Various researchers have made detailed studies of the bonding and have found that there is a transition zone between the cement matrix and the aggregate in which three layers can be distinguished. The total thickness of this so-called ITZ is in the order of 20 μm . At the aggregate surface, a thin contact layer of CH is formed with a thickness of 2–3 μm . See Fig. 1.7a and 1.7b.

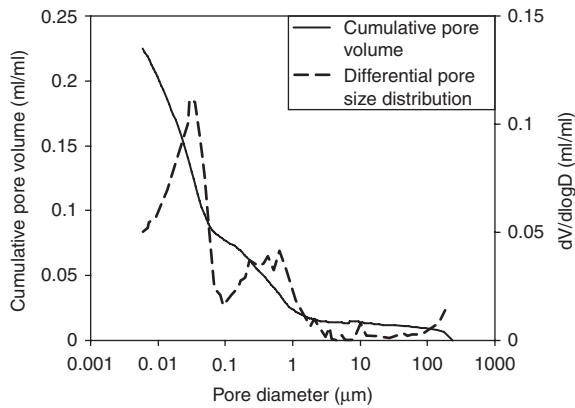
Table 1.1 Classification of pores in cement matrix^{13,14}

Pore type	Diameter	Description	Role of water	Affected properties
Capillary pores	10–0.05 μm	Large capillaries	Free, unbounded water	Strength; permeability
	50–10 nm	Medium sized capillaries	Moderate surface tension	Static and dynamic strength; permeability; shrinkage at high moisture degree
Gel pores	10–2.5 nm	Small (gel) capillaries	High surface tension	Shrinkage until 50% RH.
	2.5–0.5 nm	Micro-pores	Intensively absorbed water	Creep and shrinkage
	< 0.5 nm	Micro-pores, interlayer pores	Chemically bounded water	Creep and shrinkage

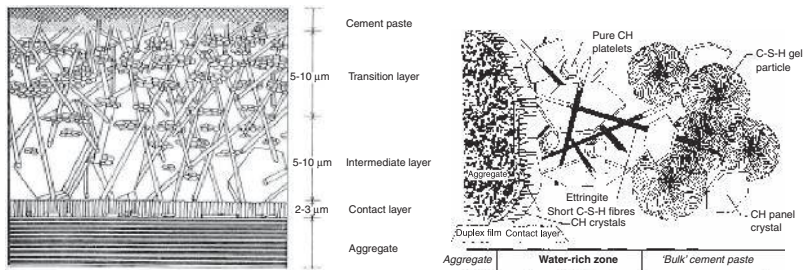


1.5 Classification of pores – schematic representation.⁸

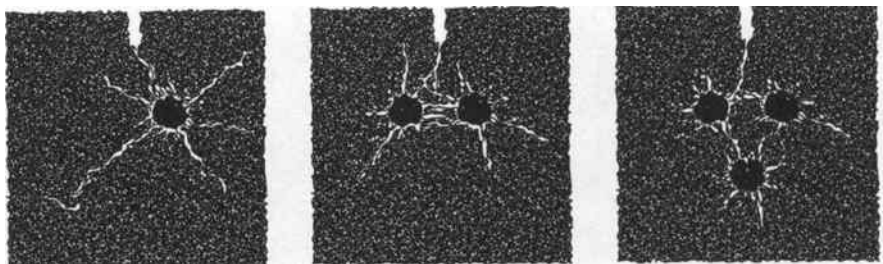
The second stratum is the intermediate layer, which consists of large CH crystals and has an open porous structure. This layer is linked to the bulk-cement matrix by the transition zone of more dense CH crystals. As the hydration process continues, the porosity of the intermediate layer reduces but remains less dense than the bulk of the hardened cement. The adhesion of water to the aggregates causes a higher w/c ratio and thus a



1.6 Characteristic representation of the pore size distribution and cumulative pore volume in cement-based materials.¹⁵



1.7 Schematic representation of the ITZ according to Reinhardt (a)¹⁴ and de Rooij (b).¹⁶



1.8 Illustration of shrinkage cracking; numerical simulation in lattice model.¹⁸

lower density in this region. Water tends to concentrate below the aggregates and so called ‘bleeding’ occurs, causing weakened zones or flaws at the lower surface of the aggregate. However, in low water cement ratio mixtures, i.e. mixtures for high strength concretes, micro-cracks may also occur.

The width and length of micro-cracks depends, among other factors, on the water cement ratio, the aggregate size and texture, and the vibration of the concrete after pouring. In fact, micro-cracking may be considered an inherent feature of concrete. Micro-cracks are defined as having a width of up to 0.1 mm and a length up to 5 mm. At higher stress levels, micro-cracks may develop into macro-cracks.¹⁷

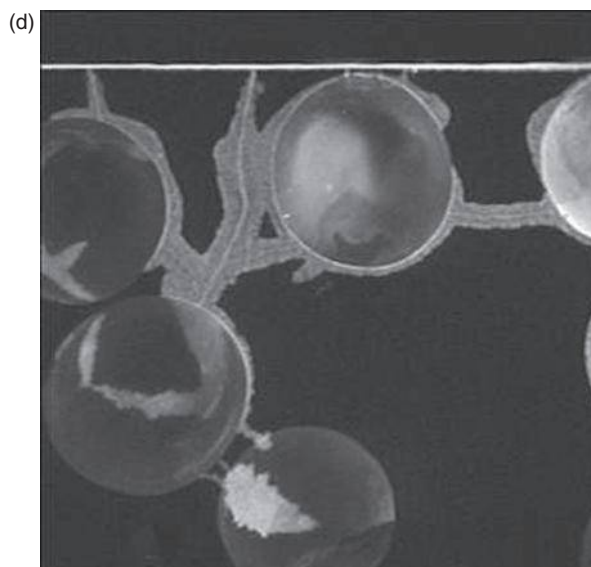
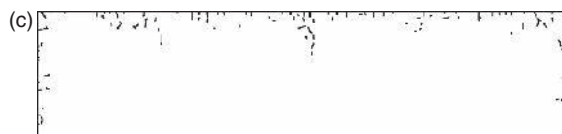
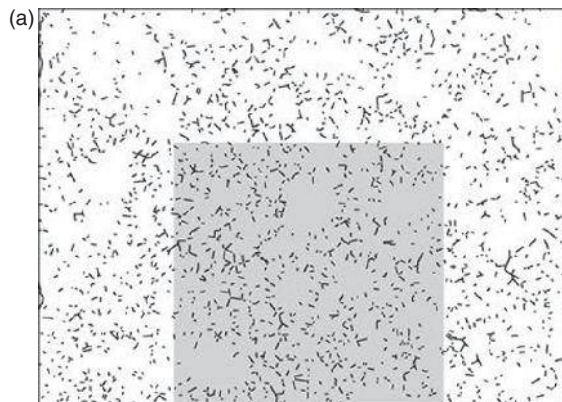
In addition to the adhesion between water and aggregates, the difference in stiffness between the aggregates and the cement matrix causes initial defects in the bonding zone. During hardening, the cement paste shrinks but is restrained by the stiff aggregates. Tensile stresses are induced in the cement matrix, which increase with the aggregate size, and radial cracks may occur when the local strength is exceeded, as illustrated in Figure 1.8. The length of these cracks will depend on many parameters (local material strength, aggregate grading and spatial distribution) and is hard to characterise in general terms. Where they occur, the length of the cracks will be in the order of the aggregate size, see for example, Fig. 1.9, which shows the shrinkage cracks in the surface area and illustrates the penetration depth of micro-cracks as being limited to the order of the maximum aggregate size.

1.4 Concrete structure and mechanical properties

A review of the hardening process of cement and the mechanical interaction with different sized aggregates enables the conclusion that a very heterogeneous system is produced at all scale levels. There are gel pores in the cement paste at a diameter of $r < 20$ nm, and a system of capillary pores at a diameter of 0.02–10 μm . At the next level, voids are produced at $r > 100$ μm , due to trapped air and bleeding effects below the aggregates. This is around the same scale as the lower scale of the aggregates, which ranges from about 0.1–20 mm. As observed above, micro-cracks occur around the aggregates due to differences in stiffness. The strength of the bonding zone (ITZ thickness about 15–25 μm) is lower than of the bulk cement paste.

The question arises as to whether all scales are relevant in studying the mechanical behaviour of concrete. At what scale is it necessary to focus in order to understand and control the behaviour of concrete under tension? The literature shows research to be focused at the nano-scale for the improvement of density and strength of the cement paste, and at the meso-level of larger aggregates in the mortar matrix, which is studied experimentally and numerically to relate the macroscopic concrete properties to this scale of heterogeneity. To the authors' knowledge, there is no study available which directly links variations in strength of the cement paste to the mechanical properties of concrete.

Multi-scale modelling is currently very popular and is developing rapidly. However, the possibilities in dealing with discrete cracking and real



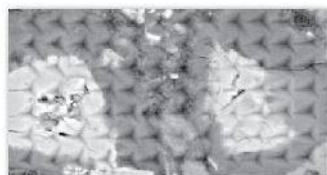
1.9 Illustration of shrinkage cracks in a special mortar of cement and spherical glass aggregate particles with a size of 6 mm. Micro-cracks only penetrate to a depth of 8 mm into the material.¹⁹ Panel (a) gives the top view of the specimen surface with the pattern of the shrinkage cracks; (b) shows the cross section with surface damage, visualized by fluorescent impregnation; (c) shows the cross section with dominant cracks (derived from (b)) and panel (d) is a detail of (b).

Indentation analysis

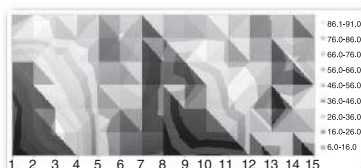
□ Fraction I, w/c = 0.40, 14 days



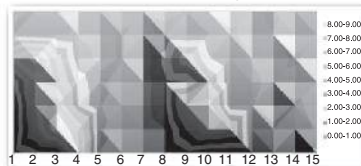
ESEM micrograph



Note: each spaced at 5 μm



Distribution map of Young's modulus

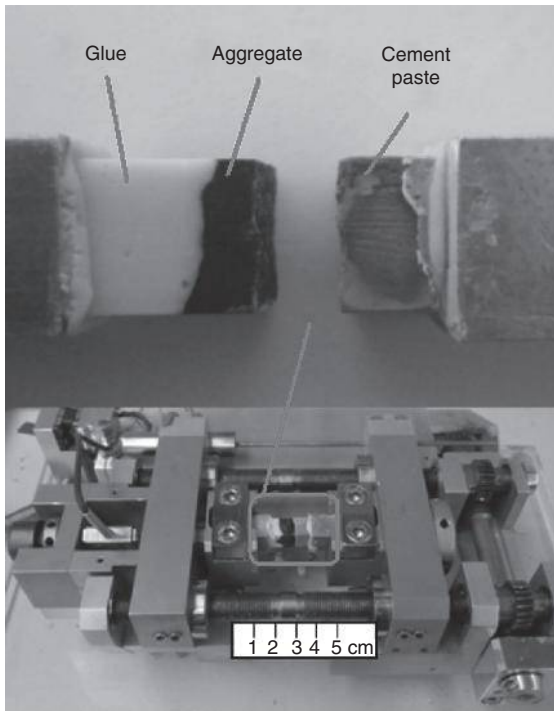


Distribution map of hardness

1.10 Nano-indentation tests on cement paste with unhydrated cement. Test results show distribution of E-modulus and Hardness (performed at MicroLab DUT).

'embedded' multi-scale modelling are still limited. Furthermore, the models need experimental input at the individual scale levels. At the nano/micro-scale for cement stone, it is possible to use SEM to observe and study the structure of the hydration products (see Section 1.2), but mechanical tests are not performed at this scale, the mechanical testing of cement paste being conducted with much larger samples. At Delft University, small-scale deformation controlled compression, tension or torsion tests are performed in the MicroLab on specimens with a cross section of 0.5 cm². These are particularly valuable experiments, because they can be combined with the environmental SEM (ESEM) to record the failure process in real time, and are suitable for quantifying the macro-response of plain cement stone, though not of the individual components. Information on the hardness, Young's modulus, strength and fracture toughness of a material at free surfaces can be obtained with a nano-indenter, see Fig. 1.10. The resistance to indentation is measured and the material properties are derived, assuming the material is isotropic for the penetration region (order of magnitude μm).

After reviewing experimental possibilities during 2012, it was concluded that it is necessary for a multi-scale approach to focus on the meso-scale as the bulk response of the cement paste and mortar at the micro-scale and the interfaces with the aggregates can be quantified.⁵ See Fig. 1.11. An attempt to bridge all scale levels, from nano- to macro- in a multi-scale approach, remains too ambitious and is not yet feasible. The research issue decides which level should be the focus. Obviously the chemical resistance



1.11 Test set-up for ITZ testing, MicroLab Delft.²⁰

of concrete depends directly on the type of cement and the pore system (see also Chapter 4), so for these issues, the nano- and micro-scale are dominant. But as the subject of this book is the mechanical response of concrete under tension, the material will be approached from the macro- to micro-level, with a focus on the meso-scale.

1.5 References

1. Dolado, J.S. and Breugel, K. van. (2011), Recent advances in modelling for cementitious materials, *Cem. Concr. Res.* **41**(7): 711–726.
2. Taylor, H.F.W. (1998), *Cement chemistry*, Thomas telford publishing
3. Mier, J.G.M. van (1997), *Fracture processes of concrete*, CRC Press.
4. Locher, F.W., Richartz, W. and Sprung, S. (1976), Setting of Cement–Part I: Reaction and Development of Structure, *Zement-Kalk-Gips INTERN*, **29**(10): 435–442.
5. Ozbek Agar A.S, Weerheijm, J. and Schlangen, E.H.J.G. (2010), *Investigation of Porous Concrete through Macro and Meso scale testing*, In Proceedings: Fracture Mechanics of Concrete Structures – FraMCOS-7, Jeju, Korea, pp. 419–427.
6. Stutzman, P.E. (2001), ‘Scanning Electron Microscopy in Concrete Petrography’, In Skalny, J., Gebauer, J. and Odler, I. (Eds.), *Proc. Materials Science of Concrete*

Special Volume: Calcium Hydroxide in Concrete, The American Ceramic Society, November 1–3, 2000, Anna Maria Island, Florida, 59–72.

7. Mindess, S. and Young, J.F. (1981), *Concrete*, Prentice Hall, Englewood Cliffs, NJ
8. Breugel, K. van (1997), *Simulation of hydration and formation of structure in hardening cement-based materials*, Delft University Press.
9. Powers, T.C. (1985), *The physical structure and engineering properties of concrete*, Research and Development Magazine No. 90, Portland Cement Association, Skokie, IL.
10. Feldman, R.F. and Sereda, P.J. (1968), A model for hydrated Portland cement paste as deduced from sorption length change and mechanical properties. *Materials and Structures*, **1**, 509.
11. Wittmann, F.H. (1977), *Grundlagen eines Modells zur beschreibung charakteristischer Eigenschaften des Betons*, DAFStb 290, Berlin.
12. Jennings, H.M. (2000), A model for the microstructure of calcium silicate hydrate in cement paste, *Cem. Concr. Res.* **30**: 101–116.
13. Haynes, J.M. (1973), Determination of pore properties of constructional and other materials – General introduction and classification of methods, RILEM Publications SARL. **6**(33): 169–174.
14. Reinhardt, H.W. (1985), *Concrete as structural material, properties and durability*, (in Dutch), Delft University Press.
15. Zhou, J., Ye, G. and van Breugel, K. (2010), Characterization of pore structure in cement based materials using pressurization-depressurization cycling mercury intrusion porosimetry (PDC-MIP), *Cem. Concr. Res.* **40**: 1120–1128.
16. Rooij, M.R. de (2000), *Syneresis in cement plaster systems*, Doctoral Thesis, Delft University.
17. Neville, A.M. (2010), *Properties of concrete*. 4th Edition. Pearson Prentice Hall, 844 p.
18. Vervuurt, A. and Mier, J.G.M. van. (1995), Optical microscopy and digital image analysis of bond-cracks in cement-based materials. In Diamond, S., Mindess, S., Glasser, F.P., Roberts, L.W., Skalny, J.P. and Wakely, L.D. (Eds.), *Microstructure of Cement-Based Systems/Bonding and Interfaces in Cementitious Materials*, MRS, Pittsburgh, PA, 370, 337.
19. Bisschop, J. (2002), *Drying shrinkage microcracking in cement-based materials*. PhD thesis Delft University of Technology, Delft University Press, the Netherlands, ISBN 90–407–2341–9 (2002) 208 p.
20. Ozbek-Agar, A.S., Weerheijm, J. Schlangen, E.H.J.G. and Breugel, K. (2013), Investigating porous concrete with improved strength: testing at different scales. *Constr Build Mater*, **41**: 480–490.

Factors affecting the tensile properties of concrete

H. W. REINHARDT,
University of Stuttgart, Germany

DOI: 10.1533/9780857097538.1.19

Abstract: This chapter reviews various influences that affect the tensile strength of concrete. These influences include composition (e.g. type of aggregate and water cement ratio), age and curing, as well as environmental effects such as sustained loading. The chapter also looks at what testing shows about such properties as stress-deformation behavior.

Key words: tensile strength of concrete, composition, age, curing, sustained loading, fatigue, testing, eigenstresses, stress-displacement curve, fracture energy, cracking.

2.1 Introduction

Tensile strength is a paramount property of concrete. It determines the load-bearing behavior of concrete structures because the compressive strength, which is usually taken as design parameter, depends also on the tensile strength on the meso-scale. Un-reinforced concrete structures rely completely on the tensile strength. The same is true for durability aspects. For instance, differential shrinkage and thermal strains can cause eigenstresses, which can lead to cracking when the tensile strength is reached. This is also the case for stresses due to imposed deformations. This chapter reviews various influences affecting the tensile strength. The influences can be a consequence of the composition of the concrete, such as the type of aggregate and the water cement ratio. They can result from the environment which is particularly a function of moisture and temperature. The curing and storage conditions play their part and the age of the concrete. There are also the effects of load duration, as the bearing strength decreases with the duration of load, but fatigue must also be considered. The testing conditions are important, since the measured values of a uniaxial test, a splitting test, and a flexural test are quite different. But it is not only the type of test, but also the size of the specimen. When no tensile tests are being performed, the tensile strength can be assessed from compressive strength with conversion

formulas. The chapter deals also with the whole stress-deformation curve and the softening in uniaxial tests. It is shown that the behavior depends strongly on the control of loading. The crack development on the meso-scale is explained.

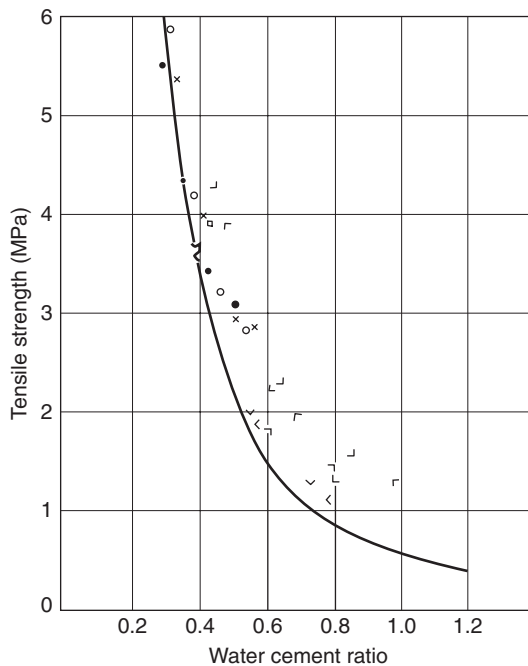
2.2 Effect of composition

High strength concrete is characterized by a dense interfacial transition zone (ITZ) and behaves differently from low strength concrete. The type of aggregate and the size of the aggregate particles can also influence the tensile strength.

2.2.1 Low to high strength concrete

Concrete is a composite consisting of matrix and aggregates. The matrix contains the hardened cement paste, fillers which may have been added to the mix, the fine powder of the aggregates, and air voids. Embedded in the matrix are the aggregates, which may be rounded sand and gravel, crushed fine and coarse rock, or artificially produced particles. The tensile strength depends on the strength of the matrix and on the adhesion (bond) of the matrix to the aggregate grains. A high water cement ratio causes low matrix strength and poor adhesion, which results in a low tensile strength of the concrete. A low water cement ratio leads to a high matrix strength and good adhesion, which can be so large that, in the case of tensile loading, the aggregate will fracture. When this happens the limit strength has been reached. An increase of tensile strength can be obtained by a larger amount of high-strength matrix and with aggregates of higher strength.

From a fracture mechanics point of view, it is the number and size of flaws in the matrix that determine the strength. Flaws can be capillary pores, air voids, or micro-cracks. The number of capillary pores is a direct function of the water cement ratio. The higher the water cement ratio, the more pores and the larger the pores. Air voids are accidental, due to incomplete compaction, or are intended by use of air-entraining agent. Micro-cracks develop during the hydration of cement. The heat of hydration leads to heating of the concrete and subsequent cooling. Since the coefficient of thermal expansion of hydrated cement paste is larger than that of most aggregates, differential strains and internal stresses develop, which may cause micro-cracks. The same is true for shrinkage of the paste. The bond between matrix and aggregates is governed by the development of the interfacial transition zone (ITZ), which may be weak due to the precipitation of calcium hydroxide crystals on the surface of the grains. In high-strength concrete, silica fume is often used, which leads to a densification of the ITZ because of the small



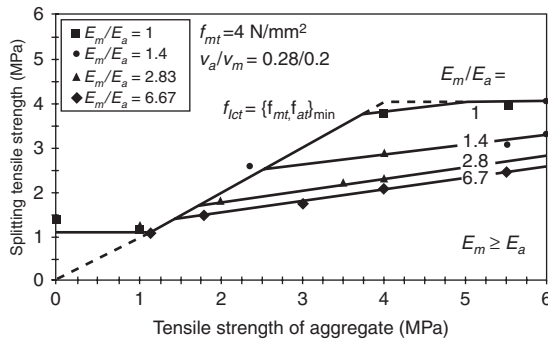
2.1 Influence of water cement ratio on tensile strength of mortar of various compositions (Graf *et al.*, 1960).

size of silica fume particles and of the consumption of calcium hydroxide during hydration.

Figure 2.1 shows an example how the water cement ratio influences the tensile strength of mortar. With a water cement ratio of 0.3, the tensile strength amounts to 6 MPa, whereas a water cement ratio of 0.7 leads to a tensile strength of 1 MPa.

2.2.2 Type of aggregate

The aggregate has an influence on the tensile strength of concrete for three reasons: the surface texture, the shape, and the strength. When the surface is rough, the bond between aggregate and matrix is stronger. Tests with rough river gravel and crushed quartz have resulted in about 20% higher tensile strength than with smooth crushed glass (Graf *et al.*, 1960). This example of extremely different strength values is not reported for natural smooth and rough aggregate surfaces. Crushed aggregates can lead to 10–20% higher tensile strength than rounded aggregates. However, flaky aggregates are less favorable, since they can break under tensile loading. Also, aggregates with a low strength, i.e. sandstone, can lead to low tensile strength of concrete.



2.2 Splitting tensile strength of LWA concrete as function of tensile strength of the aggregate (Faust, 2000). f_{mt} tensile strength of matrix, V_a aggregate volume, V_m matrix volume, f_{lct} tensile strength of lightweight concrete, f_{at} tensile strength of aggregate, E_m Young's modulus of matrix, E_a Young's modulus of aggregate.

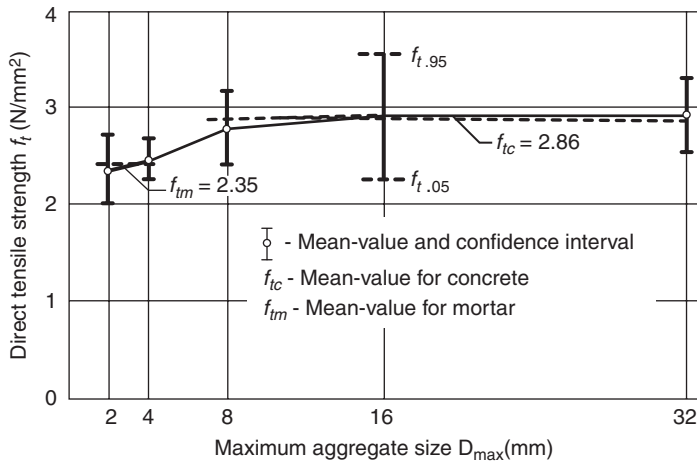
Between dense natural aggregates, there is no significant influence in tensile strength.

Lightweight aggregates (LWA) have a rough surface and can absorb water due to their porosity. This leads to a very good bond. However, the strength of LWAs is lower compared to natural aggregates. Figure 2.2 shows the result of a computer simulation whereby the tensile strength of the matrix was kept constant, and the stiffness ratio between matrix E_m and aggregate E_a was varied.

The splitting tensile strength is plotted as a function of the aggregate tensile strength. The result shows typical relationships: with low tensile strength of the aggregate, the concrete strength is only governed by the matrix strength; when the aggregate strength increases over 1 MPa, the concrete strength also increases, depending on the stiffness ratio however. The closer the stiffness ratio approaches unity the higher the concrete strength. But there is a limit, which cannot be exceeded. All examples that have been computed in Faust (2000) are similar, and show the complexity of the dependencies of the tensile strength of LWA concrete.

2.2.3 Aggregate size

A literature survey was carried out in Wolinski *et al.* (1987). It appeared that the data from various researchers were conflicting and no clear conclusion could be found. Therefore, a series of systematic tests have been performed. The result is given in Fig. 2.3. The water cement ratio was 0.5 for all mixes. The maximum aggregate size varied between 2 and 32 mm. The figure shows that the tensile strength increases from 2.35 MPa with 2 mm aggregate size to 2.78 MPa with 8 mm, and then stays almost constant at a level of 2.86 MPa.



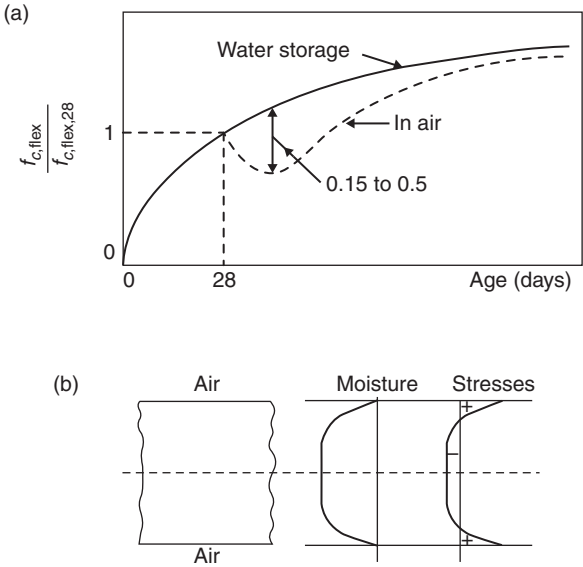
2.3 Uniaxial tensile strength as function of aggregate size (Wolinski *et al.*, 1987).

The paper concludes that there is a systematic difference between the strength of mortar (aggregate size up to 4 mm) and concrete (from 8 mm upwards). Whether this conclusion is valid for all types of concrete and aggregate sizes should be validated by experiments and numerical simulations, which have not been done so far.

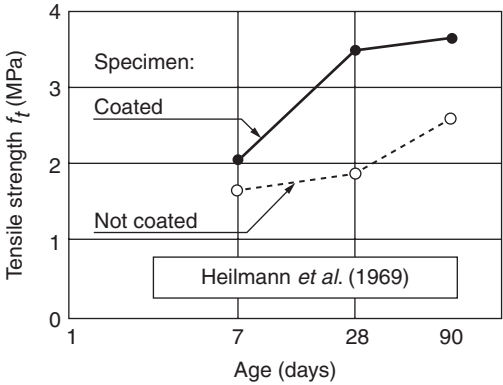
2.3 Effect of curing and moisture

Moist curing is beneficial for all mechanical properties. However, one has to guarantee that there is no moisture gradient across the cross-section. A moisture gradient would cause differential shrinkage and eigenstresses, which could reduce the tensile strength. The influence of drying on beam specimens after moist curing that are tested in flexure is most severe. A beam that has been allowed to dry before testing has 15–50% lower bending strength (modulus of rupture) than a similar specimen tested in a wet condition (Fig. 2.4a). This difference is due to the tensile stresses in the extreme fiber by restrained shrinkage as depicted in Fig. 2.4b.

The splitting strength is almost unaffected by a moisture gradient, because the splitting stresses act in the middle of the specimen remote from the surface. The uniaxial tensile strength is also affected by drying, as has been found in Heilmann *et al.* (1969). Figure 2.5 shows two relationships of tensile strength vs age: the full line represents the values of specimens that were coated at the age of one day, the dashed line corresponds to specimens that could dry after one day at 20°C/65% RH until testing. The difference between the two lines is largest at 28 days. Two effects have influenced



2.4 (a) Schematic of bending strength of concrete in moist and drying condition (Bonzel and Kadlecck, 1970) (b) eigenstresses in cross-section.



2.5 Uniaxial tensile strength as affected by moisture (Heilmann *et al.*, 1969), taken from Hordijk (1989).

the strength that cannot be separated, i.e. the moisture gradient over the cross-section, and the continuing hydration.

It is obvious that both effects were favorable in the case of coated specimens. A moisture gradient in the drying specimens led to lower strength, and so do the dry curing conditions. On the other hand, the coating has prevented eigenstresses and has caused continuing curing.

Specimens that dry from the beginning after demolding undergo tensile stress at the surface due to restrained shrinkage, and often show cracking (craquelé type cracking, crazing), which reduces the measured tensile strength. Theoretical considerations show that the tensile zone reaches about a tenth of the depth. If it is assumed that this zone is cracked, a cylinder would exhibit only 64% of the value that would be measured on a cylinder without eigenstresses. Tests reported in Bonzel and Kadlecsek (1970) show reductions of the uniaxial tensile strength between 20% and 30% of the strength that was obtained after wet curing at 28 days. The strength recovers later and can reach higher values than in the case of continuous wet curing.

2.4 Effect of temperature

Concrete can withstand high and low temperature, however, the influence on the tensile strength can be large. At 700°C, the strength vanishes almost completely whereas, at -160°C, the strength is much higher compared to ambient temperature.

2.4.1 High temperature

The ambient temperature of concrete structures ranges between -20°C and +40°C. It is common to assume that the tensile strength of concrete does not vary in this temperature range. This assumption is justified in a normal design approach. However, when the tensile strength plays a prominent role one should adjust the strength values. *fib* (fib, 2010) recommends the following temperature relations in the range of 0–80°C:

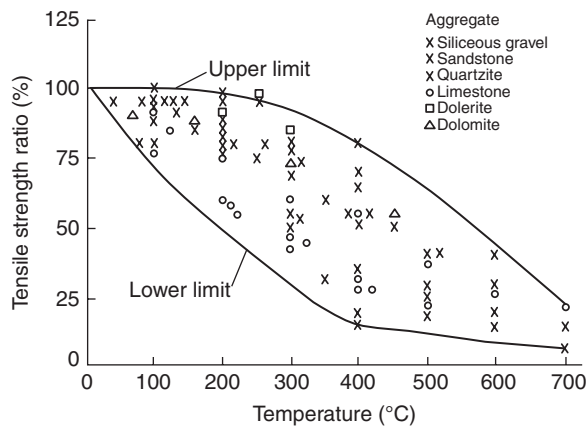
$$\text{for the uniaxial tensile strength} \quad f_{ctm}(T) = f_{ctm}(20^\circ) (1.16 - 0.008 T) \quad [2.1]$$

$$\text{for the splitting strength} \quad f_{ct,sp}(T) = f_{ct,sp}(20^\circ) (1.06 - 0.003 T) \quad [2.2]$$

$$\text{for the flexural strength} \quad f_{ct,fl}(T) = f_{ct,fl}(20^\circ) (1.1 - 0.005 T) \quad [2.3]$$

with T = temperature in °C. By evaluating the formulas it appears that, at a temperature of 0°, the strength increases by 6–16% while higher temperature lead to substantial decrease of the strength values. The basis of the formulas was a thorough literature review. Temperatures of 80°C can occur in storage tanks of warm water, in chimneys, and in cooling towers.

In case of fire, concrete is exposed to much higher temperatures, up to 1000°C and, in a hydrocarbon fire, even up to 1300°C. Results of tensile tests



2.6 Normalized tensile strength as function of temperature (Bažant and Kaplan, 1996).

on concrete have been collected. Figure 2.6 shows that there is considerable scatter on the results.

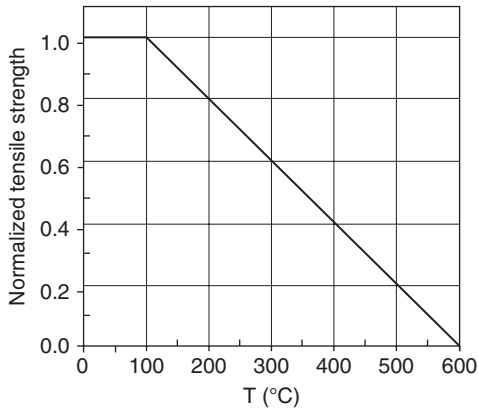
Obviously, this kind of aggregate determines the decay of strength with temperature. Limestone aggregate suffers more than quartzite or dolerite. The upper and lower boundaries converge at 700°C to a value which is only about 10% of the strength at room temperature. The reason for the decrease of strength up to about 300°C is mainly the incompatibility of thermal expansion of aggregate and hydrated cement paste. The largest mismatch occurs with limestone, which has a coefficient of thermal expansion that can be as low as one half of hydrated paste. On the other hand, the thermal expansion of quartzite and paste are similar. At higher temperatures, the intermolecular bond of the material gets weaker and causes the decrease.

The European organization for standardization (CEN) (EN 1992, 2004) has simplified the relationship between tensile strength and temperature to a linear curve, which is plotted in Fig. 2.7.

It overestimates the thermal influence on tensile strength for some aggregates in concrete, but also underestimates the influence in many cases when one compares the linear line with the experimental results of Fig. 2.6.

2.4.2 Low temperature

At low temperatures, one has to consider that the water in concrete freezes. The free water freezes already at zero degrees, and the bound water at lower temperatures depending on the pore radius in which the water is encapsulated. The smaller the pores the lower the freezing temperature. At -60°C all water is frozen. The ice in the pores supports the load-bearing resistance



2.7 Linear relationship between tensile strength and temperature (EN 1992, 2004).

of the concrete, which means that a strength increase with lower temperatures can be expected. Numerous tests have been performed on concrete in cryogenic circumstances and a strong increase has been found depending on its moisture content. The tests were performed in compression, but a conversion formula can be used transforming the compressive strength into tensile strength. The mean compressive strength is given by (Rostásy, 1984):

$$f_{cm}(T) = f_{cm,20^{\circ}\text{C}} + \Delta f_{cm} \quad [2.4]$$

$$\text{with} \quad \Delta f_{cm} = 12 \text{ m} \left[1 - \left(\frac{T+170}{170} \right)^2 \right] \quad [2.5]$$

with T in $^{\circ}\text{C}$ and m = moisture content in % by mass. The moisture content can be assumed to be 2% for general indoor elements, 4% for general outdoor elements, and 6% for elements exposed to rain (fib, 2010). The tensile strength can be assessed from

$$f_{ctm} = \alpha f_{ck}^{2/3} \quad \text{with } \alpha = 0.3 \text{ at room temperature, } \alpha = 0.2 \text{ at } -170^{\circ}\text{C} \quad [2.6]$$

with f_{ctm} the mean tensile strength, and f_{ck} the characteristic value of the compressive strength. The formulas demonstrate a large influence of low temperatures on strength.

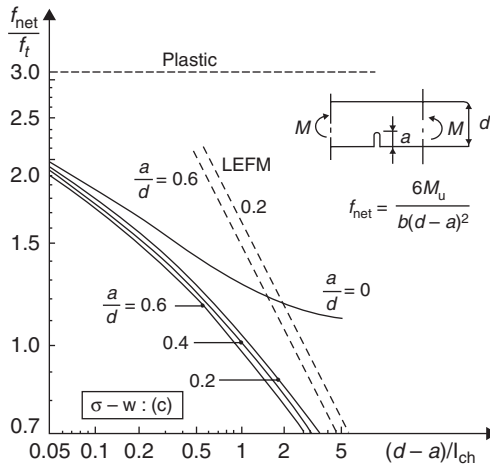
2.5 Influence of specimen size

The size of the specimen has an influence on the test results, for various reasons. According to Weibull's theory, there is a statistical influence of the

absolute size of the specimen on the result because the probability of the presence of flaws increases with volume. The strength is inversely proportional to a function of the volume ($\sigma \sim V^{-\alpha}$). A second influence stems from fracture mechanics principles, which predict an energetic influence of the size of the specimen. A third influencing factor is the non-linear stress distribution in flexural specimens, which is not accounted for in the usual theory of elasticity. Of course, there is also an influence of the heterogeneity of the material, i.e. when the specimen is too small compared to the aggregate size, that will result in an erroneous measurement. All four influencing factors affect the tensile strength, which will be shown in the following.

Uniaxial tensile tests and splitting tests on specimens with 100 mm × 200 mm resulted in strength values that were about 7.5% higher than the values of 150 mm × 300 mm specimens (Malhotra, 1970). A 9–25% decrease was reported in Walker and Bloem (1957) when the cross-section of the flexural specimens was increased from 77 mm × 102 mm to 254 mm × 254 mm. When the specimen depth was increased from 76 to 203 mm the flexural strength decreased by 40%, which was discussed with the statistical effect according to Weibull (Wright and Garwood, 1952). Another test series used cylinders with 30, 60, and 150 mm but keeping the maximum aggregate size of 20 mm the same (Rossi *et al.*, 1992). The results show a clear dependence on specimen size: the 60 mm cylinder has a 6–50% decrease of tensile strength compared to the 30 mm cylinder. The low value relates to high-strength concrete (compressive strength 128 MPa) and the high value to a medium strength concrete (35 MPa). The author explains the size effect by the heterogeneity of concrete with respect to the volume of the specimen. That high-strength concrete had the smallest decrease with size is discussed with respect to the fact that matrix and aggregates have about the same rigidity and strength. The so-called wall effect certainly plays an important part with small specimen size.

Fracture mechanics principles have long been applied to explain the size effect. Hillerborg was the first, using the fictitious crack model of non-linear fracture mechanics to explain why the size of a flexural specimen has a great effect on the measured result (Hillerborg, 1986). Concrete is modeled as a strain-softening material. When the extreme fiber of a flexural specimen reaches the tensile strength, the material starts to soften. The softening zone spreads into the beam with increasing displacement. Taking this effect into account, the beam will not fail immediately but remains stable until the maximum load has been reached. The contribution of the softening is larger the smaller the depth of the beam. Figure 2.8 shows the theoretical prediction of the flexural strength vs the depth of the beam and the notch based on a bilinear softening curve. The characteristic length is a measure of the brittleness of the concrete, which is in the order of decimeters. A very small specimen can exhibit a flexural strength that is more than twice the uniaxial strength.



2.8 Theoretical prediction of the flexural strength f_{flex} (Hillerborg, 1986), d = depth of beam, l_{ch} = characteristic length of concrete: $l_{ch} = EG_F/f_t^2$ with E = Young's modulus, G_F = fracture energy, f_t = tensile strength.

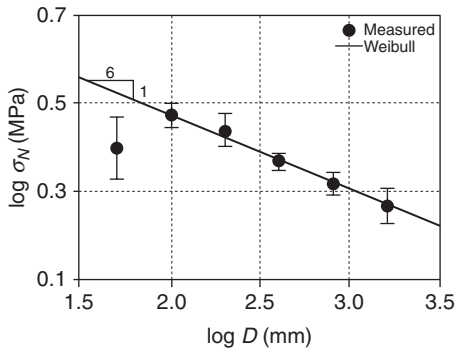
An unnotched specimen with $L_{ch} = 100$ mm with a depth of 40 mm shows a flexural strength about 1.5 times the tensile strength that is realistic and has been measured in experiments. The flexural strength of a very large specimen approaches the uniaxial tensile strength, which can be deduced from the fact that the softening zone is small compared to the dimensions of the beam. Other theories predict the size effect for splitting cylinders (Bažant *et al.*, 1991; Tang *et al.*, 1992), which is not as distinct as for bend beams.

Uniaxial tensile tests on specimens with a width ranging between 50 and 1600 mm at a constant thickness of 100 mm showed a clear influence of size (van Vliet and van Mier, 1999). The concrete mixture was always the same with 8 mm maximum aggregate size and water cement ratio of 0.5 leading to a compressive strength of 50 MPa. The results of the nominal stress (peak stress) are shown in Fig. 2.9.

The results can be approximated with a power law according to the weakest link theory of Weibull (Weibull, 1939).

$$\sigma_N \sim D^{-1/6} \quad [2.7]$$

with σ_N = nominal stress and D = width of specimen. The size effect is explained on statistical grounds (material size effect). The result of the smallest specimen does not fit into the approximation line. That is probably due to the wall effect, which is relatively larger in the small specimen, or by testing influences. Almost the same Equation as [2.7] has already been found in 1898 ($a = 1/6.4$) (de Joly, 1898).



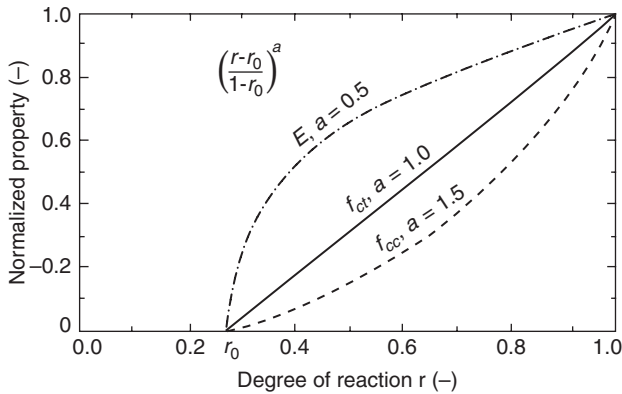
2.9 Measured values of tensile strength and Weibull approximation (van Vliet and van Mier, 1999).

The uniaxial tensile strength is a genuine property of concrete. It has to be determined on specimens that are large enough in comparison to the heterogeneity of the material. The minimum dimension of the cross-section has to be at least three times the maximum aggregate size (ASTM, 2007) which leads still to large scatter of the results. A ratio of 4 to 5 is advisable. Depending on the aim of the test, the length of the specimen can vary.

2.6 Effect of age

The effect of age on the development of mechanical properties is governed by the hydration of cement and the other hydraulic and pozzolanic components of the binder. The degree of hydration or, as it is also called, the degree of reaction, is a measure of the hardening process. The degree of reaction is defined as the ratio between the heat of hydration that has liberated at a certain time t and the maximum heat of hydration that can develop until the assumed end of reaction (De Schutter, 1996). In the very beginning of the hydration there is no contribution to strength because the material has not stiffened yet. This state finishes at the degree of reaction r_0 . r_0 is found to be 0.2 for Portland cement, 0.4 for blast furnace slag cement with a high amount of slag, and 0.03 for high-strength concrete. When the degree of reaction is 1, i.e. the cement has hydrated to the final state, the mechanical properties have developed completely. Between r_0 and 1 the normalized mechanical property follows the degree of reaction in a relation which is given by $[(r-r_0)/(1-r_0)]^a$ where a is an empirical parameter that has been determined from numerous tests. Figure 2.10 shows the relationship.

It can be seen that the elastic modulus develops the fastest, the compressive strength the slowest, and tensile strength is in between. This means that the ratio between the three quantities does not have a constant value, but varies with the hydration or varies with time.



2.10 Relationship between normalized property and degree of reaction (Gutsch, 1998).

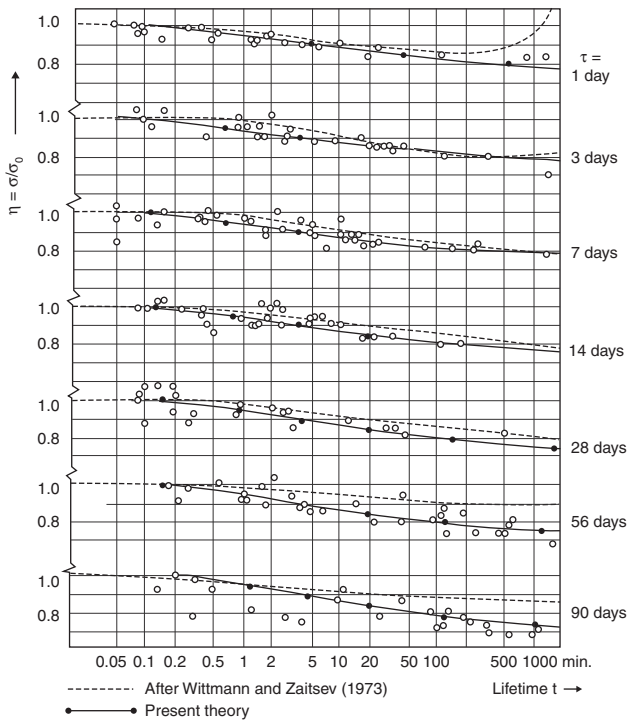
For the quantitative calculation of the influence of age on concrete strength, one is referred to the *fib* Model Code 2010 (fib, 2010). There, one can find a relation between compressive strength and age, and another for the conversion of compressive strength into tensile strength.

2.7 Effect of load duration

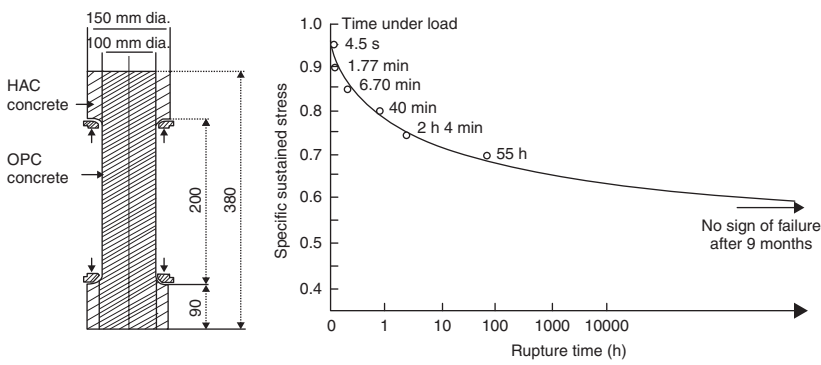
Concrete, like all other materials, consists of particles that are held together by bonds. The rate process theory (Krausz and Krausz, 1988) states that there are bonds breaking and recombining all the time. When there is no external force acting on a body, breaking and recombining bonds are equally frequent. With an external force the breaking bonds are in the majority, which means that the strength of a material decreases.

Figure 2.11 shows test results and the theoretical prediction on the basis of the rate process theory. This calculation also takes the aging effect of cement into consideration, i.e. the continuing hydration. The dashed lines (Wittmann and Zaitsev, 1974) belong to the earlier approach, compared to the full lines (Mihashi and Wittmann, 1980). According to the newer approximation, the strength decreases by about 20% after a loading time of 1000 min. The strength decrease depends also on the age. When the specimen is young at the beginning of the loading ($\tau = 1$ day) the decrease amounts to 20%; when the age is greater ($\tau = 90$ days) the decrease is 25%. The difference is due to the continuing hydration of the cement paste.

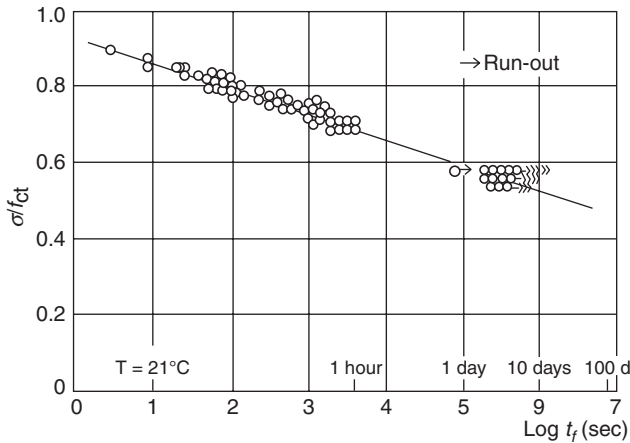
Tests on concrete cylinders with a mean compressive strength of 45 MPa are described in Al-Kubaisy and Young (1975). Figure 2.12 shows that the strength under sustained loading rapidly decreased in the first five hours and stayed constant after nine months. The authors suggest that the long-term strength (for 30 years) amounts to 55% of the short-term strength.



2.11 Tensile strength of hydrated cement paste under sustained loading, test results and prediction (Mihashi and Wittmann, 1980) and (Wittmann and Zaitsev, 1974), σ = strength at time t , σ_0 = strength under short time loading.



2.12 Specimen configuration and test results after Al-Kubaisy and Young (1975).



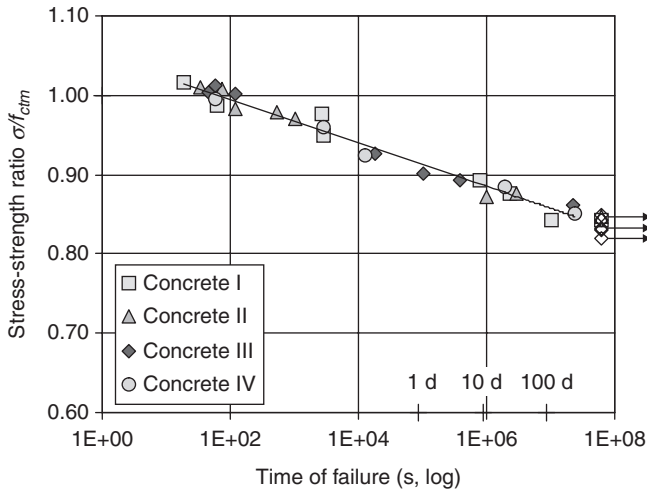
2.13 Normalized stress level vs. time to failure (Reinhardt and Cornelissen, 1985).

Other investigations on concrete with strength between 32 and 44 MPa have resulted in a good log-linear correlation of stress level and time to failure (Reinhardt and Cornelissen, 1985). The specimen failed at a stress level of 60% of the short-time strength already at day 1; however, all other specimens that were loaded longer were run-outs (Fig. 2.13).

This led to the conclusion that the long-term strength amounts to 60% of the short-term strength of 70% as the level of the long-term strength was assumed in Carpinteri *et al.* (1997), 75% of the mean short-term tensile strength was concluded from tests on notched specimens (Kordina *et al.*, 2000). The same value was reported from tests on high-strength concrete (mean compressive strength 110–120 MPa) by Han and Walraven (1993). Tests on normal strength concrete revealed a value of 0.70–0.75 (Fouré, 1982).

Cracked concrete specimens were unloaded and reloaded again to a certain load level (Barpi *et al.*, 1997). The reloading level was between 80% and 90% of the unloading level in deformation controlled tests, and the load was kept constant until failure. However, the sustained loading level was only in the order of 50% of the maximum load, which means that the long-term strength was around 50% of the short-term strength. Creep tests on concrete showed that the non-linear creep increased considerably when the load was greater than 50% of the short-term strength (Illston, 1965). This is an indication that the sustained strength is around 50% of the short-term strength.

An extensive testing program was conducted on high-strength concrete with mean compressive strength between 80 and 107 MPa (Rinder



2.14 Normalized stress-strength ratio vs. time to failure (Rinder and Reinhardt, 2004).

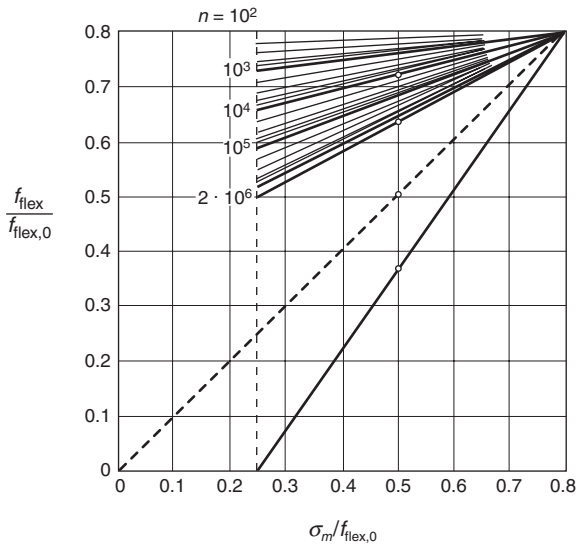
and Reinhardt, 2004). The load duration amounted to up to two years. The conclusion was that the ratio between sustained strength and short-term strength is approximately 0.75, which is derived from Fig. 2.14.

It should be noted that this ratio was found for high-strength concrete. By way of conclusion, it seems that normal strength concrete has a lower sustained strength in tension than high-strength concrete. This may be due to the better bond between aggregate and matrix, and the relatively higher elastic limit in the stress strain diagram.

2.8 Effect of cyclic loading

Most structures are loaded, not by a constant load, but by a fluctuating load. However, when the fluctuating loads are not dominant, the design takes a static loading in consideration. When the fluctuating load is dominant, for instance in concrete roads, the load has to be considered more realistically. For assessing the material resistance, loading tests have to be carried out under cyclic loads. The first to carry out cyclic tensile tests on mortar was de Joly in 1898 (de Joly, 1898), who stated that the strength at cyclic loading amounts to about 50% of the static strength. The maximum number of load cycles was 40 000 and the scatter of results was large. Therefore, the statement can only be regarded as indicative, and more recent results have to be presented.

Figure 2.15 shows a Smith diagram of the flexural strength of concrete. On the vertical axis the strength is indicated as the upper stress of the loading



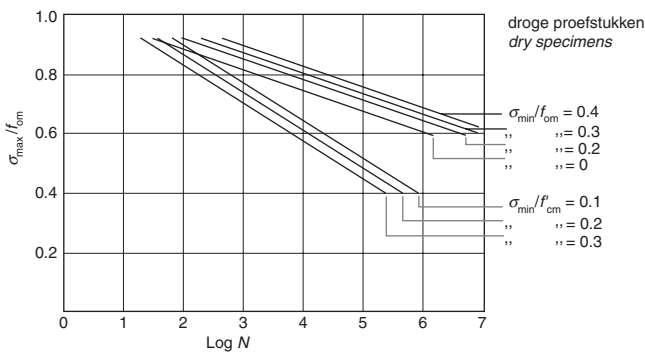
2.15 Flexural strength of concrete (Eisenmann and Leykauf, 2003).

cycles, and on the horizontal axis the mean value of the loading cycles is given. The lines in the upper part of the diagram give the upper stress of the cycles, which is at the same time the fatigue limit for a certain number of cycles. One can observe that the fatigue limit is larger for a smaller number of cycles.

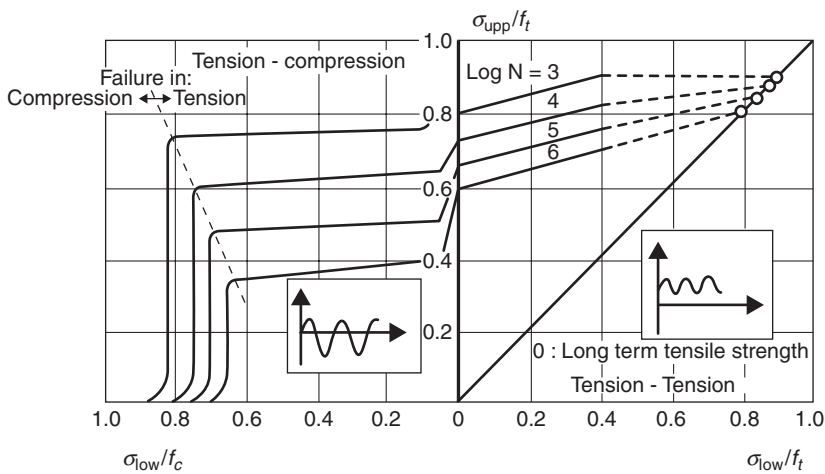
In the diagram, it is assumed that the limit for 10^2 cycles is equal to the limit under sustained constant loading, which is 0.8 times the static strength. If the number of cycles is equal to 2×10^6 a real fatigue limit is reached, which will also be valid for infinitely many cycles. For a mean value of 0.25 times the static strength, the maximum stress can be 0.5 times the static strength. The diagram of Fig. 2.15 is used for the design of concrete pavements. It has been experimentally validated for normal strength concrete.

Tests under cyclic tensile and alternate tensile compressive loading have been reported in Cornelissen (1984). The tests lead to S-N curves that are shown in Fig. 2.16. The inclination of the curves is very dependent on the lower stress level. When the lower stress is in the compression region the inclination is much larger than in the case when the lower stress is in the tension region.

The inclination of the curves is the same within the two areas. Some tests have also been performed at a frequency of 0.06 Hz, which leads to an S-N curve that is lower by about 0.08 times the maximum stress. Tests on wet specimens exhibited an S-N curve that is about 0.04 times the maximum stress below that obtained with dry specimens.



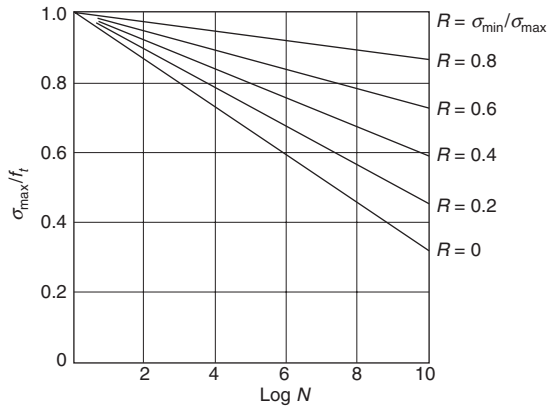
2.16 S-N curves for concrete under cyclic tensile and alternating tensile compressive loading at 6 Hz in dry condition (mean values) (Cornelissen, 1984).



2.17 Goodman diagram for concrete (Cornelissen and Siemes, 1985).

These and other results have been plotted in a Goodman diagram (Fig. 2.17).

The horizontal axis represents the minimum stress, and the vertical axis the maximum stress of the cycles with respect to the mean static strength. The right hand part of the diagram yields similar results to Fig. 2.15. The fatigue limit for 10^6 cycles is 0.6, and for 10^3 cycles it is 0.8. It should be noted that experiments have been performed on concrete with a compressive strength of 50 MPa. The tensile splitting strength was about 3 MPa. The fatigue limit changes significantly in the second quadrant, which represents the alternate tensile compressive loading. The fatigue limit for 10^6 cycles drops to 0.4 and, when the lower stress reaches about 0.65 times the mean



2.18 S-N curves for concrete in tension (Tepfers, 1979).

compressive strength, the tensile resistance approaches zero. Obviously, the compressive loading introduces cracks in the structure, which reduce the tensile capacity. Cyclic tensile tests of up to 10^5 cycles have confirmed the findings (Kessler-Kramer, 2002).

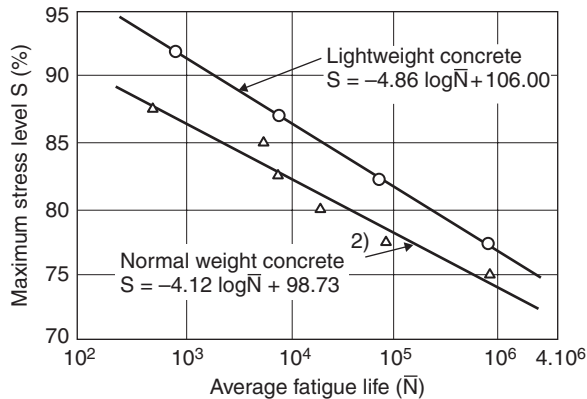
S-N curves for 10^{10} cycles have been extrapolated in Tepfers (1979). Figure 2.18 shows the results. The parameter of the curves represents the stress ratio of the loading cycles. It is obvious that a smaller lower stress leads to a steeper S-N curve. This result is in agreement with the findings in Cornelissen (1984).

It should be noted that the tests that are the basis for the diagram have been performed until 2×10^6 cycles, and that a great part of the diagram has been extrapolated on the basis of relations that have been found on compressive tests.

Tensile fatigue tests on lightweight concrete with mean static strength of 3.6 MPa was performed in Saito (1984). Figure 2.19 show the S-N curves of lightweight and normal weight concrete for failure probability of 50%.

After 2×10^6 cycles no fatigue limit has been reached. The lightweight concrete exhibits a superior cyclic strength compared to normal weight concrete. For two million cycles the strength level of lightweight concrete amounts to 75.4%, whereas for normal weight concrete it is 72.8% or, expressed in another way, the average failure cycles at 75% stress level amounts for normal weight concrete to 0.575×10^6 and for lightweight concrete to 2.391×10^6 .

The residual tensile strength has been investigated after a fixed number of preceding cycles (Meng and Song, 2007). The stress level of the preceding cycles was 75%, 80%, and 85% under which the specimens did not fail. The residual strength σ_r after n cycles has been approximated with the function (Schaff and Davidson, 1997):



2.19 Normalized S-N curves of lightweight and normal weight concrete for failure probability of 50% (Saito, 1984), (Saito and Imai, 1983).

$$\sigma_r(n) = \sigma_0 - \left(\frac{n}{b}\right)^c \quad [2.8]$$

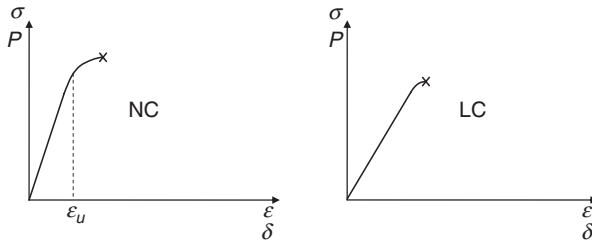
with σ_0 the static strength and b and c empirical constants, which have been determined with very good correlation. Evaluating the results it turned out that the residual strength after 10^3 cycles on a stress level of 85% was 97% of the static strength and after 2×10^3 cycles it was 93%.

2.9 Effect of type of loading

Stress-strain curves are determined by mechanical testing in testing devices either load controlled or displacement controlled. Displacement controlled testing is more sophisticated than load controlled testing, however, it is inevitable if strain-softening behavior is the purpose of the test. How displacement controlled testing can be arranged is discussed in this chapter.

2.9.1 Load-controlled tests

There are two different methods to perform loading tests; one is load controlled, and the other is displacement controlled. The load-controlled test means that the rate of loading is controlled such that the load increment per unit of time is constant ($dP/dt = \text{const}$). A consequence of such a loading regime is that the test is finished when the peak load is reached, because the specimen cannot carry a higher load. The load-displacement diagram can have various shapes. An ideal linear elastic material (for instance glass) exhibits a straight line up to failure while a strain-hardening material shows



2.20 Load-displacement curve of concrete in tension from load-controlled test (NC = normal weight concrete and LC = lightweight concrete).

a different shape. One has to notice that the displacement rate in such a test is only constant for an elastic material whereas the rate varies for all other types of material.

Concrete shows a linear response up to about 70% of the ultimate load. This means that the material behaves elastically and that the cracks that may be present inevitably do not propagate. Unloading during this stage does not result in irreversible displacement, except for some creep effects that are not discussed here. The situation is sketched in Fig. 2.20.

The elastic limit of 70% is very approximate. It can be higher for high-strength concrete and it is lower for low strength concrete, which is caused by the number of cracks in the structure, the bond between aggregate and matrix, and the onset of crack propagation. It is definitely higher for lightweight concrete, because the bond between the rather porous aggregate and the matrix is stronger and, looking to the distribution of stiffness in the structure, it means that the elastic response is mainly governed by the matrix behavior. Above the elastic limit, cracks propagate, which reduces the stiffness of the specimen. The resultant stiffness of the specimen reduces, which makes the load-displacement curve bent up to failure.

The elastic energy is represented by the area under the straight line of the load-displacement diagram. With stress σ equal to load divided by the area of the cross-section, and strain equal to displacement divided by the measuring length, and V the considered volume the elastic energy reads:

$$G = \frac{1}{2} \sigma \epsilon V \quad [2.9]$$

And, with maximum stress f_t and strain ϵ_u at maximum stress, the energy becomes:

$$G = \frac{1}{2} f_t \epsilon_u V \quad [2.10]$$

Table 2.1 Specific elastic energy of various concretes for a prismatic bar of 1 m length

Concrete ^a	E (GPa)	f_t (MPa)	G_c (J/m ²)
C 20/25	30	2.2	0.081
C 50/60	37	4.1	0.227
C 90/105	44	5.0	0.284
LC 20/27 ^b	20	1.78	0.079
LC 45/50	24	3.38	0.227
LC 80/88	28	4.28	0.327

^aC = normal weight concrete, LC = lightweight concrete,

^bdensity of LC = 1800 kg/m³.

When the energy is related to the cross-section A , we get the specific energy:

$$G_c = \frac{G}{A} \quad [2.11]$$

with the dimension Nm/m² or J/m². When Young's modulus is defined as $E = \sigma/\epsilon$ and with $L = V/A$, we get:

$$G_c = \frac{1}{2} f_t^2 \frac{L}{E} \quad \text{or} \quad G_c = \frac{1}{2} E \epsilon_u^2 L \quad [2.12]$$

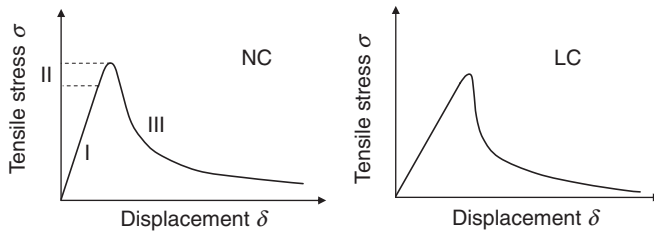
The area under the curved part of the load-displacement diagram (Fig. 2.20) belongs already to the fracture energy, which will be shown later.

A few numbers will show the magnitude of the specific elastic energy of various concretes (Table 2.1).

The quantities are taken as mean values from Eurocode 2 (EN 1992–1-1). They give an indication for various concrete strength classes and for normal weight and lightweight concretes. They show that the specific energy is rather small, which justifies the designation of concrete as brittle.

2.9.2 Displacement-controlled tests

The second method to perform a tensile test is under displacement control. This test method is very challenging because concrete is a brittle material, which requires very sensitive displacement measurements and an even more sensitive and very fast load control of the testing machine. The machine is controlled with certain constant displacement increments per unit of time ($d\delta/dt = \text{const}$). The result of such a test is a complete loading curve up to separation of the specimen, which includes the ascending part of the load and the descending part. The descending part starts after the peak load.



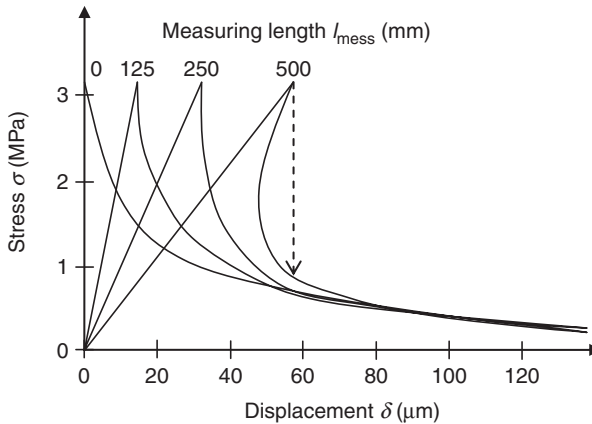
2.21 Load-displacement diagram of concrete in tension from displacement-controlled test (NC = normal weight concrete and LC = lightweight concrete).

The whole load-displacement diagram can be characterized by the following stages. Stage I, elastic which is equal to the diagram received from the load-controlled test. Stage II, non-linear loading part which may be different from Fig. 2.20 because the displacement rate is now constant and not varying. The difference, however, is small. Stage III, softening part which is due to the continuous propagation of cracks which concentrate finally in a discrete crack. This type of material behavior is called strain-softening (as opposed to strain-hardening of plastic materials). Figure 2.21 illustrates the behavior.

The shape of the softening part is strongly dependent on the length of the specimen and the measuring length. A specimen consists of at least three parts: one part containing the discrete crack and two parts adjacent to the first that are stressed and later relaxed. The crack opening is dominant for short specimens and the bulk displacement is dominant for long specimens. However, the longer the specimen the more difficult is the control of the test. The elastic uncracked parts unload and release the elastic energy into the cracking zone. The elastic unloading becomes so large with long specimens that one can observe a snap-back. On the other hand, when the length goes hypothetically vs zero there is no elastic strain and one measures only the crack opening. Figure 2.22 is the result of a computer simulation where the measuring length varies between 0 and 500 mm (Hordijk, 1989).

It shows the linear increase of displacement, which increases with measuring length. When the length is 500 mm the displacement rate is too low to compensate the elastic recovery of the uncracked parts. The consequence is a snap-back.

The fracture energy is represented by the area under the total load-displacement curve. It consists of two parts; one is under the curved part in the ascending branch, and the other is under the softening branch. The first part is due to crack propagation before a discrete crack is being formed. The cracking is not localized, but distributed over the whole specimen. The magnitude of this portion of the fracture energy is often neglected



2.22 Effect of measuring length on stress-displacement diagram in uniaxial tension (Hordijk, 1989).

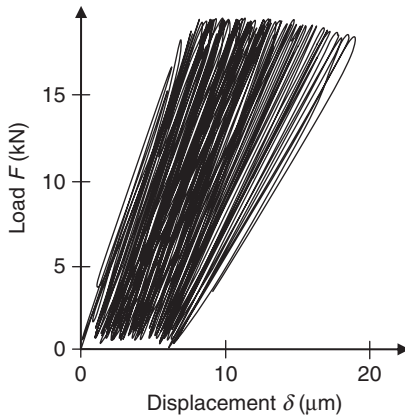
because it is in the order of the stored elastic energy, which is low. Very often, the load-displacement curve is represented by a straight line for the ascending branch and a sharp kink at the peak load (see Fig. 2.22). However, this is a simplification, because cracking is a continuous process, which starts as distributed cracking that merges later into a single crack. Therefore, a horizontal tangent at peak load is preferred.

The second part of the fracture energy is due to the formation of the discrete crack and the separation of the material. The magnitude of the fracture energy G_f is dependent on the type and composition of the material and other parameters that govern the mechanical properties, such as loading rate, temperature, and humidity. The order of magnitude is 100 N/m ($= \text{Nm/m}^2$) for plain concrete, and it is related to one crack in a cross-section. The crack opening before complete separation is in the order of $150 \mu\text{m}$. Knowing the elastic and the fracture energy, the length of a test specimen can be calculated for a stable test (neglecting the elastic energy of the test equipment) by equilibrating both energies, which is in the order of 300 mm .

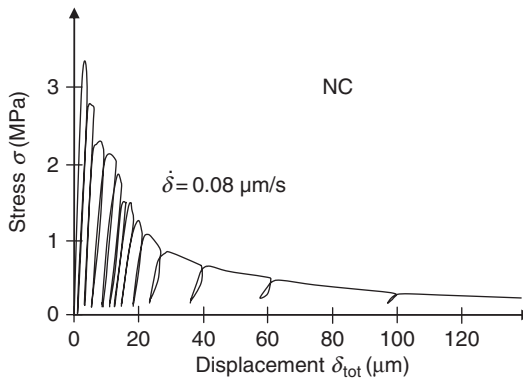
To characterize the brittleness of a material the characteristic length L_{ch} has been introduced (Hillerborg *et al.*, 1976). It is defined as

$$L_{\text{ch}} = E \frac{G_f}{f_t^2} \quad [2.13]$$

It is a measure of the ratio between fracture energy and elastic energy. If the fracture energy prevails, the material is called ductile; if the elastic energy dominates, the material is called brittle. For the asymptotic case that the fracture energy is 0 (for instance glass) the material behaves as very brittle whereas, if the material is ideally plastic the elastic energy vanishes and the material is called ductile.



2.23 Load-displacement diagram of concrete in uniaxial tensile cyclic loading (Kessler-Kramer, 2002).



2.24 Experimental result from uniaxial test (Reinhardt *et al.*, 1986).

Cyclic loading in the elastic state is often performed in order to get S-N curves (see Section 2.8). A typical example is given in Fig. 2.23 (Kessler-Kramer, 2002).

The displacement increases with each loading cycle, and the stiffness decreases slightly in the beginning and, more strongly, before failure. The loops are very close together. One should note that the upper stress level amounted to 0.9 times the static tensile strength, which means that the failure after a certain numbers of cycles is inevitable.

Cyclic loading in the softening stage shows two characteristics; first, the irreversible displacement increases and, second, the stiffness of the concrete decreases with each cycle. Figure 2.24 shows a result from uniaxial tensile experiments. One can observe the hysteresis loops with decreasing inclination and with increasing irreversible displacement.

2.10 Crack development at the meso-scale

The chapter distinguishes between distributed cracking and discrete cracking. Distributed cracking occurs already during the hydration of concrete due to differential temperature and shrinkage. Discrete cracking emanates from distributed cracks as a consequence of mechanical loading especially during softening of the material.

2.10.1 Distributed cracking

The meso-scale is situated between macro- and micro-. If concrete is analyzed at the macro scale, it means that it is regarded as homogeneous isotropic material. This is the typical scale for the analysis of structures. At micro-scale, the crystals of hydrated cement paste (hcp) are treated, particularly how they grow and interact. At meso-scale concrete is considered as two-phase material consisting of granular aggregates and matrix. The matrix which contains hcp, and additions such as fly ash, silica fume, limestone powder, etc., is regarded as cementing material and is treated as one component of the composite material. The aggregates are rounded or angular grains of various shapes. The aggregates are connected to the matrix via the ITZ, which has less strength and stiffness than the bulk matrix. This is true for normal strength concrete. For high-strength concrete, the transition zone is densified with silica fume and has similar properties to the bulk matrix. This difference has an important effect on cracking: in normal strength concrete, cracks run first through the transition zone and then detach the aggregate grain from the matrix whereas, in high-strength concrete, cracks run simultaneously through matrix and aggregate.

There are numerous flaws in the concrete in pristine state. They are distributed more or less randomly in the material. Due to the manufacturing process there may be more flaws under the grains, especially the larger grains, due to segregation and accumulation of water from the fresh concrete. Cracks due to differential strains are located almost everywhere, i.e. in the matrix and in the transition zones, but not in the aggregates. Figure 2.25 shows an example where the micro-cracks are redrawn for better visibility.

When a tensile load is applied, the existing cracks will open and close at unloading if the stresses are lower than about 70% of tensile strength. The concrete is considered as linear elastic. Above this limit, cracks will propagate, and close only partly after unloading. This can be observed by irreversible displacements at complete unloading.

There should be a remark on load duration. What has been said so far refers to monotonic loading, in the range of minutes. If the load is sustained longer, there will be creep effects and cracks will open irreversibly. The



2.25 Micro-cracks at the surface of a section through concrete (Reinhardt *et al.*, 1978).

elastic limit is often regarded as the limit of sustained strength. The literature is not consistent for all concretes.

2.10.2 Discrete cracking

A very illustrative paper (Diamond and Bentur, 1985) shows how discrete cracking develops in cement paste, mortar and concrete. In hydrated cement paste (hcp), the cracks are 'composed of linked short segments zigzagging around a generally forward propagation direction'. A discrete crack in hcp has a width of about 30 μm and tapers at the tip to 1 μm . There is not much

branching. It is interesting to note that the appearance of cracks in mortar depends largely on the drying regime before loading. Cracks in undried specimens avoid the transition zone between grains and matrix while cracks in previously dried specimens run in part through it. Branching occurs frequently. This phenomenon is more pronounced in concrete. Cracks subdivide and branch into more than one plane. It is a matter of resolution of the experimental device how many cracks are visible. The size of micro-cracks can be less than 1 μm .

There are various views on how the experimental findings can be transferred into a physical model. One view assumes that cracking of concrete manifests itself not as a sharp, single crack but rather as a cloud of micro-cracks ahead of a discrete crack. This was the reason why the 'fictitious crack model' (Hillerborg *et al.*, 1976) and the 'crack band model' (Bažant and Oh, 1983) were created. The discrete crack can start in several planes, can branch and later coalesce onto one cracking plane. Another view presented evidence that the discrete crack develops in several steps (van Mier, 1991). It starts as isolated debonding near large aggregates, creates interface grain bridges that fail finally. A microscopic picture is always two-dimensional (2D); however, a crack is a three-dimensional (3D) entity. A crack is not a line, but consists of one or several planes. The forces that are transmitted over the crack are due to bending of intact islands in the cracking planes and to aggregate interlock. Aggregate interlock leads to a friction mechanism and shear resistance. That is why load can still be transferred over crack openings, up to about 150 μm (softening).

On a specimen or a structural member, there is always a surface that is oriented to the ambient environment. This means that there are fluctuations in temperature and humidity. The fluctuations cause strains due to temperature and shrinkage differences, which cause in turn eigenstresses at the edge. These eigenstresses superimpose and facilitate cracking due to mechanical load. It is observed that cracking starts most likely from the surface and propagates into the interior.

2.11 The relationship between tensile strength and compressive strength

The relation between tensile strength and compressive strength can only be empirical, because the effects that influence compressive strength are not exactly the same as those that influence tensile strength, i.e. the type of aggregate, the paste content, and the eigenstresses due to shrinkage and temperature variations. For a good prediction, one has to establish the relation between the two every time anew. There are formulas that are average ones for a rough estimation.

A relation that was derived in 1969 reads

$$f_{\text{ctm}} = 0.3 f_{\text{ck}}^{2/3} \quad [2.14]$$

with f_{ctm} = mean tensile strength, f_{ck} = characteristic cylinder compressive strength, and 0.3 = empirical constant (Heilmann *et al.*, 1969). The formula is valid for concrete strength classes up to C50. For higher-strength classes, another relation has been established that reads

$$f_{\text{ctm}} = 2.12 \ln \left(1 + \frac{f_{\text{cm}}}{10} \right) \quad [2.15]$$

with f_{cm} mean compressive strength (fib, 2010).

The relation of Equation [2.10] can be generalized into:

$$f_t = c f_{\text{cube}}^{2/3} \quad [2.16]$$





with c a parameter that depends on the type of test and that has a certain scatter. Table 2.2 gives the validity of this parameter and the ranges that have been derived from numerous test results (Heilmann, 1969).

It can be seen that the flexural strength yields the largest values and the uniaxial tensile strength the smallest. The table allows also the conversion from flexural, to splitting, and to uniaxial strength, which leads to conversion factors of the mean values of 2.06:1.88:1.13:1.00. That means that the flexural strength is roughly twice the uniaxial strength, and the splitting strength is about 10% larger than the uniaxial strength. The coefficients of Table 2.2 have been determined from tests on normal strength concrete. The coefficient of 0.3 in Equation [2.14] is a lower limit of the empirical evaluation

2.12 The practical implications of laboratory tests

Laboratory testing is being carried out for various purposes: for exploring material properties, for validating theories, for establishing design values, or for quality control. When practice is addressed, the two last aspects are the most important. The tensile strength of concrete is usually not taken into account in the design of reinforced concrete structures. The tensile forces have to be carried by steel reinforcement. However, shear forces, which are inclined tensile forces, have to be covered by the concrete when there is no shear reinforcement present. The admissible shear stress is then directly proportional to the tensile strength of concrete (fib, 2010). For that purpose, the uniaxial tensile strength should be known from laboratory experiments or from the conversion of the compressive strength. The same is true if the concrete member undergoes torsion. If uniaxial experiments

Table 2.2 Conversion factors for Equation [2.16] for various test methods and range of validity of concrete at 28 days age

Loading scheme	Tensile strength	Lower bound	Mean	Upper bound
	Flexural strength	0.86	1.07	1.28
		0.76	0.98	1.20
				
	Splitting strength	0.48	0.59	0.70
	Uniaxial strength	0.36	0.52	0.63

Source: Heilmann, 1969.

are too difficult to perform, the splitting tensile strength can be used and reduced by 5–10%.

The flexural strength is taken for design of plain (un-reinforced) concrete structures, such as concrete roads and pavements. In this case, the size effect should be taken into account by reducing the measured strength value from the test geometry to the actual size of the structural member. The German guideline for concrete structures for protection of the environment (DAfStb, 2010) defines the flexural strength as a function of the uniaxial tensile strength as follows:

$$f_{\text{lex}} = f_t \left(1 + 0.13 \sqrt{\frac{1}{h}} \right) \tag{2.17}$$

with h = depth of structural element in meters. So, the flexural strength is greater than the uniaxial strength, and the depth influence follows fracture mechanics principles. The formula allows one to convert measurements of a certain specimen size to other depths.

Not only loading stresses occur in concrete but also eigenstresses and stresses due to imposed deformation. Calculating the cracking stress due to imposed deformation is possible by using the uniaxial tensile strength as a design value. When reinforcement is present the bond between steel and concrete and the tensile strength determine the crack distance and the crack width (Reinhardt, 1991). Eigenstresses due to shrinkage and thermal gradients cause cracking when the tensile strength at the surface of a structure is reached. However, the crack distance and width can be calculated from the fracture energy of concrete (Bažant and Cedolin, 1991).

2.13 References

- Al-Kubaisy M A and Young A G (1975), 'Failure of concrete under sustained tension', *Magazine of Concrete Research*, **27**, 171–178.
- ASTM C 192 / C192M – 07 (2007), Standard Practice for Making and Curing Concrete Test Specimens in the Laboratory.
- Barpi F, Chille F, Imperato L and Valente S (1997), 'Failure lifetime prediction of cracked concrete structures', in MRS Symp. Proc. Vol. **503** *Nondestructive Characterization of Materials in Aging Systems*, Boston, 131–136.
- Bažant Z P and Cedolin L (1991), *Stability of structures*, New York.
- Bažant Z P and Kaplan M F (1996), *Concrete at high temperatures: Material properties and mathematical models*, Harlow, Longman Group.
- Bažant Z P, Kazemi M T, Hasegawa T. and Mazars J (1991), 'Size effect in Brazilian split-cylinder tests: Measurements and fracture analysis', *ACI Materials Journal*, **88**(3), 325–332.
- Bažant Z P and Oh B H (1983), 'Crack band theory for fracture of concrete', *Materials and Structures*, **16**, 155–157.
- Bonzel J and Kadlecsek V (1970), 'Influence of curing and moisture condition on tensile strength of concrete' (in German), *beton*, **20**, 303–309 and 351–357.
- Carpinteri A, Valente S, Zhou F P, Ferrara G and Melchiori G (1997), 'Tensile and flexural creep rupture tests on partially damaged concrete specimens', *Materials and Structures*, **30**, 269–276.
- Cornelissen H A W (1984), 'Fatigue failure of concrete in tension', *HERON*, **29**(4).
- Cornelissen H A W and Siemes A J M (1985), 'Plain concrete under sustained tensile or tensile and compressive fatigue loadings', In *Prof. BOSS Conf.*, Elsevier, 487–498.
- DAfStb (2010), *German guideline for design of concrete structures in contact with water-contaminating materials* (in German), Berlin.
- de Joly M (1898), 'La résistance et l'élasticité des ciments Portland', *Annales des Ponts et Chaussées, Mémoires et Documents* **16**(3), 198–244.
- De Schutter G (1996), *Fundamental and practical study of thermal stresses in hardening massive concrete elements* (in Dutch), PhD thesis, Ghent.
- Diamond S and Bentur A (1985), 'On the cracking in concrete and fiber-reinforced cements', In S.P. Shah (Ed.), *Application of fracture mechanics to cementitious composites*, NATO ASI Series E: Applied Sciences No. 94, Dordrecht, 87–140.
- Eisenmann J and Leykauf G (2003), *Concrete pavements* (in German), Berlin.
- EN 1992-1-2:2004 (2004), EC 2: Design of concrete structures – Part 1–2: General rules – Structural fire design, CEN, Brussels.
- EN 1992-1-1:2011–01, Eurocode 2 'Design of concrete structures' – Part 1-1: General rules and rules for buildings, CEN? Brussels.
- Faust T (2000), *Production, bearing behavior and design of structural lightweight concrete* (in German), PhD thesis, Leipzig.
- fib (2010), *Model Code 2010*, Bulletin 55, Vol. **1**, Lausanne.
- Fouré B (1982), *Resistance of concrete under sustained loading* (in French), Association Française du Béton, La technique française du béton précontraint, Stockholm.
- Graf O, Albrecht W and Schäffler H (1960), *The properties of concrete* (in German). 2nd ed., Berlin.
- Gutsch A W (1988), 'Material properties of young concrete – Tests and models' (in German), *iBMB* No. 140, Braunschweig.

- Han N and Walraven J C (1993), 'Sustained loading effects in high strength concrete', In Holland I. and Sellevold E. (Eds.), *High-strength concrete*, Vol. 2, Lillehammer, 1076–1083.
- Heilmann H G (1969), 'Relations between tensile and compressive strength of concrete' (in German), *beton*, **19**(2), 68–70.
- Heilmann H G, Hilsdorf H and Finsterwalder K (1969), 'Strength and deformation of concrete under tensile stresses' (in German), *DAfStb Bulletin* **203**, Berlin.
- Hillerborg A, Modeer M and Petersson P E (1976), 'Analysis of crack formation and crack growth in concrete by means of fracture mechanics and finite elements'. *Cement and Concrete Research*, **6**, 773–782.
- Hillerborg A (1986), 'The theoretical basis of a method to determine the fracture energy G_F of concrete', *Materials and Structures* **18** (106), 291–296.
- Hordijk D A (1989), 'Deformation-controlled uniaxial tensile tests on concrete', *Stevin Laboratory Report*, **25.5**–89–15/VFA, TU Delft.
- Illston J M (1965), 'The creep of concrete under uniaxial tension', *Magazine of Concrete Research*, **17**(51), 77–84.
- Kessler-Kramer C (2002), *Tensile behavior of concrete under fatigue loading* (in German). PhD thesis, Karlsruhe.
- Kordina K, Schubert L and Troitzsch U (2000), 'Creep of concrete under tensile loading' (in German), *DAfStb Bulletin*, **498**, Berlin.
- Krausz A S and Krausz K (1988), *Fracture kinetics of crack growth*, Kluwer, Dordrecht.
- Malhotra V M (1970), 'Effect of specimen size on the tensile strength of concrete', *ACI Journal*, **67**(6), 467–469.
- Meng X and Song Y (2007), 'Residual tensile strength of plain concrete under tensile fatigue loading', *Journal of Wuhan University of Technology – Materials Science*, **22**(3), 564–568.
- Mihashi H and Wittmann F H (1980), 'Stochastic approach to study the influence of rate of loading on strength of concrete', *HERON*, **25**(3).
- Reinhardt H W (1991), 'Imposed deformation and cracking', *IABSE Report*, Vol. **62**, Zürich, 101–110.
- Reinhardt H W and Cornelissen H A W (1985), 'Concrete under sustained loading' (in German), *Baustoffe*, **85**, Festschrift for K. Wesche, Wiesbaden, 162–167.
- Reinhardt H W, Cornelissen H A W and Hordijk D A (1986), 'Tensile tests and failure analysis of concrete', *Journal of Structural Engineering*, **112**(11), 2462–2477.
- Reinhardt H W, Stroeven P, den Uijl A, Kooistra T R and Vrencken J H A M (1978), 'Influence of amplitude, stress level and frequency on fatigue strength of concrete in low-cycle fatigue experiments' (in German), *Betonwerk + Fertigteil-Technik*, **44**(9), 498–503.
- Rinder T and Reinhardt H W (2004), 'Sustained tensile strength of high-strength concrete' (in German), *beton*, **54**(7/8), 360–367.
- Rossi P, Wu X, Le Maou F and Belloc A (1992), 'Size effect on the behavior of concrete in tension' (in French), *Bulletin De Liaison Des Laboratoires Des Ponts et Chaussees*, **182**, 11–20.
- Rostásy F S (1984), 'Strengthening and brittleness of concrete by low temperatures' (in German), In *Fortschritte im konstruktiven Ingenieurbau*, Festschrift at the 60th birthday of Gallus Rehm, Berlin, 229–239.
- Saito M (1984), 'Tensile fatigue strength of lightweight concrete', *International Journal of Cement Composites and Lightweight Concrete*, **6**(3), 143–149.

- Saito M and Imai S (1983), 'Direct tensile fatigue of concrete by the use of friction grips', *Journal of American Concrete Institute*, **80**(5), 431–438.
- Schaff R J and Davidson B D (1997), 'Life prediction methodology for composite structures. Part 1: Constant amplitude and two-stress level fatigue', *Journal of Composite Materials*, **31**(2), 128–157.
- Tang T, Shah S P and Ouyang C (1992), 'Fracture mechanics and size effect of fracture in tension', *Journal of Structural Engineering–ASCE*, **118**(11), 3169–3185.
- Tepfers R (1979), 'Tensile fatigue strength of plain concrete', *ACI Journal*, **76**(8), 919–933.
- van Mier J G M (1991), 'Mode I fracture of concrete: discontinuous crack growth and crack interface grain bridging', *Cement and Concrete Research*, **21**, 1–15.
- van Vliet M R A and van Mier J G M (1999), 'Effect of strain gradients on the size effect of concrete in uniaxial tension', *International Journal of Fracture*, **95**, 195–219.
- Walker S and Bloem D L (1957), 'Studies of flexural strength of concrete – Part 3: Effects of variations in testing procedures', *Proc. ASTM*, **57**, 1122–1139.
- Weibull W (1939), 'A statistical theory of the strength of materials'. *Royal Swedish Academy of Eng. Si.Proc.*, **151**, 1–45.
- Wittmann F and Zaitsev J (1974), 'Deformation and fracture process of porous building materials under short term and long term loading' (in German), *DAfStb Bulletin*, **232**, Berlin, 65–145.
- Wolinski S, Hordijk D A, Reinhardt H W and Cornelissen H A W (1987), 'Influence of aggregate size on fracture mechanics parameters of concrete', *International Journal of Cement composites and lightweight concrete*, **9**(2), 95–103.
- Wright P J F and Garwood F (1952), 'The effect of the method of test on the flexural strength of concrete', *Magazine of Concrete Research*, **3**, 67–76.

Modelling the effect of material composition on the tensile properties of concrete

Ł. SKARŻYŃSKI and J. TEJCHMAN,
Gdańsk University of Technology, Poland

DOI: 10.1533/9780857097538.1.52

Abstract: This chapter presents the effect of micro-structure on the behaviour of plain concrete. Concrete was modelled as a random heterogeneous three-phase material. The 2D simulations were carried out with the finite element method using an isotropic damage constitutive model enhanced by a characteristic length of micro-structure by means of a non-local theory. The behaviour of notched concrete beams subjected to quasi-static three-point bending and concrete elements under uniaxial tension was studied. In the calculations with concrete beams under bending, the effect of the beam size, aggregate distribution, aggregate volume, aggregate roughness, aggregate size, aggregate stiffness, bond thickness and characteristic length on the material behaviour were numerically investigated. The numerical results were compared with our own laboratory test results using the Digital Image Correlation (DIC) method (Skarżyński *et al.* 2011), the tests by Le Bellégo *et al.* (2003) and the size effect law by Bažant (2004). In addition, the 2D representative volume element (RVE) for concrete under tension was determined. Since the RVE could not be defined in quasi-brittle materials with a standard averaging approach, due to the occurrence of a localized zone, two alternative non-standard averaging methods were presented to determine the size of the RVE in concrete subjected to uniaxial tension.

Key words: concrete, damage mechanics, micro-structure, meso-scale, representative volume element (RVE).

3.1 Introduction

The cracking process is a fundamental phenomenon in cementitious materials (Bažant and Planas 1998; Lilliu and van Mier 2003). It is a major cause of damage in concrete material under mechanical loading, contributing to a significant degradation of material strength. A realistic description of the fracture mechanism is very important to ensure safety of the structure. This mechanism is very complex, since it consists of main cracks with various

branches, secondary cracks and micro-cracks. Moreover, it strongly depends upon a heterogeneous composition of materials over many different length scales, changing e.g. in concrete from a few nanometres (hydrated cement) to millimetres (aggregate particles). Cracks are always preceded by the formation of localized zones of a certain width (called fracture process zones (FPZ)). The width of localized zones is (commonly) not negligible to cross-section dimensions of a concrete specimen and is large enough to cause significant energy release and accompanying stress redistribution in the structure (Bažant and Planas 1998). Thus, to describe strain localization, the material micro-structure has to be taken into account (Nielsen *et al.* 1995; Bažant and Planas 1998; Sengul *et al.* 2002; Lilliu and van Mier 2003; Kozicki and Tejchman 2008; He *et al.* 2009). In particular, the presence of aggregate is important, since its volume fraction can be as high as 70–75% in concrete.

A mesoscopic description of strain localization is always connected with a huge number of finite or discrete elements and a related large computational effort. To solve this problem in practice (by decreasing the number of elements in large concrete elements), some homogenization-based multi-scale models are used, where each macroscopic point at the coarse (large) scale is connected with a microscopic cell at the fine (small) scale. Thus, the most important issue in multi-scale analyses is determination of an appropriate size for a micro-structural model, the so-called RVE. The size of the RVE should fulfil two conditions: that homogenized properties become independent of micro-structural variations, and a micro-structural domain is small enough that separation of scales is guaranteed. Many researchers attempted to define the size of RVE in heterogeneous materials with a softening response in a post-peak regime (Hill 1963; Bažant and Pijauder-Cabot 1989; Drugan and Willis 1996; Evesque 2000; van Mier 2000; Bažant and Novak 2003; Kanit *et al.* 2003; Kouznetsova *et al.* 2004; Gitman *et al.* 2007; Skarżyński and Tejchman 2009). The last outcomes in this topic show, however, that the RVE cannot be defined in softening quasi-brittle materials due to strain localization, since the material then loses its statistical homogeneity (Gitman *et al.* 2007; Skarżyński and Tejchman 2009, 2010). Thus, each multi-scale approach always suffers from non-objectivity of the results with respect to a cell size (Gitman *et al.* 2008). The RVE exists solely for linear and hardening regimes.

The intention of our calculations is to describe the concrete at meso-scale by taking into account its heterogeneous and non-uniform composition (micro-structure). Concrete was assumed at meso-scale as a random material composed of three main phases: aggregate, cement matrix and bond (interface). Quasi-static FE calculations were carried out with concrete elements subjected to three-point bending and uniaxial tension. The simulations were carried out with an isotropic continuum constitutive damage

model (Marzec *et al.* 2007; Skarżyński *et al.* 2011) enhanced by a characteristic length of micro-structure by means of a non-local theory (Pijauder-Cabot and Bažant 1987; Bažant and Jirasek 2002; Bobiński *et al.* 2009).

The FE analyses are divided into two parts. In the first part (FE calculations with notched concrete beams), attention was paid to the width and shape of a localized zone appearing above the beam notch. The effect of the aggregate distribution, aggregate packing, aggregate size, aggregate roughness, aggregate stiffness, bond thickness, characteristic length and beam size on the beam behaviour was investigated. The numerical results were directly compared with corresponding laboratory test results with notched concrete beams (Skarżyński *et al.* 2009a), where the width and shape of a localized zone on the surface of notched concrete beams was determined with DIC technique. In addition, our results were compared with corresponding laboratory size effect tests by Le Bellėgo *et al.* (2003) with the same beam geometry, and the size effect law by Bažant (Bažant and Planas 1998; Bažant 2004) for notched concrete structures, where a crack grows in a stable manner prior to the maximum load. In the second part, an RVE in the concrete specimen under uniaxial tension was determined using two non-standard averaging methods.

3.2 Modelling damage in concrete

A simple isotropic damage continuum model was used, describing the material degradation with the aid of only a single scalar damage parameter D growing monotonically from 0 (undamaged material) to 1 (completely damaged material) (Katchanov 1986; Simo and Ju 1987). The stress–strain function is represented by the relationship

$$\sigma_{ij} = (1 - D)C_{ijkl}^e \varepsilon_{kl}, \quad [3.1]$$

where C_{ijkl}^e is the linear elastic material stiffness matrix and ε_{kl} is the strain tensor ('e' – elastic). The loading function of damage is

$$f(\tilde{\varepsilon}, k) = \tilde{\varepsilon} - \max\{k, k_0\}, \quad [3.2]$$

where k_0 denotes the initial value of κ when damage begins. If the loading function f is negative, damage does not develop. During monotonic loading, the parameter κ grows (it coincides with $\tilde{\varepsilon}$) and during unloading and reloading it remains constant. A Rankine failure type criterion was assumed to define the equivalent strain measure $\tilde{\varepsilon}$ (Jirasek and Marfia 2005)

$$\tilde{\varepsilon} = \frac{\max\{\sigma_i^{eff}\}}{E}, \quad [3.3]$$

where E denotes the modulus of elasticity and σ_i^{eff} are the principal values of the effective stress tensor

$$\sigma_i^{eff} = C_{ijkl}^e \varepsilon_{kl}. \quad [3.4]$$

If all principal stresses are negative, the loading function f is negative and no damage occurs.

To describe the evolution of the damage parameter D (determining the shape of a softening curve under tension), the exponential softening law was used (Peerlings *et al.* 1998)

$$D = 1 - \frac{k_0}{k} (1 - \alpha + \alpha e^{-\beta(k-k_0)}), \quad [3.5]$$

where α and β are the material constants.

The constitutive isotropic damage model for concrete requires the following five material constants: E , ν , κ_0 , α and β . The model is suitable for tensile failure (Marzec *et al.* 2007; Skarżyński *et al.* 2011) and mixed tensile-shear failure (Bobiński and Tejchman 2010). However, it cannot realistically describe irreversible deformations, volume changes or shear failure (Simone and Sluys 2004).

To properly describe strain localization, to preserve the well-posedness of the boundary value problem, to obtain mesh-independent results and, finally, to include a characteristic length of micro-structure l_c in simulations (which sets the width of a localized zone), an integral-type non-local theory was used as a regularization technique (Bažant and Jirasek 2002; Bobiński and Tejchman 2004). The equivalent strain measure $\tilde{\varepsilon}$ was replaced by its non-local value $\bar{\varepsilon}$ (Pijauder-Cabot and Bažant 1987) to evaluate the loading function (Equation [3.2]) and to calculate the damage threshold parameter κ

$$\bar{\varepsilon} = \frac{\int_V \omega(\|x - \xi\|) \tilde{\varepsilon}(\xi) d\xi}{\int_V \omega(\|x - \xi\|) d\xi}, \quad [3.6]$$

where V is the body volume, x the coordinates of the considered (actual) point, ξ the coordinates of surrounding points and ω the weighting function. As a weighting function ω , a Gauss distribution function was used

$$\omega(r) = \frac{1}{l_c \sqrt{\pi}} e^{-\left(\frac{r}{l_c}\right)^2}, \quad [3.7]$$

where l_c denotes a characteristic length of micro-structure and the parameter r is a distance between two material points. The averaging in Equation [3.7]

is restricted to a small representative area around each material point (the influence of points at the distance of $r = 3 \times l_c$ is only 0.01%). A characteristic length is usually related to material micro-structure and is determined with an inverse identification process of experimental data (Le Bellégo *et al.* 2003).

3.3 Behaviour of concrete beams under three-point bending conditions

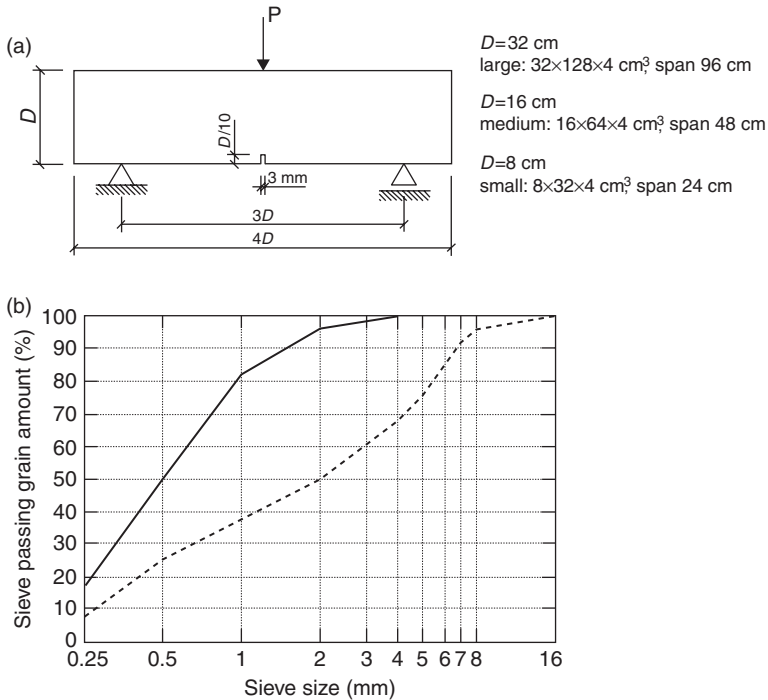
Simplified two-dimensional numerical simulations were performed with notched concrete beams $D \times L$ (D = beam height, $L = 4 \times D$ – beam length) with free ends subjected to quasi-static three-point bending. The following concrete beams were used: (a) small-size beams 80×320 mm², (b) medium-size beams 160×640 mm², and (c) large-size beams 320×1280 mm² (Fig.3.1a). The beams' span was equal to $3 \times D$. A notch with a height of $D/10$ mm was located at the mid-span of the beam bottom. The dimensions were exactly the same as in the laboratory tests by Le Bellégo *et al.* (2003) and Skarżyński *et al.* (2011). The beams were subjected to a vertical displacement in the top mid-point at a very slow rate.

3.3.1 Numerical implementation

Concrete at meso-scale was considered as a three-phase material encompassing the cement matrix, aggregate and interfacial transition zones ITZ between the cement matrix and aggregate. Aggregate was randomly distributed in cement matrix according to experimental sieve curves. Two different concrete mixes were analysed (used in experiments, Skarżyński and Tejchman 2011): sand (with a mean aggregate diameter $d_{50} = 0.5$ mm and maximum aggregate diameter $d_{\max} = 3.0$ mm) and gravel concrete ($d_{50} = 2.0$ mm, $d_{\max} = 8.0$ mm) (Fig. 3.1b). To reduce the number of aggregate particles in calculations, the size of assumed inclusions varied from $a_{\min} = 0.5$ mm up to $a_{\max} = 3$ mm in sand concrete and from $a_{\min} = 2$ mm up to $a_{\max} = 8$ mm in gravel concrete. Aggregate had mainly a circular shape for the sake of simplicity. The ITZ thickness was assumed to be $t_b = 0.05$ – 0.75 mm. Aggregate was generated according to the method given by Eckardt and Konke (2006). The circles simulating aggregate were randomly placed starting with the largest ones and preserving a certain mutual distance (van Mier *et al.* 1995)

$$D_p > 1.1 \frac{D_1 + D_2}{2}, \quad [3.8]$$

where D_p is the distance between two neighbouring particle centres and D_1 , and D_2 are the diameters of two particles, respectively. The aggregate volume



3.1 Concrete beams subjected to three-point bending: (a) geometry (Le Bellégo *et al.*, 2003; Skarżyński *et al.*, 2011), (b) grading curve for sand (continuous line) and gravel (dashed line) used for concrete (Skarżyński *et al.*, 2011).

was $\rho = 30\%$, $\rho = 45\%$ or 60% . The calculations were carried out with the set of material parameters for usual concrete only, which was prescribed to finite elements corresponding to a specified concrete phase (Table 3.1). The mesoscopic characteristic length of micro-structure was $l_c = 1.5 \text{ mm}$ (see Section 3.3.7). ITZs were assumed to be the weakest components (Lilliu and van Mier, 2003; Kozicki and Tejchman, 2008). We have assumed that ITZs have the reduced stiffness and strength as compared to the cement matrix, and that their properties do not depend on the aggregate size and shape. The FE-meshes including 12 000–1 600 000 triangular elements were assumed, where the size of triangular finite elements was: $s_a = 0.5 \text{ mm}$ (aggregate), $s_{cm} = 0.5 \text{ mm}$ (cement matrix) and $s_b = 0.1 \text{ mm} = t_b/5$ (bond). In general, the material constants should be determined with laboratory tensile tests for each phase (that is certainly possible for aggregate and cement matrix but not feasible for ITZs). The mesoscopic characteristic length $l_c = 1.5 \text{ mm}$ was simply imposed such that the numerical results agreed with the experimental observations. In our future numerical investigations, it will be directly related to concrete micro-structure (aggregate size or aggregate spacing).

Table 3.1 Material parameters assumed FE calculations of concrete notched beams under bending at meso-scale

Material parameters	Inclusions	Cement matrix	Bond
Modulus of elasticity E (GPa)	40	35	30
Poisson's ratio ν (–)	0.2	0.2	0.2
Crack initiation strain κ_o (–)	0.5	1×10^{-4}	7×10^{-5}
Residual stress level α (–)	0.95	0.95	0.95
Slope of softening β (–)	200	200	200

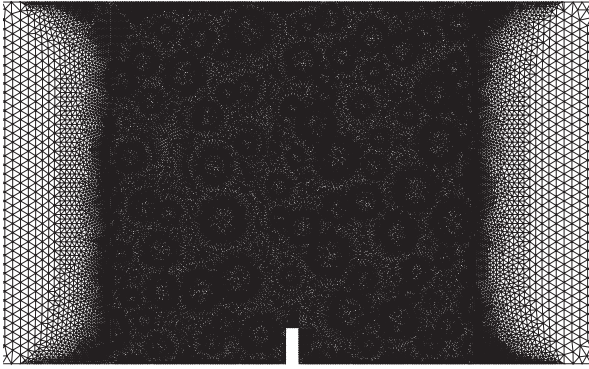
First, a small-size beam ($80 \times 320 \text{ mm}^2$) of gravel concrete was modelled: as partially homogeneous and partially heterogeneous with a meso-section in the notch neighbourhood and as an entirely heterogeneous beam at meso-scale. The width of a heterogeneous meso-scale section b_{ms} varied between $D/2$ (40 mm) and D (80 mm). These preliminary analyses allowed us to determine a representative width of a required heterogeneous region close to the notch to capture a localized zone. Next, the effect of different parameters was studied in a small-size beam. Finally, calculations were carried out with partially heterogeneous beams of a different size to determine a deterministic size effect. Three to five different stochastic realizations were usually performed for the same case. The width of a localized zone above the notch in the beams was determined at the deflection of $u = 0.15$ mm on the basis of a non-local softening strain measure $\bar{\epsilon}$ (Equation [3.6]). As the cut-off value, $\bar{\epsilon}_{\min} = 0.025$ was always assumed to be at the maximum mid-point value of $\bar{\epsilon}_{\max} = 0.08\text{--}0.13$.

The preliminary results showed that the effect of the width of the meso-scale region on the results was insignificant if $b_{ms} \geq D/2$ (Skarżyński and Tejchman 2010). In further calculations, to save computational time, a representative meso-scale section was assumed to be always equal to the beam height $b_{ms} = D$ (i.e. 80 mm for a small-size beam (Fig. 3.2), 160 mm for a medium-size beam and 320 mm for a large-size beam).

Below the effect of different parameters, such as the beam size, aggregate distribution, aggregate volume, aggregate roughness, aggregate size, aggregate stiffness, bond thickness and characteristic length, on the material behaviour (load-deflection curve and strain localization) is demonstrated. The parameters were varied independently.

3.3.2 Effect of aggregate distribution

Figures 3.3–3.6 demonstrate the effect of a stochastic distribution of the round shaped aggregate particles on the load-deflection diagram (Figs 3.3 and 3.5) and strain localization (Figs 3.4 and 3.6) in the beam $80 \times 320 \text{ mm}^2$.



3.2 FE-mesh used for calculations of meso-scale region equal to beam height (small-size beam $80 \times 320 \text{ mm}^2$, volume of circular aggregate $\rho = 30\%$).

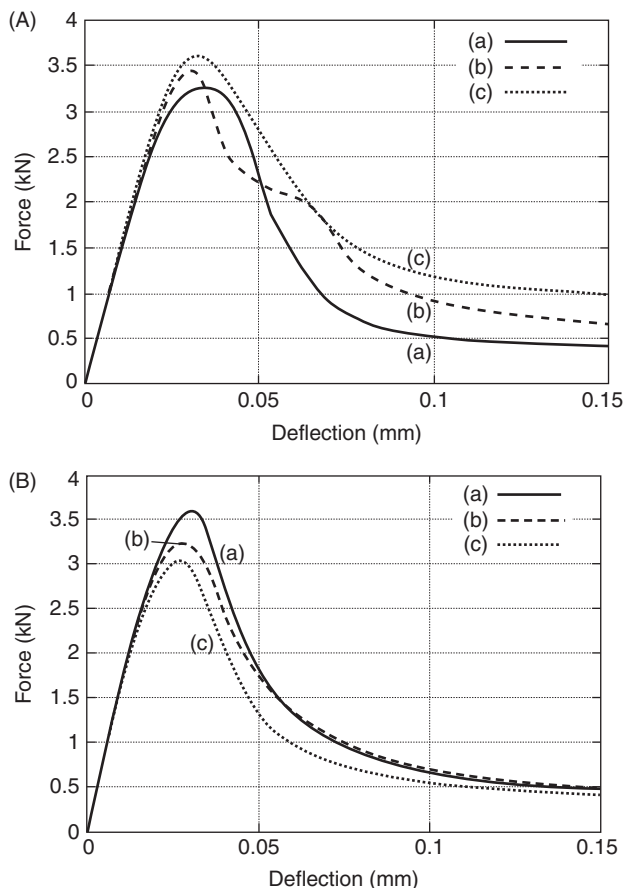
The aggregate volume was $\rho = 30\%$ (Figs 3.3 and 3.4) or $\rho = 45\%$ (Figs 3.5 and 3.6) for sand concrete ($d_{50} = 0.5 \text{ mm}$ and $d_{\max} = 3 \text{ mm}$) and for gravel concrete ($d_{50} = 2 \text{ mm}$, $d_{\max} = 8 \text{ mm}$), respectively. The bond thickness was $t_b = 0.25 \text{ mm}$.

The load-displacement curves are the same in the entire elastic regime, independently of the distribution of inclusions. However, they are significantly different after the peak is reached (Figs 3.3A and 3.5A) due to a localized zone propagating between aggregate distributed at random, which is always non-symmetric and curved. The width of the calculated localized zone is approximately $w_c = 6 \text{ mm} = 4 \times l_c = 12 \times s_{cm}$ ($\rho = 30\%$) and $w_c = 4.5 \text{ mm} = 3 \times l_c = 9 \times s_{cm}$ ($\rho = 45\%$) independently of d_{50} . The calculated localized zone is created at $u/D = 0.14$ and its width increases linearly during deformation.

3.3.3 Effect of aggregate size and aggregate volume

Figures 3.7–3.9 demonstrate the effect of aggregate size and aggregate volume in sand concrete ($d_{50} = 0.5 \text{ mm}$ and $d_{\max} = 3 \text{ mm}$) and gravel concrete ($d_{50} = 2 \text{ mm}$ and $d_{\max} = 8 \text{ mm}$) for a small-size beam ($80 \times 320 \text{ mm}^2$) using circular aggregate volume $\rho = 30\%$, $\rho = 45\%$ and $\rho = 60\%$ ($l_c = 1.5 \text{ mm}$, $t_b = 0.25 \text{ mm}$).

With increasing maximum aggregate and aggregate volume, the beam strength slightly increases (by 10–25%, Figs 3.8A and 3.8B). The width of the localized zone does not depend on the maximum aggregate size d_{\max} . However, this outcome is in contrast to statements by Pijauder-Cabot and Bažant (1987), and Bažant and Oh (1983), wherein the width of a localized zone was estimated to be about $3 \times d_{\max}$. It is also in contrast to experimental results by Mihashi and Nomura (1996), which have shown that the width of a localized zone in normal concrete increases with increasing aggregate size.

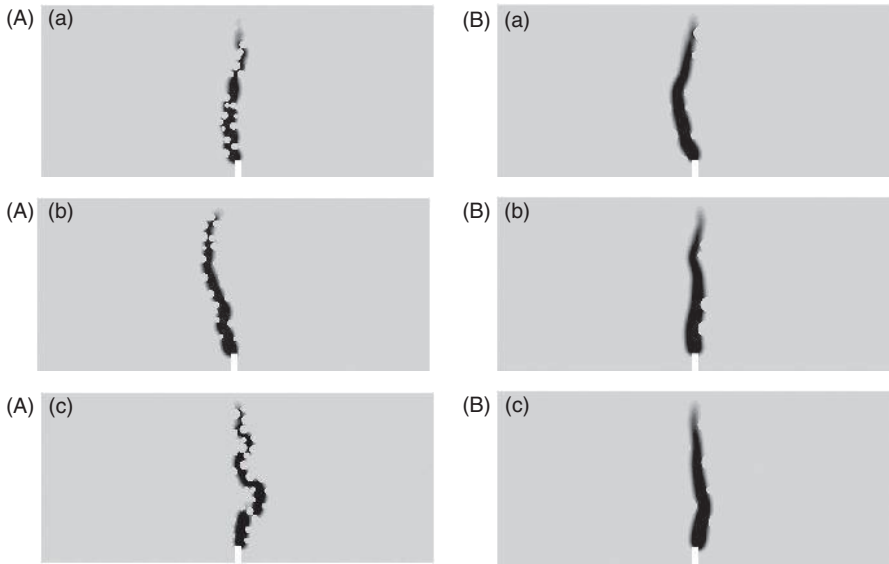


3.3 Calculated load-deflection curves for two concrete mixes and three random distributions of circular aggregate (curves 'a', 'b', 'c') in small-size beam $80 \times 320 \text{ mm}^2$ ($l_c = 1.5 \text{ mm}$, $\rho = 30\%$, $t_b = 0.25 \text{ mm}$): (A) sand concrete ($d_{50} = 0.5 \text{ mm}$, $d_{\max} = 3 \text{ mm}$), (B) gravel concrete ($d_{50} = 2 \text{ mm}$, $d_{\max} = 8 \text{ mm}$).

The width of a localized zone is influenced by the aggregate volume; a localized zone becomes narrower with increasing aggregate volume: $w_c = 6 \text{ mm}$ at $\rho = 30\%$, $w_c = 4.5 \text{ mm}$ at $\rho = 45\%$, $w_c = 3 \text{ mm}$ at $\rho = 60\%$. The shape of a localized zone is affected by d_{50} (d_{\max}) and ρ (in particular for $\rho = 60\%$).

3.3.4 Effect of aggregate roughness

The effect of the different aggregate roughness (Fig. 3.10) in a small-size beam ($80 \times 320 \text{ mm}^2$) of gravel concrete ($d_{50} = 2 \text{ mm}$ and $d_{\max} = 8 \text{ mm}$) is shown in Figs 3.11–3.14 ($\rho = 30\%$ and $\rho = 45\%$, $l_c = 1.5 \text{ mm}$, $t_b = 0.25 \text{ mm}$).



3.4 Calculated distribution of non-local strain measure for various concrete mixes and three random distributions of circular aggregate ('a', 'b', 'c') in small-size beam corresponding to load-deflection curves of Fig. 3.3 ($l_c = 1.5$ mm, $\rho = 30\%$, $t_b = 0.25$ mm): (A) sand concrete ($d_{50} = 0.5$ mm, $d_{\max} = 3$ mm), (B) gravel concrete ($d_{50} = 2$ mm, $d_{\max} = 8$ mm).

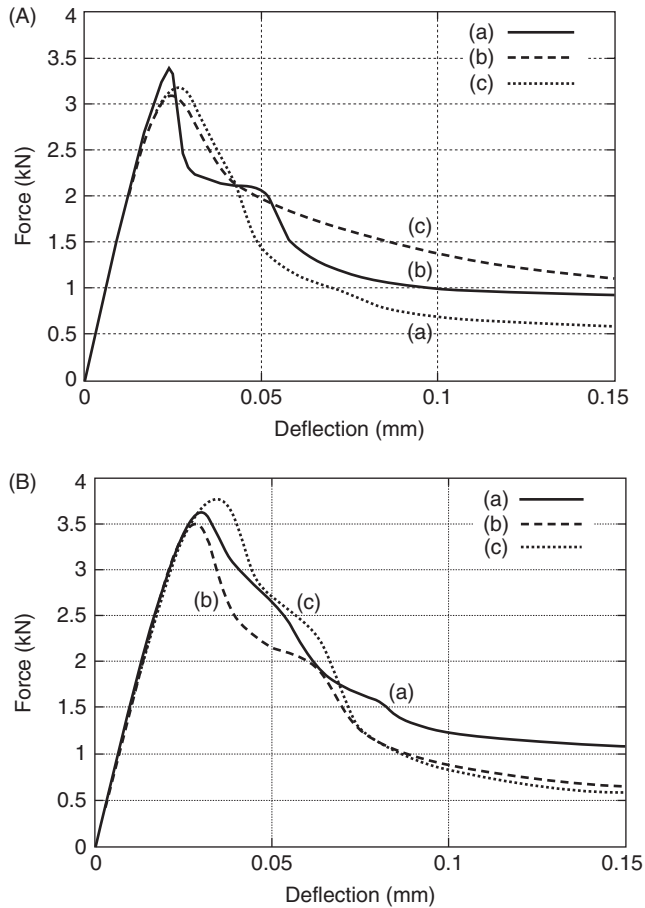
The results with the different aggregate roughness are compared using the same stochastic distribution.

The beam strength is lowest for beams with circular-shaped aggregate and increases with increasing aggregate roughness by 10–20% (Figs 3.11 and 3.13). The width of a localized zone changes between $w_c = 6$ mm for $\rho = 30\%$ and $w_c = 4.5$ mm for $\rho = 45\%$. It is not influenced by the aggregate roughness. In turn, the form of a localized zone is affected by the aggregate roughness (Figs 3.12 and 3.14).

3.3.5 Effect of aggregate stiffness

Figure 3.15 shows the effect of the aggregate stiffness in a small-size beam (80×320 mm², $d_{50} = 2$ mm and $d_{\max} = 8$ mm). The calculations were carried out with the weak aggregate (which had the same properties as the bond of Table 3.1).

For the weak aggregate, a localized zone can propagate through weak grains. The vertical force is obviously smaller and the width of a localized zone is higher than the usual aggregate.

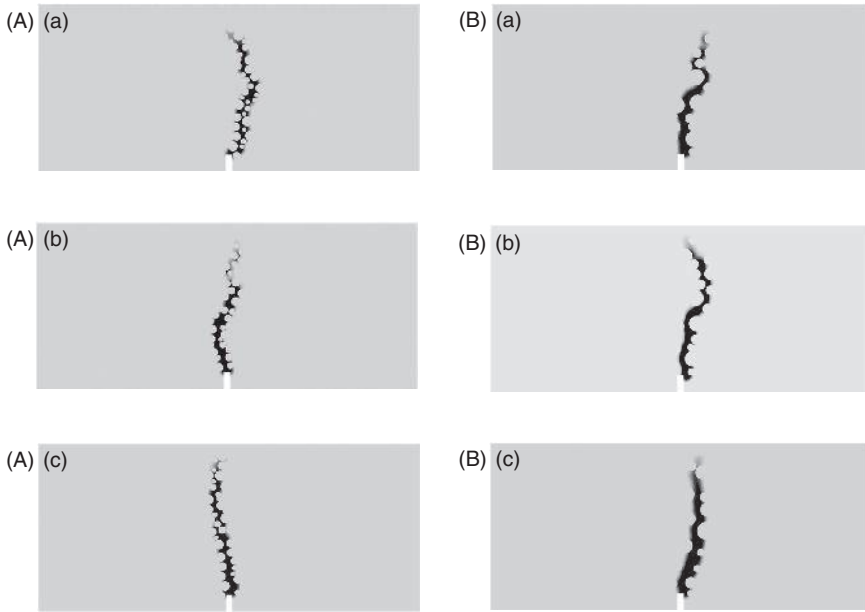


3.5 Calculated load-deflection curves for two concrete mixes and three random distribution of circular aggregate (curves 'a', 'b', 'c') in a small-size beam 80×320 mm² ($l_c = 1.5$ mm, $\rho = 45\%$, $t_b = 0.25$ mm): (A) sand concrete ($d_{50} = 0.5$ mm, $d_{max} = 3$ mm), (B) gravel concrete ($d_{50} = 2$ mm, $d_{max} = 8$ mm).

3.3.6 Effect of ITZ thickness

Figures 3.16 and 3.17 demonstrate the effect of the ITZ thickness in a small-size beam (80×320 mm²) of gravel concrete ($d_{50} = 2$ mm and $d_{max} = 8$ mm). The thickness t_b was 0.05 mm, 0.25 mm and 0.75 mm, respectively ($\rho = 45\%$, $l_c = 1.5$ mm).

Since ITZ is the weakest phase, the beam strength obviously decreases with increasing ITZ thickness. The width of a localized zone is not affected by t_b .

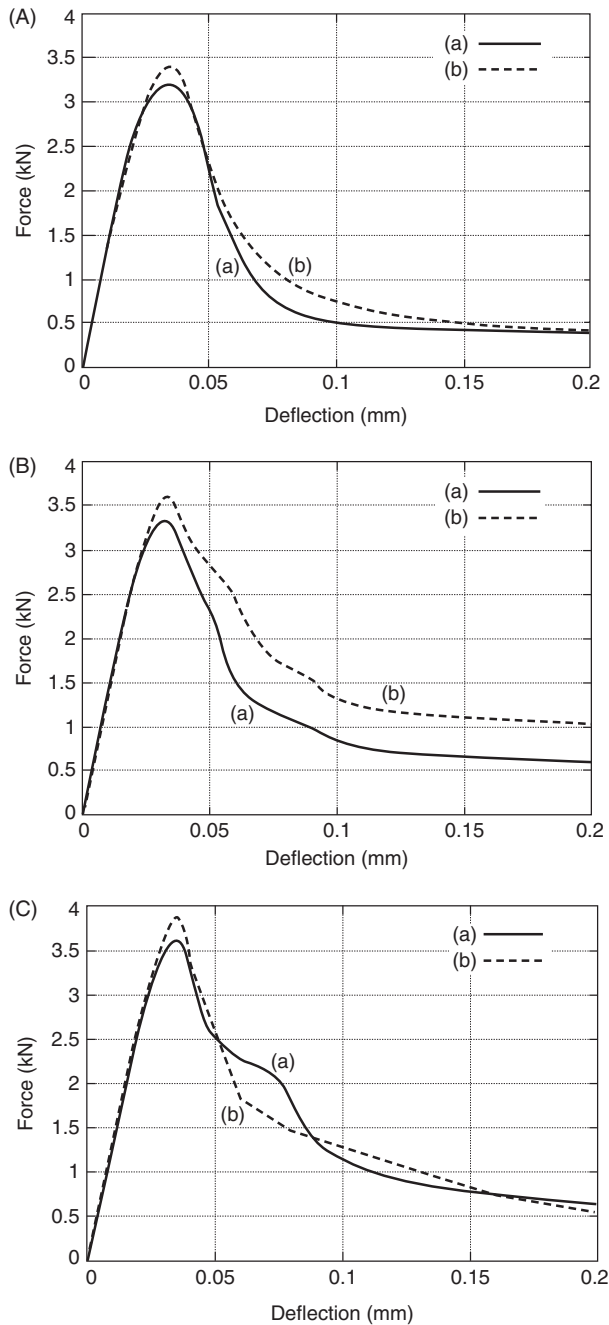


3.6 Calculated distribution of non-local strain measure for various concrete mixes and random distributions of circular aggregate ('a', 'b', 'c') in small-size beam $80 \times 320 \text{ mm}^2$ ($l_c = 1.5 \text{ mm}$, $\rho = 45\%$, $t_b = 0.25 \text{ mm}$) corresponding to load-deflection curves of Fig. 3.5: (A) sand concrete ($d_{50} = 0.5 \text{ mm}$, $d_{\max} = 3 \text{ mm}$), (B) gravel concrete ($d_{50} = 2 \text{ mm}$, $d_{\max} = 8 \text{ mm}$).

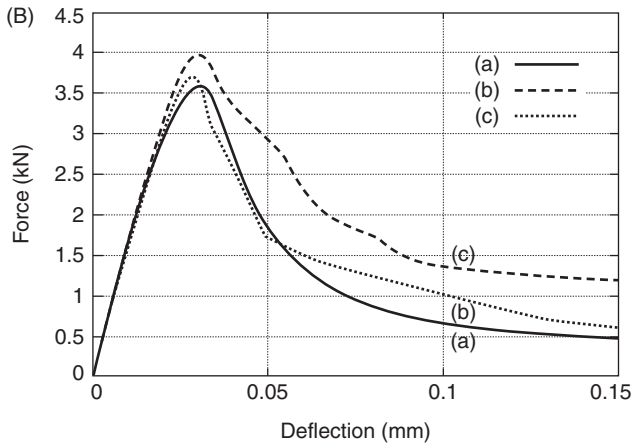
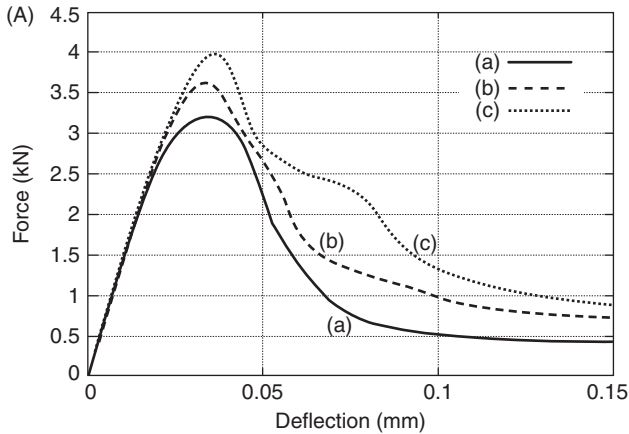
3.3.7 Effect of mesoscopic characteristic length

The effect of a characteristic length of micro-structure on the load-deflection diagram and strain localization is shown in Figs 3.18–3.21, using the same stochastic distribution of aggregate. Figures 3.18 and 3.20 demonstrate the influence of l_c on the evolution of load-deflection curves for two different mixes: sand concrete ($d_{50} = 0.5 \text{ mm}$ and $d_{\max} = 3 \text{ mm}$) with aggregate volume $\rho = 30\%$ and gravel concrete ($d_{50} = 2 \text{ mm}$ and $d_{\max} = 8 \text{ mm}$) with aggregate volume $\rho = 45\%$, respectively. In turn, Figs 3.19 and 3.21 present the distribution of a non-local softening strain measure above the notch for various l_c changing between 0.1 mm and 5.0 mm .

With increasing characteristic length, both beam strength and width of a localized zone obviously increase. The material softening decreases and material becomes more ductile. A pronounced deterministic size effect occurs. A localized zone propagating in a cement matrix between aggregate grains is strongly curved at $l_c = 0.1\text{--}2.5 \text{ mm}$, whereas it becomes straighter at



3.7 Calculated load-deflection curves for different circular aggregate densities (small-size beam $80 \times 320 \text{ mm}^2$, $l_c = 1.5 \text{ mm}$, $t_p = 0.25 \text{ mm}$): (A) $\rho = 30\%$, (B) $\rho = 45\%$, (C) $\rho = 60\%$, (a) sand concrete ($d_{50} = 0.5 \text{ mm}$, $d_{\max} = 3 \text{ mm}$), (b) gravel concrete ($d_{50} = 2 \text{ mm}$, $d_{\max} = 8 \text{ mm}$).

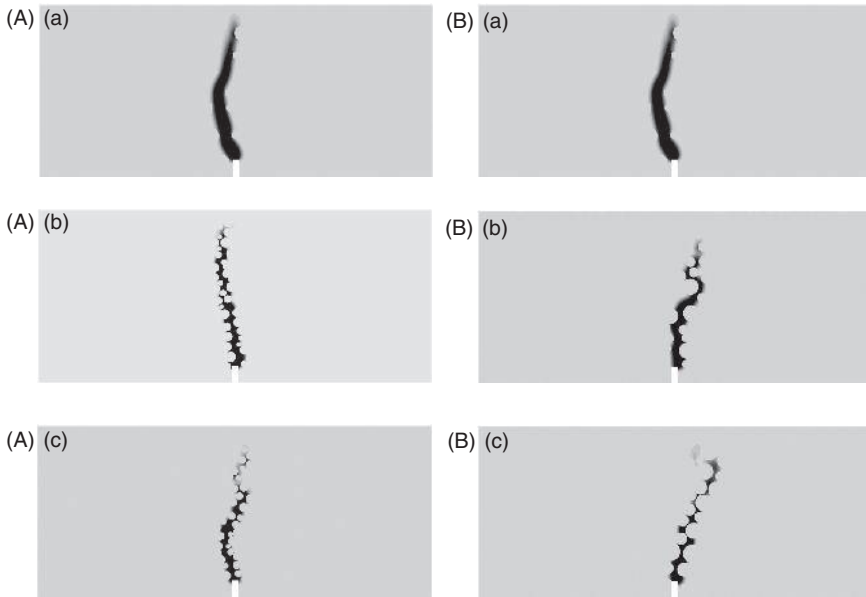


3.8 Calculated load-deflection curves for different circular aggregate density: (a) $\rho = 30\%$, (b) $\rho = 45\%$, (c) $\rho = 60\%$ (small-size beam $80 \times 320 \text{ mm}^2$, $l_c = 1.5 \text{ mm}$, $t_b = 0.25 \text{ mm}$): (A) sand concrete ($d_{50} = 0.5 \text{ mm}$, $d_{\max} = 3 \text{ mm}$), (B) gravel concrete ($d_{50} = 2 \text{ mm}$, $d_{\max} = 8 \text{ mm}$).

$l_c > 2.5 \text{ mm}$. The width of a localized zone is: $w_c = 4.5\text{--}6.0 \text{ mm} = (3\text{--}4) \times l_c$ with $l_c = 1.5 \text{ mm}$ and $\rho = 30\text{--}45\%$ ($l_c = 0.5 \times d_{\max}$ for sand concrete and $l_c = 0.2 \times d_{\max}$ for gravel concrete).

3.3.8 Effect of beam size

The effect of the beam size is presented in Figs 3.22 and 3.23. Figure 3.22 shows the numerical results of the nominal strength $\sigma_n = 1.5Pl / (bD^2)$ versus the normalized deflection u/D for three different concrete beams compared to tests by Le Bellégo *et al.* (2003). The following number of triangular



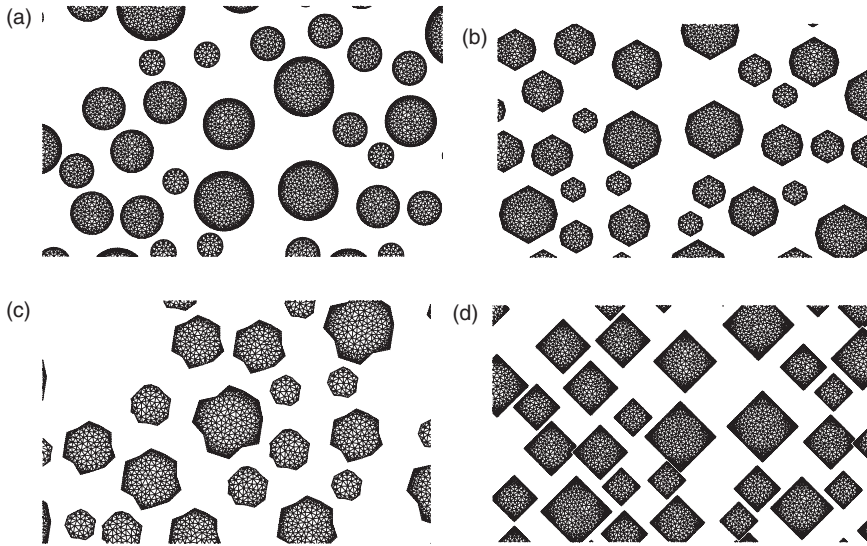
3.9 Calculated distribution of non-local strain measure for different circular aggregate densities (small-size beam $80 \times 320 \text{ mm}^2$, $l_c = 1.5 \text{ mm}$, $t_b = 0.25 \text{ mm}$): (a) $\rho = 30\%$, (b) $\rho = 45\%$, (c) $\rho = 60\%$, (A) sand concrete ($d_{50} = 0.5 \text{ mm}$, $d_{\max} = 3 \text{ mm}$), (B) gravel concrete ($d_{50} = 2 \text{ mm}$, $d_{\max} = 8 \text{ mm}$).

finite elements was used: 110 000 (small beam), 420 000 medium beam and 1 600 000 (large beam). In turn, Fig. 3.23 presents the distribution of a non-local softening strain measure in beams. The calculations were carried out with gravel concrete ($d_{\max} = 8 \text{ mm}$), circular aggregate volume of $\rho = 30\%$, bond thickness $t_b = 0.25 \text{ mm}$, and characteristic length of $l_c = 1.5 \text{ mm}$.

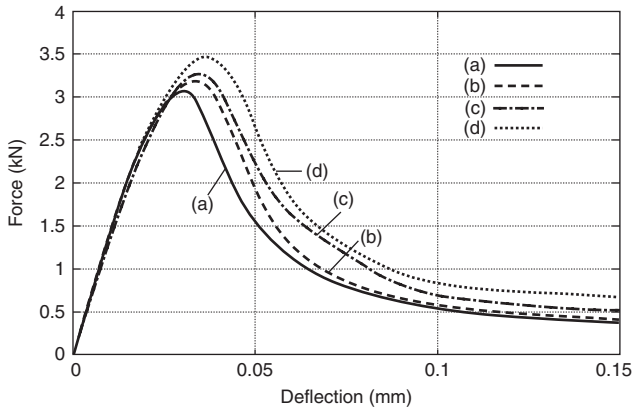
The numerical results of Figs 3.22 and 3.23 are in sufficient agreement with tests by Le Bellégo *et al.* (2003). The deterministic size effect is realistically modelled in calculations. The width of a localized zone above the notch at $u/D = 0.5$ is 6 mm ($\rho = 30\%$) for all beam sizes. A localized zone propagating between aggregate particles is always strongly curved.

Figure 3.24 shows a comparison between the measured and calculated size effect for concrete beams. In addition, the results of a deterministic size effect law by Bažant (Bažant and Planas 1998; Bažant 2004) are enclosed (which is valid for structures with pre-existing notches) wherein the nominal strength is calculated as

$$\sigma_n = \frac{Bf_t}{\sqrt{1 + (D/D_0)}}, \quad [3.9]$$

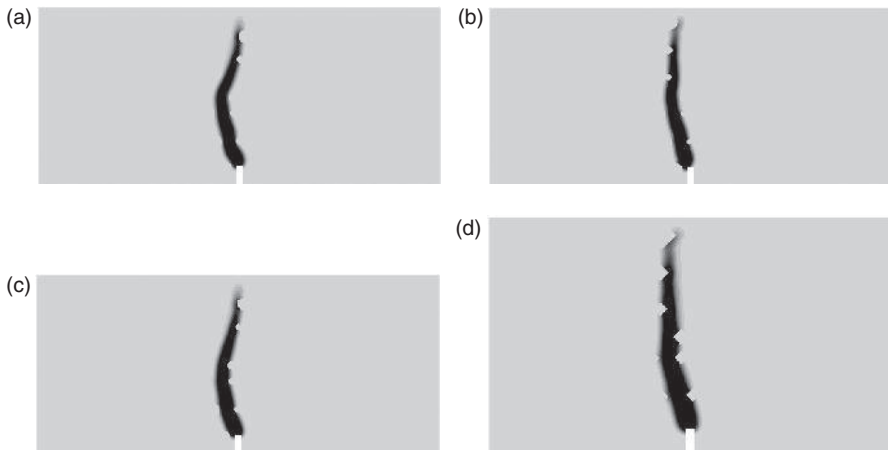


3.10 Aggregate shape assumed in calculations: (a) circular, (b) octagonal, (c) irregular (angular), (d) rhomboidal.

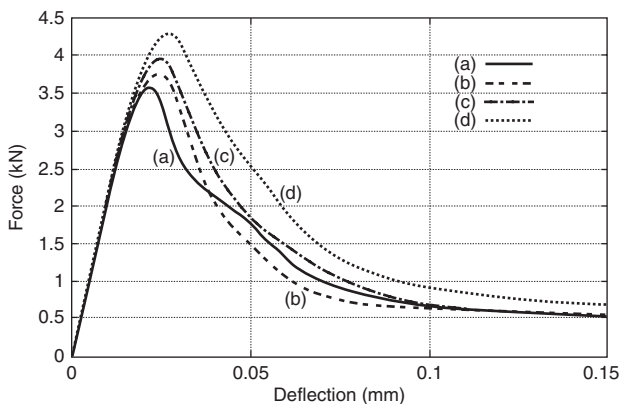


3.11 Calculated load-deflection curves for different aggregate shape of Fig. 3.10: (a) circular, (b) octagonal, (c) irregular (angular), (d) rhomboidal (small-size beam $80 \times 320 \text{ mm}^2$, $l_c = 1.5 \text{ mm}$, $\rho = 45\%$, $t_b = 0.25 \text{ mm}$, gravel concrete with $d_{50} = 2 \text{ mm}$ and $d_{\max} = 8 \text{ mm}$).

where f_t = tensile strength of concrete, B = dimensionless parameter depending upon the structure geometry and crack, D = characteristic beam size (beam height) and D_0 = size dependent parameter (called transitional size). To determine the parameters B and D_0 , a non-linear least-square



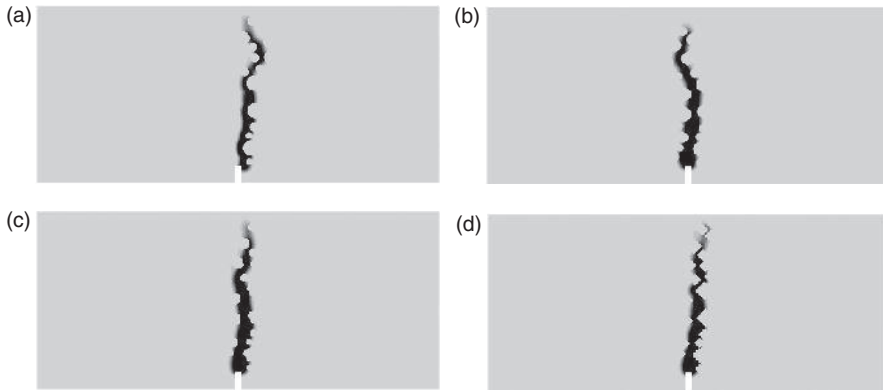
3.12 Calculated distribution of non-local strain measure for different aggregate shape of Fig. 3.10: (a) circular, (b) octagonal, (c) irregular (angular), (d) rhomboidal (small-size beam $80 \times 320 \text{ mm}^2$, $l_c = 1.5 \text{ mm}$, $\rho = 30\%$, $t_b = 0.25 \text{ mm}$, gravel concrete with $d_{50} = 2 \text{ mm}$ and $d_{\max} = 8 \text{ mm}$).



3.13 Calculated load-deflection curves for different aggregate shape of Fig. 3.10: (a) circular, (b) octagonal, (c) irregular (angular), (d) rhomboidal (small-size beam $80 \times 320 \text{ mm}^2$, $l_c = 1.5 \text{ mm}$, $\rho = 30\%$, $t_b = 0.25 \text{ mm}$, gravel concrete with $d_{50} = 2 \text{ mm}$ and $d_{\max} = 8 \text{ mm}$).

Marquardt-Lavemberg's algorithm was used. The experimental and theoretical beam strength show strong size dependence. The experimental and numerical results match well the size effect law by Bažant (Bažant and Planas 1998).

The width and shape of a calculated localized zone is in accordance with our experiments using a DIC (Skarżyński *et al.* 2011), which is a way



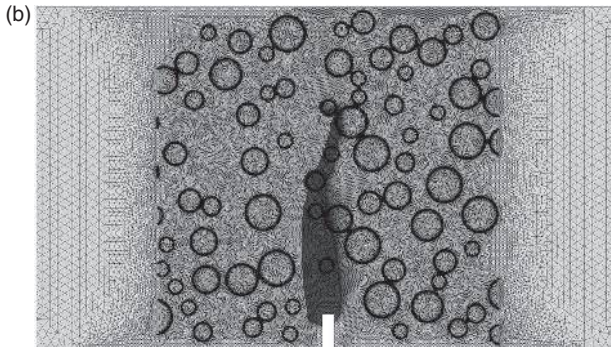
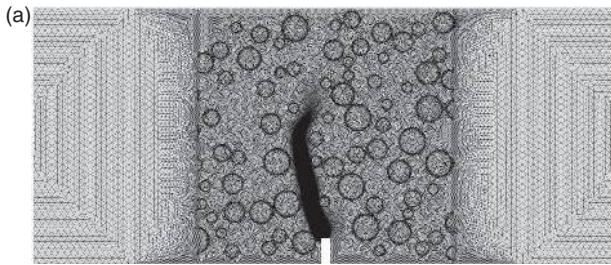
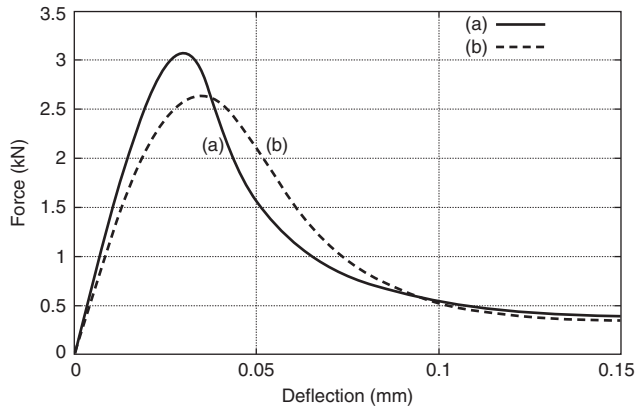
3.14 Calculated distribution of non-local strain measure for different aggregate shape of Fig. 3.10: (a) circular, (b) octagonal, (c) irregular (angular), (d) rhomboidal (small-size beam $80 \times 320 \text{ mm}^2$, $l_c = 1.5 \text{ mm}$, $\rho = 45\%$, $t_b = 0.25 \text{ mm}$, gravel concrete with $d_{50} = 2 \text{ mm}$ and $d_{\max} = 8 \text{ mm}$).

to visualize surface deformations by successive post-processing of digital images taken at constant time increments with a professional digital camera (White *et al.* 2003). Figure 3.25 shows the formation of a localized zone on the surface of concrete beams above the notch using different concrete mixes from laboratory test. A localized zone occurred before the peak on the load-deflection diagram and was strongly curved. In some cases, it branched. The width of a localized zone increased during deformation due to concrete dilatancy (Fig. 3.26). The maximum measured width of a localized zone was equal to 3.5–5.5 mm. It did not depend upon the mix type and beam size for the assumed aggregate size distributions.

To summarize, the calculated width of a localized zone increases with decreasing aggregate volume and increasing characteristic length. It is not affected by the aggregate size, aggregate roughness, bond thickness and beam height.

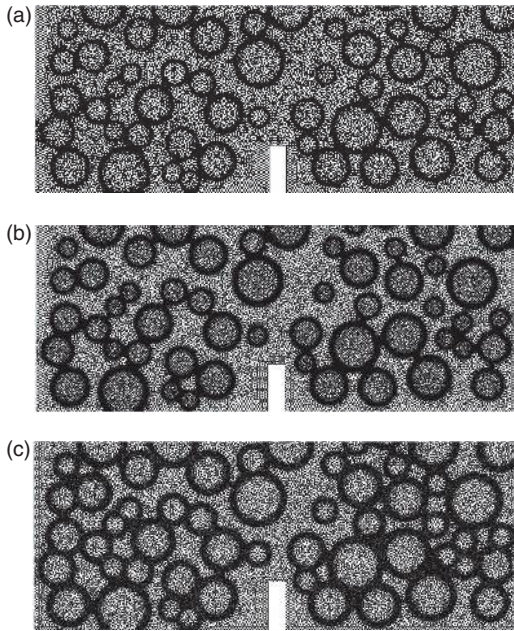
3.4 Behaviour of concrete elements under uniaxial tension

To analyse the existence of RVE under tension, a plane strain uniaxial tension test was carried out (Skarżyński and Tejchman 2012) (Fig. 3.27). The material constants for each phase are given in Table 3.2. The bond was assumed again to be the weakest component (Lilliu and van Mier 2003) and its width was 0.25 mm (Gitman *et al.* 2007). For the sake of simplicity, the aggregate was assumed to be circular. The number of triangular finite elements changed between 4000 (the smallest specimen) and 100 000 (the largest specimen). The size of the triangular elements was: $s_a = 0.5 \text{ mm}$



3.15 Effect of different aggregate stiffness in FE calculations: load-deflection curve and distribution of non-local strain measure close to notch: (a) usual circular aggregate, (b) weak circular aggregate (small-size beam $80 \times 320 \text{ mm}^2$, $l_c = 1.5 \text{ mm}$, $\rho = 45\%$, aggregate with $d_{50} = 2 \text{ mm}$ and $d_{\max} = 8 \text{ mm}$).

(aggregate), $s_{cm} = 0.25 \text{ mm}$ (cement matrix) and $s_{iz} = 0.1 \text{ mm}$ (interface). The test was performed with a quadratic concrete specimen representing a unit cell with periodicity of boundary conditions and material periodicity (Gitman *et al.* 2007; Skarżyński and Tejchman 2010).



3.16 FE-meshes with different bond thickness t_b assumed in calculations: (a) $t_b = 0.05$ mm, (b) $t_b = 0.25$ mm and (c) $t_b = 0.75$ mm (aggregate volume $\rho = 45\%$).

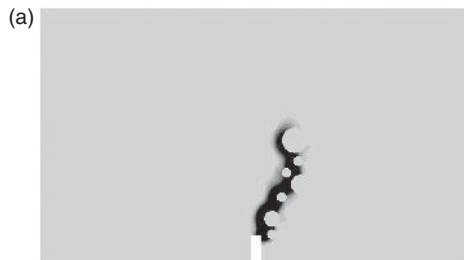
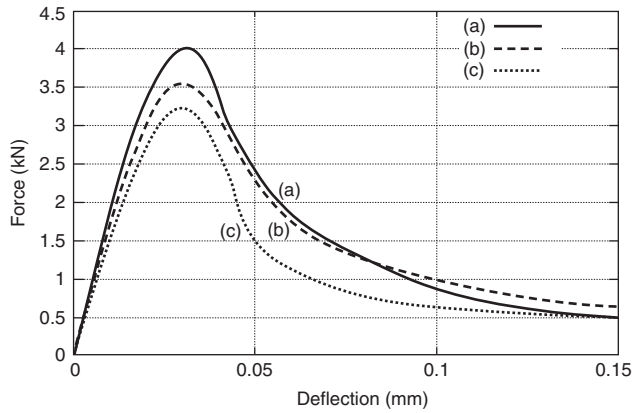
3.4.1 Numerical implementation

The unit cells of six different sizes were investigated $b \times h$: 5×5 mm², 10×10 mm², 15×15 mm², 20×20 mm², 25×25 mm² and 30×30 mm², respectively. For each specimen, three different stochastic realizations were performed (Fig. 3.28) with the aggregate volume of $\rho = 30\%$ (the results for $\rho = 45\%$ and $\rho = 60\%$ showed the same trend). A characteristic length of micro-structure was again $l_c = 1.5$ mm (see Section 3.3.6). Thus, the maximum finite element size in three different concrete phases was not greater than $3 \times l_c$ to obtain mesh-objective results (Bobiński and Tejchman 2004; Marzec *et al.* 2007).

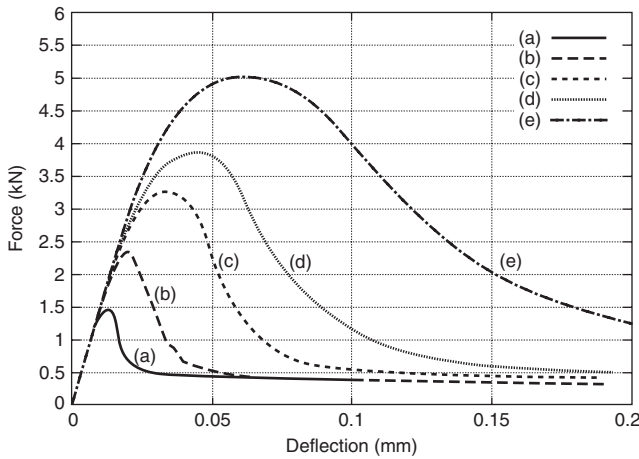
3.4.2 Standard averaging approach

The standard averaging is performed over the entire specimen domain. The homogenized stress and strain are defined in two dimensions as

$$\langle \sigma \rangle = \frac{f_y^{\text{int}}}{b} \quad \langle \sigma \rangle = \frac{f_y^{\text{int}}}{b} \quad \text{and} \quad \langle \varepsilon \rangle = \frac{u}{h}, \quad [3.10]$$



3.17 Effect of different bond thickness t_b in FE calculations: load-deflection curve and distribution of non-local strain measure close to notch: (a) $t_b = 0.05$ mm, (b) $t_b = 0.25$ mm, (c) $t_b = 0.75$ mm (small-size beam 80×320 mm², $l_c = 1.5$ mm, $\rho = 45\%$, gravel concrete with $d_{50} = 2$ mm and $d_{\max} = 8$ mm).

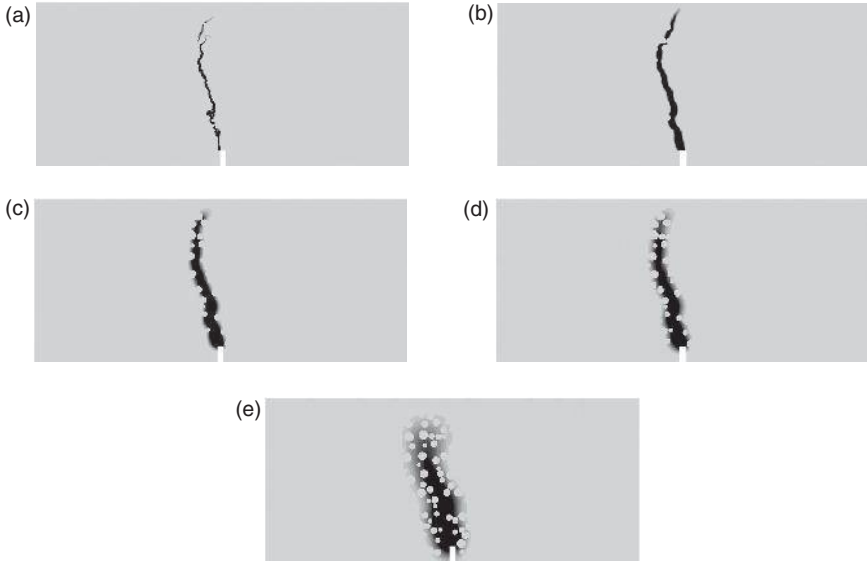


3.18 Calculated load-deflection curves for different characteristic lengths: (a) $l_c = 0.1$ mm, (b) $l_c = 0.5$ mm, (c) $l_c = 1.5$ mm, (d) $l_c = 2.5$ mm, (e) $l_c = 5.0$ mm (small-size beam 80×320 mm², sand concrete $d_{s0} = 0.5$ mm, $d_{\max} = 3$ mm, circular aggregate volume $\rho = 30\%$, bond width $t_b = 0.25$ mm).

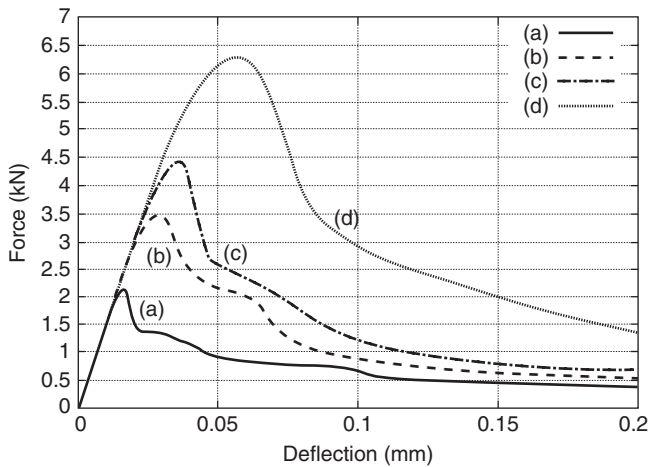
where f_y^{int} denotes the sum of all vertical nodal forces in the 'y' direction along the top edge of the specimen (Fig. 3.27), u is the prescribed vertical displacement in the 'y' direction and b and h are the width and height of the specimen.

Figure 3.29 presents the stress-strain relationships for various cell sizes and two random aggregate distributions. In the first case, the aggregate distribution was similar, and in the second case it was random in different unit cells. The results show that the stress-strain curves are only the same in an elastic regime independently of the specimen size, aggregate volume and aggregate distribution. However, they are completely different at the peak and in a softening regime. An increase of the specimen size causes a strength decrease and an increase of material brittleness (softening rate) (Fig. 3.29). The differences in the evolution of stress-strain curves in a softening regime are caused by strain localization (in the form of a curved localized zone propagating between aggregate particles (Figs 3.30 and 3.31), contributing to a loss of material homogeneity (due to the fact that strain localization is not scaled with increasing specimen size). The width of a calculated localized zone is approximately $w_c = 3$ mm = $2 \times l_c = 12 \times s_{cm}$ (unit cell 5×5 mm²), $w_c = 5$ mm = $3.33 \times l_c = 20 \times s_{cm}$ (unit cell 10×10 mm²) and $w_c = 6$ mm = $4 \times l_c = 24 \times s_{cm}$ (unit cells larger than 10×10 mm²).

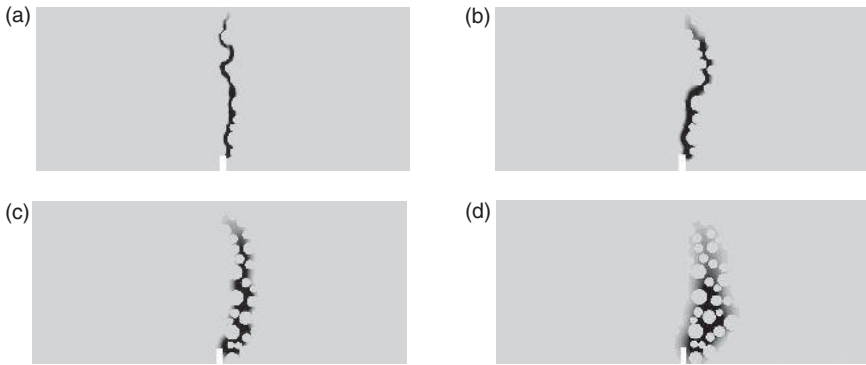
Figure 3.32 presents the expectation value and standard deviation of the tensile fracture energy G_f versus the specimen height h for three different realizations. The fracture energy G_f was calculated as the area under the stress-strain curves g_f multiplied by the width of a localized zone w_c .



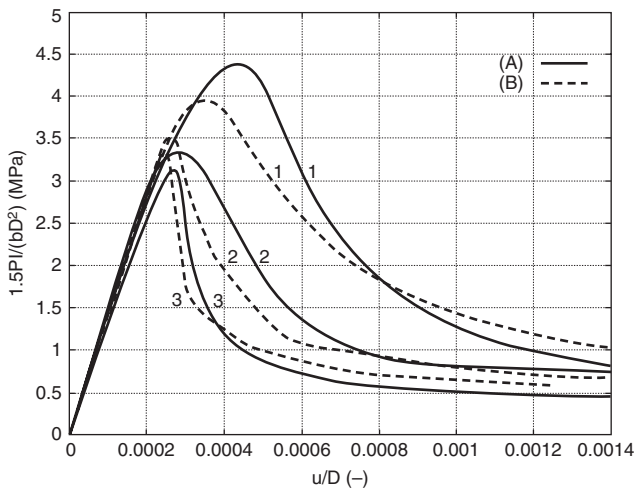
3.19 Calculated distribution of non-local strain measure for different characteristic lengths: (a) $l_c = 0.1$ mm, (b) $l_c = 0.5$ mm, (c) $l_c = 1.5$ mm, (d) $l_c = 2.5$ mm, (e) $l_c = 5.0$ mm (small-size beam 80×320 mm², sand concrete $d_{50} = 0.5$ mm, $d_{\max} = 3$ mm, circular aggregate volume $\rho = 30\%$, bond width $t_b = 0.25$ mm).



3.20 Calculated load-deflection curves for different characteristic lengths: (a) $l_c = 0.5$ mm, (b) $l_c = 1.5$ mm, (c) $l_c = 2.5$ mm, (d) $l_c = 5.0$ mm (small-size beam 80×320 mm², gravel concrete $d_{50} = 2$ mm, $d_{\max} = 8$ mm, circular aggregate volume $\rho = 45\%$, bond width $t_b = 0.25$ mm).



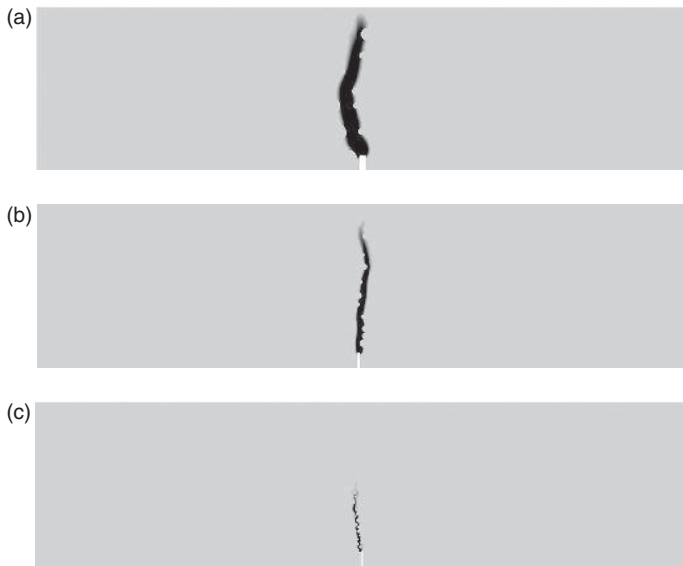
3.21 Calculated distribution of non-local strain measure for different characteristic lengths: (a) $l_c = 0.5$ mm, (b) $l_c = 1.5$ mm, (c) $l_c = 2.5$ mm, (d) $l_c = 5.0$ mm (small-size beam 80×320 mm², gravel concrete $d_{50} = 2$ mm, $d_{\max} = 8$ mm, circular aggregate volume $\rho = 45\%$, bond width $t_b = 0.25$ mm).



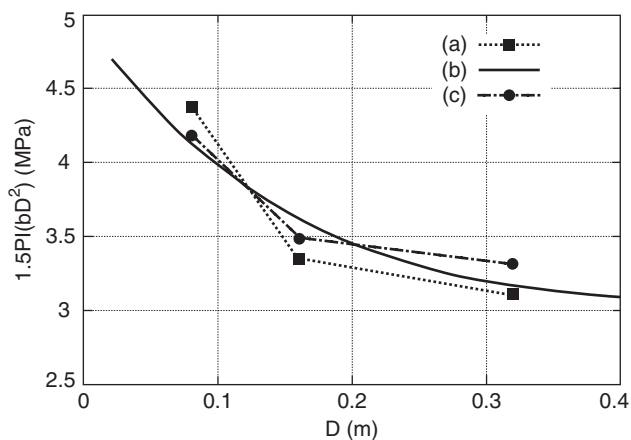
3.22 Calculated nominal strength $1.5Pl/(bD^2)$ vs normalized beam deflection u/D (u , beam deflection, D , beam height): (A) FE-results, (B) experiments by Le Bellégo *et al.* (2003): (1) small-size beam, (2) medium-size beam, (3) large-size beam (three-phase random heterogeneous material close to notch, $\rho = 30\%$, $l_c = 1.5$ mm, $t_b = 0.25$ mm).

$$G_f = g_f \times w_c = \left(\int_{a_1}^{a_2} \langle \sigma > d < \varepsilon > \right) \times w_c. \quad [3.11]$$

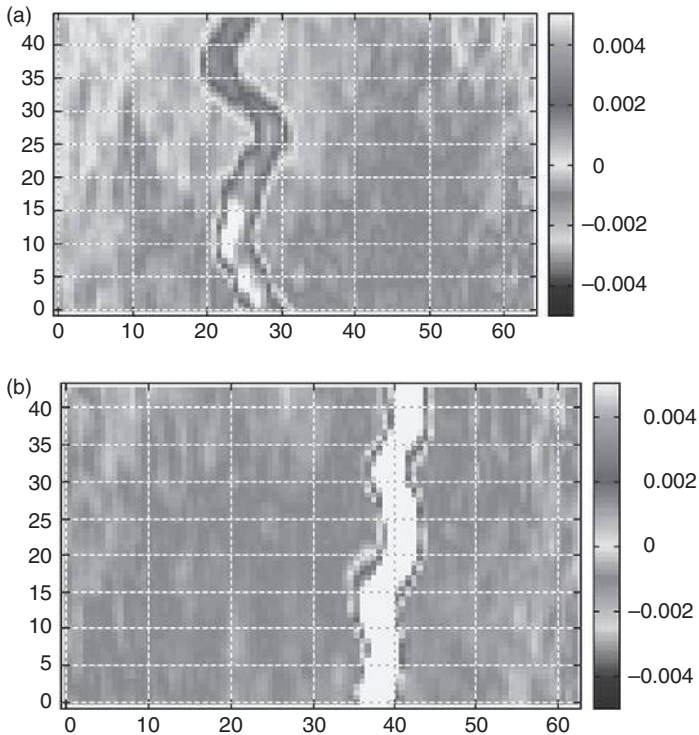
The integration limits ' a_1 ' and ' a_2 ' are 0 and 0.001, respectively (Fig. 3.29). The fracture energy decreases with increasing specimen size without reaching



3.23 Calculated distribution of non-local strain measure above notch from numerical calculations (at $u/D = 0.5$): (a) small-size beam, (b) medium-size beam, (c) large-size beam (random heterogeneous three-phase material close to notch, $\rho = 30\%$, $l_c = 1.5$ mm, $t_b = 0.25$ mm).



3.24 Calculated and measured size effect in nominal strength $1.5Pl/(bD^2)$ versus beam height D for concrete beams of a similar geometry (small-, medium- and large-size beam): (a) our FE-calculations (heterogeneous material close to notch), (b) size effect law by Bažant (2004), (c) experiments by Le Bellégo *et al.* (2003).

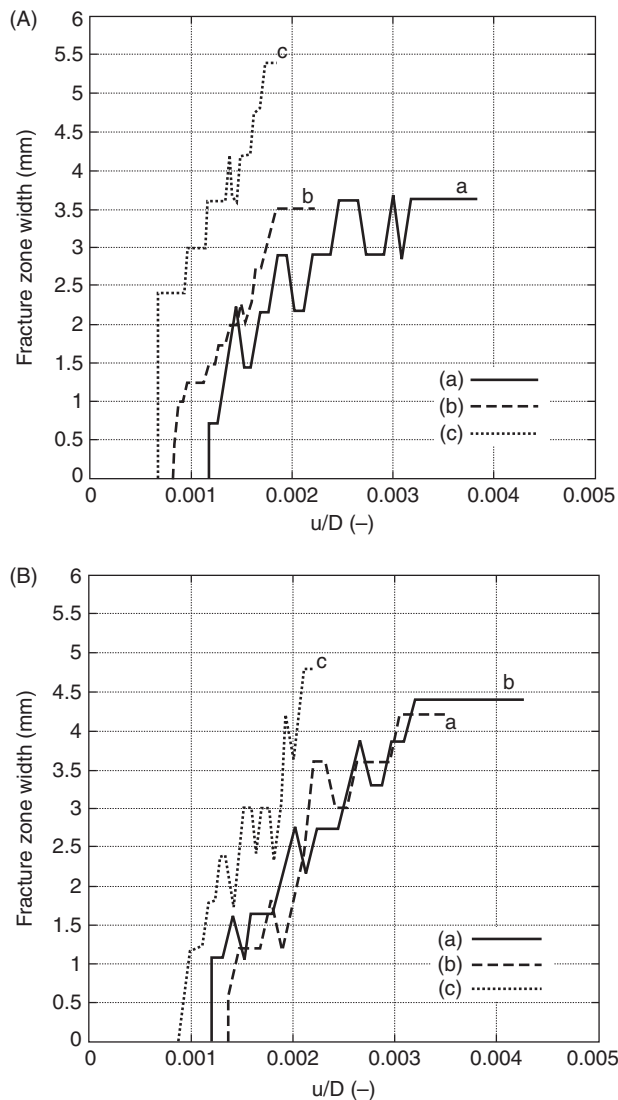


3.25 Formation of localized zone directly above notch in experiments using DIC: (a) gravel concrete medium-size beam $160 \times 640 \text{ mm}^2$, (b) sand concrete medium-size beam $160 \times 640 \text{ mm}^2$ (vertical and horizontal axes denote coordinates in (mm), colour scales denote strain intensity) (Skarżyński *et al.*, 2011).

an asymptote, i.e. the size dependence of RVE exists (since a localized zone does not scale with the specimen size). Thus, RVE cannot be found for softening materials and a standard averaging approach cannot be used in homogenization-based multi-scale models.

3.4.3 Localized zone averaging approach

Recently, the existence of RVE for softening materials was proved (based on Hill's averaging principle) for cohesive and adhesive failure by deriving a traction-separation law (for a macro crack) instead of a stress-strain relation from microscopic stresses and strains (Verhoosel *et al.* 2010a, 2010b). This was indicated by the uniqueness (regardless of a micro-sample size) of a macro-traction separation law, which was obtained by averaging responses

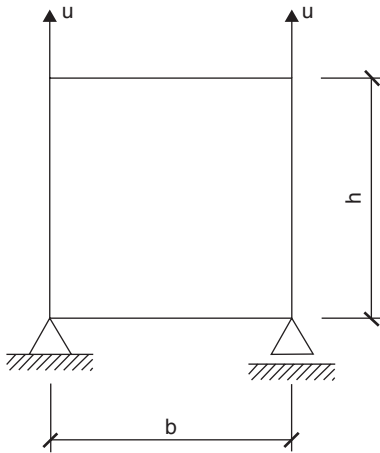


3.26 Evolution of width of localized zone in experiments using DIC vs normalized beam deflection u/D (u , beam deflection and D , beam height): (A) gravel concrete, (B) sand concrete, (a) small-size beam $80 \times 320 \text{ mm}^2$, (b) medium-size beam $160 \times 640 \text{ mm}^2$, (c) large-size beam $320 \times 1280 \text{ mm}^2$ (Skarżyński *et al.*, 2011).

along propagating micro-discrete cracks. Prompted by this approach and the fact that a localized zone does not scale with the micro-specimen size, Nguyen *et al.* (2010) proposed an approach whereby homogenized stress and strain were averaged over a localized strain domain in softening materials

Table 3.2 Material parameters assumed FE calculations of concrete elements under uniaxial tension at meso-scale

Material parameters	Inclusions	Cement matrix	Bond
Modulus of elasticity E (GPa)	30	25	20
Poisson's ratio ν (-)	0.2	0.2	0.2
Crack initiation strain κ_o (-)	0.5	8×10^{-5}	5×10^{-5}
Residual stress level α (-)	0.95	0.95	0.95
Slope of softening β (-)	200	200	200



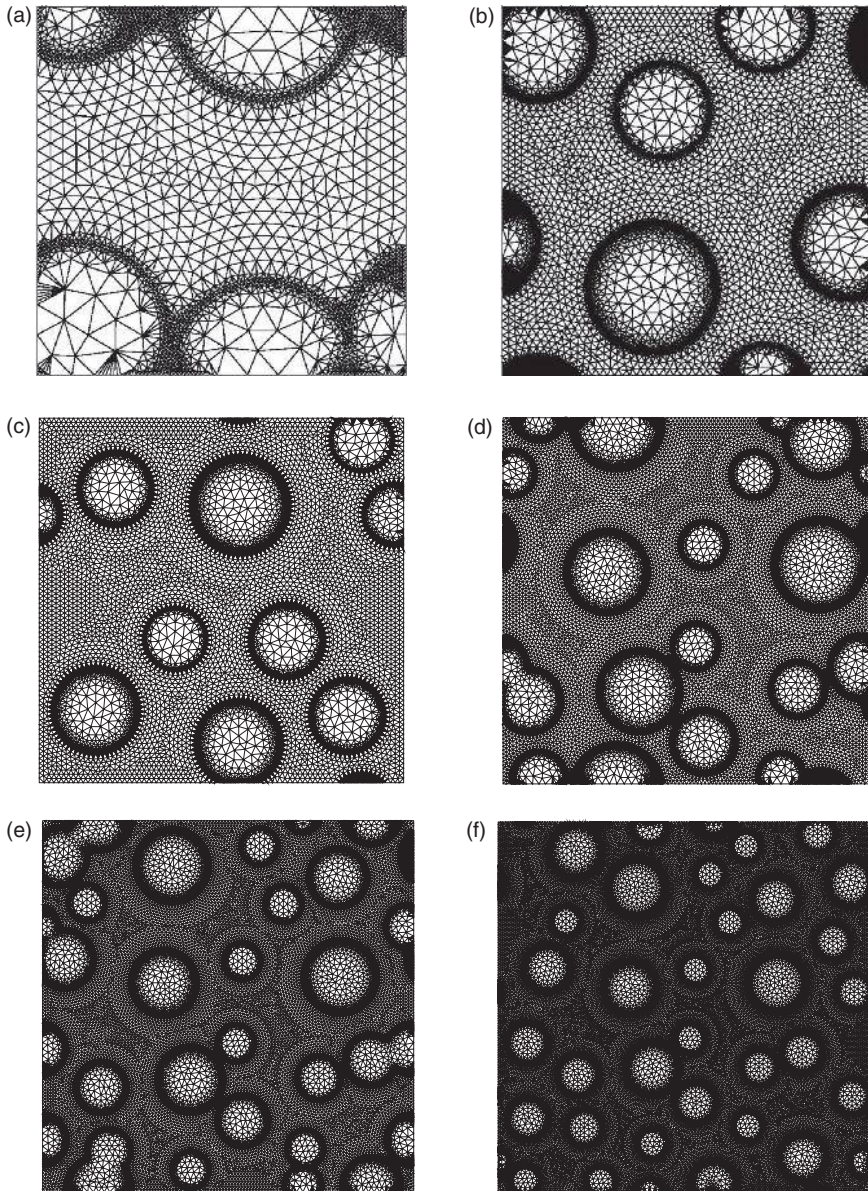
3.27 Uniaxial tension test (schematically).

(which is small compared with the specimen size) rather than over the entire specimen. We have used this method in this paper. In this approach, the homogenized stress and strain are

$$\langle \sigma \rangle = \frac{1}{A_z} \int_{A_z} \sigma_m dA_z \quad \text{and} \quad \langle \varepsilon \rangle = \frac{1}{A_z} \int_{A_z} \varepsilon_m dA_z, \quad [3.12]$$

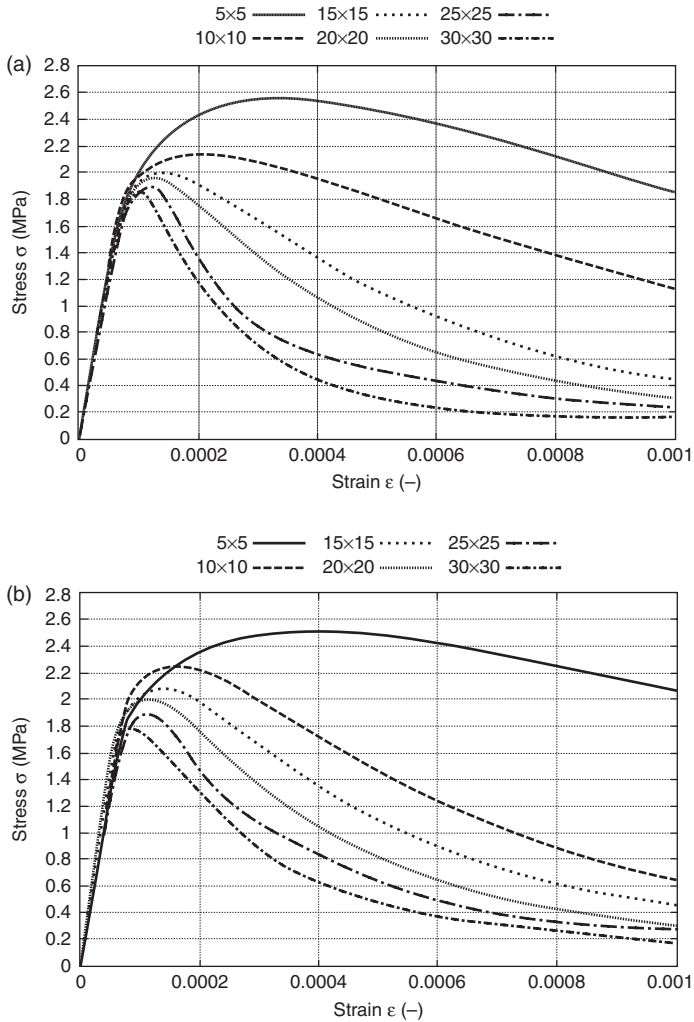
where A_z is the localized zone area and σ_m and ε_m are the meso-stress and meso-strain, respectively. The localized zone area A_z is determined on the basis of a distribution of the non-local equivalent strain measure $\bar{\varepsilon}$ (Equation [3.6]). As the cut-off value $\bar{\varepsilon}_{\min} = 0.005$ is always assumed at the maximum mid-point value, usually equal to $\bar{\varepsilon}_{\max} = 0.007-0.011$. Thus, a linear material behaviour is simply swept out (which causes the standard stress-strain diagrams to be specimen-size dependent), and an active material plastic response is solely taken into account.

Figure 3.33 presents the stress-strain relationships for various specimen sizes and two random aggregate distributions for the calculated localized



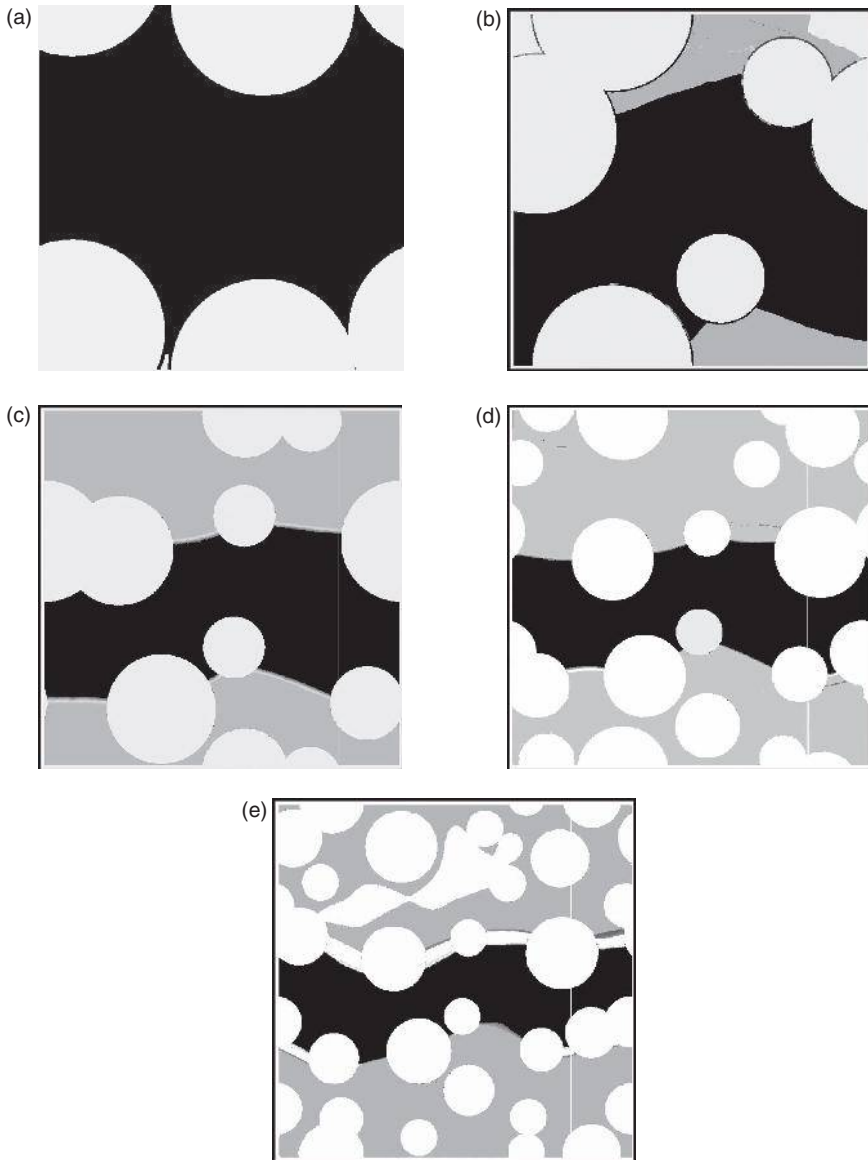
3.28 Concrete specimens of different size: (a) $5 \times 5 \text{ mm}^2$, (b) $10 \times 10 \text{ mm}^2$, (c) $15 \times 15 \text{ mm}^2$, (d) $20 \times 20 \text{ mm}^2$, (e) $25 \times 25 \text{ mm}^2$, (f) $30 \times 30 \text{ mm}^2$ (aggregate volume $p = 30\%$).

zones of Figs 3.30 and 3.31. These stress–strain curves in a softening regime (for the unit cells larger than $10 \times 10 \text{ mm}^2$) are in very good accordance with respect to their shape. In this case, the statistically representative volume element exists and is equal to $15 \times 15 \text{ mm}^2$.

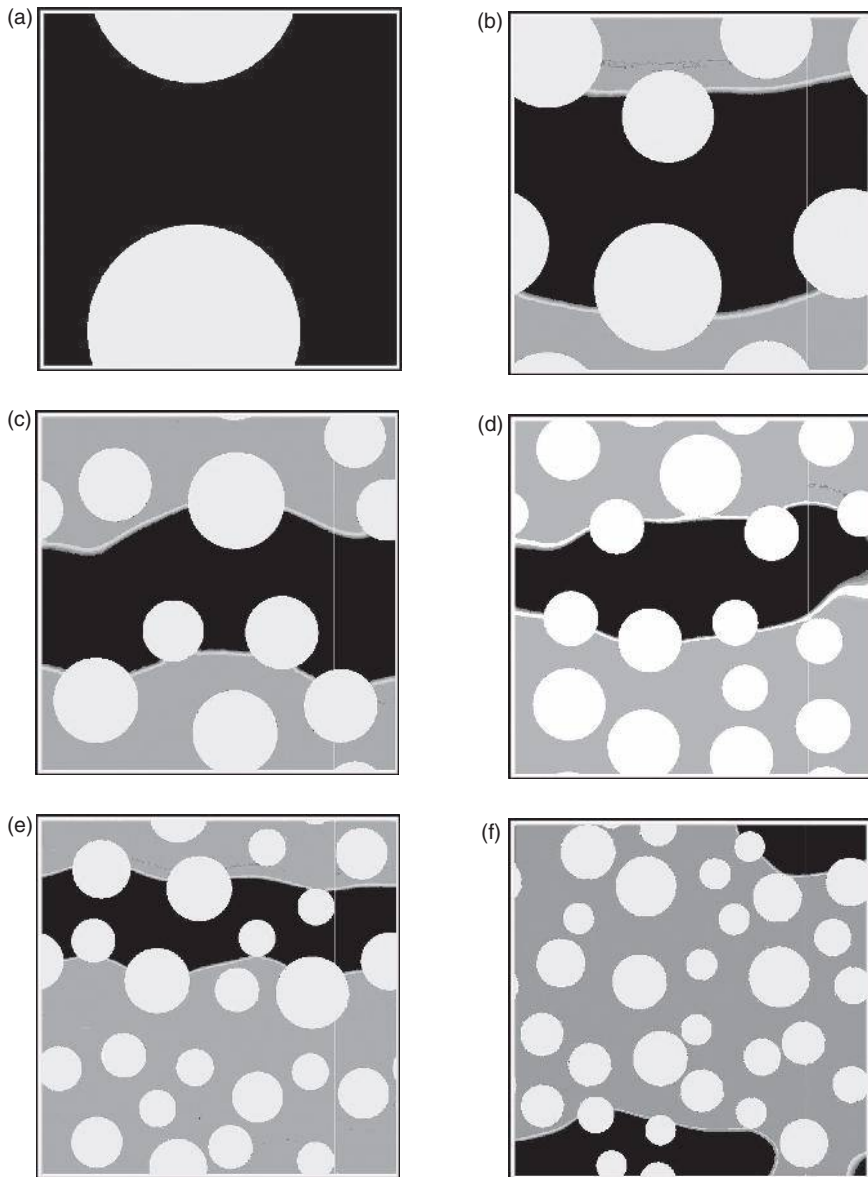


3.29 Stress–strain curves for various sizes of concrete specimens and two different random distributions of aggregate (a) and (b) using standard averaging procedure (characteristic length $l_c = 1.5$ mm, aggregate volume $\rho = 30\%$).

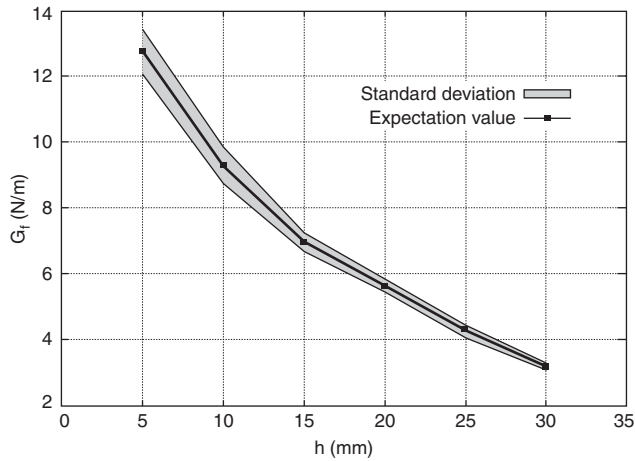
Figure 3.34 presents the expectation value and standard deviation of the tensile fracture energy G_f versus the specimen height h for three different realizations. The integration limits were $a_1 = 0$ and $a_2 = 0.004$ (Equation [3.11]). The fracture energy decreases with increasing specimen size, approaching an asymptote when the cell size is 15×15 mm². Thus, the obtained homogenized stress–strain relationships are objective with respect to the micro-sample size. RVE does not represent the entire material in its classical meaning, but the material in a localized zone (an important observation/conclusion).



3.30 Distribution of non-local softening strain measure for various specimen sizes and stress-strain curves of Fig. 3.29a using standard averaging procedure (characteristic length $l_c = 1.5$ mm, aggregate volume $\rho = 30\%$).



3.31 Distribution of non-local softening strain measure for various specimen sizes and stress–strain curves of Fig. 3.29b using standard averaging procedure (characteristic length $l_c = 1.5$ mm, aggregate volume $\rho = 30\%$).



3.32 Expected value and standard deviation of tensile fracture energy G_f vs specimen height h using standard averaging (aggregate volume $\rho = 30\%$).

3.4.4 Varying characteristic length approach

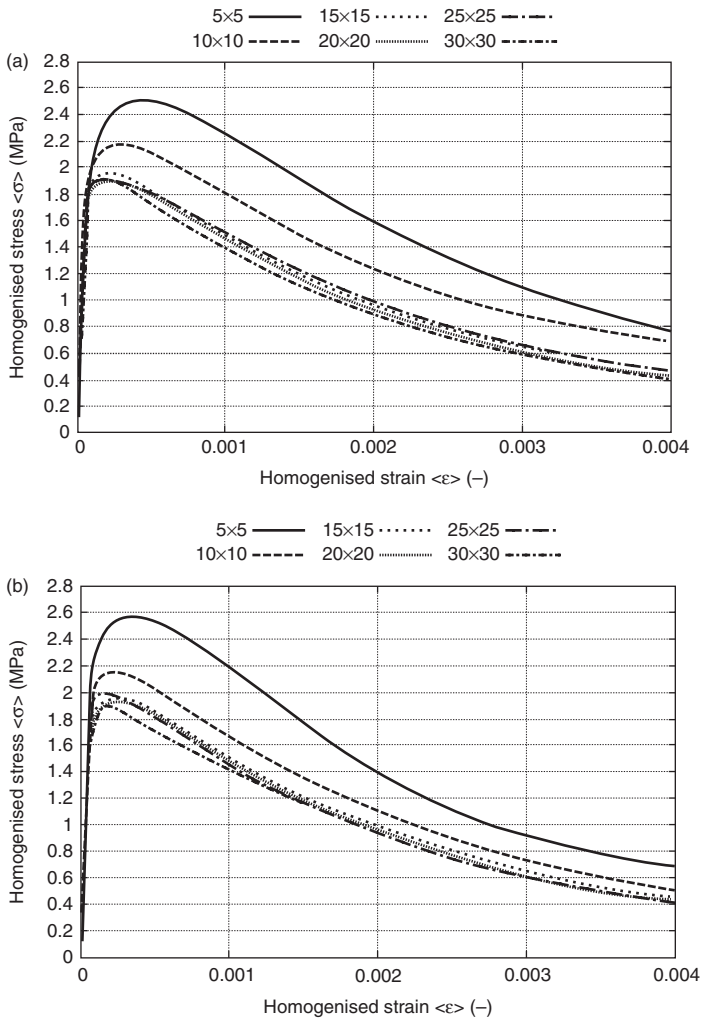
With increasing characteristic length, both the specimen strength and width of a localized zone increase. On the other hand, softening decreases them, and material behaviour is more ductile (Skarżyński and Tejchman 2009). Taking these two facts into account, a varying characteristic length related to the reference specimen size (assumed as $15 \times 15 \text{ mm}^2$ or $30 \times 30 \text{ mm}^2$) is introduced (to scale the width of a localized zone with varying specimen height) according to the formula:

$$l_c^v = l_c^{15 \times 15} \times \frac{h \text{ (mm)}}{15 \text{ (mm)}} \quad [3.13]$$

or

$$l_c^v = l_c^{30 \times 30} \times \frac{h \text{ (mm)}}{30 \text{ (mm)}}, \quad [3.14]$$

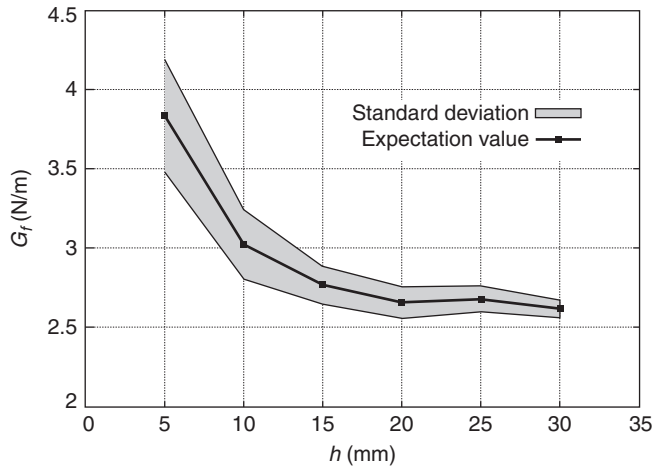
where $l_c^{15 \times 15} = l_c^{30 \times 30} = 1.5 \text{ mm}$ is a characteristic length for the reference unit cell $15 \times 15 \text{ mm}^2$ or $30 \times 30 \text{ mm}^2$ and h is the unit cell height. A unit cell larger than $30 \times 30 \text{ mm}^2$ can also be used (the width of a localized zone in the reference unit cell cannot be too strongly influenced by boundary conditions, as e.g. the cell size is smaller than $10 \times 10 \text{ mm}^2$). The characteristic length l_c^v is no



3.33 Stress–strain curves for various sizes of concrete specimens and two different random distributions of aggregate (a) and (b) using localized zone averaging procedure (characteristic length $l_c = 1.5$ mm, aggregate volume $\rho = 30\%$).

longer a physical parameter related to non-local interactions in the damaging material, but an artificial parameter adjusted to the specimen size.

The stress–strain relationships for various specimen sizes and various characteristic lengths are shown in Figs 3.35 and 3.36. A characteristic length varies between $l_c = 0.5$ mm for the unit cell 5×5 mm² and $l_c = 3.0$ mm for the unit cell 30×30 mm² according to Equation [3.13], and between $l_c = 0.25$ mm



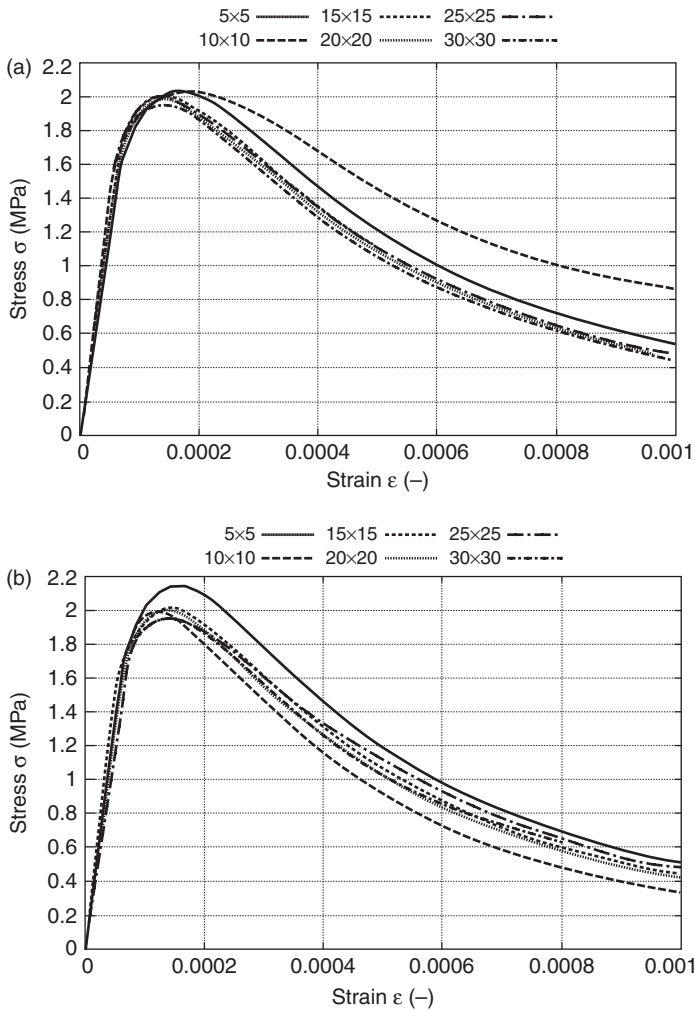
3.34 Expected value and standard deviation of tensile fracture energy G_f vs specimen height h using localized zone averaging (aggregate volume $\rho = 30\%$).

for the unit cell $5 \times 5 \text{ mm}^2$ and $l_c = 1.5 \text{ mm}$ for the unit cell $30 \times 30 \text{ mm}^2$ according to Equation [3.14]. The width of a calculated localized zone (for the reference unit cell $15 \times 15 \text{ mm}^2$) is approximately $w_c = 2 \text{ mm} = 4 \times l_c = 8 \times s_{cm}$ (cell $5 \times 5 \text{ mm}^2$), $w_c = 4 \text{ mm} = 4 \times l_c = 16 \times s_{cm}$ (cell $10 \times 10 \text{ mm}^2$), $w_c = 6 \text{ mm} = 4 \times l_c = 24 \times s_{cm}$ (cell $15 \times 15 \text{ mm}^2$), $w_c = 8 \text{ mm} = 4 \times l_c = 32 \times s_{cm}$ (cell $20 \times 20 \text{ mm}^2$), $w_c = 10 \text{ mm} = 4 \times l_c = 40 \times s_{cm}$ (cell $25 \times 25 \text{ mm}^2$) and $w_c = 12 \text{ mm} = 4 \times l_c = 48 \times s_{cm}$ (cell $30 \times 30 \text{ mm}^2$) (Figs 3.37 and 3.38). The width of a calculated localized zone (for the reference unit cell $30 \times 30 \text{ mm}^2$) is approximately $w_c = 1 \text{ mm} = 4 \times l_c = 4 \times s_{cm}$ (cell $5 \times 5 \text{ mm}^2$), $w_c = 2 \text{ mm} = 4 \times l_c = 8 \times s_{cm}$ (cell $10 \times 10 \text{ mm}^2$), $w_c = 3 \text{ mm} = 4 \times l_c = 12 \times s_{cm}$ (cell $15 \times 15 \text{ mm}^2$), $w_c = 4 \text{ mm} = 4 \times l_c = 16 \times s_{cm}$ (cell $20 \times 20 \text{ mm}^2$), $w_c = 5 \text{ mm} = 4 \times l_c = 20 \times s_{cm}$ (cell $25 \times 25 \text{ mm}^2$) and $w_c = 6 \text{ mm} = 4 \times l_c = 24 \times s_{cm}$ (cell $30 \times 30 \text{ mm}^2$) (Figs 3.39 and 3.40). A localized zone is scaled with the specimen size, and therefore the material does not lose its homogeneity and its response during softening is similar for the cell $15 \times 15 \text{ mm}^2$ and larger. Thus, the size of the RVE is again equal to $15 \times 15 \text{ mm}^2$.

The expectation value and standard deviation of the unit fracture energy $g_f = G_f/w_c$ versus the specimen height h are demonstrated in Fig.3.41. With increasing cell size, the value of g_f stabilizes for the unit cell of $15 \times 15 \text{ mm}^2$.

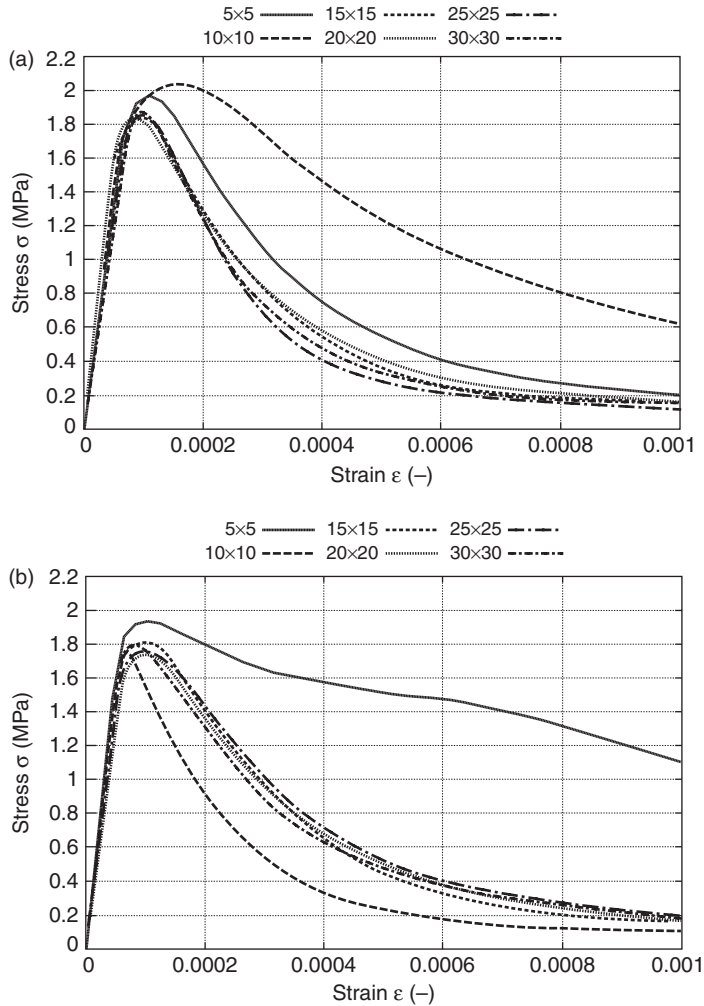
3.5 Conclusions

A meso-scale numerical model was used in this study to analyse strain localization in concrete. The FE calculations revealed that an isotropic



3.35 Stress-strain curves for various sizes of concrete specimens and two different random distributions of aggregate (a) and (b) using varying characteristic length approach (reference unit size $15 \times 15 \text{ mm}^2$, characteristic length according to Equation [3.13], aggregate volume $\rho = 30\%$).

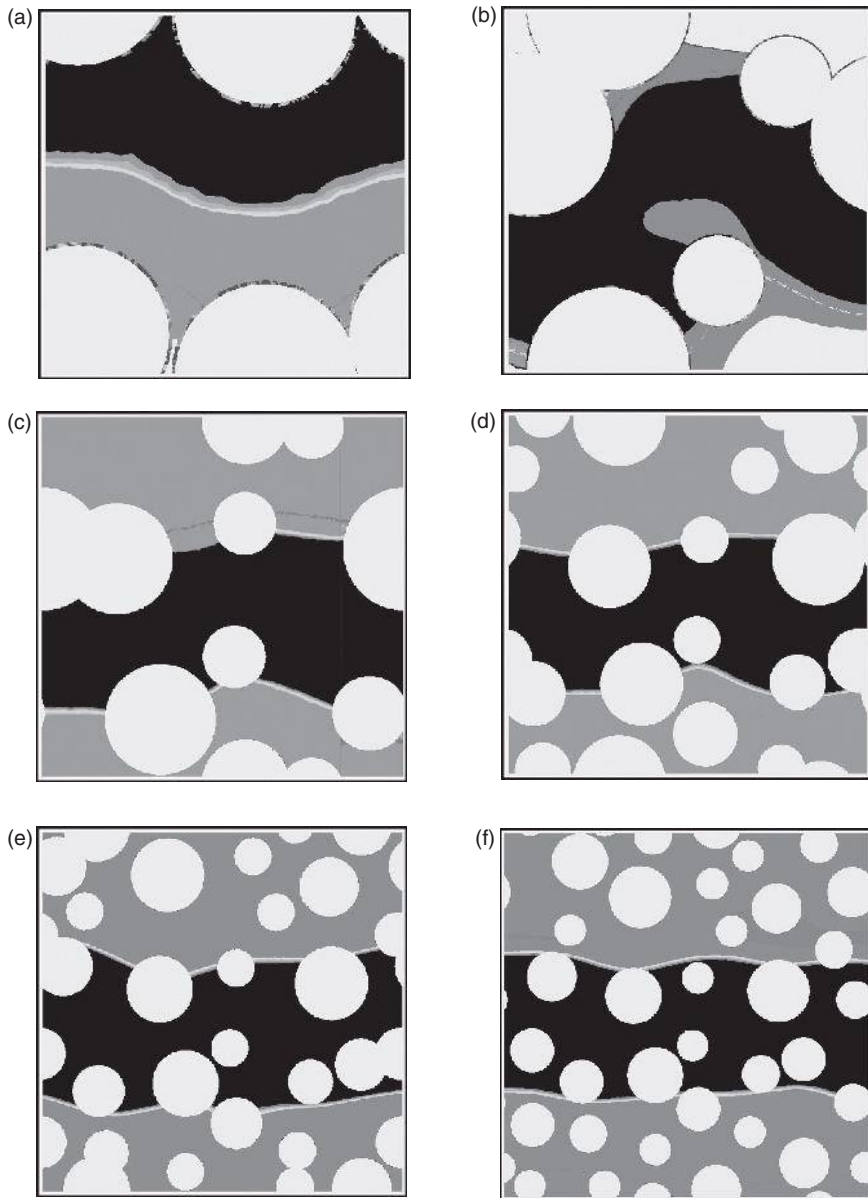
damage-continuum model enhanced by a characteristic length of micro-structure is able to capture the evolution of strain localization in concrete elements, where concrete was treated as a heterogeneous three-phase material composed of aggregate, cement matrix and bond.



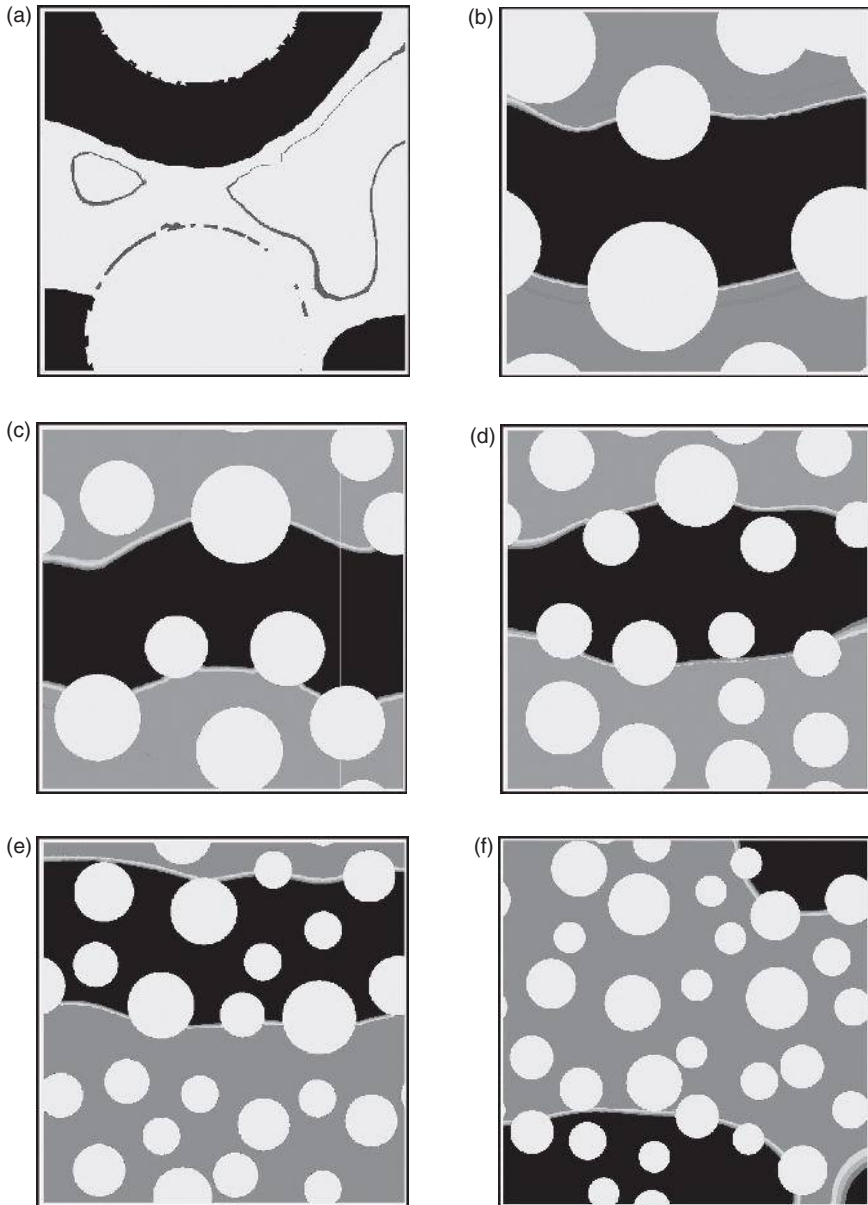
3.36 Stress–strain curves for various sizes of concrete specimens and two different random distributions of aggregate (a) and (b) using varying characteristic length approach (reference unit size $30 \times 30 \text{ mm}^2$, characteristic length according to Equation [3.14], aggregate density $\rho = 30\%$).

The following conclusions can be drawn from calculations with notched concrete beams under quasi-static three-point bending (by neglecting small aggregate grains):

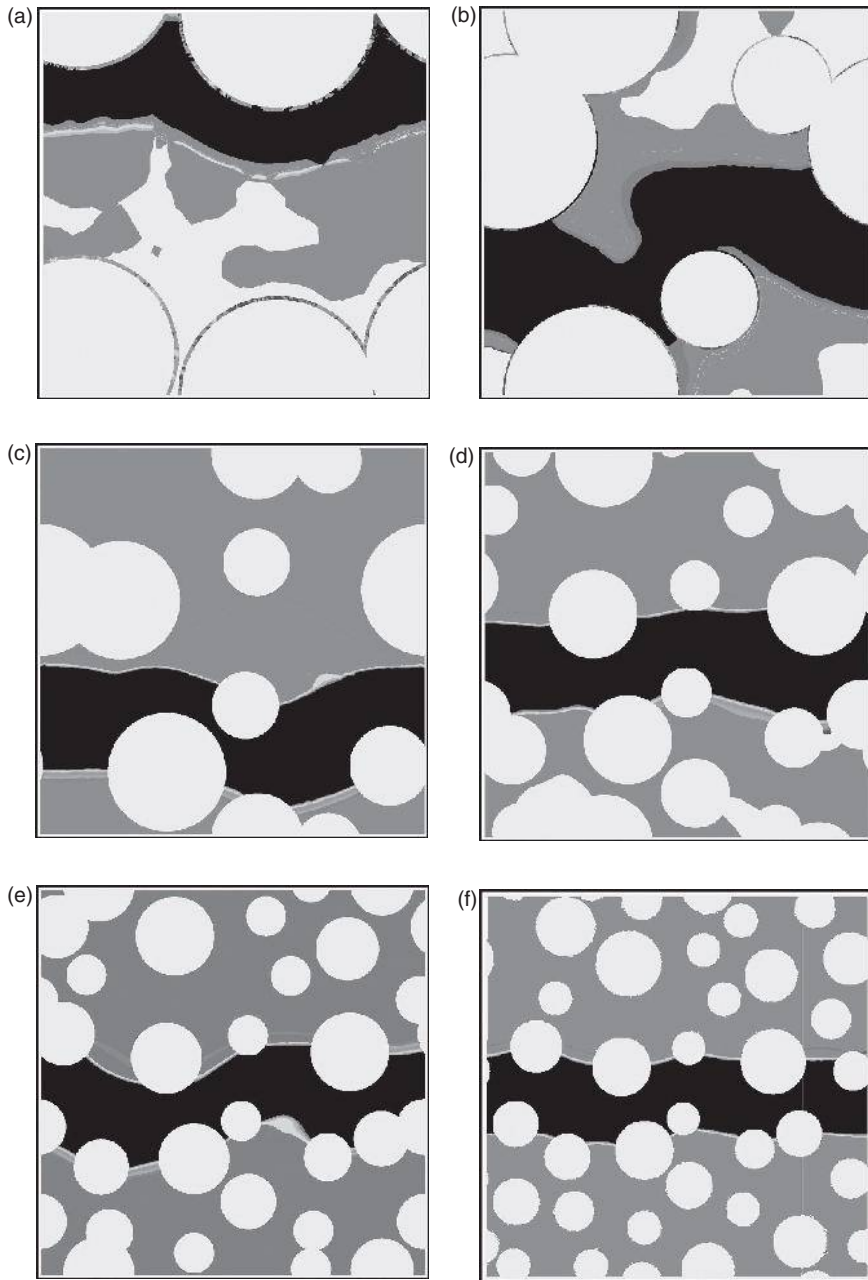
- material micro-structure at meso-scale has to be taken into account in calculations of strain localization to obtain a proper shape of a localized zone,



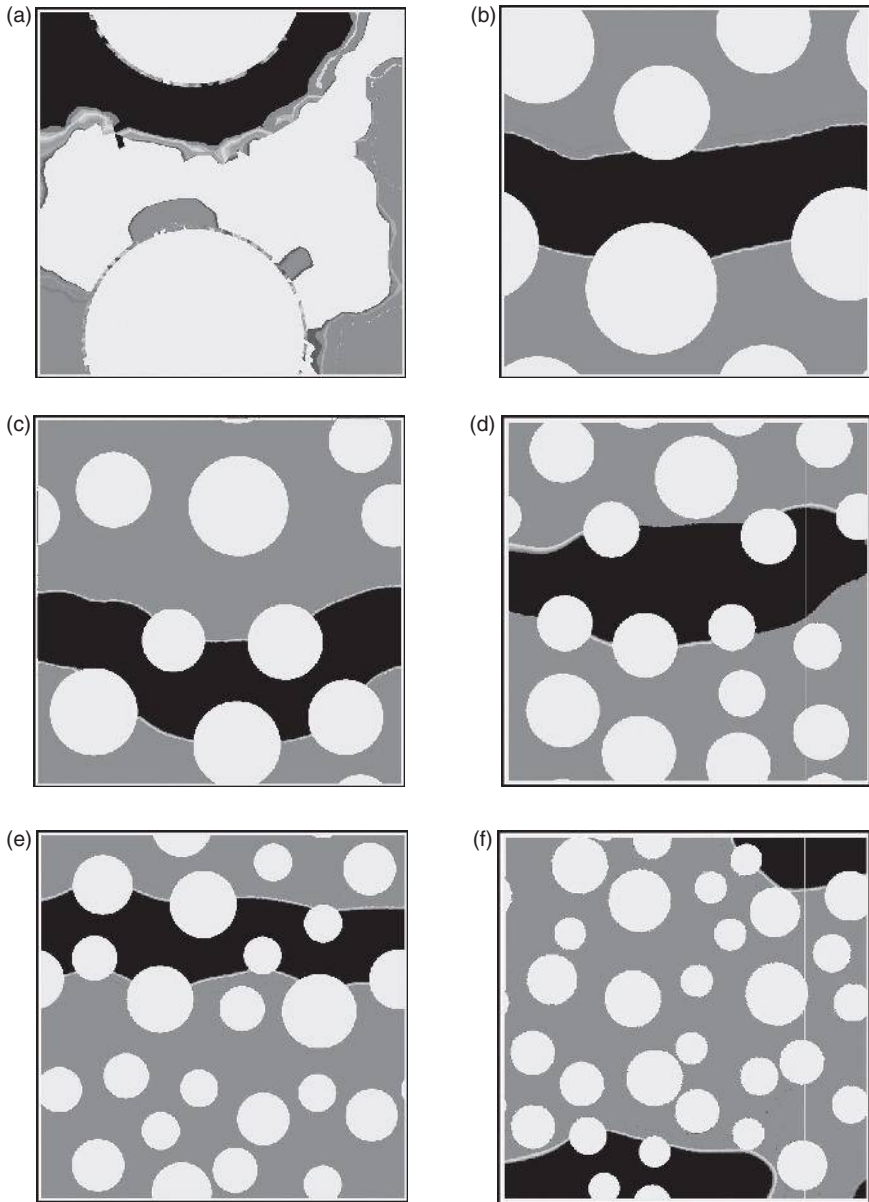
3.37 Distribution of non-local softening strain measure for various specimen sizes and stress-strain curves from Fig. 3.35a using varying characteristic length approach (reference unit size $15 \times 15 \text{ mm}^2$, characteristic length according to Equation [3.13], aggregate volume $\rho = 30\%$).



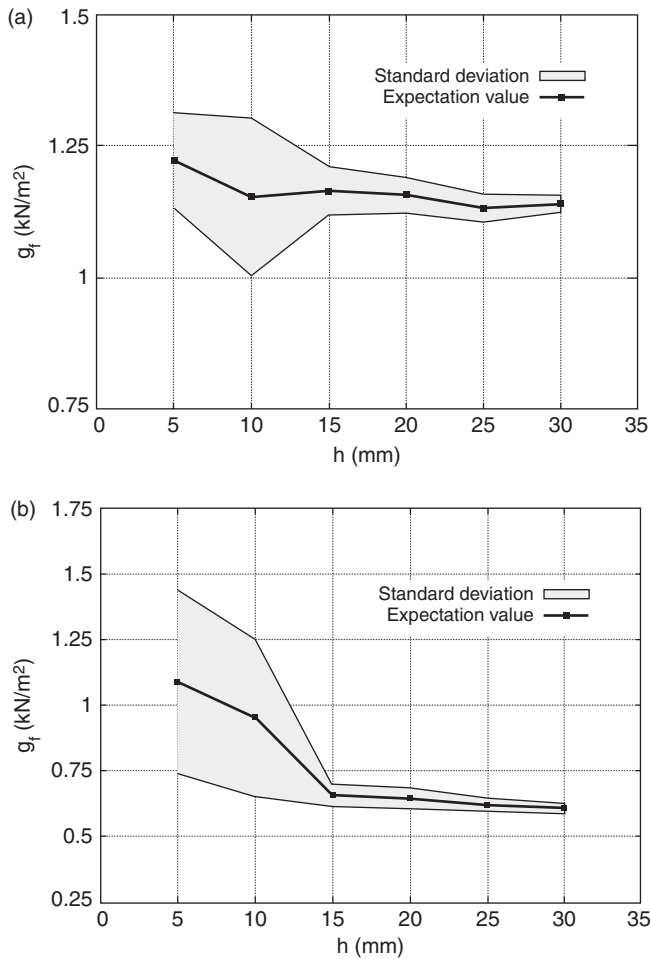
3.38 Distribution of non-local softening strain measure for various specimen sizes and stress–strain curves from Fig. 3.35b using varying characteristic length approach (reference unit size $15 \times 15 \text{ mm}^2$, characteristic length according to Equation [3.13], aggregate volume $\rho = 30\%$).



3.39 Distribution of non-local softening strain measure for various specimen sizes and stress–strain curves from Fig. 3.36a using varying characteristic length approach (reference unit size $30 \times 30 \text{ mm}^2$, characteristic length according to Equation [3.14], aggregate volume $\rho = 30\%$).



3.40 Distribution of non-local softening strain measure for various specimen sizes and stress-strain curves from Fig. 3.36b using varying characteristic length approach (reference unit size $30 \times 30 \text{ mm}^2$, characteristic length according to Equation [3.14], aggregate volume $\rho = 30\%$).



3.41 Expected value and standard deviation of unit fracture energy g_f versus specimen height h using varying characteristic length approach: (a) reference cell size $15 \times 15 \text{ mm}^2$, (b) reference cell size $30 \times 30 \text{ mm}^2$ (aggregate volume $\rho = 30\%$).

- the calculated strength, width and geometry of a localized zone are in satisfactory agreement with experimental measurements when the characteristic length at meso-scale is about 1.5 mm,
- the width of a localized zone above the notch is about $(2-4) \times l_c$. It increases with decreasing aggregate volume from $2 \times l_c$ ($\rho = 60\%$) up to $4 \times l_c$ ($\rho = 30\%$). It increases also with increasing characteristic length. It is not affected by the aggregate size, aggregate roughness, bond thickness and beam height,

- beam strength increases with increasing characteristic length, aggregate volume, aggregate roughness, aggregate stiffness and decreasing bond thickness and beam height. It depends also on a stochastic aggregate distribution,
- concrete softening is strongly influenced by the characteristic length, aggregate volume, aggregate roughness and beam height and
- the localized zone above the notch is strongly curved with $l_c = 0.1\text{--}2.5\text{ mm}$,

The following conclusions can be drawn from calculations with concrete elements under uniaxial tension:

- The RVE cannot be defined in quasi-brittle materials with a standard averaging approach (over the entire material domain) due to the occurrence of a localized zone whose width is not scaled with the specimen size. The shape of the stress–strain curve depends on the specimen size beyond the elastic region.
- The 2D RVE can be determined in quasi-brittle materials using both a localized zone averaging approach and a varying characteristic length approach. In the first case, averaging is performed over the localized domain rather than over the entire domain, by which the material contribution is swept out. In the second case, averaging is performed over the entire domain with a characteristic length being scaled with the specimen size (l_c is no longer an objective physical parameter). In both cases, convergence of the stress–strain diagrams for different RVE sizes is obtained for tensile loading. The size of a two-dimensional statistically representative volume element is approximately equal to $15 \times 15\text{ mm}^2$.

3.6 Acknowledgements

Research work has been carried out within the project: ‘Innovative ways and effective methods of safety improvement and durability of buildings and transport infrastructure in the sustainable development’ financed by the European Union (POIG.01.01.02–10–106/09–01).

3.7 References

- Bažant ZP and Oh BH (1983). ‘Crack band theory for fracture of concrete’. *Material Structures*, RILEM **16** (93), 155–177.
- Bažant ZP and Pijauder-Cabot G (1989). ‘Measurement of characteristic length of non-local continuum’. *ASCE Journal of Engineering Mechanics*, **115** (4), 755–767.
- Bažant ZP and Planas J (1998). *Fracture and size effect in concrete and other quasi-brittle materials*. CRC Press LLC, Boca Raton.

- Bažant ZP and Jirasek M (2002). 'Non-local integral formulations of plasticity and damage: survey of progress'. *Journal of Engineering Mechanics*, **128** (11), 1119–1149.
- Bažant ZP and Novak D (2003). 'Stochastic models for deformation and failure of quasibrittle structures: recent advances and new directions'. In N. Bicanic, R. de Borst, H. Mang and G. Meschke (Eds.), *Computational Modelling of Concrete Structures EURO-C*, 583–598.
- Bažant ZP (2004). 'Probability distribution of energetic-statistical size effect in quasi-brittle fracture'. *Probabilistic Engineering Mechanics*, **19**, 307–319.
- Bobinski J and Tejchman J (2004). 'Numerical simulations of localization of deformation in quasi-brittle materials within non-local softening plasticity'. *Computers and Concrete*, **1** (4), 433–455.
- Bobinski J, Tejchman J and Górski J. (2009). 'Notched concrete beams under bending – calculations of size effects within stochastic elasto-plasticity with non-local softening'. *Archives of Mechanics*, **61** (3–4), 283–307.
- Bobinski J and Tejchman J (2010). 'Continuous and discontinuous modeling of cracks in concrete elements'. In N. Bicanic, R. de Borst, H. Mang, G. Meschke (Eds.), *Modelling of Concrete Structures*, Taylor and Francis Group, London, 263–270.
- Drugan WJ and Willis JR. (1996). 'A micromechanics-based nonlocal constitutive equations and estimates of representative volume element size for elastic composites'. *Journal of the Mechanics and Physics of Solids*, **44** (4), 497–524.
- Eckardt S and Konke C (2006). 'Simulation of damage in concrete structures using multiscale models'. In N. Bicanic, R. de Borst, H. Mang and G. Meschke (Eds.), *Computational Modelling of Concrete Structures, EURO-C*, Taylor and Francis, 77–84.
- Evesque P (2000). 'Fluctuations, correlations and representative elementary volume (REV) in granular materials'. *Powders and Grains*, **11**, 6–17.
- Gitman IM, Askes H and Sluys LJ (2007). 'Representative volume: Existence and size determination'. *Engineering Fracture Mechanics*, **74** (16), 2518–2534.
- Gitman IM, Askes H and Sluys LJ (2008). 'Coupled-volume multi-scale modelling of quasi-brittle material'. *European Journal of Mechanics A/Solids*, **27** (3), 302–327.
- He H, Guo Z, Stroeve P, Stroeve M and Sluys LJ (2009). 'Influence of particle packing on elastic properties of concrete'. *Proc. First International Conference on Computational Technologies in Concrete Structures (CTCS'09)*, Jeju, Korea, 1177–1197.
- Hill R. (1963). 'Elastic properties of reinforced solids: some theoretical principles'. *Journal of the Mechanics and Physics of Solids*, **11** (5), 357–372.
- Jirasek M and Marfia S (2005). 'Non-local damage model based on displacement averaging'. *International Journal for Numerical Methods in Engineering*, **63** (1), 77–102.
- Kanit T, Forest S, Galliet I, Mounoury V and Jeulin D (2003). 'Determination of the size of the representative volume element for random composites: statistical and numerical approach'. *International Journal of Solids and Structures*, **40**, 3647–3679.
- Katchanov LM (1986). *Introduction to continuum damage mechanics*, Dordrecht: Martinus Publishers.

- Kouznetsova VG, Geers MGD and Brekelmans WAM (2004). 'Size of Representative Volume Element in a second-order computational homogenization framework'. *International Journal for Multiscale Computational Engineering*, **2** (4), 575–598.
- Kozicki J and Teichman J (2008). 'Modelling of fracture processes in concrete using a novel lattice model'. *Granular Matter*, **10** (5), 377–388.
- Le Bellégo C, Dube JF, Pijauder-Cabot G and Gerard B (2003). 'Calibration of non-local damage model from size effect tests'. *Engineering Journal of Mechanics A/Solids*, **22** (1), 33–46.
- Lilliu G and van Mier JGM (2003). '3D lattice type fracture model for concrete'. *Engineering Fracture Mechanics*, **70** (7–8), 927–941.
- Marzec I, Bobiński J and Teichman J (2007). 'Simulations of spacing of localized zones in reinforced concrete beams using elasto-plasticity and damage mechanics with non-local softening'. *Computers and Concrete*, **4** (4), 377–403.
- Mihashi H and Nomura N (1996). 'Correlation between characteristics of fracture process zone and tension-softening properties of concrete'. *Nuclear Engineering and Design*, **165** (3), 359–376.
- Nguyen VP, Valls OL, Stroeven M and Sluys LJ (2010). 'On the existence of representative volumes for softening quasi-brittle materials'. *Computer Methods in Applied Mechanics and Engineering*, **199**, 3028–3038.
- Nielsen AU, Montiero PJM and Gjorv OE (1995). 'Estimation of the elastic moduli of lightweight aggregate'. *Cement and Concrete Research*, **25** (2), 276–280.
- Peerlings RHJ, de Borst R, Brekelmans WAM and Geers MGD (1998). 'Gradient-enhanced damage modelling of concrete fracture'. *Mechanics of Cohesive-Frictional Materials*, **3** (4), 323–342.
- Pijauder-Cabot G and Bažant ZP (1987). 'Nonlocal damage theory'. *ASCE Journal of Engineering Mechanics*, **113** (10), 1512–1533.
- Sengul O, Tasdemir C and Tasdemir MA (2002). 'Influence of aggregate type on mechanical behaviour of normal- and high-strength concretes'. *ACI Materials Journal*, **99** (6), 528–533.
- Simo JC and Ju JW (1987). 'Strain- and stress-based continuum damage models – I. Formulation'. *International Journal of Solids and Structures*, **23** (7), 821–840.
- Simone A and Sluys LJ (2004). 'The use of displacement discontinuities in a rate-dependent medium'. *Computer Methods in Applied Mechanics Engineering*, **193** (27–29), 3015–3033.
- Skarżyński Ł. and Teichman J (2009). 'Mesoscopic modelling of strain localization in concrete'. *Archives of Civil Engineering*, **LV** **4**, 503–526.
- Skarżyński Ł. and Teichman J (2010). 'Calculations of fracture process zones on meso-scale in notched concrete beams subjected to three-point bending'. *European Journal of Mechanics A/Solids*, **29**, 746–760.
- Skarżyński Ł. Syroka E. and Teichman J (2011). 'Measurements and calculations of the width of the fracture process zones on the surface of notched concrete beams'. *Strain*, **s1**, e319–e332.
- Skarżyński Ł. and Teichman J (2012). 'Determination of representative volume element in concrete under tensile deformation'. *Computers and Concrete*, **1** (9), 35–50.
- van Mier JGM (2000). 'Microstructural effects on fracture scaling in concrete, rock and ice'. In J. P. Dempsey and H.H. Shen (Eds.), *IUTAM Symposium on*

- Scaling Laws in Ice Mechanics and Ice Dynamics*, Kluwer Academic Publishers, 171–182.
- van Mier JGM, Schlangen E and Vervuurt A (1995). ‘Lattice type fracture models for concrete’. In H.-B. Mühlhaus (Ed.), *Continuum Models for Material and Microstructure*, John Wiley & Sons, 341–377.
- Verhoosel CV, Remmers JJC and Gutierrez MA (2010a). ‘A partition of unity-based multiscale approach for modelling fracture in piezoelectric ceramics’. *International Journal for Numerical Methods in Engineering*, **82** (8), 966–994.
- Verhoosel CV, Remmers JJC, Gutierrez MA and de Borst R (2010b). ‘Computational homogenization for adhesive and cohesive failure in quasi-brittle solids’. *International Journal for Numerical Methods in Engineering*, **83**, 1155–1179.
- White DJ, Take WA and Bolton MD (2003). ‘Soil deformation measurement using particle image velocimetry (PIV) and photogrammetry’. *Geotechnique*, **53**, 619–631.

Modelling moisture transport in intact and fractured concrete

P. MOONEN and J. CARMELIET,
ETH Zürich and Empa Dübendorf, Switzerland

DOI: 10.1533/9780857097538.1.98

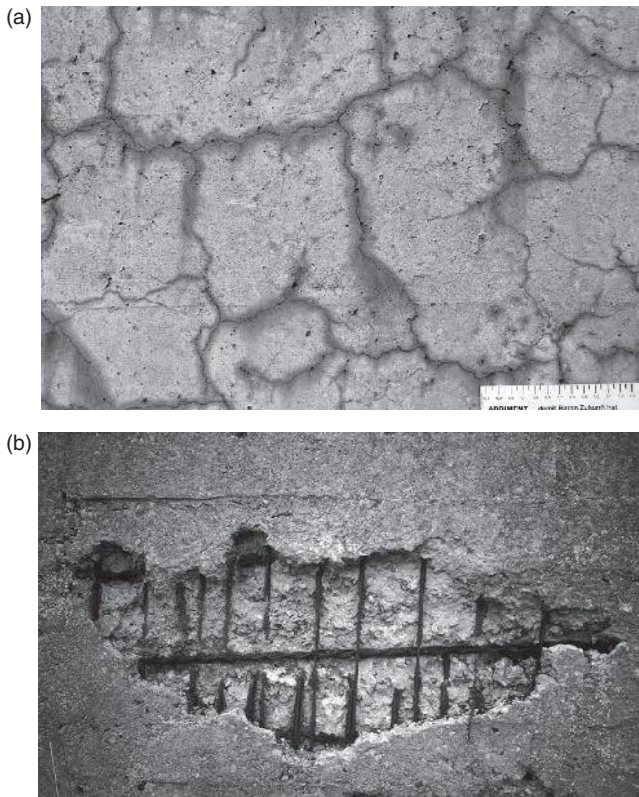
Abstract: Material degradation results from the complex interaction between physical, chemical and biological degradation processes. Moisture transport plays a crucial role in many of these processes and is therefore of particular interest. This chapter starts by reviewing the state-of-the-art in the modelling of moisture transport, both in intact and in fractured materials. It is shown that the quality of the model predictions crucially depends on two material properties, namely the capacity and the permeability, and that the experimental determination of these properties remains challenging. Next, the theory of poromechanics is introduced, describing the dependency of the stress state in the material on the amount and the distribution of moisture in the pore space. Degradation occurs when these stresses exceed the material's strength. A final case study illustrates how modelling can be used as a means to (i) gain insight, (ii) predict potential problems and (iii) propose and evaluate solutions to arrive at more sustainable structures.

Key words: material degradation, modelling, unsaturated moisture transport, retention, permeability, diffusivity, poromechanics, stress, fracture.

4.1 Introduction

During their lifetime, concrete structures are exposed to various types of degradation. We distinguish physical (e.g. frost damage), chemical (e.g. leaching) and biological causes (e.g. fungi). Water plays a central role in many of these degradation processes. Two illustrative examples of particular relevance to concrete are the alkali–silica reaction (ASR) and the corrosion of steel reinforcement.

ASR is caused by a reaction between the hydroxyl ions in the alkaline cement paste and reactive non-crystalline forms of silica in the aggregate. A gel of calcium silicate hydrate (CSH) is produced, which increases in volume by taking up water and so exerts an expansive pressure resulting in cracking and finally leading to failure of the concrete (Fig. 4.1a). ASR will



4.1 Degradation of concrete induced by (a) the ASR and (b) the corrosion of steel reinforcement.

not occur if there is no available water in the concrete, since alkali–silica gel formation involves water.

Corrosion of steel reinforcement takes place when the alkalinity of the protective layer around the reinforcement bar is reduced, e.g. by neutralization with atmospheric carbon dioxide, or when depassivating anions such as chloride are able to reach the steel. The conversion of iron to iron oxide involves a volumetric expansion, which in turn causes expansive stresses that may lead to damage (Fig. 4.1b). Again, the presence of water is a necessary condition for corrosion to occur. The permeability of the concrete is important in determining the extent to which aggressive external substances can attack the steel.

From the above examples, it is clear that a discussion on durability is in the first place a discussion on moisture transport. The presence of moisture triggers other physical, chemical and biological degradation processes. As a result of the active degradation processes, the material properties in the

wetted region are altered and stresses of various origins develop. In combination with mechanical loading, initial micro-defects may grow and coalesce into macro-cracks, thereby not only reducing the structural strength and stiffness, but also creating new pathways for preferential moisture transport, both leading to an acceleration of the degradation process.

In this chapter we present the state-of-the-art in the modelling of moisture transport, both in intact and in fractured material. Furthermore, we discuss the interaction between hygric and mechanical material behaviour. A final case study illustrates that modelling can be used as a means to (i) gain insight, (ii) predict potential problems and (iii) propose and evaluate solutions.

4.2 Modelling moisture transport in intact concrete

Our current understanding of moisture transport in porous materials such as concrete crucially relies on a number of key-developments during the twentieth century. After shortly reviewing these in Section 4.2.1, the governing equation underlying state-of-the-art transport modelling of intact porous materials is presented in Section 4.2.2. The equation expresses the delicate balance between two distinct processes taking place in the material's pore space, namely retention and transport. An in-depth discussion on these processes and the way in which they can be determined experimentally is provided in Sections 4.2.3 and 4.2.4, respectively.

4.2.1 A century of research in transport modelling

The most widely used approach to model unsaturated moisture transport in porous materials emerged from the work of Lorenzo Adolph Richards (1904–93). He elaborated on the work of Buckingham in the field of soil-water physics (Buckingham 1907), and was the first to present a partial differential equation governing water transport in unsaturated, non-deformable soils (Richards 1931). In vector format, and in SI units, his equation reads:

$$\frac{\partial \theta}{\partial \psi} \frac{\partial \psi}{\partial t} + \nabla \cdot (\mathbf{K}(\mathbf{g} + \nabla \psi)) = 0 \quad [4.1]$$

with θ (m^3/m^3) the volumetric moisture content, i.e. the volume of liquid water per unit volume of dry material, ψ (m^2/s^2) the capillary potential, t (s) the time, \mathbf{K} (s) the hydraulic permeability and \mathbf{g} (m/s^2) the gravitational acceleration. Equation [4.1] states that the volumetric moisture content can change over time as a result of flow, induced by the combined effect of gravity and a pressure gradient. Richards expressed the pressure gradient in

terms of the capillary potential ψ , as this simplified the experimental determination of the hydraulic permeability \mathbf{K} .

Various authors have proposed modifications to Equation [4.1]. Klute (1952) suggested using the moisture content X (kg/kg) as driving potential:

$$\frac{\partial X}{\partial t} + \nabla \cdot (\mathbf{K} \mathbf{g} + \mathbf{D} \nabla X) = 0 \quad [4.2]$$

with \mathbf{D} (m^2/s) the diffusivity, a concept introduced a few years earlier by Childs and George (1948):

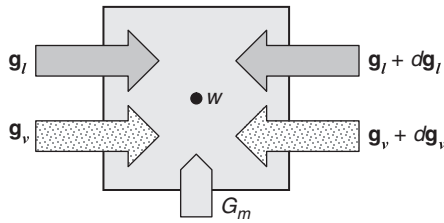
$$\mathbf{D} = \mathbf{K} \frac{\partial \psi}{\partial X} \quad [4.3]$$

Later, it was realized that a distinction needs to be made between the transport of liquid water and water vapour (Philip 1954), and the theory has been extended to non-isothermal situations (Philip and De Vries 1957). Over the years, several variables were proposed as driving potential for moisture transport, such as matric head (Milly 1980), extended relative humidity (Kießl 1983) and capillary suction (Pedersen 1990). A comparative study pointed out that relative humidity and generalized suction are both true potentials in the physical sense (Hens 1996). The specific choice is not of importance, since true potentials can be transformed into one another. Recently, the effect of deformation of the porous medium was incorporated in the theory (Jiang and Rajapakse 1994; Thomas and He 1995).

It is essential to note that the transport equations (such as Equations [4.1] and [4.2]) were mainly derived following a phenomenological approach, i.e. based on observations at the macroscopic scale. They rely on a number of important assumptions, such as (i) air transport can be neglected, (ii) validity of Darcy's law and (iii) incompressibility of the fluid. Other, more general, approaches exist, e.g. based on volume-averaging of microscopic conservation equations (Whitaker 1967; Hassanizadeh and Gray 1979). Such derivations offer more insight, but inevitably lead to a more complex framework. Nevertheless, if appropriate assumptions are made, the equations of the phenomenological approach are recovered (de Boer *et al.* 1991).

4.2.2 State-of-the-art modelling of unsaturated moisture transport

Nowadays, unsaturated moisture transport in intact porous materials is commonly modelled based on a continuum theory. Herein, it is assumed that a representative elementary volume (REV) can be defined, i.e. the smallest



4.2 Schematic representation of mass conservation in an elementary volume.

sample volume which is still representative for the bulk material (Bachmat and Bear 1986). Under the additional assumption that the material can be considered undeformable, mass conservation for a representative material sample is given by:

$$\frac{\partial w}{\partial t} + \nabla \cdot (\mathbf{g}_l + \mathbf{g}_v) = G_m \quad [4.4]$$

where w (kg/m^3) is the moisture content, \mathbf{g}_l and \mathbf{g}_v ($\text{kg}/(\text{m}^2\text{s})$) are the liquid and vapour fluxes, respectively and G_m ($\text{kg}/(\text{m}^3\text{s})$) is a mass source term. This is schematically illustrated in Fig. 4.2.

The open pore space of the material is assumed to be partially filled with liquid water and partially with a gaseous mixture of water vapour and dry air. The moisture content w (kg/m^3), i.e. the total mass of water per unit volume of material, is given by:

$$w = w_{\text{sat}} S(p_c) \quad [4.5]$$

where w_{sat} (kg/m^3) is the moisture content at saturation, $0 \leq S \leq 1$ is the degree of saturation of the porous medium and p_c (Pa) is the capillary pressure, defined as the pressure difference over the meniscus between the liquid and the gaseous phase. This quantity is theoretically minus infinity for dry materials and zero for saturated materials. However, a range of eight orders of magnitude ($-10^9 < p_c < -10$ Pa) is usually sufficient to describe the saturation levels that are found in reality. The relation between S and p_c is called the moisture-retention curve. The moisture-retention curve plays a crucial role in predicting transient hygric behaviour and its determination is the subject of the next section (Section 4.2.3).

Under isothermal conditions, the driving force for liquid-water transfer is a gradient in liquid pressure p_l , while a gradient in vapour pressure p_v involves vapour flow. Gravitational forces are usually small and can be neglected in the absence of macro-cracks or holes. The liquid and vapour fluxes can therefore be described with Darcy's law:

$$\mathbf{g}_l = -\mathbf{K}_l \nabla p_l \quad [4.6a]$$

$$\mathbf{g}_v = -\boldsymbol{\delta}_v \nabla p_v \quad [4.6b]$$

where \mathbf{K}_l (s) and $\boldsymbol{\delta}_v$ (s) are the liquid and vapour permeability, respectively. Remark that \mathbf{K}_l and $\boldsymbol{\delta}_v$ are matrices, not scalar quantities. This allows taking material anisotropy into account.

Assuming a constant total gas pressure, a gradient in liquid pressure equals a gradient in capillary pressure. Equation [4.6a] can therefore be expressed as:

$$\mathbf{g}_l = -\mathbf{K}_l \nabla p_c \quad [4.7]$$

Under equilibrium conditions, vapour pressure can be converted into capillary pressure by means of Kelvin's law (Thomson 1871):

$$RH = \frac{p_v}{p_{v,sat}} = \exp\left(\frac{p_c}{\rho_l R_v T}\right) \quad [4.8]$$

where RH is the relative humidity and $p_{v,sat}$ (Pa) the saturation vapour pressure above the meniscus between liquid and vapour phase, ρ_l (kg/m³) the mass density of liquid water, $R_v = 462$ J/(kgK) the gas constant for water vapour and T (K) the absolute temperature. Based on Kelvin's law (Equation [4.8]), Equation [4.6b] can be transformed into:

$$\mathbf{g}_v = -\mathbf{K}_v \nabla p_c \quad \text{with} \quad \mathbf{K}_v = \boldsymbol{\delta}_v \frac{p_v}{\rho_l R_v T} \quad [4.9]$$

The total mass flux \mathbf{g} (kg/(m²s)) is given by:

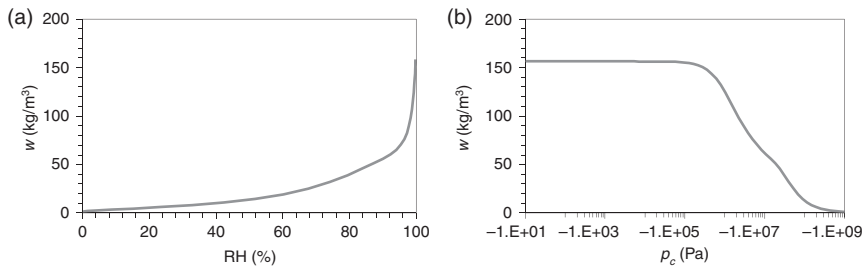
$$\mathbf{g} = \mathbf{g}_l + \mathbf{g}_v = \mathbf{K} \nabla p_c \quad [4.10]$$

where \mathbf{K} (s) is the total moisture permeability, given by the sum of the liquid and the vapour permeabilities $\mathbf{K} = \mathbf{K}_l + \mathbf{K}_v$. The moisture permeability \mathbf{K} is a key parameter in transport simulations and its description is the subject of Section 4.2.4.

The combination of Equations [4.4] and [4.10] yields the governing equation for unsaturated moisture transfer in porous media, like concrete:

$$c \frac{\partial p_c}{\partial t} + \nabla \cdot (\mathbf{K} \nabla p_c) = G_m \quad [4.11]$$

with $c = \partial w / \partial p_c$, the moisture capacity. The mass source term G_m is usually zero. The final mass-balance equation is similar to the Richards Equation [4.1], where p_c takes the function of capillary potential.



4.3 Moisture-retention capacity of concrete: (a) hygroscopic curve $w(RH)$ and (b) moisture-retention curve $w(p_c)$.

4.2.3 Moisture retention

When oven-dry porous material is exposed to a moist environment, moisture is adsorbed at the pore surface as a result of two distinct sorption processes, namely molecular adsorption and capillary condensation, and an increase in weight is observed. A plot of the mass gain as a function of the relative humidity of the environment is called the hygroscopic curve (Fig. 4.3a). Based on Kelvin's law (Equation [4.8]), relative humidity can be converted into capillary pressure. The corresponding graph essentially contains the same information, but is termed the moisture-retention curve (Fig. 4.3b).

In practice, the relationship $w(p_c)$ is obtained from a combination of experimental tests, such as isothermal ad- or de-sorption measurements, pressure-membrane or pressure-plate apparatus (PMA or PPA) experiments and mercury intrusion porosimetry (MIP). A combination of tests is required, since single tests are not able to accurately cover the entire range of capillary pressures. Isothermal ad- or desorption measurements are for instance good for the low relative humidity range, i.e. large $|p_c|$. MIP, on the other hand, can cover a larger range in p_c , but tends to overestimate the retention in the low- $|p_c|$ region and underestimate the retention in the high- $|p_c|$ region due to the so-called ink-bottle effect. The magnitude of the ink-bottle effect can be assessed by performing one or more intrusion-withdrawal cycles (Wardlaw and McKellar 1981). A further complication is the occurrence of hysteresis between wetting and drainage, as a result of the complex pore structure. Roels *et al.* (2001) proposed a simple hysteresis model to obtain the main drainage curve (PMA, MIP) from the main wetting curve, the latter based on quantitative image analysis. From this concise overview, it is clear that the accurate determination of $w(p_c)$ is not an easy task, and may take several weeks depending on the type of material and the sample size.

Based on the experimentally determined main wetting and drying curves, any intermediate or secondary curve can be obtained using a suitable hysteresis model. It was to the credit of Poulouvassilis (1962) to apply the

general independent-domain theory of hysteresis (Everett and Whitton 1952) to describe capillary hysteresis. Later, Mualem and Dagan (1975) presented a dependent-domain theory of hysteresis. In contrast to the independent-domain theory, the dependent-domain theory can capture processes such as pore blockage against air entry upon pore drainage. In later publications, these modelling concepts were further elaborated.

Another approach consists in trying to approximate, e.g. the main wetting curve, by means of an analytical expression. Carmeliet and Roels (2002) give an overview of several possible uni-modal and bi-modal functions, and present a method to estimate the unknown parameters objectively. They confirm the observation of Durner (1992, 1994), that the observed relation between the degree of saturation and the capillary pressure is well-approximated by means of a superposition of van Genuchten type functions (Fig. 4.5b):

$$S(p_c) = \sum_{i=1}^{nps} l_i \left(1 + (c_i | p_c |)^{n_i} \right)^{-\left(1 - \frac{1}{n_i}\right)} \quad [4.12]$$

where nps is the modality of the function, which can be related to the number of pore systems in the porous medium, $0 \leq l_i \leq 1$ is the weight factor of subsystem i of the multimodal function ($\sum l_i = 1$), and $c_i > 0$ and $n_i > 0$ are shape parameters of the i th subsystem. Once the parameters l_i , c_i and n_i are determined, Equation [4.12] can be used in numerical simulations of moisture transport. Other closed-form expressions were e.g. proposed by Gardner (1958) and Brooks and Corey (1964).

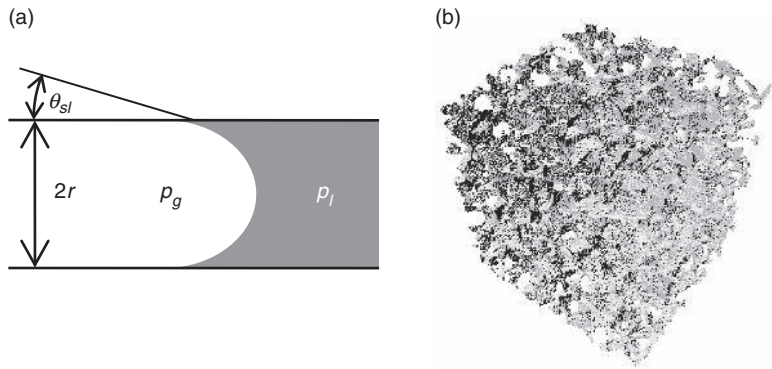
There is a strong link between the pore-size distribution of the material and $S(p_c)$. In a cylindrical pore (Fig. 4.4a), the relation between the pore radius r and the capillary pressure p_c is given by the (Young-)Laplace equation:

$$p_c = p_l - p_g = -\frac{2\gamma_{gl}}{r} \cos(\theta_{sl}) \quad [4.13]$$

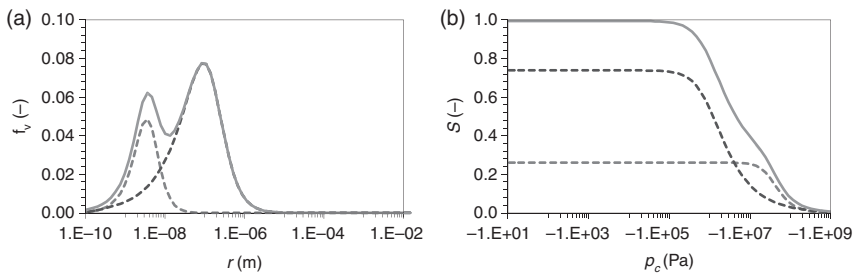
with γ_{gl} the surface tension along the meniscus between the liquid and gaseous phase and θ_{sl} the contact angle. Equation [4.13] is named after Thomas Young (1773–1829), who developed the qualitative theory of surface tension, and Pierre-Simon Laplace (1749–1827), who completed the mathematical description. If we consider the porous medium as a bundle of non-intersecting capillary tubes, the *apparent* pore volume distribution is given by:

$$f_v(r) = -\Psi_0 \frac{\partial S(p_c(r))}{\partial \log(-p_c(r))} \quad [4.14]$$

with Ψ_0 the open porosity. The term *apparent* indicates that a real porous medium is geometrically much more complex, as illustrated in Fig. 4.4b.



4.4 Illustration of (a) an idealized cylindrical pore and (b) a real pore network.



4.5 (a) Pore-size distribution and (b) corresponding contributions to the moisture-retention curve.

Figure 4.5 shows (a) the apparent pore volume distribution for a specimen of concrete and (b) the degree of saturation as a function of the capillary pressure. The material exhibits a broad range of pore radii, from 10^{-10} to 10^{-5} m (Fig. 4.5a). Two subsystems can be clearly identified, as they form a narrow distribution around certain characteristic pore radii (dotted distributions in Fig. 4.5a). At the corresponding capillary pressure (Equation [4.13]), that entire pore system will wet or drain, resulting in a sudden change of the overall degree of saturation (Fig. 4.5b). Since the saturation level can be converted into moisture content by means of Equation [4.5], the moisture-retention curve exhibits a similar degree of non-linearity (Fig. 4.3b).

4.2.4 Moisture transport

Like the moisture-retention curve, the accurate determination of moisture permeability remains challenging and the reliability of hygric simulations crucially depends on that knowledge. Basically three strategies exist. The

moisture permeability can be obtained (i) from the diffusivity, or (ii) as the sum of a liquid and a vapour permeability, or (iii) by means of a network approach. In this section, a concise overview is given of the pros and cons of each of these approaches.

Diffusivity approach

Several simple analytical relationships between diffusivity and moisture content have been proposed in literature. Gardner and Mayhugh (1958) proposed the exponential diffusivity relation:

$$D_w(w) = D_{w_0} \exp\left\{\beta \frac{\theta - \theta_0}{\theta_{cap} - \theta_0}\right\} \quad [4.15]$$

with D_{w_0} (m^2/s) the diffusivity at a reference moisture content θ_0 , θ_{cap} (m^3/m^3) the moisture content at capillary saturation and β (-) a fitting parameter. The work of Brutsaert (1979) led to the following expression for D_{w_0} :

$$D_{w_0} = \gamma \left(\frac{A}{\theta_{cap} - \theta_0} \right)^2 \quad [4.16]$$

with A ($\text{m}/\text{s}^{1/2}$) the sorptivity of the material and γ (-) a fitting parameter.

The unknown parameters in these expressions are determined by comparison with experimental data, usually a one-dimensional water absorption test in which both the mass gain and the moisture content profiles are monitored as a function of time. Descamps (1997) compares three possible techniques, namely the Boltzmann transform method, the flow-gradient method and the optimization method. He concludes that the spline-function optimization method outperforms the other two methods. The most frequently used method is, however, the Boltzmann transform method. The latter can only be applied if the Boltzmann conditions are fulfilled.

As can be expected, analytic expressions have a limited validity. The unsaturated moisture permeability can, for example, be anisotropic (Bear *et al.* 1987), while most analytic relations are only valid for homogeneous isotropic media.

Determination of liquid permeability

Van Genuchten *et al.* (1999) distinguish three classes of methods to determine the hydraulic properties of soils, namely pore-size distribution methods, inverse methods and methods based on pedotransfer functions. The same methods can be applied to porous materials such as concrete.

In pore-size distribution models the unsaturated hydraulic conductivity is estimated from the distribution, connectivity and tortuosity of the pores.

One popular model of this type was developed by Mualem (1976) by assuming water flow through cylindrical pores and incorporating the equations of Darcy and Poiseuille. In this model the relative hydraulic conductivity function is linked to the moisture-retention curve:

$$K(p_c) = K_s K_r \quad \text{and} \quad K_r = S^\tau \left[\frac{\int_0^S 1/p_c \, dS}{\int_0^1 1/p_c \, dS} \right]^2 \quad [4.17]$$

with K_s (s) the saturated conductivity, K_r (-) the relative conductivity and τ an empirical shape factor which takes into account the tortuosity of the pore space.

In inverse methods, the unknown parameters of closed-form expressions such as Equations [4.12] and [4.17] are estimated from observed time series of infiltration, water content and/or pressure head (e.g. Šimůnek and van Genuchten 1996; Abbaspour *et al.* 1997). Inverse methods often suffer from non-uniqueness of the results. This problem can be overcome by performing the optimization on two or more independent data sets (Hopmans and Šimůnek 1999).

Pedotranfer functions utilize various regression analysis and data mining techniques to extract rules, associating basic soil properties (e.g. the particle size distribution, bulk density, organic matter content) with more difficult to measure properties. To the authors' knowledge, this method has not yet been applied to porous materials such as concrete. This method is therefore not further discussed.

Determination of vapour permeability

The vapour resistance of a material is expressed using a vapour resistance factor μ (-), indicating how many times less vapour can diffuse through the material than through stagnant air, per unit of time. The vapour resistance factor can be obtained from dry and wet cup measurements.

$$\delta_v = \frac{\delta_a}{\mu} \quad [4.18]$$

with δ_a (s) the vapour permeability of air, determined from:

$$\delta_a = \frac{D_v}{R_v T} \quad [4.19]$$

with D_v (m²/s) the diffusion coefficient of water vapour in dry air at temperature T (K) and R_v the gas constant of water vapour. According to Schirmer (1938), the dependency of the diffusion coefficient of water vapour in air on pressure and temperature is given by:

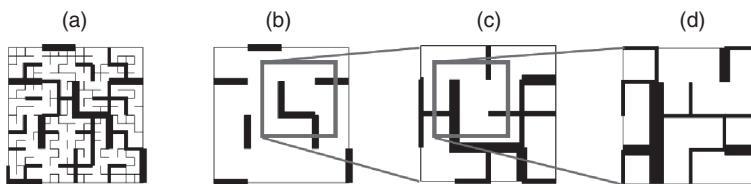
$$D_v = 2.3 \cdot 10^{-5} \frac{p_0}{p_0 + p_v} \left(\frac{T}{T_0} \right)^{1.81} \quad [4.20]$$

with p_0 (Pa) and T_0 (K) the reference pressure (101 323 Pa) and temperature (273.15 K), respectively, and p_v (Pa) the vapour pressure. A good overview on relations found by other authors is given by Galbraith (1992).

Network approach

Conceptually, porous media are often considered as bundles of non-intersecting cylindrical tubes. This is, for instance, the underlying assumption of Equation [4.14] for the determination of the apparent pore-size distribution. In contrast, network models consider porous media as an interconnected network of capillary tubes, with tube diameters based on the real pore-size distribution. Network models emerged from the work of Fatt (1956) in petroleum engineering. About 20 years later, Chatzis and Dullien (1977) combined network models with percolation concepts. Multiscale percolation systems were introduced by Neimark (1989). In the multiscale approach the pore space is described as a superposition of several pore sub-systems situated in different pore-size ranges. A crucial point is the modelling of the interconnection between the different scales. Xu *et al.* (1997) used hierarchic lattices, in which networks of lower pore-size range were connected to larger scales using rescaling and normalization techniques. Alternatively, Carmeliet *et al.* (1999) proposed a multiscale approach based on the concept of examining the porous space at different levels of magnification (Fig. 4.6).

At each level of magnification an isotropic non-planar 2D cross-squared network of capillary tubes is created. The pore radii of the tubes are randomly obtained from a normalized pore radius distribution, dependent on the level of magnification. Given the fluid distribution in the network corresponding to a known capillary pressure p_c , the permeability can be calculated by imposing a unit pressure gradient over the network. This



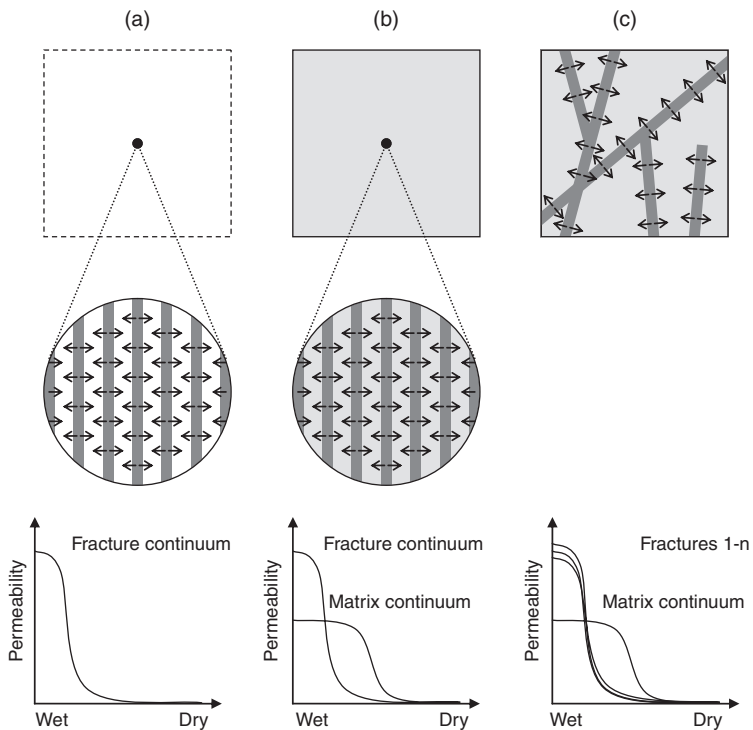
4.6 Schematic representation of (a) the pore system in a porous material and (b–d) the same pore system at different levels of magnification.

process is repeated for different capillary pressures and the relationship between capillary pressure and permeability is determined.

The strength of network models is that they can predict the highly non-linear relationship over the total moisture content range by combining the liquid and vapour transfer. Carmeliet *et al.* (1999) proved that the multiscale approach efficiently and accurately simulates the enhancement of the water vapour permeability due to capillary condensation as well as the steep increase of the moisture permeability at the critical moisture saturation.

4.3 Modelling moisture transport in degraded concrete

Several paradigms exist regarding the modelling of moisture transfer in fractured porous media. The most important are (i) dual porosity, (ii) dual permeability and (iii) discrete fracture models (Fig. 4.7). The key principles,



4.7 Different conceptual models for modelling transport in fractured porous media : (a) dual-porosity models, (b) dual-permeability models, and (c) discrete fracture models.

as well as the main advantages and disadvantages, of each of these modelling concepts are explained below.

4.3.1 Dual-porosity models

The underlying idea of a dual-porosity model is that a fractured porous medium contains two regions with opposite characteristics, namely the fractures and the material itself. The former contributes largely to the porosity, but negligibly to the capacity, while the latter makes a minor contribution to the porosity, but determines the capacity. Since the permeability of the material is much smaller than that of the fractures, flow inside the matrix is not considered. Flow through the fracture network and flow exchange between the matrix and the fracture are nevertheless included in an averaged sense (Fig. 4.7a). Warren and Root (1963) were among the first to use a dual-porosity model in their study of naturally fractured reservoir flow. Since that time, numerical modelling using dual-porosity models has been the subject of numerous investigations. A concise overview is given in Šimůnek *et al.* (2003). The main advantage is the simplicity of the method. The main disadvantage is that the application of the method is restricted to situations where the matrix has a negligible effect on the permeability.

4.3.2 Dual-permeability models

More complicated models consider transport in both the fracture and the matrix region (Fig. 4.7b). Therefore, these models are generally termed dual-permeability models. Nevertheless, since dual-permeability models are also based on the assumption that two regions with distinct porosity exist in the material, some authors classify them as dual-porosity models. Most dual-permeability models employ two water-retention functions – one for the matrix and one for the fracture – but three permeability functions, namely one for the fracture, one for the matrix, and one for the fracture–matrix interface. The latter describes the exchange of moisture between the two pore systems. Dual-permeability models date back to a seminal paper by Barenblatt *et al.* (1960), who presented the basic concepts of the motion of liquids in fissured rocks. It is assumed that the fractures are much smaller than the domain under study, as such that the fractured porous medium can be considered as a superposition of the fracture continuum and the (unfractured) material matrix. At each point in space, two pressure fields exist, i.e. the pressures in the fractures and the pressures in the pores of the matrix. The pressure difference between them is the driving force behind the mass exchange between both regions. Similar to the dual-porosity models, the geometry and connectivity of the fractures are not explicitly taken into

account. Available dual-permeability models (e.g. Jarvis *et al.* 1991; Gerke and van Genuchten 1993) differ mainly in how they implement water flow in and between the two pore regions. The interested reader is referred to Šimůnek *et al.* (2003) for a more extensive overview.

4.3.3 Discrete fracture models

In contrast to the two approaches mentioned above, discrete network models explicitly take into account the geometry and the hydraulic properties of each fracture (Fig. 4.7c). Castillo *et al.* (1972) presented one of the first studies examining flow in a (simplified) fracture network, but without considering matrix diffusion. The numerical model proposed by Berkowitz *et al.* (1988) incorporates matrix diffusion by using the principle of superposition of one-dimensional fracture elements onto two-dimensional porous matrix elements. More recent models (e.g. Shikaze *et al.* 1994; Therrien and Sudicky 1996; Moonen *et al.* 2010) consider moisture transfer in discrete fractures embedded in the material matrix. These fully coupled models assume continuity in the pressure head at the fracture–matrix interface, which allows a simultaneous solution of the transport equations in the fracture network and in the porous matrix. The special feature of the model proposed by Moonen *et al.* (2010) is that it allows the combination of discrete fracture modelling for the large fractures with dual-permeability modelling for the microscopic cracks in the porous material matrix. In this way, the advantages of both techniques are combined. The excellent performance of this method was verified by Alfaiate *et al.* (2010).

4.4 Interaction between moisture transport and material behaviour

The presence of moisture highly influences the mechanical behaviour of porous materials. Upon wetting, the material starts swelling and its stiffness and strength both decrease. When the free swelling is hindered, hygric eigenstresses develop and damage in the form of cracks may appear. These cracks often act as preferential pathways for liquid-water transfer, leading to an accelerated wetting of the porous material surrounding the crack. The preferential wetting/drying and swelling/shrinking of the area next to the fracture may, in turn, result in an additional loading of the crack and lead to an acceleration of the damage process.

The influence of moisture on the mechanical behaviour of the material can be described successfully by means of the effective-stress principle. This principle was first formulated by Terzaghi (1936) for saturated porous media, and later by Bishop (1959) for the unsaturated case. Both formulations were rather empirical. A very similar expression was rigorously derived

by Hassanizadeh and Gray (1980) using averaging theory and a systematic exploration of the entropy inequality using the Coleman–Noll procedure (Coleman and Noll 1963). In the derivation, interfacial phenomena were not explicitly included. Interface thermodynamics was taken into account in the work of Gray and Schrefler (2001), providing a similar expression to that of Bishop (1959), but including additional terms that e.g. account for the curvature of the solid–fluid interface. Although such studies are theoretically valuable, their practical use is rather limited, since crucial information, such as the average interface curvature, is usually unavailable in reality. But interface thermodynamics can also be taken into account indirectly, using the theory of poromechanics (Coussy 1995). This is a macroscopic thermodynamic approach, and therefore no information on the geometry of the microstructure is required.

The poromechanical effective-stress principle for a macroscopically homogeneous material reads:

$$\boldsymbol{\sigma}^s = \boldsymbol{\sigma} - b^s p^s \mathbf{I} \quad [4.21]$$

where \mathbf{I} is the second order unit tensor, $\boldsymbol{\sigma}^s$ is the partial stress tensor of the solid material, $\boldsymbol{\sigma}$ is the effective-stress tensor, b^s is the Biot coefficient introduced to account for the deformability of the matrix, and p^s the solid pressure, defined as (Coussy 2004):

$$p^s = p^g - S^l (p^g - p^l) - U \quad \text{with} \quad U = \int_{S_l} (p^g - p^l) dS_l \quad [4.22]$$

The term U is the macroscopic contribution of the interfaces to the solid pressure.

Several material models have been developed to describe the dependency of the effective-stress tensor on material deformation. The simplest model assumes an isotropic linear elastic material and is given by:

$$\boldsymbol{\sigma} = \mathbf{D} \boldsymbol{\varepsilon} \quad [4.23]$$

with $\mathbf{D} = \lambda \mathbf{I} \otimes \mathbf{I} + 2\mu \mathbf{I}$ the elasticity tensor, \mathbf{I} and \mathbf{I} the second and fourth order unit tensors, and λ and μ the Lamé constants. $\boldsymbol{\varepsilon}$ is the second order strain tensor. Linear elasticity is suitable for modelling the mechanical behaviour of many quasi-brittle materials under moderate loading conditions. For higher load levels, more advanced models incorporating material damage must be used, such as the stress-based continuum damage model by Simo and Ju (1987).

4.5 Case study: application of outside render to masonry walls

In this section we illustrate how the theory described in this chapter can be employed to analyse problems of practical importance. As an example,

we investigate the application of a mineral mortar to a masonry wall. It is shown that the application method determines the quality of the render.

4.5.1 Numerical model

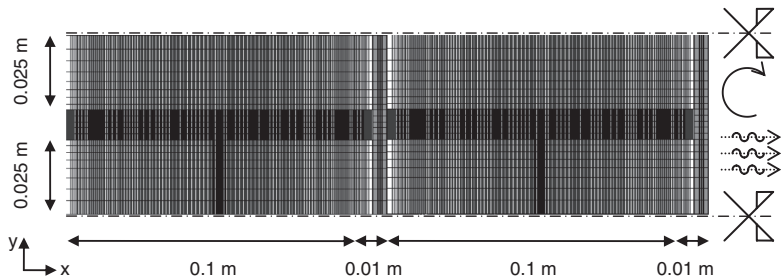
We consider a two-dimensional, periodic cell in a vertical cross section of a double-wythe masonry wall (Fig. 4.8). Three-dimensional effects are not accounted for. The wall is composed of bricks ($L \times W \times H = 0.21 \times 0.1 \times 0.05$ m) with a 0.01 m mortar joint between them. The wall is not pointed. At the outside, a mineral-based plaster of 0.01 m thickness is applied. The inside surface is left unfinished. Insulation material is not present.

At the symmetry axes of the model, the displacements are restricted in the y-direction ($\bar{u}_y = 0$) and no-flux boundary conditions are imposed ($\bar{g} = 0$). In order to prevent rigid body motion, the displacement in horizontal direction of the bottom-left node of the computational model is restricted ($\bar{u}_x = 0$). Gravitational effects are neglected. This implies that the compressive load of the brickwork above the investigated periodic cell is not taken into account. Plane strain conditions are assumed. The in- and out-side surfaces are exposed to climatic boundary conditions, expressed by:

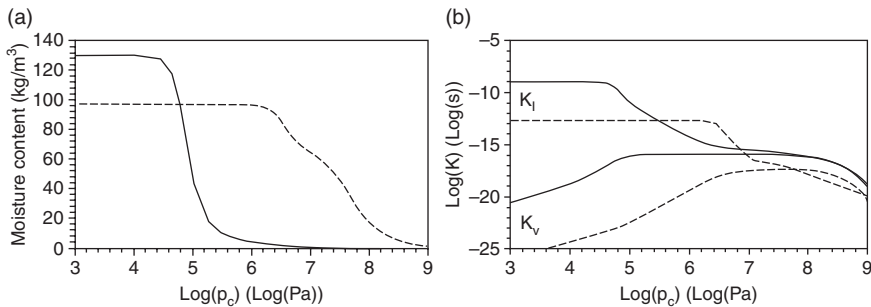
$$\bar{g} = \beta(\bar{p}_v - p_v) \quad [4.24]$$

Equation [4.24] describes the exchange of mass with the environment by means of evaporation or condensation. The coefficient β is a mass transfer coefficient taken equal to 18.5×10^{-9} s/m for exchange with an indoor environment and 140.0×10^{-9} s/m for exchange with the outdoor climate. Rain is not considered. The indoor environment is assumed to have a constant temperature of 293.15 K and a relative humidity of 50%. The temperature and relative humidity of the outdoor climate are 283.15 K and 85%, respectively.

All materials are considered linear elastic and isotropic (Equation [4.23]). Lamé constants $\lambda = 3.09$ GPa and $\mu = 7.22$ GPa are assumed for brick,



4.8 Periodic cell of the double-wythe masonry wall used in this study.



4.9 (a) Moisture content and (b) liquid and vapour permeability as a function of capillary pressure for brick (solid line) and mortar/render (dashed line).

0.66 and 0.99 GPa for mortar and 1.86 and 4.35 GPa for render, respectively. Hygric effects are taken into account by means of the effective-stress principle (Equations [4.21] and [4.22]). A Biot coefficient of 0.6 is assumed for all materials. The moisture capacity is modelled as a linear superposition of van Genuchten type functions, according to Durner (Equation [4.12]). The liquid permeability is obtained using the model of Mualem (Equation [4.17]). The hygric material properties of the three materials are depicted in Fig. 4.9. The mechanical strength of the render is assumed to develop gradually towards its final value of 4 MPa. This is a simplified way to describe the hardening during hydration. In practice all properties will gradually change during hardening, but insufficient experimental data were found to include this in the simulation. Following Moonen *et al.* (2008), discrete cracks are introduced in the mortar when the effective stress exceeds the tensile strength. The crack orientation is orthogonal to the principal stress direction.

4.5.2 Render applied to a saturated masonry wall

To simulate the behaviour of a wet render, applied to a saturated wall, we assume an initial capillary pressure of -10^4 Pa for both components ($S \approx 99\%$). The initial temperature of the structure is assumed to be equal to the inside temperature (293.15 K). We solve for capillary pressures and displacements. Plate I (see colour section between pages 208 and 209) illustrates the resulting failure pattern after one day of drying (top figure) and the near-equilibrium state after 100 days (bottom figure).

In the first hours of drying, the saturation in the surface layer of the render decreases rapidly. Thereby, hygric stresses develop, exceeding the tensile strength of the young material. As a result, a distributed network of fine surface cracks is formed (see arrows in Plate Ia).

Additionally, moisture diffuses from the brick via the render towards the surface. Because of the difference in moisture properties, the degree of saturation at the brick–render interface will decrease faster in the brick than in the render. The brick deforms during the drying process, and subjects the render to tensile loading and bending. Because the joints were not fully pointed, a small cavity exists. This cavity locally hinders the supply of moisture from the bulk of the wall towards the surface. Therefore, drying of the render is not uniform, and a shrinkage-induced stress concentration arises at the position of the joint. These effects combine to cause crack initiation (Plate Ia).

Moisture also diffuses from the brick towards the indoor environment. Nevertheless, less drying is observed at this side. This results from a combination of factors: (i) The indoor mass transfer coefficient (β) is lower than the outdoor one, therefore the corresponding mass flux towards the indoor environment is smaller as well. Moreover, since both the degree of saturation and the liquid permeability of the mortar remain approximately constant until the capillary pressure drops below $\approx -10^{6.4}$ Pa, the large mass flux towards the outdoor climate can take place for a long period of time. (ii) Despite the low relative humidity, the indoor vapour pressure is higher than the outdoor vapour pressure at the given temperatures, which results in a net mass flux from inside to outside. (iii) The capillary moisture content of the brick material is higher than that of mortar, which implies that more water needs to be removed from the brick to decrease its degree of saturation. The combination of these three factors explains the higher drying rate to the outside climate under the given combination of initial conditions, boundary conditions and material properties.

As drying proceeds, the stresses in the render resulting from the restrained shrinkage increase, and one of the existing cracks propagates further. The crack in the render creates a pathway between the cavity and the outside environment (Plate Ib). In a later stage, moisture might enter via this channel, expose the brick-render interface to wetting, and trigger an acceleration of the degradation process.

4.5.3 Render applied on a dry masonry wall

A dry masonry wall is modelled by assuming an initial capillary pressure of -10^8 Pa ($S \approx 1\%$). The render is wet when applied, and therefore an initial capillary pressure of -10^4 Pa ($S \approx 99\%$) is chosen. The boundary conditions towards the outside environment are similar to those in the previous example, but we assume a higher outdoor wind speed, resulting in a higher surface transfer coefficient ($\beta = 280.0 \times 10^{-9}$ s/m). Plate II (see colour section between pages 208 and 209) shows the failure pattern after 1 min, 20 min, 3 h and 12 h of drying.

The difference in vapour pressure between the surface of the saturated render and the surrounding air controls the drying process. The high wind

speed (modelled by the high value for β) leads to a high drying rate. The degree of saturation in the surface layer of the render decreases rapidly. Already after one minute, the drying-induced hygric stress reaches the tensile strength of the fresh material and small surface cracks appear (Plate IIa). Furthermore, the large difference in capillary pressure between brick and render causes drying at the reverse side of the render. The drying-induced shrinkage of the render is hindered by the stiffer brick material. As a result, a series of parallel cracks is initiated orthogonal to the brick–render material interface (Plate IIa).

As the drying proceeds many surface cracks appear (Plate IIb). After three hours of drying, the crack pattern at the surface is fully formed (compare Plate IIc and IId). As the drying proceeds, the bending in the render vanishes and the cracks close (not shown).

4.6 Summary and future trends

Degradation of materials usually does not have a single identifiable cause, but results from the complex interaction between different types of degradation mechanisms. Moisture transport plays a crucial role in many of these processes and is therefore of particular interest.

Degradation should only occur after a long period of time. For studying such slow processes, modelling approaches are very well suited. This chapter gives a short overview on modelling unsaturated moisture transfer in porous materials such as concrete, and the underlying assumptions. It has been shown that the quality of the simulations crucially depends on two material properties, namely the capacity and the permeability. The experimental determination of these properties remains challenging. A possible way out is to measure the pore-size distribution of the material by means of quantitative imaging techniques. The capacity is proportional to the pore-size distribution. The permeability can be obtained from the pore-size distribution using a network approach. Once the properties are determined at the macro-scale, moisture-transfer simulations can be performed.

It has been shown that the presence of moisture inside the pore system generates hygric stresses, as described by the theory of poromechanics. In combination with stresses induced by other processes, these might lead to cracking. Cracks alter the permeability of the porous material. Moisture transfer in the bulk is diffusion-dominated. Moisture transfer in cracks is, however, driven by capillary suction. Several modelling techniques have been mentioned to incorporate the change in permeability due to crack formation in the moisture-transfer simulations. The most promising tool is a continuous–discontinuous framework. Therein, the crack pattern is explicitly modelled.

A coupled hygro-mechanical model including fracture processes is the basis for any sustainability analysis. These models need to be tested, based on experimental data. Validation is crucial to put trust in these models. Only then can the model be applied to study e.g. the influence of the design of a structural component on its lifetime, the remaining service lifetime of a component, critical crack opening (e.g. nuclear plants, underground storage of waste), etc.

4.7 References

- K.C. Abbaspour, M.Th. van Genuchten, R. Schulín and W. Schlappi, 1997. A sequential uncertainty domain inverse procedure for estimating subsurface flow and transport parameters, *Water Resources Research*, **33**(8), 1879–1892.
- J. Alfaiate, P. Moonen, L.J. Sluys and J. Carmeliet, 2010. On the use of strong discontinuity formulations for the modeling of preferential moisture uptake in fractured porous media, *Computer Methods in Applied Mechanics and Engineering*, **199**(45–48), 2828–2839.
- Y. Bachmat and J. Bear, 1986. Macroscopic modelling of transport phenomena in porous media. 1: The continuum approach, *Transport in Porous Media*, **1**, 213–240.
- G.I. Barenblatt, Iu.P. Zheltov and I.N. Kochina, 1960. Basic concepts in the theory of seepage of homogeneous liquids in fissured rocks (strata), *Prikladnaya Matematika I Mekhanika*, **25**(5), 852–864.
- J. Bear, C. Braester and P.C. Menier, 1987. Effective and relative permeabilities of anisotropic porous media, *Transport in Porous Media*, **2**, 301–316.
- B. Berkowitz, J. Bear and C. Braester, 1988. Continuum models for contaminant transport in fractured porous formations, *Water Resources Research*, **24**(8), 1225–1236.
- A.W. Bishop, 1959. The principle of effective stress, *Teknisk Ukeblad*, **39**, 859–863.
- R.H. Brooks and A.T. Corey, 1964. *Hydraulic properties of porous media*, Hydrology papers 3, Colorado State University, Fort Collins, Colorado.
- W. Brutsaert, 1979. Universal constants for scaling the exponential soil water diffusivity?, *Water Resources Research*, **15**(2), 481–483.
- E. Buckingham, 1907. *Studies on the movement of soil moisture*, USDA Bureau of Soils Bulletin No 38. U.S.D.A., Washington, DC.
- J. Carmeliet, F. Descamps and G. Houvenaghel, 1999. A multiscale network model for simulating moisture transfer properties of porous media, *Transport in Porous Media*, **35**, 67–88.
- J. Carmeliet and S. Roels, 2002. Determination of the moisture capacity of porous building materials, *Journal of Thermal Envelope And Building Science*, **25**, 209–237.
- E. Castillo, G.M. Karadi and R.J. Krizek, 1972. Unconfined flow through jointed rock, *JAWRA Journal of the American Water Resources Association*, **8**(2), 266–281.
- I. Chatzis and F. A. L. Dullien, 1977. Modelling pore structure by 2-D and 3-D networks with application to sandstones, *Journal of Canadian Petroleum Technology*, **16**(1), 97–108.
- E.C. Childs and N. C. George, 1948. Soil geometry and soil-water equilibria. *Discussions of the Faraday Society*, **3**, 78–85.

- B.D. Coleman and W. Noll, 1963. The thermodynamics of elastic materials with heat conduction and viscosity, *Archive for Rational Mechanics and Analysis*, **13**, 168–178.
- O. Coussy, 1995. *Mechanics of porous continua*, Wiley, Chichester.
- R. De Boer, W. Ehlers, S. Kowalski and J. Plischka, 1991. *Porous media, a survey of different approaches*, Forschungsbericht aus dem Fachbereich Bauwesen, Heft 54, Universität-Gesamthochschule Essen.
- F. Descamps, 1997. *Continuum and discrete modelling of isothermal water and air flow in porous media*, dissertation, Catholic University of Leuven, Leuven, Belgium.
- W.Durner, 1992. *Predicting the unsaturated hydraulic conductivity using multi-porosity water retention curves*. In M. Th. van Genuchten, F. J. Leij and L. J. Lund (Eds.), Proc. Int. Workshop, Indirect Methods for Estimating the Hydraulic Properties of Unsaturated Soils, University of California, Riverside, CA, 185–201.
- W. Durner, 1994. Hydraulic conductivity estimation for soils with heterogeneous pore structure, *Water Resources Research*, **30**(2), 211–233.
- D.H. Everett and W. I. Whitton, 1952. A general approach to hysteresis, *Transactions of the Faraday Society*, **48**, 749–752.
- I. Fatt, 1956. The network model of porous media: I. Capillary pressure characteristics, *Petroleum Transactions AIME*, **207**, 144–159.
- G.H. Galbraith, 1992. *Heat and mass transfer within porous building materials*, dissertation, Department of Mechanical Engineering, University of Strathclyde, Glasgow, Scotland.
- W.R. Gardner, 1958. Some steady state solutions of the unsaturated moisture flow equation with application to evaporation from a water table. *Soil Science*, **85**, 228–232.
- W.R. Gardner and M.S. Mayhugh, 1958. Solutions and tests of the diffusion equation for the movement of water in soil, *Soil Science Society of America Journal*, **22**, 197–201.
- H.H. Gerke and M.Th. van Genuchten, 1993. A dual-porosity model for simulating the preferential movement of water and solutes in structured porous media. *Water Resources Research*, **29**(2), 305–319.
- W.G. Gray and B.A. Schrefler, 2001. Thermodynamic approach to effective stress in partially saturated porous media, *European Journal of Mechanics A-Solids*, **20**(4), 521–538.
- S.M. Hassanizadeh and W.G. Gray, 1979. General conservation equations for multi-phase systems: 1 Averaging procedure, *Advances in Water Resources*, **2**, 131–144.
- S.M. Hassanizadeh and W.G. Gray, 1979. General conservation equations for multi-phase systems: 2 Mass, momenta, energy and entropy equations, *Advances in Water Resources*, **2**, 191–203.
- S.M. Hassanizadeh and W.G. Gray, 1980. General conservation equations for multi-phase systems: 3. Constitutive theory for porous media flow, *Advances in Water Resources*, **3**, 25–40.
- H. Hens, 1996. IEA Annex 24: *Heat, air and moisture transfer through new and retro-fitted insulated envelope parts*. Task 1: Modelling. Acco, Leuven.
- J.W. Hopmans and J. Šimůnek, 1999. Review of inverse estimation of soil hydraulic properties, In M.Th. van Genuchten, F.J. Leij, and L. Wu (Eds.), *Proceedings of the International Workshop on Characterization and Measurement of the*

- Hydraulic Properties of Unsaturated Porous Media* (Riverside, California, October 22–24, 1997), University of California, Riverside, California, 643–659.
- N.J. Jarvis, P.-E. Jansson, P.E. Dik and I. Messing, 1991. Modelling water and solute transport in macroporous soil. I. Model description and sensitivity analysis, *Journal of Soil Science*, **42**, 59–70.
- Q. Jiang and R.K.N.D. Rajapakse, 1994. On coupled heat-moisture transfer in deformable porous media, *The Quarterly Journal of Mechanics and Applied Mathematics*, **47**(1), 53–68.
- K. Kiessl, 1983. *Kapillarer und dampfförmiger feuchtetransport in mehrschichtigen bauteilen*. Dissertation, Universität-Gesamthochschule Essen, Germany.
- A. Klute, 1952. A numerical method for solving the flow equation for water in unsaturated materials, *Soil Science*, **73**(2), 105–116.
- P.C.D. Milly, 1980. *The coupled transport of water and heat in a vertical soil column under atmospheric excitation*. Dissertation, Massachusetts Institute of Technology, United States.
- P. Moonen, J. Carmeliet and L.J. Sluys, 2008. A continuous-discontinuous approach to simulate fracture processes in quasi-brittle materials, *Philosophical Magazine*, **88**(28–29), 3281–3298.
- P. Moonen, L.J. Sluys and J. Carmeliet, 2010. A continuous-discontinuous approach to simulate physical degradation processes in porous media, *International Journal for Numerical Methods in Engineering*, **84**(9), 1009–1037.
- Y. Mualem, 1976. A new model for predicting the hydraulic conductivity of unsaturated porous media, *Water Resources Research*, **12**(3), 513–522.
- Y. Mualem and G. Dagan, 1975. A dependent domain model of capillary hysteresis, *Water Resources Research*, **11**(3), 452–460.
- A.V. Neimark, 1989. Multiscale percolation systems, *Soviet Physics, Journal of Experimental and Theoretical Physics*, **69**(4), 786–791.
- C.R. Pedersen, 1990. *Combined heat and moisture transfer in building constructions*. Dissertation, Technical University of Denmark, Denmark.
- J.R. Philip, 1954. Some recent advances in hydrologic physics, *Journal of the Institute of Engineers Australia*, **26**, 255–259.
- J.R. Philip and D.A. de Vries, 1957. Moisture movement in porous materials under temperature gradients, *Transactions, American Geophysical Union*, **38**(2), 222–232.
- A. Poulouvassilis, 1962. Hysteresis of pore water, an application of the concept of independent domains, *Soil Science*, **93**, 405–412.
- L.A. Richards, 1931. Capillary conduction of liquids through porous mediums, *Physics*, **1**, 318–333.
- S. Roels, J. Elsen, J. Carmeliet and H. Hens, 2001. Characterisation of pore structure by combining mercury porosimetry and micrography, *Materials and Structures*, **34**, 76–82.
- R. Schirmer, 1938. Die Diffusionszahl von Wasserdampf-Luftgemischen und die Verdampfungsgeschwindigkeit, *VDI Beiheft Verfahrenstechnik*, **6**, 170.
- S.G. Shikaze, E. A. Sudicky and C. A. Mendoza, 1994. Simulation of dense vapor migration in discretely fractured geologic media, *Water Resources Research*, **30**(7), 1993–2009.
- J.C. Simo and J.W. Ju, 1987. Strain- and stress-based continuum damage models – 1. Formulation, *International Journal of Solids and Structures*, **23**(7), 821–840.

- J. Šimůnek, N.J. Jarvis, M.Th. van Genuchten and A. Gärdenäs, 2003. Review and comparison of models for describing non-equilibrium and preferential flow and transport in the vadose zone, *Journal of Hydrology*, **272**, 14–35.
- J. Šimůnek and M.Th. van Genuchten, 1996. Estimating unsaturated soil hydraulic properties from tension disc infiltrometer data by numerical inversion, *Water Resources Research*, **32**, 2683–2696.
- R. Therrien and E. A. Sudicky, 1996. Three-dimensional analysis of variably-saturated flow and solute transport in discretely-fractured porous media, *Journal of Contaminant Hydrology*, **23**(1–2), 1–44.
- H.R. Thomas and Y. He, 1995. Analysis of coupled heat, moisture and air transfer in a deformable unsaturated soil, *Geotechnique*, **45**(4), 677–689.
- W. Thomson, 1871. LX. On the equilibrium of vapour at a curved surface of liquid, *Philosophical Magazine Series 4*, **42**(282), 448–452.
- M.T. van Genuchten, M.G. Schaap, B.P. Mohanty, J. Simunek and F.J. Leij, 1999. Modeling flow and transport processes at the local scale. In J. Feyen and K. Wiyono (Eds.), *Modelling of Transport Process in Soils at Various Scales in Time and Space*, Wageningen Pers, Wageningen, The Netherlands, 23–45.
- NC Wardlaw and M McKellar, 1981. Mercury porosimetry and the interpretation of pore geometry in sedimentary rocks and artificial models. *Powder Technology*, **29**, 127–143.
- J.E. Warren and P.J. Root, 1963. The behavior of naturally fractured reservoirs, *Society of Petroleum Engineers Journal*, **3**(3), 245–255.
- S. Whitaker, 1967. Diffusion and dispersion in porous media, *Journal of the American Institute of Chemical Engineers*, **13**(3), 420–427.
- K. Xu, J.F. Daian and D. Quenard, 1997. Multiscale structures to describe porous media, Part I: theoretical background and invasion by fluids, *Transport in Porous Media*, **26**, 51–73.

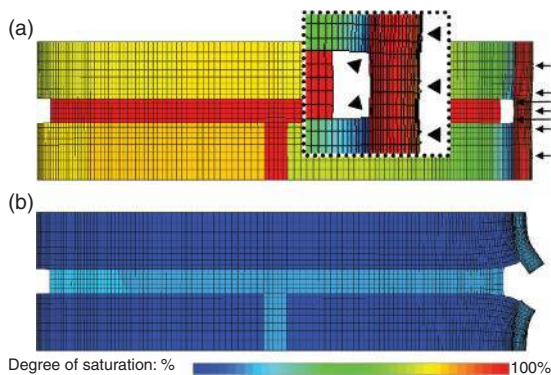


Plate I (Chapter 4) Deformed configuration of a wet render, applied to a wet masonry wall (a) after 1 day of drying, and (b) at equilibrium. Deformations are magnified by a factor 1000. Colours correspond to the degree of saturation. Arrows indicate the positions where cracks initiate.

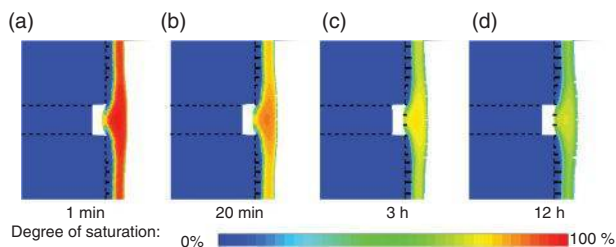


Plate II (Chapter 4) Deformed configuration of a wet render, applied to a dry masonry wall after (a) 1 min, (b) 20 min, (c) 3 h and (d) 12 h of drying. Deformations are magnified by a factor 1000. Colours correspond to the degree of saturation. Dashed lines indicate material boundaries. Cracks are overlaid with black lines to increase visibility.

Modelling the response of concrete structures to dynamic loading

W. RIEDEL, Ernst Mach Institut, Germany and
P. FORQUIN, University of Lorraine, France

DOI: 10.1533/9780857097538.2.125

Abstract: Chapters 5–10 will deal with the rate dependent to shock induced dynamic behaviour and modelling of concrete in tension. It can be caused in practical applications by structural dynamic response, stress wave superposition or a mixture of both. In every case the type of loading mechanism has very strong implication on the occurring and achievable peak strain rates. The current chapter will therefore introduce dynamic tensile loading states on the basis of practical applications. They range from moderate rate earthquake loading, across blast response to high and hypervelocity impact. The discrimination of structural and wave dynamic response mechanisms is a necessary basis to understand the description of dynamic material response regimes of concrete in Chapters 6 to 10.

Key words: bending and shear failure, compression, shock, release waves, lateral dispersion, earthquake, blast, impact, contact detonation.

5.1 Introduction: dynamic loading regimes affecting concrete structures

Dynamic tensile response of concrete structures, its consequences on the material level and modelling approaches are the topics of Chapters 5 to 11. Across the dynamic regime both inertia forces on structural and local level, and dynamic material response, have to be described appropriately and separately. The latter is usually characterized by rates of loading in terms of ‘strain rate’ or ‘stress rate’ (Equation [5.1a,b], with strain ϵ or stress σ changing over time t).

$$\dot{\epsilon} = \frac{\partial \epsilon}{\partial t} \quad \dot{\sigma} = \frac{\partial \sigma}{\partial t} \quad [5.1a,b]$$

The mechanical properties of concrete are rate dependent, especially in tension. Two regimes can be distinguished, which will be described here-under and, finally, compared in Fig. 5.4. The regime depends on the type of dynamic loading and the structure. Both will play a decisive role in which stress or strain rates will occur.

The basic macroscopic deformation mechanisms which can lead to dynamic tension are:

1. Strong oscillations, as, for example, excited by an earthquake. Selected global deformation modes of low frequencies (3–30 Hz) and strain rates ($\partial\epsilon/\partial t < 10^{-1}/s$) activate **inertia forces**, but only an insignificant or very low strength increase.
2. **Rate effects** on concrete strength ($10^{-1} < \partial\epsilon/\partial t < 10^2/s$) occur **during structural response** to impulsive aerial loading, such as air blast (>100 Hz) or soft impact of a deformable airframe (10–100 Hz). A broad band of frequencies and deformation modes are excited.
3. **Stress waves and dynamic strain fields** of high frequencies ($>>100$ Hz) and strain rates $\partial\epsilon/\partial t < 10^3/s$ are generated by localized impact loading i.e. by a rigid penetrator at velocities well below 1000 m/s. They lead to **high triaxial compressions**, shear and dynamic membrane tension loading. Release wave superposition resulting in dynamic tensile states ('spallation') starts to occur.
4. Contact detonation or hypervelocity impacts generate **shock waves** with **shock heating** of the material. Highest rate tensile states from **superposition of release waves** ('spallation') become a dominant failure mechanism on the opposite free surface.

Dynamic phenomena accumulate from low to very high rates, so that a complex mix of structural and material dynamic influences governs regimes 2 and 3. At the highest stress levels with shock waves, however, structural dynamic response becomes insignificant to the extent of concrete cracking and failure, since it comes into play at much later timescales (see Fig. 5.4).

In the following, the above dynamic loading regimes are highlighted with one example each for final comparison in Fig. 5.4. Validated and predictive numerical simulations based on hydrocodes and plasticity models (see Chapter 10) are mainly used to demonstrate and investigate them. The examples will serve as an introduction to detailed descriptions of experimental, engineering and computational techniques in Chapters 6 to 11. Only a limited number of exemplary references, rather than complete surveys, for each application area are given for the sake of a compact comparison of the different regimes.

5.2 Earthquake loading and impact deflection: inertia effects

Serving as a first example is the earthquake response of the ‘security scraper’ concept designed with an ultra-high performance concrete core against aircraft impact (Nöldgen, 2011, 2012). The high-rise building, designed for an altitude of 500 m (or more), bears a gravity load of 6000 MN on a ground cross-section of 60 × 60 m with an overall bending stiffness of 33 MN/m. The well-known ground motion of the ‘El Centro’ earthquake is exercised to excite the first global deformation mode increasingly over a time of 207 s. At this point, the building’s peak tip deflection is 1.83 m, which exceeded the design wind case of 1.06 m (Nöldgen, 2011) and the recommended maximum value $x < h/500$ for high-rise buildings (König and Liphardt, 2003). The oscillation period is $T \sim 14$ s, Plate III (see colour section between pages 208 and 209).

At close to the limit of bending strength, it is assumed that 90% of the tensile strength $f_t = 9$ MPa of the ultra-high performance concrete is activated. This corresponds to a loading rate of 2.3 MPa/s, according to Equation [5.2], in a quarter oscillation from zero to peak deflection within 3.5 s. Using a typical Young’s modulus of 53 GPa in Equation [5.3], this shows a gross strain rate of $4 \times 10^{-5}/s$ for the global deformation portion.

$$\dot{\sigma}_{\max} \approx \frac{\sigma_{\max,t}}{T/4} = \frac{0.9f_t}{14s/4} = \frac{0.99\text{ MPa}}{3.5s} = 2.3\text{ MPa/s} \quad [5.2]$$

$$\dot{\epsilon}_{\max} = \frac{\sigma_{\max}}{E} = 4.10^{-5}/s \quad [5.3]$$

Higher modes, and smaller and stiffer buildings, will provide eigenfrequencies and loading rates that are higher by one or two orders of magnitude. On the local scale, i.e. the connections of structural elements to storey plates, higher strain rates of up to 1/s can be reached. For global structural integrity, however, it already becomes apparent here that rate-increased material strength is not a major influence. Appropriate damping and yielding (plasticity demand) properties are more important. The same observation is valid also for the global structural response following an aircraft impact (Plate III, lower left, red line, (Nöldgen, 2011)). But in the local impact zone, much higher loading rates occur on a local scale, as described in Section 5.4.

5.3 Blast response: rate-dependent strength

The second example investigates the six-storey, wall-stiffened concrete frame building in Plate IV (see colour section between pages 208 and 209).

It is subjected to an external blast load of 500 kg trinitrotoluene (TNT) equivalent, at a distance of 10 m. The redundant load-bearing R/C structure can easily withstand this loading on a global scale. Single wall sections close to the charge respond by bending. Their deformation is most commonly and efficiently assessed using engineering approaches such as single-degree-of-freedom (SDOF) models, as described in comprehensive detail in the US tri-service manuals (TM5-1300 1990) and the later release of Unified Facilities Criteria 3-340-02 (UFC, 2008) and Chapter 11. Alternatively, finite element simulations can be used to analyse the dynamic tensile states induced by the air-shock loading (Riedel *et al.*, 2010a). Moreover, it makes sense to validate finite element method (FEM) tools and their rate-dependent material descriptions under such simple component geometries, in order to have confidence with more complex surface shapes, i.e. with curvature and openings.

In the example, the wall slab is mainly challenged by dynamic bending, since the reflected blast overpressure of 4.2 MPa does not exceed the compressive strength and direct shear capacity of the conventional concrete member. This is observed consistently in shock-tube tests and numerical simulations. Plate IV (see colour section between pages 208 and 209) shows computed peak strain rates of $\partial\epsilon/\partial t \sim 30/s$ in the tensile zone of the mid-section after damage evolution. In this regime, dynamic strength increase becomes significant and has to be included in modelling approaches, irrespective of whether finite element methods or simplified single- or two-degree-of-freedom models are used, as in Chapter 11.

5.4 Projectile impact loading: compressibility and high triaxial stresses

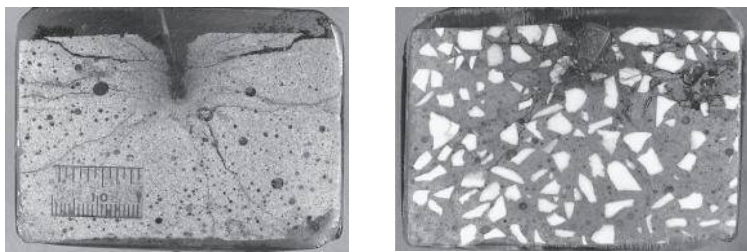
Several damage modes under triaxial compression and extension in concrete structures are activated by impact of rigid projectiles (Li *et al.*, 2005; Forquin *et al.*, 2008; Forquin and Hild, 2010). They spread into the target during projectile penetration, leading to fracture modes such as ‘scabbing’ (also called ‘cratering’) on the front face, ‘spalling’ on the rear face and radial cracking around the tunnel. These fracturing processes strongly influence the ballistic resistance of concrete targets, particularly in the case of slabs that are thin compared to the projectile diameter.

The first example investigates a ballistic impact experiment with an ogival pointed penetrator on a concrete slab, performed by Cargile (Plate V (see colour section between pages 208 and 209), (Cargile, 1999)). The penetrator hits a concrete target 127 mm thick at 316 m/s. The cratering on the front face and spalling on the rear face can be clearly observed, see Plate Va. Moreover, several radial cracks have propagated from the tunnel through the whole target, as visible on the lower left view. Recently Erzar (2010) numerically analysed the configuration in order to identify tensile and shear

loading which induced these fracture processes. As shown in Plate Vb, axial and hoop tensile loading explain the cratering on the front face and radial cracking inside the target. Related axial and radial strains are plotted as functions of time in Plate Vc, with typical strain rates of $50 < \partial\epsilon/\partial t < 300/\text{s}$.

Dynamic tensile states mainly occur due to a radial-strain field imposed by the intruding penetrator. In this regime, compaction and triaxial strength properties of the concrete in the range of several hundred MPa, derived from specialized triaxial machines at the University of Grenoble (Gabet *et al.*, 2008; Vu, 2009) or at ERDC-WES (Williams *et al.*, 2010), are of key importance, see Plate VI (see colour section between pages 208 and 209). Stress waves do occur, but only exceeding the concrete strength close to the penetrator nose because of limited velocity and the pointed contact surface.

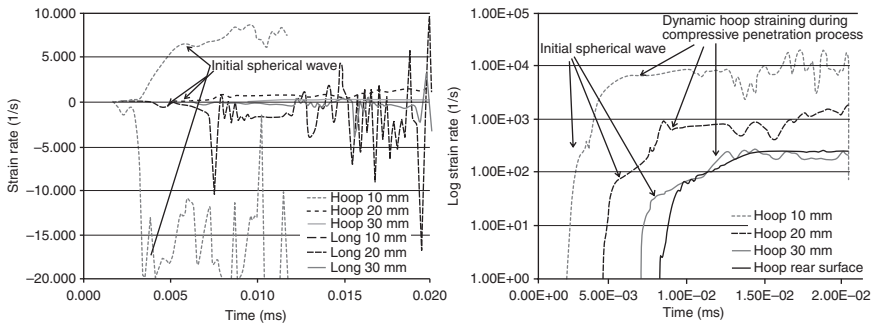
Deep penetration of a blunt, hard steel projectile (diameter 5.3 mm, length 8 mm and mass 1.2 g) at 750 m/s (Forquin *et al.*, 2006) serves as a second example. Targets made of a cementitious matrix, with and without alumina aggregates, are placed in an aluminium casing to keep the concrete fragments in place. Each target has been infiltrated after impact with a hyper-fluid coloured resin, cut and polished for subsequent analysis. Several distinct damage types are clearly observable on the cross-sectional views in Figs 5.1a and 5.1b. In the vicinity of the tunnel, the mortar matrix is totally pulverized and rearranged, due to the level of confining pressure and crushing of concrete pores. Moreover, several long cracks radiating from the tunnel region are observable. On the front surface, the penetration of the projectile induced a ‘saucer-shaped cratering’ as the result of heavy compression in the direction normal to the tunnel axis, leading to a cone-like expulsion of material on the front surface.



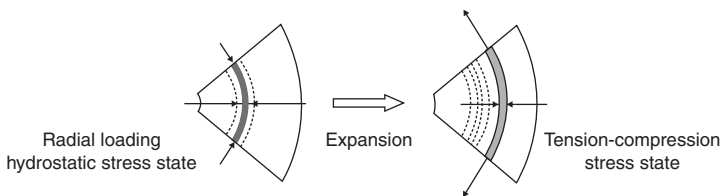
(a) Mortar without aggregates, impact velocity: 756 m/s, depth of penetration: 15 mm, straight tunnel

(b) Mortar reinforced with alumina aggregates, impact velocity: 759 m/s, depth of penetration: 7.7 mm, unbalanced projectile

5.1 (a, b) Ballistic impact of a steel projectile (mass: 1.3g, $\phi = 5.3$ mm, hardness: 65 HV) against a cementitious matrix reinforced with (right) and without (left) ceramic particles saucer-shaped cratering on the front face (‘scabbing’), compaction, collapse of pores close to the penetration channel and radial cracks initiated from pores, hampered by particles (reprinted from Forquin *et al.*, 2006 with permission from EDP Sciences).



5.2 Addition numerical analysis of ballistic impact in Forquin *et al.* (2006) and Plate VII hoop tensile rates of several 100/s are reached in the initial stress wave, up to 30000/s during compressive longitudinal/hoop extension loading of the later penetration process.



5.3 Dynamic triaxial compression leading to hoop tension states, described by Riou (1998) and Riedel (2010); reprinted with permission from Elsevier.

Numerical simulations are again used to investigate the transient states in the targets. The commercial finite element code Abaqus/Explicit and the Krieg, Swenson Taylor plasticity model for the cementitious matrix (Forquin *et al.*, 2009) are the basis (see Chapter 10). In the model, limit states are defined in terms of principle stress difference versus mean stress, and mean stress versus volumetric strain (see Chapter 10). Plate VII (see colour section between pages 208 and 209) shows on the one hand a field of pressure of about 650 MPa in front of the projectile. On the other hand, a tensile hoop stress field propagates through the target, which explains the radial cracks visible in subsequent study. The analysis in Fig. 5.2 shows strain rates, associated with tensile hoop stresses for the initial wave propagation from below, to several hundred 1/s. At later stages the progressing penetrator forces the material under longitudinal compression and hoop tension to rates from 600 to 30000/s.

The simulations highlight that, for increased impact velocities below and above 1000 m/s, tensile damage is also induced by the initial, preceding stress waves before the strain fields are imposed on later penetration stages. As highlighted in Fig. 5.3, the tensile cracking occurs as a result of diverging stress waves, leading to lateral expansion of the material while axial compressions are still present. Riou *et al.* (1998) and Riedel *et al.* (2010)

investigated and described this effect for ceramics and Forquin and Hild (2008) for ultra-high performance concretes on the basis of 'Edge-on Impact Experiments' and numerical studies. This experiment type is later modified and applied to concrete in Section 6.6 and Plate X (see colour section between pages 208 and 209).

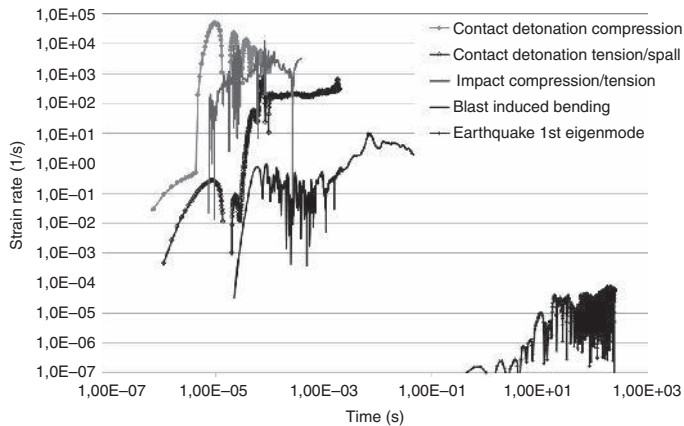
In summary, the impact of a hard projectile on a concrete target at an impact velocity of several tens to hundreds metres per second induces damage modes, such as scabbing, on the front face, spalling on the rear face, and radial cracking, pore collapse and confined shearing around the penetration channel. These result from a complex multi-axial stress loading (confined compression and dynamic extension) with typical hoop strain rates ranging from 50/s to $\partial\epsilon/\partial t < 500$ /s in the initial spherical stress wave and up to $\partial\epsilon/\partial t \approx 10\,000$ /s in the compressive extension field in front of the penetrator. The dynamic behaviour of concrete under such loading rates, as well as the whole fracturing process of the target, has to be described in the modelling to perform predictive numerical simulations of the impact of a rigid projectile against a concrete structure.

5.5 Contact detonations and explosive formed projectiles (EFPs): shock and release properties

Stress-wave induced failure mechanisms gain increasing importance, compared to penetration-imposed strain fields, with increasing penetrator velocity. Such 'hypervelocity impacts' can result from very fast ammunition (up to 1600 m/s), explosive formed projectiles (EFPs) (4000–7000 m/s), shaped charges (up to 10000 m/s), or meteoroid impact (3000–70000 m/s).

These highest strain rates are also reached by contact detonation, where very high pressure detonation products locally penetrate the concrete element. The example in Plate VIII (see colour section between pages 208 and 209) shows a strong shock wave of more than 6 GPa generated by a contact detonation of the high explosive pentaerythritol tetranitrate (PETN – often also referred to as 'nitropenta') in the kg range onto concrete plate of 23.5 cm thickness. It is reinforced by two layers of 6 mm diameter reinforcement bars with 10 cm spacing. In the zone directly under the contact charge, extreme compression rates of 10⁵/s occur in the shock wave in the concrete (see Fig. 5.4 'compression'). Here the shock properties of concrete dominate.

Plate IX (see colour section between pages 208 and 209) shows the difference between static and dynamic compression of concrete grout under uniaxial strain (Riedel *et al.*, 2008). The lower line with the unloading states is reached in a slow isothermal oedometer test with heavy confinement, forcing a 1D strain state. The shock states are generated by inverse plate impact experiments with dynamic 1D self-confinement in the centre of the plate. The figure shows that, for example at a compressive strain level of 0.3, a



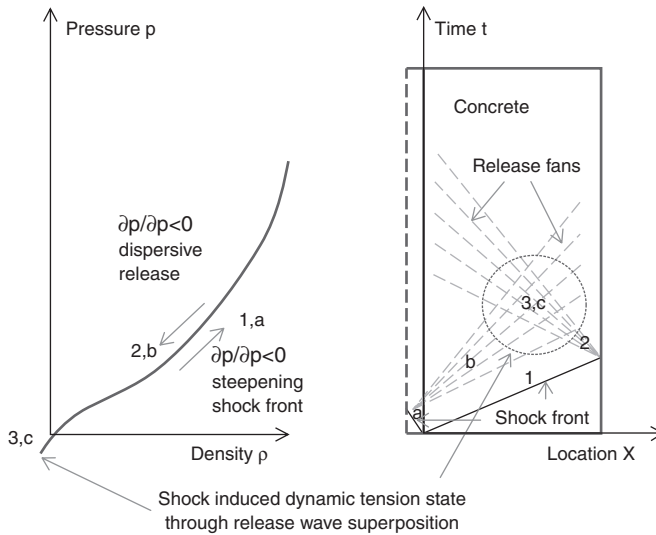
5.4 The range of dynamic loading scenarios in terms of strain rate vs time.

difference from 1 to 5 GPa can be observed between static, isothermal loading and dynamic shock compression under the same strain state. Thus, correct shock properties are a precondition for correct stress-wave amplitudes before reflection into dynamic tension. Quasi-static triaxial compression tests are questionable for measuring the shock response of concrete, even if they reach hundreds of MPa of well-defined and controllable confinement stress.

Due to the short pulse length and dissipation processes, such as pore compaction and shock heating, the pressure waves rapidly decay in Plate VIII (see colour section between pages 208 and 209). Note that two different scales are necessary to show the pressures on the front and rear surfaces in one diagram.

At the free rear surface the shock is reflected as release wave (Fig. 5.5). In contrast to the incident shock, the release wave is of dispersive nature. Stronger unloading portions propagate slower than smaller amplitudes, thus a release fan rather than a sharp wave front propagates back into the concrete. For the two reasons, the damping on the incident compression wave and the dispersive nature of the release wave, the tensile states resulting from release wave superposition are of much lower strain rates compared to the compression rates on the loaded surface. The resulting strain rates of several 100/s, up to a maximum of 1000/s in the 'tension/spall' zone are shown in Fig. 5.4. It is important to note that the dynamic tension is not reached in one release (or decompression) fan, but only upon superposition of two or more release fans, i.e. following after the initial shock into the material.

Further intensifying the loading would not lead to increased strain rates, but to the destruction of the concrete by the incident compression waves. Thus, this type of loading indicates clearly an upper limit of purely tensile



5.5 Initial shock (1,a), dispersive release waves (2,b) and superposition in the target (3,c) leading to highest rate dynamic tensile states.

strain rates around some 1000/s (for concrete), which cannot be physically exceeded in practical applications. This limitation is defined by the compressive strength and the dispersive nature of release waves. Higher (hoop) tensile rates are only observed under impact, as in Section 5.4, but then always in combination with longitudinal compression.

5.6 Concluding remarks

Summing up, the observed domains of strain rates and load durations across the dynamic application range can be displayed with the help of double-logarithmic scaling in Fig. 5.4.

- Earthquake loading has typical durations of some tens to hundreds of seconds. Inertia forces dominate, and rate effects on material response are negligible or at least very small.
- Air-blast loading and aerial low velocity impact (<100 m/s) act in tens to hundreds of milliseconds, with active strain rate-dependent material behaviour in the range of $\partial\epsilon/\partial t < 10/\text{s}$. Support conditions play an important role in the structural response.
- Localized impact and penetration problems of some 100 m/s provide dynamic straining around the penetrator which leads to hoop extension. Compression/compaction properties and triaxial strength at several 100 MPa and strain rates of several hundred 1/s are dominant. Stress-wave

propagation starts to gain importance with increasing velocity towards 1000 m/s and blunt loading, but shock properties are still secondary. Strain rates $\partial\epsilon/\partial t$ of a few hundreds are reached in the hoop tension zone of the initial loading wave, longitudinal compression/hoop tension rates in front of the penetrator can reach and exceed $10^4/s$, but do not occur as pure tension.

- Contact detonations or hypervelocity impacts (>1500 to >10000 m/s) are dominated by stress-wave propagation and release/spallation. The higher the impact velocity or pressure, the more important become the shock properties as input conditions for tension states during release. Although compression rates around $10^5/s$ are common, tensile rates are limited for concrete to two orders of magnitude less to about 1000/s. The reason is compressive destruction of the concrete at higher loading intensities and the dispersive nature of the release wave.

As a consequence, some requirements on testing techniques can be drawn from this analysis:

- Dynamic direct tension experiments with the sample in equilibrium are promising in the range of moderate strain rates of several 1/s up to some 10/s.
- Highest rate dynamic tensile states of 100–1000/s or more can only be reached by impact-induced tension or superposition of release waves, resulting from compression waves below the compressive strength. Wave analysis within the sample is required, rather than force equilibrium considerations on boundary surfaces.
- The investigation of spherical/cylindrical compression waves leading to hoop extension with tension-compression states is of interest in investigating concrete material states in front of intruding penetrators.

Requirements on concrete models across the different regimes can be stated as follows:

- Earthquake simulations do not require dynamic material data. Inertia activated in modal deformations, plasticity and connections dominate.
- Dynamic aerial impact loads, such as air blast and soft airframe impact, require consideration of rate-dependent strength properties and appropriate models for failure and softening. Cracking, rather than a large damage zone, is in the focus.
- Localized penetration at ballistic velocities requires careful triaxial strength and compression descriptions at several 100 MPa, and strain rates in the range of 100/s to several 1000/s. Quasi-plastic behaviour under triaxial compression, and brittle behaviour at low confinements,

have to be captured. Post-peak softening and flow resistance of failed concrete under compression are important.

- High to hypervelocity impact and contact detonations require the above qualities with a consistent link to the shock properties of the material. The dramatic difference between isothermal and shock compression has to be captured. Support conditions and connections become insignificant, since they act orders of magnitudes later.
- For all loading conditions leading to dynamic tensile failure, alternative discretization techniques beyond FEM such as extended finite element method (XFEM), discrete element methods, smooth particle hydrodynamics (SPH) and other mesh-free methods should be considered. They can provide synergies with the constitutive models, avoiding simplistic numerical workarounds such as element erosion.
- For all loading situations with clearly defined phenomenology (bending or shear motion under blast, cratering under contact detonation), engineering tools are applicable for simple geometries such as reinforced slabs and columns. They allow fastest design, and are an additional independent analysis tool to be employed together with finite element (FE) modelling and experiments, as appropriate.

As a final, most general, requirement, the deformation mechanisms in the material level should be understood, as a basis for physical and phenomenological models on all scales. Key influence parameters on the local crack level should be identified, such as moisture content, influence of the interface transitions zone or aggregate geometries and strength.

5.7 References

- Cargile J.D. (1999). *Development of a constitutive model for numerical simulation of projectile penetration into brittle materials*. Technical report SL-99-11, U.S. Army Corps of Engineers, ERDC.
- Erzar B. (2010). *Ecaillage, craterisation et comportement en traction dynamique de betons sous impact: approches experimentales et modelisation*. PhD-thesis, University of Metz, France.
- Forquin P., Arias A. and Zaera R. (2006). An experimental method of measuring the confined compression strength of high-performance concretes to analyse their ballistic behaviour. *J. Phys. IV, DYMAT*, **134**, 629–634.
- Forquin P., Arias A. and Zaera R. (2008). Role of porosity in controlling the mechanical and impact behaviours of cement-based materials. *Int. J. Impact. Eng.*, **35**(3), 133–146.
- Forquin P., Arias A. and Zaera R. (2009). Relationship between mesostructure, mechanical behaviour and damage of cement composites under high-pressure confinement. *Exp. Mech.*, **49**, 613–625.
- Forquin P. and Hild F. (2008). Dynamic fragmentation of an ultra-high strength concrete during edge-on impact tests. *ASCE J. Eng. Mech.*, **134**(4), 302–315.

- Forquin P. and Hild F. (2010). A probabilistic damage model of the dynamic fragmentation process in brittle materials. *Advances in Applied Mech.* **44**, 1–72.
- Gabet T., Malécot Y. and Daudevielle L. (2008). Triaxial behaviour of concrete under high stresses: influence of the loading path on compaction and limit states, *Cem. Concr. Res.* **38**, 403–412.
- König, G. and Liphardt, S. (2003). Hochhäuser aus Stahlbeton, *Betonkalender Teil I*, 1–70.
- Li, Q.M., Reid, S.R., Wen, H.M. and Telford A.R. (2005). Local impact effects of hard missiles on concrete targets. *Int. J. Impact Eng.*, **32**, 224–284.
- Nöldgen, M. (2011). *Modeling of Ultra High Performance Concrete (UHPC) under impact loading – Design of a high rise building core against aircraft impact*, Forschungsergebnisse aus der Kurzzeitdynamik, Fraunhofer Verlag, Heft 19, ISBN 978-3-8396-0286-7.
- Nöldgen M., Fehling E., Riedel W. and Thoma K. (2012). Vulnerability and robustness of a security skyscraper subjected to aircraft impact, *Comput.-Aided. Civ. Inf.*, **27**(5), 358–368.
- Riedel W., Wicklein M. and Thoma K. (2008). Shock properties of conventional and high strength concrete, experimental and mesomechanical analysis, *Int. J. Impact. Eng.*, **35**/3, 155–171
- Riedel W., Thoma K., Mayrhofer Chr. and Stolz A. (2010a). Engineering and numerical tools for explosion protection of reinforced concrete, Multi-Science Publishing, *Int. J. Prot. Struct.*, **1**, 85–101.
- Riedel W., Hiermaier S. and Thoma K. (2010b). Transient stress and failure analysis of impact experiments with ceramics, Elsevier, *Mater. Sci. Eng., B*, **173**, 139–147.
- Riou P., Cottenot C.E. and Boussuge M. (1998). Anisotropic damage model for impacted ceramic material: Application to silicon carbide, *Int. J. Imp. Eng.*, **21**, 683–693.
- TM 5–1300 (1990). *Structures to resist, the effects of accidental explosions*, Army Technical Manual 5-1300/Navy Publication NAVFAC P-397/Air Force Manual (AFM) 88-22, Department of the Air Force.
- UFC 3–340–02 Unified Facilities Criteria (2008). *Structures to resist the effects of accidental explosions*. Department of the Army, the NAVY and the Air Force, Washington, DC, USA.
- Vu X.H., Malécot Y., Daudeville L. and Buzaud E. (2009). Experimental analysis of concrete behavior under high confinement: effect of the saturation ratio, *Int. J. Solids Struct.*, **46**, 1105–1120.
- Williams, E. M., Graham, S. S., Akers, S. A., Reed, P. A. and Rushing, T. S. (2010). Constitutive property behavior of an ultra-high-performance concrete with and without steel fibers. *Comput. Concrete, Int. J.*, **7**(2), 191–202.

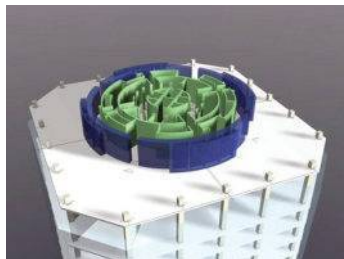
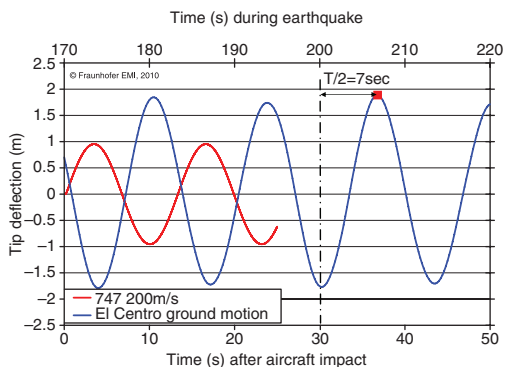
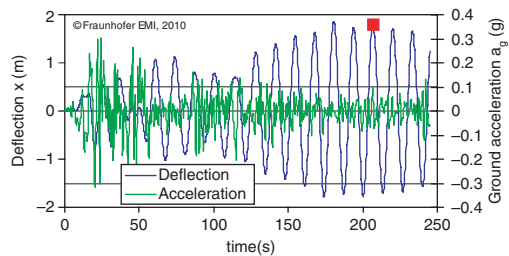


Plate III (Chapter 5) Global dynamic response of the high-rise building concept 'Security Scraper' (Nöldgen, 2011) with an ultra-high performance concrete core subjected to earthquake loading and aircraft impact.

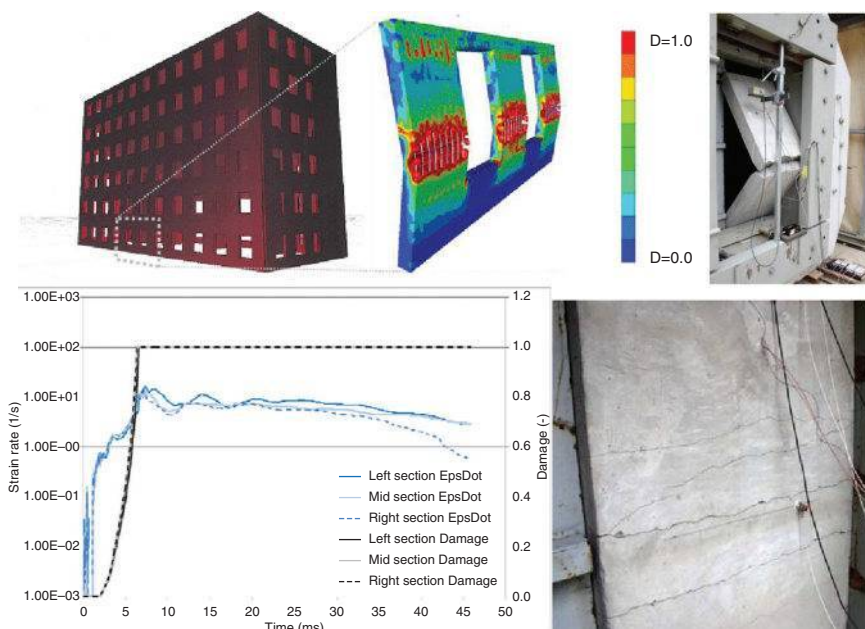
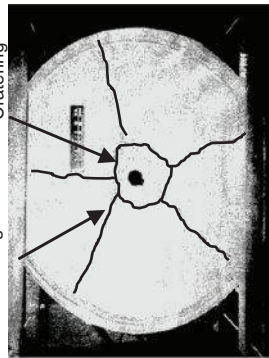
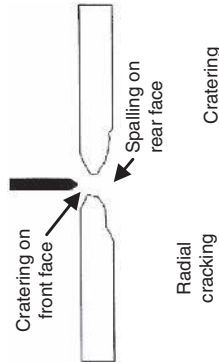


Plate IV (Chapters 5 and 10) Reinforced concrete frame building loaded by an external blast load in simulation and shock-tube tests; reprinted from Riedel (2010) with permission from Multi-Science Publishing; Lower: tensile cracks (right) by dynamic bending at local strain rates $1 < \partial \epsilon / \partial t < 30/s$ (left) recorded in validated simulations.

(a) Impact experiments

Impact velocity: 316 m/s
Projectile diameter: 50.8 mm
Slab thickness: 127 mm



(b, c) Numerical simulation

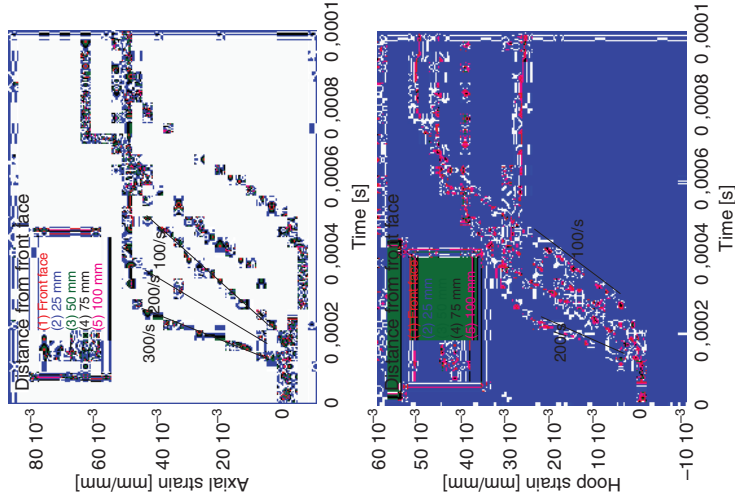
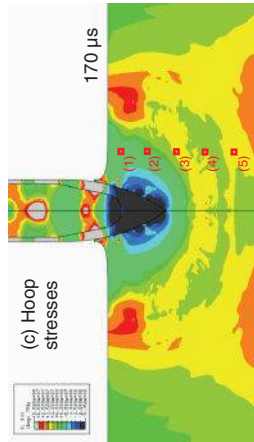
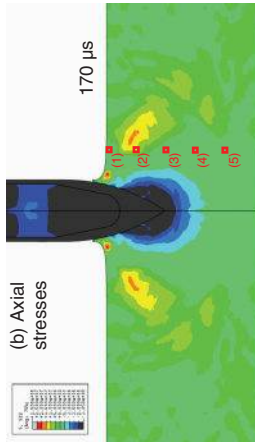


Plate V (Chapter 5) Impact of a kinetic penetrator against a thin concrete slab (Cargile, 1999) and numerical simulation of the test (Krieg, Swenson and Taylor model) (Erzar, 2010).

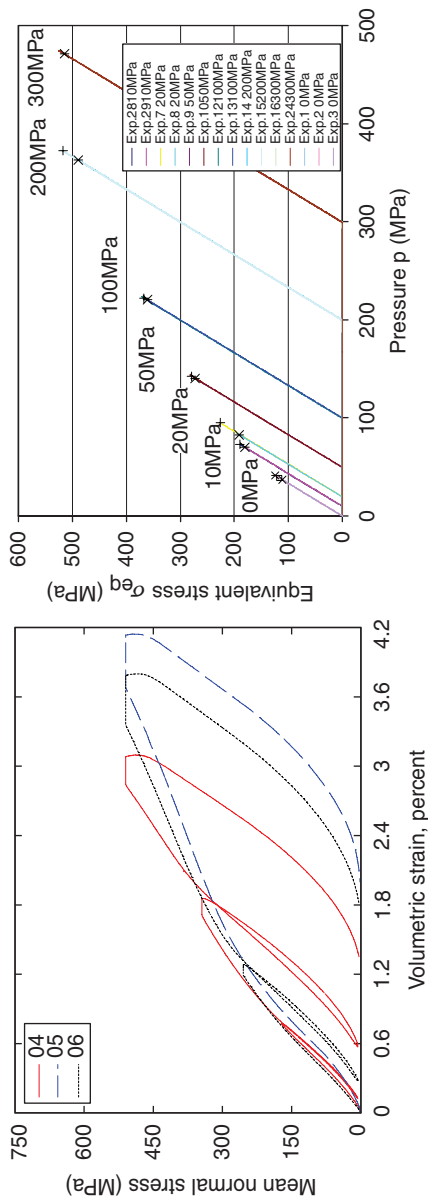
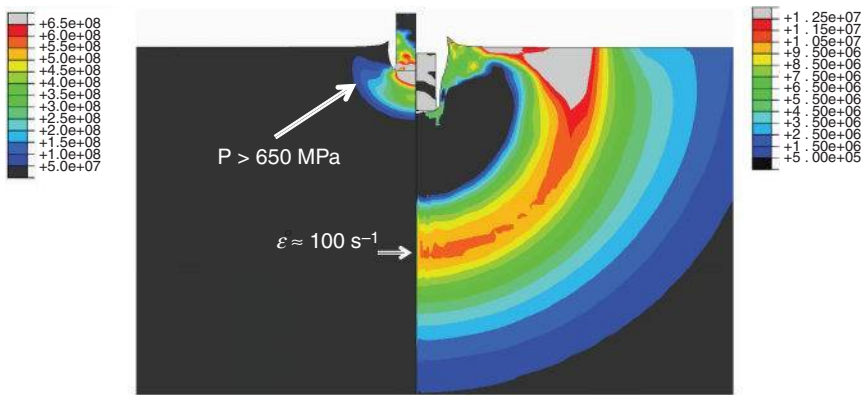


Plate VI (Chapters 5 and 10) Example data of compaction and strength measurements of concrete under increasing triaxial compressions (courtesy of ERDC). Lateral confinement stress specified in right figure.



Hydrostatic pressure [Pa] ($t = 5\mu\text{s}$)

First principle stress [Pa] ($t = 15\mu\text{s}$)

Plate VII (Chapters 5 and 10) Numerical simulation of a ballistic impact against a mortar matrix (impact velocity: 750 m/s), Krieg, Swenson and Taylor model; reprinted from Forquin *et al.* (2006) with permission from EDP Sciences.

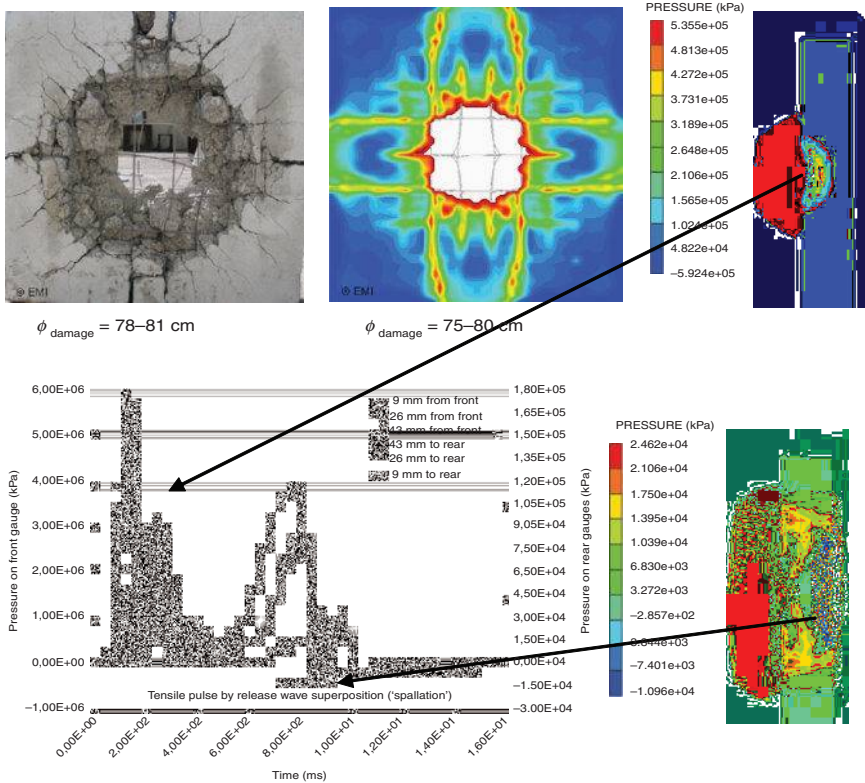


Plate VIII (Chapter 5) Rear surface of a reinforced concrete plate after contact detonation.

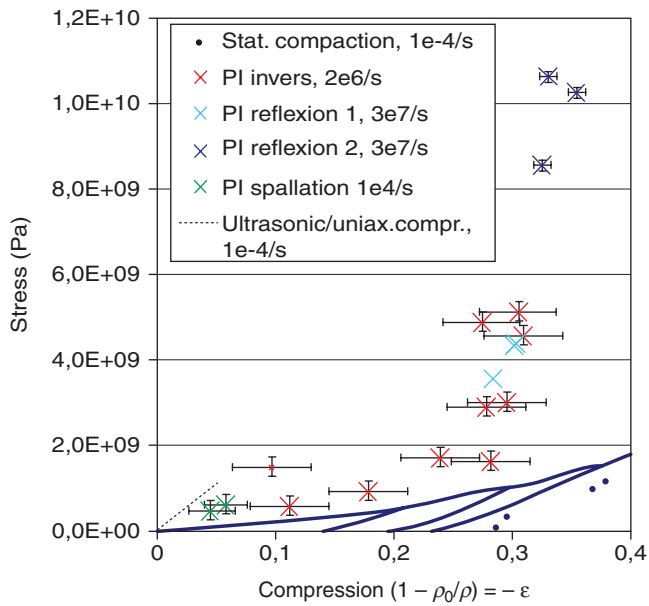


Plate IX (Chapters 5 and 10) Difference of isothermal 1D compression to planar shock states in concrete grout for moderate to strong shock waves of 0.5–12 GPa (Riedel, 2008).

Dynamic test devices for analyzing the tensile properties of concrete

P. FORQUIN, University of Lorraine, France, W. RIEDEL, Ernst Mach Institut, Germany and J. WEERHEIJM, TNO and Delft University of Technology, The Netherlands

DOI: 10.1533/9780857097538.2.137

Abstract: Owing to their low tensile failure strain, concrete is a difficult material to test under dynamic tensile loading. Indeed, conventional testing apparatuses such as high-speed hydraulic presses or Split Hopkinson Bar facilities rely on a mechanical balance of the specimen implying a short round-trip time in the specimen in comparison with the loading time to failure and consequently loading-rates below few hundreds of GPa/s. Above this threshold the specimen is clearly unbalanced and these methods are inadequate. Other techniques, such as spalling tests, plate-impact experiments that do rely on stress-wave analysis or edge-on impact tests that are used to visualize the tensile damage in the target, then come into play. In this chapter, different experimental methods are sorted in four sets to point out their field of use, their limitations and a number of results obtained in the literature.

Key words: testing devices, dynamic tensile loading, concrete tensile strength, concrete fracture energy, spalling, impact test.

6.1 Introduction

This chapter describes the testing devices used to identify the main mechanical properties involved in the response of concrete to dynamic tensile loading, which are strength, Young's modulus, and fracture energy. The following section briefly sets out the main experimental methods that are used to characterize this tensile response depending on the loading rate to be reached. Four sets of experimental methods are distinguished, namely those in which a mechanical balance of the specimen is obtained, those relying on the reflection of a compressive pulse on a free surface (1D uniaxial stress state or uniaxial strain state), and those based on the impact of a metallic projectile against a concrete target. Depending on the experimental technique and the processing method, several material properties are used to measure the ultimate strength (maximum tensile stress), the softening behavior, the fracture energy, and the kinetics of damage and cracking patterning. Some

experimental results obtained with conventional concretes, microconcretes, or high-strength concretes are used to indicate the influence of free water and strain rate on their tensile behavior.

6.2 Different experimental methods to characterize the tensile response of concrete

As discussed in the previous chapter, severe damage modes are observed in concrete structures when they are subjected to impulse loading through impact with a rigid projectile or blasting (Li *et al.*, 2005; Forquin *et al.*, 2008). Scabbing on the front face, spalling on the rear face, and multiple fracturing radiating from the penetration tunnel are induced by tensile stress. The range of strain rates may vary greatly, depending on the kind of loading. Strain rates below 1/s are usually observed in the case of earthquakes or soft impact from a ‘deformable projectile.’ Strain rates from 1/s to 100/s are involved with blast loading and impact with a rigid projectile. Higher strain rates (100/s to 1000/s) may be observed in the case of hyper-velocity impact or contact detonation. Four kinds of experimental methods have been developed and published in the literature to characterize the mechanical response of concretes under tensile loading over a wide range of loading rates:

- The first set gathers experimental results to obtain a mechanical balance of the specimen. Input and output forces are equal and inertial effects are negligible in comparison to the level of loading applied to the specimen. Direct tensile experiments by hydraulic press or split Hopkinson pressure bar (SHPB) are included in this first set of experimental methods, as well as Brazilian tests (i.e. diametral compression of a disc) through SHPB devices (Ross *et al.*, 1996). Usually strain rates do not exceed about 10/s.
- In the second set the specimen is unbalanced but loaded in a quasi-uniaxial stress state, for example in the spallation configuration based on the use of an SHPB. The specimen is unbalanced, since one end is in contact with the bar whereas the other end is let free. Typical strain rates in the range of 20–200/s are reached with this technique (Schuler *et al.*, 2006; Weerheijm and van Doormaal, 2007; Erzar and Forquin, 2010a, 2011).
- The third set includes experimental methods in which the specimen is unbalanced and loaded in a uniaxial strain state. Such loading is obtained in plate-impact experiments or very fast impulse loading of a thin disc of small thickness-to-diameter ratio. Given the size of the concrete sample, the loading duration is necessarily short (a few microseconds or less). This technique is used for exploring the strength of mortar and concrete-like materials under strain rates of few thousands/s to 1e4/s (Kipp *et al.*, 1999; Grote *et al.*, 2001).
- A fourth set of experimental methods may be defined to investigate the tensile damage of concrete under impact loading. For instance, edge-on

impact (EOI) experiments have been developed to visualize fragmentation in brittle materials, and to quantify the cracking density through post-mortem analysis (Forquin and Hild, 2008, 2010). The experimental results obtained may be compared to numerical predictions in terms of kinetics of damage and cracking pattern. More recently, this experimental method has benefited from recent progress in the domain of ultra-high-speed imaging and full-field measurements. Typical strain rates of few 100s/s are obtained through EOI tests. Note that in these tests no uniaxial tensile stress conditions occur, whereas tensile failure occurs in a multiaxial compression tension state.

The principles, data processing, and the limitations of each of these experimental techniques, are discussed in this chapter. The influence of microstructural parameters (free water, grain size, fibers) is also briefly addressed.

6.3 Characterizing the tensile strength and fracture energy of concrete at intermediate loading rates ($\dot{\sigma} \leq 100$ GPa/s or $\dot{\epsilon} \leq 2$ /s)

6.3.1 Introduction: experimental techniques used at intermediate loading rates

High-speed hydraulic presses and Split Hopkinson Bar devices are commonly used to investigate the dynamic tensile behavior of concrete at loading rates below 100 GPa/s. Classical processing methods are used to process the data relying on the assumption of mechanical balance of the sample. Influence of strain rate, free water, and aggregates size at intermediate loading rates is briefly pointed up in this section.

Over the last two decades, several techniques have been developed to investigate the behavior of concretes and rock-like materials at intermediate tensile loading rates (in the range of 10^{-2} /s to few 1/s). Three experimental methods proposed in the literature are presented below:

- The direct tensile test performed on a high-speed hydraulic press (Toutlemonde, 1992; Erzar and Forquin, 2010b, 2011),
- The gravity driven Split Hopkinson Bars (SHB) facility developed at Delft (Kormeling, Zielinski, Rossi, Toutlemonde, and Weerheijm),
- The SHB facility developed at Ispra (Italy) based on the rupture of a blocking bolt (Cadoni *et al.*, 2006).

These methods rely on classical data processing. For instance, in the first method, a loading cell is mounted in the vicinity of the end of the specimen to measure the dynamic load applied to the concrete sample. In the last two methods, incident, reflected, and transmitted pulses recorded on input and

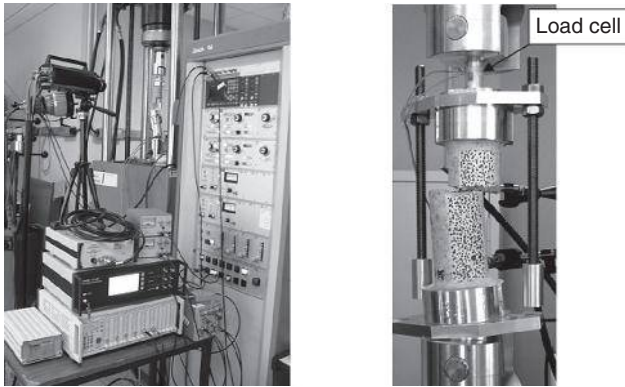
output Hopkinson bars allow measurement of the stress and strain state in the sample based on the data processing proposed by Kolsky (1949). Thus, a correct balance of the specimen is assumed in each method. Balance of input and output forces implies a short round-trip time in the specimen in comparison with the loading time to failure. As consequence the strain rate is limited as in Equation [6.1]:

$$T_{\text{loading}} = \frac{\varepsilon_{\text{failure}}}{\dot{\varepsilon}} \gg T_{\text{round-trip}} = \frac{2L}{C_{\text{wave}}}, \quad [6.1]$$

where $L, C_{\text{wave}}, \varepsilon_{\text{failure}}$ denote respectively the length of the sample, the wave speed, and the failure strain of the tested material. Considering classical values of $L, C_{\text{wave}}, \varepsilon_{\text{failure}}$ and five wave round-trips in a concrete sample, the maximum strain rate cannot exceed about few 0.1/s to a few 1/s depending on the specimen length. Above this threshold the specimen is clearly unbalanced and these methods are inadequate. Other techniques, such as spalling tests, that do rely on stress-wave analysis rather than on a mechanical balance of the specimen, then come into play.

6.3.2 Direct tensile tests performed through a high-speed hydraulic press

As discussed in Chapter 2, hydraulic test devices may be used to characterize the tensile strength and fracture energy of concrete in quasi-static conditions. A high-speed hydraulic press may be used to perform dynamic tensile tests on concrete samples over loading rates ranging from $1\text{e-}3/\text{s}$ to about $1/\text{s}$. Toutlemonde (1992) investigated the strain-rate sensitivity of dry and wet concrete by performing dynamic tensile experiments in the LEM3 laboratory through a Zwick press, allowing jack speeds of up to few m/s. The maximum loading rate reached during these experiments was 500 MPa/s (about $0.01/\text{s}$). More recently, a new device has been developed in LEM3, including a damping system and two kneecaps settled on both specimen ends to ensure a perfect uniaxial stress state in the sample without any bending effects. A load cell was also specially designed and calibrated for measuring the axial loading as near as possible to the specimen (Fig. 6.1). The axial strain in the sample was deduced from strain gages, linear variable differential transformer (LVDT) sensors, or laser extensometers. The mantle's surface was scratched with sandpaper to improve adhesion on the sample. Concrete cylinders, measuring 45.7 mm in diameter and 120 or 140 mm in length, were tested in dried or fully saturated conditions. This experimental technique was employed to measure the strength of conventional concretes, mortars, and microconcretes at strain rates ranging from $0.01/\text{s}$ to $0.5/\text{s}$. A digital ultra-high-speed camera (UHSC)



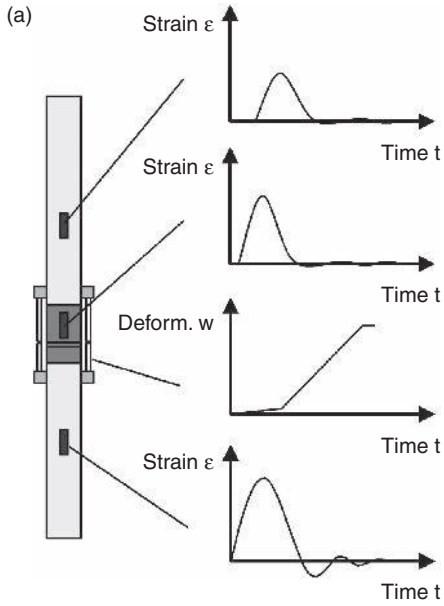
6.1 Direct tensile tests performed on a high-speed hydraulic press (LEM3 lab., Metz) (Forquin and Erzar, 2010).

was also used to visualize the cracking inception by using a Digital Image Correlation (DIC) technique (Fig. 6.1).

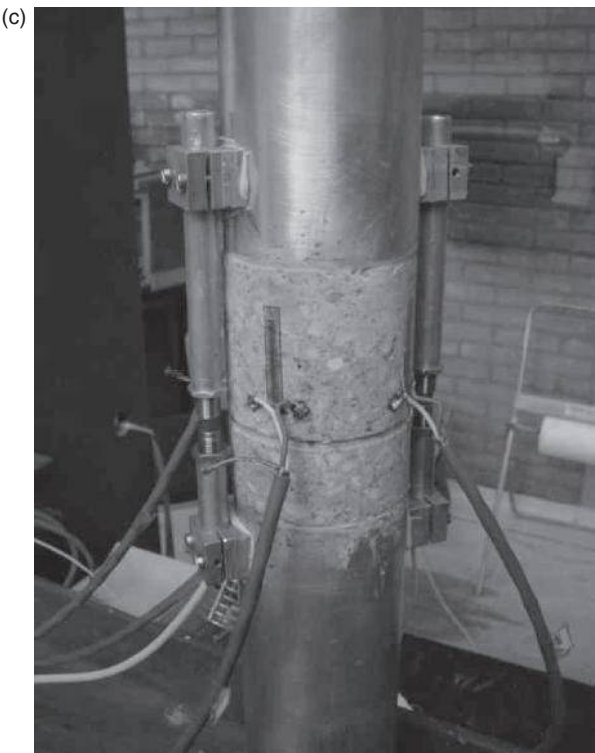
6.3.3 Gravity driven SHB facility at Delft

To study the rate dependency of concrete it would be ideal to perform deformation-controlled tests, just as in statics. Maintaining the specimen geometry and complete control of the softening branch would directly allow identification of rate effects on strength and softening behavior. Deformation-controlled hydraulic testing is possible up to 5000 MPa/s (10^{-1} 1/s), but beyond these loading rates inertia effects and wave phenomena are no longer negligible. For higher loading rates, up to 50 GPa/s the Split Hopkinson Tensile Bar (SHTB) technique may be used. It is a technique with control of the applied loading pulse but without any control of the deformation. Reinhardt and co-workers developed in the 1980s a gravity-driven SHB to test concrete in a loading-rate regime of 10–50 GPa/s. The SHB was developed to study the rate effect on tensile strength. At a later stage, a testing procedure was developed to additionally study the fracture energy. Because hydraulic test devices are already discussed in Chapter 2, in this section we focus on the SHB device developed by Reinhardt at Delft University of Technology (DUT) and the set-up at ISPRA.

The SHB at the Stevin Laboratory of DUT consists of two cylindrical aluminum bars (\varnothing 74 mm) between which the concrete specimen (length 100 mm) is bonded (see Fig. 6.2 and Table 6.1 for the dimensions). The tensile-stress wave is generated with a drop weight, which slides along the lower bar and hits an anvil at the bottom end. The DUT set-up differs slightly from the traditional SHB configuration and analysis. Instead of a step-load, a tensile pulse with a long ascending branch is generated, and the concrete



6.2 The SHB at Delft (a) measurement scheme; (b) set-up; (c) instrumented notched specimen.



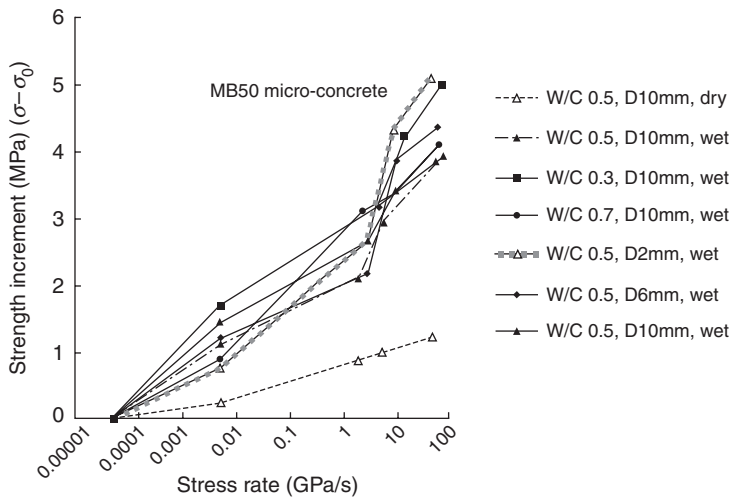
6.2 Continued

Table 6.1 Specification gravity driven SHB at Delft

Diameter	Length incident bar	Length transmitter bar	Loading rates	f_t -tested
74 mm	3.50 m	6.75 m	5–50 GPa/s	1–10 MPa

specimen fails during this phase. The amplitude and shape of the loading pulse depend on the drop-weight mass, the impact velocity controlled by the drop height, and the layer applied between the drop weight and the anvil. These parameters control the loading rate at testing. The loading rate that can be generated with the SHB at the DUT ranges from 1 to 50 GPa/s, and strain rates of up to 5/s (see Fig. 6.23), the regime just before enhanced rate effects on strength occur for normal concrete.

The tensile wave travels upwards through the aluminum bar and the specimen, fracturing the specimen when the tensile strength of the concrete is reached. The amplitude of the pulse transmitted to the upper bar represents the strength of the concrete specimen. The loading rate is derived from the slope of the transmitted stress pulse. Without additional measurements on



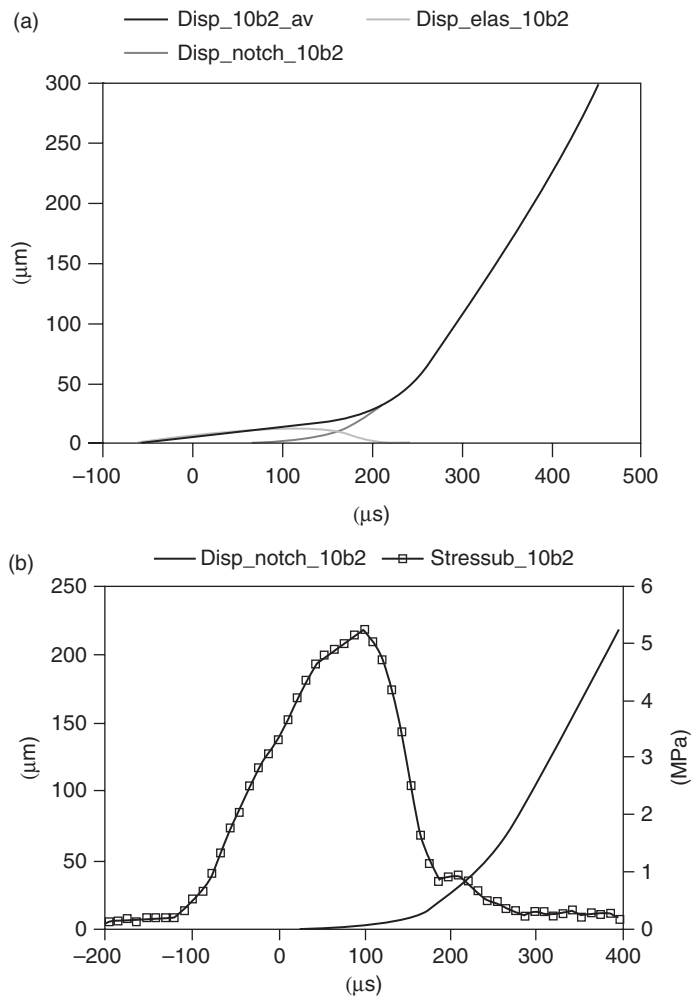
6.3 Direct tensile tests performed with hydraulic press and SHB device on conventional concrete considering different max. aggregates size (2–10 mm), water to cement ratio (0.3–0.7), and free water content. Stress-rate ranges from 0.05 MPa/s to 50 GPa/s. (Toutlemonde, 1992).

the specimen response, the corresponding strain rate is derived using the static Young's modulus value of the concrete tested.

It is a very basic test device to determine the dynamic strength of concrete and it requires only simple data analysis. During operation the incident and transmitted pulses are recorded by multiple strain records to check and quantify the uniaxial stress condition during loading, and asymmetry in failure.

This SHB set-up at the DUT has been used by several researchers in the past (Kormeling, Zielinski, Rossi, Toutlemonde, and Weerheijm). Strength data obtained for normal strength concrete at different moisture levels, steel fiber concrete, and also the rate effect on steel bonding, are studied in this set-up. Some results obtained by Toutlemonde (1992) with the Delft SHB facility are shown in Fig. 6.3. He performed dynamic tensile experiments with concrete of various maximum aggregate sizes (2, 6, 10 mm), water to cement ratio (0.3, 0.5, 0.7), and free-water content (dry or wet samples). Toutlemonde noted there was a very small influence of concrete compositions, but a major influence of free water. This conclusion was confirmed in several later works.

Weerheijm extended the possibilities of determining also dynamic fracture energy using notched specimens. These are applied to avoid multiple fracture and to obtain data for a single fracture zone, as in static-deformation controlled tests. To measure the deformation of the fracture zone directly, two displacement transducers are placed on both sides of the specimen, glued to the aluminum bars. The elastic deformation outside the fracture zone is measured by strain gages on the specimen (see Fig. 6.2). By combining the

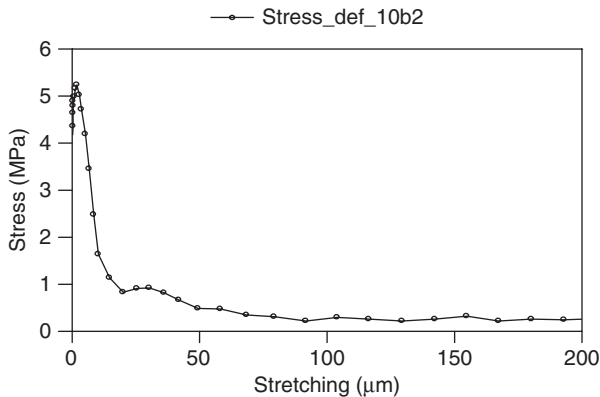


6.4 Example of displacement time records (a); stress and deformation time record (b).

synchronized measurements, the stress deformation curve, and thereby the fracture energy for the single fracture zone, are obtained.

An example of a displacements measurement, the subtraction of the elastic portion, and the resulting deformation of the fracture zone (called *disp_notch*), is presented in Fig. 6.4. The figure also shows the synchronized stress and deformation records for the notched zone. The combination of these records results in the stress deformation curve as presented in Fig. 6.5.

The obtained stress deformation curve deviates from static tests. The displacement measurement in the static tests consists of two parts: the contribution of the crack opening, and the contribution of elastic deformation over



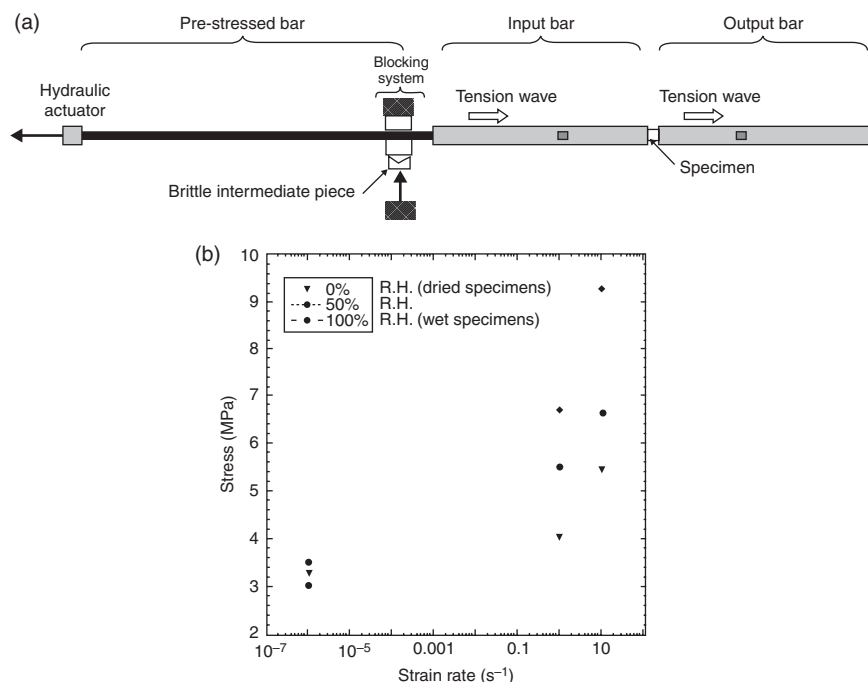
6.5 Example of stress deformation curve (synchronized raw data).

the total measuring length. In the SHB tests, on the contrary, the elastic deformations are subtracted already from the total deformations, so the elastic ascending branch is not present in the stress deformation curve. Note that the area under both the static and SHB curves represents the fracture energy. See also Hillerborg (1985) and the discussion on fracture energy in Chapter 7.

6.3.4 SHB facility at ISPRA

An experimental set-up has been developed in the Joint-Research-Centre at ISPRA to test concretes and geomaterials at intermediate strain rates. This impressive device is composed of two aluminum alloy Hopkinson bars 2 m long (Fig. 6.6). The square cross-section is subdivided into 25 ‘minibars’ over 1 m. Each mini bar is instrumented by strain gages giving the records of incident, reflected, and transmitted signals. The specimen, a cube of 200 mm, is glued with an epoxy resin to 25 instrumented bundles linked to the input bar, and to 25 instrumented bundles connected to the output bar. In the first step, a cable 100 m in length and linked to the input bar is preloaded. The input bar is held by a blocking device so that the specimen is initially stress-free. In the second step, the blocking system is released by the rupture of bolts, so that an incident wave propagates through the input bar. One portion of the incident wave is transmitted to the output bar through the specimen, and the other part is reflected in the opposite direction. A classical processing of data (Kolsky, 1949) is applied to the experimental data to obtain the nominal stress and strain within the specimen as function of time.

This experimental device provides several benefits. The wave dispersion phenomenon is eliminated despite the size of the specimen, as each mini bar in the bundle is of small diameter. Moreover, the kinetics of damage are analyzed, by comparing the data provided by each strain gage. Some results of quasi-static and dynamic tests are plotted on Fig. 6.6. As observed



6.6 Tensile tests performed in the Joint-Research-Centre of Ispra. (a) Principle of HBB tests (Hopkinson Bar Bundle System) (Cadoni *et al.*, 2006); (b) Quasi-static and dynamic strength of concrete obtained for three strain rates and two moisture contents. (Cadoni *et al.*, 2001).

previously by Rossi (1991), Toutlemonde (1992), and Ross (1996), sensitivity to strain rate and moisture content is clearly pointed out.

In the following two sections, other experimental techniques are presented in which the concrete sample is in an unbalanced state. Varying the size of the specimen and the wavelength of the applied loading, a uniaxial stress state or a uniaxial strain state is obtained. Strain rates around 100/s (spalling tests) to a few 1000s/s (spalling by plate-impact experiments) are reached.

6.4 Characterizing the tensile strength and fracture energy of concrete at high loading rates ($100 \text{ GPa/s} \leq \dot{\sigma} \leq 1000 \text{ GPa/s}$ or $20/\text{s} \leq \dot{\epsilon} \leq 200/\text{s}$)

The spalling technique based on the use of a single Hopkinson bar has been widely employed to characterize the tensile strength and fracture energy of concretes in the range of loading rates from 100 to 1000 GPa/s. Various testing devices and processing methods considered in the literature are detailed in this section. The strength data exhibits the strength enhancement with strain rate and the effect of moisture on the tensile response of concretes.

6.4.1 Introduction: benefits and disadvantages of spalling tests

In a spalling test the sample is intentionally in an unbalanced state, in contact with a Hopkinson bar on one end and free on the other. This methodology analyzes the propagation of individual stress waves within the sample, rather than aiming for dynamic equilibrium between sample ends. The principle of a spalling test is as follows. A short cylindrical projectile launched by a gas-gun facility is used to generate a compressive pulse on one end of a metallic (steel or aluminum alloy) Hopkinson bar. The pulse length is defined by the length and wave speed of the striker and is shorter than the concrete sample extension. From the striker's free surface a release wave is reflected downstream into the striker and bar. An alternative method to generate short pulses of high amplitude onto the input bar is the use of a small explosive charge rather than a striker. This incident compression and decompression wave propagates through the bar towards the contact surface of the concrete sample (see Fig. 6.9). Due to the impedance mismatch between the metal of the bar and the concrete, a part of the incident wave is reflected in the opposite direction (upstream), whereas the other part is transmitted into the sample. This compressive pulse reflects as a release wave on the free surface upstream back into the specimen. Superposition of both release waves, the upstream release from the free sample end and the downstream release from the striker's free surface, leads to dynamic tension. If the length and sound-speed of striker and sample are correctly matched, dynamic tension is achieved within the material sample.

Several benefits and disadvantages may be noted. On the one hand, the use of release wave superposition for producing a dynamic tensile loading allows avoidance of difficulties due to adhesion. Indeed, the specimen is only put in contact with the Hopkinson bar for transmitting the compressive pulse and its release. Secondly, previous limitations concerning the level of strain rate to ensure a balance of the specimen disappear, since this hypothesis is unnecessary in the processing (to be discussed later). Last, but not least, considering specimens of small diameter in comparison to their length, a quasi-uniaxial (1D) stress state may be obtained that facilitates the processing and the use of localized instrumentation, such as strain gages or laser interferometers.

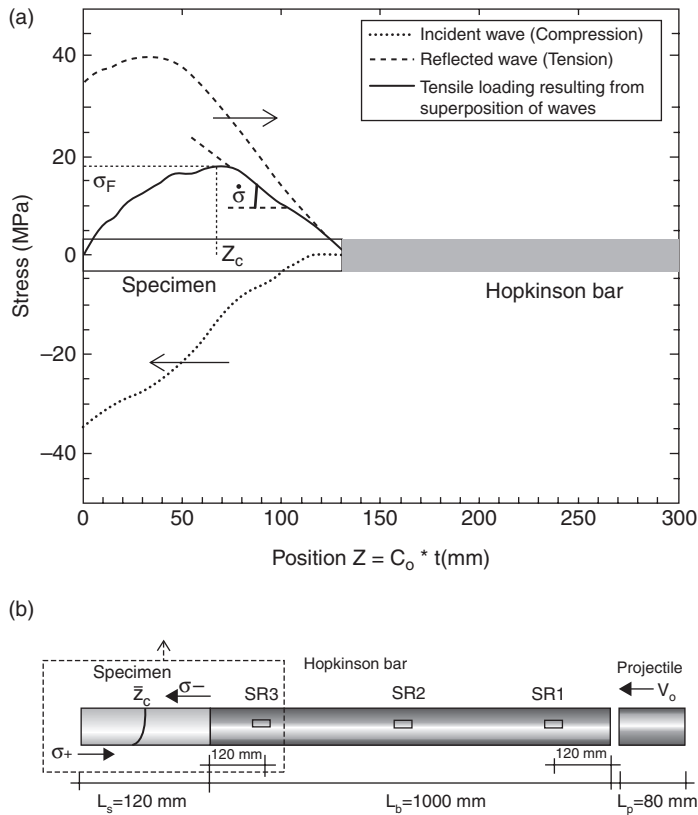
On the other hand, further limitations may be noted in this kind of experiment. In particular, this technique is restricted to a limited range of very high strain rates (about 10/s to 200/s). The release wave superposition has to happen in the sample in order to obtain a dynamic tension state. Therefore, the tensile loading must occur before the release wave from the sample's free end reaches the contact surface with the bar (Equation [6.2]).

$$T_{\text{loading}} = \frac{\varepsilon_{\text{failure}}}{\dot{\varepsilon}} < T_{\text{round-trip}} = \frac{2L}{C_{\text{wave}}} \quad [6.2]$$

Note that this inequality is opposite to that introduced in Equation [6.1] for a well-balanced specimen. Considering classical values of L , C_{wave} , $\epsilon_{\text{failure}}$, respectively the length of the sample, the wave speed, and the failure strain of the tested concrete, it follows that the minimum strain rate that may be obtained in a spalling test is about 10/s. Another limitation of spalling tests is due to the compressive pulse that precedes the tensile loading within the concrete sample. Indeed, to avoid any compression damage that might influence the response in tension, the incident compressive pulse must not exceed about 30% of the dynamic compressive strength of the material. Due to wave dispersion in the Hopkinson bar and a specimen of large diameter, the maximum frequency of the compressive pulse, as well as the strain rate, is limited (Erzar and Forquin, 2011a). In practice, the strain rate in spalling tests on unscaled concrete is so far limited to strain rates of 200/s. However, this order of magnitude represents the physical limit of tensile strain rates, where strength still has to be considered (see Section 6.5).

Dynamic tensile tests by spalling have been performed on concrete for several decades. Landon and Quinney (1923) investigated the dynamic failure of concrete by using an explosive charge at the end of a cylindrical specimen 74 mm in diameter and 914 mm in length. The authors noticed a dynamic failure consisting of multiple fracture planes. More recently, Goldsmith *et al.* (1966) and Birkimer and Linderman (1971) obtained similar results by launching a steel sphere against a concrete cylinder instrumented by strain gages. McVay (1988) carried out experiments of contact detonation against concrete slabs to generate scabbing on the rear face of the target. Spalling tests based on the use of a single Hopkinson bar were pioneered by Klepaczko and Brara (2001) and Schuler *et al.* (2004, 2006). The Hopkinson bar was instrumented with strain gages in order to obtain the transmitted pulse from incident and reflected waves taking account of wave dispersion (Fig. 6.7). The two methods used to deduce the dynamic strength based on the velocity of fragments and the position of fracture planes have been recently discussed by Erzar and Forquin (2010a). It was concluded that the method developed by Schuler *et al.* (2006), based on momentum conservation evaluated through the pullback velocity, allows much more accurate results.

Almost at the same time as Klepaczko and Brara at Metz University and Schuler at Ernst Mach Institute (EMI) Freiburg, Weerheijm *et al.* (2003) and Weerheijm and van Doormaal (2004, 2007) substantially refined instrumented spalling tests to derive the dynamic strength and fracture energy analogue with the SHB measurement set-up in Delft. Both Schuler and Weerheijm used experimental devices based on a large Hopkinson bar of 74.5 mm in diameter and 5.5 m in length to allow the analysis of unscaled concrete. Millon *et al.* (2009) recently refined the instrumentation of the EMI Hopkinson bar, especially to achieve higher accuracy of fragment velocity measurements and crack opening.



6.7 Dynamic tensile tests by spalling (Klepaczko and Brara, 2001).

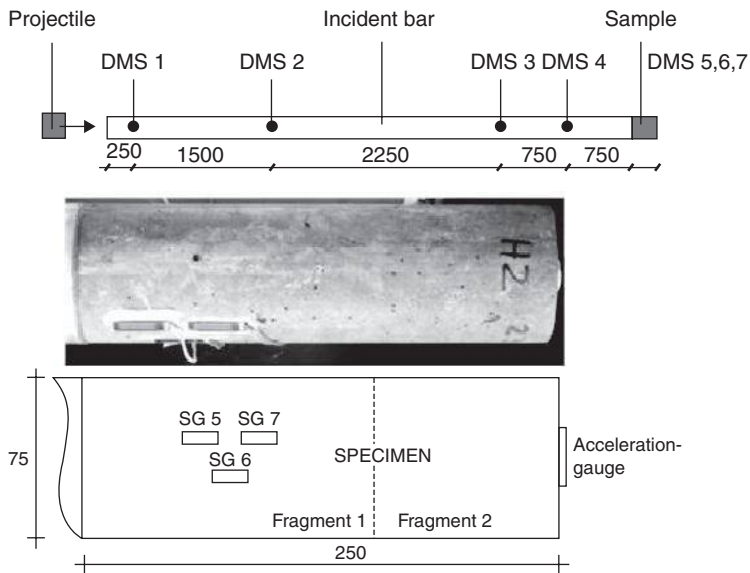
(a) Incident, reflected waves and resulting tensile wave in the concrete sample. (b) Sketch of the set-up: Projectile, Hopkinson bar, Specimen.

The configurations and measurement techniques at EMI, Metz and Delft, and some results obtained with conventional strength to UHPC, are presented in the following sections in more detail.

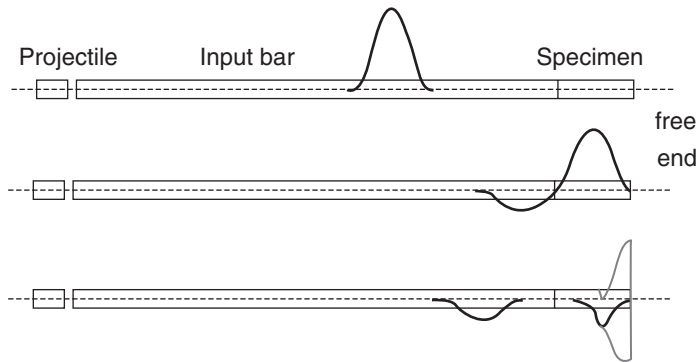
6.4.2 Test device and methodology used at the Ernst Mach Institute

The test device and the methodology at the Ernst Mach Institut Freiburg, site Efringen-Kirchen had originally been developed by Schuler and colleagues (2004) (Schuler and Hansson, 2006; Schuler *et al.*, 2006). Details of the derivation are provided in the references. In the following, the spallation configuration and the main experimental results are briefly summarized.

The principle of these experiments is the generation of tensile stresses in the specimen due to a compressive load. The set-up for the testing device is shown in Fig. 6.8. It consists of an incident bar, a striker bar, and its acceleration facility, as well as a specimen. The specimen is loosely bonded, but



6.8 Specimen-geometry for spallation tests on the 75 mm diameter Hopkinson Bar at Ernst Mach hop Institut (Schuler and Hansson, 2006; Millon *et al.*, 2009). DMS = strain gauge (SG).



6.9 Dynamic loading in the spallation configuration (Schuler and Hansson, 2006).

with good aerial contact, to the right-hand side of the Hopkinson Bar. The experimental process is shown in Fig. 6.9. Due to the impact of a striker of defined length and mass on the incident bar, a loading pulse is generated in the bar propagating downstream. The pulse is twice the length of the striker bar and composed of a compressive wave and a decompressive wave from its free end. The compressive wave leads to compression of the bar material, and the decompressive wave leads to a release back to the initial stress state. The loading pulse reflects at the specimen's free

end and runs back upstream. Due to the superimposition of the incident and the reflected decompression portions of the pulse, tensile stresses are generated in the specimen, leading to its fragmentation if the material's tensile strength is overcome. The spallation process on a concrete material is shown in a sequence of pictures in Fig. 6.10. Out of this process the essential dynamic properties, such as tensile strength, Young's modulus, and fracture energy, can be derived.

Cylindrical specimens with a diameter of 75 mm and a length of 250 mm (Fig. 6.8) are used in this configuration. For the determination of the Young's modulus and the tensile strength, undisturbed propagation of the stress waves in the material is required.

The tensile strength of concrete $f_{t,dyn}$ is calculated using the stress–particle velocity relationship, or Novikov formula (Equation [6.3]) from the ‘pull-back velocity’ Δv_{pb} measured on the rear free surface of the specimen (Fig. 6.11) (Novikov *et al.*, 1966):

$$f_{t,dyn} = \frac{1}{2} \rho c_0 \Delta v_{pb} \quad [6.3]$$

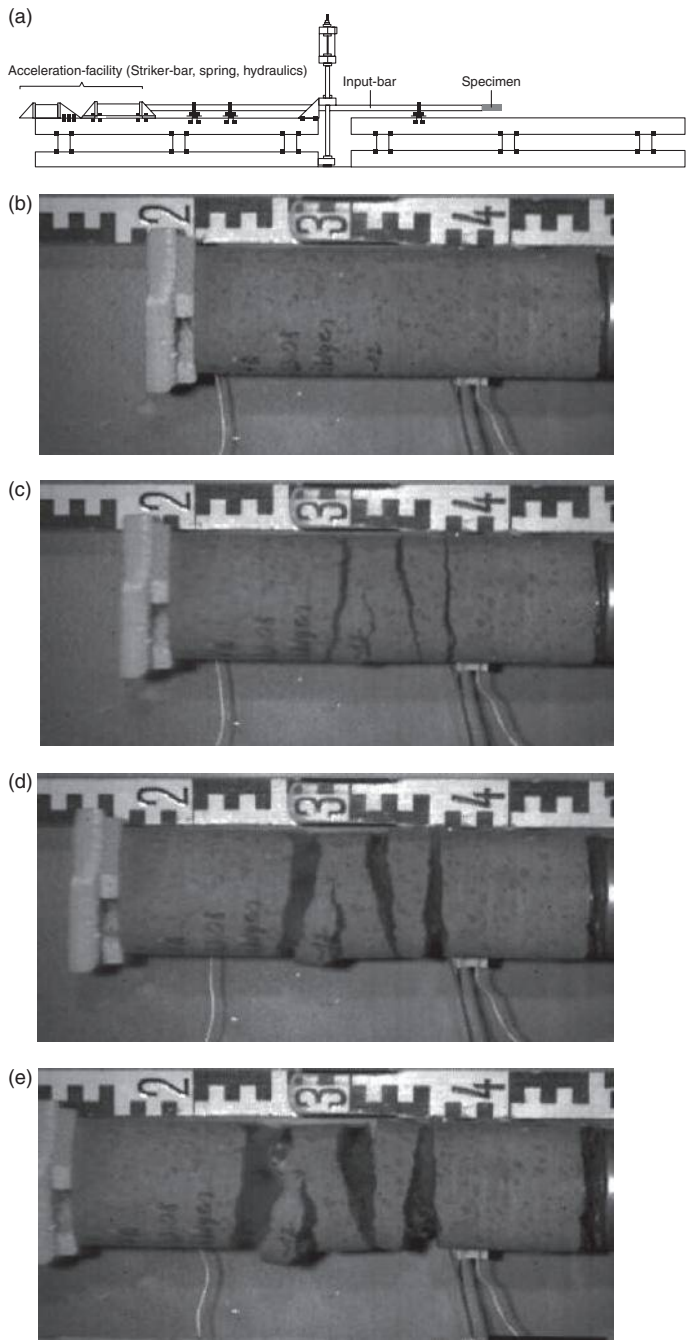
where c_0 is the one-dimensional wave speed expressed as function of the Young's modulus E and density ρ of the media:

$$c_0 = \sqrt{\frac{E}{\rho}} \quad [6.4a]$$

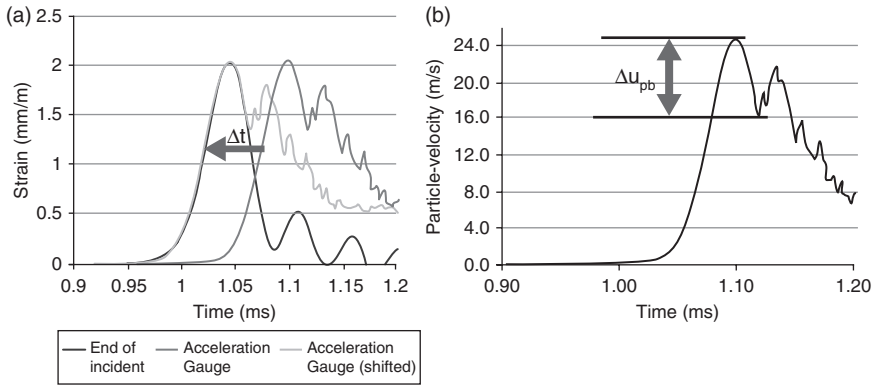
Equation [6.3] is derived from the momentum equation for elastic stress-wave propagation in an one-dimensional bar, leading to the equation of motion (Equation [6.4b]). $u(x,t)$ denotes displacements along the x coordinate direction. Equation [6.4c] represent a set of solutions of the equation of motion. Substitution in Hooke's law provides the fundamental ‘stress particle–velocity relationship’ between stress σ and ‘particle velocity’ v_p in the bar (Equation [6.4d]). The ‘free surface hypothesis’ finally states that v_p in the bar is about half the value $v_{p, \text{free surface}}$, which is measured at the stress-free boundary. Applying the final equation (Equation [6.4d]) to the maximum deceleration Δv_{pb} allows direct derivation of the peak tensile stress amplitude $f_{t,dyn}$. This wave portion is reflected from the spall plane during crack opening back to the free surface as Equation [6.3].

$$\frac{E}{\rho} \frac{\partial^2 u}{\partial x^2} = \frac{\partial^2 u}{\partial t^2} \quad [6.4b]$$

$$\frac{\partial u}{\partial t} = c_L \frac{\partial u}{\partial x} \quad \text{into} \quad \sigma = E \varepsilon = E \frac{\partial u}{\partial x} \quad [6.4c]$$



6.10 Spallation process of concrete due to tensile loading on UHPC:
(a) Hopkinson-Bar (b)-(e) fracture at 0, 4, 8, 12 ms.



6.11 (a) Derivation of c_L from the shifted strain records; (b) recorded velocity-time signal at the end of the sample with 'pullback velocity' Δv_{pb} .

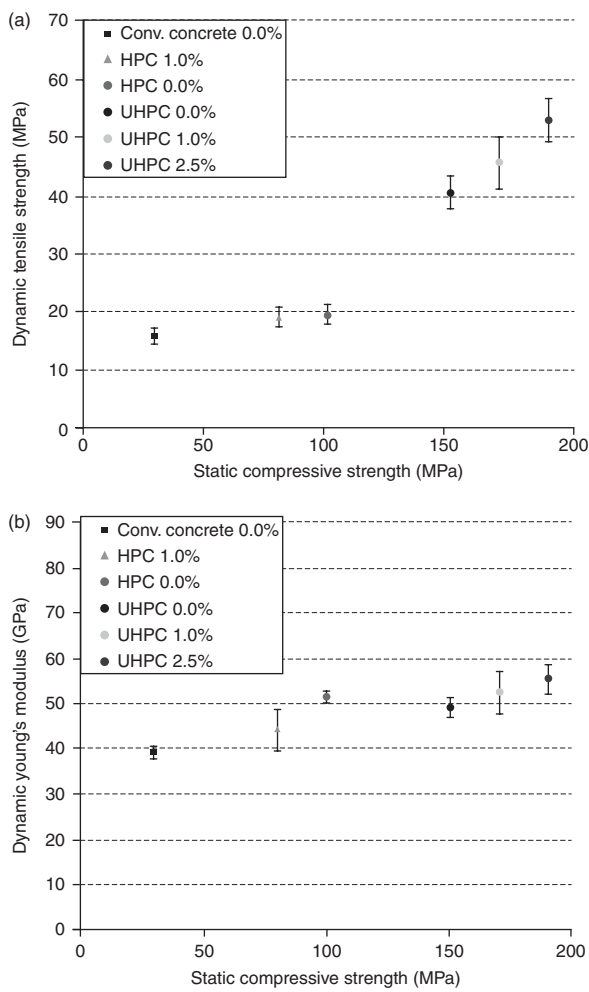
$$\sigma = \frac{E}{c_0} \frac{\partial u}{\partial t} = c_0 \rho \frac{\partial u}{\partial t} = c_0 \rho v_p = \frac{1}{2} c_0 \rho v_{p, \text{free surface}} \quad [6.4d]$$

The stress and strain rates can be calculated using the rise time of the pull-back signal and range between 10 and 180/s for EMI's Hopkinson bar. It mainly depends on the material's stiffness and strength, and thus the necessary input momentum to fail the sample. In order to derive the dynamic Young's modulus of the concrete sample in the same test the stress-wave propagation, along the bar and in the concrete, is studied. A first step dispersion correction (Equation [6.5]), described i.e. by Gong *et al.*, (1990), is applied to propagate the loading wave from the last strain gage on the aluminum input bar to the interface with the concrete sample. The various velocities of the different wavelengths n are corrected by phase shifts ϕ_{dn} .

$$\varepsilon_{\text{alu}} = \frac{A_0}{2} + \sum_{n=1}^{\infty} D_n \cos(n\omega_0 t - (\phi + \phi_{dn})) \quad [6.5]$$

The time Δt of the wave propagation along the sample length L is determined by shifting the strain-time-signal of the sample's free end into the strain-time-recording at the interface of sample and input bar. This procedure is shown in Fig. 6.11a. c_0 is determined as distance L divided by the time shift Δt .

Figure 6.12 and Table 6.2 show results by Millon *et al.* (2009) and Schuler and Hansson (2006) on concrete qualities from conventional strength (CC) over high-performance concrete (HPC) to UHPC with steel fiber content of 0–1.0%. The experiments show an increasing effect of the concrete quality



6.12 Dynamic Young's Modulus and tensile strength for conventional to UHPC concrete and 0% and 1% of steel fiber content at strain rates around 100/s (Millon *et al.*, 2009). (a) Dynamic tensile strength versus static compressive strength and (b) dynamic Young's modulus versus static compressive strength.

in all measured properties. The wave propagation velocity grows moderately with increasing strength from 4100 m/s (conventional concrete) up to 4600 m/s (UHPC), leading to an increased Young's modulus. The comparison of the tensile strength shows a discrimination of concrete materials into two classes. Conventional concrete and HPC show similar values, with a slight increase with higher concrete quality. In comparison to these standardized materials, UHPC offers significantly increased tensile strength. The reason lies in the composition of the material and its strongly improved microstructure, leading to a dense

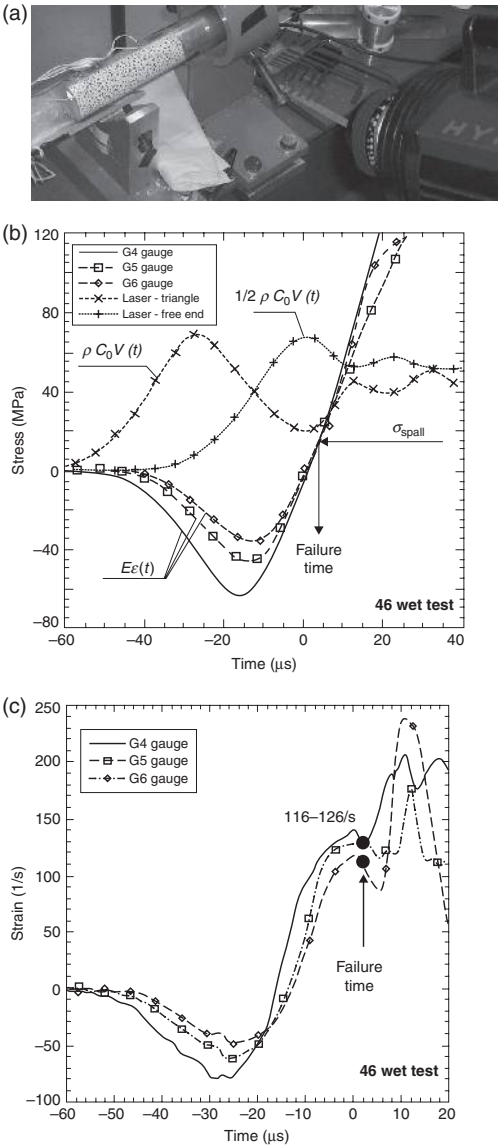
Table 6.2 Dynamic (and static) material properties for different concrete qualities measured on the EMI Hopkinson bar ($\dot{\epsilon} \approx 10^2/s$, $\dot{\sigma} \approx 10^3 \text{ GPa/s}$)

	Wave speed (m/s)	Tensile strength (MPa)	Young's modulus (GPa)
Conventional concrete	4110	15.5 (2.9)	39.6 (31.9)
HPC	4540	19.8 (5.2)	51.4 (45.2)
HPC 1 Vol.-% fiber reinforced	4460	19.3 (4.8)	47.5 (42.3)
UHPC	4620	40.7 (5.9)	50.6 (52.7)
UHPC 1 Vol.-% fiber reinforced	4655	42.7 (6.6)	53.1 (53.0)
UHPC 2.5 Vol.-% fiber reinforced	4695	55.3 (10.3)	56.6 (59.6)

matrix with a good bond between the components. Furthermore, the use of high-strength components has a positive effect. In general, steel fiber reinforced concretes behave better with a limited effect on the tensile strength, but with a large improvement of the fracture energy and the softening branch of the load displacement curve (cf. Fig. 6.19). The strain-rate sensitivity or dynamic increase factors (DIFs) of each property, have been investigated by Millon *et al.* (2009). He stated a negligible strain-rate effect (<1.2) on the Young's modulus, but substantial increase factors of 3.5–5.0 on tensile strength, for all concrete qualities.

6.4.3 Experimental technique developed in Lorraine University (Metz)

A new dynamic testing facility has been developed in LEM3 laboratory (Lorraine University (Metz)) to test concrete specimens under spalling loading for strain rates ranging from 30/s to 200/s (Erzar and Forquin, 2010a). The device includes a gas-gun, used to launch a cylindrical projectile 70 or 80 mm in length to strike a Hopkinson bar (diameter: 45 mm, length: 120 mm), both made of the same high-strength aluminum alloy. Figure 6.13 provides an illustration of the experimental set-up and data processing applied for a spalling test performed on a microconcrete. The instrumentation includes three strain gages (G4, G5, G6) bonded on the concrete sample respectively at 60, 40 and 30 mm from the free end. Moreover, two laser interferometers are used to record the particle velocity near the bar specimen contact (Laser-triangle) and on the rear face (Laser-free end). The processing method used to treat the data is as follows. First, the time interval between both laser signals allows deduction of the wave speed of the tested concrete C_0 and the dynamic Young's modulus E_{dyn} with Equation [6.6]. Then the pullback velocity is measured from the particle-velocity signal recorded on the rear face, and the spall strength can be obtained from the Novikov formula (Equation [6.3]). Finally, by reporting the strength value on the gage signals (converted in elastic stress, Fig. 6.13b) the failure time and strain rate at failure are identified (Fig. 6.13b and 6.13c).



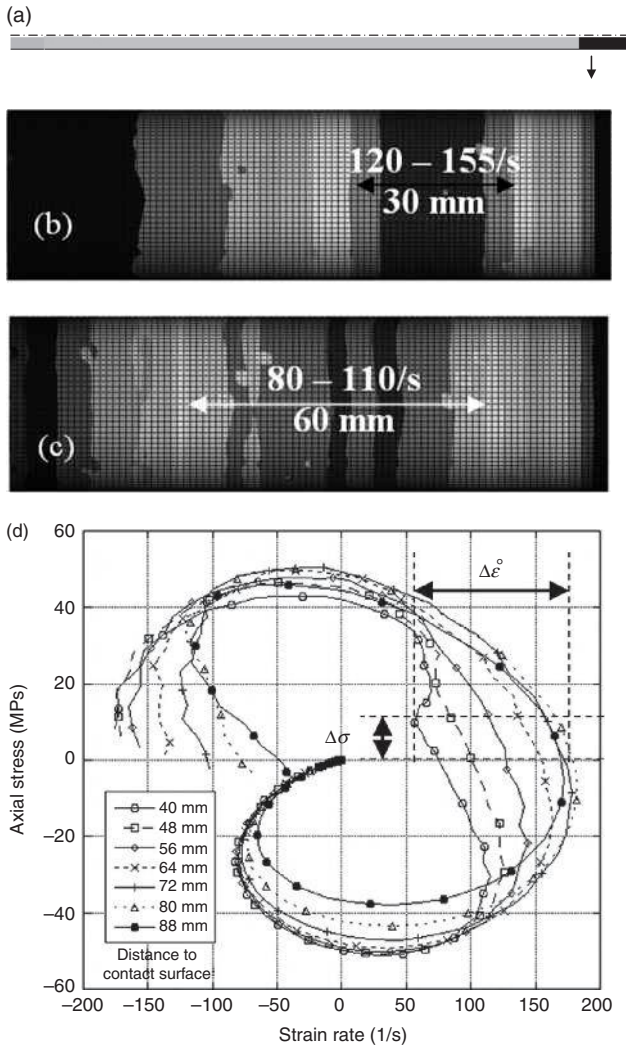
6.13 (a) Experimental device used for spalling tests (LEM3 laboratory); (b) and (c) experimental data for a spalling test performed on a wet microconcrete.

Several advances have been proposed to improve the analysis of spalling tests. First, in each test, an instrumentation including strain gages and laser interferometers of high bandwidth (1.5 MHz) have been used, in order to avoid difficulties due to inertia and adhesion of the accelerometer. The validity of data processing based on the use of Novikov formula was discussed by means of a series of numerical simulations involving different

damage and fracture models and assumed strength levels varying from 10 to 40 MPa (Erzar and Forquin, 2010a). Compression pulses used in the computation were directly obtained from real tests. It was shown that a maximum error a few percent might be expected from this data processing.

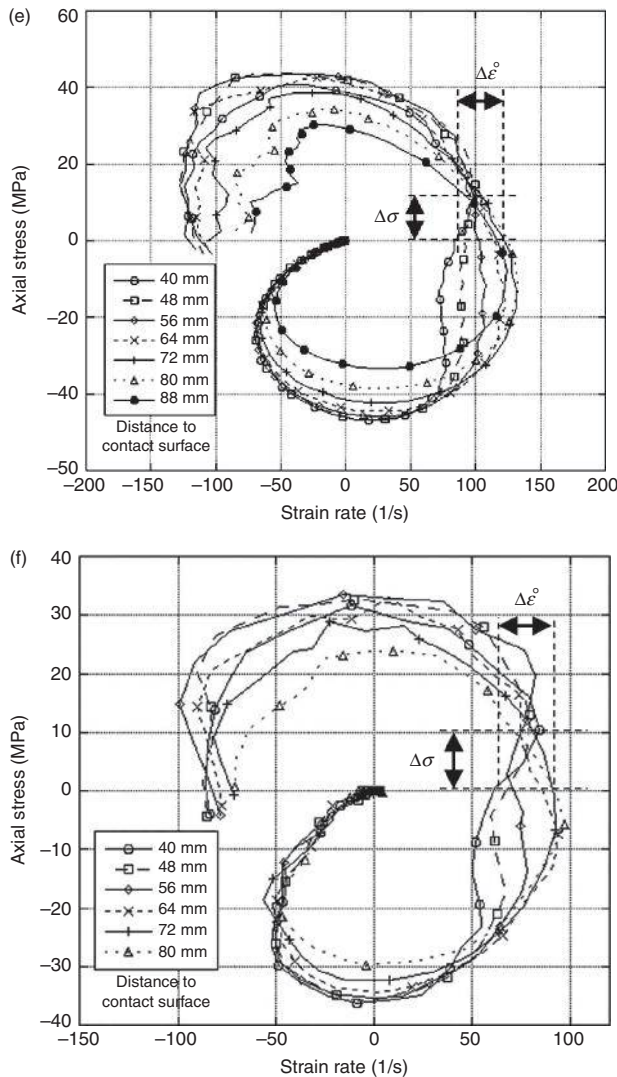
Moreover, with the initial goal of producing reproducible compressive pulses without any influence of parallelism defects at the projectile Hopkinson bar interface, smooth-end projectiles have been designed using numerical simulation tools. A series of computations involving the whole device (projectile, Hopkinson bar, and concrete sample) have been carried out, varying the radius of the hemispheric cap of the projectile. It has been demonstrated that a large radius of about 1.7 m might improve the tensile loading within the concrete cylinder without causing any plastic strain in the Hopkinson bar close to the impacted surface. Figure 6.14 provides an illustration of this phenomenon. On the one hand, a flat-end projectile provides a strongly non-uniform spatial strain-rate field when the level of tensile stress reaches about 20 MPa within the specimen (Fig. 6.14b). On the other hand, the optimized projectile allows obtaining a much more homogeneous strain-rate field (Fig. 6.14c). This result is more noticeable when plotting the axial stress as function of strain rate for several points distributed along the specimen (Fig. 6.14d, 6.14e and 6.14f). For tensile stresses growing from 0 to 10 MPa, the strain rate ranges between 90 and 120/s with the smooth-end projectile (Fig. 6.14e), whereas strain rates ranging from 60/s to 170/s may be observed with a flat-end projectile (Fig. 6.14d) (Erzar and Forquin, 2010a).

Several spalling tests performed on MB50 microconcrete and R30A7 conventional concrete have been conducted using a digital Shimadzu UHSC to visualize the fracturing process of the samples. Two pictures of a UHSC are illustrated on Fig. 6.15a. Cracks are clearly observable on both pictures. However, as shown by DIC processing (Correli software), cracks are initiated much earlier. Indeed, a multiple fracturing process is observed in the specimen less than 35 μ s after the inception of the tensile loading ($T = 0$). The field of axial displacement measured by DIC shown at $T = 83 \mu$ s (Fig. 6.15b) allows detection of four distinct fracture planes. Thus, the tensile damage in the concrete sample subjected to a spalling test is the result of inception and growth of multiple cracking in a very short time following the inception of tensile stresses in the sample (Forquin and Erzar, 2010). In addition, post-mortem analysis of several specimens was conducted. The sample was infiltrated by a colored hyperfluid resin then cut and finely polished. Failure patterns revealed a large number of oriented cracks perpendicular to the loading axis, and an increase of cracking density with the level of strain rate in dry rather than in specimens. More recently, a new processing technique has been proposed by Pierron and Forquin (2012) based on the use of the Virtual Fields Method (VFM). First, images of a grid bonded onto the specimen are recorded by means of a digital ultra high speed camera to obtain axial displacement maps at the surface of the specimen. Second, a specific



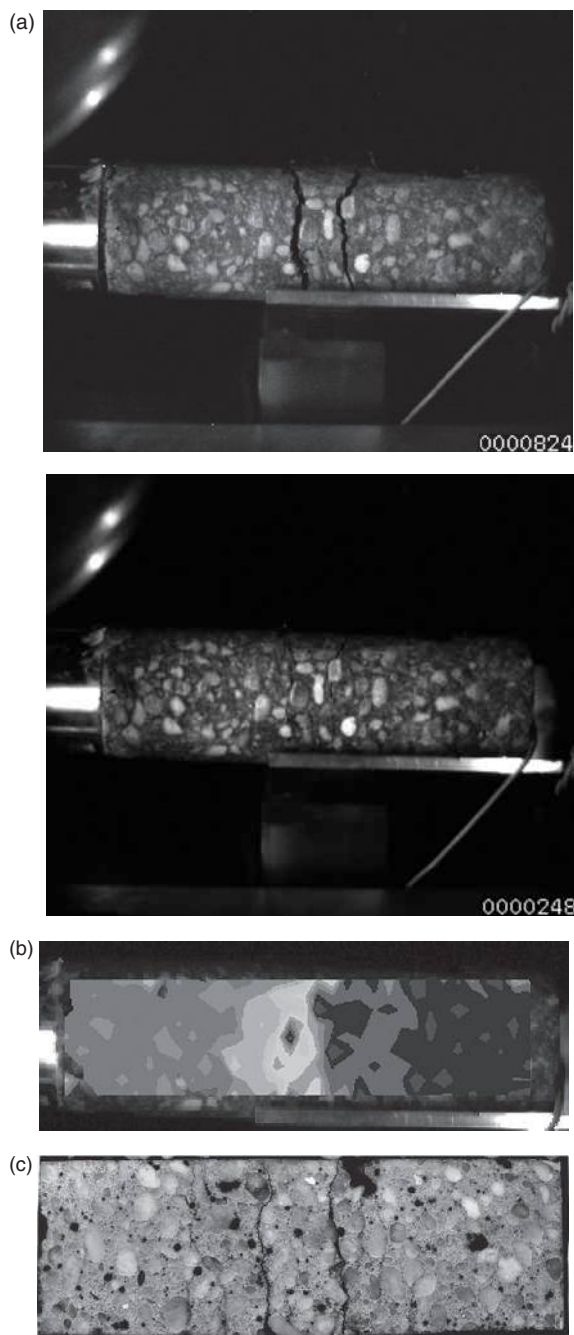
6.14 Numerical simulations of a spalling test with an elastic model (specimen length: 120 mm). (a) Sketch of the numerical configuration; (b) and (c) field of strain rate in the specimen respectively for a flat-end projectile and for the optimized geometry of projectile when maximum stress in the specimen reaches about 20 MPa ($V_{\text{impact}} = 10$ m/s); (d) results obtained for a flat-end projectile at $V_{\text{impact}} = 10$ m/s; (e) results for the optimized geometry of projectile at $V_{\text{impact}} = 10$ m/s; (f) results for the optimized geometry of projectile at $V_{\text{impact}} = 6$ m/s (Erzar and Forquin, 2010).

virtual field allows to use the VFM for deducing the average Young's modulus and axial stress in any cross-section from the acceleration map. Finally it is possible to reconstruct local stress-strain curves and to derive a tensile strength value.

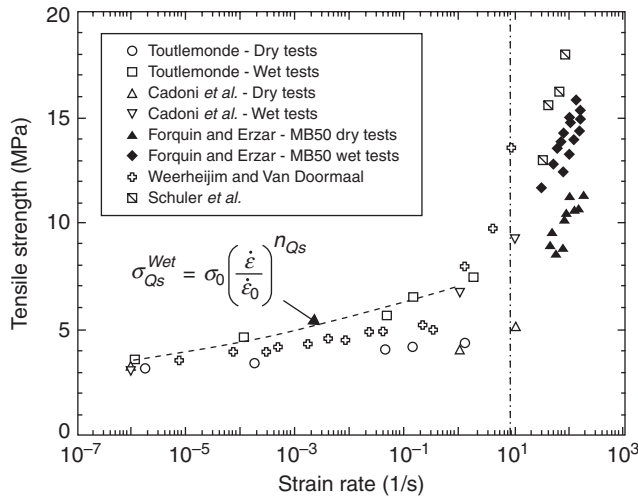


6.14 Continued

Experiments performed on wet and dry MB50 microconcrete are shown in Fig. 6.16 and compared to data given by Cadoni *et al.* (2006), Toutlemonde (1992), Schuler *et al.* (2006), and Weerheijm and Van Doormaal (2007). A strong increase of strength is noted in dry and wet concretes when subjected to spalling tests, whereas a limited or quasi-nil strength enhancement was observed respectively in wet and dry concretes at strain rates below 1/s. Moreover, the dynamic strength of wet specimens is clearly above that of dry specimens, confirming the major influence of moisture on the tensile strength observed at low and intermediate strain rates (Rossi *et al.*, 1992; Toutlemonde, 1992). See also the discussion and results given in Chapter 7.



6.15 Visualization of damage in a wet concrete sample subjected to a spalling test by using a UHS camera and after a post-mortem study.
(a) Pictures of Shimadzu Ultra-High Speed Camera; (b) digital image correlation processing (Correli^{LMT} Software) and (c) post-mortem analysis.



6.16 Quasi-static and dynamic tensile strength of dry and saturated MB50 microconcrete obtained by spalling technique. Comparison with data from Cadoni *et al.* (2006), Toutlemonde (1992), Schuler *et al.* (2006), and Weerheijm and Van Doormaal (2007).

$$\sigma_{QS}^{wet} = \sigma_0 \left(\frac{\dot{\epsilon}}{\dot{\epsilon}_0} \right)^{n_{QS}} \quad [6.6]$$

where $\dot{\epsilon}$ is the strain rate, $\dot{\epsilon}_0$ is a reference strain rate arbitrarily defined and σ_0 and n_{QS} are parameters to be identified.

6.4.4 Dynamic fracture energy in concretes by spalling: test methodologies at Delft and the Ernst Mach Institute

Schuler (2006) derived the fracture energy based on the momentum transfer between the fragments during crack opening. Therefore the stress and velocity distribution over the time is calculated. The stress $\sigma(t)$ on the sample interface with the bar is determined using Equation [6.5] and from there propagated into the sample assuming linear elastic behavior in Equations [6.7] and [6.8]. When the stress wave reaches the sample's free end it is reflected as a rarefaction wave, appearing as a – sign in the second term of Equation [6.7]. During release, the velocity v is further increased, and thus a + sign occurs for the second term in Equation [6.8].

$$\sigma(x, t) = \sigma \left(1 - \frac{x}{c_L} \right) - \sigma \left(1 + \frac{x - 2x_{end}}{c_L} \right) \quad [6.7]$$

$$v(x, t) = \frac{c_L}{E} \sigma \left(1 - \frac{x}{c_L} \right) + \frac{c_L}{E} \sigma \left(1 + \frac{x - 2x_{end}}{c_L} \right) \quad [6.8]$$

Thereby, the velocity distributions as well as the mean velocities are calculated in the two fragments just before and after cracking. They are compared to the fragment velocity evaluations from high-speed videos (Schuler, 2006), later replaced by optical high-speed extensometer recordings (Millon *et al.*, 2009).

The derivation of the fragment mean velocity before and after fracture is the base of the calculation of the fracture energy. The difference, or dissipated kinetic energy, is interpreted as the fracture energy needed to open the crack and to cause fragmentation.

$$G_f = \int F d\delta = \int \frac{dI}{dt} \delta dt \quad [6.9]$$

$$G_f = \Delta v m \delta \quad [6.10]$$

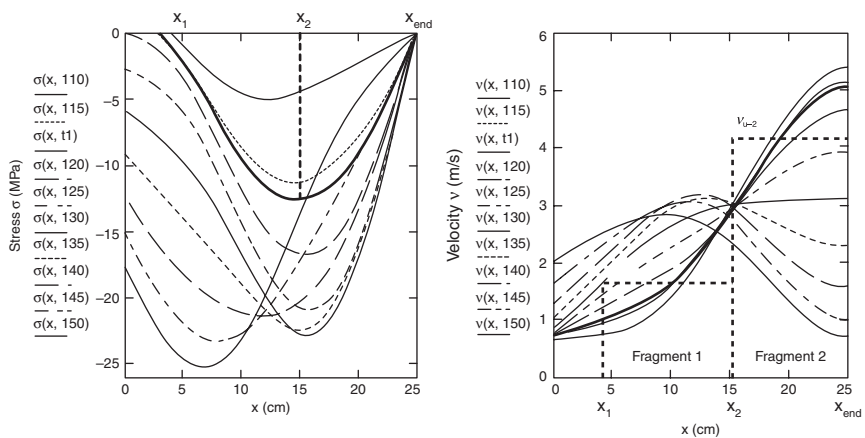
The total energy G_f consumed by the fracture process is equal to the integral of the force F during the crack-opening displacement δ (Equation [6.9]), which can also be expressed as change in momentum I . Equation [6.9] leads to the simple Equation [6.10] calculating the fracture energy from the crack opening velocity δ' and the reduction Δv of the velocity of fragment 2 between crack initiation and the fully opened crack.

Undisturbed cylindrical specimens tend to provide fracture zones and multiple fracture planes (Schuler 2006); see also the method described in Section 6.3.3 for the moderate loading rate regime. This fact compromises the calculation of the specific fracture energy per unit surface area $G_f' = G_f / A$, which is the actual material parameter. Therefore, Schuler introduced additionally notched specimens to provide one clear fracture area A (Fig. 6.18). Ever since, notched specimens to derive the specific fracture energy on one fracture plane and unnotched samples to derive the dynamic strength in undisturbed one-dimensional samples have been used at EMI.

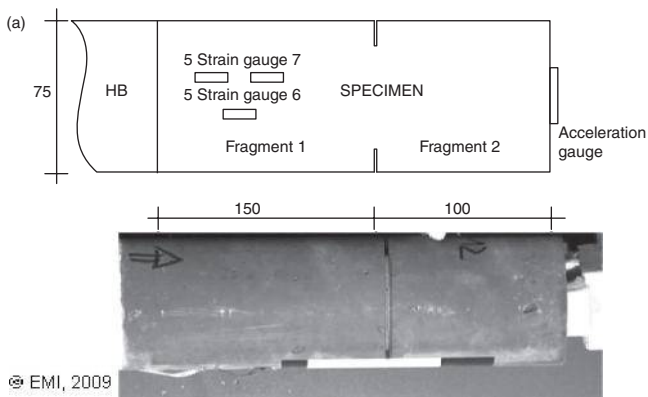
The accuracy of the velocity measurements, and consideration of the material scattering, have been identified as main influences during application and refinement of this technique over the last years. Schuler originally used 2D high-speed digital recordings with a spatial resolution of about 0.5 mm (1024×512 pixel) with typically 1000–8000 frames/s. Millon *et al.* (2009) refined the method by introducing a 1D optical extensometer to resolve displacements below 0.005 mm with a sampling rate of 10^6 /s (1 MHz), getting close to measure the actual crack opening process at the early stages of Fig. 6.18b. The refined measurements lead clearly to an increase of the derived fracture energies by several 10%.

The material scattering, on a batch of more than 25 tests with virtually identical initial conditions with respect to the specific fracture energy, has been recently studied in cooperation with Nanyang Technological

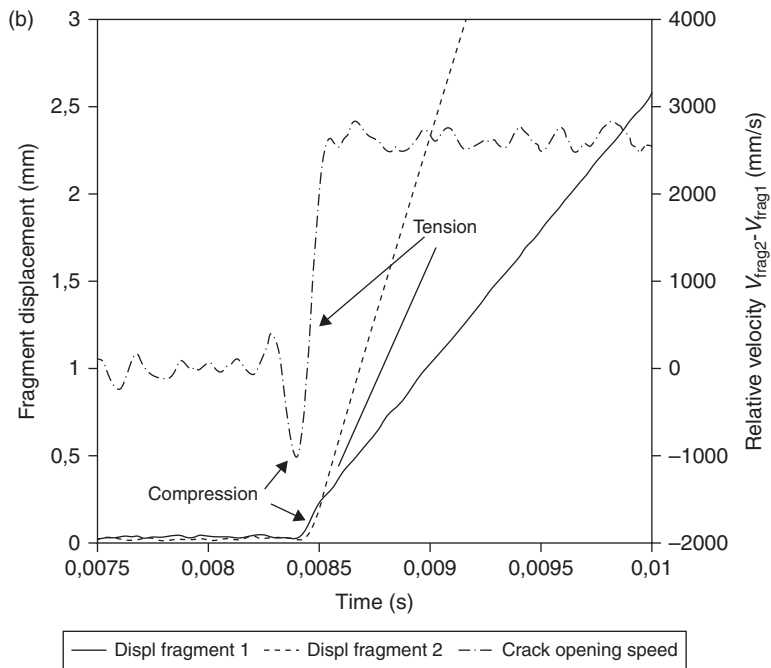
University, Singapore. Despite thorough sample preparation, very repeatable striker impact velocities (standard deviation <7%) and application of the high-resolution optical extensometer, a wide variation of G_f' from 290 to 1030 N/m, with a noticeable standard deviation of 205 N/m (35%), has been derived (Fig. 6.18c). The average specific fracture energy of 592 N/m clearly exceeds Schuler's value 380 N/m derived by 4–7 samples per input condition. In conclusion, it can be stated that significant scattering of the fracture energy seems to be an intrinsic material property of concrete. The mean fracture energy of 728 N/m (with standard deviation of 310 N/m), derived from eight tests with local strain gages by Weerheijm and Vegt at Delft, falls reasonably well within the range of results measured at EMI with the same



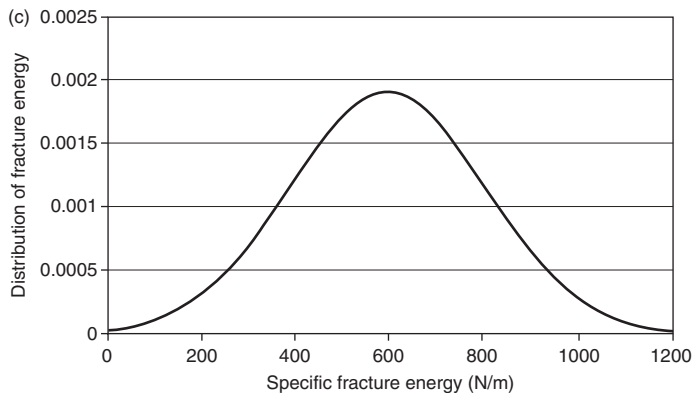
6.17 Stress and velocity evolution in the spallation sample at 5 ms time steps and the instant of fracture (bold lines), reprinted from Schuler (2006).



6.18 (a) Notched specimen and analytically calculated velocity distribution before fracture.



6.18 (b) Optical extensometer recordings of fragment displacements and relative velocity.



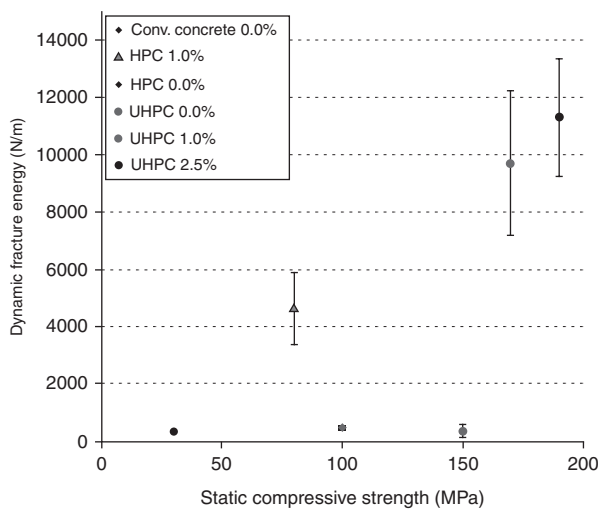
6.18 (c) Normal distribution of fracture energy as derived from >25 SHB repetitions with identical input parameters: average $G_f' = 592$ N/m with a standard deviation of 205 N/m.

sample dimensions (Weerheijm *et al.*, 2009). Other test series performed by Weerheijm and Vegt, with slightly different test conditions, confirm the conclusion that the scatter in fracture energy is an intrinsic concrete property at high loading rates.

Table 6.3 Results of the Hopkinson Bar experiments for the dynamic (and static) fracture energy ($\dot{\epsilon} \approx 10^2/S$, $\dot{\sigma} \approx 10^3$ GPa/s) (Millon *et al.*, 2009).

	Specific fracture energy G_f' (N m ⁻¹)
Conventional concrete	592 ^a ± 205 (150)
HPC	480 (160)
HPC 1 Vol.-% fiber reinforced	4200 (2270)
UHPC	360 (230)
UHPC 1 Vol.-% fiber reinforced	10 070 (10 300)
UHPC 2.5 Vol.-% fiber reinforced	11 290 (13 900)

^aOriginal value of 380 N/m (Schuler 2004, 2006) recently refined by optical extensometer measurements on large number of samples.



6.19 Dynamic fracture energy for conventional to UHPC concrete for 0% and 1% of steel fiber content at strain rates of 70–160 1/s (Millon *et al.*, 2009).

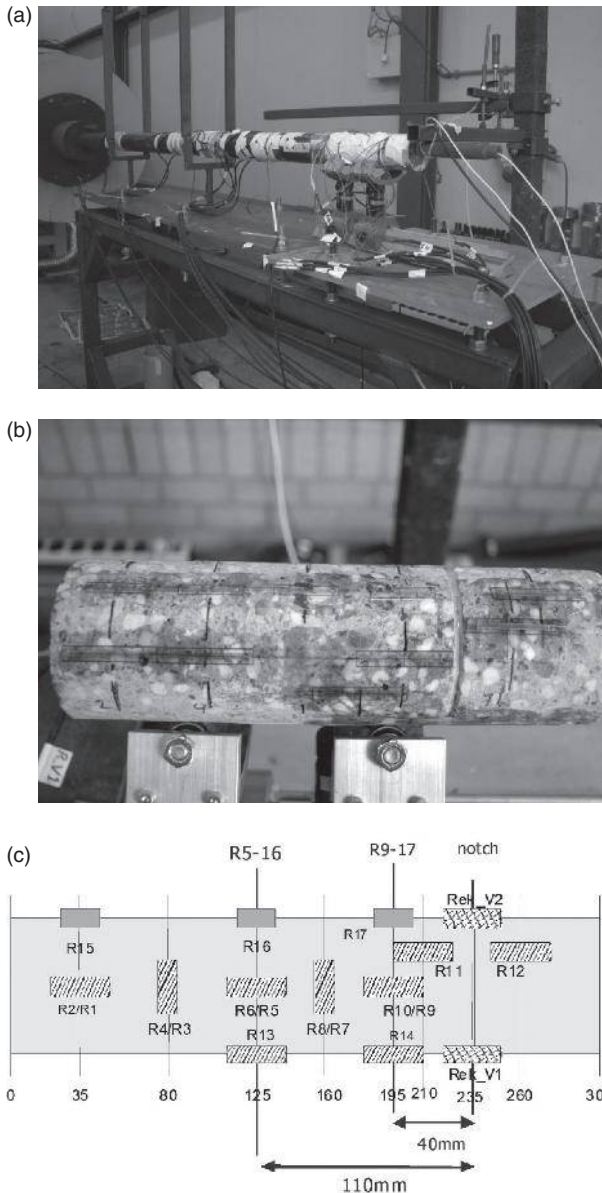
The following conclusions can be drawn from application to various concrete qualities in Table 6.3 and Fig. 6.19. The measured fracture energies show, in comparison to the tensile strength and the Young's modulus, no significant influence of the bulk concrete quality. The addition of steel fibers leads to a remarkable increase of both the ductility and fracture energy. The latter property increases by a factor of 10–30. The experiments show that already a small fiber content of 1% is sufficient to increase the fracture energy significantly (Table 6.3).

Table 6.3 allows derivation of the DIF for measured fracture energies at strain rates around 30–165/s, again comparable to quasi-static notched-beam bending tests at about 10^{-4} /s (Millon *et al.*, 2009). Pronounced dynamic increases around 300% are observed for conventional concrete and HPC

without fiber. UHPC concrete with 1% fiber content yields to the same fracture energy as under static conditions in the spallation tests, within the experimental scattering. The strain-rate effect is low, but the absolute values for the static and the dynamic fracture energy are high. Independently of the concrete quality, a lower rate effect is observable compared to the tensile strength. Thereby, with increasing concrete strength higher loads and higher strain rates are required to produce fragmentation in the experiment.

In the set-up and analysis presented above, nowadays optical extensometers are used to monitor the fracture process and gain data to derive the dynamic fracture energy. This diagnostic technique is related to the method developed in Delft by Weerheijm and Vegt. They worked on a method to derive the stress deformation curve, and thereby the fracture energy, directly from strain and deformation recordings (Weerheijm *et al.*, 2001, 2004; Vegt *et al.*, 2007). The set-up in Delft consists of a horizontal steel bar (length 2 m, \varnothing 74 mm), supported by strings (Fig. 6.20). The compression pulse is generated with small explosive charges. The diagnostics and data acquisition are designed to reconstruct the stress distribution along the specimen as a function of time. To derive the full load deformation curve, notched specimens are used. The stress distribution in the notched section is combined with the deformation recordings for the whole response process up to failure, so the dynamic fracture process is reconstructed from the recordings. To examine the possibilities to reconstruct the whole response process, the specimen is instrumented with a large set of strain gages.

The applied diagnostics of the modified split Hopkinson bar (MSHB) are similar to the equipment of the gravity driven split Hopkinson bar. The generated pulse in the steel (incident) bar is recorded by two sets of strain gages at the steel bar to check the amplitude, energy, and reproducibility of the loading pulse induced by the explosive charge. A part of this incident pulse is transmitted to the concrete specimen (dimensions: \varnothing 74 mm, length 300 mm). The reflected part is recorded by the strain gages on the steel bar, while the transmitted pressure pulse, the wave propagation and reflection process within the specimen are recorded with a number of strain gages distributed along the notched specimen (Fig. 6.20). The functions of the strain gages are as follows. Two pairs of strain gages (R1-R4) are located near the contact surface to record the transmitted pulse and check symmetry, in case of occasional bending. In combination with the other longitudinal gages (R5/6, R13, and R9/10), wave velocity and dispersion are recorded. From the wave velocity, the dynamic Young's modulus is derived assuming 1D stress condition ($E_{\text{dyn}} = \rho c_0^2$). Using the E_{dyn} the transmitted stress pulse is calculated from strain gages R1/2 and compared with the recorded incident and reflected pulses in the steel bar. Reliable data on the wave velocity is needed to check the load transmission process and to quantify the loading conditions in the concrete specimen. The experiments showed that 3–4 gages are needed to derive representative, reliable data on wave velocity and E_{dyn} .



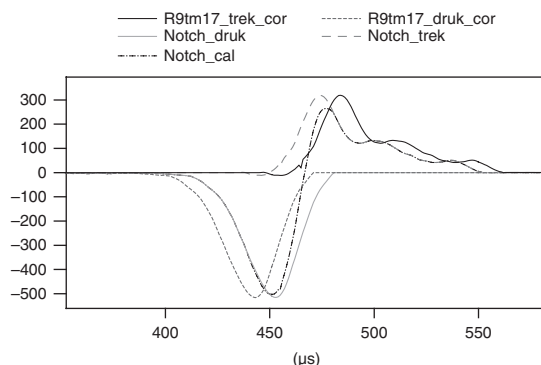
6.20 (a) 74mm MSHB in Delft for high loading rates (1000 GPa/s); (b) instrumented specimen; (c) specimen instrumentation scheme.

To reconstruct the stress conditions along the specimen in time, the assumption is that the concrete is a perfect linear elastic material in compression and no damage occurs. This assumption is checked on the condition of constant c_0 – values between the strain gages and the condition of no residual strains at location R1-R4. Note, that the amplitude of the loading

pressure pulse was limited to about 1/3 of the static concrete compressive strength. This restriction appeared to be sufficient to fulfill the above mentioned conditions.

Besides the quantified loading pulse and the reconstructed stress history along the concrete specimen, the deformation in the fracture zone had to be recorded to derive the full stress deformation relation. The dynamic strength and total fracture energy are derived from this relation. Because of the high loading rate the mass of the displacement gages needs to be mass-less to prevent distortion of the recording by mechanical vibrations of the gage system. A new measuring device was developed, consisting of a 30 mm strain gage glued onto a synthetic foil. The ends of the foil are bonded onto the specimen, leaving a certain unbonded area around the notch. The supporting foil behaves linearly and is able to stretch for a certain distance before it breaks (Vegt *et al.*, 2007). The new device was extensively tested, calibrated, and proved to fulfill the requirements.

The measured deformations at the notch are combined with the resulting stresses in the notch to obtain the desired stress deformation curve. This method is consistent with the method applied in statics and for the SHB in the moderate loading regime. Figure 6.21 presents examples of the recorded pressure pulses, the tensile pulse recorded beyond the failure zone, and the reconstructed stress condition in the notched zone. Figure 6.22 shows the deformation time record and the reconstructed stress deformation curve. The applied diagnostic technique enables determination of the fracture

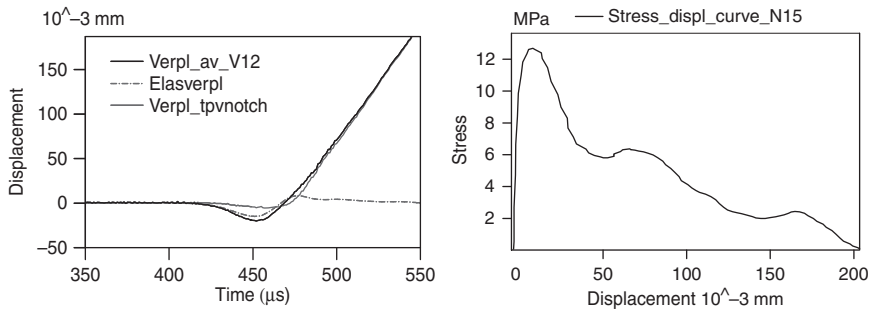


6.21 Examples of recorded and reconstructed strain-time records (units: μ -strain and μ sec). The curve indicated with 'Notch-druk' gives the incident LE-pressure curve at the notch as a function of time. The curve 'R9tm17_trek_cor' is the transmitted tensile pulse recorded at R9-17. This pulse is shifted in time ('Notch-trek' curve) to synchronize incident and reflected pulses at the notch. The sum of the incident and transmitted curve results in the stress condition at the notch as a function of time (the curve 'Notch_cal'). Note the steepened slope of the resulting tensile pulse in the notched area.

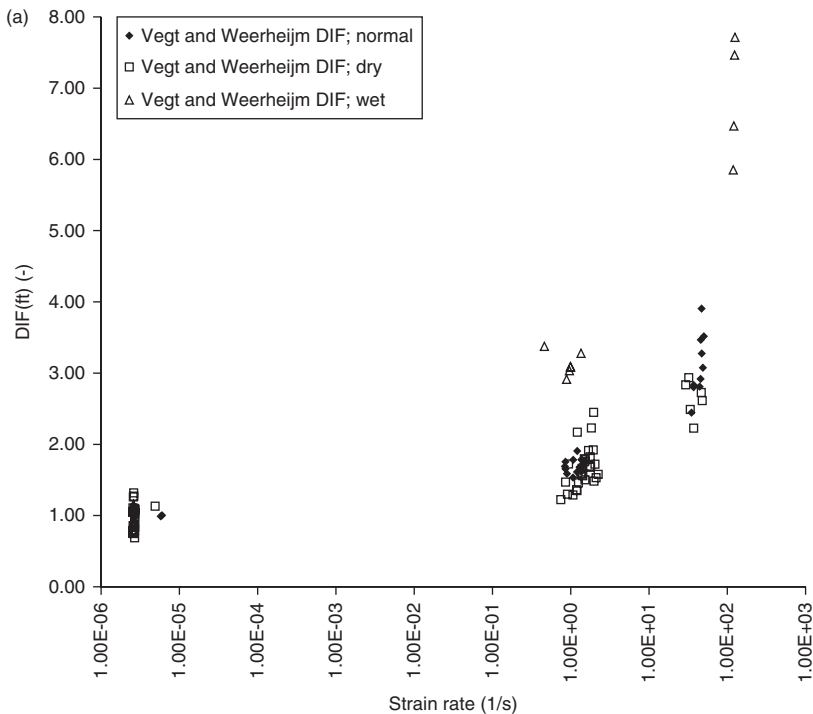
energy consistently with the methods applied in statics and the moderate loading regime.

The prime focus of the test set-up and diagnostics is on the fracture energy, but of course data on the dynamic Young's modulus and strength are also obtained.

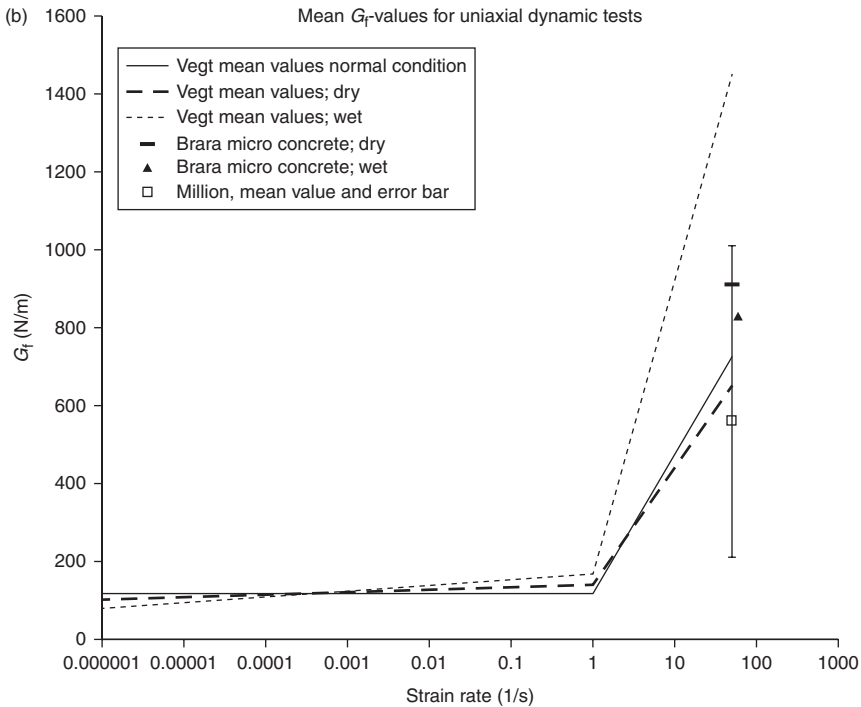
Figure 6.23 gives some of the results obtained with the set-ups at Delft. The strength data exhibits the enhanced increase beyond strain rates of $1/s$



6.22 Reconstructed load-deformation curve (right) from stress state (left) and recorded deformation at the notched zone.



6.23 (a) DIF tensile strength data Vegt *et al.* (2007) and (b) mean values fracture energy data.



6.23 Continued

and the effect of moisture on the rate effect. See also the discussion and data given in Chapter 7 and 10.

Concerning the fracture energy data, it is emphasized that the scatter is large for the high loading rate regime (see Section 6.4.4). This scatter is an intrinsic property of concrete, and should be considered in defining test programs.

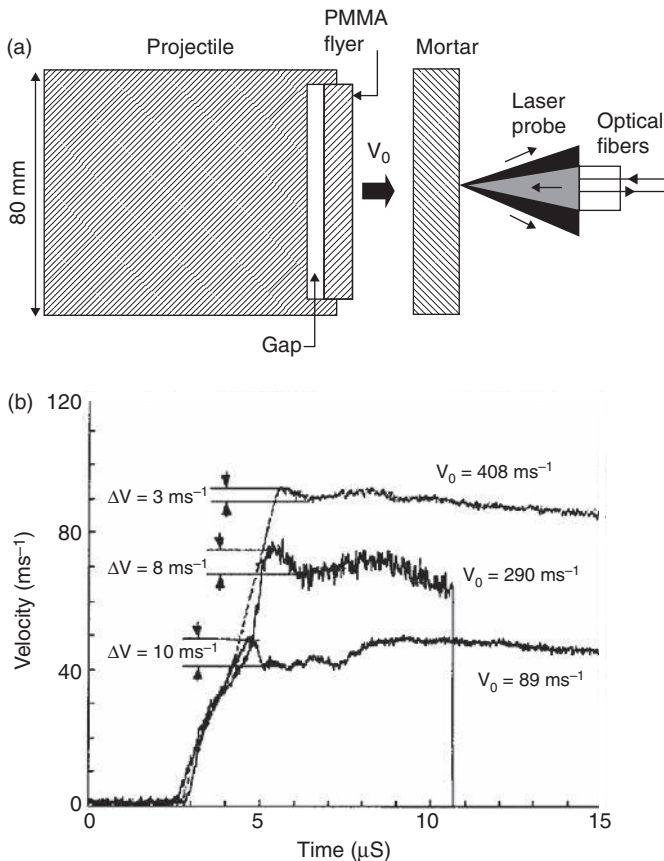
6.5 Characterizing the tensile strength of concrete at very high loading rates ($\dot{\sigma} \geq 10^5$ GPa/s or $\dot{\epsilon} \geq 2000$ /s)

Spall experiments with plate-impact technique have been widely used to characterize the dynamic strength of brittle and ductile materials (Antoun *et al.*, 2002). The principle of these tests is the following. A thin disc, launched at a velocity of few tens to few hundreds of meters per second, hits a target made of the material to be characterized. Compressive waves, propagated in the projectile and in the target, reflect as release waves on free surfaces of the target and projectile. A fast dynamic tensile loading initiates when both release (decompression) waves cross each other, leading to a dynamic failure in a uniaxial strain state. This technique was employed for studying

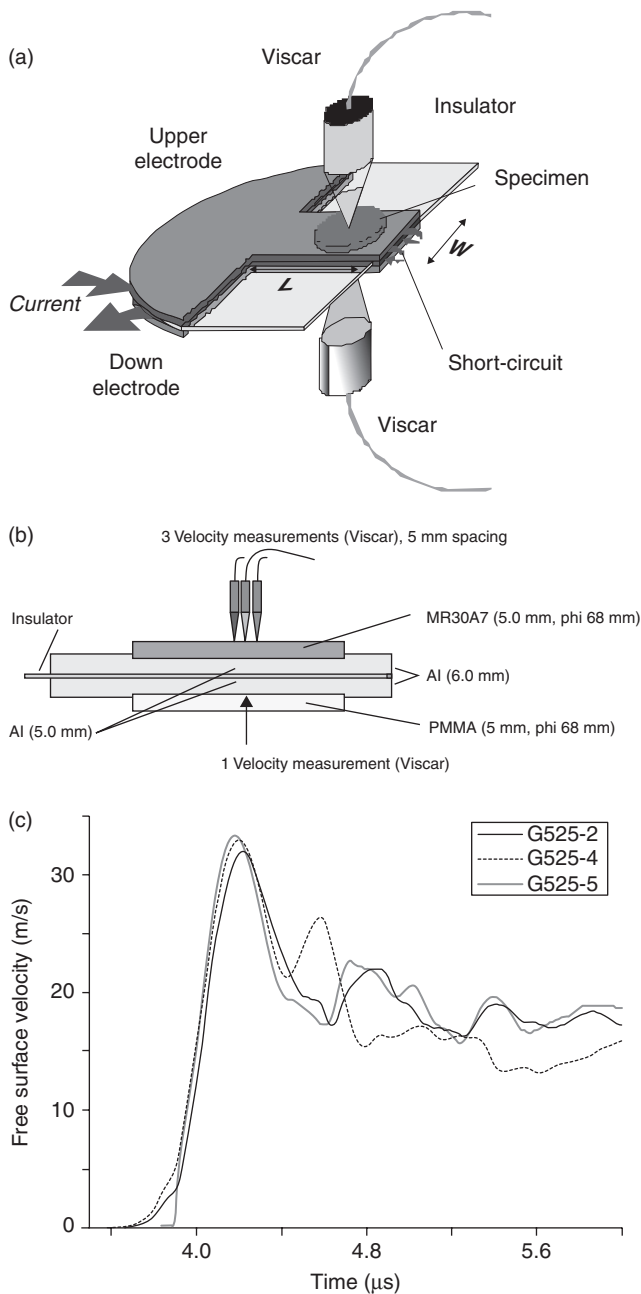
the ductile failure of metals induced by void- or microcrack-growth coalescence (Antoun *et al.*, 2002). This technique was also used to characterize the spall strength of ceramics (Coscolluela, 1992; Cagnoux, 1994; Bartkowski and Dandekar, 1996; Hiltl and Nahme, 1997). The spall strength is derived from the formula proposed by Novikov *et al.* (1966):

$$\sigma_{\text{spall}} = \frac{1}{2} \rho C_L v_{\text{pb}}, \quad [6.11]$$

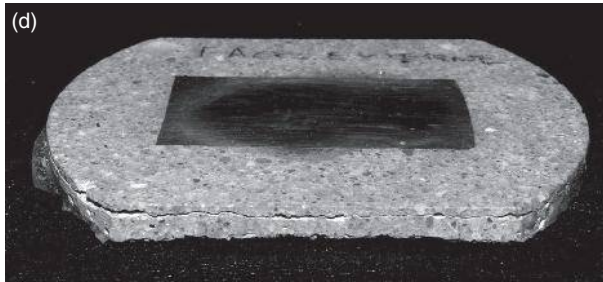
where ρ , C_L denote respectively the density and the longitudinal wave speed ($C_L = \sqrt{(\lambda + 2\mu) / \rho}$) and v_{pb} denotes the pullback velocity corresponding again to the difference of velocities between the maximum value and the velocity at rebound, both measured on the rear face of the specimen. A laser interferometer is generally used to record this velocity.



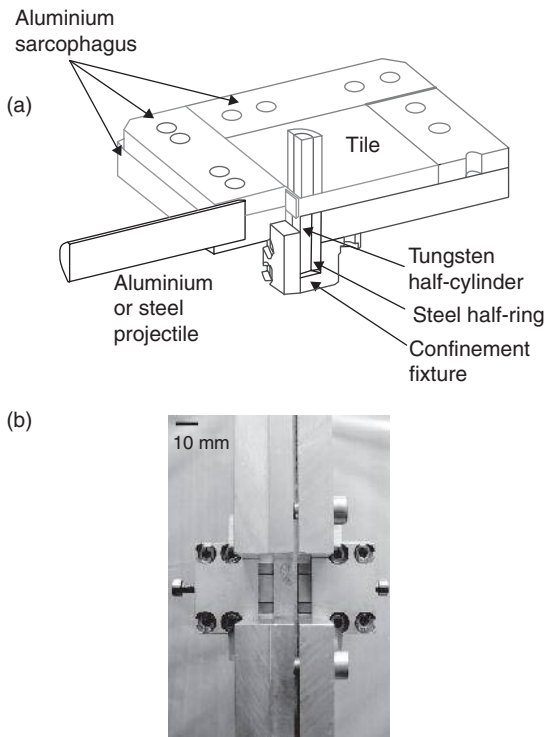
6.24 Spalling tests by plate-impact technique performed on mortar specimens (Grote *et al.*, 2001). (a) Plate impact set-up and (b) velocity profiles recorded on the rear face of mortar sample.



6.25 Spalling experiments performed with GEPI (Générateur Electrique de Pressions Intenses) facility at Gramat (a) Scheme of an electrode in the load region. (b) Spall experiment performed with a mortar specimen 5 mm thick. (c) Free surface velocities measured by VISAR interferometer. (d) Recovered specimen (Erzar *et al.*, 2009).

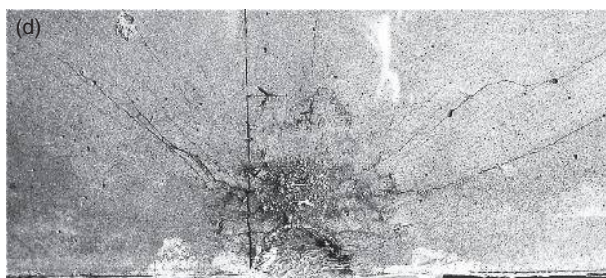
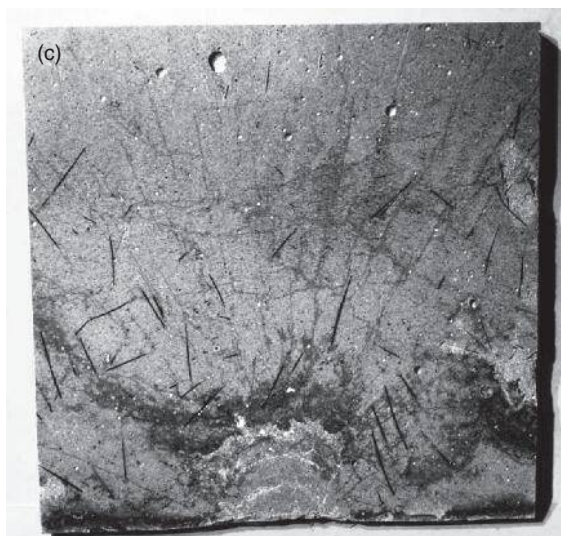


6.25 Continued



6.26 EOI experiments performed with Ductal® Ultra-High-Strength Concrete (Forquin and Hild, 2008). (a) Schematic of the sarcophagus configuration; (b) front view of the device with confinement system; (c) damage pattern after EOI of an aluminum projectile (impact velocity = 88 m/s); (d) and a steel projectile (impact velocity = 130 m/s).

Grote *et al.* (2001) conducted plate-impact experiments to characterize the spall strength of mortar specimens by using a PMMA striker (Fig. 6.24). The authors obtained a spall strength of 42.3 MPa with the lowest impact velocity (89 m/s), whereas lower strengths (33.9 and 12.7 MPa) were obtained at higher impact velocities (respectively 290 and 408 m/s). The compressive



6.26 Continued

pulse that preceded the tensile loading supposedly weakened the sample in the two last experiments.

A similar technique was used by Kipp *et al.* (1997) to investigate the spall strength of conventional concretes (max. grain size: 10 mm) in plate-impact experiments. Despite the scatter in the results the authors evaluated a spall strength of about 30 MPa. However, as in the Grote *et al.* test series, the strain rate of the loading remains unknown.

More recently a new testing device, GEPI, was developed in the CEA (Commissariat à l'Energie Atomique et aux Energies Alternatives) – Centre de Gramat (Hereil *et al.*, 2003). A very short and intense current (about 3.5 MA in 500 ns) is used to accelerate an electrode by the Laplace effect (Fig. 6.25a). The electrode initially in contact with the concrete sample plays a similar role to an impactor in the case of a plate-impact experiment. So, the pressure pulse reflects as a tensile pulse on the rear free surface of the target. A spall fracture occurs in a state of uniaxial strain, unlike spalling tests with a Hopkinson bar where a uniaxial stress state is obtained.

A spall experiment configuration used to characterize the tensile strength of MR30A7 mortar is shown on Fig. 6.25b. Three VISAR laser interferometers are directed towards the free surface of the specimen. A PMMA sample is placed in contact with the lower electrode, so this fourth velocity measurement serves as a chronometry indicator to calculate the longitudinal wave speed in concrete. Experimental data from VISAR interferometers are plotted on Fig. 6.25c. The average strain rate is about 4500 s^{-1} , and the spall strength of about 49 MPa is quite similar to the values obtained by Grote *et al.* (2001) and Kipp *et al.* (1997) in plate-impact tests (about 40–50 MPa). However, the major advantages of this pulsed-power technology, in comparison with a conventional plate-impact experiment, lies in the fact that, on the one hand, a slower rise time of the incident pulse is obtained so the strain rate of the tensile loading may be easily computed while, on the other hand, the sample can be recovered for post-mortem analysis (Fig. 6.25d).

6.6 Edge-on impact tests performed on concrete

EOI configurations had been first developed at EMI in Germany (Hornemann *et al.*, 1984; Strassburger *et al.*, 1994) and by the Centre Technique d'Arcueil (CTA) in France (Denoual *et al.*, 1998; Riou *et al.* 1998; Forquin and Hild, 2008). During an EOI test, a cylindrical projectile hits the edge of a tile to be fragmented. In the same way as for a real impact, a compressive wave propagates within the target, inducing a radial motion of the material along the axis centered on the impact point. This radial motion creates tensile hoop stresses that may induce intense damaging of the target from oriented microcracks. Riedel *et al.* (2010) numerically analyzed the sequence of loading conditions leading to failure using Smoothed-particle hydrodynamics (SPH) and Lagrangean hydrocodes. Steinhäuser *et al.* (2009) used the test to validate discrete element simulations.

Two configurations are usually considered for these tests. In the first (open configuration), the development of the fragmentation process is visualized in 'real time' by means of an optical 'Schardin camera' or, nowadays, also digital UHSC. In the second configuration (sarcophagus configuration), the specimen is placed within an aluminum casing to keep all fragments in place after the test. Next, the fragmented target is infiltrated by a colored hyperfluid resin and finely polished so the macroscopic and microscopic post-mortem cracking pattern may be observed.

EOI experiments have been conducted by Forquin and Hild (2008) to investigate the damage modes induced by impact loading in UHPC (Ductal®) targets. A slab of size $300 \times 150 \times 15 \text{ mm}^3$ is impacted on the edge by a metallic projectile (diameter: 20 mm, length: 50 mm) travelling at 90–130 m/s. A schematic of the sarcophagus configuration is shown on Fig. 6.26a. In this configuration, a 'dynamic confinement system,' composed of two

half-cylinders made of tungsten and two half-crowns made of steel, is put in contact with the lateral faces of the concrete tile near the impact point. This confinement system ensures a plane strain compression loading in front of the projectile. Consequently, the hydrostatic pressure in this area increases and it allows one to benefit from the large increase of strength of rock and concrete materials with the level of confinement pressure. Therefore, the extent of compressive damage is reduced and the modeling of the test is easier. As no additional static loading is used to ensure a good confinement, the confinement system is really effective during the back-and-forth time of waves in the confinement (about a dozen microseconds). This is why this system is called dynamic confinement.

Results of EOI tests carried out on the Ductal® fibered concrete are shown in Fig. 6.26c and 6.26d. In the first test, an aluminum projectile hits the target at 90 m/s, whereas a steel projectile impacting at 130 m/s was used in the second configuration. In both cases, an intense fragmentation is visible far beyond the area of confinement. It is composed of numerous cracks oriented in the radial direction (from the impact point). Moreover, in the second test (steel projectile, impact velocity of 130 m/s), complex cracking mechanisms may be observed close to the comminuted area. In particular cracks, called snail cracks, oriented at 45° with respect to the radial and hoop directions are noted. These cracks, developed in mode II with rubbing lips, correspond to a confined compressive damage due to high compression stresses induced close to the area of confinement. Furthermore, it is noted that fibers did not prevent crack initiation and propagation, even if they provided a substantial residual strength to the fragmented target (Forquin and Hild, 2008).

More recently, EOI experiments have been conducted on microconcrete and common concrete samples in the LEM3 laboratory. The concrete target, a plate 15 mm thick was impacted by an aluminum alloy projectile 22.5 mm in diameter. Again, both configurations (i.e. open and sarcophagus configurations) have been considered for these tests. This technique was used to analyze the damage kinetics during the test (Erzar, 2010b; Erzar and Forquin, 2011).

The tests performed on dry and water-saturated specimens revealed an important red of oriented crack and a notable influence of water content: indeed higher cracking density was noted in dry specimen compared to wet specimens. This result is consistent with spalling tests in which wet specimens showed higher tensile strength than dry specimens.

6.7 Conclusions

Several sets of experimental methods are proposed in the literature to characterize the tensile response and fracture energy of concretes in dynamic conditions. High-speed hydraulic press or SHB facilities may be used to

characterize the tensile behavior of concretes at intermediate loading rate (strain rate range $1\text{e-}3/\text{s}$ – $10/\text{s}$). Spalling experiments performed with a single Hopkinson bar are commonly used to reach higher strain rates ($10/\text{s}$ – $200/\text{s}$). In this configuration, the specimen is intentionally unbalanced and stress-wave analysis is applied. The plate-impact technique allows reaching much higher strain rates, but with a state of uniaxial strain. As in spalling tests, a pressure pulse reflects as a tensile pulse on the rear free surface of the target. However, the tensile pulse duration is very short (less than a few ns). Impact tests as EOI experiments are employed to visualize the kinetics of damage and to improve understanding of the fragmentation process at high loading rates.

Among the main experimental results obtained with conventional concretes, microconcretes, high-strength concretes and mortars, strong strain-rate sensitivity is noted above $1/\text{s}$ as well as a clear influence of free-water content on their tensile strength and fracture energy. Aggregate size seems to have a limited effect on strength enhancement. Moreover, post-mortem analyses of spalled or impacted specimens have revealed a strong increase of cracking density above $1/\text{s}$.

Several limitations are also pointed out, for instance concerning the post-peak behavior of concrete at high or very high strain rates, resulting from the short pulse duration applied in spalling tests, especially at a very high strain rate. Scatter in the results is noted for the measurement of fracture energy at very high strain rates, which seems to result from the variability in concrete microstructure, but this needs further study. Moreover, some difficulties arise for characterizing the tensile strength of concrete at extremely high loading rates in plate-impact tests. Indeed, as shown by Grote *et al.* (2001), the compressive pulse that precedes tensile loading may weaken or damage the sample. Some further work should enable overcoming these gaps, benefiting from recent progress in numerical modeling and experimental tools.

6.8 References

- Antoun T., Seaman L., Curran D.R., Kanel G.I., Razorenov S.V. and Utkin A.V. (2002) *Spall fracture*, Springer Ed., New York, ISBN 0–387–95500–3.
- Bartkowski P.T. and Dandekar D. P. (1996) *Spall strengths of sintered and hot pressed silicon carbide*, Army Research Laboratory. Report.
- Birkimer D.L. and Lindemann R. (1971) Dynamic tensile strength of concrete materials. *ACI Journal*, **68**(8), 47–49.
- Cadoni E., Albertini C. and Solomos G. (2006) Analysis of the concrete behaviour in tension at high strain-rate by a modified Hopkinson bar in support of impact resistant structural design. *J. Phys. IV France*, **134**, 647–652.
- Cadoni E., Labibes L., Albertini C., Berra M. and Giangrasso M. (2001) Strain-rate effect on the tensile behaviour of concrete at different relative humidity levels. *Mater. Struct./Matériaux et Constructions*, **34**, 21–26.

- Cagnoux J. (1994) *Caractérisation dynamique de nouvelles céramiques pour blindages (TiB₂, B₄C, SiC)*. rapport n° T94-45, Centre d'Etudes de Gramat.
- Coscolluela A. (1992) *Plasticité, endommagements et ruptures des aluminés sous sollicitations dynamiques triaxiales : influence de la taille de grains*. PhD-thesis, Bordeaux I University.
- Erzar B. (2010b) *Ecaillage, craterisation et comportement en traction dynamique de betons sous impact: approches experimentales et modelisation*. PhD-thesis, University of Metz, France.
- Erzar B., Buzaud E., Pontiroli C. and Forquin P. (2009) Tensile strength of mortar over a wide range of strain rate. *DYMAT*, **1**, 603–609.
- Erzar B. and Forquin P. (2010) An experimental method to determine the tensile strength of concrete at high rates of strain. *Exp. Mech.*, **50**(7), 941–955.
- Erzar B. and Forquin P. (2011) Experiments and mesoscopic modelling of dynamic testing of concrete. *Mech. Mater.*, **43**, 505–527.
- Forquin P., Arias A. and Zaera R. (2008) Role of porosity in controlling the mechanical and impact behaviours of cement-based materials. *Int. J. Impact. Eng.*, **35**(3), 133–146.
- Forquin P. and Erzar B. (2010) Dynamic fragmentation process in concrete under impact and spalling tests. *Int. J. Fracture*, **163**, 193–215.
- Forquin P. and Hild F. (2008) Dynamic fragmentation of an ultra-high strength concrete during edge-on impact tests. *ASCE J. Eng. Mech.*, **134**(4), 302–315.
- Forquin P., and Hild F. (2010) *A probabilistic damage model of the dynamic fragmentation process in brittle materials*. Advances in Applied Mech. Giessen & Are feds. **44**, 1–72. Academic Press, San Diego, CA.
- Goldsmith W., Polivka M. and Yang T. (1966) Dynamic behaviour of concrete. *Exp. Mech.*, **6**, 65–79.
- Gong J.C., Malvern L.E. and Jenkins D.A. (1990) Dispersion investigation in the Split Hopkinson pressure bar. *J. Eng. Mater. Technol.*, **112**, 309–314.
- Grote D.L., Park S.W. and Zhou M. (2001) Experimental characterization of the dynamic failure behavior of mortar under impact loading. *J. Appl. Phys.*, **89**(4), 2115–2123.
- Hereil P.L., Lassalle F. and Avrillaud G. (2003) GEPI: An ice generator for dynamic material characterisation and hypervelocity impact, *AIP Conf. Proc.*, **706**(1) 1209–1212.
- Hillerborg A. (1985) The theoretical basis of a method to determine the fracture energy G_f of concrete. *RILEM Mater. Struct.*, **18**(106), 291–296.
- Hiltl M. and Nahme H. (1997) Dynamic behaviour of a shock-loaded glass-ceramic based on the Li₂O-Al₂O₃-SiO₂ system, *J. Phys. IV*, **7**, C3, 587–592, DOI: dx.doi.org/10.1051/jp4:19973101
- Kipp M.E., Chhabildas L.C. and Reinhart W.D. (1997) Elastic shock response and spall strength of concrete. *AIP Conf. Proc.*, **429**, 557–560.
- Klepaczko J.R. and Brara A. (2001) An experimental method for dynamic tensile testing of concrete by spalling. *Int. J. Impact Eng.*, **25**, 387–409.
- Kolsky H. (1949) An investigation of mechanical properties of materials at very high rates of loading. *Proc. Phys. Soc. London, B*, **62**, 676–700.
- Landon J.W. and Quinney H. (1923) Experiments with the pressure Hopkinson bar, *Proc. R. Soc. Lond. A*, **103**, 622–643.
- Li Q.M., Reid S.R., Wen H.M. and Telford A.R. (2005). Local impact effects of hard missiles on concrete targets. *Int. J. Impact Eng.*, **32**, 224–284.

- McVay M.K. (1988) *Spall damage of concrete structures*. Technical Report No. SL-88-22, US Army Engineer Waterways Experiment Station, Vicksburg, June 1988.
- Millon O., Nöldgen M., Thoma K., Riedel W. and Fehling E. (2009) Fiber-reinforced ultra-high performance concrete under tensile loads, *9th Int. Conf Mechanical and Physical Behaviour of Materials under Dynamic Loading – DYMAT*, 2009, **1**, 671–677.
- Novikov S.A., Divnov I.I. and Ivanov A.G. (1966) The study of fracture of steel, aluminium and copper under explosive loading, *Fiz. Met. Metalloved.*, **21**(4), 608–615.
- Pierron F., Forquin P. (2012) Ultra high speed full-field deformation measurements on concrete spalling specimens and stiffness identification with the Virtual Fields Method, *Strain*, **48**(5), pp. 388–405.
- Ross C.A., Jerome D.M., Tedesco J.W. and Hughes M. (1996) Moisture and strain rate on concrete strenght. *ACI Mater. J.*, **93**, 293–299.
- Rossi P. (1991) Influence of cracking in the presence of free water on the mechanical behaviour of concrete. *Mag. Concr. Res.*, **43**, 53–57.
- Rossi P., van Mier J.G.M., Boulay C. and le Maou F. (1992) The dynamic behaviour of concrete: influence of free water. *Mater. Struct.*, **25**, 509–514.
- Riedel W., Hiermaier S. and Thoma K. (2010) Transient stress and failure analysis of impact experiments with ceramics, Elsevier, *Mat. Sci. Eng. B*, **173**, 139–147, DOI:10.1016/j.mseb.2009.10.038
- Schuler H. (2004) *Experimentelle und numerische Untersuchungen zur Schädigung von stoßbeanspruchtem Beton*, Forschungsergebnisse aus der Kurzzeitdynamik, Heft 6, Freiburg i. Br.: Fraunhofer-EMI, ISBN 3–8167–6463–0.
- Schuler H., Mayrhofer C. and Thoma K. (2006) Spall experiments for the measurement of the tensile strength and fracture energy at high strain rates, *Int. J. Impact. Eng.*, **32**, 1635–1650.
- Schuler H. and Hansson H. (2006) Fracture behavior of High Performance Concrete (HPC) investigated with a hopkinson-bar, *J. Phys. IV France*, **134**, 1145–1151.
- Steinhauser M.O., Grass K., Strassburger E. and Blumen A. (2009) Impact failure of granular materials – non-equilibrium multiscale simulations and high-speed experiments, *Int. J. Plasticity*, **25**, 161–182.
- Vegt, I., Weerheijm, J. and Van Breugel, K. (2007) The fracture energy of concrete under impact tensile loading- a new experimental technique. *CONSEC Conference*, Tours, France.
- Weerheijm, J., van Doormaal J.C.A.M. and van de Kastele R.M. (2003) Development of a new test set-up for dynamic tensile tests on concrete under high loading rates Part 2: Results test series B and C. TNO-PML report, PML 2003-A87.
- Weerheijm J. and van Doormaal J.C.A.M. (2004) Tensile failure at high loading rates; Instrumented spalling tests. *International Conference FramCoS*, 5, April 2004.
- Weerheijm J. and van Doormaal J.C.A.M. (2007) Tensile failure of concrete at high loading rates: new test data on strength and fracture energy from instrumented spalling test. *Int. J. Impact Eng.*, **34**, 609–626.
- Weerheijm J., Vegt I. and Breugel van K. (2009) *The rate dependency of concrete in tension – New data for wet, normal and dry conditions*. Proc. DYMAT, Brussels, 95–101.

(a)



(b)

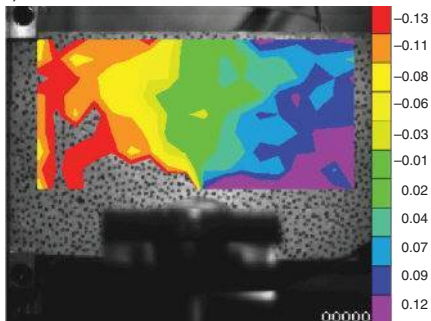


Plate X (Chapter 5) EOI experiments performed on concrete specimens in LEM3 lab. (Lorraine University) (Erzar, 2010) (a) Experimental set-up: gas gun, impact chamber, target and its confining system, UHS camera and lightening. (b) Far field measurement by DIC method: transverse displacement in pixel.

Response mechanisms of concrete under impulsive tensile loading

J. WEERHEIJM, TNO and Delft University of Technology, The Netherlands and P. FORQUIN, University of Lorraine, France

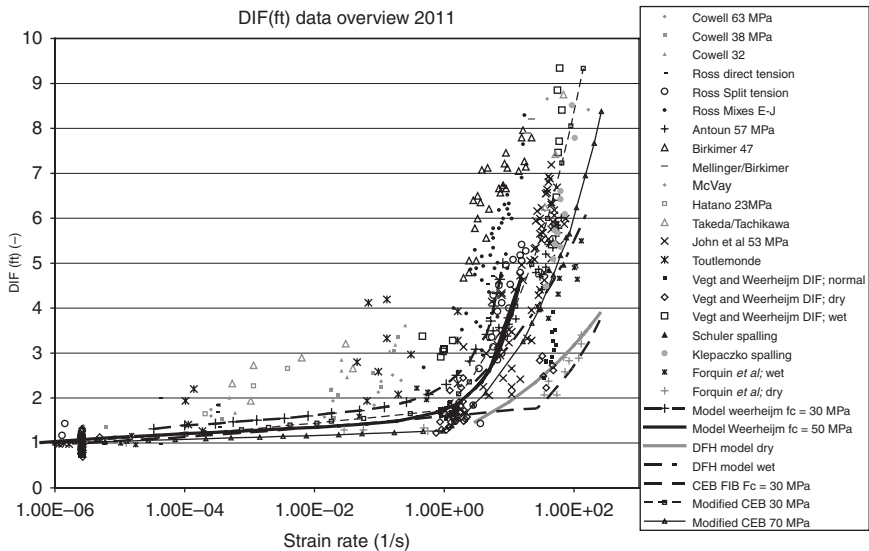
DOI: 10.1533/9780857097538.2.181

Abstract: The response of concrete up to complete failure in tension is represented in the load deformation relation. The characteristic parameters are the ultimate strength, stiffness in the ascending branch and the fracture energy. All these parameters depend on concrete composition and environmental conditions, as discussed in the previous chapters. The observed response of concrete at macro-level is determined by the damage initiation and damage accumulation mechanisms at meso- and micro-scale levels. The failure process is governed by (i) the stress condition, (ii) the mechanisms governing microcrack nucleation, propagation and obscuration of critical flaws, (iii) the ability to absorb energy in fracture, and (iv) the energy flow from the surrounding material into the fracture zone. In dynamics, all four conditions vary in time and depend on the loading rate. This chapter discusses the background and mechanisms of the rate-dependent behaviour of concrete, focusing on the effects of (i) inertia and limited cracking velocity at material level, (ii) concrete composition at meso-level, and (iii) moisture content and pore distribution. The available experimental data on dynamic strength and fracture energy are presented and related to response mechanisms for the different loading rate regimes.

Key words: dynamic loading, rate dependency, tensile strength, fracture energy, damage modelling, dynamic testing, fracture process, crack velocity, concrete heterogeneity, meso-scale, inertia effects.

7.1 Introduction: concrete response mechanisms under impulsive tensile loading

Concrete is probably the most rate-dependent structural material. Especially in tension, concrete exhibits a pronounced increase in strength for high loading rates. One can distinguish two regions of rate dependency. For loading rates, ranging from static (10^{-4} GPa/s) to intermediate (50 GPa/s), a moderate rate effect in tensile strength is observed. Beyond the rate of 50 GPa/s (strain rates $>1/s$) a very steep strength increase occurs. Figure 7.1 shows sets of experimental data and model predictions, which will be discussed in Section 7.2.6.



7.1 Experimental data and model predictions of the dynamic increase factor (DIF) (ratio apparent dynamic and static tensile strength) as a function of the strain rate.

The transition to high rate dependency occurs for concrete at low loading rate values in comparison with other materials, such as ceramics and metals. The main causes for this are their low quasi-static strength ($f_{t,stat}$) and the coarse heterogeneity of concrete, the failure being dominated by processes at meso-level with an aggregate skeleton at a scale in the order of 10 mm.

The key difference between the responses to static and dynamic loading is ‘time’. The supplied energy propagates through the structure at a certain velocity, and damage does not occur instantaneously because the fracture process takes some time. To study and understand the rate effect in material response, we have to analyse how the failure mechanisms are affected by ‘time’, and at which time scale the fracture process within the heterogeneous concrete material develops.

Other important aspects in dynamic response analysis are ‘the role of inertia’ and the distinction between ‘material response and structural response’. Especially at higher loading rates, the observed response in tests is the result of the dynamic structural response of the specimen as well as the real material response. The inertia at structural level will influence the average stress distribution, while inertial effects inducing some limitations in crack initiation and propagation at meso- and micro-levels will affect the fracture process within the material. As discussed in Chapter 10, the deformation rate in the fracture process zone becomes so fast at high loading rates that the inertia generated in this zone affects the strength observed

in tests. Cotsovos and Pavlovic (2007) postulates that all experimentally observed rate effects are due to structural response. The authors do not support this extreme statement but cautious analysis to separate structural and material response is required. Therefore the term ‘apparent dynamic strength’ is mentioned in the caption of Fig. 7.1. This chapter focuses on the material response mechanisms.

The rate effect on tensile strength has been studied and reported by many authors (e.g. Ross, Grady, Tedesco, Reinhardt, Malvern). Not all the details of the mechanisms are understood yet, but the headlines are known. However, the research and knowledge on the rate effects on the full failure process of microcracking and macrocrack formation is very limited. In Section 7.3 some ideas are presented on the rate dependency of the fracture energy and the shape of the load deformation curve.

This chapter is divided into two main parts, one on the dynamic strength (Section 7.2) and the other on the rate effects on the failure process and the fracture energy (Section 7.3). First, the governing mechanisms are presented, followed by some of the available models and data.

7.2 The effect of cracking rates on the tensile strength of concrete

The mechanisms resulting in the moderate and enhanced rate effect on tensile strength are discussed in this section. The heterogeneous composition, see Chapter 1, the fracture mechanics principles and crack propagation provide the basis to understand and explain the dynamic concrete response.

7.2.1 Mechanical response

As discussed in Chapter 1 the tensile strength (f_t) is determined by the fracture process at micro- and meso-scales. The failure process starts with bond fracture at about $0.6 f_t$, followed by matrix fracture at a load of $0.8 f_t$. Beyond this level, the microcracks in the mortar start to grow, bridging of the bond cracks occurs, and when the maximum resistance is reached, crack propagation becomes unstable and final failure occurs by the formation of macrocracks.

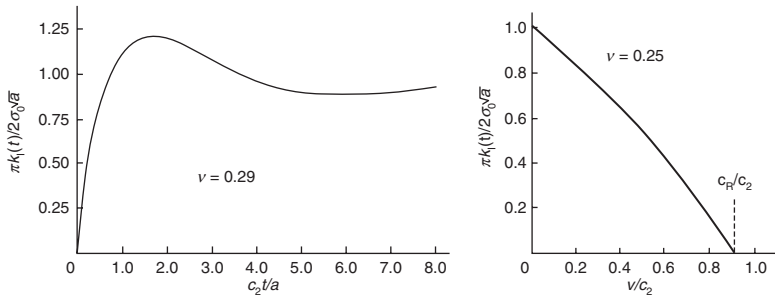
To study the rate effect on strength, the initiation of bond cracks and microcracks in the cement and mortar phase have to be addressed. Zielinski and Weerheijm amongst others (Zielinski, 1982; Weerheijm and Karthaus, 1985; Reinhardt and Weerheijm, 1991; Weerheijm 1992, 1998, 2006) applied fracture-mechanics principles to the meso-structure to study the rate effect on tensile strength. The model is described in detail in Weerheijm (1992) and is applicable for the moderate as well as the high loading rate regime. Here it is merely introduced, as it helps to identify the dominant mechanisms.

In summary, the tensile-fracture process is modelled by crack growth in a fictitious-failure plane. The initial damage stage is represented by equally distributed penny-shaped flaws (radius a_o) at intermediate distances ($2b$). Around the initial flaws two zones are distinguished. One zone, A_b , represents bond failure and the other zone, $A_m + A_a$, represents mortar and aggregate fracture. The geometry of the fictitious-fracture plane follows, on one hand, from the requirement that the dissipated energy in the fracture plane of the real material corresponds with the dissipated energy in the model. On the other hand, crack extension in the fictitious-fracture plane is described by using the stress and displacement fields given by Linear Elastic Fracture Mechanics (LEFM). Application of the strength criterion of the LEFM yields that a_o and a_c are the critical crack sizes at $0.6 f_t$ and $0.8 f_t$ respectively. With these criteria, the geometry of the fictitious-fracture plane is defined when the static strength, Young's modulus, Poisson's ratio, aggregate fraction and the specific surface energies, are known. The fictitious-fracture plane represents concrete composition and static strength properties. The stress field around the cracks is calculated for uniaxial tensile loading. Crack extension is predicted as a function of time, and follows from the balance of energies in the region around the crack tip. The model predicts a moderate strength increase for loading rates up to 15 GPa/s, when the geometry of the fracture plane is changed according to a higher energy demand (Zielinski, 1982). Otherwise, no strength increase is predicted for this loading rate regime. For higher loading rates, an enhanced strength increase is predicted according to the experimental data in Fig. 7.1. The model addresses the two dominant aspects of strength rate dependency, which are the effect of the loading rate on (i) crack initiation and (ii) crack growth. These aspects are discussed next in more detail.

7.2.2 The effect of the transition from moderate to enhanced cracking rates on strength

To understand and model the dynamic concrete response the questions to be addressed are: (i) does energy demand change and alters the fracture plane, (ii) does the strength criterion for crack-growth initiation change, and (iii) does the internal stress distribution change due to increasing strain/loading rate and crack velocity? The last aspects are studied by Freund, Barrenblatt and Sih. Their work shows that the dynamic stress intensity factor ($K_{I,d}$) around flaws initially increases proportionally with $t^{1/2}$ after impact and rapidly approaches the static value. They also proved that $K_{I,d}$ decreases with increasing crack velocity, see Figs 7.2a and 7.2b.

Let us first focus on the role of micro-inertia on the dynamic stress intensity factor of a penny-shaped crack before crack initiation (Chen and Sih, 1977). In Fig. 7.2 time is scaled with the shear-wave velocity (denoted as c_2)



7.2 Ratio of dynamic and static stress intensity factor due to shock impact on penny shaped crack. (a, left) Ratio in time, before crack initiation and (b, right) ratio as function of the crack growth velocity (Chen, 1977).

and the flaw radius (a). After the shock hits the flaw, the stresses are at first lower than in static state. Until $c_2 \cdot t/a = 1$ the reduced stresses will definitely result in delayed crack initiation. After a while, five wave rays along the crack surfaces, equilibrium static-stress distribution is reached. Note that this phenomenon is seen in many wave problems, that after a number of wave reflections an average, quasi-static situation is reached. The effect of discontinuities in geometry, stiffness or loading is smoothed.

Because the dynamic strength is directly coupled to crack initiation, two regimes emerge from the theory (see Equations [7.1] and [7.2]). In Region I, no rate effects on strength will occur because internal stress distribution is similar to statics. Region II exhibits rate effects on strength, which increase with increased loading rate. In this region micro-inertial effects are dominant, which lead to limitations in crack nucleation. In this discussion, the conditions that limit the velocity of crack propagation have not yet been considered (see also Section 7.2.4).

$$\dot{\sigma} < \frac{C_r \cdot f_{t,st}}{a} \quad \text{Region I, no rate effects on strength due to micro-inertia on crack initiation} \quad [7.1]$$

$$\dot{\sigma} \geq \frac{C_r \cdot f_{t,st}}{a} \quad \text{Region II, rate effects on strength due to micro-inertia on crack initiation} \quad [7.2]$$

in which

a = radius characteristic flaw size (m)

$f_{t,st}$ = static tensile strength (Pa)

C_r = Rayleigh wave velocity (m/s)

$\dot{\sigma}$ = loading rate (Pa/s)

Table 7.1 Loading rate beyond which ft becomes rate dependent.
Data for $\dot{a} = 1000 \text{ m/s}$ and $f_t = 3 \text{ MPa}$

a_o (mm)	Δa (mm)	$\dot{\sigma}_{\text{crit}}$ (GPa/s)	$\dot{\epsilon}_{\text{crit}}$ (1/s)
1	20	15	0.5
1	10	30	1
1	5	60	2
1	2	150	5

Let us apply this theoretical result to real concrete. Concrete composition, water cement ratio and curing conditions determine the initial damage level, the internal stresses and initial defects. For statics Reinhardt discussed these effects in Chapter 2. To give some rough numbers, the heterogeneity and the characteristic flaw size are determined by the aggregate size (order $0.1 \Phi_{\text{aggr}} \approx 1 \text{ mm}$). Applying Equation [7.1] for $f_{t,\text{st}} = 3 \text{ MPa}$ and $C_r = 1800 \text{ m/s}$, only beyond $\dot{\sigma} = 5000 \text{ GPa/s}$ ($\dot{\epsilon} = 1501/\text{s}$), rate effects can occur due to delayed crack initiation. The test data show that significant rate effects already occur beyond 50–100 GPa/s. Obviously, the effect of micro-inertia on crack initiation is not the factor that dominates the apparent rate dependency of the tensile strength.

The next step is to consider crack growth. Before the maximum strength is reached, the initial defects (microcracks) have to grow, which takes time. During this time, t_{ft} , the dynamic load increases. The effect on the observed dynamic strength depends on (i) the required crack growth (Δa), (ii) the crack velocity (\dot{a}), and (iii) the loading rate ($\dot{\sigma}$). As a first estimate at which loading rates with a 10% strength increase can be observed, we have assumed an average value of $\dot{a} = 1000 \text{ m/s}$ and calculated for some Δa -values the t_{ft} and the corresponding loading rate at which 0.3 MPa is reached. The results are given in Table 7.1, and show that the onset of the rate dependency for the concrete tensile strength corresponds with the experimental data (Fig. 7.1).

Reality is of course more complex. As described later, the dynamic failure of concrete is the result of inception and propagation of a number of cracks initiated from critical defects randomly distributed in the volume. Moreover, the crack velocity is not constant and the $K_{I,\text{dyn}}$ also depends on \dot{a} . The results of Freund, presented in Fig. 7.2b, show that the stresses in front of the crack tip gradually decrease with increasing crack velocity. Ultimately, at crack velocities equal to C_r , the ‘new crack size information’ cannot be transferred in time to the material in front of the crack tip, resulting in $K_I = 0$. The model developed by Weerheijm (1992) predicts the crack growth by calculating the energy flux into the fracture zone and the energy

absorption rate by crack growth, and takes all the effects on the dynamic stress field (K_{Id}) into account. This more thorough analysis shows that the changes in K_{Id} due to dynamic loading and the crack velocity only play a role for loading rates beyond $\dot{\sigma} \approx 50 \text{ GPa/s}$ ($\dot{\epsilon} \approx 2(1/s)$), the same threshold we obtained from first-order approach.

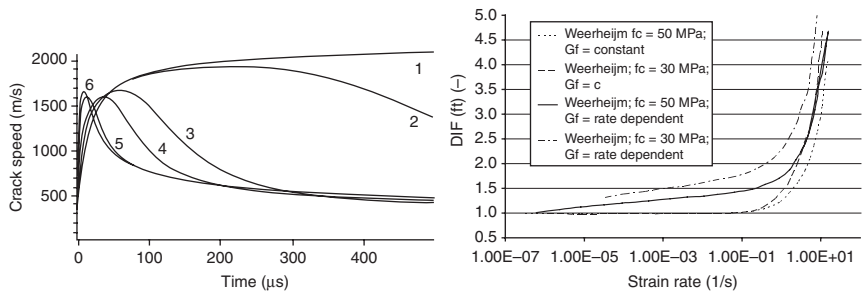
From the presented analysis and discussion we conclude for loading rates $\dot{\sigma} < \dot{\sigma}_{\text{transition}}$ ($\approx 50 \text{ GPa/s}$ for ordinary concrete):

- the decisive, internal stress distribution is not affected by dynamic loading conditions or crack velocity;
- if the strength criterion for crack growth initiation (K_{Ic}) is not affected by the loading rate, no rate effect on strength will occur.

From these observations and conclusions it is evident that the observed rate dependency of the tensile strength in tests for the regime $\dot{\sigma} < 50 \text{ GPa/s}$ must be caused by an enhanced resistance to crack initiation bearing no relation to micro-inertia effects. The moisture contents and the pore structure are the keys to explain the observed strength increase. This is discussed in Section 7.2.5.

7.2.3 Mechanical response under high loading rate regimes ($\dot{\sigma} > 50 \text{ GPa/s}$)

For this regime extensive rate effects are observed. In Section 7.2.2 it was shown that, on the one hand, the internal stress distribution around existing microcracks changes for loading rates larger than about 5000 GPa/s . On the other hand, above $\dot{\sigma}_{\text{transition}}$ the limited cracking velocity is seen to play a major role on the strength enhancement with stress rate. Since the 1980s, the influence of micro-inertia and cracking velocity on the dynamic tensile strength and number of fragments in brittle materials has been investigated (Kipp *et al.*, 1980; Grady and Kipp, 1987). Kipp *et al.* (1980) introduced the idea that the fracture process under tension is governed by inertia. They used the stress distribution around a single crack due to transient tensile load. Based on LEFM and the assumption of a critical stress intensity factor which depends on the loading rate, but constant during the fracture process, they derived for high loading rates the relation (Equation [7.3]) with $\beta = 1/3$. The ‘power-law’ dependency emerges also from rate theory and is used to fit test data for both loading rate regimes, deriving the coefficients for A and β (see also Section 7.2.6 where some examples are given).



7.3 (left) Crack-tip velocity of a single crack as a function of the loading rate; $C_r = 2050$ (m/s), Lines 1–6 represent $\dot{\sigma} = 0.1, 10, 50, 100, 500$ and 1000 (GPa/s) (right) DIF tensile strength, some experimental data and model prediction for low (dashed line) and normal quality concrete (solid line) (Weerheijm, 1992).

$$\text{DIF} = \frac{f_{t,\text{dyn}}}{f_{t,\text{stat}}} = A \cdot \left(\frac{\dot{\sigma}}{\dot{\sigma}_o} \right)^\beta \quad [7.3]$$

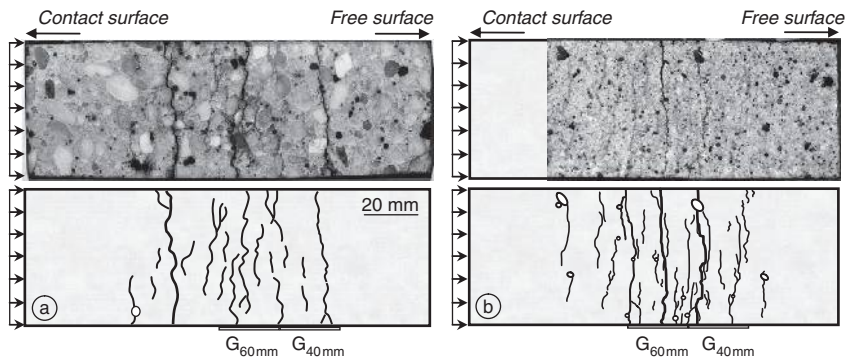
Based on similar ideas and fracture mechanics principles, the authors introduced the fracture model with the fictitious-fracture plane as mentioned in Section 7.2.1 (Weerheijm *et al.*, 1985, 1992, 1998). The advantages of this model are that coefficients and parameters are derived from the static concrete properties; without any modification the model covers the whole range from static to high loading rates and the crack growth, and damage development is followed in time. The latter helps in understanding the rate dependency related to the material structure. As an illustration, the crack-tip velocity of a single crack in a matrix with average concrete properties is given in Fig. 7.3 for various loading rates. For static loading the terminal velocity equals the Rayleigh wave velocity (C_r), as it should. It is interesting that for higher loading rates the terminal velocity decreases and an asymptote of about 500 m/s is predicted. Analysis of the various energy terms showed that the kinetic and deformation energy, normalized by the external work, increased significantly with increased loading rate. The energy supply rate becomes too high to be absorbed by the fracture process immediately, resulting in an equilibrium in which a major part is stored around the crack tip as deformation and kinetic energy. This is equivalent to a change in stress distribution, a reduced $K_{I,c}$ due to the contribution of inertia to the force equilibrium, as was discussed in Section 7.2.2. Curbach obtained similar results for the terminal crack velocities (Curbach and Eibl, 1990) with finite element (FE) analyses and experiments on a notched specimen.

The rate dependency predicted by the model is illustrated in Fig. 7.3b for two concrete qualities, $f_c = 30$ and 70 MPa. The low-strength concrete with the coarser heterogeneity is more rate sensitive than the higher-strength concrete. Based on the model, the steep strength enhancement will occur at higher loading rates for concrete with finer aggregate grading and higher bond and matrix strength. These results illustrate that the rate dependency of the tensile strength is captured by the approach of representative initial defects in a schematic ‘potential fracture plane’, and the crack growth in the plane of defects is due to dynamic tensile loading. The rate dependency is well presented for all loading rates. However, with this schematized approach, no 3D-effects are captured. Whether the width of the fracture zone and the amount of microcracking are affected by the loading rate is not addressed. In the following section a more advanced model that captures 3D-effects is presented.

7.2.4 Multiple fragmentation due to the limited cracking velocity

Introduction

Post-mortem analysis conducted on spalled specimens (see Chapter 6) has revealed an important increase of cracking density with strain rate. For instance, failure patterns of concrete specimens subjected to spalling tests are displayed in Fig. 7.4. Several tens of individual cracks are clearly visible for both concrete (common concrete $\phi_{\text{aggr}} 10$ mm and microconcrete $\phi_{\text{aggr}} 2$ mm). The cracking density was evaluated for the microconcrete specimen (Fig. 7.4b) from the average distance between two vertical macrocracks (about $d = 3\text{--}4$ mm), corresponding to a few tens of initial decisive cracks/cm³ (i.e. a cracking density in the range of $(1/d)^3 \approx 1\text{e}7\text{--}1\text{e}8$ cracks/m³). At strain rates of $20\text{--}200\text{ s}^{-1}$ (or $\dot{\sigma} = 500\text{--}5000\text{ GPa/s}$), such as occurrence in the spalling tests, a large number of cracks simultaneously initiate and propagate, to interact and to coalesce or to stop. On the one hand, ‘moving cracks’ are initiated from critical existing flaws, the critical flaws being large pores, lumps or microcracks in the cement matrix, or defects in the ITZ (Interfacial Transition Zone) at the aggregate matrix interface. A dynamic process occurs at the microscale. On the other hand, the local stress state is modified around these moving cracks by a stress-relief wave propagating on both sides of the crack. Consequently, the fast decrease of microscopic tensile stress in the vicinity of existing cracks may prevent any new crack nucleation in these interaction zones and the potential critical defects are ‘obscured’.



7.4 Post-mortem analysis of two concrete specimens after spalling tests. (a) Dry common concrete ($\dot{\epsilon} = 120/\text{s}$) (Erzar and Forquin, 2011a), (b) dry micro-concrete ($\dot{\epsilon} = 130/\text{s}$) (Forquin and Erzar, 2009).

To model this complex dynamic fracture process, some simplifying hypotheses may be considered:

- Cracks are initiated from point defects randomly and uniformly distributed in the volume of the considered concrete specimen. Therefore, density of critical defects can be expressed as function of the applied stress, $\lambda_t(\sigma)$.
- Obscuration zones grow in a self-similar way and with a diameter proportional to the crack length, so the size of the obscuration zone at time T corresponding to a single crack initiated at time t , reads:

$$V_0(T-t) = S(V_{\text{crack}}(T-t))^n \quad [7.4]$$

where S is a shape parameter of the obscuration volume equal to $4\pi/3$ when assuming that they are similar to spheres in a 3D medium ($n = 3$), π for a disk in a 2D medium ($n = 2$) and $S = 1$ in a 1D medium ($n = 1$). The cracking velocity V_{crack} is supposed to be constant for sake of simplification.

Two cases are considered for critical defects: if a critical defect is not located in any obscuration zones, it is triggered as soon as its critical stress is reached; otherwise, as the local stress is supposed to decrease in obscuration zones, critical defects are supposed to be defused (i.e. obscured).

Modelling of the multiple fragmentation process: the Denoual-Forquin-Hild (DFH) model (Denoual and Hild, 2000; Forquin and Hild, 2010)

The condition of non-obscuration at a time T for a given flaw located at a point (M) may be expressed considering its past history: this condition is that no

critical defect exists in its ‘horizon’, the horizon being the space time domain around (M, T) in which any crack will always obscure the point M at time T :

$$\text{Horizon of } (M, T) = \{\underline{x}, t\} \in [V_0(T - t) = S(kC(T - t))^n] \cap \Omega \quad [7.5]$$

In which kC is the crack velocity given as a constant fraction (k) of the wave velocity C . Now the condition of non-obscuration of a point M at time T may be expressed in terms of probability applying the ‘weakest-link hypothesis’ to the space time domain corresponding to its horizon: the probability of non-obscuration is equal to the product of elementary probabilities of no-inception of new cracks P_{ϵ}^i in each elementary space-time zones ($dZ \times dt$) of Ω belonging to the horizon of the point M at time T :

$$P_{\text{no}}(M, T) = \prod_{[\text{horizon of } (M, T) \in \Omega]} P_{\epsilon}^i \quad [7.6]$$

If one assumes that the material contains point defects of density λ_t (hypothesis of a Poisson point process of intensity λ_t), the elementary probability of no-inception of new crack P_{ϵ}^i in $dZ \times dt$ reads (Forquin, 2003; Forquin and Hild, 2010):

$$P_{\epsilon}^i(\underline{x}, t) = \exp\left(-\frac{\partial \lambda_t(\underline{x}, t)}{\partial t} dZ dt\right) \quad [7.7]$$

Thus the general form of the probability of non-obscuration P_{no} of a point M at a time T reads (Forquin and Hild, 2010):

$$P_{\text{no}}(M, T) = \exp\left(-\iint_{(\underline{x}, t) \in [\text{horizon of } (M, T) \in \Omega]} \frac{\partial \lambda_t(\underline{x}, t)}{\partial t} dZ dt\right) \quad [7.8]$$

In the particular case of a uniform stress field, the non-obscuration probability reads (Forquin and Hild, 2010):

$$P_{\text{no}}(T) = \underbrace{\exp\left(-\int_{t_Z}^T \frac{d\lambda_t(t)}{dt} Z_0(T - t) dt\right)}_{\text{Multiple fragmentation}} \times \underbrace{\exp\left(-Z \int_0^{t_Z} \frac{d\lambda_t(t)}{dt} dt\right)}_{\text{Single fragmentation}} \quad [7.9]$$

where t_Z is the interacting time corresponding to the intersection between the horizon of (M, T) and the boundary of the whole domain of size Z :

$$Z = S(kC(T - t_Z))^n \quad [7.10]$$

At high strain rates a multiple fragmentation occurs and the horizon of (M , T) is small compared to the size of the domain (Z). Therefore, t_z tends to zero and the obscuration probability becomes the damage variable proposed by Denoual and Hild (2000) (left part of Equation [7.9]). On the other hand, at low strain rates, single fragmentation occurs and the interacting time t_z tends to the current time T . Consequently, the obscuration probability tends to the failure probability proposed by Weibull (1939) (right part of Equation [7.9]).

Now, the crack density λ_{cracks} may be computed as function of the obscuration probability P_o and the increment of critical defects considering that new cracks may emerge only in non-obscured zones (Denoual and Hild, 2000; Forquin and Hild, 2010):

$$\frac{\partial \lambda_{\text{cracks}}}{\partial t} = (1 - P_o) \frac{\partial \lambda_t}{\partial t} \quad [7.11]$$

Moreover, a damage variable may be defined in the framework of Continuum Damage Mechanics. By averaging over a representative zone, the obscuration probability P_o is equivalent to an obscured volume fraction, with $P_o = 0$ for the virgin material and $P_o = 1$ for the fully obscured one, and the macroscopic stress Σ is computed from the obscuration probability and the microscopic stress:

$$\Sigma = (1 - D) \sigma = (1 - P_o) \sigma + P_o \sigma_{\text{coh}}(\varepsilon) \quad [7.12]$$

where $\sigma_{\text{coh}}(\varepsilon)$ corresponds to the residual strength (cohesion strength) of the material despite the total obscuration of the domain Ω . An empiric function of the cohesion strength has been proposed by Erzar and Forquin (Erzar and Forquin, 2010) to describe the loss of cohesion strength with strain for dry and wet (fully saturated) concrete:

$$\sigma_{\text{coh}}(\varepsilon) = \sigma_0^{\text{dry}} \exp\left\{-\left(\frac{\varepsilon}{\varepsilon_0^d}\right)^n\right\} + \sigma_0^{\text{water}} \exp\left\{-\left(\frac{\varepsilon}{\varepsilon_0^w}\right)\right\} \quad [7.13]$$

where σ_0^{dry} , σ_0^{water} , ε_0^d , ε_0^w , n are material parameters to identify. The first term of Equation [7.13] describes the cohesion strength of a fully damaged dry concrete, whereas the second one accounts for the addition of cohesion strength of wet concrete induced by the presence of free water in open porosity and connected microcracks. As shown by Erzar (2010), as the ultimate strength (i.e. maximum macroscopic strength) is reached when P_o is small ($P_o < 0.15$) the cohesion strength has a limited influence on the ultimate strength, and the ultimate strength may be approximated by:

$$\Sigma_u = \max_T [(1 - D(T)) \sigma(T)] \approx \max_T [(1 - P_o(T)) \sigma(T)] \quad [7.14]$$

Analytical solution and model predictions

Analytical predictions may be obtained considering several simplifications: a constant stress rate ($\dot{\sigma}$) may be assumed in addition to a shape of obscuration zone given by Equation [7.4] and a density of critical defects given as a power-law function of the applied stress:

$$\lambda_r(\sigma) = \lambda_0 \left(\frac{\langle \sigma \rangle}{S_0} \right)^m \quad [7.15]$$

where m and S_0^m / λ_0 are interpreted as Weibull parameters when single fragmentation occurs. For wet concrete in dynamic conditions, it should be noted that the characteristic strength S_0 has to be corrected with the stress-rate sensitivity observed below 50 GPa/s. Now, one can compute the ultimate stress Σ_u of the material by neglecting the cohesion strength of the material (Equation [7.12]) (Denoual and Hild, 2000):

$$\Sigma_u = \left(S_0 \lambda_0^{-\frac{1}{m}} \right)^{\frac{m}{m+n}} (\dot{\sigma})^{\frac{n}{m+n}} \left(S_n^{\frac{1}{n}} V_{\text{crack}} \right)^{-\frac{mn}{m+n}} \left(\frac{1}{e} \frac{(m+n-1)!}{m!n!} \right)^{\frac{1}{m+n}} \quad [7.16]$$

Moreover, based on previous simplifications (i.e. a constant stress rate and an obscuration zone and a density of critical defects given by Equations [7.4] and [7.13]) the final cracking density may be computed by integrating Equation [7.9]:

$$\lambda_{\text{cracks}}^{T=\infty} = \left(S_0 \lambda_0^{-\frac{mn}{m+n}} \right) (\dot{\sigma})^{\frac{mn}{m+n}} \left(S_n^{\frac{1}{n}} V_{\text{crack}} \right)^{-\frac{mn}{m+n}} \left(\frac{(m+n)!}{m!n!} \right)^{\frac{m}{m+n}} \Gamma \left(1 + \frac{m}{m+n} \right) \quad [7.17]$$

where Γ is the Euler function of the second kind (Spanier and Oldham, 1987),

$$\Gamma(1+x) = \int_0^{\infty} \exp(-u) u^x du \quad [7.18]$$

In conclusion, this micromechanics-based modelling of the fragmentation process allows prediction of the strain rate sensibility and cracking density of concrete and concrete-like materials based on the knowledge of the population of critical defects and the cracking velocity of the material. Identification of material parameters (i.e. Weibull parameters and cracking velocity) and some comparison between experimental data and model predictions are given below.

Identification of material parameters

Predictions of the so-called ‘dynamic fragmentation model’ rely on the characterization of three types of parameters: those describing the population of critical defects dispersed within the material, those describing the size of obscuration zone related to cracking velocity, and those describing the cohesion strength of the damaged material. As explained above, the ultimate strength (i.e. maximum macroscopic stress) and the cracking density depend mainly on the first two sets of parameters. Identification of these parameters is discussed below.

The parameter m

Various types of flaws such as large pores, lumps, microcracks and small pores in the ITZ at the aggregate matrix interface, and fractured aggregates may initiate unstable cracks in concrete, leading to the fragmentation of a specimen under a dynamic tensile loading. One way to identify the density of critical defects of Equation [7.13] is to perform quasi-static bending tests. However, some difficulties arise: indeed, on the one hand, big specimens might lead to stable crack propagation so the maximum force would not provide the stress level corresponding to the crack inception. On the other hand, small specimens might provide an effective volume too small in comparison with the Representative Elementary Volume (RVE).

The bending tests (at least a dozen) provide a distribution of failure stresses σ_F defined as:

$$\sigma_F = \max_{\Omega} \sigma_1 \quad [7.19]$$

where σ_1 is the local maximum principal stress in the specimen. Now, the Weibull parameters, namely, the Weibull scale parameter (S_0^m / λ_0) and the Weibull modulus (m) may be deduced. One way to obtain these parameters is to deduce the Weibull modulus for example from the ratio of the standard deviation of failure stresses (σ_{sd}) to the average failure stress (σ_w), and the Weibull scale parameter (S_0^m / λ_0) from the average failure stress (Forquin and Hild, 2010):

$$\frac{\sigma_{sd}}{\sigma_w} = \frac{\sqrt{\Gamma(1+(2/m)) - \Gamma^2(1+(1/m))}}{\Gamma(1+(1/m))} \quad [7.20]$$

$$\sigma_w = S_0 (\lambda_0 Z H_m)^{-1/m} \Gamma\left(1 + \frac{1}{m}\right) \quad [7.21]$$

where Z is the size of the whole volume, surface or length and H_m is the stress heterogeneity factor (Hild *et al.*, 1992) expressed as:

$$H_m = \frac{1}{Z} \int_{\Omega} \left(\frac{\langle \sigma_1 \rangle}{\sigma_F} \right)^m dZ \text{ when } \sigma_F > 0 \quad [7.22]$$

A classical alternative to Equation [7.18] for determining the Weibull modulus is to resort to the so-called Weibull (1939) diagram in which $\ln[-\ln(1 - P_F)]$ vs $\ln(\sigma_F)$ is interpolated by a linear function, the slope of which is the Weibull modulus m .

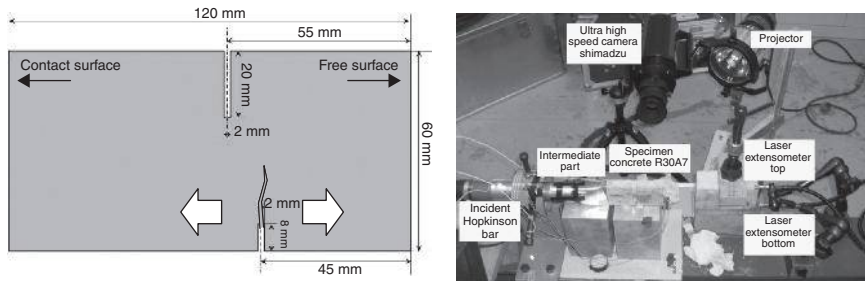
Finally, a transition criterion may be defined between single and multiple fragmentation processes considering the strain rate for which Equations [7.21] and [7.16] give the same ultimate strength:

$$\sigma_w(Z) = \Sigma_u(\dot{\sigma}) \quad [7.23]$$

Finally, because of the size effect observed at low strain rates (Equation [7.21]), the transition stress rate may vary slightly depending on the geometry of the specimen used in quasi-static loading and, consequently, the bigger the samples, the lower the quasi-static strength and the lower the transition loading rate.

The parameter V_{crack} , the cracking velocity in concrete

For the sake of simplification, the model cracks are assumed to propagate with a constant velocity V_{cracks} . It may be expressed as a fraction of the one-dimensional wave speed ($V_{\text{cracks}} = k C_0$ with $C_0 = \sqrt{E/\rho}$), where k is a constant parameter to determine. Based upon the concept of conservation of energy, an analytical solution for k was proposed (Broek, 1982; Kanninen and Popelar, 1985). It was demonstrated that when the crack length becomes significantly larger than the initial crack size, the cracking velocity tends to a limit close to $0.38 C_0$. However, according to Freund (1972, 1990), cracks in brittle materials may accelerate up to the Rayleigh wave speed C_r , e.g., $C_r = 0.59 C$ with $\nu = 0.2$. Moreover, the parameter k was investigated in several brittle materials, in particular when transparent. For example, experimental studies showed a limiting velocity about $0.5 C_r$ in glass, about $0.6 C_r$ in Plexiglas and about $0.4 C_r$ in Homalite-100 (Ravi-Chandar and Knauss, 1982, 1984a, 1984b, 1984c, 1984d; Knauss and Ravi-Chandar, 1985, 1986; Sharon *et al.*, 1995). Strassburger and Senf (1995) also investigated the terminal crack velocity in a silicon carbide and in glass materials and observed a crack velocity of approximately one half of C_r in both cases. Note that we modelled the crack velocity in the fictitious-fracture plane (see Section 7.2.3). Expressed in C_r , the crack velocities varied between 0.75 and $0.4 C_r$ during



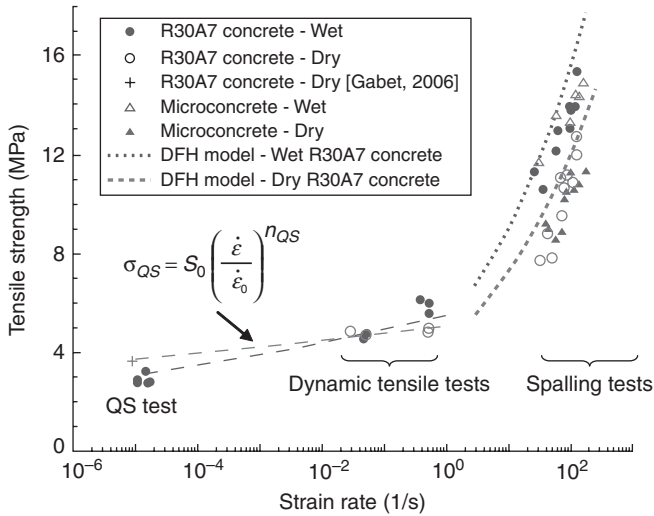
7.5 Optimized specimen geometry used in the rocking spalling tests (left). Experimental set up used for dynamic crack propagation testing (right) (Forquin and Cheriguène, 2011).

the fracture process. Therefore, it is reasonable to assume a crack velocity in brittle materials within the range $0.4 C_r$ to $0.6 C_r$ (or $0.23 C_0$ to $0.35 C_0$ with $\nu = 0.2$).

More recently, a new testing technique has been developed in LEM3 laboratory (Metz) to characterize the cracking velocity in concrete and concrete-like materials (Forquin and Cheriguène, 2011). The set-up and the specimen geometry are shown in Fig. 7.5 A projectile is launched against a Hopkinson bar so that a compressive wave propagates through it. A part of the incident pulse transmitted to the specimen is reflected as a tensile pulse on the free surface. The parallelepipedic specimen is pre-notched with two notches so a rocking effect is applied to the rear part of the specimen that favours the triggering of an unstable crack on the smaller notch tip without damaging the sample. Also, an ultra-high-speed camera is used to film the specimen response and perform a Digital Image Correlation post-treatment (Forquin *et al.*, 2007). A processing method based on the Crack Opening Displacement (COD) measurement is employed to characterize the crack propagation (Forquin *et al.*, 2004) (see Chapter 5, Fig. 5.8). Finally a mean value of crack propagation velocity about 1300 ± 50 m/s ($V_{\text{cracks}} = 0.32 C_0$ to $0.35 C_0$) was found for dry and wet concrete that matches with experimental and theoretical values mentioned above.

Comparison of the DFH model predictions with experimental data

Numerous validation works of the DFH fragmentation model have been proposed in the literature considering different kinds of brittle materials: ceramics (Denoual and Hild, 2000; Forquin *et al.*, 2003), rocks (Grange *et al.*, 2008), ultra-high-performance concrete (Forquin and Hild, 2008), glass (Brajer *et al.*, 2003), dry and wet microconcrete (Forquin and Erzar, 2010) and common concrete (Erzar and Forquin, 2011a, 2011b). For concrete, the



7.6 Results of quasi-static and dynamic tests performed with MB50 microconcrete and R30A7 common concrete. QS test refers to quasi static test.

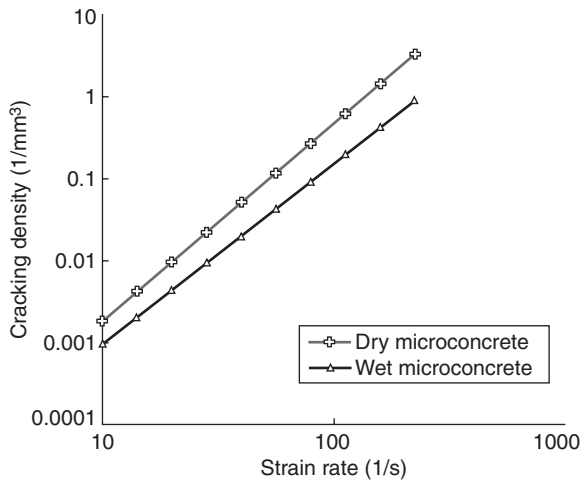
modelling has been validated by means of edge-on-impact tests and spalling tests.

A comparison is given in Fig. 7.9 between the spall strength obtained in spalling tests (strain rate range: 30–150/s) and the macroscopic ultimate strength predicted by Equation [7.14]. For the moderate regime the rate effect is given in the power-law format (see also Section 7.2.3):

$$\sigma_{QS}^{\text{wet}} = S_0^{\text{wet}} \left(\frac{\dot{\epsilon}}{\dot{\epsilon}_0} \right)^{n_{QS}^{\text{wet}}}, \quad \sigma_{QS}^{\text{dry}} = S_0^{\text{dry}} \left(\frac{\dot{\epsilon}}{\dot{\epsilon}_0} \right)^{n_{QS}^{\text{dry}}} \quad [7.24]$$

where n_{QS} is the strain rate sensitivity of concrete identified in the strain rate range ($10^{-6} - 1$ [1/s]). According to experimental data obtained with a common concrete, this exponent is worth $n_{QS}^{\text{wet}} = 0.05$ and $n_{QS}^{\text{dry}} = 0.025$ (Fig. 7.6). Finally, the dynamic strength enhancement is quite well predicted for dry or wet microconcrete (Forquin and Erzar, 2009) as for a common dry or wet concrete (Erzar and Forquin, 2011a).

In advance of the discussion on the fracture energy and microcracking during the failure process in Section 7.3, it is worth mentioning that the DFH model also provides data on the amount of microcracking in the failure zone (Equation [7.15]). The predicted cracking density is plotted as function of the strain rate considering data of dry and wet MB50 microconcrete (Fig. 7.7). A strong increase of cracking density with loading rate is noted



7.7 Predictions of DFH fragmentation model in terms of cracking density-vs-strain rate for dry and wet MB50 microconcrete.

for both dry and wet concrete. A higher cracking density is predicted in dry concrete than in wet concrete. Model predictions have been compared to damage patterns of spalling specimens by Forquin and Erzar (2010).

7.2.5 The effect of moisture content on dynamic strength

The effect of moisture content on the dynamic concrete strength was extensively studied in the 1990s. Frequently referenced literature from that period includes (Reinhardt *et al.*, 1990; Rossi, 1991; Rossi *et al.*, 1992, 1996; Cadoni *et al.*, 2001). It is generally accepted that the rate effect on strength in the moderate regime is caused by moisture in pores. Experimental data prove the effect of moisture, while the explanation is given by the so-called Stefan effect.

Referring to Chapter 1, we distinguish free and chemically bonded water in concrete. The latter is an integral component in the hydrated cement paste (HCP) and is not lost during drying. The free water is in the pores, voids and cracks. The free water can evaporate and the moisture content of concrete can vary with temperature, humidity and time. Considering these facts the observed rate dependency of the tensile strength on the moisture level must be related to the free water.

The commonly accepted explanation is the so-called Stefan effect (Cotterill, 1964). When two parallel circular plates (radius r) are separated by an incompressible fluid with viscosity μ and thickness h , the pulling force needed to separate these plates at a velocity V , is proportional to V and the

viscosity. When we neglect the static component due to surface tension of the outer meniscus surfaces, the expression for the force due to the dynamic separation of the plates is given by:

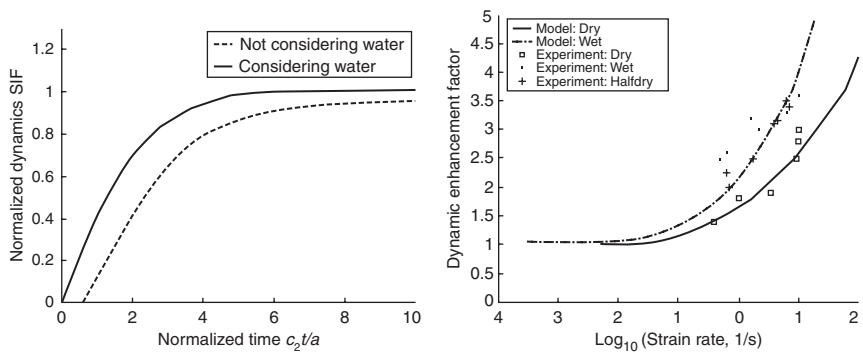
$$F = \frac{3\pi\mu r^4}{2h^3} \cdot V \quad [7.25]$$

Translating the Stefan effect to concrete and the rate dependency, the free water in the fully saturated pores will lead to additional resistance, which increases with increasing loading rate and reduced pore diameter. To quantify and model the ‘Stefan effect’ for real concrete is not easy, even in laboratory conditions. The porosity and the pore-size distribution vary with the concrete and depend on curing conditions. The saturation level of the pores has to be known in order to quantify their contribution to the additional resistance. Commonly this detailed information is not determined and/or given. Most dynamic strength data is related to ‘dry’ and ‘wet’ concrete. ‘Dry’ is defined as ‘no free water’ and ‘wet’ as fully saturated. The authors performed an extensive study on the influence of the moisture content on the dynamic response and quantified the pore distribution and saturation level (see Weerheijm and Vegt, 2006, 2009). Curing conditions were carefully controlled to avoid additional damage due to temperature effects. The modelling work is still on-going. In this chapter we limit ourselves to referring to the work of Rossi (1991) and (Zheng and Li, 2004; Zheng *et al.*, 2005).

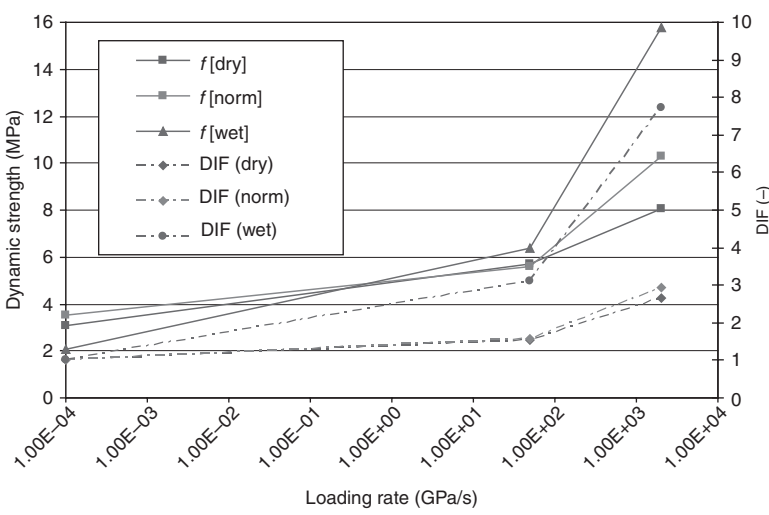
Zheng followed the work of Rossi and developed a phenomenological model following a similar approach to capture the rate effect as presented in the Sections 7.2 and 7.3. The cracks can propagate when the strength and energy criteria are fulfilled. The stress condition in front of the cracks is characterized by the dynamic stress intensity factor K_{Id} . When the pores/cracks are fully saturated, the Stefan effect will increase the strength criterion threshold and delay the crack initiation. Referring to Section 7.2.2 presenting the K_{Id} , the additional strength results in a time delay for crack initiation. Zheng solved the problem analytically for cracks under linear load increase. The results are depicted in Fig. 7.8 giving the correction function $f(c_2, t/a)$ according to Equation [7.26] covering moisture and inertia effects. The figure also illustrates the effect on the tensile strength.

$$K_{I,dyn} = \sigma(t) \cdot \sqrt{\pi a} \cdot f\left(c_2, \frac{t}{a}\right) \quad [7.26]$$

These results are not calibrated to real concrete, but reflect the effect of moisture in the pores and predict that the enhancing moisture effect with increasing loading rate. According to this approach, the moisture effect, i.e. the additional strength threshold, is not limited. In real concrete the water is



7.8 Dynamic stress intensity factor as a function of time (left) and strength enhancement factor (right) for a linearly increasing load (after Zheng, 2004).



7.9 Experimental data. Rate effects on strength for dry, normal and wet concrete (Weerheijm and Vegt, 2009).

not pure, the adhesion strength between water and pore/crack surface is limited, and the strength of the surrounding mortar, cement stone can become decisive for failure. Probably the ‘Stefan’ effect becomes more moderate at high loading rates or even vanishes beyond a certain loading rate. The data we obtained are given in Fig. 7.9. They show that for the concrete we tested up to loading rates of 2000 GPa/s, the moisture effect on strength became more pronounced with increasing loading rate, according the phenomenological model of Zheng. This is reflected in the absolute ($f_{t,\text{dyn}}$) and relative

(DIF) strength data. From the review on the moisture effect on the dynamic concrete response, it is evident that for predictive models the pore structure of concrete has to be incorporated.

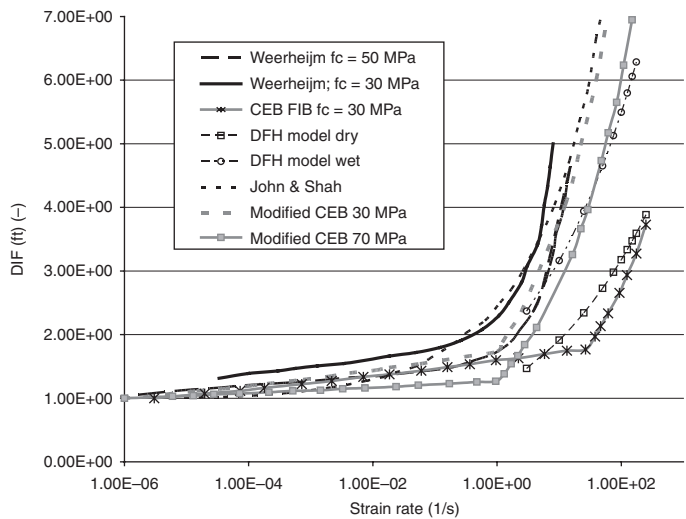
7.2.6 Strength data and empirical models

The models and tendencies described in the previous sections show that besides the static reference strength and mechanical properties, the decisive concrete material parameters for the rate dependency are: (i) scale of heterogeneity reflected in the size and distribution of initial defects, (ii) parameters related to crack inception and cracking velocity, and (iii) the moisture content in combination with the capillary pore distribution.

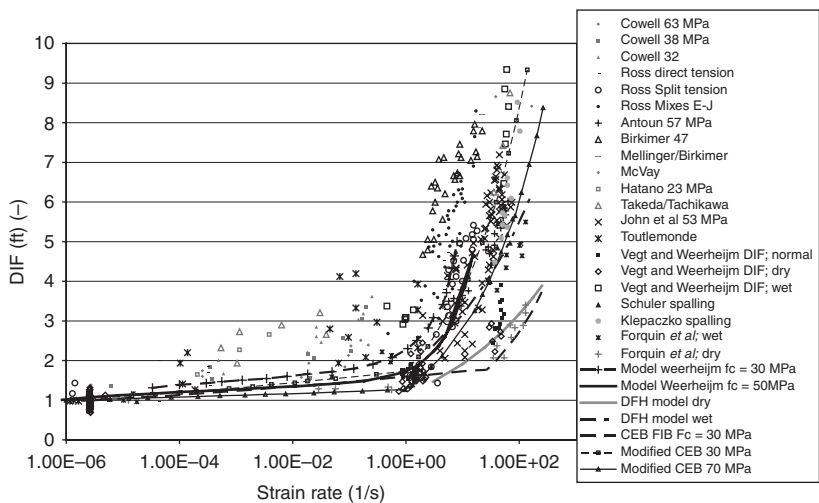
In Chapter 2 it was described how these and other concrete properties are affected by concrete composition, water cement fraction (wcf), curing conditions, etc. Reviewing the experimental data from literature showed that most researchers use their own 'reference concrete' and their specific equipment (see also Chapter 6). In general it must be concluded that 'all' reported experiments are performed with different concrete materials with non-standardized test methods. Therefore, scatter in the results is inevitable and, unfortunately, large. In Fig. 7.1 old and new data were given for a wide range of concrete. Within the scope of this chapter it is impossible to discuss the different test series and explain the (possible) causes of the scatter. We refer to e.g. Malvern and Rose (1998), who did a data and source comparison; Crawford repeated this action, and Schuler also analysed tensile data. We will limit ourselves to mentioning some general tendencies in the experimental data, compare the data with some model predictions and relate the tendencies to the response mechanisms discussed in this chapter.

Various semi-empirical models are given in the literature. The CEB-FIB formula is probably the most cited model, and is based on data up to 1988. The rate dependency is given as a function of the concrete compressive strength (f_c). Low f_c -values lead to more pronounced rate effects. Related to all currently available data, it predicts quite low values and is not suitable for wet conditions. Ross and Malvern modified the CEB-FIB expression based on scaling rules, resulting in more pronounced rate effects. John and Shah also studied the dynamic properties of concrete extensively. Based on a dynamic crack opening model and their data, they derived a model for the DIF (John, *et al.*, 1986). These models are depicted in Fig. 7.10 together with the physics-based models the authors developed. The model and data are combined in Fig. 7.11. They show that the modified CEB, and the models of Shah and Weerheijm, reflect the general trend of the data.

The DFH model provides correct prediction of the strength enhancement of a microconcrete and a common concrete tested in Metz in dry and saturated conditions (Erzar and Forquin, 2011a). However, the testing conditions



7.10 Some semi-empirical and physics-based models for the DIF of the concrete tensile strength. To be noted that different quasi-static strengths (and specimen sizes) have been considered for the quasi-static strength of each concrete grades.



7.11 Experimental data and models for DIF (ft).

considered in quasi-static experiments (smaller specimens and higher strain rates) provide relatively higher quasi-static strengths, leading to an apparently lower DIF under dynamic loading. Because the rate effects on strength depend on the concrete composition and heterogeneity, physics-based models

especially should reflect the material dependency (influence of the population of critical defects, the cracking velocity and the cohesion strength in the fractured zones). Note that the presented results of the Weerheijm model are determined for concrete tested with the set-up in Delft (see Chapter 6).

In summary, the experimental data and the physics-based models reflect the mechanisms that we have presented and discussed in this chapter. The tendencies are:

- The transition from the moderate to extreme rate dependency occurs at strain rates in the order of $1/s$ (loading rate of 50 GPa/s). This transition point shifts to higher strain rates when the heterogeneity of concrete decreases as the quasi-static strength increases.
- The rate dependency reflected in the dynamic increase factor (DIF) values increases with decreasing concrete quality.
- The DIF values for mortar are slightly lower than for common concrete (Fig. 7.6), apparently because it is less heterogeneous and the size of the largest defects is smaller, which provides higher quasi-static strength compared to the dynamic strength.
- The DIF value strongly depends on the moisture content in the capillary pores and consequently on the pore structure, and so it depends on the concrete quality.

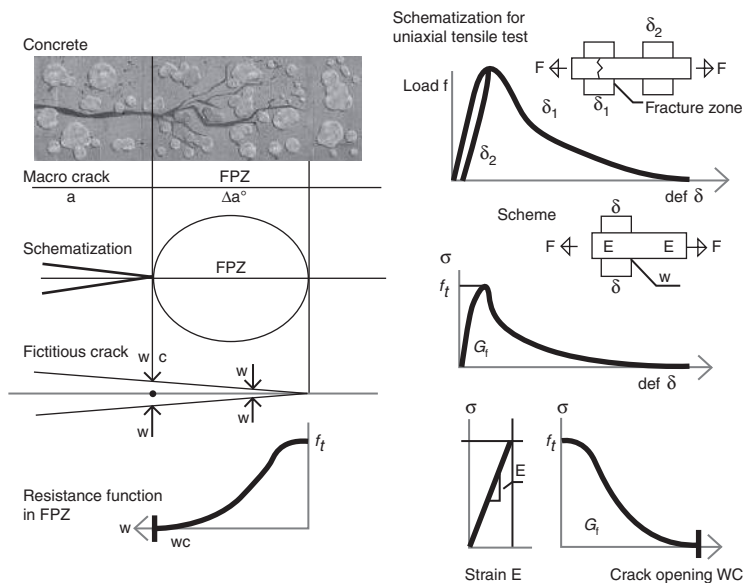
7.3 The effect of cracking rates on the fracture process under moderate and high loading regimes

The response of concrete up to complete failure in tension is represented in the load-deformation relation. The characteristic parameters are ultimate strength, stiffness in the ascending branch, and fracture energy. The rate effects on strength are discussed in the previous sections. In this section we address the post-peak failure process, the softening behaviour. The failure process is governed by (i) the stress condition, (ii) the ability to absorb energy in fracture, and (iii) the energy flow from the surrounding material into the fracture zone. In dynamics all three conditions vary in time and depend on the loading rate. Especially at loading rates beyond 50 GPa/s, the contribution of these mechanisms in the pre-peak response are strongly rate dependent resulting in the observed extensive strength increase. Besides the strength amplitude, the amount of microcracking and the width of the fracture zone determine the fracture energy. Data and models on these parameters are scarce. In Section 7.2.4 the authors presented a model on multiple cracking and fragmentation. In this section we will give a semi-quantitative analysis of the dynamic mechanisms supported by experimental data.

7.3.1 Definition of fracture energy parameters

The concrete response in tension up to failure is studied and described extensively in the literature (e.g. Bazant, Carpinteri, Wittmann, Hillerborg, Reinhardt, van Mier). When the material strength is locally exceeded, damage will start to grow. Available deformation energy flows into the fracture zone and is absorbed in the fracture process. Because of the coarse heterogeneity the fracture does not consist of the formation of a single crack. The macrocrack is preceded by a zone in which multiple microcrackings occur. This zone is called the fracture process zone (FPZ). First the microcracks start to grow, interfering with each other, with defects and aggregates. After a while a dominant macrocrack is formed, which also grows. This process is well represented in the fictitious-crack model of Hillerborg (Hillerborg *et al.*, 1976; Hillerborg 1985) (see Fig. 7.12).

The approach is quite similar to the energy balance approach, in which a certain amount of energy is absorbed by the formation of a unit area of crack surface. When a crack propagates, a certain amount of (deformation) energy is released. Crack propagation is controlled by the balance of released and absorbed energy (the energy criterion). In the fictitious-crack model the crack initiation is controlled by the strength criterion, the maximum material strength, f_t . To help the discussion and description of the Mode I fracture process we recall and suggest the following definitions:



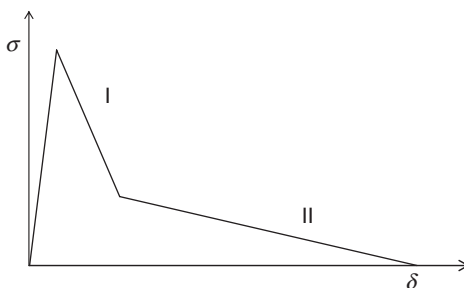
7.12 Crack-tip fracture process. In this figure WC stands for the critical crack width.

- The FPZ is the zone ahead of the tip of a physical, macrocrack. Microcracking in the FPZ leads to the growth of the macrocrack. The FPZ is coupled to the material characteristics at meso- and micro-level.
- The Fracture Zone (FZ) covers the material that is involved in the energy exchange of the fracture process. In this zone, the final failure crack is formed by the branching and coalescence of individual microcracks (see Fig. 7.1 for the uniaxial tensile test). The zone includes the FPZ of these macrocracks plus the surrounding material from which deformation energy is released into crack formation.
- The material fracture energy G_f is the energy absorbed within a single FZ and equals the surface below the stress deformation curve for uniaxial tensile loading.

7.3.2 Dynamic conditions

Using the schematized softening curve with two descending branches (see Fig. 7.13) the first steep branch is coupled to the phase of microcracking, while the long tail branch is related to the macrocracking and final failure. The questions are: (i) how is the amount of microcracking within the FZ affected by the loading rate, (ii) is the macrocracking process rate-dependent, and (iii) does the width of the FZ (l_{FZ}) depend on the loading rate?

To find answers to these questions, let us return to the simple, basic idea: ‘damage starts to grow from representative defects; with increasing load, first the larger defects start to grow, followed by the smaller defects’. At low loading rates the increase in load during the failure process will be limited and the size of the representative, decisive defects does not change. Only this set of cracks starts to grow, the stress in the material adjacent to these cracks is released and no other defects are activated (see Section 7.2.4). At high loading rates this might change. Due to the fast load increase, smaller defects become critical and start to grow before the stress release from



7.13 Schematic stress deformation curve

the initially activated cracks occurs. This will result in more microcracking within the FZ and an increase in the fracture energy.

It would be interesting to study the initiation and growth of different sized defects numerically in the mesoscopic model. Some numerical mesoscopic studies have been reported (Erzar, 2010; Pedersen, 2010; Zhou and Hao 2008) but do not address the growth of different sized defects. However, these studies confirm that the amount of microcracking increases with increasing loading rate. Zhou shows, simulating the dynamic splitting tests, that for loading rates beyond 100 GPa/s the failure mode changes and the amount of microcracking increases.

Fortunately, the fracture mechanics principles also give quantitative guidance. For crack initiation, first the strength criterion must be fulfilled. In analogue with the dynamic effects on the concrete strength at macro-level (see Sections 7.2.2 and 7.2.3), the strength criterion at meso- and micro-levels is affected by the moisture content and the micro-inertia effects. Let us assume that the moisture content is constant and focus first on the contribution of micro-inertia.

Schematizing concrete as a homogeneous material with equally distributed sets of initial flaws with sizes a_1, a_2, a_3 , etc. (e.g. $a_i = 2 \cdot a_{i+1}$), and assuming that the critical stress intensity factor (K_{Ic}) does not change the critical load level, $\sigma_{i+1} = 4 \cdot \sigma_i$ to activate the set of cracks ' a_{i+1} '. Experiments and numerical simulations indicate that t_{frac} is in the order of 100 μsec . For a concrete with tensile strength $f_t = 3 \text{ MPa}$, this means that the smaller set of cracks cannot be activated at loading rates less than 90 GPa/s. In equation format, additional microcracking may occur if:

$$\dot{\sigma}_{\text{micro}+} > \left[\left(\frac{a_i}{a_{i+1}} \right)^2 - 1 \right] \cdot \frac{f_t}{t_{\text{frac}}} \quad (\text{for } K_{Ic} \text{ is constant}) \quad [7.27]$$

Equation [7.24] shows the tendencies in rate effects on the fracture energy. The density of microcracking will increase with increasing loading rate, but only beyond a certain threshold. The threshold for dependency decreases for more heterogeneous (larger t_{frac}) and lower strength concrete.

In Section 7.2 we saw that, following fracture mechanics principles, K_{Ic} decreases beyond a certain loading rate, resulting in a steep strength increase (see Equations [7.2] and [7.3]). Including the rate effect on strength, the threshold for rate effects on the fracture energy due to additional microcracking is:

$$\dot{\sigma}_{\text{micro}+} > \left[\left(\frac{a_i}{a_{i+1}} \right)^2 - 1 \right] \cdot A \cdot \left(\frac{\dot{\sigma}}{\dot{\sigma}_o} \right)^\beta \cdot \frac{f_{t,\text{stat}}}{t_{\text{frac}}} \quad [7.28]$$

with $\dot{\sigma}_o$ and $\dot{\sigma}$ the loading rates at static and dynamic loading, respectively, β the power coefficient that depends on the concrete properties, but is in the order of 1/3 and A is a calibration coefficient.

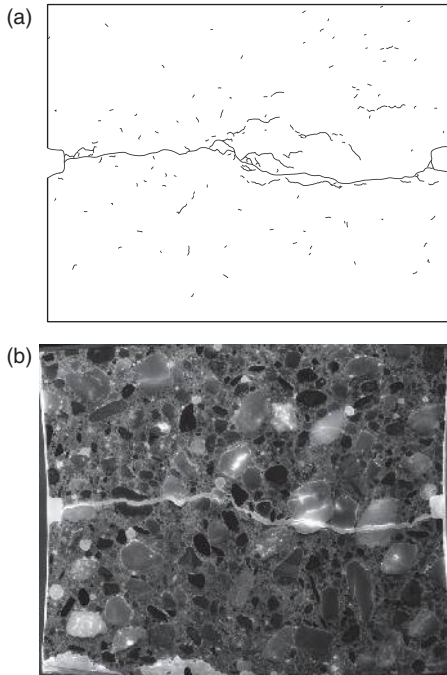
Referring to the stated question (i) ‘how is the amount of microcracking within the FZ affected by the loading rate?’ the conclusion is: additional microcracking is only possible at high loading rates. Rate effects on fracture energy are activated at higher loading rates than for strength. The DIF on tensile strength (DIF_f) cannot be used to quantify the rate effect on fracture energy G_f .

In the preceding discussion we identified some thresholds and general conditions but did not provide a model to quantify the additional microcracking and the DIF_{Gf} . To the authors’ knowledge, these models are not available yet. We mainly have to rely on the scarce experimental data and qualitative analyses of the dynamic fracture process.

7.3.3 Experimental data on the dynamic fracture process and fracture energy

We defined FZ as the zone with a single macrocrack including the FPZ, with microcracking and the surrounding material contributing to the energy exchange which drives the fracture process. The width of the FZ (l_{FZ}) and the microcrack density determine G_f . Theoretically, the maximum of l_{FZ} is determined by $l_{FZ} = 2C_0 \cdot t_{\text{frac}}$. The wave velocity c_0 in concrete is about 3500 m/s, which means that only for t_{frac} in the order of a few microseconds does $l_{FZ, \text{max}}$ have the order of the aggregates, as in statics. But the scarce data on t_{frac} shows that the failure time is in the order of 100 μsec , so the FZ can include so many aggregates that the condition of a single macrocrack will not be fulfilled. Multiple fracture planes will be formed, as is also seen in dynamic tests. We have to conclude that, also for the possible rate effect on the width of the FZ, we have to rely on experimental data, or dedicated computational simulations.

Data on dynamic fracture energy in literature are mostly derived from dynamic bending tests (equivalent with RILEM test) and are polluted with structural responses, leading to over-prediction of rate effects. To analyse G_f in tension, the uniaxial tests are preferred (see Chapter 6). In dynamics, the SHB and uniaxial spalling tests are appropriate and give information on G_f , t_{frac} ; with post-test analysis, info on the amount of microcracking and l_{FZ} is also obtained. In these tests, multiple macrocracks occur when un-notched specimen are used. Reviewing the literature with the selection criterion of ‘data on a single failure zone’ only a few data are left (see Chapter 6) (Weerheijm and van Doormal, 2004, 2007; Schuler *et al.*, 2006;



7.14 Digitized crack pattern (top) and picture of the same fracture zone (bottom).

Vegt *et al.*, 2006, 2007, 2009; Weerheijm *et al.*, 2009; Forquin and Erzar, 2010). The most consistent set of data is given by Vegt. It consists of strength, fracture energy data, as well as quantitative data on micro- and macro-crack patterns. We will use this data set to analyse the rate effect on the fracture process and fracture energy.

The test method and diagnostics are given in Chapter 6. Tests were performed for dry, normal and wet conditions. Details of composition, curing and test conditions are given in (Vegt *et al.*, 2006, 2009). The characteristics for normal, lab-curing conditions are: (i) cube compression strength 48 MPa, (ii) splitting tensile strength 3.4 MPa, (iii) Young's modulus 35 GPa, and (iv) the maximum aggregate size 8 mm.

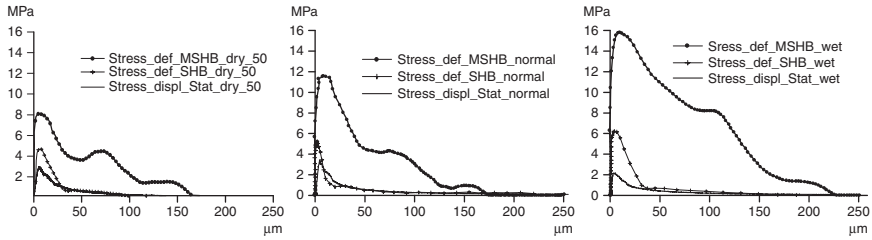
The experimental results on strength and fracture energy are summarized in Table 7.2. In the post-test microscopic analysis on 'thin sections', the crack patterns were analysed and quantified. Figure 7.14 illustrates the kind of data that are obtained from the post-test analysis. Some microcracks are directly connected to the macro crack but most microcracks are isolated in the FZ. The length of the macrocracks (l_{mac}), the length of connected microcracks ($l_{\text{mic,c}}$) and isolated microcracks ($l_{\text{mic,i}}$) were measured, as well as the physical width (l_{FZ}) of the FZ. The data are given in Table 7.3 for three

Table 7.2 Data on strength and fracture energy (Vegt et al., 2009)

σ (GPa/s)	Dry			Normal			Wet		
	f_t (MPa)	G_r (N/m)	DIF _{ft}	DIF _{Gr}	f_t (MPa)	G_r (N/m)	DIF _{ft}	DIF _{Gr}	f_t (MPa)
10 ⁻⁴	3.05	105.5	1.0	1.0	3.30	120.2	1.0	1.0	2.05
40	4.73	138.6	1.6	1.3	5.58	120.4	1.7	1.0	6.35
1700	8.05	653.5	2.6	6.2	10.47	679.0	3.2	5.6	16.04
									G_r (N/m)
									80.3
									167.1
									1475
									7.7
									18.4

Table 7.3 Data on fracture patterns (Vegt et al., 2009)

σ (GPa/s)	Dry			Normal			Wet		
	l_{fz} (mm)	l_{mac} (mm)	$l_{mic,tot}$ (mm)	DIF _{micro}	l_{fz} (mm)	l_{mac} (mm)	$l_{mic,tot}$ (mm)	DIF	DIF _{micro}
10 ⁻⁴	8.7	90	84	1.0	6.1	80	141	1.0	1.0
40	8.8	88	97	1.2	8.1	86	94	0.7	1.1
1700	44.1	79	172	2.0	19.1	81	170	1.2	2.1
									$l_{mic,tot}$ (mm)
									135
									144
									283
									7.7
									18.4



7.15 Stress displacement and deformation curves for dry (left), normal (middle) and wet (right) condition.

loading rates and three moisture levels. The diagnostics of the experiments enables derivation of the load deformation curve and reconstruction of the failure process in time. Figure 7.15 gives the curves for the normal and wet curing conditions. The data comprises a lot of information, but in this section we limit ourselves to the main findings.

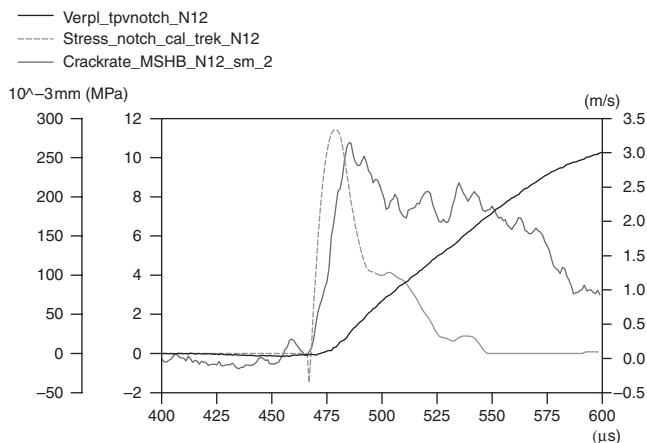
The observations for static and moderate load regime are:

- The softening curves have two branches.
- The last (macrocrack) branch is not affected by the loading rate.
- The length of the final macrocrack is not affected by the loading rate or curing condition; apparently it is dominated by concrete structure/aggregate grading.
- The macrocrack is fully opened at $\delta_{\text{frac}} \approx 150\text{--}200\mu\text{m}$ and is not affected by loading rate or curing.
- For dry conditions, δ_{frac} is smaller ($\approx 100\mu\text{m}$) at both the static and moderate rate.
- Up to $\dot{\sigma} = 40\text{ GPa/s}$, additional microcracking is marginal for the dry and wet conditions, and for normal curing conditions it is even reduced. The threshold of 40 GPa/s corresponds with the theoretical analysis represented in Equations [7.23] and [7.24].
- The width of the FZ is not affected by the loading rate.

From the observations we conclude that the second branch is coupled to the opening of the macrocrack. The data of the moderate regime shows that the second branch is not affected by the loading rate, neither by material or structural response.

Finally, we will have a closer look at the fracture energy G_f which is given by:

$$G_f = \int_{t_{\text{frac}}} \frac{F(t)}{A_{\text{cross}}} \cdot \dot{\delta}(t) \cdot dt. \quad [7.29]$$



7.16 Stress $\sigma(t)$ -curve (indicated as Stress_notch), deformation $\delta(t)$ -curve (indicated as Verpl_tpvnotch_N12) and velocity $\dot{\delta}(t)$ -curve (addressed as crackrate_MSHB) recordings of the failure zone for spalling tests on normal concrete.

The first branch of the softening curve is determined by microcracking (initiation and growth) and is coupled to the material response. The rate effect on G_f is caused by the additionally absorbed energy to form the microcrack surfaces and the contribution of moisture and micro-inertia to $F(t)$ in Equation [7.25]. The observed reduced amount of microcracking at $\dot{\sigma} = 40 \text{ GPa/s}$ for concrete with normal curing conditions, while G_f equals the static value, illustrates that both components contribute. The data in Table 7.3 also show that the increase in fracture energy is not linearly proportional to the number (length) of additional microcracks.

For the high loading regime the observations are quite different.

- The two branches are still present, but much less obvious.
- The macrocrack is fully opened at $\delta_{\text{frac}} \approx 230 \mu\text{m}$.

Because the total length of macrocracking is similar to the values for the other loading rates, it seems that the second branch is affected by structural inertia effects. The inertia might delay the opening of the macrocrack and will be recorded as additional resistance. However, in the spalling test we recorded the deformation of the FZ, δ_{frac} , as a function of time. These data show that during the second branch the velocity, $\dot{\delta}_{\text{frac}}(t)$, is constant (see Fig. 7.16). So the additional resistance observed during the formation of the final macrocrack is not caused by structural inertia effects and have to be coupled to the material response itself.

Table 7.4 Ratios of l_{FZ} and $l_{micc,tot}$ related to static conditions

$\dot{\sigma}$ (GPa/s)	Dry		Normal		Wet	
	Ratio l_{FZ}	Ratio $l_{micc,tot}$	Ratio l_{FZ}	Ratio $l_{micc,tot}$	Ratio l_{FZ}	Ratio $l_{micc,tot}$
1700	5.1	2.0	3.1	1.2	7.9	2.1

To understand the significant increase in fracture energy for the high loading rate regime, we have to consider the microcracking data in more detail. The observations on microcracking for the high loading rate regime are:

- The width of FZ increases significantly.
- The amount of microcracking increases considerably.

To ratios of l_{FZ} and $l_{micc,tot}$ for static and high dynamic are given in Table 7.4. Obviously the width of FZ increases more than the total amount of microcracking. The average density of microcracks decreases, and most probably the density in the direct vicinity of the macrocrack is not affected by the loading rate.

Looking at the macrocracking process, the material in the direct vicinity of the final macrocrack is unloaded and additional microcracking will not occur in this zone. However, at high loading rates the width of the failure zone is much wider and the process of microcracking can continue at some distance from the macrocrack. The additional microcracking, during the formation of the final macrocrack, explains why the ‘two branches’ of the softening curve are much less pronounced for high loading rates. Note that the presented DHF model (Section Modelling of the multiple fragmentation process: the DFH model (Denoual and Hild, 2000; Forquin and Hild, 2010)) predicts for the high loading rate regime enhanced microcracking (see Fig. 7.7) but the experimentally observed difference between dry and wet concrete is not supported.

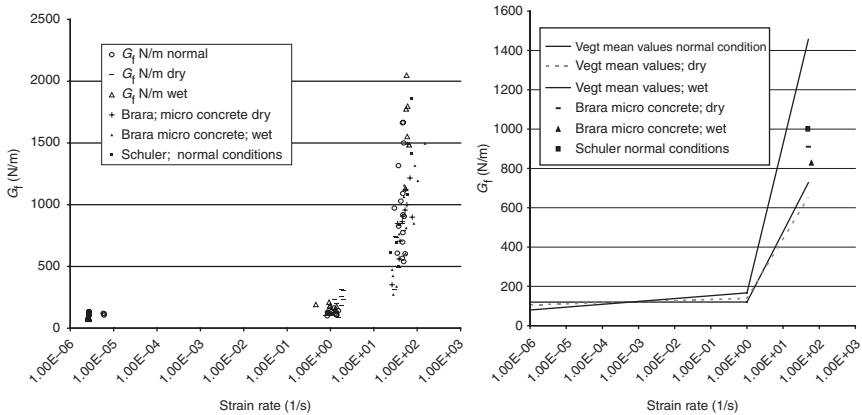
Although we concluded that structural inertia effects do not influence the second softening branch in the stress deformation relation of the spalling test, there is still an effect that disturbs the derived material softening curve (see Chapter 6). In the spalling set-up, the reflected tensile wave interferes with the failure zone during the fracture process, which results in additional stress pulses that propagate from the failure zone to the free end. This pulse travels forward and backward between the failure zone and the free end causing the ‘bumps’ in the stress deformation curves. Because of these phenomena, the G_f -values given in Table 7.2 might overestimate the true dynamic fracture energy.

Concluding remarks on the dynamic fracture energy:

- The fracture energy is determined by the resistance to microcracking and the energy absorbed in the micro- and macro-cracking.
- The fracture energy has to be related to a FZ with a single, final macrocrack.
- The fracture failure process represented by the stress deformation curve is characterized by two branches. The first steep branch is related to the microcracking process, while the second branch is related to the final macrocrack formation and final failure.
- Rate effects on G_f are related to (i) additional microcracking and (ii) the additional resistance to microcrack initiation and growth due to micro-inertia effects.
 - The instrumented spalling tests the authors performed showed that the structural inertia effects on the macrocracking process are negligible in the applied set-ups.
 - The quantified rate-effect data for G_f and f_t are material properties including the micro-inertia effects.
- Up to a $\dot{\sigma}_{lim}$ - threshold additional microcracking is negligible and rate effects on G_f are only caused by additional strength and resistance to microcracking.
- Similar to the rate effect on strength, two regimes can be distinguished for the fracture energy. Pronounced rate effects on G_f occur for $\dot{\sigma} \geq \dot{\sigma}_{lim}$. The pronounced rate effect on fracture energy occurs at a higher loading rate than for the tensile strength.
- The width of the FZ only increases in the high loading rate regime. Therefore, the internal length scale in numerical calculations has to be adapted for rate effects in the high loading regime only.

Finally, the few available data on dynamic fracture energy from uniaxial tests are given in Fig. 7.17. Note that these data are obtained with different test set-ups and measurement techniques (see also Chapter 6). The scatter in the results for the high loading rates is large, therefore the mean values are also given. A comparison and discussion on these results is given in Weerheijm (2009). Here we limit ourselves to some observations.

The data on dynamic fracture energy are scarce and the test and diagnostic methods are not standardized yet. Therefore, international cooperation and a benchmark program of dynamic tensile testing are recommended. A direct comparison of data and exchange of information can lead to standardization in dynamic testing, and will enable the comparison of dynamic test data.



7.17 G_f -values from uniaxial tensile tests: (left) all data and (right) mean values.

7.4 Conclusions

At the end of this chapter we want to emphasize the importance of combined experimental, analytical and computational research, especially in dynamics. In this chapter we have focused on the main effects of dynamics on crack initiation and propagation at the material meso-level and the experimentally observed rate effects on strength and fracture energy could be explained. However, even with advanced diagnostics, real-time data on the fracture process is hard to get, and also on the macrocracking process recorded at the free specimen surface (see also Chapter 6). With the advanced computational models (see Chapter 10) the failure process of material and structure can be represented in detail. By combined research the bias on the experimentally observed rate effects can be reduced, or even eliminated.

A second remark concerns the discussion of whether the observed rate effects are due to ‘structural inertia’ in the mechanical response of the specimen, or if micromechanical processes are involved in the strong increase of strength with strain rate. In this chapter we have showed that the rate effects can and should be directly related to the fracture process associated with critical defects (porosities, microcracks, lumps, aggregates matrix interface), to the propagation of cracks at a limited cracking velocity, and to a cohesion strength in FZs. If the crack initiation and propagation process is modelled a static in the (detailed) numerical model, and preferably probabilistic, material model should be used. If not, and the numerical model is more global, the rate effect should be treated as a material property and a damage model is recommended.

A third remark concerns the large scatter in the experimental results given in the literature. In our opinion, it is caused by (i) the scattering in concrete composition and microstructures, and (ii) the testing procedures employed to characterize the quasi-static and dynamic tensile strength of concrete. The testing procedures might vary for instance in terms of size of specimens, set-up, and instrumentation used, curing and drying conditions of concrete.

7.5 References

- Brajer X., Forquin P., Gy R. and Hild F. (2003). The role of the surface and volume for the fracture of glass under quasi-static and dynamic loadings – *J. Non-Cryst. Solids.*, **316**, 42–53.
- Broek, D. (1982). *Elementary engineering fracture mechanics*. the Netherlands: Martinus Nijhoff, The Hague.
- Cadoni, E., Labibes, K., Albertini, C. and Berra, M. (2001). Strain rate effect on the tensile behaviour of concrete at different relative humidity levels, *Mater. Struct.*, **34**, 21–26.
- Chen, E.P. and Sih, G.C. (1977). *Transient response of cracks to impact loads*. In Mechanics of Fracture 4, Elastodynamic crack problems. Edited by Sih, G.C. Noordhoff Int. Publishing, Leyden. The Netherlands.
- Cottrell, A.H. (1964). *The mechanical properties of matter*. New York; John Wiley & Sons Inc.
- Cotsovos, D.M. and Pavlovic, M.N. (2007). Numerical investigation of concrete subjected to high rates of uniaxial tensile loading. *Int. J. Impact Eng.*, **35**, 319–335, doi:10.1016/j.ijimpeng.2007.03.006.
- Curbach, M. and Eibl, J. (1990). Crack velocity in concrete. *Int. J. Eng. Fract. Mech.*, **35** (1/2/3), 321–326.
- Denoual C. and Hild. F. (2000). A damage model for the dynamic fragmentation of brittle solids. *Comp. Meth. Appl. Mech. Eng.*, **183**, 247–258.
- Erzar B. and Forquin P. (2010). An experimental method to determine the tensile strength of concrete at high rates of strain. *Exp. Mech.*, **50** (7), 941–955.
- Erzar, B. (2010). *Ecaillage, craterisation et comportement en traction dynamique de betons sous impact: approches experimentales et modelisation*. PhD-thesis, University of Metz, France, 2010.
- Erzar B. and Forquin P. (2011b). Free water influence on the dynamic tensile behaviour of concrete, *Appl. Mech. Mater.*, **82**, 45–50.
- Erzar B. and Forquin P. (2011a). Experiments and mesoscopic modelling of dynamic testing of concrete, *Mech. Mater.*, **43**, 505–527.
- Forquin P., Charles Y., Rota L. and Hild F. (2004). A method to determine the macroscopic toughness scatter of brittle materials. *Int. J. Fracture.*, **125** (1), 171–187.
- Forquin P. and Hild F. (2008). Dynamic fragmentation of an ultra-high strength concrete during edge-on impact tests. *ASCE J Eng Mech.*, **134** (4), 302–315.
- Forquin P. and Hild F. (2010). A probabilistic damage model of the dynamic fragmentation process in brittle materials. *Adv. Appl. Mech. Giessen and Are feds.*, **44**, 1–72. Academic Press, San Diego, CA.
- Forquin P. and Erzar B. (2010). Dynamic fragmentation process in concrete under impact and spalling tests. *Int. J. Fracture*, **163**, 193–215.

- Forquin P. and Cheriguène R. (2011). *A rocking spalling test to characterize the crack velocity in concrete*. SEM 2011, Uncasville, Connecticut, USA.
- Grady, D.E. and Kipp, M.E. (1987). *Dynamic rock fragmentation*, In B.K. Atkinson (ed.), *Fracture mechanics of rock*, Academic Press, London.
- Grange S., Forquin P., Mencacci S. and Hild F. (2008). On the dynamic fragmentation of two limestones using edge-on impact tests. *Int. J. Impact Eng.*, **35**, 977–991.
- Hild, F., Billardon, R. and Marquis, D. (1992). Hétérogénéité des contraintes et rupture des matériaux fragiles. *C. R. Acad. Sci. Paris II*, **315**, 1293–1298.
- Hillerborg, A., Modeer, M. and Petersson, P.E. (1976). Analysis of crack formation and crack growth in concrete by means of fracture mechanics and finite elements. *Cem. Concr. Res.*, **6**, 773–782.
- Hillerborg, A. (1985). The theoretical basis of a method to determine the fracture energy G_f of concrete. *RILEM Mater. Struct.*, **18** (106), 291–296.
- John, R., Shah, S.P. and Jenq, Y.S. (1986). *A fracture mechanics model to predict the rate sensitivity of mode I fracture of concrete*. Northwestern University, Evanston.
- Kanninen, M. F. and Popelar C. H. (1985). *Advanced fracture mechanics*. Oxford (UK): Oxford University Press.
- Kipp, M.E., Grady, D.E. and Chen, E.P. (1980). Strain rate dependent fracture initiation. *Int. J. Fract.*, **16**, 471–478.
- Malvar, J. and Ross, A.C. (1998). *Review of strain rate effects in concrete*. ACI Materials Journal. Technical paper no. 95-M73.
- Pedersen, R.R. (2010). *Computational modelling of dynamic failure of cementitious materials*. PhD-thesis Delft University of Technology, 2010.
- Reinhardt H.W., Rossi, P. and van Mier, J.G.M. (1990). Joint investigation of concrete at high rates of loading. *Mater. Struct.* **23**, 213–216.
- Reinhardt, H.W. and Weerheijm, J. (1991). Tensile fracture of concrete at high loading rates taking account of inertia and crack velocity effects. *Int. J. Fracture*, **51**, 31–42.
- Ross, C.A., Jerome D.M., Tedesco J.W. and Hughes, M.L. (1996). Moisture and strain rate effects on concrete strength. *ACI Material J.*, **96**, 293–300.
- Rossi, P., van Mier, J.G.M., Boulay, C. and le Maou, F. (1992). The dynamic behaviour of concrete: influence of free water. *Mater. Struct.*, **25**, 509–514.
- Rossi P. (1991). Influence of cracking in the presence of free water on the mechanical behaviour of concrete. *Mag. Concr. Res.*, **43**, 53–57.
- Schuler, H., Mayrhofer, C. and Thoma, K. (2006). Spall experiments for the measurement of the tensile strength and fracture energy of concrete at high strain rates. *Int. J. Imp. Eng.*, **32**, 1635–1650.
- Spanier, J. and Oldham, K.B. (1987). *An atlas of functions*. Springer, New York (USA).
- Strassburger, E. and Senf, H. (1995). *Experimental investigations of wave and fracture phenomena in impacted ceramics and glasses*. EMI Report, ARL-CR-214.
- Vegt, I., Weerheijm, J. and Van Breugel, K. (2006). *Moisture content and the effect on dynamic concrete behaviour*. Proceedings of the 2nd Int. Conf. on Design and Analysis of Protective Structures, Singapore, 13–15 November 2006.
- Vegt, I., Weerheijm, J. and Van Breugel, K. (2007). *The fracture energy of concrete under impact tensile loading- a new experimental technique*. CONSEC Conference June 2007, Tours, France.

- Vegt, I., Weerheijm, J. and Breugel van K. (2009). *The rate dependency of concrete under tensile impact loading fracture energy and fracture characteristics*. Conference Proceedings 13th ISIEMS.
- Weerheijm, J. and Karthaus, W. (1985). *Tensile fracture model for concrete under dynamic tensile loading*. Proc. Int. Conf. on The interaction of non-nuclear munitions with structures, Panama City Beach.
- Weerheijm, J. (1992). *Concrete under impact tensile loading and lateral compression*. Doctoral thesis, Delft University.
- Weerheijm, J. (1998). *Prediction of dynamic tensile strength*. In W. Bounds (ed.), Concrete and blast effects. ACI, SP-175.
- Weerheijm, J. and van Doormaal J.C.A.M. (2004). Tensile failure at high loading rates; Instrumented spalling tests. International Conference FramCoS 5, April 2004.
- Weerheijm, J. (2006). Axial dynamic tensile strength of concrete under static lateral compression. *Key Eng. Mater.*, **324–325**, 991–994.
- Weerheijm, J. and van Doormaal, J.C.A.M. (2007). Tensile failure of concrete at high loading rates: New test data on strength and fracture energy from instrumented spalling tests. *Int. J. of Imp. Eng.*, **34**, 609–626.
- Weerheijm, J., Vegt, I. and Breugel van K. (2009). *The rate dependency of concrete in tension – New data for wet, normal and dry conditions*. Proc. DYMAT 2009, Brussels, 95–101.
- Weibull, W. (1939). *A Statistical Theory of the Strength of Materials Report 151*, Roy. Sweden Institute of Engineering Research.
- Zielinski, A.J. (1982). *Fracture of concrete and mortar under uniaxial impact tensile loading*. Doctoral thesis, Delft University of Technology.
- Zheng, D. and Li, Q. (2004). An explanation for rate effect of concrete strength based on fracture toughness including free water viscosity. *Eng. Fract. Mech.*, **71**, 2319–2327.
- Zheng, D., Li, B. and Wang, L. (2005). A microscopic approach to rate effect on compressive strength of concrete. *Eng. Fract. Mech.*, **72**, 2316–2327.
- Zhou, X.Q. and Hao, H. (2008). Mesoscale modelling of concrete tensile failure mechanisms at high strain rates. *Comput. Struct.*, **86**, 2013–2026.

Modelling the dynamic response of concrete with mesoscopic heterogeneity

Y. LU, University of Edinburgh, UK

DOI: 10.1533/9780857097538.2.218

Abstract: Concrete is heterogeneous in nature. The needs of modelling concrete with explicit inclusion of the heterogeneity will arise when the mechanical processes at this level become of particular interest, either due to the target scale of observation, or more so if the heterogeneity is deemed to play a critical role in the material response under a particular loading condition. This chapter deals with modelling mesoscopic heterogeneity of concrete for high strain rate loading. For completeness in the treatment of this subject, both tensile and compressive loading as applied externally will be included. In fact, at the mesoscale the mechanisms underlying the damage process are closely associated with fracture or generalized tension even under compression. The chapter begins with an overview of the nature of the mesoscopic heterogeneity and its computational representation. Different modelling techniques are briefly reviewed and discussed. A finite element based mesoscale modelling framework is then described in more detail. The model is employed in various investigations into the meso-mechanisms affecting the dynamic behaviour of concrete in high strain rate compression and tension, and representative numerical simulations are introduced and the main observations summarized. In particular, the contribution of the heterogeneity in the dynamic compressive and tensile strengths of concrete, the dynamic structural (inertia) effects, and the strain rate limits in dynamic compression and Brazilian splitting tension tests are highlighted from a mesoscopic numerical simulation point of view. In the last part of the chapter, a simplified scheme for representing concrete heterogeneity, in which regular spatial discretization is utilized in conjunction with a stochastic material property distribution, is introduced along with example applications.

Key words: concrete, heterogeneity, mesoscale model, dynamic behaviour, strain rate effect, splitting tension.

8.1 Introduction

Concrete is heterogeneous by nature. The behaviour of such a material is complicated by a combination of brittleness, micro-fracture, heterogeneity, and multi-phase interactions. In most modelling applications, however,

concrete is treated as a homogeneous material with uniform material properties as obtained from testing of standard concrete specimens such as cubes and cylinders, of which the size is typically at least a few times that of the largest aggregates. Strictly speaking, such properties are valid only when the critical regions in the structure being analysed are subject to a distribution of stress and strain similar to that in the standard test samples. In other words, the homogenization treatment is valid only when both of the following conditions are true: a) the stress distribution is relatively uniform within a characteristic size which is comparable to the size of standard concrete specimens, such that concrete exhibits its bulk behaviour, and b) the response of interest is macroscopic, or more specifically, the scale of observation is at or above one order of magnitude larger than the material heterogeneity. The implication for the computational modelling is that the basic element size need not be smaller than the characteristic size, i.e., 3–4 times the size of the largest aggregates; otherwise, the use of homogenized properties and the computed response at the element level would be questionable due to the incompatibility between the spatial discretization and the bulk material properties being used.

The aforementioned conditions may be more easily satisfied when analysing larger structures and under a quasi-static loading condition. Under dynamic loading, however, this is hardly the case due to the abrupt spatial variation of the stress and strain that is typically associated with the transient stress wave effect at high strain rates. For the purpose of the present discussion we shall refer to the high strain rate regime as starting from the order of 1 s^{-1} and above. To capture the stress wave effect, a refined spatial discretization on or below the aggregate size level may be necessary. Consequently, the description of the mechanical properties of the material would only make sense if heterogeneity is appropriately taken into account.

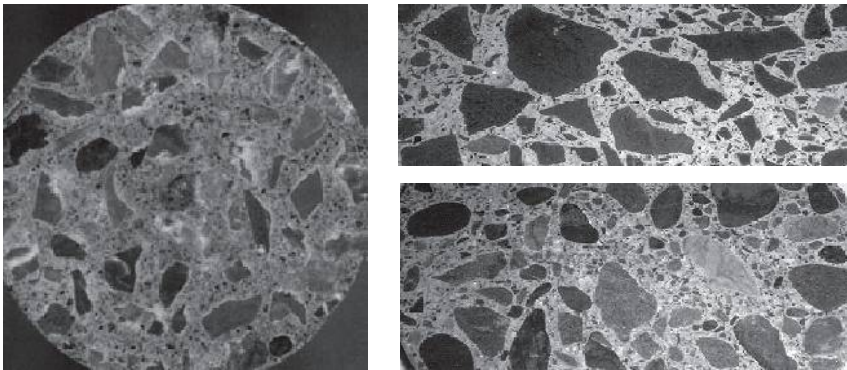
This chapter is concerned with the modelling of concrete using a non-homogenous approach for high strain rate applications. Different non-homogeneous modelling schemes are considered, namely (a) a meso-scale model with an explicit description of the mesoscopic heterogeneity, including random meso-geometric structure and distinctive material properties for different phases, and (b) an approximate mesoscale model, either with simplified mesoscale geometry, for example using round/sphere-shaped aggregates, or with an equivalent statistical distribution of material properties. The chapter is organised as follows. Following the introduction in Section 8.1, an overview of the mesoscopic heterogeneity and associated modelling considerations are given in Section 8.2, along with a discussion on the necessity of an explicit representation of the heterogeneity under high strain rate conditions. Section 8.3 provides a review of the types of mesoscale model and their applications in the dynamic analysis of concrete. Section 8.4 introduces a continuum FE based mesoscale model with random polygon aggregates in

2D and suited for general analysis under complex and dynamic loading conditions. To enable the 2D mesoscale model for dynamic analysis of concrete with a more realistic representation of the 3D stress condition, a pseudo-3D mesoscale model configuration is described in Section 8.5. A series of simulation studies using the above mesoscale model for concrete under high rate compression are introduced, and the mechanisms contributing to the bulk dynamic strength increase are discussed from a mesoscale perspective, and the need for re-visiting some of the conventional high strain rate test results is highlighted. Section 8.6 looks into the simulation of dynamic tensile behaviour of concrete in a Brazilian splitting condition, and Section 8.7 provides a brief introduction of simplified mesoscale modelling with stochastic material properties. Example analyses using such a modelling approach in real application problems involving fragmentation are given in Section 8.8. The chapter ends with a summary of concluding remarks in Section 8.9.

8.2 The mesoscopic structure of concrete and computational considerations

At the mesoscopic level, concrete may be regarded as a composite comprising of three distinct phases, namely, coarse aggregate, mortar matrix and interfacial transition zone (ITZ). Figure 8.1 shows selected section views of typical concrete mesoscopic structure.

Modelling of the mechanical behaviour of concrete may be done on different physical scales, ranging from homogenized continuum to a microscopic description where the particulates in the cement paste may be explicitly modelled (Emery *et al.*, 2007). The selection of an appropriate level of modelling for concrete depends on the scale of observation, characteristics of response and degree of accuracy sought, as well as the computational cost.



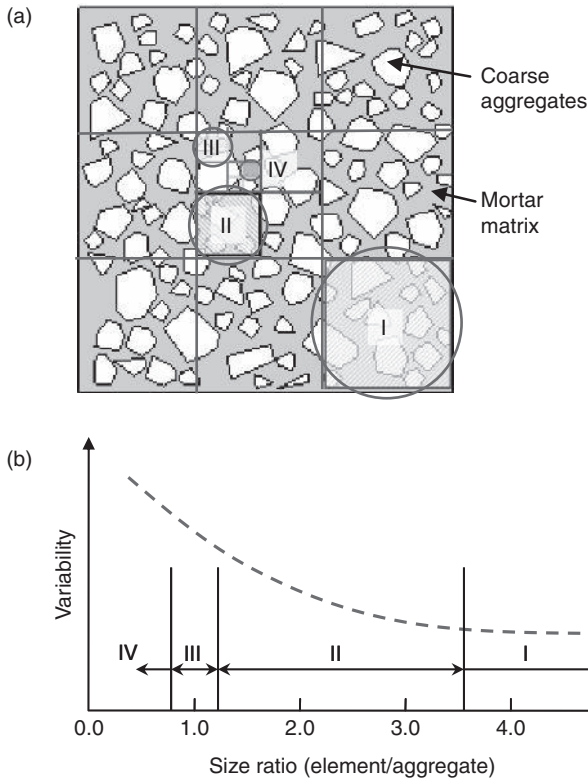
8.1 Typical concrete mesoscopic geometry (after Grote *et al.*, 2001, left; and Mackechnie, 2004, right).

Generally speaking, modelling of concrete in macroscale with homogenized material properties is computationally economical, and can be suitable for a wide range of applications. However, homogeneous models take no regard of the material composition; and moreover, because the constitutive laws in such models are derived from the nominal stress–strain response of standard specimens whose sizes are at least 3–4 times that of the largest aggregates in the composite, the applicability of the macroscopic model is generally limited to problems in which the global response is of primary interest in the analysis; and moreover, the spatial variation of the stress and strain should not be drastic within the above characteristic dimension. An implication of such a requirement in a finite element context is that the basic element size (or the FE mesh resolution) should normally be on or above the order of the characteristic length, so as to maintain consistency with the macro-material property description. From there, the statistics in the bulk properties of concrete as observed from testing standard concrete samples may be incorporated by adopting an appropriate stochastic property distribution (e.g. Rossi and Richer, 1987).

For an analysis where finer spatial resolution than the characteristic size of bulk concrete, or a representative volume element (RVE) (Aboudi, 1991; Hill, 1963; Zohdi and Wriggers, 2001), is required to properly describe the responses, homogenization can no longer be justified. There is no experimental data to support homogenization with stable material properties at such a scale level. It is conceivable that the properties of the material would exhibit a much increased scatter as the element size is reduced into the sub-RVE regime. Rossi *et al.* (1992, 1997) studied the variance of the concrete material properties for a variety of sample sizes with a volume ratio between the sample and the largest aggregate ranging from 10 to 7000, or roughly a ratio of 2.2~19.1 in terms of nominal length, and implemented the statistics in their probability models as a representation of the mesoscopic heterogeneity. However, the statistics cannot be extrapolated to spatial discretization falling into a sub-RVE size regime.

For a conceptual discussion, four levels of spatial discretization may be defined for the purpose of classifying the material descriptions, as schematically illustrated in Fig. 8.2. Herein we define the element size ratio as the ratio of the basic cell size in a computational model to the nominal size of the aggregates:

- Level I: element size ratio $\geq 3\sim 4$; homogenization and use of the standard (bulk) material test data are deemed appropriate. Variation of the material properties is minimal and may well be represented by the statistics derived from standard concrete sample tests.
- Level II: element size ratio well above 1.0 but less than the order of $3\sim 4$; material properties at the element size level are not generally known,



8.2 (a) Schematic of four levels of discretization and (b) the corresponding variability of mechanical properties of individual elements.

and the variability of the material properties can be expected to increase with the decrease of the element size in the above range. Homogenization may be possible but the increased variability of the material properties needs to be properly taken into account.

- Level III: element size ratio on the order of 1.0; material properties at the element level can vary through a wide range, from one that largely resembles a pure aggregate, to one that falls between mortar and ITZ.
- Level IV: element size ratio falls well below unity; in this case, only a mesoscale model with appropriate representation of the mesoscale geometry may be considered as rational. Use of indiscriminate spatial discretization, even with a consideration of statistical properties of the constituent materials, would not be physically justifiable due to inevitable disruption of the morphology of the composite.

Spatial discretization at levels I and II may be suitable mainly in quasi-static loading analysis and for relatively large structures. Homogenization is most appropriate for these levels of discretization; however, care should be taken with regard to the increased variability of the material properties, especially for the smaller end of level II discretization and when a detailed distribution of stress and strain is sought from such models.

For a typical high strain rate analysis with a strain rate in a range of $10\sim 100\text{ s}^{-1}$, spatial discretization at levels III and IV are common practice due to the need of capturing the transient stress wave effects. High impulsive loading such as blast and impact often generates a stress-strain field with a drastic temporal and spatial variation. In the initial phase of such responses, the stress and strain gradient can be so significant that it cannot be ignored over a size scale that is comparable to the heterogeneity (particularly coarse aggregates) in concrete.

Plate XI (see colour section between pages 208 and 209) illustrates the response of a concrete sample to dynamic compression at a nominal strain rate of 100 s^{-1} , modelled using a homogeneous and a heterogeneous meso-scale model, respectively (Lu *et al.*, 2010). The effect of heterogeneity on the distribution of damage is strikingly visible. A direct implication of such an effect will be the mobilization of the much stronger aggregates in the load resistance, and hence contributing to a certain extent to the experimentally observed bulk dynamic strength increase (i.e. DIF). Apparently, this mechanism is not represented in an homogenized model, and neither is it reasonably represented in physical tests where scaled concrete, e.g. mortar, is employed. Similar argumentation may be applied to the initial local response of concrete components when subjected to an impact or a close-in blast.

Clearly, without a realistic representation of the mesoscopic heterogeneity, including the composition and geometry, it would not be possible to preserve the underlying mechanisms and hence for the model to be robust enough to cater for different high rate loading conditions.

Much has been accomplished in the mesoscale modelling of concrete in the quasi-static literature, as will be briefly reviewed in the next section. Generally speaking, each model in this category involves a set of assumptions concerning structural idealisation, material description and failure criteria which are catered for in the particular modelling framework and loading conditions. Although such models have been fairly successful in their specific applications, they lack sufficient robustness for applications beyond the situations for which they were originally suited. Moreover, extension of these works to more general applications has been largely hindered by the fact that most of the proposed procedures are implemented in dedicated programmes, where there is usually a restricted choice concerning the material constitutive models and the capability in handling complex stress conditions, especially under dynamic loading, is often limited.

Consequently, it has been difficult to conduct systematic investigations into the concrete failure mechanisms under various loading conditions using a mesoscale model. The attempt to use mesoscale modelling for the dynamic analysis of concrete materials is a rather recent development and models, ranging from simplified (such as elliptical or spherical) to random polygonal aggregate representations, have been developed, as will be briefly reviewed in Section 8.3.4.

It is noteworthy that a mesoscale model with a detailed description of the meso-geometry requires refined meshes at the millimetre scale, i.e., level IV discretization, and this is obviously costly in terms of the computational effort. In cases where less detailed results are acceptable, level III discretization may be appropriate, and this could be particularly suitable for the analysis of large structures or structural components. As mentioned earlier, discretization at this level implies large variability of the material properties at the element level, and to reflect such variability a stochastic sampling process may be involved such that individual elements will possess different properties to resemble a targeted statistical distribution. This scheme will be discussed together with the mesoscale model in later sessions.

8.3 Types of mesoscale model and their applications in the dynamic analysis of concrete

Mesoscale modelling of concrete has been a topic of extensive research in the quasi-static literature. Three main alternative approaches have been employed, namely lattice models, discrete element models, and continuum-based FE models. A key challenge associated with the lattice models is the difficulty in determining the equivalent model parameters. Similar issues exist in the discrete element methods (DEM) approach where the virtually continuous interface between aggregates and the mortar matrix (at least up to a moderate non-linear response stage) is represented through artificial local contacts. The determination of the modelling parameters in a continuum-based FE model, on the other hand, is seemingly more straightforward.

8.3.1 Lattice models

The concept of lattice models was initially introduced 70 years ago to provide an alternative to solving classical problems of elasticity (Hrennikoff, 1941). With the evolution of computing power from the late 1980s, lattice models have gained increasing popularity for modelling brittle failure in heterogeneous or disordered materials. Starting with the early continuum model named ‘numerical concrete’ by Wittmann and co-workers (Wittmann

et al., 1984), several mesoscale models have been proposed in subsequent years (Bazant *et al.*, 1990; de Schutter and Taerwe, 1993; Schlangen and van Mier 1992a; Schlangen and van Mier, 1992b; van Mier and Vonk, 1991) in an effort to simulate progressive failure in concrete.

Lattice models are characterized by a grid of truss or beam elements, generally in the form of triangular or rectangular shapes (Arslan *et al.*, 2002; Lilliu and van Mier, 2003; Schlangen, 1993; van Mier and van Vliet, 2003), which represent the continuous medium in a simplified manner. The use of beam elements enables the transfer of moments, axial and shear forces via the basic lattice elements.

When heterogeneity is to be simulated in the framework of lattice models, the geometry of aggregate shape may be superimposed on top of the mesh grid, thus defining different mechanical properties for the lattice elements falling respectively into the aggregate, matrix or interface domains, effectively mimicking the three-phasic nature of the composite. Alternatively, a lattice with variable (random) element length may be generated (Chiaia *et al.*, 1997; Man and van Mier, 2008). Although any aggregate shape could in principle be superimposed, circular (2D) or spherical (3D) shapes have been preferred in the literature, thus ignoring any aggregate angularity effect (Schlangen, 1993; van Mier *et al.*, 2002). Other variants of lattice models include, for example, that presented by Leite *et al.* (2004, 2007), where a stochastic-heuristic algorithm is developed for an improved generation of the three-dimensional concrete mesoscale structure with elliptical aggregates, making it possible to create aggregate contents as high as in real concrete. The system of lattice elements is then generated by projection onto the mesoscale structure, so that elements representing aggregates, mortar, and mixed aggregates and mortar (with possibility of including the interface properties) can be identified and properties allocated. All types of linear elements are available, e.g., truss and frame elements, for the lattice elements. Another approach is to simulate heterogeneity, while keeping a regular lattice grid, by means of random distributions of the properties of the beams, similar to the random distribution of material properties in a continuum framework, as will be described in Sections 8.6 and 8.7.

A commonly encountered issue in the lattice representation is an imperfect shape of the resulting stress–strain curves showing sharp drops due to element removal when a failure criterion is met, usually by a tensile strength limit. Moreover, the element removal strategy, which is usually employed to simulate cracking, does not account for possible crack closure, and does not guarantee consistent fracture energy consumption. It should be noted that the elastic properties of the composite strongly depend on the regularity of the lattice scheme (van Mier *et al.*, 1997), and may lead to problems such as a zero Poisson's ratio for a regular square lattice. A further point worth noting is that the lattice modelling method is intrinsically

discretization-dependent, similar to the behaviour of a standard continuum model when softening is involved.

8.3.2 Discrete element and discrete particle methods

The discrete element approach was first proposed in late 1970s for the study of granular geomaterials (Cundall and Strack, 1979). Such an approach models the material as a collection of rigid or deformable particles, assembled through contact and cohesion. DEM has been used extensively in the study of granular flow and joint rock mass problems (e.g., Ghaboussi and Barbosa, 1990; Omachi and Arai, 1988). More recently DEM has been extended to the study of heterogeneous quasi-brittle continua such as concrete, e.g., Donzé *et al.* (1999), Camborde *et al.* (2000), Azevedo *et al.* (2008), where the continuum behaviour is described through enhanced cohesion and bonds at the contacts. The advantage of DEM in modelling geomaterials apparently arises from its ability to adapt to problems involving fracturing and fragmentation and the associated discontinuities. However, the determination of the bond strength at discrete contact points in representing what is essentially a continuum interface makes the modelling parameters sensitively problem-dependent.

A similar feature of discretization in the modelling of a continuum solid was introduced for concrete by Bazant and his co-workers in their microplane series models (Bazant *et al.*, 1996; Zubelewicz and Bazant, 1987). In terms of the numerical analysis, the nature is similar to the lattice models, in the sense that in both cases the resulting system is a complex beam structure. However, herein each lattice node corresponds to the centre of one aggregate, while each beam represents the behaviour of the contact between two adjacent particles, resulting in a lattice particle system. Cusatis *et al.* (2003) extended the above framework by incorporating a confinement-shear lattice model for concrete damage. The confinement-shear lattice struts transmit not only axial forces (tension or compression) but also shear forces; in particular, the tensile and shear behaviours of the connecting struts are sensitive to the lateral confining pressure. This class of lattice particle model has also been used in the simulation of high loading rate problems, such as impact and penetration of concrete targets (Cusatis *et al.*, 2008).

8.3.3 Continuum (Finite Element) model

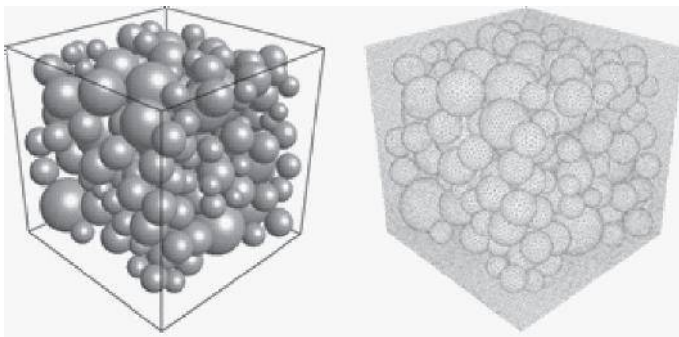
Mesoscale modelling of concrete using a continuum-based finite element framework allows for the multi-phasic but mesoscopically ‘continuous’ nature of concrete to be explicitly represented. One of the main advantages of these models is that they represent composite materials in a more

realistic fashion, considering continuum fields of the state variables outside the cracking zone. The evolving discontinuity due to fracture can be simulated by damage laws associated with the description of the constituent materials. Most of the early mesoscale models were actually developed in this framework (e.g. von Mier and Vonk, 1991; Wang *et al.*, 1999; Wittman *et al.*, 1984).

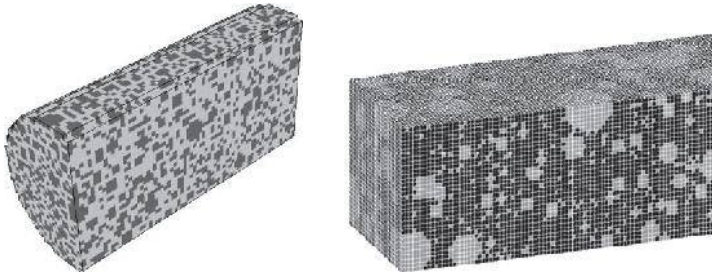
Generation of the meso-geometry and the FE meshing are the main challenges. A commonly adopted method for generation of the meso-geometry is the so-called take-and-place approach (or sometimes called a random sequential addition (RSA) method), and some forms of its variants (e.g. De Schutter and Taerwe, 1993; Eckardt *et al.*, 2004; Wang *et al.*, 1999). For simplicity, the ITZ phase is ignored in some cases (e.g., Eckardt *et al.*, 2004; Wriggers and Moftah, 2006). Van Mier and van Vliet (2003) presented the so-called random particle drop method to deal with a higher aggregate volume fraction. For 3D mesoscale models, simplified geometries with spherical or elliptical inclusions are often employed. Figure 8.3 shows a typical 3D model with spherical inclusions.

Alternative methods for the generation of a mesoscale geometry exist. Instead of a take-and-place approach, concurrent algorithm-based simulation (CAS) can be used, in which a structure of aggregates is generated with a dynamic DEM analysis. A special compaction technique can be used to generate a 3D densely packed structure which can be transferred to input for 2D finite element method (FEM) analyses (He *et al.*, 2011; He *et al.*, 2012).

For meshing of the mesoscale models, aligned meshing is the most widely used technique, in which the finite element boundaries are coincident with material interfaces and therefore there are no material discontinuities within the elements (Caballero *et al.*, 2006; Wang *et al.*, 1999; Wriggers and Moftah 2006; see also Chapter 4 of this book by Skarzynski and Tejchman). Some authors prefer unaligned meshing, in which material interfaces may be



8.3 Biphase spherical mesoscale model of concrete and FE mesh: 40% aggregate volume (after Wriggers and Moftah, 2006).



8.4 Bi-phasic mesoscale FE model (left: Dupray *et al.*, 2009; right: Riedel *et al.*, 2008).

positioned within a finite element (Zohdi and Wriggers, 2001). Additionally, structured (Caballero *et al.*, 2006) or non-structured meshing (typically based on a Delaunay triangulation, see e.g. Wang *et al.*, 1999) may be chosen. Non-structured meshes often yield a larger number of degrees of freedom for meshing the same geometry, increasing the computational cost.

Another category of mesoscale models makes use of the regular FE mesh but create the heterogeneity by joining adjacent elements to form aggregates in approximate shapes and following a certain size distribution. Dupray *et al.* (2009) used such an approach to create biphasic mesoscale models, where the size of aggregates followed a histogram (distribution) of six classes, as depicted in the Fig. 8.4a, left. Non-linear behaviour is allocated only to mortar, using an explicit damage-plasticity model. Similar biphasic mesoscale models have been used in some other studies e.g. Riedel *et al.* (2008) for shock response, Wriggers and Moftah (2006) for uniaxial compression, Akers and Phillips (2004) for contact detonation and Caballero *et al.* (2006) for tension and compression.

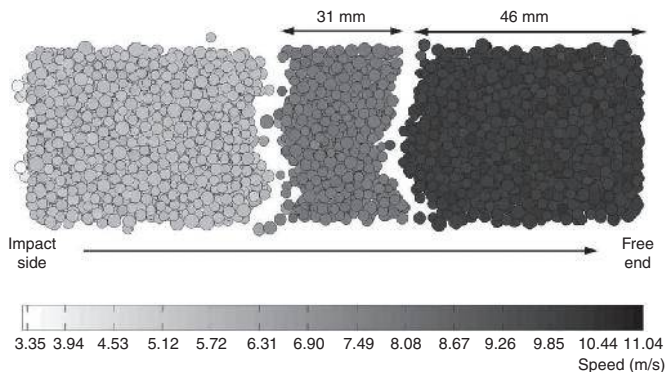
8.3.4 Applications of mesoscale models in high strain rate analysis of concrete

Mesoscale analysis of concrete for high strain rate loading poses additional demands due to the dynamic effects involved and the requirements for the constituent material models to be capable of accommodating the pressure and rate dependency.

Donzé *et al.* (1999) used a DEM model to study the compressive behaviour of concrete under high strain rate. Their numerical results clearly indicate that the compressive strength increases as the strain rate increases. As the model did not involve viscoelasticity, which was deemed by some researchers to be a possible explanation of the strain rate enhancement (e.g. Gopalaratnam *et al.*, 1996), the fact that their numerical results fit the

experimental data favourably could only be attributed to the dynamic structural effect, or more specifically the inertia as identified qualitatively in some earlier publications (e.g. Bischoff and Perry, 1991; Brace and Jones, 1971; Janach, 1976; Reinhardt and Weerheijm, 1991). In the DEM framework, the inertia effects will tend to locally oppose the opening of cracks, which is dependent on the loading time. This was confirmed by examining the propagation distance of the damage area, in that as the strain rate increases, the extent of the damage lessens. It was also observed that this damage is not homogeneous and tends to propagate inwardly from the lateral free surfaces of the specimen, thus forming a contact cone as seen in real experiments (Janach, 1976). Unlike quasi-static experiments where fracturing is well localized into narrow shear zones (Lockner and Moore, 1992), here the damage area appears to be more diffuse. Similar observations of the inertia effect on the dynamic strength increase under compression have also been made in a number of more recent studies, e.g. Nard and Bailly (2000), Li and Meng (2003) and Lu *et al.* (2009).

Using the same DEM approach, Henzt *et al.* (2004) carried out simulations of tensile Split Hopkinson Pressure Bar (SHPB) tests, at strain rates ranging from 36 to 70 s⁻¹. Without any changes in the model as used for the above-mentioned compression analysis, the tensile simulation did not show any strain rate enhancement as observed in the compression simulation. On the other hand, imposing an increase in the local tensile strength was observed to be sufficient to fit the experimental results. It was therefore argued that firstly the inertia alone cannot explain the increase of tensile strength in this range of strain rates, and secondly the rate sensitivity in tension is more a material-intrinsic effect. Figure 8.5 shows a simulated SHPB tension failure. As a matter of fact, the disassociation of the dynamic tensile strength increase with the structural



8.5 Simulation of direct tension with DEM: introducing the strain rate dependence in the contact-bond strength enabled the simulation to fit the experimental result well (after Henzt *et al.*, 2004).

effect was observed as well in several earlier studies using FE simulations (e.g. Hughes *et al.*, 1993; Ruiz *et al.*, 2000).

Cusatis *et al.* (2008) used an enhanced lattice-particle model in the simulation of the mesoscale behaviour of concrete for static as well dynamic loading. As briefly mentioned in the previous section, the computational algorithm of this model essentially follows the lattice framework, while the constitutive description of the lattice struts adopted the microplane model for brittle materials (Cusatis *et al.*, 2003).

Zhou and Hao (2008a, 2008b) conducted numerical studies of the compression and tension response of concrete under high strain rates using simple mesoscale models with spherical aggregates in 2D. The dominant inertia effects on the compressive strength enhancement, and the insensitivity of the tensile strength to the structural effect, were confirmed in their mesoscale simulations.

Lu and Tu (2008) developed a 2D mesoscale model framework to cater for general FE analysis under complex and dynamic loading conditions. The model is featured by random polygon aggregates with ITZ being represented by a thin layer of solid elements. To enable a realistic simulation of the 3D structural effect in the mesoscale model, which is deemed to be crucial in the strain rate effect in compression, a pseudo-3D scheme is proposed (Lu *et al.*, 2010). Details of this approach and the associated simulation results will be given later in Sections 8.4–8.6.

Brara *et al.* (2001) performed dynamic tension tests of concrete using Hopkinson bar apparatus in a spalling test setting. Tests were conducted on wet concrete specimens and the results demonstrated a DIF of tensile fracture ranging from around 4 for a strain rate of 20 s^{-1} to the order of 12 for strain rate of 100 s^{-1} . In conjunction with the experiment, a numerical simulation was conducted using a DEM model in which a cumulative fracture criterion was employed for the links between the particles. The criterion was based on some physical notion accounting for the thermally activated rate process, but effectively in a form with an explicit inclusion of the strain rate. Loading was imposed by an incident wave on the left-hand side of the specimen. The simulation was able to reproduce the dynamic response of the spalling specimens. A typical failure pattern is depicted in Plate XII (see colour section between pages 208 and 209).

Mahabadi *et al.* (2010) presented a numerical exploration study using combined FEM/DEM simulation for dynamic Brazilian test of rocks. The employed FEM/DEM is a hybrid model developed by Munjiza *et al.* (1999) in which individual discrete elements have FE mesh within themselves to handle the continuum deformation whereas the DEM capability allows for discontinuity to develop. As such, the model is actually subject to similar issues as in typical DEM models, in that the behaviour in the continuum stage is indirectly stimulated through equivalent contact systems. Such a

combined FEM/DEM is more relevant to the analysis of rock mass where the discontinuation is well defined while in the deformation within each intact rock block can be significant.

Zhu and Tang (2006) carried out a numerical simulation of the rock failure process in Brazilian disk tests. In the model used, the rock sample was discretized into fine mesoscopic elements in a finite element framework, and the heterogeneity was simulated by stochastic sampling of the material properties in accordance with the Weibull distribution. Strain rate dependence is considered in the material failure (strength) criteria.

In this book in Chapter 11, Pedersen *et al.*, presents a meso-scale model with the ITZ being modelled with separate continuum elements in combination with spherical and polygonal aggregates. The influence of loading rate and moisture content is investigated for Hopkinson bar tests. The major conclusion of this work is that the tensile strength of the ITZ is an important parameter which defines the global strength as well as the size of the fracture process zone.

8.4 A comprehensive mesoscale continuum model for the dynamic analysis of concrete

In this section, a comprehensive mesoscale model suited for analysis involving complex stress–strain and load conditions, including dynamic loading, is introduced with some necessary details to facilitate discussion on the pros and cons. The complete treatment can be found in Tu and Lu (2011). The procedure consists of three main processes namely: generation of the concrete mesoscopic structure, generation of the mesoscale FE mesh, and non-linear dynamic analysis. The mesoscale structure is composed of three phases, i.e., aggregates, mortar matrix, and the ITZ. The aggregates are created with 2D random polygon shapes following prescribed probabilistic shape and size distributions. For the modelling of the ITZ, two alternative approaches are examined, namely a cohesive interface model and an equivalent layer of solid elements model. The non-linear dynamic analysis is carried out using commercial dynamic analysis software, in the present case LS-DYNA (2007).

8.4.1 Generation of coarse aggregates

In normal concrete, the coarse aggregates are generally defined to consist of particles having a nominal size greater than 4.75 mm, and they occupy around 40–50% of the mixture volume (Wriggers and Moftah, 2006). In a 2D model, the volumetric proportion is represented by the area ratio. Actual aggregates may appear in different shapes depending on their source of origin; the naturally formed gravels tend to have a rounded shape, while crushed stone

aggregates have an angular or polygonal shape. In the present study, we shall consider mainly the polygon-shaped aggregates. Other special shapes, such as round or elliptical, are relatively simple to generate, and they may also be approximated by polygons with specially chosen shape parameters.

Different size distributions may be considered. Herein the Fuller curve is employed,

$$P(d) = 100.0 \times (d/d_{\max})^n \quad [8.1]$$

where P is the volume percentage of aggregates below size d , d_{\max} is the maximum size of the aggregate particle. The exponent n generally takes a value in the range of 0.45–0.70.

In the numerical simulation, the grading curve expressed in Equation [8.1] can be discretized into a predefined number of segments (denoted by i_{\max}), each covering a size range of $[d_i, d_{i+1}]$. Thus the amount of aggregates within each grading segment is:

$$A_{a,i} = \frac{P(d_{i+1}) - P(d_i)}{P(d_{\max}) - P(d_{\min})} \times A_a \quad [8.2]$$

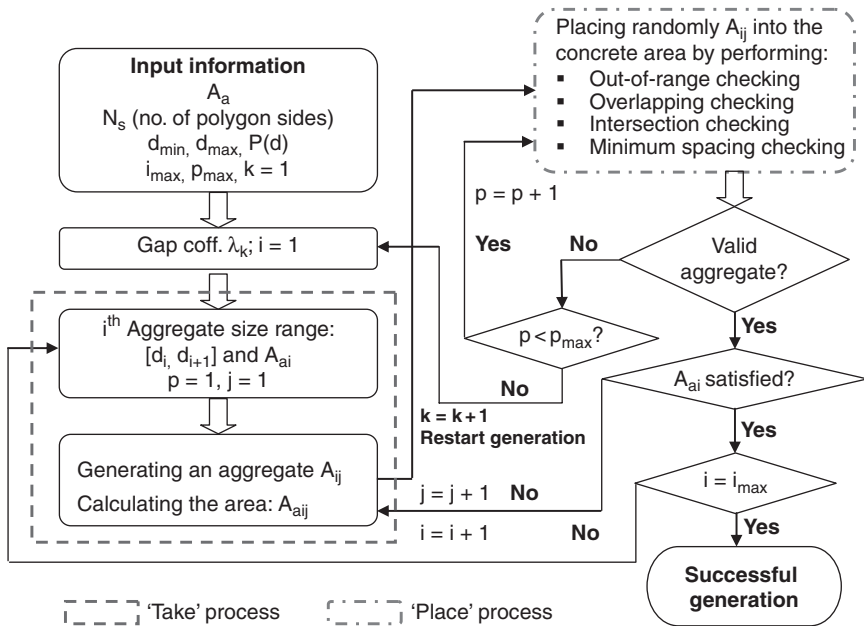
where A_a is the total amount (area) of aggregates in concrete.

The generation of the random geometry of aggregates is implemented using the commonly adopted take-and-place method. In this procedure, the ‘take’ process generates each time an individual aggregate in accordance with the random size and shape descriptions in the local coordinate system. The ‘place’ process subsequently positions the aggregate into the predefined concrete area, ensuring a rational separation with aggregates that are already placed in the domain. Figure 8.6 shows a flowchart of the procedure, which is programmed herein using MATLAB. The take-and-place process is executed in a sequential manner, starting with the largest aggregate size group $[d_1, d_2]$ (for easy packing), and carrying on until the smallest size group is completed.

8.4.2 Generation of FE mesh

Meshing of the mesoscopic structure of concrete is a classical challenge. With the availability of advanced meshing techniques in the latest commercial FE codes, this task is made much simpler and faster. Herein we employ the ANSYS pre-processor (2011) to perform meshing of the random 2D mesoscale structure.

Let A_c denote the spatial domain of a concrete sample, A_a the collective area of the aggregates (with A_a^i being i_{th} aggregate), and A_m the area not occupied by the aggregates. A_m is actually a complex multi-connectivity region. A_m can be generated by applying the well-known ‘overlapping’



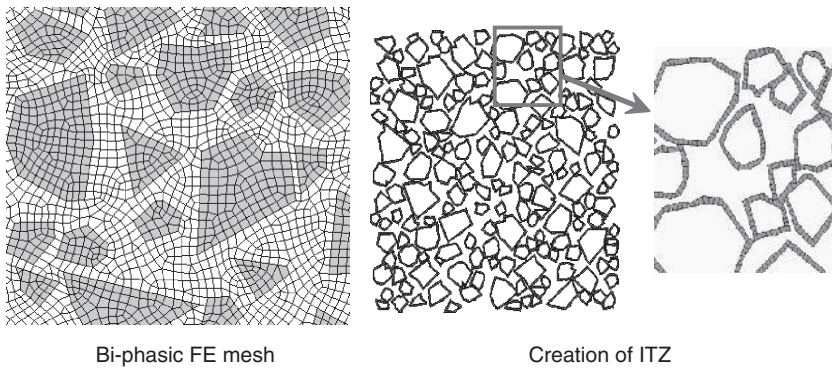
8.6 Flowchart of generation of polygonal aggregates and meso-geometry in 2D.

Boolean operation between all A_u^i and the entire concrete area A_c . A two-phasic mesh is thus generated. This mesh would have originally shared nodes at the interface between the two materials. If the ITZ surrounding the aggregates is to be modelled explicitly, for example by zero-thickness interface elements such as the Goodman model (Kwan *et al.*, 1999), a duplicate set of nodes can be created at the interface locations. An alternative way of modelling the ITZ is to use a thin layer of solid elements having grossly equivalent properties as the ITZ. This approach avoids the use of the zero-thickness elements and hence does not require a duplicate set of nodes at the interface.

Figure 8.7 shows an example of the mesoscale mesh for concrete. The mesh data can then be exported, herein to MATLAB, to finish with the model input data as required by the chosen FE analysis solver for the onwards non-linear dynamic analysis.

8.4.3 Material models and other numerical considerations

The evolution of damage in normal concrete at the mesoscale is largely governed by local fracture in mortar and ITZ, while aggregates generally



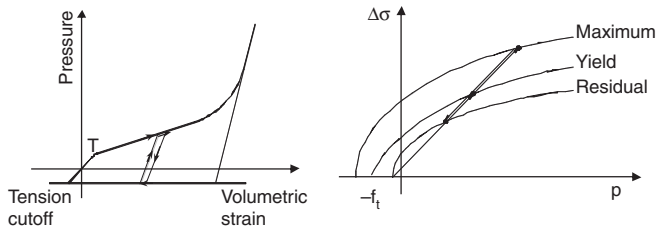
Bi-phasic FE mesh

Creation of ITZ

8.7 Illustration of FE mesh for mesoscale model of concrete.

remain elastic under quasi-static loading. From this point of view, aggregates may be modelled simply as an elastic material with a Young's modulus and Poisson's ratio suitable for the type of aggregates considered. It should be pointed out that in the high strain rate regime aggregates may respond to a much higher stress level than the mortar matrix due to the propagating wave effect, and for this reason an appropriate damage model may have to be employed for a realistic representation of the aggregate responses. The need for a sophisticated damage model for aggregates may be verified by examining the stress level that may be mobilized in the aggregate phase for a particular loading condition.

Mortar is considered to have similar properties to the bulk (macro) properties of concrete; however, it has a smaller 'representative volume' due to the finer grain size, and this has implications when it comes to the choice of the characteristic length (affecting fracture energy) for the mortar elements. ITZ, on the other hand, is the least known phase, and large uncertainties are expected to be associated with its mechanical properties. It is generally understood that the real ITZ has a thickness in the range of 20–50 μm (e.g. Scrivener *et al.*, 2004), and its mechanical properties are different from the cement paste. It is generally found that, as the ITZ bond strength increases, the strength of concrete also increase, whether in tension, flexure or compression (Mindess *et al.*, 2002). Whereas cracking in tension is expected to be dominated by the actual ITZ, the boundary between ITZ and mortar becomes blurred when concrete is under compression due to the complex stress state in the interfacial region. This phenomenon supports the adoption of an equivalent layer of solid elements as the representation of the ITZ. This approach will not have a sensitive effect on the tension behaviour as compared to the use of some interfacial link elements, but is deemed to improve the model behaviour under compression in which complex stress conditions develop at the ITZ regions. When an equivalent layer of solid



8.8 Compaction curve (left) and three strength surfaces (right) of the Concrete Damage Model.

element is employed to represent the ITZ, the material model as used for mortar may be sufficient, with however a discounted strength. Man and van Mier (2008) adopted a layered ITZ approach in their study of the size effect on strength and fracture energy using lattice beam model, where the ITZ is represented by a layer of beam elements connecting the aggregate and the mortar lattice beam elements.

In much of the previous mesoscale modelling studies, relatively simple material models have commonly been used to simplify the modelling requirements. Nowadays, many comprehensive and advanced constitutive models are available in general purpose finite element analysis codes for describing the quasi-brittle behaviour of concrete-like materials (see, e.g., Tu and Lu, 2009). Herein we employ the Concrete Damage Model (Malvar *et al.*, 1997, 2000) to model mortar and the equivalent ITZ. This material model is capable of describing the material failure due to tension, shear, as well as compression under various stress conditions, and it also includes pressure and strain rate dependent features.

The basic considerations in the Concrete Damage Model follow the classical damage-plasticity framework. The total stress is uncoupled into an isotropic and a deviatoric part. The isotropic behaviour is controlled by a compaction curve relating the current pressure to the current and previous compressive volumetric strain, and the deviatoric stress is defined as a linear combination of failure surfaces based on a three-invariant formulation. Figure 8.8 depicts the compaction curve, and the three strength surfaces, namely an initial yield surface, a maximum failure surface and a residual surface. The general strength criterion is given by a uniform expression as:

$$\Delta\sigma = \sqrt{3J_2} = f(p, J_2, J_3) \quad [8.3]$$

where $\Delta\sigma$ and p denote the principal stress difference and pressure, respectively. J_2 and J_3 are the stress invariants. In the principal stress space, the meridian of the strength surface is governed by $f(p, J_2, J_3) = \Delta\sigma^c \times r'$, where $\Delta\sigma^c$ represents the compressive meridian and r' is a function of the Lode

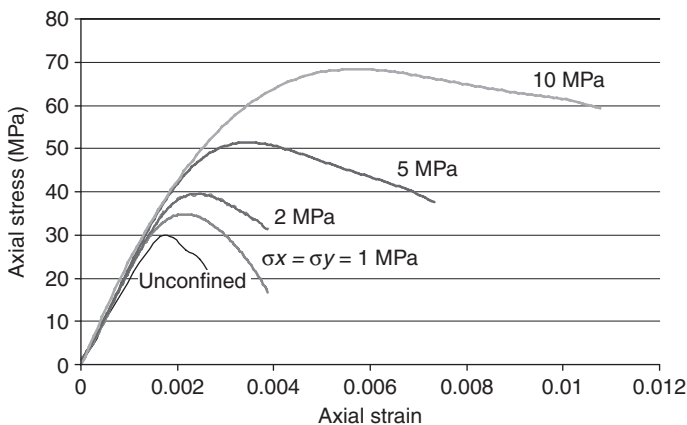
angle. The compressive meridians of the three strength surfaces have a similar form as:

$$\Delta\sigma = a_0 + \frac{p}{a_1 + a_2 p} \quad [8.4]$$

where a_0 , a_1 and a_2 are free parameters. For the failure surface, $a_0 = 0$. Thus, for the three failure surfaces eight free parameters need be determined, based on experimental data.

The loading path after yield is defined by interpolation between the respective strength surfaces. The development of non-linearity is controlled by a variable called yield scale factor η , which in turn is determined by a damage function λ . Different damage evolution in tension and compression is realized by different definitions of the λ function. For typical classes of concrete, recommended specifications of these parameters can be found from relevant literature (e.g., Malvar *et al.*, 1997) and an automatic generation option is available (Malvar *et al.*, 2000).

Considering the critical importance of the model in representing the pressure-confinement effect in the dynamic response of concrete under high strain rate loading, the model is examined extensively in this regard using a single-element setting. Figure 8.9 shows the axial compressive stress-strain curves for 30-MPa concrete under four different levels of the confining stresses, namely 1, 2, 5 and 10 MPa, respectively. It can be observed that the achieved compressive strength and ductility increase with the increase of the lateral confining stress. The trend agrees well with general experimental observations.



8.9 Single-element analysis of the axial compressive stress-strain curves under different levels of lateral confining stress.

For the strain rate enhancement in the material strength, the model implements a radial rate enhancement on the failure surface. It is possible to use different rate enhancements for tension and compression, respectively, and the enhancement option can be turned on or off as required.

As always is the case in a finite element analysis with a local material description, numerical localization will inevitably occur when softening is involved, leading to mesh sensitive results. In the Concrete Damage Model, a length scale is introduced for the stress-softening related parameters to be adapted to enable the preservation of the fracture energy when softening localization happens, such that:

$$\int_0^{\varepsilon_{\max}} \sigma d\varepsilon = G_f / h_c \quad [8.5]$$

where G_f is the fracture energy per unit area, h_c is the characteristic dimension of the element. In addition, the model introduces a user-defined localization width ' l_w ' to enable another layer of control over the fracture energy, such that in situations where the localization in the FE model may deem to span more than one element due to particular stress conditions, ' l_w ' may be set to the anticipated width instead of equating h_c to ensure that the fracture energy within ' l_w ' would be equal to the total G_f .

When an equivalent layer of solid elements is employed to represent the ITZ, the mechanical properties of such an ITZ layer may reasonably be assumed to resemble those of mortar with however a reduced strength. Therefore, two basic variables need to be decided: (a) thickness of the equivalent layer and (b) strength reduction. Due to the tiny thickness of the real ITZ, it is neither practical nor necessary for the equivalent layer to match the real thickness of the ITZ. A rigorous approach to the selection of the equivalent layer thickness may require a sensitivity analysis as to how the thickness would affect the results under a particular loading condition. Provided the mesh resolution is sufficiently fine, which would normally be required to deal with the mesh irregularities associated with the random aggregate shapes, for example at 1/10th of the nominal aggregate dimension, it is reasonable to simply use a single layer of mortar elements immediately surrounding each aggregate as the ITZ, as indicated in Fig. 8.7. The equivalent properties can then be assigned to these ITZ elements and calibrated. In the present analyses the mesh resolution is typically at 1/10th of the nominal size of the aggregates, namely 0.5 mm for the 50 mm specimens and 1–2 mm for the 150 mm specimens, the equivalent ITZ layer has thus been at these thicknesses for 50 mm and 150 mm specimens, respectively. Considering that the strength of the real ITZ would be around 50% of the mortar, and that the equivalent ITZ layer is a combination of the real ITZ and a slice of mortar, it is reasonable to assume a reduced strength to be about 75% of the mortar strength for the equivalent ITZ. Calibration results

under a variety of loading conditions indicate that the above properties for the equivalent ITZ provide consistent and comparable overall results with relevant experimental data. It is also useful to note that the results are not very sensitive to further refinement of the equivalent ITZ thickness (e.g. from 1 to 0.25 mm in the 50 mm specimens).

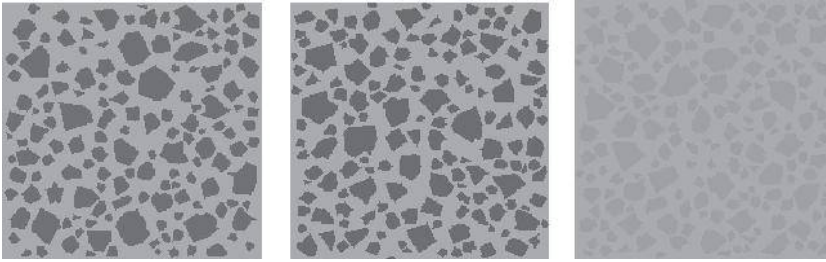
In the mesoscale model, the ITZ elements must be identified out of the mortar phase first. A convenient approach to doing this is to use a 'selecting elements by path' function which is available in ANSYS and other FE pre-processing tools. To pick out elements surrounding an aggregate, the path can be defined effectively by a polygon which is a slightly expanded version of the actual aggregate. Such paths can be conveniently generated during the creation of the aggregates in the take-and-place procedure.

The option to use zero-thickness interface elements for the modelling of ITZ in a general ITZ model depends, understandably, upon the capacity of the interface elements in catering to complex stress conditions. A classical cohesive model, as available in LS-DYNA (2007), is suited for modelling the interface failure involving interaction between mode I and mode II fractures. When the element is subjected to compression, the model implements a penalty algorithm to work out a repulsive force to avoid inter-node penetration. Such cohesive elements prove to work well under tension-dominated loading, but perform poorly when the specimen is subjected to compression, as will be shown in Section 8.4.4.

In the mesoscale model, the process of fracture initiation and coalescence will manifest as severe local non-linearity and material degradation, and this can create considerable numerical difficulty in achieving a converged solution if an iterative non-linear solution approach is adopted. For this reason, and in view of an accommodation for dynamic analysis, an explicit time integration approach is adopted in solving the non-linear quasi-static and dynamical response, while elements with a single integration point are employed. The use of this type of elements helps to avoid the numerical problems that could occur in fully-integrated elements in case of large deformations, for instance shear locking and solution instability. However, such elements can be susceptible to the problem arising from the so-called 'hourglass' modes. For a full discussion about the numerical considerations related to the integration scheme and the hourglass control, readers are referred to Tu and Lu (2011).

8.4.4 Validation of the model and the influence of non-homogeneity in mortar and aggregates on the bulk concrete behaviour

The above described mesoscale model is validated firstly under quasi-static loading, and the results are compared with experimental observations.



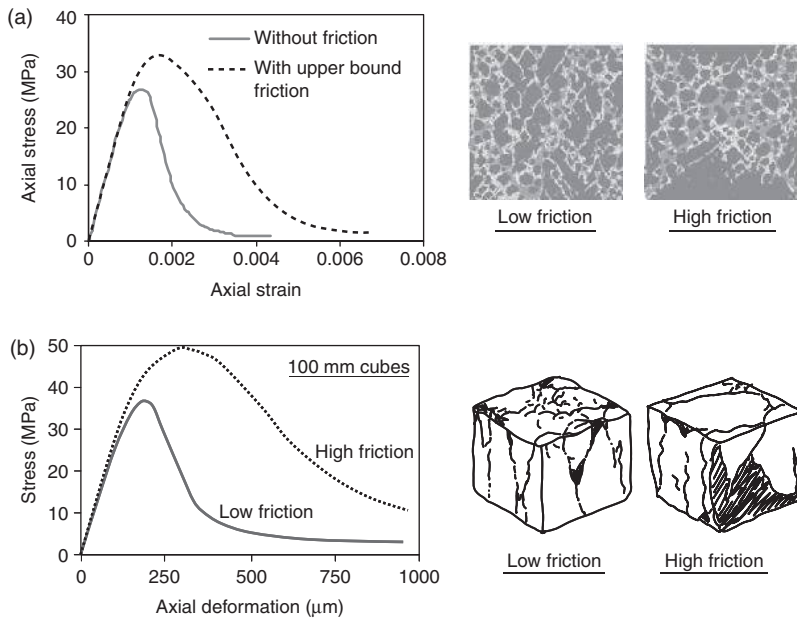
8.10 Typical samples of aggregate distribution (overall specimen size 150×150 mm).

2D mesoscale models are firstly created for 150×150 cubic specimens in a plane stress condition. Figure 8.10 depicts a few samples of the created mesoscale geometries. The specimens are subjected to axial compression which is imposed by applying displacement on the top end while the bottom end is fixed in the loading direction. Two different lateral constraints are imposed on the top and bottom faces, i.e., free sliding and fully confined, to represent the lower and upper bounds of the frictions between the specimen and the loading platens as in a physical experiment. The target compressive strength is set at 30 MPa, for which mortar is assigned a strength of 35 MPa, and the equivalent ITZ has a reduced strength of 27 MPa.

Figure 8.11a shows the achieved nominal compressive stress–strain curves, along with the fracture patterns. For a comparison, a set of experimental results is shown in Fig. 8.11b. As can be seen, the computed stress–strain curves and the damage patterns agree favourably with the experimental observations.

By way of verification, the sensitivity of the overall specimen response to the detail of a sample set of aggregates and to the randomness of the mechanical properties within the mortar and ITZ phases, respectively, are evaluated. The randomness of the properties within the mortar and ITZ phases are simulated by a random distribution of the properties within the collection of mortar and ITZ elements, respectively, in accordance with a prescribed probability distribution. As shown in Fig. 8.12, the influence of the randomness in the detailed aggregate geometry and in the properties within the mortar and ITZ is found to be limited mainly in the softening branch of the response. These results suggest that, comparing to the meso-heterogeneity with the three distinctive phases of aggregate, mortar and ITZ, the randomness within each phase plays a secondary role in affecting the overall behaviour of the specimens and hence may be neglected. In all subsequent analyses, the properties for the mortar elements and ITZ elements are assumed to be homogeneous.

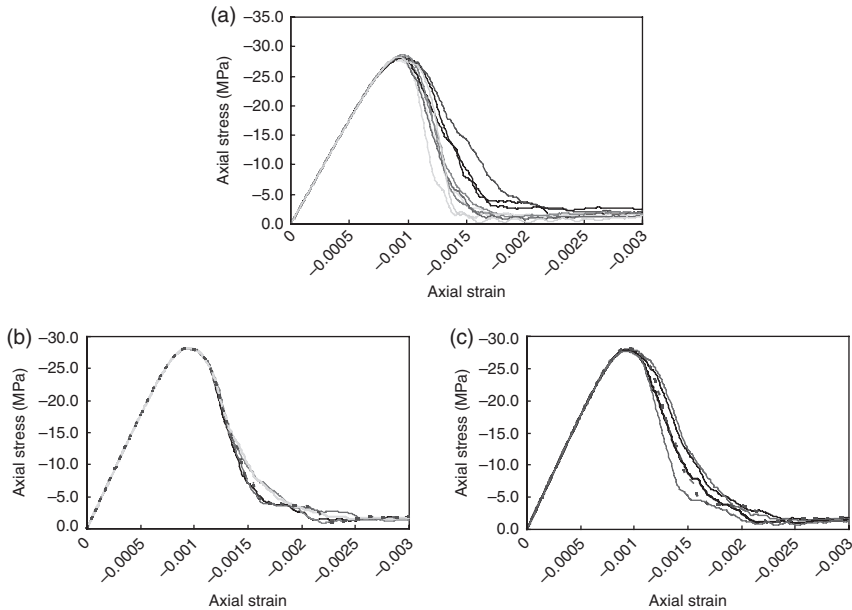
The behaviour of the above mesoscale model is also examined under uniaxial tension. For the grade 30 MPa concrete under consideration, the direct



8.11 Mesoscale simulation results under quasi-static compression and comparison with typical experimental observations (friction low/high refers to friction between specimen and loading platens).

tensile strength is expected to be around 2.5 MPa. A similar displacement controlled loading scheme as in compression is employed. A typical simulated fracture process of concrete under uniaxial tension is depicted in Plate XIIIa (see colour section between pages 208 and 209). The corresponding tensile stress-strain curve is shown in Plate XIIIb.

It can be observed that at the peak stress, numerous micro-cracks have developed and are located mostly in the mortar aggregate interface zones. As the strain increases, concentrated macro-cracks start to emerge, and this brings the specimen into the softening stage. Because of the stress relief, unloading and recovery of the elastic deformation takes place in areas outside the strain localization regions. The majority of micro-cracks that have developed earlier cease to open further (i.e. no further increase in the tensile damage). As the applied extension further increases, the concentrated macro-cracks propagate transversely, cutting through the mortar aggregate interface regions, and eventually coalesce to form virtually a single major crack across the entire width of the specimen. The entire simulated fracture process is in good agreement with experimental observations (Gopalaratnam and Shah, 1985; Ueda *et al.*, 1993).

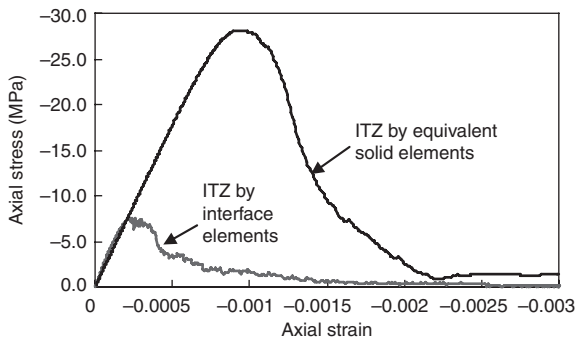


8.12 Sensitivity of compressive behaviour to randomness in aggregate arrangement and non-homogeneity within mortar and ITZ phases.

(a) Different samples of aggregate geometry, (b) randomness within mortar and (c) randomness within ITZ.

Shown in Plate XIIIb is also the computed tensile stress–strain curves when the ITZ is modelled using the interface cohesive model. The result is almost identical with that obtained using the equivalent solid layer of ITZ. However, as mentioned earlier, the use of the cohesive elements becomes problematic when the interface is subjected to complex stress conditions, and this is evidenced from the results when the model is subjected to compression, as illustrated in Fig. 8.13. The mesoscale model with cohesive ITZ elements fails to produce a realistic compressive response of concrete, while the model using the equivalent ITZ scheme shows a superior performance.

The poor performance of using the cohesive interface element may largely be attributable to the inability of this element in representing the shear fracture strength of the ITZ under a compressive stress condition. As generally known, the shear fracture strength of the ITZ in concrete-like materials is strongly dependent on the normal stress at the interface. With the presence of a compressive stress, the shear strength is expected to increase significantly, for example by 2–3 times at a moderate compressive stress level (Nagai *et al.*, 2005). Unfortunately, this important mechanism is not well represented in a general cohesive material model as used herein.



8.13 Compressive stress-strain curves produced by mesoscale model with two different ITZ schemes.

8.5 A pseudo-3D (sandwich) mesoscale model for the dynamic analysis of concrete in compression

The 2D mesoscale model proves to perform well under quasi-static compression and tension. Considering the significance of the 3D structural effects, in particular the inertia effect, in the response of concrete under high strain rate loading, it is necessary to address the simulation of the 3D effects before the mesoscale model may be reliably applied in the dynamic analysis. In this section a pseudo-3D mesoscale model (Lu *et al.*, 2010) is discussed.

8.5.1 Model configuration

In lieu of a true 3D mesoscale model, which would be considerably more complex in terms of the mesoscale geometry and the FE mesh when polygon aggregates are involved, herein we employ a pseudo-3D model configuration on the basis of the above 2D mesoscale model. The key purpose of such a pseudo-3D model is to facilitate the development of a realistic 3D inertia effects as in a real 3D environment, while allowing the full mesoscale features to be represented within the primary mesoscale part of the model.

At this juncture, it may be worth commenting briefly on the option of an axisymmetric model. From a global perspective a concrete cylinder under axial loading may be treated as an axisymmetric problem, and thus may simply be modelled using a 2D axisymmetric model. However, this treatment cannot be extended to the case of mesoscale modelling, since with an axisymmetric model, the aggregates effectively become continuous circular hoops, which obviously do not represent the true effect of the discrete aggregates.

A sandwich layout can be well suited to achieve the desired 3D effects. Such a configuration is composed of a layer of the plane mesoscale model and a body of the homogeneous concrete material, thus forming a complete 3D specimen shape. The mesoscale layer is sandwiched in the homogeneous concrete, and a sliding interface is enabled between the mesoscale layer and the homogeneous part of the model. In this way, the mesoscale layer will deform independently within its own plane, as in the case of a 2D mesoscale model, while in the direction normal to the plane it will be subjected to the confining stress from the homogeneous body of concrete. Provided the properties of the homogeneous portion of the model resemble the bulk properties of concrete, the lateral inertia effect on the sandwiched mesoscale layer in the normal direction should be similar to that in a true 3D mesoscale model. Consequently, the behaviour of the mesoscale portion within its plane should closely resemble what happens in a true 3D mesoscale model. The effectiveness of such a pseudo-3D model configuration will be illustrated in the following sections.

For a cubic specimen, a pseudo-3D mesoscale model can be set up by sandwiching the mesoscale model (plate) into the middle of a homogeneous cube. Considering the symmetry, only half of the cube is required in the analysis, as shown in Plate XIV (see colour section). For a 50 mm cubic specimen, the halved model will consist of a $50 \times 50 \times 24$ mm homogeneous portion, and a $50 \times 50 \times 1$ mm mesoscale portion. The symmetrical condition is imposed on the outer face of the mesoscale portion.

Plate XV (see colour section between pages 208 and 209) shows a typical stress contour in the above sandwich model. The overall stress contour shows a clear resemblance of the 3D effect, while the essential mesoscale features are maintained in the mesoscale part of the model.

For the modelling of a cylindrical specimen using the concept of the pseudo-3D mesoscale model, a cylinder shaped sandwich configuration is appropriate. With the consideration of symmetry, a half-cylinder model with a layer of mesoscale model attached to the symmetrical plane will suffice, as shown in Plate XIV (see colour section between pages 208 and 209). To save the computational cost, without affecting the accuracy, the mesh size in the homogeneous portion may be made coarser. For the mesh shown in Plate XIV, the total number of elements is around 40 000, which is just about four times the number in the 2D mesoscopic model.

The effectiveness of the above sandwich model for cylinder specimens is verified by comparing the general development of damage with a comparative 3D homogenous model, as illustrated in Plate XVI (see colour section between pages 208 and 209).

It can be observed that the overall damage patterns agree well between the two models. Damage is initiated from the loading side and propagates towards the support end. The central zone of the specimen exhibits considerably less damage than the outer region, indicating a significant confining

effect. Besides, damage in the mesoscale model shows a clear effect of the aggregates, with the damage in the ITZ region occurring first on the loading side and then developing around the aggregates.

A further check is made with regard to the influence of the mesoscale layer thickness on the simulated strength in the mesoscale part of the model. Three different thicknesses were analysed, namely 0.5, 1.0 and 2.0 mm. Results indicate the variation of the strength is well within 2%, indicating good stability in this respect.

8.5.2 Mesoscale analysis of strain rate effect in dynamic compression

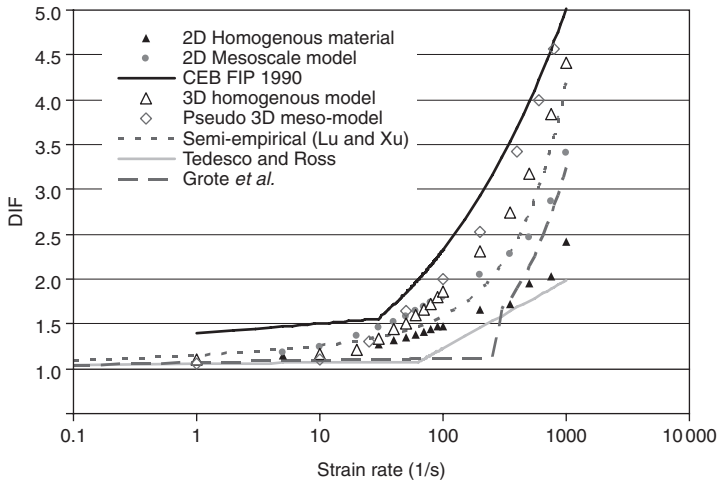
With the above pseudo-3D mesoscale, a series of calculations were carried out to examine the variation of the apparent compressive strength of concrete with the increase of the strain rate. For a comparison, a 2D mesoscale model, a 2D homogeneous model and a 3D homogeneous model are also analysed for the same variation range of the strain rate. To observe the dynamic structural effect, in all these models no embedded strain rate enhancement factor is considered in the properties of the constituent materials. From the simulation results, the DIF is calculated as the ratio between the nominal strength under the dynamic compression and that under a quasi-static compression. The nominal dynamic strength is obtained from the average stress on both the loading and supporting faces. This effectively resembles the ‘three-wave’ approach in standard SHPB tests. It should be worth noting that the adequacy of such an approach under a very high strain rate regime can be questionable, as will be discussed in Section 8.5.3. For the pseudo-3D mesoscale model, only the sandwiched mesoscale portion is considered in the above evaluation of the dynamic strength.

Figure 8.14 shows the variation of the DIF with the strain rate from the above numerical experiments. Shown in the figure are also four empirical curves for comparison, namely:

i) CEB-FIP DIF model (CEB, 1993):

$$DIF = \begin{cases} (\dot{\epsilon} / \dot{\epsilon}_s)^{1.026\alpha_s} & \text{for } \dot{\epsilon} \leq 30 \text{ s}^{-1} \\ \gamma_s (\dot{\epsilon} / \dot{\epsilon}_s)^{1/3} & \text{for } \dot{\epsilon} > 30 \text{ s}^{-1} \end{cases} \quad [8.6]$$

where $\dot{\epsilon}_s = 30 \times 10^{-6} \text{ S}^{-1}$ (static strain rate), $\log \gamma = 6.156\alpha_s - 2$, $\alpha_s = 1 / (5 + 9f_{cs} / f_{c0})$, f_{cs} is static compressive strength, and $f_{c0} = 10 \text{ MPa}$.



8.14 Compression DIF from numerical experiments comparing to empirical formulas.

ii) Empirical model by Tedesco and Ross (1998):

$$DIF = \begin{cases} 0.00965 \log \dot{\epsilon} + 1.058 \geq 1.0 & \text{for } \dot{\epsilon} \leq 30 \text{ s}^{-1} \\ 0.758 \log \dot{\epsilon} - 0.289 \leq 2.5 & \text{for } \dot{\epsilon} > 30 \text{ s}^{-1} \end{cases} \quad [8.7]$$

iii) Empirical model by Grote *et al.* (2001):

$$DIF = \begin{cases} 0.0235 \log \dot{\epsilon} + 1.07 & \text{for } \dot{\epsilon} \leq 266.0 \text{ s}^{-1} \\ 0.882 (\log \dot{\epsilon})^3 - 4.40 (\log \dot{\epsilon})^2 + 7.22 \log \dot{\epsilon} - 2.64 & \text{for } \dot{\epsilon} > 266.0 \text{ s}^{-1} \end{cases} \quad [8.8]$$

iv) A regression model derived from semi-empirical data in Lu and Xu (2004):

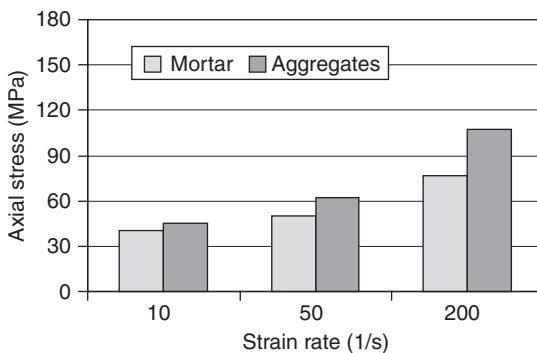
$$DIF = \begin{cases} 1 + 0.15 \dot{\epsilon}^{0.2} + 0.0013 \dot{\epsilon}^{1.1} & \text{for compression} \\ 1 + 1.505 \dot{\epsilon}^{0.295} & \text{for tension} \end{cases} \quad [8.9]$$

It should be noted that the dimension of the concrete specimen (50 mm) in the numerical experiment is adequate for strain rates up to about 100 s^{-1} . The simulations in the higher strain rate range do not satisfy the stress equilibrium and strain uniformity requirements for the size of the specimen,

therefore the DIF results in this range may be considered for a reference purpose only. Further discussion in this regard will be given in Section 8.5.3.

Based on the results shown in Fig. 8.14, the following observations may be drawn: (1) all the models exhibit a significant increase in the nominal compressive strength as the strain rate increases, despite that no strain rate enhancement has been considered at the material constitutive property level, and all the simulated DIF curves resemble the general trend as given by the empirical formulas; (2) the lateral inertia confinement effect, as demonstrated from the results using the homogeneous models, is shown to be a major contributor to the observed DIF. It is noteworthy that, due to a lack of realistic representation of the lateral inertia confining effect, the 2D homogeneous model markedly underestimates the DIF in the specimen; (3) the mesoscale heterogeneity proves to also play a sensible role in the total DIF, especially in the high strain rate regime. The results from the pseudo-3D mesoscale model appear to be consistent with the results from the 3D homogeneous model, indicating an effective incorporation of the 3D confining effect. Compared to the 2D mesoscale model, the results from the pseudo-3D model shows a further increase in the DIF.

To further illustrate the magnitude of contribution from the material heterogeneity, Fig. 8.15 depicts the proportion of the stresses that are developed in the aggregates as compared with the stress in the mortar matrix as the nominal strain rate increases. It can be clearly observed that, while the stress distribution is grossly uniform up to a strain rate of 10 s^{-1} , the stress in the aggregates is about 20% higher than in the mortar at a strain rate of 50 s^{-1} , and it further increases to about 30% under a strain rate of 200 s^{-1} . Considering that the volume ratio of aggregates is at around 50%, an increase in the aggregate stress will manifest sensitively as an increase in the overall strength, and hence contributing to the increase of the DIF.



8.15 Variation of peak stresses in mortar and aggregates with increase of strain rate.

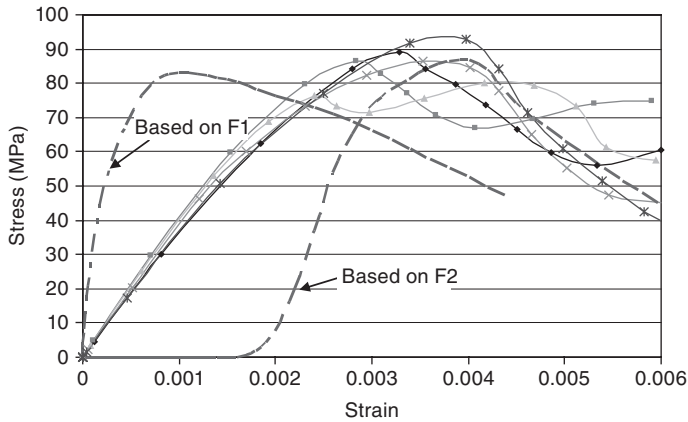
8.5.3 The strain rate limit of concrete in the SHPB compression test and its implications for the interpretation of test data

Another issue that potentially has a great implication on the interpretation of high strain rate results from SHPB type of tests is the strain rate limit, which sets an upper bound if reasonable stress uniformity is to be achieved for a given size of test samples. It is generally accepted that 3–4 stress reverberations are required in an SHPB test for the establishment of a relatively uniform stress state. Accordingly, an upper limit strain rate can be established for a given specimen of length as:

$$\dot{\epsilon} = \frac{\epsilon_f}{t} < \frac{\epsilon_f c_0}{n l_s} \quad [8.10]$$

where l_s is the length of the specimen, ϵ_f denotes the failure strain, c_0 is the acoustic wave speed, and $n \geq 3$. To give an example, for a 30 MPa concrete specimen of 50 mm length, the strain rate limit according to the above formula is roughly about 50 s^{-1} . This means for tests beyond such a strain rate limit, either a shorter specimen needs to be used, or stress non-uniformity at failure would occur, rendering the corresponding test results questionable. As a matter of fact, numerous existing tests in the literature did not strictly satisfy such a strain rate limit requirement.

In a recent study by Song and Lu (2011), the development of stress and the progressive failure in a concrete cylinder under very high strain rate compression is scrutinized. A few key findings are summarized in what follows. Artificially dividing the 50 mm length of a specimen into five sequential strips along the loading direction, the developing stress distributions can be examined in detail as the stress wave propagates and reverberates between the two ends of the specimen. Plate XVII (see colour section between pages 208 and 209) shows the time histories of the axial stresses in the five individual strips for a nominal strain rate of 50 s^{-1} and 200 s^{-1} , respectively. As can be clearly observed under the strain rate of 50 s^{-1} , a relatively homogeneous stress state is attained throughout the entire specimen before the maximum stress is reached. In contrast, damage and failure develops in a layer by layer fashion under the strain rate of 200 s^{-1} . It is noteworthy that, despite the progressive failure pattern, the maximum stress developed in each individual layer does not differ significantly. This implies that using the nominal stress either on the incident front or on the transmitter end can reasonably represent the bulk strength of the specimen, as illustrated in Fig. 8.16. Moreover, because of the considerable non-uniformity in the strain distribution within the specimen, such that part of the specimen is still unstrained while the front layers fail, it would be hard to estimate the actual local strain from the velocities inferred



8.16 Stress–strain curves inferred from three different wave approaches in comparison with actual curves within individual strips. Nominal rate = 200 s^{-1} . F_1 = force on incident face. F_2 = force on transmission face.

from the two end faces; averaging out the velocity over the specimen length will obviously under-predict the local strains and hence can cause inflated Young's modulus. An appropriate correction would be required on the nominal strain before it could be used in an estimation of the Young's modulus.

8.6 Mesoscale modelling of the tensile behaviour of concrete in dynamic splitting (Brazilian) tension

Splitting tests in a Brazilian disk configuration are commonly used in determining the tensile strength of concrete-like materials under quasi-static loading. This technique has also been extended to high strain rate tests using an SHPB apparatus. The basic premise of this extension stems from the assumption that an equilibrium condition similar to that under static loading can be established in the dynamic test before the test specimen reaches the tension failure. Such a condition would effectively impose a strict rate limit, beyond which readings from the SHPB splitting tests would not be valid for the inference of the tensile strength. This requirement is recognised in the literature but unfortunately has not always been observed in the past experiments, especially in the high strain rate regime. In this section, some recent numerical simulation studies using both homogeneous and meso-scale models will be introduced. The issues to be examined include the transition of the stress conditions from relatively low to high strain rate regimes, the significance of the structural effect in the apparent tensile strength of concrete, as well as the contribution of the mesoscale heterogeneity in the dynamic tensile strength enhancement.

8.6.1 A brief review of numerical studies on Brazilian tests

There is a large body of literature concerning the experimental aspects of the dynamic Brazilian tests, which will not be discussed here. However, it is useful to provide a quick overview of some previous numerical studies using a Brazilian set-up to investigate the dynamic responses of the specimen.

Hughes *et al.* (1993) performed FE analysis of high strain rate splitting tensile tests. They examined the splitting stress distribution. By increasing the tensile strength (cut-off) in the material model to an appropriate value, the FE results match well the experimental data for a given stress (strain) rate; therefore, a tensile strength increase under dynamic loading was deemed to be a material property rather than any structural effect. It was also observed that the tensile strength enhancement becomes more pronounced at strain rates above approximately 5 s^{-1} .

Ruiz *et al.* (2000) presented a 3D FE analysis of dynamic Brazilian tests on concrete cylinders, using a cohesive material model based on Camacho and Ortiz (1996). It was shown that because the cohesive model has an intrinsic time scale, the model was able to capture the rate dependency of the damage. This result also led the authors to attribute most of the strain rate sensitivity of concrete in tension to dynamic micro-cracking and fracture, in other words a material property from a macroscopic point of view.

The above model with a cohesive law was also applied in a modified form by Yu *et al.* (2004) to study the Brazilian experiments of ceramics tested by Galvez *et al.* (1997). Similar resemblance with the experimental results was obtained in terms of fracture patterns as well as the overall rate enhancement effect.

In the numerical calculations of the Brazilian tests, convenience loading is usually applied in a displacement controlled manner similar to the compression simulations described earlier. This is achieved via a prescribed velocity history at the contact between the striker bar and the specimen, i.e., on the loading strip. The width of the strip, as in physical tests, is typically set to $1/8$ (or $1/12$) of the specimen diameter. When simulating a specific SHPB test, the velocity history profile may be estimated to match a target incident stress profile occurring in the incident bar according to the following equation (Nicholas and Recht, 1990):

$$v_i = \frac{\sigma_i}{\rho c} \quad [8.11]$$

where ρ and c are respectively the one-dimensional density and wave speed of the incident bar, and σ_i is the incident stress. On the other hand, the contact between the specimen and the transmitter bar, i.e., the support strip, may be assumed as rigid support.

Besides, for comparison with experiments, the rise time and duration may also be determined in accordance with those from the selected physical tests. In the study by Ruiz *et al.* (2000), such information was extracted from tests by Hughes *et al.* (1993) and Tedesco *et al.* (1993), and the rise time ranges in 41~85 μs , while velocity ranges in 1.5~6.7 m/s and the corresponding incident stress varies in 60.2~264.3 MPa. The constant velocity duration was kept at 100 μs in all cases. It should be noted that, while the above rise time range may be adequate for the velocity (and hence strain rate) examined in the comparison with experiments, in their parametric studies where the velocity was allowed to vary in a broad range of 1~100 m/s, the use of a standard rise time of 50 μs could be problematic, especially in the higher-velocity end as will be discussed in the next section.

8.6.2 The limiting strain rate and the load rise time for a Brazilian test

The basis of the splitting test is established from the elastic theory. When a pair of compression forces, P , are applied on the opposite sides of a disk, the material in much of the central region of the diameter in the loading axis is subjected to a uniform tensile stress in the perpendicular direction, σ_t , and a varying compressive stress, σ_c , in the loading direction:

$$\sigma_t = \frac{2P}{\pi LD} \quad [8.12]$$

$$\sigma_c = \frac{2P}{\pi LD} \left[\frac{D^2}{z(D-z)} - 1 \right] \quad [8.13]$$

where P is the compression force, z is the distance of the element to the point of loading, and L is the thickness (length) of the disk.

From Equation [8.12] it is possible to determine the tensile strength from the maximum compression force recorded, P_{\max} . (It should be noted, though, that the rupture zone is under a biaxial stress state, and the presence of a compressive stress will increase somewhat the tensile strength thus obtained. This needs to be taken into account when comparing the results with direct tension tests.)

With an SHPB apparatus, the applied forces at the loading (incident) and supporting (transmitter) ends may be determined from the strains measured in the incident and transmitter bars, respectively, as:

$$P_1 = AE(\epsilon_i + \epsilon_r) \quad [8.14]$$

$$P_2 = AE\epsilon_t \quad [8.15]$$

where ε_i , ε_r , ε_t are the incident, reflected and transmitted strains, respectively, A and E are the cross section area and Young's modulus of the Hopkinson bars, respectively. Assuming a similar equivalent state as in the static condition, the tensile stress in the specimen can be determined by using Equation [8.11] with P equal to either P_1 or P_2 , or an average of both. Depending upon the applied load pulse profile, an estimation of the effective strain rate may be made by the following equation:

$$\dot{\varepsilon}_t = \frac{\Delta\sigma_t}{E_c(\Delta t)} \quad [8.16]$$

where $\Delta\sigma_t$ denotes the increment of the tensile stress over a time duration Δt and E_c is the Young's modulus of concrete.

Concerning the validity of the splitting SHPB test in terms of the establishment of an equilibrium state, and hence a uniform tensile stress state over the splitting diameter, Rodríguez *et al.* (1994) carried out a simple but quite illustrative elastic FE analysis. The specimen was 10 mm in height and 20 mm in diameter, and had the elastic properties of a ceramic material, with Young's modulus of 200 GPa, Poisson's ratio of 0.33 and density of 2690 kg/m³. The dynamic load was applied through imposing a trapezoidal velocity history to one end of the specimen with a maximum value of 13 m/s and a rise time of 20 μ s, as obtained from their Hopkinson bar tests. The observation was made by examining the development of (elastic) stress so as to determine whether the specimen would fail before or after reaching the quasi-static equilibrium. It was found that with the stress wave reverberations taking place a more uniform stress distribution was being established, and in that particular specimen 8 μ s was found to be the minimum time to complete the process in reaching a symmetrical distribution and the equilibrium state. After that time, the tensile stress in the splitting region was well represented by Equation [8.12].

A quick deduction from the above result to the test of concrete would point to a timescale of around 50 μ s for the establishment of a uniform stress distribution in a normal concrete specimen of 50 mm in diameter. It is interesting from here to make an estimate of the tensile strain rate limit that would permit 50 μ s of loading time before reaching the tensile failure strain. For this estimation, we assume a gradual increase of the loading (strain) rate until the dynamic tensile strength is attained, thus,

$$\varepsilon_{dt} = \int \dot{\varepsilon} dt \equiv \frac{1}{2} \dot{\varepsilon}_{t,\max} \tau \quad [8.17]$$

and

$$\varepsilon_{dt} = \frac{f_{dt}}{E_c} = \frac{\alpha f_{st}}{E_c} = \alpha \varepsilon_{st} \quad [8.18]$$

where f_{dt} and f_{st} are the dynamic and static tensile strength, respectively, and E_c is the Young's modulus. ε_{dt} is the dynamic tensile failure strain, ε_{st} is the quasi-static tensile failure strain, α is the tensile dynamic strength increase factor, and τ denotes the duration of loading before failure. Thus,

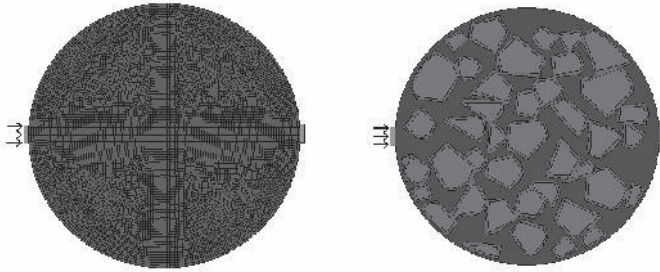
$$\dot{\varepsilon}_{t,\max} = \frac{2\alpha\varepsilon_{st}}{\tau} \quad [8.19]$$

For an indicative purpose, let us assume a quasi-static tensile failure strain of $100 \mu\varepsilon$, hence for $\tau = 50 \mu\text{s}$, $\dot{\varepsilon}_{t,\max} = 4\alpha \text{ s}^{-1}$. From here one can easily calculate a limit strain rate that would be on the order of 10 s^{-1} for a concrete cylinder of diameter 50 mm. Even for smaller cylinders, for example with a diameter of 10 mm for a mortar sample, the maximum allowable strain rate would still just be about 50 s^{-1} . It is worth noting here that attempting to boost the maximum strain rate by adopting a very short rise time (ultimately using a step increase) would only make the situation worse, as in that case the specimen would reach the failure strain even faster, making it more difficult to reach an equilibrium state. Moreover, employing a very short rise time would render the specimen more susceptible to premature local failure, as will be illustrated later.

The above estimation raises a logical question with regard to the extent to which the past experimental data on the dynamic tensile strength increase as derived from Brazilian tests would have been reliable. An in-depth investigation into this subject is beyond the scope of the present discussion. In what follows we shall demonstrate a few numerical simulations on the dynamic splitting tests, with a particular interest in observing the variations in the stress and fracture (damage) distributions under different targeted strain rates and the effect of the rise time. For generality, we shall firstly examine the development of the splitting failure process using a homogeneous model. Similar analyses are then performed using the mesoscale model to illustrate the possible influence the meso-heterogeneity may introduce in a dynamic splitting test condition.

Figure 8.17 shows the basic configurations for both homogenous and mesoscale models. The concrete employed in these examples is of 30 MPa grade, and the diameter of the disk is 50 mm. Load is imposed on the incident end by a velocity condition with a gradual rise stage followed by a constant velocity.

The cap velocity in the constant stage is set at 12.5 m/s. The corresponding nominal tensile strain rate, as confirmed from an elastic analysis assuming no premature failure before reaching an equilibrium state, would be on an order of 50 s^{-1} . As we shall see slightly later this would not actually be attainable, due to the limited failure strain of the material; as a result the achieved strain rate will be far lower than the above indicative level. Four different rise times are numerically examined, namely, 5, 10, 20 and 40 μs , respectively. Plate XVIII (see colour section between pages 208 and 209) shows the damage (crack) patterns.



8.17 Dynamic splitting simulation: homogeneous vs mesoscale models.

From Plate XVIII it can be observed that the specimen is subject to severe local impact damage when the rise time is less than $20\ \mu\text{s}$, which means the specimen cannot develop into a splitting tension mode before the onset of local failure, and this in effect invalidates the results in terms of splitting tension. When the loading rise time is increased to $40\ \mu\text{s}$, a splitting damage pattern indeed occurs. However, upon a close examination of the tensile stress–strain history (not shown) it can be found that failure (and the peak incident force) is reached much earlier than the attainment of the target strain rate, and the actually achieved strain rate is much lower at only about $20\ \text{s}^{-1}$.

The above exploratory results further confirm the conceptual discussion made earlier that an upper strain rate limit does have a binding effect for a valid Brazilian test for the dynamic tension of concrete. For normal concrete in a 50 mm disk, a $10\ \text{s}^{-1}$ limit appears to be realistic, and higher tensile strain rates would not be attainable either because of a premature failure (in the case of a prolonged rise time) or a much distorted stress distribution (in the case of a steep rise phase).

Next we shall examine the damage patterns of the specimen when the target strain rate is adjusted to $1\ \text{s}^{-1}$ and $10\ \text{s}^{-1}$, respectively. For these strain rates the imposed velocity cap is set at 0.25 and 2.5 m/s, respectively, while the rise time for both scenarios is set at $50\ \mu\text{s}$. Plate XIX (see colour section between pages 208 and 209) depicts the typical damage patterns. As can be seen, satisfactory uniformity is achieved in the distribution of tensile stress and damage under the strain rate of $1\ \text{s}^{-1}$. For the strain rate of $10\ \text{s}^{-1}$, a reasonable uniformity persists; however, progressive development of damage (fracture) starts to emerge, indicating that a strain limit on the order of $10\ \text{s}^{-1}$, as conceptually established earlier, indeed holds. In both cases, the achieved tensile stress and that calculated using Equation [8.11] correlates very well, with a difference well within 10% for both strain rate cases.

The simulation results in terms of the tensile strength as inferred using Equation [8.11] tend to support the previous observations in that, unlike

the case of the dynamic compression, the dynamic structural effects play a rather insignificant role in the increase of the splitting forces. The majority of the increase in the splitting forces from physical tests tends to be attributable to non-structural, micro-processes at the local material level (e.g. Weerheijm *et al.*, 2007). Without incorporating the DIF in the constitutive strength of the concrete material model (or for this effect a timescale in the material constitutive description), the specimens would exhibit no apparent increase in the splitting forces as the strain rate increases.

It is also worth mentioning that in the simulation for the nominal strain rate of 50 s^{-1} with a steep rise stage, the maximum acting forces (thereby the deduced 'dynamic tensile strength') tends to show a much increased value than in the lower strain rate simulations. As explained earlier this increase is largely due to the non-splitting effect and therefore should not be misinterpreted as a valid dynamic structural effect on the splitting tensile strength.

The simulation is then carried out using the mesoscale model under a similar loading condition for each of the three loading rates mentioned above. The resulting damage patterns are shown in Plate XX (see colour section between pages 208 and 209). As can be observed, the general fracture patterns from the mesoscale analysis agree with those from the homogeneous models; however, the detailed distributions are apparently affected by the presence of the aggregates. Further comparison of the failure splitting forces (and hence the splitting tensile strength) with the results from the homogeneous models indicates that the presence of the heterogeneity (stronger aggregates) tends to introduce an appreciable amount of increase in the dynamic splitting tensile strength. For the range of strain rates investigated, the increases that may be attributable to the heterogeneity ranges are on the order of 20%.

8.7 Modelling of heterogeneity in concrete with stochastic material properties

A seemingly efficient approach to represent non-homogeneity in a computational model, without the need to involve a detailed description of the morphology of the actual heterogeneity, is to introduce a stochastic distribution of material properties among the elements in the computational domain. In a way, such treatment may be regarded as an equivalent technique, wherein the heterogeneities larger than the spatial discretization are virtually diffused and therefore could not be fully represented.

8.7.1 A brief overview

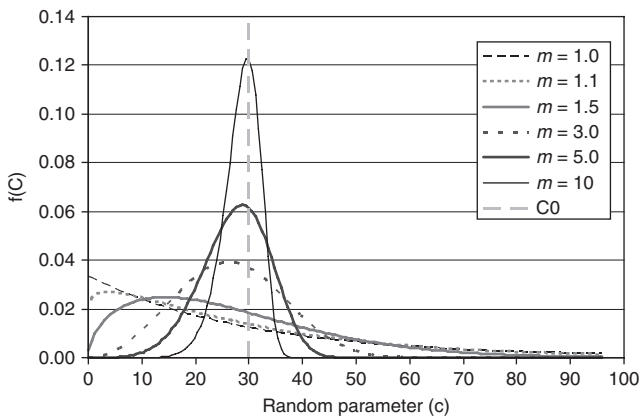
Rossi *et al.* were among the first to propose a probabilistic description of the material properties in a finite element model to capture the initiation and propagation of cracks in concrete specimens, see e.g. Rossi and Richer

(1987) and Rossi and Wu (1992). In their models, concrete strength, Young's modulus, element volume ratio (to the largest aggregates) were taken into account in the derivation of the probabilistic distribution functions for the concrete properties associated with each individual elements. The volumetric ratio was introduced to reflect the varying probabilistic properties (variance) at different levels of observations.

A number of studies have been reported using essentially a similar probabilistic approach, as mentioned above in numerical simulation of the behaviour and failure of rock materials, e.g. Blair and Cook (1998), Tang *et al.* (2000a, 2000b), Fang and Harrison (2002), Ma *et al.* (2006), Dong *et al.* (2006). The heterogeneities in these studies are modelled by random sampling of the basic material properties for each individual element following a Weibull distribution:

$$\phi(C; C_0, m) = \frac{m}{C_0} \left(\frac{C}{C_0} \right)^{m-1} e^{-(C/C_0)^m} \quad [8.20]$$

where C denotes the random parameter variable, e.g., strength, and C_0 is its mean value. m is the shape parameter and it translates herein as a homogeneity index of the material; a larger value of m implies a more homogeneous material, see Fig. 8.18. Considering the fact that the basic mechanical properties, such as the Young's modulus and tensile/compressive strength, are usually closely correlated, it may be appropriate to choose a governing parameter, such as the compressive strength, to be sampled randomly in accordance with the Weibull distribution. The remaining property parameters are then determined on the basis of the sampled compressive strength.



8.18 Probability density functions generated from Weibull distribution with different shape parameter (homogeneity index).

In the section that follows, an illustrative application of the generalized heterogeneous concrete model involving stochastic distribution of concrete material properties at each individual material point (element), reported in Dong *et al.* (2006), is given. The models are applied for the analyses of the strain rate effect on 50 mm cylindrical specimens under splitting tension and compression, respectively.

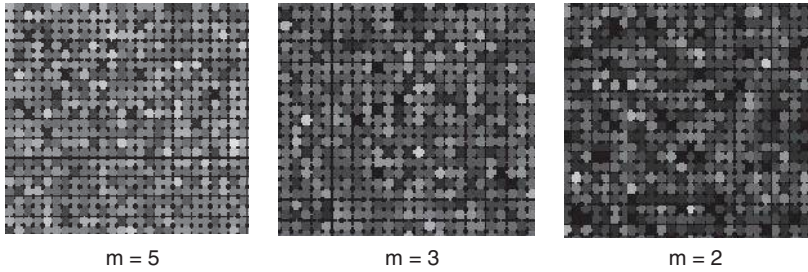
8.7.2 Stochastic heterogeneous modelling of concrete and its application in analysing dynamic tension and compression

In this modelling study with stochastic material properties, the computational model is developed using the smoothed particle hydrodynamics (SPH) solver. However, the general model consideration is not restrictive, and a similar analysis may be carried out using a classical finite element model. Being a meshless technique, SPH can be employed for solving computational continuum dynamics problems involving the development of discontinuities. Its particular advantage over the classical grid-based Lagrange method is the ability to track large deformations without involving the grid tangling problem. Thus, SPH is well suited for simulating fracture and fragmentation of brittle solids (Benz and Asphaug, 1995), as well as complex fracture in geological rock formations and in brittle materials (e.g. Gray *et al.*, 2000; Ma *et al.*, 2006; Ma *et al.*, 2010).

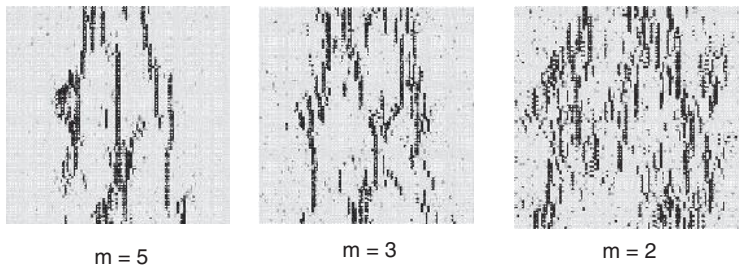
In this simulation, the concrete material is modelled with Johnson Holmquist (JH) model (Johnson and Holmquist, 1994) using the dynamic analysis code AUTODYN (2005). The choice of JH model was partly because of its comprehensive capability in describing pressure-dependent strength and evolution of damage, and partly because of the ease in customizing the model to accommodate random properties for individual elements.

The JH model is essentially a generalized Mohr Coulomb model. Similar to the Concrete Damage Model described earlier in Section 8.4.3, it includes a representation of the intact and fractured strength, a pressure–volume relationship that can include bulking, and a damage model that transitions the material from an intact state to a fractured state. To represent the heterogeneity in the numerical model, each element (SPH particle herein) has its individual material property represented by a characteristic parameter such as compressive strength, which is sampled randomly from a specified Weibull distribution function. Figure 8.19 depicts several example model material distributions with different degrees of heterogeneity.

The influence of the degree of heterogeneity as represented by the stochastic material properties can be studied readily by subjecting models with different heterogeneity parameter m to a given load condition. Figure



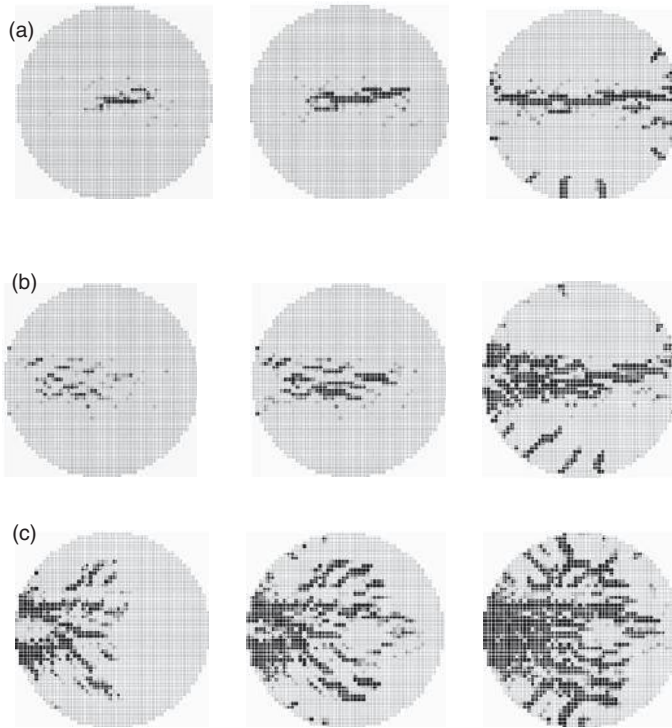
8.19 Close-up of numerical specimens with increasing degree of heterogeneity (decreasing m): higher contrast indicates higher heterogeneity and vice versa.



8.20 Variation of crack patterns as degree of heterogeneity increases.

8.20 illustrates the distribution of the cracks in a cubic specimen when subjected to dynamic compression with a nominal strain rate of 50 s^{-1} . It can be observed clearly that as the degree of heterogeneity increases, the crack pattern becomes increasingly diffused and tends to exhibit general resemblance to the patterns obtained from the mesoscale model. However, due to the inability of such a stochastic model to represent the meso-geometry, it will not be possible to capture the crack distribution in line with the actual layout of the heterogeneity, especially when larger aggregates are involved.

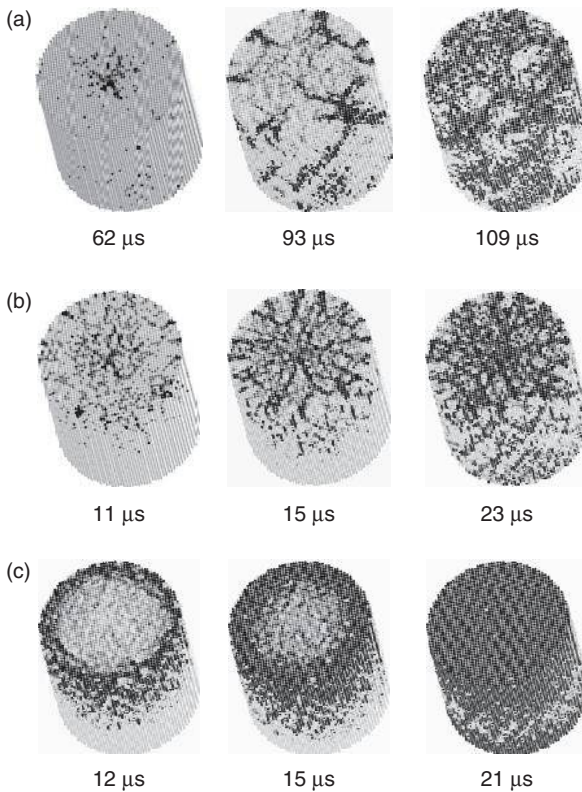
Figure 8.21 illustrates the development of the damage (crack) patterns from simulations of Brazilian splitting tension under different loading rates, which correspond to a nominal tensile strain rate of 2, 10 and 50 s^{-1} , respectively. Similar to the observations made in Section 8.5, the failure patterns of the concrete specimen change with the increase of the loading velocity or strain rate. Under a relatively low strain rate (2 s^{-1} herein), the failure pattern is similar to the generally observed quasi-static splitting failure mode. Major fracture initiates around the centre of the disc and it propagates in both directions towards the loading/support ends. Finally the specimen is split into two halves. Comparing to the splitting fracture from the mesoscale model, it is clear that in the stochastic model herein the fracture distribution



8.21 Failure processes of heterogeneous specimen under different loading rates. (a) Nominal tensile strain rate = 2 s^{-1} , (b) nominal tensile strain rate = 10 s^{-1} and (c) nominal tensile strain rate = 50 s^{-1} .

in the centre area tends to trace the path of the weakest elements, whereas in a mesoscale model it is apparently affected by the meso-geometry such that the splitting fracture is in line with the path of the aggregate–mortar interface within a certain band of the central area of the disc.

The simulated failure processes for a statistical model under compression with a loading rate $\dot{\epsilon}$ equal to 10 s^{-1} , 50 s^{-1} and 100 s^{-1} , respectively, are depicted in Fig. 8.22. The general observations are consistent with those presented in Section 8.5.2. At the relatively lower strain rate of $\dot{\epsilon} = 10 \text{ s}^{-1}$ (Fig. 8.22a), no significant damage occurs before the specimen enters a global failure state, and there are a few major crack lines as generally observed in quasi-static loading regimes. When $\dot{\epsilon} = 50 \text{ s}^{-1}$ (Fig. 8.22b), crack initiates from the incident loading end but in general damage is still well distributed over the entire specimen before final failure. It is noteworthy that radial fractures are formed during the propagation of the stress wave along the loading axis. When the loading rate reaches a high value of $\dot{\epsilon} = 100 \text{ s}^{-1}$ (Fig. 8.22c), failure occurs almost instantaneously on the incident end when load is applied, and propagates as the stress wave travels towards the opposite end. The phenomena are



8.22 Failure processes of heterogeneous concrete specimens under different strain rates. (a) Nominal compressive strain rate = 10 s^{-1} , (b) nominal compressive strain rate = 50 s^{-1} and (c) nominal tensile strain rate = 100 s^{-1} .

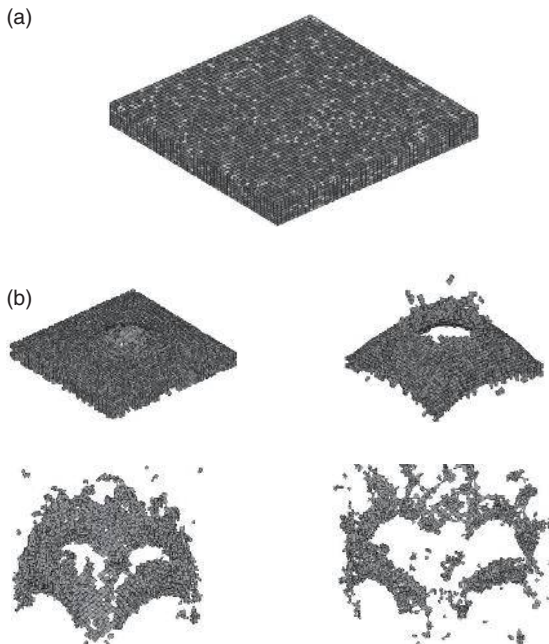
consistent with the observations made earlier with the mesoscale model. The bulk dynamic compressive strength in the statistic model also exhibits a similar increase trend as observed in the mesoscale modelling results. The results in terms of the apparent DIF from the compression simulations are consistent with other numerical observations in that the dynamic structural effect tends to be the major cause of the observed bulk DIF under compression.

8.8 Modelling of spalling and fragmentation in concrete structures with a stochastic material property distribution

In many applications of concrete structures under high rate loading such as blast, it is often required to predict in finer detail the break-up process and the throw of fragments after the structure has failed.

There exist a range of techniques in the literature that may be employed to handle large and discontinuous deformations in a complex loading environment (Lu, 2009), for example the meshfree methods, such as SPH described in the previous section, and DEM. However, for cases where the response of the structure in its continuum state constitutes an essential part of the analysis, especially where complex geometrical layout is involved, the use of finite element method is still an indispensable choice. In such a situation, the incorporation of the statistical property distribution scheme in conjunction with a controlled use of the element erosion technique provides an effective means to simulate fracture and fragmentation while minimizing the problem with mesh distortion. This is in addition to the apparent advantage of such a scheme in representing the physical heterogeneity in the material.

Figure 8.23 illustrates a FE model with a stochastic property distribution for a concrete slab subjected to a close-in blast causing considerable fracture and fragmentation of the slab. The analysis was performed using LS-DYNA, with which the blast load may be applied either by a coupled (via blast-structure interaction) or uncoupled (as imposed loading) approach. For simplicity and without losing generality, a limited number of material types (sub-groups) are defined to represent the statistical distribution of



8.23 Modelling of concrete slab fragmentation under blast load. (a) FE model of concrete slab with heterogeneity by material randomization and (b) Simulation results under high intensity blast loading.

the concrete being modelled. The proportion of elements falling into each subgroup and the characteristic material properties for the subgroup can be determined in accordance with a prescribed probability density function, such as the Weibull distribution with a specific value for the shape parameter. The allocation of each individual element into a particular subgroup can then be done through random sampling.

The use of such a heterogeneous model allows for the realization of a progressive fragmentation process even in areas of excessive deformation as failure will tend to initiate in weaker elements. Where an erosion or element elimination technique needs to be invoked, different elimination criteria may be considered for different groups of elements, and this helps alleviate the issue with loss of mass in the calculation cycles, and at the same time enables realization of fragmentation.

In the current example, the concrete material is assumed to have a nominal strength of 50 MPa, and it is modelled by six material sub-groups. The simulation of the break-up and fragmentation of the slab is achieved via the erosion technique, with a varying erosion limit for different groups of materials. Figure 8.23b depicts the break-up and throw of fragments in the concrete slab.

In summary, the material randomization scheme mentioned above resembles some essential effects of a detailed mesoscale model, with however a considerably simplified implementation procedure as compared to a large-scale mesoscale model. Such a simplification makes it possible to include the material heterogeneity in real applications where a non-homogeneous distribution of the material properties in the model is desirable.

8.9 Conclusions

Concrete is inherently heterogeneous. Homogenization in the numerical modelling of concrete is strictly justifiable only for applications where the stress and strain distribution does not vary considerably over a size scale comparable to a representative volume element or a characteristic length, which is typically a few times of the aggregate size. This general condition can hardly be satisfied when the loading rate is high. Therefore, modelling of the material heterogeneity becomes a particularly significant topic in the analysis of concrete under high strain rate loading.

Mesoscale models of concrete may be developed with various degrees of sophistication, and the choice is largely dependent upon the response characteristics as well as the scale of observation. Due to the complexities associated with transient stress waves and the evolution of damage under high strain rate loading, a more realistic mesoscale model would be desired for investigations into the meso-mechanical processes underlying the bulk dynamic behaviour of such heterogeneous material. Such a model should

preserve the essential mesoscale compositions of the material, namely the three distinctive phases of aggregates, mortar matrix, and the ITZ, as well as the geometry of the heterogeneity. As an alternative approach, simplified mesoscale models with regular grid discretization but a stochastic distribution of material properties may be employed. The latter option can be well suited in the analysis of large specimens or structural components involving extensive fracture and fragmentation processes.

Numerical experiments using mesoscale models provide new insight into the meso-mechanical processes of concrete under high rate loading. For concrete under compression, results demonstrate an increasingly more significant contribution of the meso-heterogeneity in the dynamic strength enhancement or the DIF, and this is in addition to the generally known dynamic structural effect, namely the inertia confinement. For concrete in tension, however, no evidence from the numerical investigations tends to show any significant structural effect in the increase of the bulk tensile strength. This is in agreement with previous numerical studies, and such observations effectively suggest that the increase in the dynamic tensile strength should indeed be attributable to micro-mechanical reasons, and thus be treated primarily as a material property from a modelling point of view, unless such micro-mechanical mechanisms can be well represented in the computational model.

Numerical simulations also clearly demonstrate the complications that tend to arise when the strain rate exceeds a certain limit for a particular specimen dimension, such that propagating failure occurs before a desired uniform stress distribution may possibly be established. An implication is that averaging of the externally measured data on the specimen becomes less representative of the true material response, and this is particularly the case on the high strain rate end of the dynamic regime. For dynamic tension tests using a Brazilian disc set-up, attempting to test the specimens at strain rates beyond a suitable limit could ultimately render the test data irrelevant for observing the tensile behaviour of the material.

8.10 Acknowledgements

Numerical studies from the author's research group as included in this chapter have been conducted over a period spanning a few years, and several former and current research students/associates have been involved. Their contributions, particularly those from Zhenguo Tu and Zhenhuan Song, are gratefully acknowledged.

8.11 References

Aboudi, J. (1991). *Mechanics of composite materials: A unified micromechanical approach*, Elsevier, Amsterdam.

- Akers S.A. and Bruce Phillips R. (2004). *Concrete modeled as an inhomogeneous material: numerical simulations of contact detonations charges*. 18th International Symposium on Military Aspects of Blast and Shock, Bad Reichenhall, Germany. ANSYS Academic Research, Release 11.0, ANSYS, Inc., Canonsburg, PA, 2007.
- Arslan, A., Ince, R. and Karihaloo, B.L. (2002). Improved lattice model for concrete fracture, *J. Eng. Mech. ASCE*, **128**(1), 57–65.
- AUTODYN (2005). *AUTODYN – Explicit software for nonlinear dynamics*. Release Notes Version 4.1. Century Dynamics, Inc.
- Azevedo, M.N., Lemos, J.V. and de Almeida, J.R. (2008). Influence of aggregate deformation and contact behaviour on discrete particle modelling of fracture of concrete, *Eng. Fract. Mech.*, **75**(6), 1569–1586.
- Bazant, Z.P., Tabarra, M. R., Kazemi, T. and Pijaudier-Cabot, G. (1990). Random particle model for fracture of aggregate or fiber composites, *J. Eng. Mech.*, **116**(8), 1686–1705.
- Bazant, Z.P., Xiang, Y. and Prat, P.C. (1996). Microplane model for concrete. I: Stress–strain boundaries and finite strain. *J. Eng. Mech.*, **122**(3), 245–254.
- Benz, W. and Asphaug, E. (1995). Simulations of brittle solids using smooth particle hydrodynamics. *Comput. Phys. Commun.*, **87**, 253–265.
- Bischoff, P.H. and Perry, S.H. (1991). Compression behaviour of concrete at high strain rates. *Mater. Struct.*, **24**, 425–450.
- Blair, S.C. and Cook, N.G.W. (1998). Analysis of compressive fracture in rock using statistical techniques: Part I. A non-linear rule-based model. *Int. J. Rock. Mech. Min. Sci.*, **35**, 837–848.
- Brace, W.F. and Jones, A.H. (1971). Comparison of uniaxial deformation in shock and static loading of three rocks, *J. Geomech. Abstr.*, **13**(6), 4913–4921.
- Brara, A., Camborde, F., Klepaczko, J.R. and Mariotti, C. (2001). Experimental and numerical study of concrete at high strain rates in tension. *Mech. Mater.*, **33**, 33–45.
- Caballero, A., Carol, I. and Lopez, C.M. (2006). A meso-level approach to the 3d numerical analysis of cracking and fracture of concrete materials. *Fatigue. Fract. Eng. Mater. Struct.*, **29**(12), 979–991.
- Camacho GT and Ortiz M. (1996). Computational modelling of impact damage in brittle materials. *Int. J. Solids. Struct.*, **33**(20–22), 2899–2938.
- Camborde, F., Mariotti, C. and Donzé, F.V. (2000). Numerical study of rock and concrete behaviour by discrete element modeling. *Comput. Geotech.*, **27**, 225–247.
- CEB (1993), *CEB-FIP Model Code 1990*, Comité Euro-International du Béton. Redwood Books.
- Chiaia, B., Vervuurt, A. and Van Mier, J. G. M. (1997). Lattice model evaluation of progressive failure in disordered particle composites. *Eng. Fract. Mech.* **57**(2/3), 301–318.
- Cundall, P.A. and Strack, O.D.L. (1979). A discrete numerical model for granular assemblies. *Geotechnique*, **29**, 47–65.
- Cusatis, G., Bazant, Z.P. and Cedolin, L. (2003). Confinement-shear lattice model for concrete damage in tension and compression: 1. Theory, *J. Eng. Mech.*, **129**(12), 1439–1448.
- Cusatis, G., Mencarelli, A., Pelessone, D. and Baylot, J. T. (2008). *Lattice Discrete Particle Model (LDPM) for fracture dynamics and rate effect in concrete*. Proc. 18th Analysis and Computation Speciality Conf., ASCE Structures Congress 2008, April 24–26, Vancouver, Canada.

- De Schutter, G. and Taerwe, L. (1993). Random particle model for concrete based on Delaunay triangulation, *Mater. Struct.*, **26**, 67–73.
- Dong, A.A., Lu, Y. and Ma, G.W. (2006). *Numerical simulation study of strain rate effect on dynamic behaviour of concrete material*, Proc. Design and Analysis of Protective Structures (DAPS06), Singapore, 280–288.
- Donzé, F.V., Magnier, S.-A., Daudeville, L., Mariotti, C. and Davenne, L. (1999). Numerical study of compressive behavior of concrete at high strain rates. *J. Eng. Mech.*, **125**(10), 1154–1163.
- Dupray, F., Malecot, Y., Daudeville, L. and Buzaud, E. (2009). A mesoscopic model for the behaviour of concrete under high Confinement, *Int. J. Numer. Anal. Meth. Geomech.*, **33**, 1407–1423.
- Eckardt, S., Hafner, S. and Konke, C. (2004). *Simulation of the fracture behaviour of concrete using continuum damage models at the mesoscale*. In: Proceedings of ECCOMAS, Jyväskylä.
- Emery, J. M., Hochhalter, J. D. and Ingraffea, A. R. (2007). Computational fracture mechanics of concrete structures: a retrospective through multiple lenses. *FraMCoS-6*, Jun 17–22, Catania, Italy.
- Fang, Z. and Harrison, J.P. (2002). Development of a local degradation approach to the modeling of brittle fracture in heterogeneous rocks. *Int. J. Rock. Mech. Min.*, **39**, 443–457.
- Galvez, F., Rodriguez, J. and Sanchez, V. (1997). Tensile strength measurements of ceramic materials at high rates of strain. *J. Phys.*, **7**, 151–156.
- Ghaboussi, J. and Barbosa, R. (1990). Three-dimensional discrete element method for granular materials. *Int. J. Num. Anal. Method. Geo.*, **14**, 451–472.
- Gopalaratnam, V., Gerstle, W., Isenberg, J. and Mindness, S. (1996). *State-of-the-art report on dynamic fracture*. Rep., ACI Committee 446, American Concrete Institute, Detroit.
- Grote, D.L., Park, S.W. and Zhou, M. (2001). Dynamic behavior of concrete at high strain-rates and pressures: I. Experimental characterization. *Int. J. Imp. Eng.*, **25**, 869–886.
- He, H., Stroeven, P., Stroeven, M. and Sluys, L.J. (2011). Influence of particle packing on fracture properties of concrete. *Comput. Concr.*, **8**(6), 677–692.
- He, H., Stroeven, P., Stroeven, M. and Sluys, L.J. (2012). Influence of particle packing on elastic properties of concrete. *Mag. Concrete. Res.*, **64**(2), 163–175.
- Hentz, S., Donzé, F.V. and Daudeville, L. (2004). Discrete element modeling of concrete submitted to dynamics loading at high strain rates, *Comput. Struct.*, **82**, 2509–2524.
- Hill, R. (1963). Elastic properties of reinforced solids: some theoretical principles, *J. Mech. Phys. Solids*, **11** (5), 357–372.
- Hrennikoff, A. (1941). Solution of problems of elasticity by the framework method. *J. Appl. Mech.*, **12**, 169–175.
- Hughes, M. L., Tedesco, J. W. and Ross, C. A. (1993). Numerical analysis of high strain rate slitting-tensile tests. *Comput. Struct.*, **47**(4/5), 653–671.
- Janach, W. (1976) The role of bulking in brittle failure of rocks under rapid compression. *Int. J. Rock. Mech. Min. Sci. Geomech. Abstr.*, **13**(6), 177–186.
- Johnson, G.R. and Holmquist, T.J. (1994). *An improved computational constitutive model for brittle materials*. High Pressure Science and Technology 1994, American Institute of Physics, 981–984.
- Kwan, A.K.H., Wang, Z.M. and Chan, H.C. (1999). Mesoscopic study of concrete II: nonlinear finite element analysis. *Comput. Struct.*, **70**, 545–556.

- Le Nard, H. and Bailly, P. (2000). Dynamic behaviour of concrete: the structural effects on compressive strength increase. *Mech. Cohes-Frict. Mat.*, **5**, 491–510.
- Leite, J.P.B., Slowik, V. and Apel, J. (2007). Computational model of mesoscopic structure of concrete for simulation of fracture processes. *Comput. Struct.*, **85**, 1293–1303.
- Leite, J.P.B., Slowik, V. and Mihashi, H. (2004). Computer simulation of fracture process of concrete using mesolevel models of lattice structures. *Cem. Concr. Res.*, **34**(6), 1025–1033.
- Li, Q.M. and Meng, H. (2003). About the dynamic strength enhancement of concrete-like materials in a split Hopkinson pressure bar test. *Int. J. Impact. Eng.*, **40**, 343–360.
- Lilliu, G. and van Mier, J. (2003). 3D lattice type fracture model for concrete. *Eng. Frac. Mech.*, **70**, 927–941.
- Lockner, D. A. and Moore, D. E. (1992). Microcrack interaction leading to shear fracture. Proc. of the 33rd US Symposium on Rock Mechanics, 3–5 June 1992, Santa Fe, NM, 807–816.
- LS-DYNA (2007). *Keyword user's manual, version 971*. Livermore Software Technology Corporation.
- Lu, Y. (2009). Modelling of concrete structures subjected to shock and blast loading: an overview and some recent studies. *Struct. Eng. Mech.*, **32**(2), 235–250.
- Lu, Y. and Tu, Z.G. (2008). *Simulation of concrete fragmentation with a mesoscale approach*, 4th Int. Conf. on Advances in Structural Engineering and Mechanics (ASEM'08), 26–28 May 2008, Jeju, Korea.
- Lu, Y. and Xu, K. (2004). Modelling of concrete materials under blast loading, *Int J Soilds. Struct.*, **41**(1), 131–143.
- Lu, Y., Song, Z.H. and Tu, Z.G. (2009). *Numerical simulation study of the strain rate effect on concrete in compression considering material heterogeneity*, Proc., DYMAT 2009, 7–11 September 2009, Brussels.
- Lu, Y., Song, Z.H. and Tu, Z.G. (2010). Analysis of dynamic response of concrete using a mesoscale model incorporating 3D effects, *Int. J. Prot. Struct.*, **1**(2), 197–217.
- Ma, G.W., Dong A.A. and Li J.C. (2006). *Modeling strain rate effect for heterogeneous brittle materials*. 1st Int Conf. on Analysis and Design of Structures against Explosive and Impact Loads, Sept. 15–17, 2006, Tianjin, China.
- Ma, GW., Wang, X.J. and Li, Q. M. (2010). Modeling strain-rate effect of heterogeneous materials using SPH method. *Rock. Mech. Rock. Eng.*, **43**, 763–776.
- Mackechnie, J.R. (2004). *Properties of New Zealand concrete aggregates*. Technical Report 11 (TR 11), Cement & Concrete Association of New Zealand.
- Mahabadi, O. K., Cottrell, B. E. and Grasselli, G. (2010). An example of realistic modelling of rock dynamics problems: FEM/DEM simulation of dynamic Brazilian test on barre granite, *Rock. Mech. Rock. Eng.*, **43**, 707–716.
- Malvar, L.J., Crawford, J.E. and Morrill, K.B. (2000). K&C concrete material model release III-automated generation of material model input. K&C Technical Report TR-99–24-B1.
- Malvar, L.J., Crawford, J.E. and Wesevich, J.W. (1997), A plasticity concrete material model for Dyna3D, *Int. J. Impact. Eng.*, **19**(9/10), 847–873.
- Man, K.T. and van Mier, J. G. M. (2008). Size effect on strength and fracture energy for numerical concrete with realistic aggregate shapes. *Int. J. Fract.*, **154**, 61–72.
- Mindess, S., Young, J.F. and Darwin, D. (2002). *Concrete*. 2nd ed., Prentice Hall.

- Munjiza, A., Andrews, K.R.F. and White, J.K. (1999). Combined single and smeared crack model in combined finite-discrete element analysis. *Int. J. Numer. Methods. Eng.*, **44**, 41–57.
- Nicholas, T. and Recht, R.F. (1990). *Introduction to impact phenomena*. In Zukas J.A. (ed.), *High velocity impact dynamics*, Wiley: New York, 1–63.
- Omachi, T. and Arai, Y. (1988). Dynamic failure of rockfill models simulated by the distinct element method, In Swoboda G. (ed.), *Numerical Methods in Geomechanics*, Innsbruck, A. A. Balkema, 1855–1860.
- Reinhardt, H.W. and Weerheijm, J. (1991). Tensile fracture of concrete at high loading rates taking account of inertia and crack velocity effects. *Int. J. Fracture.*, **51**, 31–42.
- Riedel, W., Wicklein, M. and Thoma, K. (2008). Shock properties of conventional and high strength concrete: experimental and mesomechanical analysis. *Int. J. Imp. Eng.*, **35**, 155–171.
- Rodriguez J., Navarro C. and Sanchez-Galvez V. (1994). Splitting tests: an alternative to determine the dynamic tensile strength of ceramic materials. *J. Phys. IV*, **4**(C8), 101–106.
- Rossi, P. and Richer, S. (1987). Numerical modelling of concrete cracking based on a stochastic approach. *Mater. Struct.*, **20**(5), 334–337.
- Rossi, P. and Wu, X. (1992). Probabilistic model for material behavior analysis and appraisalment of concrete structures. *Mag. Concrete Res.*, **44**, 271–280.
- Rossi, P., Ulm, F.-J. and Hachi, F. (1997). Compressive behavior of concrete: physical mechanisms and modeling. *J. Eng. Mech.*, **122**(11), 1038–1043.
- Ruiz, G., Ortiz, M. and Pandol, A. (2000). Three-dimensional finite-element simulation of the dynamic Brazilian tests on concrete cylinders. *Int. J. Numer. Meth. Engng.*, **48**, 963–994.
- Schlangen, E. (1993). Experimental and numerical analysis of fracture process in concrete (PhD thesis). Delft University of Technology, The Netherlands.
- Schlangen, E. and Van Mier, J. G. M., (1992a). Experimental and numerical analysis of micromechanisms of fracture of cement-based composites. *Cem. Concr. Compos.*, **14**(2), 105–118.
- Schlangen, E. and van Mier, J. (1992b). Simple lattice model for numerical simulation of fracture of concrete materials and structures. *Mater. Struct.*, **25**, 534–942.
- Song Z.H. and Lu, Y. (2011). Mesoscopic analysis of concrete under excessively high strain-rate compression and implications on interpretation of test data. *Int. J. Imp. Eng.*, **46**, 41–55.
- Tang, C.A., Liu, H., Lee, P.K.K., Tsui, Y. and Tham, L.G. (2000a). Numerical studies of the influence of microstructure on rock failure in uniaxial compression-Part I: effect of heterogeneity. *Int. J. Rock. Mech. Min.*, **37**, 555–569.
- Tang, C.A., Tham, L.G., Lee, P.K.K., Tsui, Y. and Liu, H. (2000b). Numerical studies of the influence of microstructure on rock failure in uniaxial compression-Part II: constraint, slenderness and size effect. *Int. J. Rock. Mech. Min.*, **37**, 571–583.
- Tedesco, J.W. and Ross, C.A. (1998). Strain-rate-dependent constitutive equations for concrete. *ASME J. Press. Vessel. Technol.*, **120**, 398–405.
- Tedesco, J.W., Ross, C.A. and Kuennen, S.T. (1993). Experimental and numerical-analysis of high-strain rate splitting tensile tests. *ACI Mater. J.*, **90**(2), 162–169.
- Tu, Z.G. and Lu, Y. (2009). Evaluation of typical concrete material models used in hydrocodes for high dynamic response simulations. *Int. J. Impact. Eng.*, **36**, 132–146.

- Tu, Z. and Lu, Y. (2011). Mesoscale modelling of concrete for general FE analysis – Part 1: Model development and implementation. *Struct. Eng. Mech.*, **37**(2), 197–213.
- van Mier, J. and van Vliet, M. (2003). Influence of microstructure of concrete on size/scale effects in tensile fracture. *Eng. Fract. Mech.*, **70**(16), 2281–2306.
- van Mier, J. G. M. and Vonk, R. A. (1991). Fracture of concrete under multiaxial stress – recent developments. *Mater. Struct.*, **24**(1), 61–65.
- Van Mier, J.G.M., Chiaia, B.M. and Vervuurt, A. (1997). Numerical simulation of chaotic and self-organizing damage in brittle disordered materials. *Comp. Meth. Appl. Mech. Engrg.*, **142**, 189–201.
- van Mier, J.G.M., van Vliet, M.R.A. and Wang, T.K. (2002). Fracture mechanisms in particle composites: statistical aspects in lattice type analysis. *Mech. Mater.*, **34**, 705–724.
- Wang, Z.M., Kwan, A.K.H. and Chan, H.C. (1999). Mesoscopic study of concrete I: generation of random aggregate structure and finite element mesh. *Comput. Struct.*, **70**, 533–544.
- Weerheijm, J., Vejt, I. and van Breugel, K. (2007). Research developments and experimental data on dynamic concrete behaviour. *Advances in Construction Materials*, Part **IX**, 765–773.
- Wittmann, F.H., Roelfstra, P.E. and Sadouki, H. (1984). Simulation and analysis of composite structures. *Mater. Sci. Eng.*, **68**, 239–248.
- Wriggers, P. and Moftah, S.O. (2006). Mesoscale models for concrete: Homogenisation and damage behaviour. *Finite. Elem. Anal. Des.*, **42**, 623–636.
- Yu, R.C., Ruiz, G. and Pandolfi, A. (2004). Numerical investigation on the dynamic behavior of advanced ceramics. *Eng. Fract. Mech.*, **71**, 897–911.
- Zhou, X.Q. and Hao, H. (2008a). Modelling of compressive behaviour of concrete-like materials at high strain rate. *Int. J. Solids. Struct.*, **45**, 4648–4661.
- Zhou, X.Q. and Hao, H. (2008b). Mesoscale modelling of concrete tensile failure mechanism at high strain rates, *Comput. Struct.*, **86**(21–22), 2013–2026.
- Zhu, W.C. and Tang, C.A. (2006). Numerical simulation of Brazilian disk rock failure under static and dynamic loading. *Int. J. Rock. Mech. Min. Sci.*, **43**, 236–252.
- Zohdi, T.I. and Wriggers, P. (2001). Computational micro-macro material testing, *Arch. Comp. Meth. Eng.*, **8**(2), 131–228.
- Zubelewicz, A. and Bažant, Z. P. (1987). Interface element modeling of fracture in aggregate composites. *J. Eng. Mech.*, **113**(11), 1619–1630.

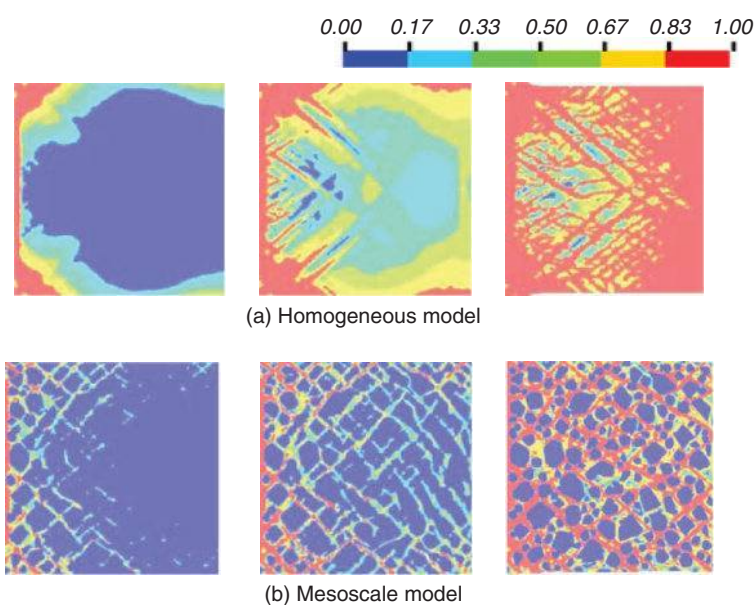


Plate XI (Chapter 8) Comparative simulation of damage patterns using homogeneous and mesoscale models, respectively. Strain rate = 100 s^{-1} , colour scale 1.0 = total failure.

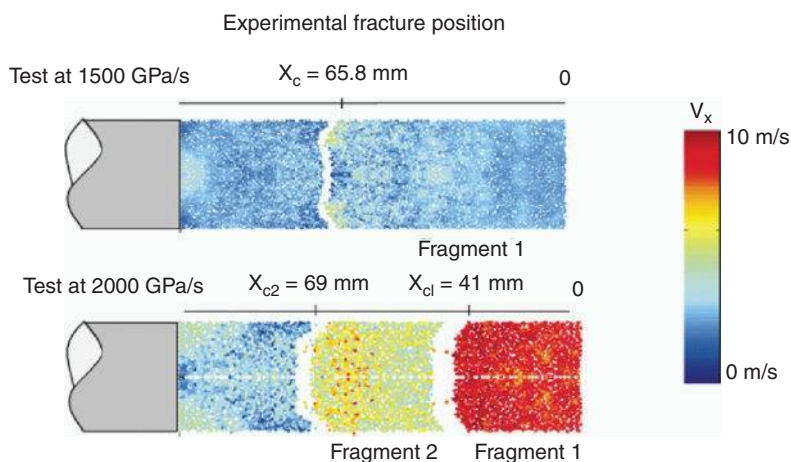
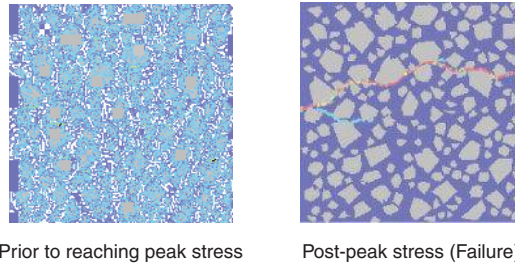
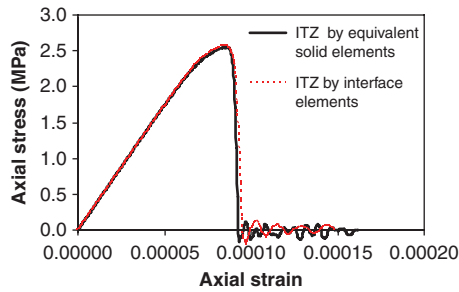


Plate XII (Chapter 8) Numerical simulation of fracture in spalling tests and post-mortem velocities of ejection (after Brara *et al.*, 2001).

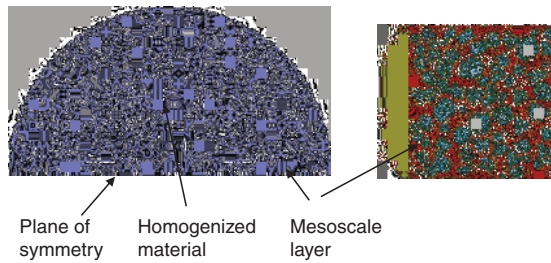


(a) Development of crack patterns (red lines indicate total fracture / macro crack)

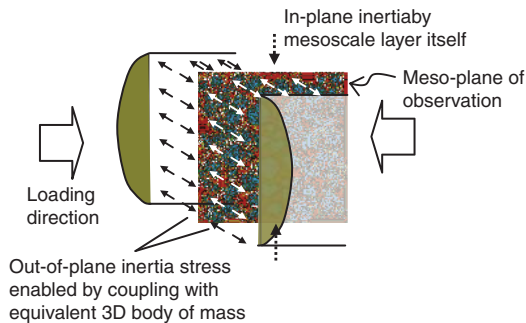


(b) Stress-strain curve (nominal strain across whole length)

Plate XIII (Chapter 8) Typical simulation results under uniaxial tension.

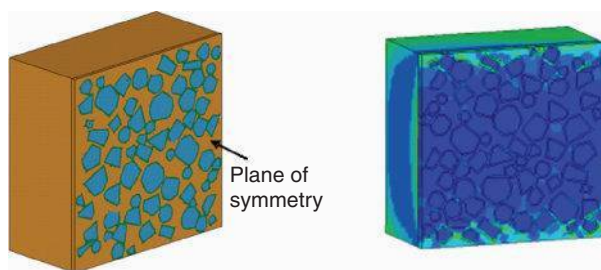


(a) Sandwich mesoscale model for cylinder



(b) Pseudo 3D stress environment

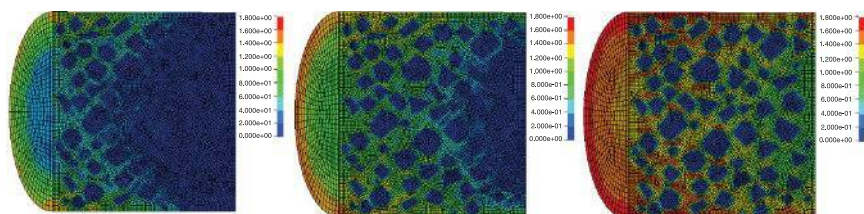
Plate XIV (Chapter 8) Sandwich model (cylinder).



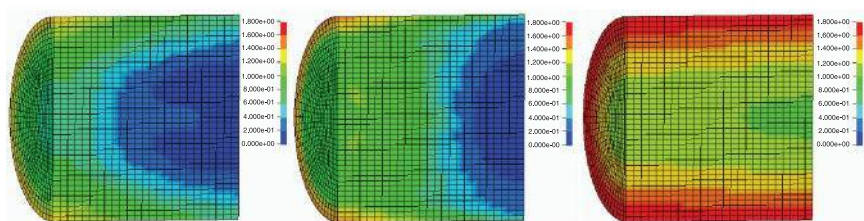
(a) Geometry of the sandwich model
contour

(b) Representative stress
distribution

Plate XV (Chapter 8) Configuration of a pseudo-3D mesoscale model for a cubic specimen and representative stress distribution.

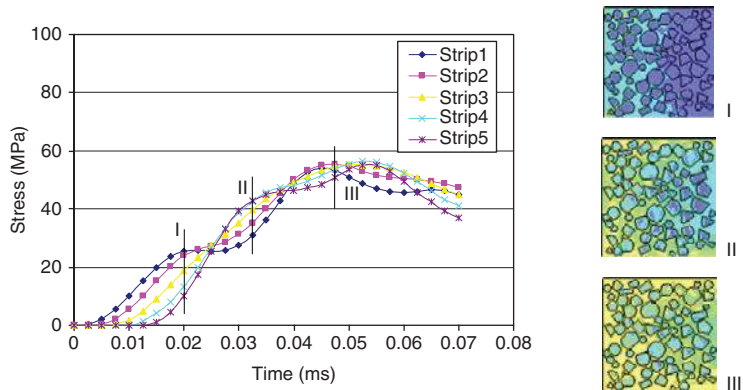


(a) Pseudo 3D mesoscale model

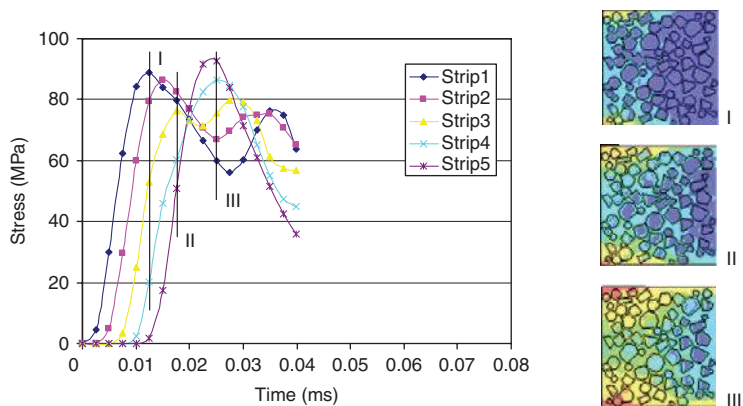


(b) 3D homogeneous model

Plate XVI (Chapter 8) Comparison of damage patterns in the pseudo-3D mesoscale model and 3D homogeneous model, strain rate 50 s^{-1} .



(a) Nominal strain rate = 50 s^{-1}



(b) Nominal strain rate = 200 s^{-1}

Plate XVII (Chapter 8) Stress time histories in five equally divided strips along loading direction.

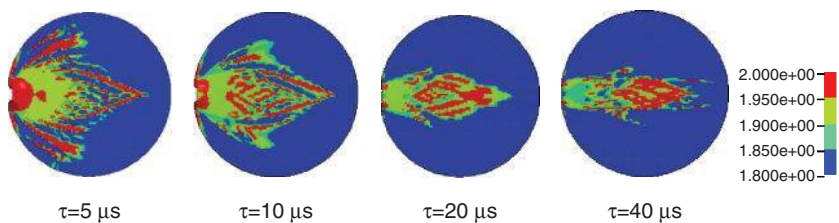


Plate XVIII (Chapter 8) Damage patterns for a target strain rate of 50 s^{-1} with different rise times (colour scale: 2.0 indicates total failure).

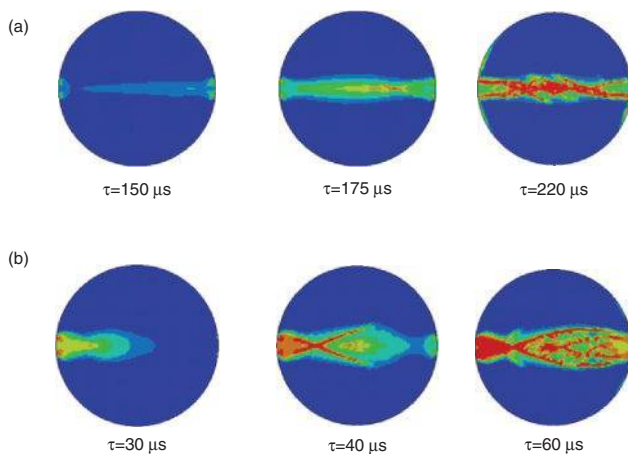


Plate XIX (Chapter 8) Typical damage patterns for strain rates of 1 s^{-1} and 10 s^{-1} . (a) Nominal tensile strain rate = 1 s^{-1} , (b) Nominal tensile strain rate = 10 s^{-1} .

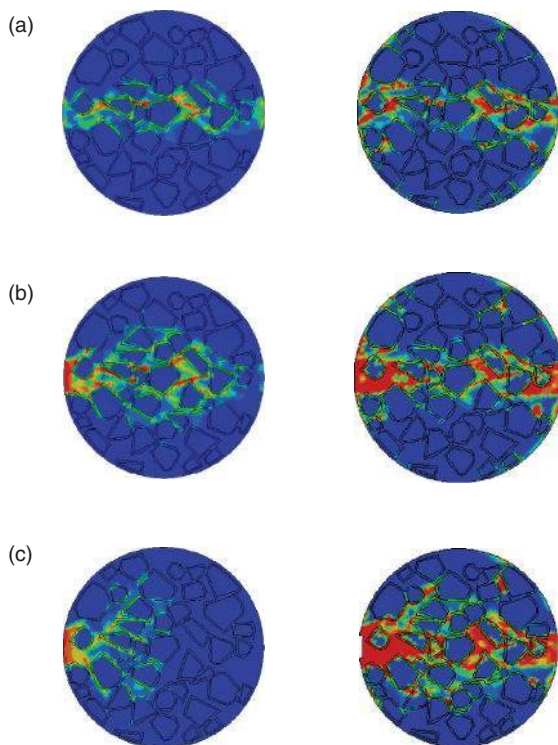


Plate XX (Chapter 8) Typical damage characteristics in mesoscale model under different splitting tensile strain rates. (a) Nominal tensile strain rate = 1 s^{-1} , (b) Nominal tensile strain rate = 10 s^{-1} , (c) Nominal tensile strain rate = 50 s^{-1} .

Mesoscopic modeling of concrete under different moisture conditions and loading rates

R. R. PEDERSEN, Aalborg University, Denmark,
A. SIMONE and L. J. SLUYS,
Delft University of Technology, The Netherlands

DOI: 10.1533/9780857097538.2.268

Abstract: We present a mesoscopic finite element model for simulating the rate- and moisture-dependent material behavior of concrete. The idealized mesostructure consists of aggregates surrounded by an interfacial transition zone embedded in the bulk material. We examine the influence of the most significant constitutive model parameters on global and local response. Different distributions and shapes of the aggregates are tested. Three model parameter sets, corresponding to different moisture conditions, are employed in the analysis of two specimens in which the applied loading rate is significantly different. The results indicate that the loading rate has a stronger influence than the saturation level on fracture processes and global strength.

Key words: mechanical properties, mesoscopic modeling, concrete, finite element analysis.

9.1 Introduction

Experimental results show that concrete is a heterogeneous brittle material that fractures through the formation, growth and coalescence of microcracks. Failure processes in concrete depend on the loading rate and are significantly influenced by micro-inertia of the material adjacent to a propagating microcrack and moisture in the capillary pores. These phenomena show that fracture processes of concrete involve multiple length scales defined at various levels (from small length scales associated to microcracks to macroscopic length scales characterizing the width of the fracture process zone). Realistic numerical simulations of fracture processes should adequately represent the influence of these length scales on the mechanical response. An explicit model of the mesostructure, coupled with a regularized bulk material model, is a simple yet effective approach to the characterization of length scale effects at different levels. In this contribution we will employ

a two-dimensional plane-stress rate-dependent visco-elastic visco-plastic damage (VEVPD) continuum model,¹ developed by the authors, which successfully reproduced, in macroscopic simulations, rate-dependent tensile strength results obtained in an experimental campaign conducted at Delft University of Technology.²⁻⁶ With the VEVPD macroscopic model we were also able to provide an estimate of the rate- and moisture-dependent size of the fracture process zone (FPZ). This measure, however, was in poor agreement with the corresponding experimental observations. Here we will show that the prediction capabilities of the VEVPD continuum model can be greatly improved by explicitly modeling the mesostructure including aggregates and interfacial transition zone (ITZ).

While the literature abounds with mesoscopic models of concrete, only a handful of them⁷⁻¹⁰ has been adequately designed to describe their behavior. Leaving aside the issue of mesoscopic representation of concrete¹¹⁻¹³, here discussed in Section 9.3, a key component of concrete modeling is the correct management of its strain-softening behavior. Lattice models¹⁴⁻²⁰ have been abundantly used for this purpose because of their simplicity. Their major drawback is, however, the strong dependence of the results on the lattice geometry Fig. 9.8. Some authors have nevertheless reported that mesh dependency can be eliminated²² or strongly reduced²³ by considering lattices with a fixed minimum distance between lattice elements²⁴ representing the distance between aggregates. Such an approach is, however, questionable since the stress field is so poorly described that key phenomena such as damage initiation in the ITZ cannot be adequately represented. Even when a detailed characterization of the stress field is achieved, the quality of the solution is strongly related to the quality of the employed discretization technique. Although the use of aggregates might alleviate the issue of mesh dependency when the continuum is not regularized^{17, 25-28} or when the cohesive surface methodology^{29, 30} is employed,³¹⁻³³ only a mesoscopic model based on a regularized continuum description can efficiently deliver reliable results.⁷⁻¹⁰ ‘Weakly’ regularized continuum descriptions^{34, 35} cannot for instance deliver information about the width of the damage band based on the fracture energy approach. The constitutive model employed in this study, proposed in Reference 1 and summarized in Section 9.2, is regularized and accounts for the essential dependencies of the global tensile strength and local fracture characteristics on the saturation level and the applied loading rate. The model parameters must, however, be calibrated so that the numerical results in terms of local data (FPZs) as well as global data (tensile strength) reflect the experimental findings. This is not a trivial task, and a trial-and-error procedure was used in order to determine a suitable set of model parameters for each saturation level that could be consistently adopted for all applied loading rates.

With reference to the experimental results,²⁻⁶ we have studied a Split Hopkinson Bar (SHB) apparatus subjected to intermediate loading rates

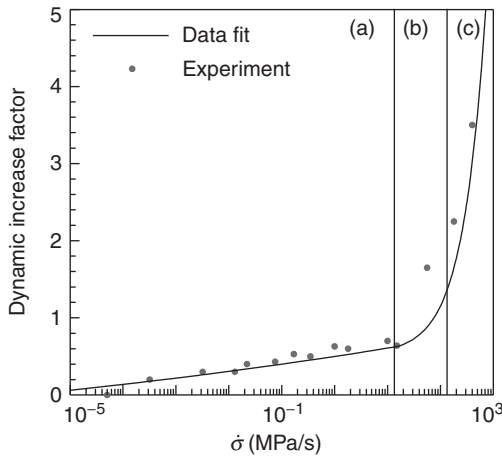
and a Modified Split Hopkinson Bar (MSHB) apparatus subjected to high loading rates. These test set-ups are used to determine the influence of the loading rate and saturation level on the formation of fracture planes during the failure process as influenced by the shape and spatial arrangement of the aggregates and the properties of the ITZ material. More specifically, in the analysis of the SHB apparatus (Section 9.4), the normal saturation level is considered and a model parameter that controls the moisture content in the numerical model is varied to examine the influence on the global tensile strength of the sample and the characteristics of the FPZ in various mesoscopic realizations. The impact of the aggregate shape on the mechanical response is studied by means of the MSHB apparatus in Section 9.5 where we have chosen a single mesoscopic representation and shown local comparisons between experimental and numerical results for three different saturation levels.

9.2 Constitutive modeling of concrete

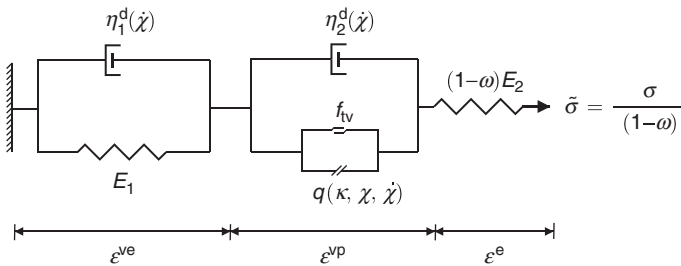
We summarize the governing equations of the constitutive model that will be employed for the mesoscopic analyses. The model, which includes visco-elasticity and coupled visco-plasticity and damage degradation mechanisms, has been applied to the macroscopic description of dynamic fracture in concrete.¹ For the sake of completeness, relevant aspects of the model are reported below.

It is well known that the mechanical properties of concrete depend on the loading rate – the physical mechanisms responsible for these rate effects have been thoroughly discussed in Rossi *et al.*³⁶ and Klepaczko and Brara.^{37,38} The dependence of the tensile strength on the loading rate can be represented in terms of the ratio of the dynamic to static strength, known as dynamic increase factor, by the curve sketched in Fig. 9.1 (refer also to Fig. 9.2 in Reference 59). The curve can be approximately divided into three branches, representing low ($\dot{\sigma} < 10$ MPa/s), intermediate ($10 \text{ MPa/s} < \dot{\sigma} < 100 \text{ MPa/s}$) and high ($\dot{\sigma} > 100 \text{ MPa/s}$) loading rates. For low and intermediate loading rates, the measured rate effect is associated with a viscous phenomenon known as the Stefan effect, which takes place in the capillary pores.^{39,40} This phenomenon can be reproduced by considering two circular plates separated by a thin water film. The force necessary to pull the plates apart depends on the loading rate and the adhesion forces between water and the plate material. The Stefan effect in this idealized mechanical system is described by the Stefan-Reynolds equation,^{41,42} according to which the adhesion force between the two plates can be expressed as⁴³

$$f_{\text{iv}} = \frac{2V\gamma^s \cos\phi}{w^2} + \frac{3\eta V^2}{2\pi w^5} \dot{w}, \quad [9.1]$$



9.1 The increase of tensile strength as a function of the loading rate. Three regions can be identified: low (a), intermediate (b), and high (c) loading rate.



9.2 Rheological representation of the VEPD model (adapted from Reference 1).

where w is the distance between the plates, related to the pore size, \dot{w} is the rate of the opening/collapse of the pores, V is the water volume, η is the water viscosity, γ^s is the surface tension, and ϕ is the wetting angle. The water volume V can be determined from a quasi-elastic neutron scattering technique,⁴⁴ and the pore-size distribution can be estimated from mercury-intrusion porosimetry tests.⁴⁵ According to Equation [9.1], the viscous strengthening effect associated with the presence of water in the pore system depends mainly on the porosity, the degree of saturation, and corresponding water-induced stresses.^{1,46} Therefore, when the pore system, water-induced stresses or moisture level changes, the viscous hardening forces are affected accordingly. The water-induced stresses are, for instance, affected by the deformation of the concrete specimen; furthermore, the appearance of microcracks certainly changes the initial state of the pore

system and the corresponding adhesion forces. In this respect, an important component of the constitutive model is the definition of a function q , which takes the above physical aspects of the viscous hardening effect into account. This hardening force is made a function of both the equivalent visco-plastic strains associated with failure and equivalent visco-elastic strains associated with the viscous forces (Stefan effect) in the pores according to

$$q(\kappa, \chi, \dot{\chi}) = f_t g(\kappa) h(\chi, \dot{\chi}), \quad [9.2]$$

where f_t is the static tensile strength. The function g , defined as an exponential softening curve and function of the equivalent visco-plastic strain κ , reads

$$g(\kappa) = \exp(-\beta_1 \kappa), \quad [9.3]$$

with β_1 a parameter governing the slope of the softening branch. The second function, h , reflects the complex physical interaction between moisture and microstructural solid skeleton. Here, the viscous hardening force

$$h(\chi, \dot{\chi}) = \left\{ 1 - \chi_a^d(\dot{\chi}) \log \left(\frac{\chi}{\chi_s} \right) \right\}, \quad [9.4]$$

proposed by Sercombe *et al.*,⁴⁷ is adopted. In Equation [9.4], by using the log function, small values of the equivalent visco-elastic strain χ , relatively to χ_s , result in an increase of the tensile strength. The parameter χ_s is the maximum value of the equivalent visco-elastic strain when the Stefan effect is active. When χ exceeds this value, i.e. when there is no Stefan effect, the h function is less than 1. Consequently, under static loading conditions and a high degree of saturation, the initial tensile strength decreases. The rate-dependent factor $\chi_a^d(\dot{\chi})$, where $\dot{\chi}$ is the rate of the equivalent visco-elastic strain, sets the evolution rate of the increase factor. From these considerations, the initial yield stress f_{iv} depends on the visco-elastic response according to $f_{iv} = f_t h(\chi, \dot{\chi})$. Upon increasing loading rates, the evolution rate of the equivalent visco-elastic strain decreases. This implies a slower decay of the viscous hardening force compared to static loading conditions. Physically, this corresponds to the retardation effect of microcracking. The evolution of the equivalent visco-elastic strain χ can be computed from a rheological Kelvin element as

$$\eta_1^d \frac{\partial \chi}{\partial t} = |\mathbf{s}| - E_1 \chi, \quad [9.5]$$

where E_1 is the visco-elastic spring stiffness, η_1^d is the dynamic viscosity defined in Equation [9.11], and \mathbf{s} is the deviatoric stress tensor. When the value of the equivalent visco-elastic strain is known, the visco-elastic strain tensor can be computed from

$$\dot{\boldsymbol{\varepsilon}}^{ve} = \dot{\chi} \mathbf{b}, \quad [9.6]$$

where \mathbf{b} is a scaling matrix defined as

$$\mathbf{b} = \mathbf{s} / |\mathbf{s}|. \quad [9.7]$$

It is important to emphasize that the viscous hardening effect is only valid for relatively low loading rates, with a dynamic increase factor below 1.5 (refer to region (b) in Fig. 9.1). The strengthening effect at higher loading rates is mainly caused by a change of fracture planes and by the effect of micro/meso-inertia.^{4,37,38,48} These phenomena are the consequence of the extremely short time to failure and a fast energy transfer from the bulk material into the crack tips^{49–51} which generate crack branching and an increase of energy dissipation. Under these conditions, cracks propagate through parts of the material with a high tensile strength and the final fracture planes do not necessarily propagate through the weakest parts of the material.

A visco-plastic model is adopted to represent the rate effects associated with the inertia effect at the micro-and meso-scale. The visco-plastic strain contribution is expressed according to the formulation proposed by Perzyna.⁵² When the yield criterion is violated in the effective stress space, i.e. when $f \geq 0$ with f the yield function, the visco-plastic strain rate is expressed in the associative form as

$$\dot{\boldsymbol{\varepsilon}}_{vp} = \frac{1}{\tau_2^d} \phi f_{\sigma}, \quad [9.8]$$

where $f_{\sigma} = \partial f / \partial \boldsymbol{\sigma}$. The visco-plastic relaxation time $\tau_2^d = \eta_2^d / f_{tv}$, where η_2^d is the viscosity and f_{tv} is the initial tensile strength function of the visco-elastic strain rate $\dot{\chi}$. The overstress function ϕ is defined as

$$\phi = \left(\frac{f}{f_{tv}} \right)^N, \quad [9.9]$$

where N is a real number ≥ 1 . From the above considerations, the total strain in the VEVDP model is expressed as

$$\boldsymbol{\varepsilon} = \boldsymbol{\varepsilon}^e + \boldsymbol{\varepsilon}^{ve} + \boldsymbol{\varepsilon}^{vp}, \quad [9.10]$$

where the strain tensor is split into elastic, $\boldsymbol{\varepsilon}^e$, visco-elastic, $\boldsymbol{\varepsilon}^{ve}$, and visco-plastic, $\boldsymbol{\varepsilon}^{vp}$, contributions. With this strain decomposition, it is possible to distinguish between the separate effects of visco-elasticity and visco-plasticity, representing the Stefan effect and the micro-inertia of the material surrounding the crack tip, respectively. A rheological representation of the model is reported in Fig. 9.2. The viscosity parameters in the visco-elastic visco-plastic element are rate-dependent according to the

following relationship between static, η_i^s and dynamic, η_i^d , viscosities ($i = 1, 2$):

$$\eta_i^d = \eta_i^s \left(1 + \nu(n) (\dot{\chi})^{\frac{1-n}{n}} \right), \quad [9.11]$$

where the function ν is defined as

$$\nu(n) = \begin{cases} 0 & \text{if } n=1 \\ 1 & \text{otherwise} \end{cases} \quad [9.12]$$

with n a real number between 0 and 1 ($1-n$) controls the sensitivity of the viscosity parameters to the applied loading rate.

The elastic stiffness E_2 is reduced by the damage variable ω as indicated in the rheological model in Fig. 9.2. The coupling between plasticity and damage is based on the effective stress concept and the hypothesis of strain equivalence.^{1,53} The Cauchy stress tensor $\boldsymbol{\sigma}$ is then computed according to

$$\boldsymbol{\sigma} = (1 - \omega) \tilde{\mathbf{D}}^{\text{pd}} : \boldsymbol{\varepsilon}, \quad [9.13]$$

where $\tilde{\mathbf{D}}^{\text{pd}}$ is the consistent tangent operator,¹ $\boldsymbol{\varepsilon}$ is the strain tensor, and the damage variable ω ($0 \leq \omega \leq 1$) in Equation [9.13] is updated through

$$\omega = 1 - \exp(-\beta_2 \kappa), \quad [9.14]$$

where β_2 regulates the slope of the damage evolution law, and κ is a history term representing a measure of the deformation accumulated in the plastic regime. To add further flexibility to the model, the damage evolution parameter β_2 is made a function of the damage parameter ω according to

$$\beta_2^* = \beta_2 \{ 1 + (\beta_\omega - 1) \omega^{\beta_\omega(1-\omega)} \}, \quad [9.15]$$

where β_ω ($0 \leq \beta_\omega \leq 1$) is a factor reflecting the brittleness of the material (β_2^* is therefore adopted in the model in place of β_2 ; $\beta_\omega = 1$ implies $\beta_2^* = \beta_2$). Further details regarding the implementation of the model can be found in Pedersen *et al.*¹ A nomenclature of the VEVPD model parameters is presented in Table 9.1 and the adopted values of the parameters for dry, normal, and wet concrete specimens can be found in Table 9.2.

9.3 Mesoscopic modeling of concrete

The model described in the previous section can reproduce the global response observed in experiments when employed in a macroscopic model, that is, when the microstructure is not explicitly represented. However, the estimation of the model parameters from experimental data conducted by Pedersen *et al.*¹ revealed several limitations of the model, which were

Table 9.1 Model parameters in the mesoscopic VEPD model

Parameter	Unit	Description
E_2	MPa	Young's modulus in elastic material
E_1	MPa	Young's modulus in visco-elastic material
ρ	Ns ² /mm ⁴	Mass density
ν	–	Poisson's ratio
η_1^s	MPa s	Viscosity in visco-elastic material
τ_2^s	s	Relaxation time in visco-plastic material
χ_a	–	Amplitude in viscous hardening function
χ_s	–	Threshold in viscous hardening function
β_1	–	Softening parameter in plastic hardening function
β_2	–	Softening parameter in damage evolution function
β_w	–	Parameter to control the damage softening parameter
f_t	MPa	Tensile strength
N	–	Exponent in visco-plastic overstress function
n	–	Exponent in rate-dependent viscosity function

Table 9.2 Macroscopic model parameters used in the SHB and MSHB tests for different degrees of saturation

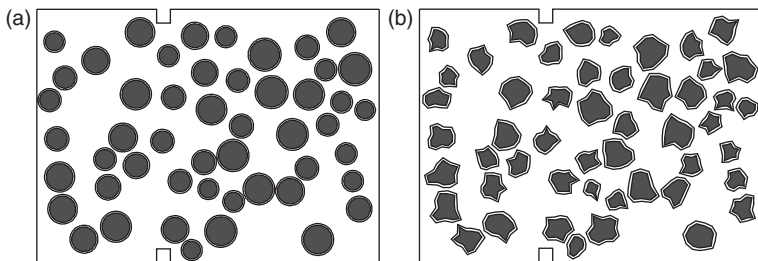
Parameter	Unit	Degree of saturation		
		Dry	Normal	Wet
E_2	MPa	38 000	44 000	46 000
E_1	MPa	60 000	60 000	60 000
ν	–	0.2	0.2	0.2
ρ	Ns ² /mm ⁴	2200×10^{-12}	2300×10^{-12}	2400×10^{-12}
η_1^s	MPa s	2000	10 000	60 000
τ_2^s	s	0.08	0.08	0.08
χ_a	–	0.025	0.025	0.025
χ_s	–	0.000 04	0.000 04	0.000 02
β_1	–	1250	1250	1250
β_2	–	12 100	8600	4400
β_w	–	0.20	0.15	0.10
f_t	MPa	3.0	3.0	2.4
N	–	1	1	1
n	–	0.6	0.6	0.6

partially solved through the recalibration of some model parameters. We have, for instance, noticed that the size of the FPZ is extremely sensitive to the applied loading rate. The source of this problem lies in the definition of the value of the relaxation time τ_2 , which is responsible for the regularization of the strain-softening regime through the introduction of rate effects in quasi-static simulations. Without a proper calibration of τ_2 , the numerical process zone obtained in dynamics simulations resulted wider than the experimental one at high loading rates, while being comparable

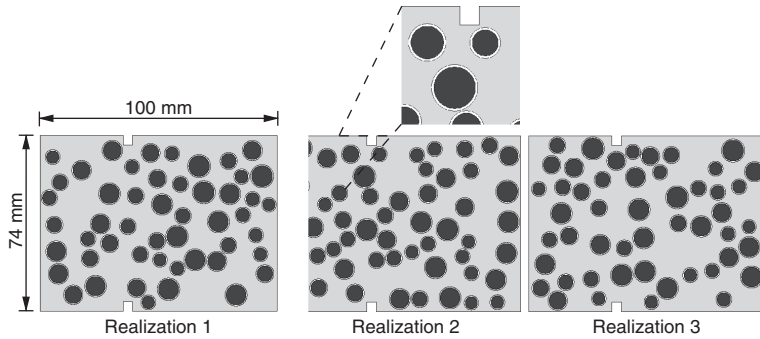
at smaller loading rates. An indirect recalibration of τ_2 was performed by considering an evolving damage evolution parameter β_2 in Equation [9.15]. The observed brittle behavior just after the peak load could be captured and, at the same time, the far post-peak response could be reproduced as well. However, although we observed an improvement in terms of global response, the local FPZ remained still not comparable to the experimental results.

The explicit representation of microstructural features has a strong impact on the definition of the localization zone width. As such, a mesoscopic representation of concrete, in which the ITZ is explicitly represented and shape, size and distribution of aggregate particles resemble realistic concrete in a statistical sense, might avoid the recalibration of the relaxation time parameter τ_2 just described. Special procedures have been developed for the generation of representative random aggregate structures.^{7,11} In the examples reported in this paper, we have considered both circular and polygonal aggregates, keeping the same aggregate volume fraction as shown in Fig. 9.3. Considering circular aggregates, a Mori-Tanaka homogenization scheme can be used to determine the stiffness of the constituents at the meso-level so that the homogenized stiffness reflects the material stiffness in the macroscopic model. Since the polygonal aggregates occupy the same physical volume, we have used the same homogenized stiffness as for the circular aggregates. The value of the Young's modulus and Poisson's ratio of the three constituents is calibrated to be similar to the homogenized stiffness and Poisson's ratio of the macroscopic model listed in Table 9.2.

The relative influence of the aggregate distribution on the fracture characteristics is analyzed by examining the three particle distributions shown in Fig. 9.4 with the VEPD constitutive model. Although the aggregate volume fraction is the same, differences in the spatial distribution of the aggregates might lead to different fracture planes. Furthermore, the aggregates and their spatial distribution introduce a physically more realistic FPZ. In this respect the width of the fracture zone is controlled by both the relaxation time and the aggregate distribution.



9.3 Typical circular (a) and polygonal (b) aggregates.



9.4 Three different realizations with the same volume fraction of aggregates. The ITZs shown in white separates the aggregates (dark gray) from the cement paste (light gray). Particle density is approximately 30%; maximum aggregate diameter $d_{\max} \approx 8$ mm.

The ITZ around each aggregate is characterized by a different microstructure compared to the surrounding cement paste. Instead of describing its complex structure, we restrict ourselves to variations of its tensile strength, f_t^{ITZ} , which is assumed to follow the Weibull statistical distribution

$$p = \frac{k}{\lambda} \left(\frac{f_t^{\text{ITZ}}}{\lambda} \right)^{k-1} e^{-(f_t^{\text{ITZ}}/\lambda)^k}, \quad [9.16]$$

where k and λ are shape and scale parameters, respectively – we used $\lambda = 10$ and $k = 1-3$ for $f_t^{\text{ITZ}} = 1-3$ MPa. Each finite element associated with the ITZ material is therefore given a random tensile strength; the values in neighboring elements are not correlated. The remaining model parameters of the ITZ follow the model parameters related to the macroscopic bulk material given in Table 9.2. Note that the Young's modulus and Poisson's ratio of the ITZ and aggregate materials are calibrated employing the Mori-Tanaka homogenization scheme as discussed above. The aggregates follow a linear elastic material behavior. Accordingly, the material densities for the constituents are determined from the volume fractions and the macroscopic density from Table 9.2. Furthermore, except for the Young's modulus, the Poisson's ratio, the density, and the initial tensile strength, the same material parameters are used for ITZ and bulk materials i.e. the two materials obey the same evolution laws for damage, softening and the Stefan effect – ITZ and bulk materials are in reality characterized by different porosity and should therefore be represented using different parameters in the evolution law describing the Stefan effect; here we neglect these differences and focus on the relative influence of aggregate shape and tensile strength of the three constituents (this issue is further discussed in Section 9.4.3).

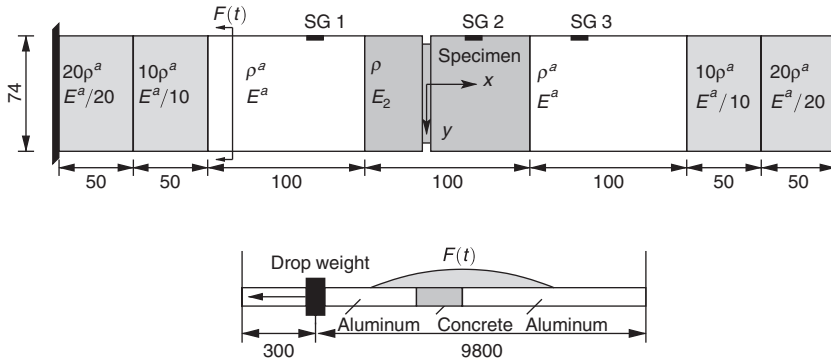
In the following sections we will study in detail the role of the heterogeneous mesostructure of concrete on the impact response of a SHB and a Modified Split Hopkinson Bar (MSHB) test set-up. In the SHB test we focus on the influence of different conditions on the fracture characteristics and the global tensile strength such as (i) the saturation level, by changing the viscosity parameter η_i^s , (ii) the initial tensile strength, and (iii) the aggregate shape and configuration. The material definition for normal saturation level from Table 9.2 is adopted in these analyses. In the MSHB test we examine the influence of the different saturation levels from Table 9.2 on the global and local response and compare the results to experimental findings.

9.4 The Split Hopkinson Bar test

A gravity driven SHB apparatus was used in Reference 54 to study the behavior of concrete in the intermediate loading rate range in region (b) depicted in Fig. 9.1. With this numerical exercise we want to illustrate three important issues: (i) the influence of the tensile strength of the ITZ material on the global tensile strength of the specimen, (ii) the influence of different distributions of aggregates, including their shape, on the overall dynamic tensile strength, and (iii) the role of the rate-dependent properties of the bulk material. The material parameter set for normal saturation level reported in Table 9.2 is adopted in this section.

The SHB set-up consists of two vertical cylindrical aluminum bars (diameter 74 mm) between which the concrete specimen is glued. The geometry and boundary conditions of the SHB specimen are shown in Fig. 9.5 along with the simplified model used in the numerical analyses. In the numerical model, the two aluminum bars have been shortened for numerical convenience. Consequently, their material properties have had to be altered so that (i) the arrival time of the tensile wave from SG 1 to the specimen is comparable to that measured in the experiments (elastic wave velocity $C_e = \sqrt{E/\rho}$), and (ii) acoustic impedances ($z = A\sqrt{E/\rho}$) of aluminum and concrete are identical. With these constraints, Young's modulus and density of the two aluminum bars are taken equal to $E_2^a = 4570$ MPa and $\rho^a = 19950 \times 10^{-12}$ Ns²/mm⁴, respectively. Wave reflection is avoided using elements with a reduced Young's modulus, but similar acoustic impedance, at both ends of the two aluminum bars as shown in Fig. 9.5a. Plane-stress three-node elements have been used in all the analyses.

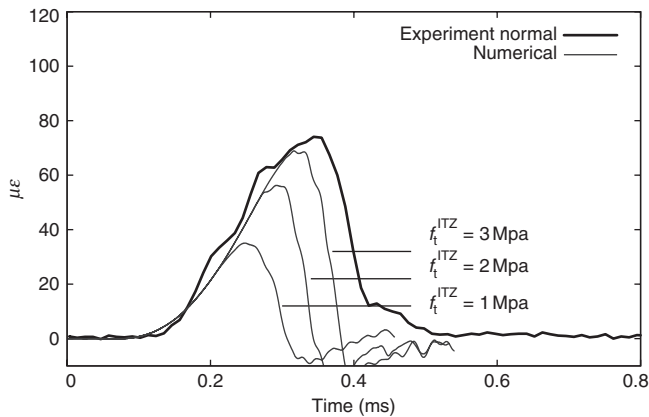
In the analyses, we considered realization 3 shown in Fig. 9.4 with material properties according to a normal degree of saturation as listed in Table 9.2. The ITZ material properties follow those of the bulk with the exception of Young's modulus and Poisson's ratio, which are determined from the homogenization scheme in Appendix A, and tensile strength. There is



9.5 A two-dimensional model of the SHB test set-up: (a) material properties and boundary conditions – the properties of the material on the right- and left-hand sides have been calibrated in order to represent a wave-absorbing material, whereas the white and gray zones are given the properties of steel and concrete, respectively and (b) the drop weight that introduces the tensile stress wave $F(t)$. All dimensions in mm.

no exact relation between the tensile strength of the bulk material and the strength f_t^{ITZ} of the ITZ material. However, it is well known that f_t^{ITZ} is lower than the bulk tensile strength. Thus, in a preliminary analysis, we have tested three different values of the ITZ tensile strength (1, 2 and 3 MPa) – note that these values are given as input to the Weibull distribution of the ITZ tensile strength in Equation [9.16]. The numerical study on the influence of the tensile strength of the ITZ material revealed that this parameter has a significant impact on the global tensile strength of the specimen as evident from the transmitted strain wave reported in Fig. 9.6. The corresponding final fracture planes related to the different tensile strengths are shown in Plate XXI (see colour section between pages 208 and 209). The local response in Plate XXIC is similar to the macroscopic FPZs reported in Reference 1, suggesting that the influence of the mesostructure is, in this case, minor. A similar observation holds for the global response shown in Fig. 9.6. As evident from Plate XXIA, the most vulnerable material points are located in the ITZ elements and in the regions connecting them. When the tensile strength of the ITZ is increased, relatively more bulk material is damaged and the fracture planes become less defined (Plate XXIC).

Experimental evidence suggests that the tensile strength of the ITZ material is lower than the bulk tensile strength. Consequently, the numerical results presented in Fig. 9.6 indicate that the experimental results can be reproduced only if the model parameters in the mesoscopic model are redefined – we will show how we have approached this issue in Sections 9.4.2 and 9.4.3. Next, we analyze the impact on the mechanical response of



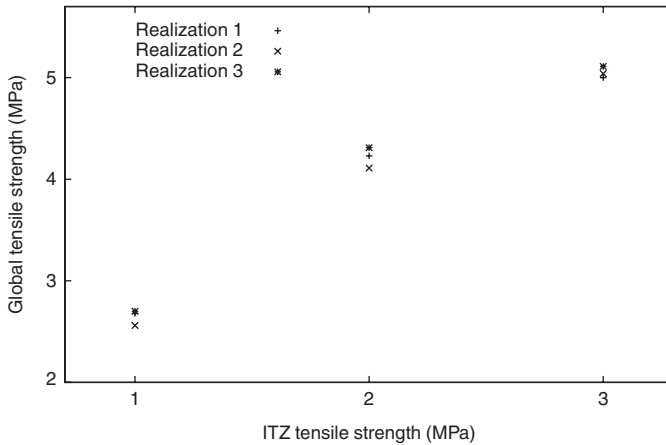
9.6 Time-strain curves at the upper bar (SG 3) for the normal saturation level material set. The corresponding fracture planes are shown in Plate XXI (see colour section between pages 208 and 209).

the different realizations shown in Fig. 9.4 for different tensile strengths of the ITZ material.

9.4.1 Different aggregate distributions

The realizations in Fig. 9.4 are considered in order to determine the influence of the aggregate distribution on the global strength and number of fracture planes. We consider variations of the ITZ tensile strength for a normal degree of saturation ($f_t^{\text{ITZ}} = 1, 2, 3$ MPa for each distribution). Figure 9.7 shows that there is no significant variation of the global tensile strength for the three aggregate distributions. The overall tensile strength is obtained by multiplying the measurement of the transmitted strain wave reported in Fig. 9.6 with the Young's modulus of the aluminum upper bar. The final fracture patterns are shown in Plate XXII (see colour section between pages 208 and 209) for different aggregate distributions with $f_t^{\text{ITZ}} = 1$ MPa. In the three realizations, the final failure consists of one or two dominant fracture planes. For realization 2 damage initiates at the notches, whereas for realizations 1 and 3 failure initiates between aggregates and the free boundary.

The characteristics of the FPZ from the remaining combinations of f_t^{ITZ} and aggregate distributions follow the same trend as shown in Plates XXI and XXII. This is also confirmed by a low variation of the global strength obtained from the different realizations as shown in Fig. 9.7. When f_t^{ITZ} is lower compared to that of the bulk material, cracks are mainly located in the ITZ materials. However, more cracks are formed in the bulk material when f_t^{ITZ} is increased. The previous analyses showed that $f_t^{\text{ITZ}} = 2$ MPa provided



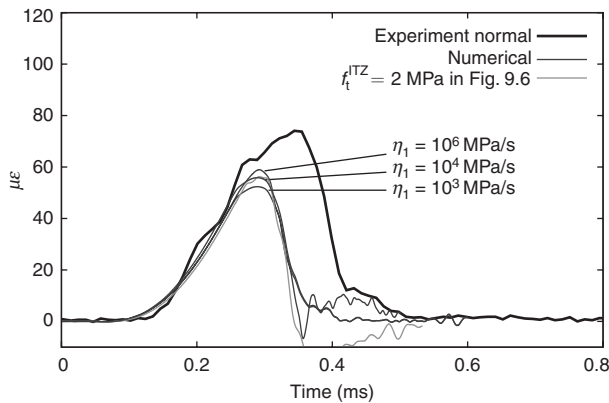
9.7 Tensile strength of the concrete specimen as a function of the tensile strength of the ITZ for the three realizations in Fig. 9.4.

the best results in terms of the global strength and the FPZ. Therefore, in the following simulations we choose $f_t^{\text{ITZ}} = 2$ MPa in the Weibull distribution (Equation [9.16]). Since the global tensile strength turns out to be lower than the strength obtained with the macroscopic model (refer to Fig. 9.6), a recalibration of the material properties of the bulk and ITZ material is necessary. In the following examples, we show the influence of variations of the parameter η_i^s on the mechanical response.

9.4.2 Influence of bulk viscosity

The previous set of analyses proved that the tensile strength of the ITZ material is an important parameter that influences both global and local response, whereas the global tensile strength is almost independent of the aggregate configuration. In the following analyses we use $f_t^{\text{ITZ}} = 2$ MPa and $f_t = 3$ MPa for the bulk material. We now consider variations of the viscosity parameter η_i^s in the bulk material for a normal degree of saturation by keeping all remaining model parameters fixed. The viscosity parameter η_i^s reflects the Stefan effect and is related to the microstructure via the moisture content and the pore-size distribution as discussed in Reference 1. The Stefan effect is responsible for the increase in the tensile strength observed in the experiments for intermediate loading rates (region (b) in Fig. 9.1) through the hardening function in Equation [9.4].

The results of our simulations, reported in Fig. 9.8, indicate that the influence of η_i^s in the bulk material on the global tensile strength is not significant. Indeed, the results are qualitatively identical to those shown in Fig. 9.6

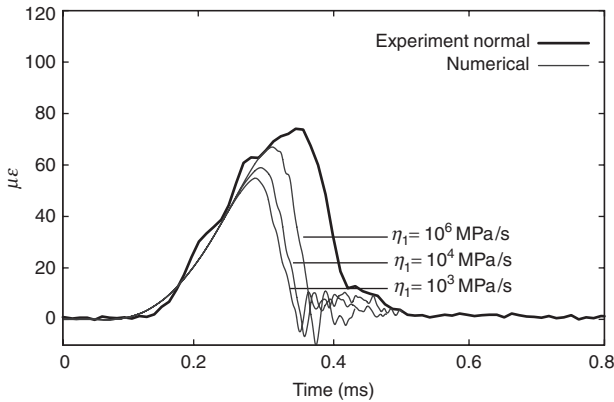


9.8 Time-strain measurement of transmitted wave for different viscosities η_i^s of the bulk material.

with $f_t^{ITZ} = 2$ MPa and $\eta_i^s = 10^4$ MPa/s (normal saturation level) for both the bulk and ITZ material. This conclusion, which holds for the other saturation levels as well, is a further indication of the relatively low influence of the bulk properties with respect to those of the ITZs. The corresponding FPZs are reported in Plate XXIII (see colour section between pages 208 and 209). The number and orientation of the fracture planes are independent of the viscosity parameter η_i^s . However, increasing the viscosity in the bulk material reduces the diffusion of damage around the aggregates as a consequence of the strength increase of the material. Further, we observe that the fracture planes shown in Plates XXI and XXIII are comparable. The small deviations in the results can be explained from a different distribution of the tensile strength of the ITZ material in the simulations.

9.4.3 Influence of bulk and ITZ viscosity

Next, the viscosity η_i^s is varied in both bulk and ITZ material considering the same values as in the previous example. The time strain response is reported in Fig. 9.9. Unlike the results reported in Fig. 9.8, the viscosity parameter η_i^s has now a higher impact on the global tensile strength. Actually, we see that it is possible to approach the experimental measurement when a viscosity $\eta_i^s = 10^6$ MPa/s is used. Therefore, it is important to properly define the material properties of the ITZ elements, as they are the first active elements in the localization process while the surrounding bulk material is predominantly elastic. However, the overall failure process does not seem to be influenced, as evident from the comparison of the final fracture planes reported in Plates XXIII and XXIV (see colour section between pages 208 and 209).



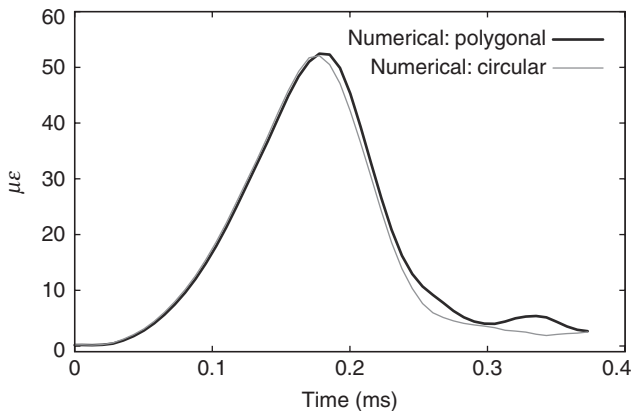
9.9 Time-strain measurement of transmitted wave for different viscosities η_i^s of bulk and ITZ material.

The recalibration of the VEPD model is further complicated when different nonlinear material behaviors are considered in the same mesoscopic model. In general, the ITZ material has a higher porosity than the bulk material and its pore-size distribution is different. Therefore, the viscosity parameter η_i^s , related to the Stefan effect, and the tensile strength must be different in the two systems. Hence, in principle, in our mesoscopic model we need to calibrate a viscosity parameter for each porous system, i.e. define a viscosity parameter for both the ITZ and bulk material. However, we do not have any experimental evidence of the characteristics of the different porous systems. Therefore, we use the same viscosity parameter for both systems. We emphasize that the experiments can be reproduced both if a relatively high or low viscosity parameter is used for the ITZ material compared to the bulk material. The only restriction is that the selected parameters must be consistent, so that the numerical results fit the experimental output for a range of applied loading rates – with the parameters listed in Table 9.2 we are able to fit the experimental output obtained with three different loading rates.

9.4.4 Influence of aggregate shape

The analyses in Section 9.4.3 showed that the properties of the ITZ material have a significant influence on the global response and a less marked influence on local fracture characteristics. Next, we compare results obtained with circular and polygonal aggregates. We use the input parameters corresponding to the normal saturation level.

In Fig. 9.3, polygonal aggregates are employed for realization 1 shown in Fig. 9.4 – note that in both cases volume fraction and center of gravity of the aggregates are the same. Fracture patterns obtained with the mesoscopic



9.10 Strain measurement of the transmitted tensile wave from simulations with polygonal and circular aggregates in the mesoscopic model.

analyses with polygonal and circular aggregates are reported in Plate XXV (see colour section between pages 208 and 209). We obtain approximately identical widths of the FPZs. Further, both aggregate geometries activate the same fracture planes. The only difference can be observed in the fracture planes, which in the case of polygonal aggregates are more distinctive and well defined. Furthermore, Fig. 9.10 shows that the time strain response is not significantly affected by the aggregate shape. Hence, the total energy dissipation is almost identical in the two cases. These results are in line with the finding in Reference 26.

9.5 Modified Split Hopkinson Bar test

The Modified Split Hopkinson Bar (MSHB) is now analyzed, considering a high loading rate (region (c) in Fig. 9.1). We use the rate-dependent mesoscopic model and the model parameters from the SHB simulations in the previous section. This is in line with the definition of a set of model parameters that is consistent with all possible loading rates as previously discussed. In the same spirit, through an extensive parametric study, we have determined a parameter set for each saturation level (refer to Table 9.2). This parametric study also showed that an improved grading of polygonal aggregates had a significant impact on the results, which is in contrast with the conclusions from the SHB tests. Therefore, we focus on more realistic microstructures with improved grading plus polygonal aggregates, as shown in Fig. 9.11.

In this section we will focus on the analysis of the effect of variations in the tensile strength of the ITZ material and the saturation level. The experimental data reported by Vegt *et al.*²⁻⁶ will be compared to the numerical

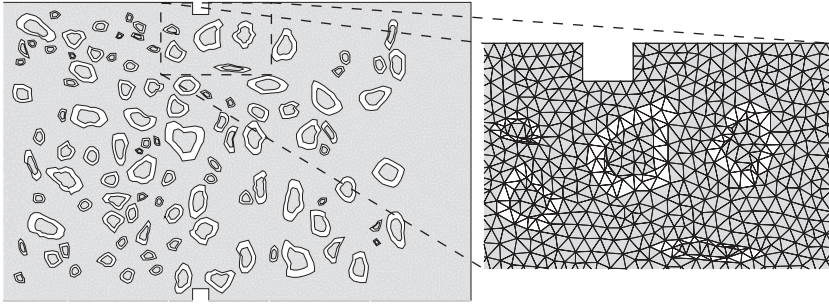
results. Note that the character of the structural set-up in the experiments makes it very difficult to obtain reliable data for the FPZ.

However, estimates of the width of the FPZs from the MSHB tests are presented in Reference 5 for the three saturation levels. Here we use the measured strains in the comparison between numerical and experimental results. The FPZs obtained with the numerical mesoscopic model are shown in order to illustrate the influence of the saturation level on the size of the fracture zones.

The computational model of the MSHB test set-up is reported in Fig. 9.12. In the experiments, a compression wave, generated from an explosive charge, propagates in the steel bar and is transmitted to the concrete specimen. In the model, the load $F(t)$ is applied to the middle of the steel bar. This results in a tensile wave propagating to the left-hand side and a compression wave propagating to the right-hand side. Reflection of the tensile wave at the left free end is avoided using elements with a reduced Young's modulus but with similar acoustic impedance. The length of these zones and the position where the load is applied depend on the stress-wave velocity. Failure is initiated at the notches when the compression wave is reflected at the right free end. Consequently, the position of the notches controls the stress state around them and in this way failure initiation. The optimal position of the notches depends on the wave length, the wave velocity, and the geometry of the specimen. In the experiments, each saturation level was characterized by a different wave velocity. Therefore, the dynamic Young's modulus E_2 is calibrated to 45 000, 48 000 and 53 000 MPa for low, medium and high saturation level, respectively (see Table 9.2). The Young's modulus and Poisson's ratio for the three constituents are determined using the homogenization procedure described in Appendix A although the aggregates are polygonal.

9.5.1 Tensile strength of ITZ

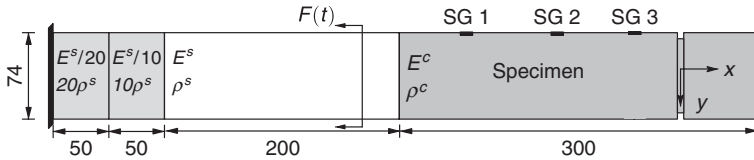
Classical visco-plastic models are known to be very sensitive to the applied loading rate as discussed in Reference 1. For a specific relaxation time, both the material tensile strength and the width of the damage zone increase with the applied loading rate. However, the problem lies in the relatively fast increase, compared to the tensile strength, of the width of the damage zone. Therefore, if a visco-plastic model is employed to reproduce the increase in tensile strength reported in Fig. 9.1c, a simple remedy to avoid this problem consists in using an artificially high initial tensile strength and a low relaxation time. However, in the VEVDP model a physically realistic value for the tensile strength can be used with a relatively high relaxation time because part of the strengthening effect is covered by the Stefan effect, which is controlled by the visco-elastic model.



9.11 Mesostructure with bulk material, aggregate, and ITZ (linear triangular elements are used).

The Stefan effect is less pronounced in the high loading rate regime, where the local inertia effect is the predominant contribution to the observed increase in tensile strength. The literature distinguishes between local inertia effect and structural inertia effect. Local inertia effect is assumed to be a material property and covers the complex mechanisms taking place in the crack tip zone of a fast propagating crack.⁵ In Reference 55, an explicit model of the local inertia effect stemming from the growth of microcracks is presented. The model is based on a non-local damage approach, where the equivalent damage equation is extended with an inertia term. Structural inertia⁵⁶ is related to the type of boundary and load conditions and should automatically contribute to the mechanical response independently of the applied constitutive relation if a transient analysis has been considered. However, Cotsovos and Pavlović⁵⁷ concluded that a significant change in the density has a relatively small effect on the response of concrete specimens under high rates of loading. In our rate-dependent mesoscopic model, micro-inertia effects are included automatically because the relaxation time τ_2 is very sensitive to the applied loading rate – this results in spreading of the FPZs. Furthermore, we observe from our results that structural inertia⁵⁶ is separated from the material inertia because the set of model parameters can be used for three different structural test set-ups with different strain rates.

Next we examine the influence of the strength of the ITZ material. The number of fracture planes related to the tensile strength of the ITZ material is examined with reference to the model parameters corresponding to the normal saturation level (see Table 9.2). The damage patterns are shown in Plate XXVI (see colour section between pages 208 and 209) for three different tensile strengths of the ITZ material. As previously discussed in Section 9.4, the width of the macroscopic damage profile in the mesoscopic SHB tests is recovered when the tensile strength of the ITZ and bulk material is identical. However, this is not the case in the MSHB tests where an opposite trend is observed.



9.12 A two-dimensional model of the MSHB test set-up. The properties of the material on the left-hand side have been calibrated in order to represent a wave-absorbing material, whereas the white and gray zones are given the properties of steel and concrete, respectively. Dimensions in mm.

9.5.2 Influence of saturation level

The MSHB test set-up with three different moisture levels is considered using the mesoscopic model and the model parameters from the SHB tests. The model parameters are listed in Table 9.2, and the tensile strength f_t^{ITZ} follows the same distribution as that used in the SHB tests with an average input strength $f_t^{\text{ITZ}} = 2$ MPa – in the definition of the ITZ tensile strength we have followed the arguments described in Section 9.4. Note that the reported strain measurements are from SG 3 in Fig. 9.12.

Dry material

The local and global response for the dry material are reported in Plate XXVII (see colour section between pages 208 and 209). The numerical strain follows approximately the normal strains measured in the experiments. Quantitatively, we can say that the size of the numerical FPZ increases compared to the numerical results obtained with the SHB tests. This is in line with the conclusions in Reference 5.

Normal material

The local and global response for the material with a normal saturation level are reported in Plate XXVIII (see colour section between pages 208 and 209). When the global response is matched for the normal saturation level, the corresponding FPZ is very similar to the FPZ obtained with the dry material. Therefore, the conclusions reached in the dry material test hold in this case as well. The results agree with the experimental results on the fracture zones reported in Reference 5.

Wet material

Plate XXIX (see colour section between pages 208 and 209) shows the local and global response for the case of material with a high saturation level

i.e. wet material. The experimental observations⁵ indicate that the amount of microcracks depends on the applied loading rate and the saturation level. Normal and dry material show a very similar behavior, whereas more microcracks are observed in the wet material experimental data.⁵ Therefore, numerical and experimental results are in disagreement in this case.

A wider FPZ can be obtained if the amplitude of the incoming compression wave is increased. We observe from the time strain plot in Plate XXIX that the amplitude can be increased by approximately 15% and still fit within the experimental measurement. This implies that more material points are damaged. We also know that the strength increase originating from the Stefan effect is higher for the wet material as compared to normal and dry materials. Consequently, the material is in this case characterized by a higher tensile strength. This might explain Plate XXVI where less material points are damaged when compared to the FPZ from materials with dry and normal saturation levels. It is also worth noting that the value of the damage softening parameter β_2 from Table 9.2 for the wet material is the smallest amongst the three materials. A small β_2 value implies a ductile material behavior and correspondingly a slow damage progress. Furthermore, the loading time (length of loading wave) compared to the SHB tests is much smaller. Therefore, the fast loading wave and the slow damage process could explain the narrow FPZ when compared to experiments. Finally, according to Reference 6, the standard deviation on the fracture energy for wet material is approximately 35%. We assumed a similar behavior for the width of the FPZ. Therefore, with some effort, adjusting the softening parameter β_2 for the wet material, the numerical FPZ may come closer to the experimental result when experimental uncertainties are considered. In conclusion, the experimental observations on an increased width of the FPZ for wet material may be reproduced numerically with the above mentioned modifications. This means that no clear trend on the dependence of the FPZ on the saturation level can be extracted from the numerical results of the MSHB tests. However, the numerical results showed the clear trend that the width of the FPZ is very sensitive to the applied loading rate. The FPZs in the MSHB tests are clearly larger than those obtained in the SHB tests. Hence, the width of the FPZs grows with increasing loading rate.

9.6 Summary and conclusions

The main objective of this work was to analyze the dynamic response of concrete specimens subjected to different degrees of saturation and different loading rates. Experimental results from Delft University of Technology²⁻⁶ show that failure processes in concrete depend on the loading rate and moisture in the capillary pores. In this contribution we have proposed a mesoscopic model that combines a regularized constitutive model¹ and an explicit model of the mesostructure including aggregates and ITZ. The resulting mesoscopic

model was used to predict the above mentioned experiments. We have shown that an improved prediction of the tensile strength and the size of the FPZ as a function of loading rate and saturation level can be achieved with the proposed mesoscopic model. In this numerical exercise we studied the role of four relevant model components on global tensile strength and size of the FPZ: (i) the tensile strength of the ITZ material, (ii) the model parameter that controls the moisture content, (iii) the aggregate shape and distribution, and (iv) the applied loading rate. We found that the tensile strength of the ITZ material is an important parameter that defines the global strength as well as the final size of the FPZ. This holds for both intermediate and high loading rates. The moisture content is responsible for the initiation of microcracks in the specimen. Therefore, the distribution of the aggregates and corresponding ITZs defines the initial damage state. However, the results clearly indicate that the loading rate has the strongest impact on the final size of the FPZ and the global tensile strength.

The results presented in this study demonstrate that a mesoscopic model clearly improves the description of failure processes in concrete and makes the comparison to experimental observations more objective.

9.7 Acknowledgments

This research is supported by the Netherlands Science Foundation STW (under grant DCT.6262) and the Ministry of Public Works and Water Management. The experimental data were kindly provided by I. Vegt and J. Weerheijm (TU Delft).

9.8 References

1. R. R. Pedersen, A. Simone, and L. J. Sluys, 2008. An analysis of dynamic fracture in concrete with a continuum visco-elastic visco-plastic damage model. *Engineering Fracture Mechanics*, **75**:3782–3805.
2. I. Vegt, K. van Breugel, and J. Weerheijm, 2007. *Failure mechanisms of concrete under impact loading*. In A. Carpinteri, P. Gambarova, G. Ferro, and G. Plizzari (eds.), *New Trends in Fracture Mechanics of Concrete – FraM-CoS 2007*, Catania, Italy, 17–22 June 2007. Taylor & Francis, London/Leiden/New York/Philadelphia/Singapore. ISBN 978-0-415-44065-3.
3. I. Vegt, J. Weerheijm, and K. van Breugel, 2007. *The fracture energy of concrete under impact tensile loading a new experimental technique*. In F. Toutlemond, K. Sakai, O. Gjørv, and N. Banthia (eds.), *Proceedings of the 5th international Conference on Concrete under Severe Conditions of Environment and Loading – CONSEC’07*, Tours, France, 4–6 June 2007.
4. J. Weerheijm, 2007. Tensile failure of concrete at high loading rates: New test data on strength and fracture energy from instrumented spalling tests. *International Journal of Impact Engineering*, **34**:609–626.
5. J. Weerheijm and I. Vegt, 2011. How to determine the dynamic fracture energy of concrete. Theoretical considerations and experimental evidence. *Applied Mechanics and Materials*, **82**:51–56.

6. J. Weerheijm, I. Vegt, and K. van Breugel, 2009. *The rate dependency of concrete in tension. new data for wet, normal and dry conditions*. In DYMAT 2009–9th International Conference on the Mechanical and Physical Behaviour of Materials under Dynamic Loading, **1**:95–101, [10.1051/dymat/2009013], Brussels, Belgium, 7–11 September 2009. EDP Sciences (www.dymat-proceedings.org). ISBN 978-2-7598-0472-6.
7. S. Eckardt and C. Könke, 2008. Adaptive damage simulation of concrete using heterogeneous multiscale models. *Journal of Algorithms and Computational Technology*, **2**(2):275–297.
8. O. Lloberas-Valls, D. J. Rixen, A. Simone, and L. J. Sluys, 2012. Multiscale domain decomposition analysis of quasi-brittle heterogeneous materials. *International Journal for Numerical Methods in Engineering*, **89**(11):1337–1366.
9. Ł. Skarżyński and J. Tejchman, 2010. Calculations of fracture process zones on meso-scale in notched concrete beams subjected to three-point bending. *European Journal of Mechanics-A/Solids*, **29**(4):746–760.
10. J. F. Unger and S. Eckardt, 2011. Multiscale modeling of concrete. *Archives of Computational Methods in Engineering*, **18**(3):341–393.
11. S. Honkeafner, S. Eckardt, T. Luther, and C. Könke, 2006. Mesoscale modeling of concrete: Geometry and numerics. *Computers and Structures*, **84**:450–461.
12. Z. M. Wang, A. K. H. Kwan, and H. C. Chan, 1999. Mesoscopic study of concrete I: Generation of random aggregate structure and finite element mesh. *Computers and structures*, **70**(5):533–544.
13. P. Wriggers and S. O. Moftah, 2006. Mesoscale models for concrete: Homogenisation and damage behaviour. *Finite Elements in Analysis and Design*, **42**(7):623–636.
14. N. Benkemoun, M. Hautefeuille, J.-B. Colliat, and A. Ibrahimbegovic, 2010. Failure of heterogeneous materials: 3D meso-scale fe models with embedded discontinuities. *International Journal for Numerical Methods in Engineering*, **82**(13):1671–1688.
15. P. Grassl and R. Rempling, 2008. A damage-plasticity interface approach to the meso-scale modelling of concrete subjected to cyclic compressive loading. *Engineering Fracture Mechanics*, **75**(16):4804–4818.
16. L.-P. Guo, A. Carpinteri, R. Roncella, A. Spagnoli, W. Sun, and S. Vantadori, 2009. Fatigue damage of high performance concrete through a 2D mesoscopic lattice model. *Computational Materials Science*, **44**(4):1098–1106.
17. J. Kozicki and J. Tejchman, 2008. Modelling of fracture process in concrete using a novel lattice model. *Granular Matter*, **10**(5):377–388.
18. J. P. B. Leite, V. Slowik, and J. Apel, 2007. Computational model of mesoscopic structure of concrete for simulation of fracture processes. *Computers and Structures*, **85**(17–18):1293–1303.
19. G. Lilliu and J. G. M. van Mier, 2003. 3D lattice type fracture model for concrete. *Engineering Fracture Mechanics*, **70**(7–8):927–941.
20. K. Nagai, Y. Sato, and T. Ueda, 2004. Mesoscopic simulation of failure of mortar and concrete by 2D RBMS. *Journal of Advanced Concrete Technology*, **2**(3):359–374.
21. M. Ostoja-Starzewski and G. Wang, 2006. Particle modeling of random crack patterns in epoxy plates. *Probabilistic Engineering Mechanics*, **21**(3):267–275.
22. G. Cusatis, 2011. Strain-rate effects on concrete behavior. *International Journal of Impact Engineering*, **38**:162–170.

23. P. Grassl and M. Jirasek, 2010. Meso-scale approach to modelling the fracture process zone of concrete subjected to uniaxial tension. *International Journal of Solids and Structures*, **47**(7–8):957–968.
24. A. Zubelewicz and Z. P. Bažant, 1987. Interface element modeling of fracture in aggregate composites. *Journal of Engineering Mechanics*, **113**(11):1619–1630.
25. F. Dupray, Y. Malecot, L. Daudeville, and E. Buzaud, 2009. A mesoscopic model for the behaviour of concrete under high confinement. *International Journal for Numerical and Analytical Methods in Geomechanics*, **33**(11):1407–1423.
26. S.-M. Kim and R. K. Abu Al-Rub, 2011. Meso-scale computational modeling of the plastic-damage response of cementitious composites. *Cement and Concrete Research*, **41**:339–358.
27. A. K. H. Kwan, Z. M. Wang, and H. C. Chan, 1999. Mesoscopic study of concrete II: Nonlinear finite element analysis. *Computers and structures*, **70**(5):545–556.
28. J. D. Eshelby, 1957. The determination of the elastic field of an ellipsoidal inclusion and related problems. *Proceedings of the Royal Society of London. Series A*, **241**:376–396.
29. M. G. A. Tijssens, L. J. Sluys, and E. Van der Giessen, 2000. Numerical simulation of quasi-brittle fracture using damaging cohesive surfaces. *European Journal of Mechanics A/Solids*, **19**(5):761–779.
30. X.-P. Xu and A. Needleman, 1994. Numerical simulations of fast crack growth in brittle solids. *Journal of the Mechanics and Physics of Solids*, **42**(9):1397–1434.
31. A. Caballero, I. Carol, and C. M. López, 2006. A meso-level approach to the 3D numerical analysis of cracking and fracture of concrete materials. *Fatigue and Fracture of Engineering Materials and Structures*, **29**(12):979–991.
32. L. Snozzi, A. Caballero, and J. F. Molinari, 2011. Influence of the meso-structure in dynamic fracture simulation of concrete under tensile loading. *Cement and Concrete Research*, **41**(11):1130–1142.
33. M. G. A. Tijssens, L. J. Sluys, and E. Van der Giessen, 2001. Simulation of fracture of cementitious composites with explicit modeling of microstructural features. *Engineering Fracture Mechanics*, **68**(11):1245–1263.
34. D. Nguyen, C. Lawrence, C. La Borderie, M. Matallah, and G. Nahas, 2010. A mesoscopic model for a better understanding of the transition from diffuse damage to localized damage. *European Journal of Environmental and Civil Engineering*, **14**(6–7):751–776.
35. W. C. Zhu and C. A. Tang, 2002. Numerical simulation on shear fracture process of concrete using mesoscopic mechanical model. *Construction and Building Materials*, **16**(8):453–463.
36. P. Rossi, J. G. M. van Mier, C. Boulay, and F. L. Maou, 1992. The dynamic behaviour of concrete: Influence of free water. *Materials and Structures*, **25**(9):509–514.
37. A. Brara and J. R. Klepaczko, 2006. Experimental characterization of concrete in dynamic tension. *Mechanics of materials*, **38**:253–267.
38. J. R. Klepaczko and A. Brara, 2001. An experimental method for dynamic tensile testing of concrete by spalling. *International Journal of Impact Engineering*, **25**:387–409.
39. E. Cadoni, K. Labibes, C. Albertini, M. Berra, and M. Giangrasso, 2001. Strain-rate effect on the tensile behaviour of concrete at different relative humidity levels. *Materials and Structures*, **34**:21–26.
40. C. A. Ross, D. M. Jerome, J. W. Tedesco, and M. L. Hughes, 1996. Moisture and strain rate effects on concrete strength. *ACI Material Journal*, **96**:293–300.

41. A. V. Nguyen, 2000. Historical note on the Stefan–Reynolds equations. *Journal of Colloid and Interface Science*, **231**(1):195.
42. B. Steinhaus, P. T. Spicer, and A. Q. Shen, 2006. Droplet size effects on film drainage between droplet and substrate. *Langmuir*, **22**:5308–5313.
43. P. Rossi, 1991. A physical phenomenon which can explain the mechanical behaviour of concrete under high strain rates. *Materials and Structures*, **24**(6):54–62.
44. H. N. Bordallo, L. P. Aldridge, and A. Desmedt, 2006. Water dynamics in hardened ordinary portland cement paste or concrete: From quasielastic neutron scattering. *The Journal of Physical Chemistry B*, **110**:17966–17976.
45. S. Roels, J. Elsen, J. Carmeliet, and H. Hens, 2001. Characterisation of pore structure by combining mercury porosimetry and micrography. *Materials and Structures*, **34**:76–82.
46. Z. P. Bazant, A. B. Hauggaard, S. Baweja, and F. J. Ulm, 1997. Microprestress-solidification theory for concrete creep. I: Aging and drying effects. *Journal of Engineering Mechanics*, **123**(11):1188–1194.
47. J. Sercombe, F.-J. Ulm, and H.-A. Mang, 2000. Consistent return mapping algorithm for chemoplastic constitutive laws with internal couplings. *International Journal for Numerical Methods in Engineering*, **47**:75–100.
48. H. W. Reinhardt and J. Weerheijm, 1991. Tensile fracture of concrete at high loading rates taking account of inertia and crack velocity effects. *International Journal of Fracture*, **51**:31–42.
49. J. F. Boudet, S. Ciliberto, and V. Steinberg, 1996. Dynamics of crack propagation in brittle materials. *Journal de Physique II*, **6**:1493–1516.
50. J. Fineberg, S. P. Gross, M. Marder, and H. L. Swinney, 1991. Instability in dynamic fracture. *Physical Review Letters*, **67**:457–460.
51. E. Sharon, S. P. Gross, and J. Fineberg, 1996. Energy dissipation in dynamic fracture. *Physical Review Letters*, **76**:2117–2120.
52. P. Perzyna, 1966. *Fundamental problems in viscoplasticity*. Advances in Applied Mechanics, **9**:243–377. Academic Press, New York.
53. J. W. Ju, 1989. On energy-based coupled elastoplastic damage theories: Constitutive modeling and computational aspects. *International Journal of Solids and Structures*, **25**(7):803–833.
54. I. Vegt, J. Weerheijm, R. R. Pedersen, and L. J. Sluys, 2006. *Modelling of impact behaviour of concrete -an experimental approach*. In G. Meschke, R. de Borst, H. A. Mang, and N. Bîćanić (eds.), Computational Modelling of Concrete Structures – EURO-C 2006, Mayrhofen, Tyrol, Austria, 27–30 March 2006. Taylor & Francis, London/Leiden/New York/Philadelphia/Singapore. ISBN 0 415 39749 9.
55. U. Haußler-Combe and M. Kitzig, 2009. Modeling of concrete behavior under high strain rates with inertially retarded damage. *International Journal of Impact Engineering*, **36**:1106–1115.
56. J. Ozbolt, A. Sharma, and H. W. Reinhardt, 2011. Dynamic fracture of concrete compact tension specimen. *International Journal of Solids and Structures*, **48**:1534–1543.
57. D. M. Cotsovos and M. N. Pavlovic, 2008. Numerical investigation of concrete subjected to compressive impact loading. Part 2: Parametric investigation of factors affecting behaviour at high loading rates. *Computers and Structures*, **86**:164–180.
58. P. Onck and E. Van der Giessen, 2000. A relationship among the components of the Eshelby tensor and its physical meaning in general inclusion problems. *Philosophical Magazine Letters*, **80**(6):367–370.

59. R. Desmorat, M. Chambart, F. Gatuingt, and D. Guilbaud, 2010. Delay-active damage versus non-local enhancement for anisotropic damage dynamics computations with alternated loading. *Engineering Fracture Mechanics*, **77**(12):2294–2315.

9.9 Appendix A: computation of the homogenized material tensor for different saturation levels

Next, we use the Mori-Tanaka homogenization scheme to determine the material tensor for the constituents of the mesoscopic model. In the Mori-Tanaka scheme a combined stiffness \mathbf{D}_c is formulated as

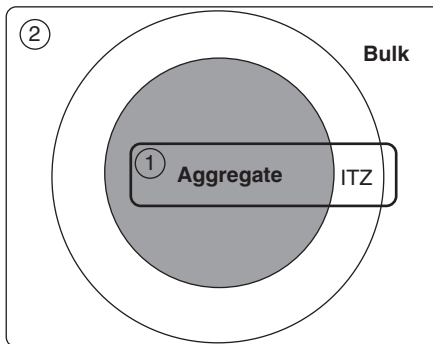
$$\mathbf{D}_c = \mathbf{D}_0 \left[\mathbf{I} + (f\mathbf{L})^{-1} (f \{ \mathbf{S} - \mathbf{I} \} \mathbf{L}) \right]^{-1} \quad [9.17]$$

where \mathbf{S} is the Eshelby tensor for spherical particles.⁵⁸ The volume fraction of the embedded material is denoted by f and \mathbf{I} is the unit tensor. The tensor \mathbf{L} in Equation [9.17] reads

$$\mathbf{L} = -[(\mathbf{D} - \mathbf{D}_0)\mathbf{S} + \mathbf{D}_0]^{-1}(\mathbf{D} - \mathbf{D}_0), \quad [9.18]$$

where \mathbf{D} and \mathbf{D}_0 are the material stiffness tensor of the embedded material and reference material, respectively.

The Mori-Tanaka homogenization is performed in two steps as shown in Fig. 9.13. In the first step, ①, the aggregates with material tensor \mathbf{D} are embedded in the ITZ material with material tensor \mathbf{D}_0 , which results in a material with a material tensor \mathbf{D}_c . In the second step, 2, the material tensor \mathbf{D} is set equal to this combined material tensor \mathbf{D}_c and is embedded in the bulk material with the material tensor \mathbf{D}_0 . Finally, this provides the



9.13 Mesostructure with bulk material, aggregate and interfacial transition zone – ① refers to the first step in the Mori-Tanaka scheme, where aggregates are embedded in the ITZ material; and ② refers to the second step, where the output from ① is embedded in the bulk material.

combined macroscopic material tensor \mathbf{D}_c , which can be compared to the macroscopic material tensors used in Reference 1.

In order to use the Mori-Tanaka scheme to determine the homogenized material tensor for the adopted mesostructures, we need to define the volume fractions f to be used as inputs in Equation [9.17]. The volume fraction of aggregate material in the ITZ material is found to be 72% and the volume fraction of ITZ and aggregate material in the bulk material is 33%, see Fig. 9.4.

The material tensor for the reference material when using Lamé parameters reads

$$\mathbf{D}_0 = \begin{bmatrix} \lambda_i + 2\mu_i & \lambda_i & 0 \\ \lambda_i & \lambda_i + 2\mu_i & 0 \\ 0 & 0 & \mu_i \end{bmatrix} \quad [9.19]$$

where i ($= 1, 2, 3$) refers to the three different constituents (aggregate, ITZ and bulk material), and the material tensor for the embedded material \mathbf{D} is defined in the same way. The Lamé parameters are determined using the iterative scheme for the different constituents until the macroscopic material tensor used in Reference 1 is achieved. The Eshelby tensor for spherical inclusions²⁸ is defined as

$$\mathbf{S} = \begin{bmatrix} \frac{7-5\nu}{15(1-\nu)} & \frac{5\nu-1}{15(1-\nu)} & 0 \\ \frac{5\nu-1}{15(1-\nu)} & \frac{7-5\nu}{15(1-\nu)} & 0 \\ 0 & 0 & \frac{4-5\nu}{15(1-\nu)} \end{bmatrix}. \quad [9.20]$$

For linear elastic problems and spherical or elliptical inclusions, the Eshelby tensor is exact.

The two-step Mori-Tanaka scheme is now employed to compute the material tensor for a material with high saturation level using the Young's modulus and Poisson's ratio of the three constituents ($E_a = 51\,150$ and $\nu_a = 0.28$ for aggregate material, $E_{ITZ} = 25\,000$ and $\nu_{ITZ} = 0.22$ for ITZ material, and $E_b = 40\,000$ and $\nu_b = 0.22$ for bulk material). The final macroscopic material tensor reads:

$$\mathbf{D}_{\text{macro}} = \begin{bmatrix} 48800 & 15900 & 0 \\ 15900 & 48816 & 0 \\ 0 & 0 & 16700 \end{bmatrix}. \quad [9.21]$$

In Table 9.2, Poisson's ratio $\nu = 0.2$ and Young's modulus $E = 46\,000$ MPa for wet material. In a plane-stress configuration these values result in a macroscopic constitutive tensor \mathbf{D} with $\mathbf{D}_{11} = 47917$ MPa, which compares well with the value of \mathbf{D}_{11} in the predicted macroscopic material tensor above.

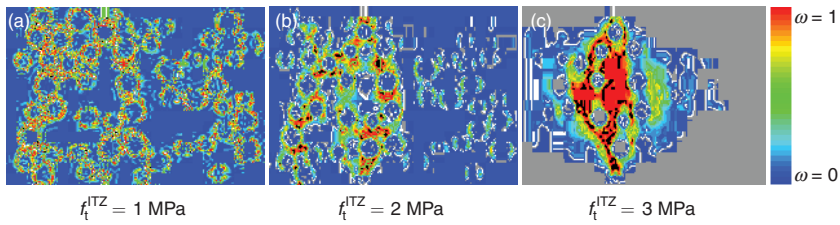


Plate XXI (Chapter 9) Fracture planes corresponding to different values of the strength of the ITZ in realization 3.

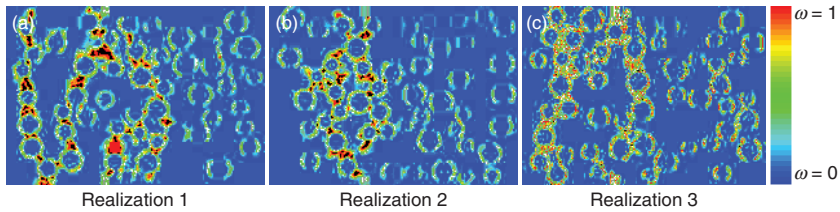


Plate XXII (Chapter 9) Fracture planes for the realizations reported in Fig. 9.4. The tensile strength of the ITZ is set equal to 1 MPa.

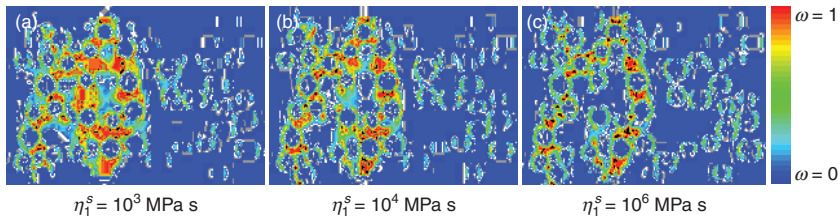


Plate XXIII (Chapter 9) Fracture planes corresponding to different values of the viscosity η_1^s MPa s for the bulk material in realization 3.

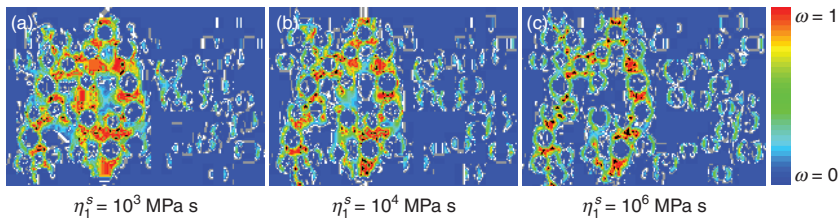


Plate XXIV (Chapter 9) Fracture planes corresponding to different values of the viscosity η_1^s for bulk and ITZ material in realization 3.

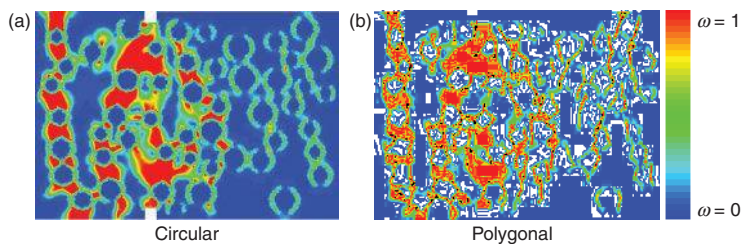


Plate XXV (Chapter 9) (a) circular (b) polygonal. Damage profiles in specimens with different aggregate shapes in realization 1.

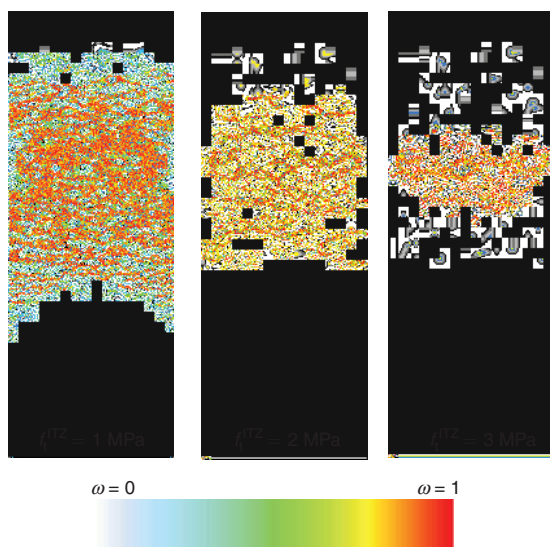


Plate XXVI (Chapter 9) FPZs for different tensile strength of the ITZ material.

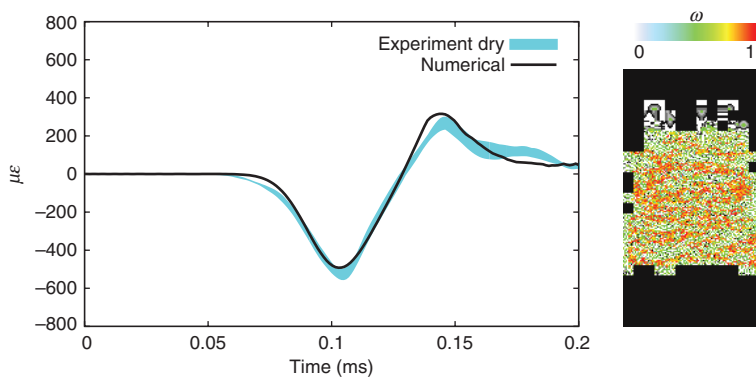


Plate XXVII (Chapter 9) Results for dry material. Left: experimental and numerical strain measurement. Right: the FPZ obtained with the mesoscopic model.

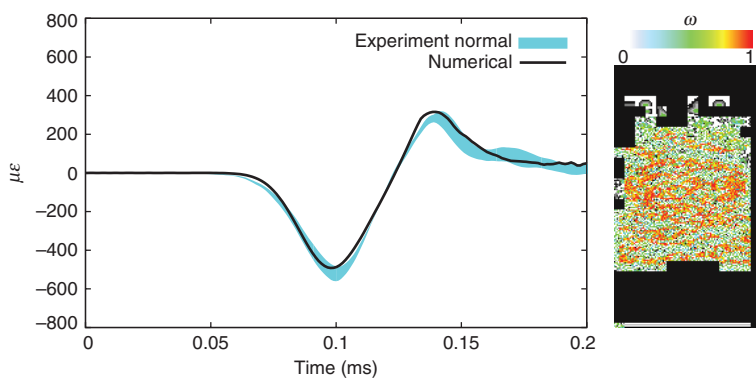


Plate XXVIII (Chapter 9) Results for normal material. Left: experimental and numerical strain measurement. Right: the FPZ obtained with the mesoscopic model.

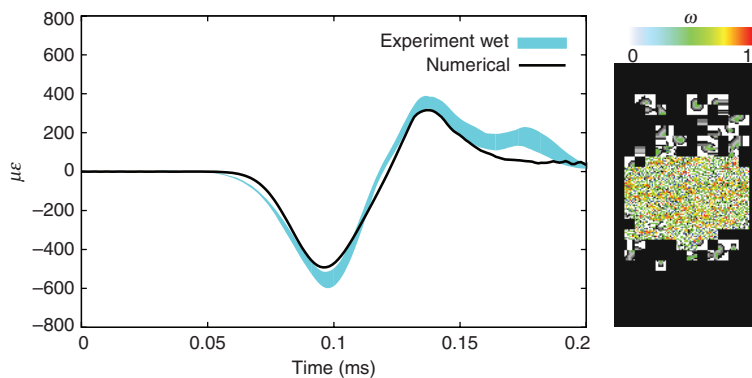


Plate XXIX (Chapter 9) Results for wet material. Left: experimental and numerical strain measurement. Right: the fracture process zone obtained with the mesoscopic model.

Modelling the response of concrete structures from strain rate effects to shock induced loading

J. OŽBOLT, University of Stuttgart, Germany and
W. RIEDEL, Ernst Mach Institut, Germany

DOI: 10.1533/9780857097538.2.295

Abstract: Impact loading on concrete gives rise to a strain rate influence on strength, stiffness, ductility and failure mode. Moreover, inertia is activated, which influences the resistance and failure mode of concrete structures. In most macroscopic models currently used in engineering applications, the influence of inertia forces on dynamic strength enhancement is still part of the constitutive law, instead of emerging automatically from dynamic analysis. Detailed numerical analysis based on the microplane model shows that the progressive increase of apparent tensile strength can be attributed to structural inertia invoked by the softening of concrete, and not to material strength.

Key words: dynamic fracture, impact, rate sensitivity, true and apparent strength, finite element analysis.

10.1 Introduction to the modelling of loading-rate effects on concrete

The experimental and theoretical evidences show that loading rate significantly influences the resistance and failure mode of concrete structures (Kipp *et al.* 1980; Mihashi and Wittmann 1980; Reinhardt 1982; Reinhardt *et al.* 1985; Banthia *et al.* 1987; Brandon 1987; Curbach 1987; Bischoff and Perry 1991; Reinhardt and Weerheijm 1991; Holmquist *et al.* 1993; Lu and Xu 2004; Schuler 2004; Ožbolt and Reinhardt 2005, Ožbolt *et al.* 2006, 2011; Ortlepp, 2006; Pedersen 2009; Larcher 2009; Reinhardt *et al.* 2010; Mechtcherine *et al.* 2011; Ožbolt and Sharma 2011, 2012). In the case of linear elastic material there is no rate sensitivity. However, in materials that exhibit damage and fracture phenomena, such as concrete, there is significant loading-rate influence on material and structural response. This implies that rate sensitivity is closely related to damage (softening) of the material, i.e. more damage and a higher level of heterogeneity (larger softening zone) will enhance the influence of loading rate on the structural response. Confirmation of this is to be found in the fact that concrete-like materials exhibit the highest rate sensitivity for dominant tensile load.

The response of concrete structures depends on time-dependent loading through three different effects (Ožbolt *et al.* 2006, 2011): (1) the rate dependency of the growing micro-cracks (influence of inertia at the micro-crack level), (2) the viscous behaviour of the bulk material between the cracks (creep of concrete or viscosity due to the water content), and (3) the influence of structural inertia forces, which can significantly change the state of stresses and strains in the material. The first two effects can be accounted for by the constitutive law (see Chapter 9) and the third effect should be automatically accounted for with dynamic analysis, whereby the rate-dependent constitutive law interacts with structural inertia (Ožbolt *et al.* 2011). Depending on the material type and the loading rate, the first, second or third effect may dominate. For quasi-brittle materials, such as concrete, the first two effects are important for relatively low and medium strain rates. However, for higher strain rates (impact) the last effect dominates. Moreover, structural inertia can change the failure mode, e.g. from a mode-one failure at low loading rates to a mixed or punching failure at very high loading rates. Finally, inertia at the crack tip (fracture process zone) of a single propagating crack is also responsible for crack branching phenomena. As discussed by Ožbolt *et al.* (2011), inertia changes the stress distribution around the crack tip, which forces a single crack to split into two cracks.

Experimental evidence shows that concrete under tensile load exhibits the strongest influence on loading rate. To experimentally study the uniaxial tensile behaviour of concrete is difficult even under static load. Therefore, indirect methods, such as the Brazilian test, compact tension tests, etc., are often employed. Moreover, even numerically it is very difficult to perform the direct dynamic uniaxial tests to study/describe the tensile behaviour of concrete, since at high loading rates the failure always occurs locally, near the loading points. Therefore, under dynamic loads the problem is studied through indirect tests, such as split Hopkinson bar tests (Reinhardt *et al.* 1985; Weerheijm 1992; Schuler 2004; Pedersen 2009; Mechtcherine *et al.* 2011, see Chapter 10). In the split Hopkinson bar test, the measurement of concrete strength is based on the theory of uniaxial wave propagation through elastic media and measurements of strain and strain rates in the bar. The results of experiments show that for strain rates larger than approximately 1 s^{-1} , resistance increases progressively with increase of strain rate. The question that arises, and is still under discussion, is the reason for such an increase, and whether the experimentally measured resistance should be attributed to the material strength only or whether there are other effects that need to be considered.

Regardless of the influence of strain rate, the complex transfer of energy between two or more colliding bodies, or in the case of explosion, is an additional problem. For this reason, strain rate is not the only problem to be considered. According to Bentur *et al.* (1987) and Banthia *et al.* (1987), because

of very high strain gradients it is experimentally difficult to meet the energy balance for very high loading rates (see also Chapter 8). On the other hand, it is numerically relatively simple to calculate the transfer of kinetic energy into other energy forms. Accordingly, it is useful to perform numerical simulations in order to better understand the processes that take place in a very short period of time.

10.1.1 Overview of modelling frameworks

There are different frameworks for modelling of rate-dependent behaviour of concrete-like materials. The rate theory is employed to explain the first two above-mentioned reasons for strain-rate sensitivity (micro-cracking and viscosity) (Mihashi and Wittmann 1980; Krausz and Krausz 1988). The theory assumes that crack initiation on an atomic scale is governed by the activation energy, i.e. in a non-stressed material there is an equal number of bond-breaking and bond-healing steps in time. When an external force acts on the material there is a surplus of energy, which causes more bond-breaking than bond-healing steps. Since the number of bond-breaking steps is assumed to be constant in time, a longer loading time causes more ruptures than a shorter loading time. Expressed in terms of strength, it means that sustained loading and creep causes a reduction of strength, whereas very short loading causes an increase of strength. This means that high loading rates increase the apparent strength of the material. According to Mihashi and Wittmann (1980) the increase of strength, compressive, tensile and flexural, can be expressed by:

$$\frac{f_d}{f_s} = \left(\frac{\dot{\sigma}}{\dot{\sigma}^0} \right)^\alpha \quad [10.1]$$

with f_d = dynamic strength, f_s = static strength under monotonic load, $\dot{\sigma}$ = stressrate under dynamic load, $\dot{\sigma}^0$ = stressrate under static load and α = parameter dependent on load and type of material and the way of loading. Equation [10.1] accounts for the effect of inertia at the micro-scale; however, it does not consider the effect of inertial forces on the macro-scale.

The model of Bažant *et al.* (2000a) is based on the same principle. Again, the influence of macro-inertia forces is not considered. The influence of the loading rate is divided in two parts: (i) the effect of viscosity, and (ii) the effect of strain-dependent growth of micro-cracks. The first effect is described by a relatively simple visco-elastic model. The influence of the strain-dependent growth of micro-cracks on the other hand is based on the theory of activation energy. Both parts are captured in the relation:

$$\sigma(\varepsilon) = \sigma^0(\varepsilon) \left[1 + C_2 \ln \left(\frac{2\dot{\varepsilon}}{C_1} \right) \right] \quad [10.2]$$

where σ = stress at dynamic load, σ^0 = stress at static load, $\dot{\varepsilon}$ = strain rate, and C_1 and C_2 are constants determined from experiments. This model has been used in various forms in the microplane model for concrete (Bažant *et al.* 2000a; Ožbolt *et al.* 2001, 2006, 2011).

Inertia effects at the material macro-level are taken into account in the model of Reinhardt and Weerheijm (1991), and by Lu and Xu (2004). The authors look at a cluster of penny-shaped cracks in a plane perpendicular to the tensile-loading direction. When a crack propagates into the material with a certain velocity, the crack faces move. For this movement, the energy balance is computed, which is the sum of external work W , deformation energy V , kinetic energy T , fracture energy D and initial energy E_0 at time t_0 , thus:

$$-W + V + T + D - E_0 = 0 \quad [10.3]$$

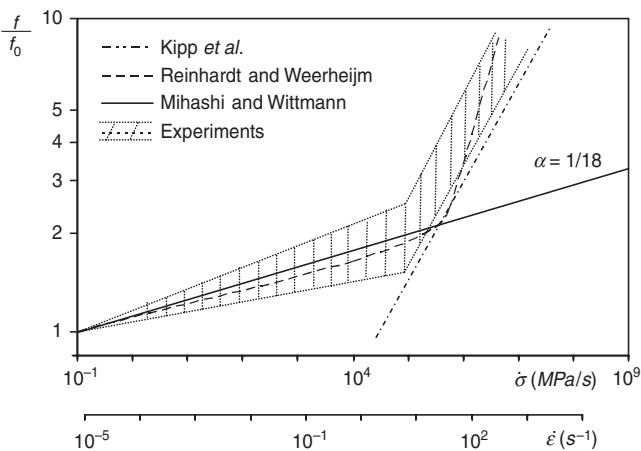
The faster the crack propagates, the larger are the kinetic energy and the deformation energy. The calculations show that the rate of energy supply becomes too high to be absorbed in the fracture process, resulting in an equilibrium in which a major part of the supplied energy is stored as kinetic and deformation energy around the crack tip. This means that the stress distribution around the crack tip changes, and the stress-intensity factor decreases with increasing loading rate. This is in agreement with Freund (1972a, 1972b), who predicts that the stress-intensity factor even vanishes when the crack propagates with the speed of the Rayleigh wave. The consequence of this result is that the strength of a material increases with loading rate. The rate of strength increase is not constant for all loading rates, but is rather small for low and medium strain rates, while there is a steep increase at high loading rates. At very high loading rates the strength increases with the cube root of strain rate (Kipp *et al.* 1980).

The major problem with this and similar modelling approaches that account for the influence of inertia forces on material strength at the constitutive level is the fact that in reality at high loading rates the increase of strength is always related to the change of the failure mode and crack branching phenomena. From the physical point of view it would be more appropriate that in the modelling the constitutive laws were responsible only for the increase of the true material strength due to strain rate. These effects should come automatically out of the model if the modelling were performed at the micro-scale – discrete modelling of the structure of concrete. The effects of inertia on the macro-scale (e.g. crack branching), or

increase of material strength due to the interaction between constitutive law and inertia (e.g. lateral confinement through inertia in case of uniaxial compression), should come automatically from dynamic analysis performed at the macro-scale. For instance, in the case of uniaxial compression, increase of the overall resistance by higher loading rates should not be a priori implemented into the constitutive law, but must come implicitly from the interaction between macro-inertia and rate-dependent constitutive law. Of course, for this it is important that one has a constitutive law that is able to properly account for the interaction with inertia forces, i.e. crack branching and change of the failure mode should be an outcome of the model.

In the literature, there are various two- and three-dimensional phenomenological models, continuous or discrete, that are based on the coupling of elastic, plastic, damage and viscous units in different combinations (Curbach 1987; Holmquist *et al.* 1993; Rabczuk and Belytschko 2004; Ožbolt *et al.* 2006, 2011; Larcher 2009; Pedersen 2009). Depending on the model, the strain-rate dependent material behaviour in the entire strain-rate range described will be either better or worse.

The result of several theories is summarized in Fig. 10.1. As can be seen, for strain rates larger than about 10 s^{-1} , the total resistance starts to increase progressively. It has been recently discussed that for low and medium strain rates up to 10 s^{-1} , the total resistance is controlled by viscosity and strain-dependent micro-crack growth (Ožbolt *et al.* 2011; Ožbolt and Sharma 2012). However, at very high strain rates (impact), the inertial



10.1 The material resistance as a function of stress- and strain-rate: (a) Mihashi and Wittmann (1980), (b) Reinhardt and Weerheijm (1991) and (c) Kipp *et al.* (1980).

forces dominate and cause progressive increase of structural resistance and have dominant influence on failure mode and crack propagation (Ožbolt *et al.* 2011; Ožbolt and Sharma 2012). In the concrete community, there is still discussion as to whether the progressive strength increase is true material strength or apparent material strength. Comparing the results of the models shown in Fig. 10.1, it can be seen that according to the model of Mihashi and Witmann (1980) the material strength increases linearly in the log-log scale. All other models predict the progressive increase of material resistance in the case of very high loading rates, as also observed in experimental investigations. This important question is discussed in more detail in the following section.

Due to the complexity of the problem, the above-mentioned phenomena can best be studied by using numerical methods. In the numerical modelling, which can be of smeared or discrete type, different constitutive laws and modelling techniques can be used (Rabczuk and Belytschko 2004; Ožbolt *et al.* 2006; Larcher 2009; Pedersen 2009). The influence of viscosity and the strain-rate dependent growth of micro-cracks (micro-scale effects) are accounted for by the constitutive law. These two effects take place in the pre-peak regime of the material behaviour, and are relevant for the increase of true material strength due to strain rate. Because of the influence of local inertia at the tips of micro-cracks, the stress-intensity factor decreases with increase of strain rate. Consequently, material resistance (strength) increases. The viscosity effect (Stefan effect) and the rate-dependent micro-crack growth take place at the level of the material structure (pore system and micro-cracks). They can be modelled only on the micro-scale. Therefore, in the meso- or macro-scale analysis these effects should be a part of the constitutive law. The same is principally valid for rate-dependent concrete fracture energy, with the difference that post-peak micro-cracking also influences fracture energy.

In contrast to micro-inertia effect (micro-scale), the influence of structural inertia can be accounted for in the macro-analysis. At macro-scale there are principally two groups of inertia forces: (i) inertia, due to the softening (post-peak) that takes place in the fracture process zone, and (ii) inertia, activated in the undamaged part of the material (e.g. between cracks).

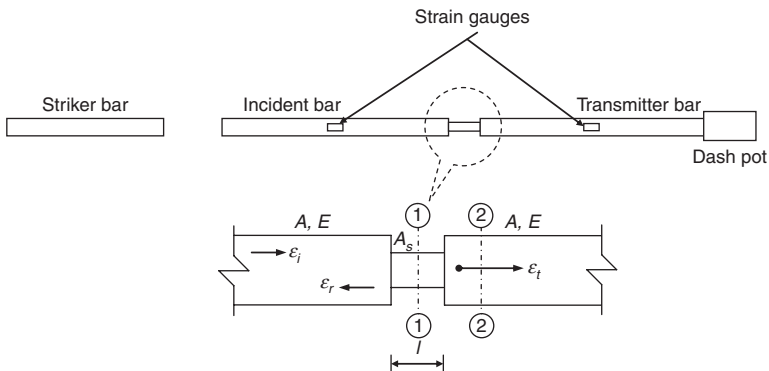
The first group, which will be later discussed in more detail, is related to the size of the fracture process zone. With increase of ductility and non-homogeneity, the size of the softening (process) zone increases and the influence of inertia becomes stronger. For normal strength concrete, this size is in the range of approximately 100 mm. Therefore, this influence can be taken into account in macroscopic analysis, for instance using finite element methods. It becomes important in case of higher loading rates and is not related to the true material strength. The second group, that of inertial

forces activated between macro-cracks, interact with the constitutive law. For instance, in the case of uniaxial compression lateral inertia has the effect of confinement, which increases axial resistance of concrete. This should be automatically accounted for in dynamic analysis and it should not be a part of the rate-dependent constitutive law.

To account for the effects of inertia forces at macro-scale it is important that constitutive law and (or) the corresponding discretization method are employed, which can account for realistic interaction between structural inertial forces and constitutive law. Discrete models and microplane models are able to account for these effects automatically; however, tensorial models (e.g. plasticity and damage-based models) seem to be incapable of accounting for these effects. Therefore, in tensorial models the effect of structural inertia forces is usually indirectly accounted for through constitutive law, which is principally incorrect on the scale of material sample calculations (see discussion below).

10.2 Measuring the strain-rate dependent strength of concrete

Hopkinson (1914) experimentally tested the behaviour of various materials at high strain rates. On a long bar he generated a compressive pulse by explosive charge or impacting bullet. On the end of the bar the compressive loading wave reflected as a tensile-loading wave and would cause fracturing of brittle materials such as concrete, rock, etc. Later, Kolsky (1953) made the method operable for practical measurements. The method is known as the split Hopkinson (pressure) bar, schematically shown in Fig. 10.2 for compressive testing. The bar can be modified such that the specimen can also be tested for different loading conditions.



10.2 Schematic of split Hopkinson bar.

where M_c and \ddot{u}_c are equivalent mass and acceleration of the concrete softening zone, respectively. Note that \ddot{u}_c is the acceleration activated in the micro-cracked continuum as a consequence of material softening. Obviously, when the material exhibits softening in a non-negligible proportion of the material volume (quasi-brittle materials), the measured stress σ_t in the split Hopkinson bar test cannot be attributed only to material strength. It comprises the material resistance $\sigma_{t,s}$ and the contribution of the inertia forces $\sigma_{t,i}$.

As discussed before, the rate-sensitive material resistance derives from the pre-peak rate-dependent response (viscosity and rate-dependent growth of micro-cracks), whereas the contribution of structural inertia comes from inertia forces that are activated as a consequence of softening that takes place in the fracture process zone. The larger the fracture process zone of the material, the larger will be the contribution of inertia. Moreover, it can be expected that for the same size of the fracture process zone, the influence of inertia will be stronger in case of larger specimen, since then for the same crack extension the energy released from the structure is also larger. This will invoke higher accelerations in the process zone, and consequently higher inertia forces will be activated.

The above effects also confirm experimental observations, e.g. extremely brittle materials, such as glass, exhibit almost no rate sensitivity due to the fact that the size of the fracture process zone is very small (Peroni *et al.* 2011). Furthermore, it should be pointed out that, at higher loading rates and with larger test specimens, there is more than only one discrete crack, i.e. with increase of loading rate the size of the softening material volume increases. This explains the progressive increase of the contribution of inertia to apparent strength σ_t .

Equation [10.4] is based on the theory of elasticity. However, due to micro-cracking of concrete in a non-negligible part of the specimen volume, the stiffness of the concrete specimen is reduced, which implies that wave propagation through softened part of concrete is slower. The consequence is that strain rate from Equation [10.4] is not calculated correctly.

According to Equation [10.6] the measured resistance in the split Hopkinson test consists of two contributions: (1) the true material strength, and (2) the contribution of stress that comes from inertia of the softening zone (fracture process zone). For concrete, the true stress is an approximately linear function of the strain rate (log-log scale) and it is due to the rate-dependent micro-crack growth and viscous behaviour of cement paste of concrete (Freund 1972; Mihashi and Wittmann 1980; Ožbolt *et al.* 2006, 2011; Pedersen 2009). This contribution can be modelled by the constitutive law, which can be calibrated based on the experimental results on relatively low or medium strain rates, where inertia due to fracture process zone (FPZ) is negligible. Although there are constitutive models that explicitly account for the influence of inertia forces on the macro- and meso-scale (see Fig.

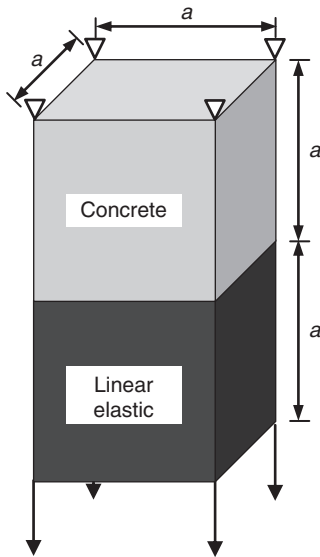
10.1), the contribution of these inertia forces ($\sigma_{i,i}$) should come automatically from dynamic analysis; however, the constitutive law must be realistic, in order to account correctly for the interaction with inertia (Ožbolt *et al.* 2011). It is important to note that as long as the modelling scale allows representing cracks individually, no additional inertia term coupled to the softening volume needs to be added to the constitutive law.

10.2.1 True and apparent dynamic tensile resistance of concrete

To confirm the theoretical considerations discussed in the previous section, finite element analyses for two geometries are carried out. In the first study, a relatively simple cohesive-elastic finite element (FE) model is investigated. This model principally corresponds to the measurement set-up of the split Hopkinson bar. Subsequently, to demonstrate that in real structure concrete dynamic fracture is controlled only by the true material strength, the simulation of the compressive pulse in a concrete bar, which is reflected from the free end-surface of the bar and causes tensile fracture, is carried out. In numerical analyses, the rate-dependent microplane model is used as a constitutive law (Ožbolt *et al.* 2011). As a regularization method, a simple energy criterion (crack band method) is employed (Bažant and Oh 1983).

Simple cohesive-elastic FE model

The geometry of the numerical specimen consists of two 3D eight-node solid finite elements. It approximately represents the experimental set-up from Fig. 10.3. The first element is cohesive, and represents a concrete specimen which, after reaching tensile strength, undergoes softening (micro-cracked continuum). The second element is linear elastic and corresponds to the part of the experimental set-up from Fig. 10.3. The properties of the cohesive element (concrete) are taken as: Young's modulus $E_c = 30\,000$ MPa, Poisson's ratio $\nu = 0.18$, tensile strength $f_t = 3.5$ MPa, uniaxial compressive strength $f_c = 40$ MPa, concrete fracture energy $G_F = 0.09$ N/mm and mass density $\rho_c = 2400$ kg/m³. It is assumed that the elastic element has the same elastic properties and density as the cohesive element. The model is loaded by controlling the displacement rate of the nodes at the free surface of the elastic element in the axial direction (see Fig. 10.4). Loading force and reaction are monitored. Compared to the experimental set-up from Fig. 10.3, the reaction represents true material resistance and the load is the resistance measured in the split Hopkinson bar test set-up. The analysis is performed for three different specimen sizes, $a = 25, 50$ and 100 mm, where a is element size, i.e. half the concrete specimen size. Note that in this simple model the size (volume) of the cohesive zone is equal to the element size. The

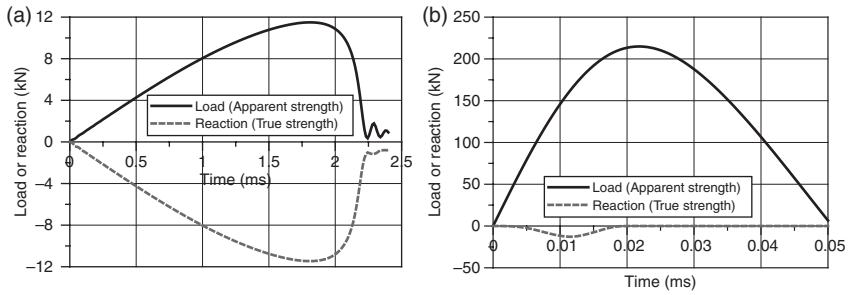


10.4 Simple cohesive-elastic FE model.

constitutive law of the cohesive model is the rate-dependent microplane model (Ožbolt *et al.* 2011).

In static analysis the load and reaction must be the same. This is also the case in dynamic analysis, but only if both elements are linearly elastic. However, the question is whether they are the same in the case of dynamic analysis, where the concrete element, after reaching tensile strength, undergoes softening. If they are not equal, the material resistance measured in the split Hopkinson bar test is not the true material strength, i.e. it is apparent strength.

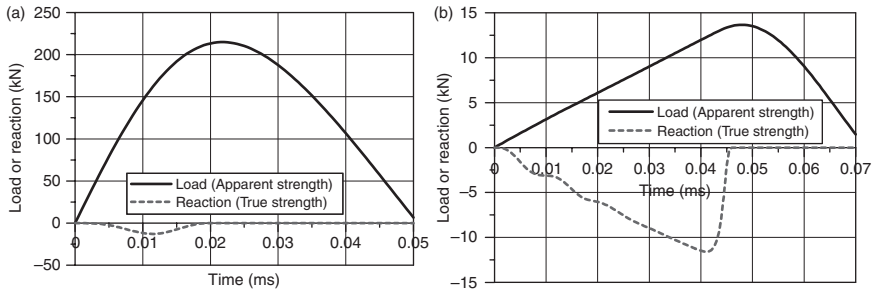
In Fig. 10.5 are plotted typical reaction forces – and the load-time response ($a = 50$ mm) for two different loading rates, 0.2 s^{-1} and 200 s^{-1} . The strain rates are calculated as the prescribed displacement rate over the length of the cohesive element. For a relatively low strain rate, the load and reaction are almost the same; however, for a very high strain rate, the reaction is much smaller than the load. This implies that because of softening of the cohesive material the inertia forces are activated. These forces in the elastic element generate stresses that are much higher than the stresses in the cohesive element. Therefore, the numerical results show that, in general, strength as measured in the elastic element cannot be the true material strength. This is apparent strength, which consists of the true material strength and the contribution of inertia forces, as discussed in previous section. The same can also be shown by the analytical solution recently presented by Kožar and Ožbolt (2010).



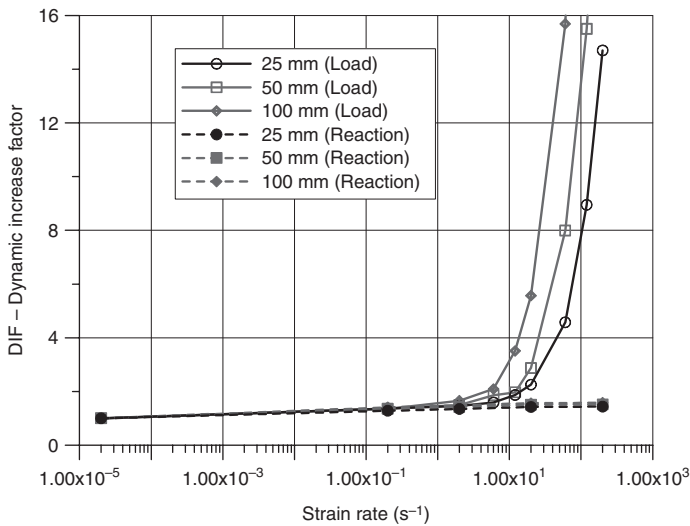
10.5 Typical reaction- and load-time response ($a = 50$ mm): (a) Strain rate = 0.2 s^{-1} and (b) Strain rate = 200 s^{-1} .

Due to the fact that inertia forces are related to the size of the softening zone (FPZ), it can be expected that for brittle materials (e.g. glass) the influence of inertia on the apparent strength is negligible. To prove this, the above analysis is repeated but assuming brittle behaviour of cohesive element. The fracture energy of the cohesive material is taken as $G_F = 0.0009 \text{ N/mm}$. All other properties are taken as before. In Fig. 10.6 reaction- and load-time response ($a = 50$ mm) for loading rate of 200 s^{-1} (a) for the cohesive element, and (b) the brittle element, are again plotted. It can be seen that for the brittle element, even at very high strain rates, the reaction and load are nearly the same. This proves that for brittle material the strength measured in the elastic element is the same as true material strength, i.e. the apparent strength is nearly the same as true strength. However, due to inertia, the load oscillates with respect to time.

Similar to the brittleness of the material, the size of the FPZ should have influence on inertia forces. The same fracture energy but a larger fracture zone should cause stronger influence of inertia on apparent strength. This also shows the experiments, e.g. the Dynamic Increase Factor (DIF) of low quality concrete is larger than that of high quality concrete (CEB 1988; *fib* 2010). Furthermore, the same is the case with mass density and size of the specimen. In Fig. 10.7 calculated DIF for true (reaction) and apparent (load) strength are plotted for three different specimen sizes ($a = 25, 50, 100$ mm) and for different strain rates. It can be seen that for strain rates up to approximately 2 s^{-1} the true and apparent strengths are almost the same. However, for higher strain rates the true strength increases approximately linearly in semi-log scale, whereas the apparent strength exhibits a progressive increase. As expected, the increase is stronger if the element size is larger. Contrary to this, the true strength shows almost no sensitivity to the size of the element. The increase of the true strength with increase of the strain rate is controlled by the energy activation theory, which is the part used in the microplane constitutive law.



10.6 Typical reaction- and load-time response ($a = 50 \text{ mm}$, strain rate = 200 s^{-1}) for: (a) cohesive element and (b) brittle element.

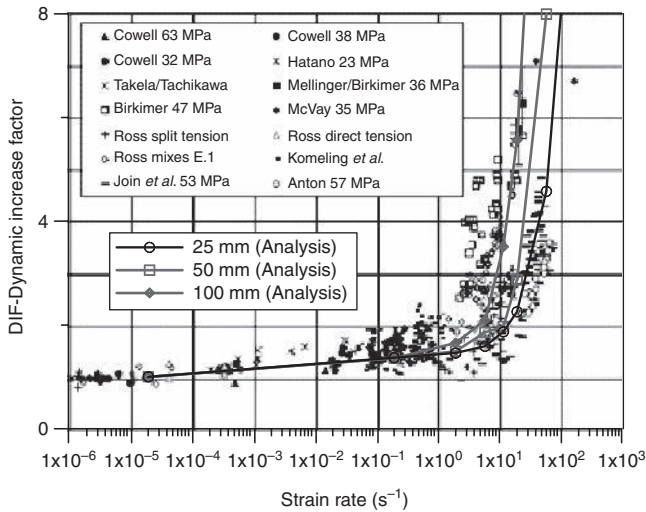


10.7 Calculated DIF for true (reaction) and apparent (load) strength.

In Fig. 10.8 numerical results for apparent strength are compared with the apparent strength measured in the experiments. Note that the experimental data represent measurements on specimens of different sizes and shapes, different concrete qualities and different water content. Therefore, it is not surprising that there a relatively large scatter of test data with respect to the measured strain rate. It is surprising that, in spite of the very simple numerical model, the numerical results nicely fit a band of experimental results.

Compressive pulse in a concrete bar

In the previous simple numerical example it is argued that in the split Hopkinson bar test the experimentally measured rate-dependent strength

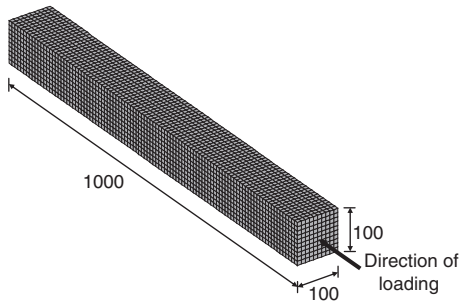


10.8 Comparison of numerically and experimentally observed apparent strength.

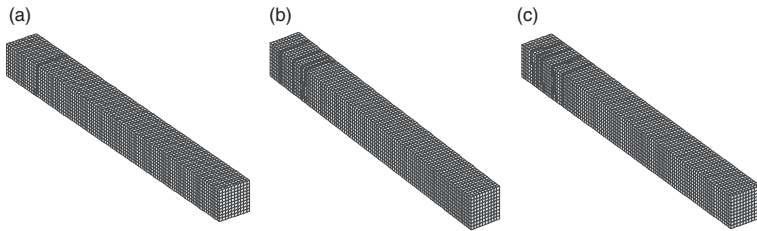
is not true strength but apparent strength, which is for very high strain rates much larger than the true material strength. In the second example simulation the compressive pulse in a concrete bar (original Hopkinson bar), which is reflected from the free end-surface of the bar and causes tensile fracture, is carried out for different loading rates. The aim is to demonstrate the effect of high strain rates on material strength and concrete fracture energy by evaluating the results of the numerical analysis. Moreover, it will be demonstrated that because of inertia more than only one mode-I cracks in concrete specimen are generated.

The geometry, finite element discretization and loading of the concrete bar are shown in Fig. 10.9. To prevent local crushing of the concrete at the application of the loading impulse, the bar is assumed to be confined in the lateral direction (plane strain loading). The properties of concrete are taken as: Young's modulus $E_c = 30\,000$ MPa, Poisson's ratio $\nu = 0.18$, tensile strength $f_t = 2.75$ MPa, uniaxial compressive strength $f_c = 40$ MPa, concrete fracture energy $G_F = 0.06$ N/mm and weight density $\rho_c = 2400$ kg/m³. The dynamic analysis is performed for different loading impulses that are applied at the top of the concrete bar. The applied impulses are: $0.5 \text{ mm}/10^{-4} \text{ s}$ (loading rate 5 m/s), $1 \text{ mm}/10^{-4} \text{ s}$ (loading rate 10 m/s), $2 \text{ mm}/10^{-4} \text{ s}$ (loading rate 20 m/s) and $4 \text{ mm}/10^{-4} \text{ s}$ (loading rate 40 m/s). The constitutive law is the same as the cohesive constitutive law of the model shown in Fig. 10.4.

In Fig. 10.10 are shown failure modes (cracks in the form of maximal principal strain) for three different loading rates: 10 m/s, 20 m/s and 40 m/s. For low loading rates no cracking of the concrete bar is observed; however,



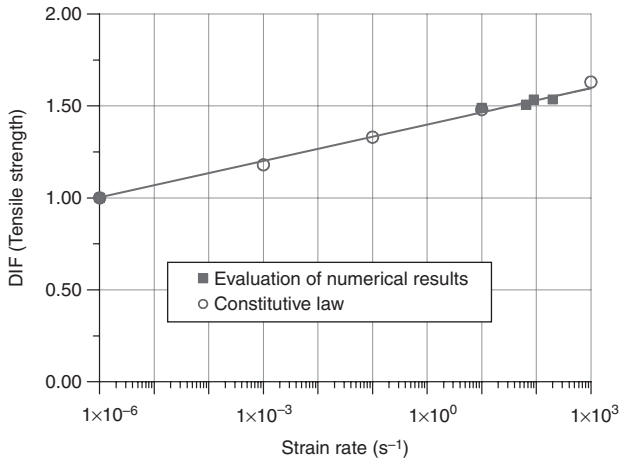
10.9 Geometry (all in mm) and FE discretization of the analysed original split Hopkinson bar.



10.10 Failure modes for the bar at different loading rates: (a) 10 m/s, (b) 20 m/s and (c) 40 m/s. Cracks (dark zones) are plotted in terms of max. principal strain.

with increase of the loading rate (impulse) the release wave reflected from the free surface of the concrete bar superimposed with the release from the loading surface causes cracking. For 10 m/s loading rate (impulse) a single mode-I crack is obtained (Fig. 10.10a). However, as in experimental investigations, with an increase of loading rate the number of cracks increases and the typical crack spacing of 50 mm is obtained (Fig. 10.10b and 10.10c). Moreover, at high loading rates there is a tendency for crack branching, which will be later discussed in more detail. The reason for multiple cracking is inertia forces, which are generated as a consequence of the softening of a relatively large zone of the material due to superposition of loading and reflecting pulses.

The strain rates at cracks are evaluated from numerical results for the loading rates of 5 m/s, 10 m/s, 20 m/s and 40 m/s as 10 s^{-1} , 65 s^{-1} , 90 s^{-1} and 200 s^{-1} , respectively. To show the influence of strain rate on the true strength and fracture energy of concrete, maximal average stress (strength) over the cracked cross-section of the bar (single crack, first from the free end of the bar, see Fig. 10.11) is evaluated from numerical results for quasi-static loading and for four loading rates, which correspond to strain rate of: 10 s^{-1} , 65 s^{-1} , 90 s^{-1} and 200 s^{-1} .

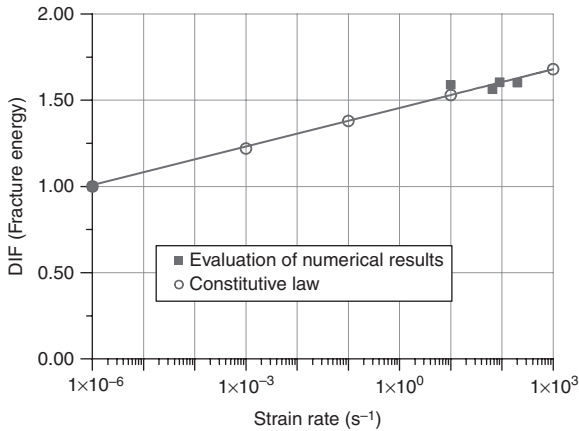


10.11 DIF for concrete strength as a function of strain rate.

The crack opening rates, which are obtained by multiplying strain rate with the element size (10 mm) are: 0.1 m/s, 0.65 m/s, 0.9 m/s and 2 m/s. Dynamic fracture energy is calculated as work of fracture over the same crack.

Figure 10.11 shows the DIF for concrete strength as a function of strain rate. It can be seen that there is an approximately linear increase of strength with increase of strain rates in semi-log scale and that the fit of calculated data coincide with the data coming out of the constitutive law. For strain rates of 10, 65, 90 and 200 s^{-1} , DIF are 1.52, 1.51, 1.54 and 1.54, respectively. This was expected since the true material strength depends only on the constitutive law, i.e. on the outcome of the rate sensitive microplane model.

Figure 10.12 plots the DIF for concrete fracture energy. Similar to the results obtained for dynamic strength, it can be seen that the dynamic fracture energy of concrete exhibits approximately linear increase in semi-log scale. For the evaluated strain rates the corresponding values for DIF are 1.49, 1.56, 1.60 and 1.60, respectively. The increase of fracture energy is almost the same as the increase of strength. Since brittleness of the material is inversely proportional to fracture energy and proportional to the square of strength, as far as only one crack is concerned it is obvious that with increase of strain-rate brittleness increases. However, the increase of brittleness at high strain rate can be compensated by the fact that for high strain rates more than only one crack is generated. For strain rates of 65 and 200 s^{-1} the brittleness is almost the same. However, comparing Fig. 10.10a and 10.10c, it can be seen that in the case of higher strain rate (Fig. 10.10c) the energy consumed by fracture is much higher due to the multiple cracking and crack branching phenomena.



10.12 DIF for fracture energy as a function of strain rate.

If one were to account for the total fracture energy consumed by concrete fracture, instead of only for the specific fracture energy as shown in Fig. 10.12, then an increase of strain rate from 65 s^{-1} (single crack, see Fig. 10.10a) to 200 s^{-1} (approximately four cracks, see Fig. 10.10c) would indicate a progressive increase of the total fracture energy as a function of strain rate. Unfortunately, in the literature this kind of evaluation of results of impact experiments on Hopkinson bar and other geometries is sometimes performed, i.e. the total energy is not related to the total crack surface. Schuler (2004) made an estimation to account for multiple cracks in un-notched specimens correlating with single cracks in notched specimens. Nowadays, the latter type is mostly used to confine the crack to one plane as described in Section 6.3.4 and shown in Fig. 6.10. This means accepting the compromise of a slightly disturbed one-dimensional stress propagation to circumvent the problem of multiple crack planes.

The evaluation of the numerical results shows that the true material strength is controlled by the rate-dependent constitutive law, i.e. by the micro-cracking phenomena (inertia at the micro-cracking level) and viscosity at the pre-peak regime. The same is the case for fracture energy. The phenomena that control rate-dependent strength and fracture energy are taking place at micro-level. They should be distinguished from the effects of inertia forces at macro-scale which are, among other effects, responsible for the apparent strength. In the rate-sensitive microplane model used here the pre- and post-peak regimes at the micro-scale are modelled based on the energy activation theory. Due to the fact that the microplane model, similarly to the discrete models, accounts for the interaction between different directions in the material, the influence of structural inertia comes automatically from dynamic analysis.

10.2.2 Modelling phenomena related to rate-dependent fracture of concrete

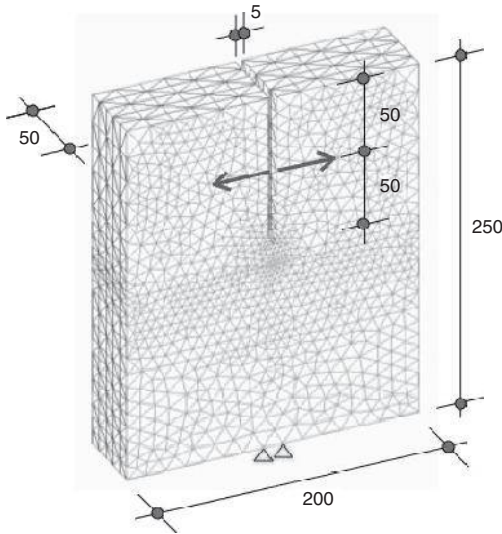
Theoretical, experimental and numerical studies show that the failure mode, crack pattern and velocity of the crack propagation are influenced by the loading rate (Freund 1972a,b; Curbach and Eibl 1990; Ožbolt and Reinhardt 2005; Ožbolt *et al.* 2006, 2011; Travaš *et al.* 2009). Principally, with increase of loading rate, the failure mode tends to change from mode-I to mixed mode. Responsible for this are, as already discussed, the structural inertia forces, which homogenize material in the impact zone and force the damage (crack) to move away from the zone of high inertia forces. Therefore, there is a change of mode-I fracture to mixed mode. Moreover, when a crack starts to propagate relatively quickly, inertia forces at the crack tip tend to prevent crack propagation. Consequently, single cracks split into two inclined cracks (branching) because the stress-intensity factor at the crack tip decreases with increase of crack speed.

The velocity of crack propagation also depends on loading rate. The maximal theoretical crack velocity is equal to Rayleigh wave speed $v_R = C_R (G_c/\rho_c)^{0.5}$ where the constant C_R depends on Poisson's ratio, G_c is the shear modulus and ρ_c is the density of the material. For normal strength concrete, the Rayleigh wave speed is approximately equal to 2100 m/s (see Chapter 11). However, experimental (Curbach and Eibl 1990), theoretical (Freund 1972a, 1972b) and numerical investigations (Rabczuk and Belytschko 2004; Ožbolt *et al.* 2011) indicate that a single mode-I type of crack cannot reach this theoretical speed of propagation. According to these investigations, the maximal crack speed in concrete is between 500 and 600 m/s. Moreover, after the crack speed reaches a certain critical value there is crack branching (Freund 1972a, 1972b; Rabczuk and Belytschko 2004; Kožar and Ožbolt 2009; Reinhardt *et al.* 2010; Ožbolt *et al.* 2011). These phenomena are here illustrated in examples of the compact tensile specimen and L-shaped specimen.

Compact tensile specimen

Because of its relatively compact size, the so-called compact tension specimen (CTS) is frequently used to measure the fracture properties of concrete and other quasi-brittle materials. To demonstrate the influence of loading rate on the resistance, failure mode and speed of crack propagation, transient 3D finite element analysis of the CT specimen using the rate-sensitive microplane model was carried out (Ožbolt *et al.* 2011).

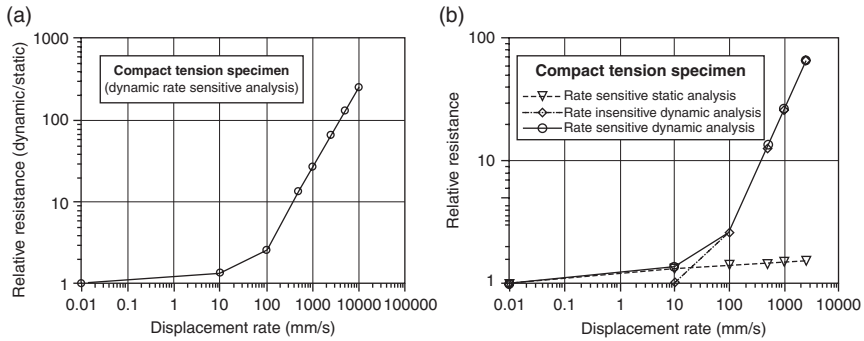
The geometry, boundary conditions and finite element mesh of the specimen are shown in Fig. 10.13. The dimensions of the specimen are: width–height–thickness = 200 × 250 × 50 mm and the notch length is 100 mm.



10.13 Geometry of the CTS (all in mm), finite element mesh, loading (displacement control) and boundary conditions. Failure suppressed around loading points for very fast tension speeds.

The analysis is carried out for normal strength concrete with the following macroscopic properties: Young's modulus $E_c = 30\,000\text{ N/mm}^2$, Poisson's ratio $\nu = 0.18$, uniaxial compressive strength $f_c = 40.0\text{ N/mm}^2$, tensile strength $f_t = 3.50\text{ N/mm}^2$, fracture energy $G_F = 0.09\text{ N/mm}$ and concrete mass density $\rho_c = 2400\text{ kg/m}^3$. The spatial discretization is performed by standard four-node solid finite elements with constant strain field (see Fig. 10.13). The load is applied by controlling horizontal displacement of the notch, applied 50 mm from the top of the specimen. The specimen is first analysed assuming a quasi-static loading condition. Subsequently, dynamic analysis is carried out with the following displacement rates $\Delta/dt = 10, 100, 500, 1000, 2500, 5000$ and $10\,000\text{ mm/s}$. Moreover, in order to demonstrate the influence of inertia forces and rate sensitivity on the response of the specimen, additional rate-sensitive static analysis and dynamic analysis using rate insensitive constitutive law are carried out.

It has to be pointed out that, especially for the very high tension speeds above 1000 m/s , compressive and shear failure around the loading points are suppressed in order to obtain the highest crack opening speed. In real experiments the highest speeds would not be realised, because the specimen would fail on the loading points rather than on the notch tip. Nevertheless, the 'numerical experiment' with elastic loading area and fast failure modes starting from the notch is deemed useful to explain the change of failure modes.



10.14 Relative resistance (rate-dependent resistance/quasi-static resistance) for: (a) dynamic analysis for range up to 10 m/s, and (b) the same as (a) comparison between static analysis with rate sensitivity and dynamic analysis with and without rate sensitivity.

The peak load measured relative to the quasi-static resistance is plotted as a function of displacement rate in Fig. 10.14a. It is assumed that the quasi-static load corresponds to a displacement rate of 0.01 mm/s. As can be seen from Fig. 10.14a, up to a displacement rate of 100 mm/s there is a relatively low increase of resistance with increase of displacement rate. However, for higher displacement rates there is progressive increase of resistance. As already discussed, this progressive increase is due to structural inertia forces, which have in the case of higher displacement rates a major influence on structural response (Ožbolt *et al.* 2006). To confirm this, two additional series of analysis are carried out, i.e. static analysis with rate sensitivity, and dynamic analysis without rate sensitivity. The results are summarized in Fig. 10.14b for displacement rates up to 2500 mm/s. The comparison of results shows that for displacement rates up to 10 mm/s, strain rate controls the response; however, for higher displacement rates structural inertia (dynamic analysis) dominates and strain rate has much less influence on the total response. The results of static rate-sensitive analysis show that the resistance increases as a linear function of the displacement rate (log-log scale). The results for the CT specimen show that the true tensile resistance of the concrete specimen increases as a linear function of the loading rate. The progressive increase (apparent strength) can obviously be attributed to inertia.

Plate XXX (see colour section between pages 208 and 209) shows predicted crack patterns in terms of maximal principal strains, assuming a critical crack width $w_{cr} = 0.2$ mm. It can be seen that for a quasi-static load and for relatively low displacement rates (up to 100 mm/s) there is a single mode-I crack, which propagates from the notch tip. However, for higher displacement rates ($\Delta/dt > 500$ mm/s) there is a branching of the crack and multiple cracking. For instance, for displacement rate $\Delta/dt = 1000$ mm/s a single crack starts from

the notch tip and subsequently branches into two inclined cracks. For higher displacement rates ($\Delta/dt > 2500$ mm/s) the crack branching starts already at the crack tip at onset of cracking and subsequently additional branching (multiple branching) is observed. Obviously, for higher displacement rates there is a cluster of multiple cracks with a rather complex mixed failure mode.

Structural inertia forces are responsible for the change of the failure mode. The analyses without inertia forces (static analysis with rate sensitivity) indicate no change of the failure mode, i.e. independent of the displacement rate there is mode-I fracture (single crack). In distinction to this, dynamic analysis without rate sensitivity predicts the same failure modes and crack branching as shown in Fig. 10.9. When in dynamic analysis the crack reaches the critical velocity of approximately 500 to 600 m/s, crack branching is observed. This is illustrated in Plate XXXI (see colour section between pages 208 and 209). The figure shows crack velocities at different cracking stages ($\Delta/dt = 1000$ and 2500 mm/s). The data are obtained by the evaluation of the numerical results. It is interesting to observe that crack branching always takes place when the crack velocity reaches approximately 500 m/s. Furthermore, Plate XXXI also shows that the crack velocity depends on the crack path. For instance, in the case of a displacement rate of 1000 mm/s the maximal crack propagation of 480 m/s is observed before crack branching and the minimal crack velocity of 40 m/s is measured, close before the termination of the analysis. Although the displacement rate is constant during the entire loading history (1000 mm/s), there is a span of the crack velocity from 40 to 480 m/s.

The main reason for the crack branching are structural inertia forces at the crack tip, which prevent mode-I propagation and force the crack to split (branch) into two new cracks. The direction of propagation of a new crack depends on the propagation of the loading waves in the damaged structure, which in turn depends on material properties, current fracture configuration, geometry and displacement (loading) rate. The inertia that causes branching is principally the same as the inertia responsible for apparent strength in the case of the split Hopkinson bar test. The difference is due only to the state of stresses and strains. In the case of Hopkinson bar there is a uniaxial stress-strain state and possibility for crack branching is much lower than in the CT specimen where the stress-strain state is different. However, at high loading rates in both cases inertia of the FPZ controls the response and not the pre-peak and post-peak micro-cracking and viscosity, which are responsible only for true material strength and fracture energy.

Although the inhomogeneity of concrete is not the major reason for crack branching, it probably also plays an important role. It can be expected that a higher level of inhomogeneity tends to generate crack branching at lower crack velocities. In the split Hopkinson bar tests branching is more related to material inhomogeneity, whereas in the CT specimen branching

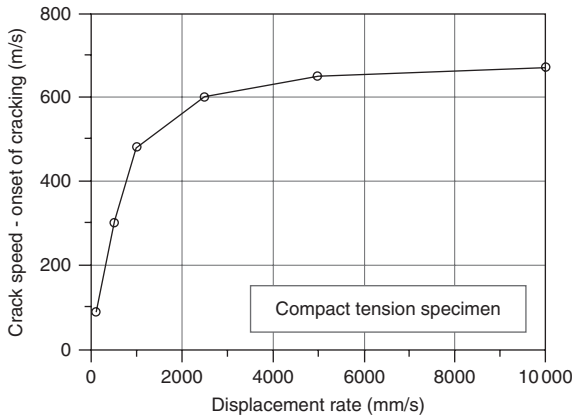
is more influenced by the stress–strain state. Note that for the concrete used here Rayleigh wave speed $v_R = C_R (G_c/\rho_c)^{0.5} = 2140$ m/s with $C_R = 910$ (for crack velocity in m/s). The results are also in good agreement with theoretical and experimental measurements of the crack speed, showing that maximal crack speed cannot reach the theoretical limit of the Rayleigh wave speed (Freund 1972a,b; Curbach and Eibl 1990; Rabczuk and Belytschko 2004; Larcher 2009). The maximal measured crack velocity in concrete was approximately 500 to 600 m/s (Curbach 1987; Larcher 2009).

The results of the analysis are obtained using spatial finite element discretization as shown in Fig. 10.13, which is based on the randomly generated four-node simple constant strain solid elements, together with the localization limiter based on the energy criteria (crack band method). In order to confirm that the crack branching predicted by the finite element model from Fig. 10.13 is mesh independent, additional analysis is performed, where relatively fine standard eight-node solid elements with linear strain field are employed. The comparison of the crack path and calculated crack velocities ($\Delta/dt = 1000$ mm/s) for two completely different spatial discretizations show that the results of the analysis are principally mesh independent (see Plate XXXII in colour section between pages 208 and 209), in the sense that the observed crack branching does not depend on the discretization. The crack path is slightly influenced by the mesh since, in case of four-node finite elements, the discretization is relatively coarse compared to the eight-node element mesh. Furthermore, for the finer hexa-mesh the evaluation of crack velocities is more precise due to the finer spatial discretization. Note that a more serious mesh sensitivity study, which is out of the scope of the present paper, would require detailed and systematic variation of mesh size and shape.

The results of the analysis show that crack velocity depends on the crack path and on the displacement rate. Principally, the crack speed is highest at the onset of crack branching, where it reaches a velocity of approximately 500 to 600 m/s. Furthermore, the crack velocity at the onset of cracking (notch tip) depends on the displacement rate. It increases with the displacement rate and reaches a maximal value of 625 m/s ($\Delta/dt = 10\,000$ mm/s). The crack velocity at the onset of cracking as a function of displacement rate is plotted in Fig. 10.15. It can be seen that the crack velocity increases with the increase of displacement rate up to $\Delta/dt = 2500$ mm/s. With further increase of displacement rate the crack speed at the onset of cracking does not increase, and instead crack branching at the onset of cracking is observed.

L-shaped specimen

The L-specimen poses a very interesting problem from the point of view of crack propagation and fracture of concrete and is often used to demonstrate the capabilities of material models as well as the phenomenon of mesh



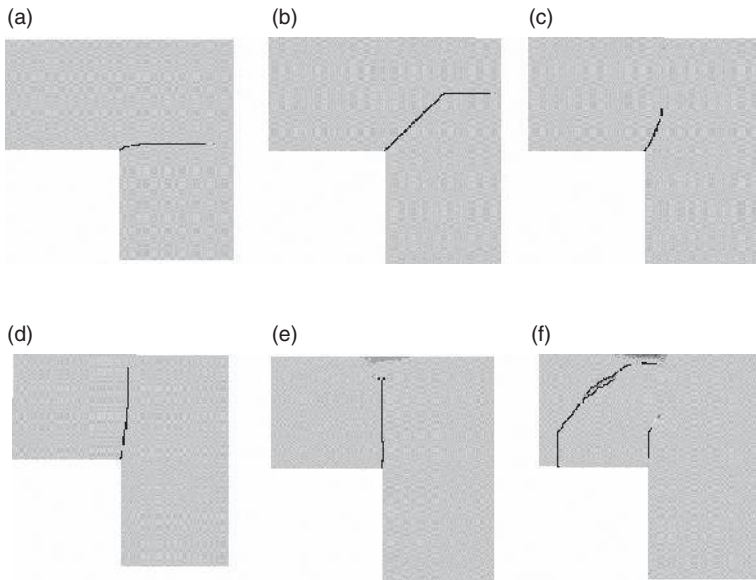
10.15 Crack speed at onset of cracking as a function of displacement rate.

sensitivity (Winkler *et al.* 2001; Özbolt *et al.* 2002). The L-specimen tested by Winkler *et al.* (2001) was considered for this numerical study (Fig. 10.16). In the first instance, the specimen was analysed under static loads to compare the results of analysis with experiment. The same model was then subjected to high loading rate to investigate the influence of loading rate on failure mode and fracture propagation of the specimen (Özbolt and Sharma 2012).

In the numerical model, meshing was done with eight-node solid elements with linear strain field. To keep the number of elements low, only one row of elements was considered for the analysis (plane stress condition), with the thickness of the slice as 2.5 mm. The analysis is carried out for normal strength concrete with the following properties: Young's modulus $E_c = 25\,850\text{ N/mm}^2$, Poisson's ratio $\nu = 0.18$, uniaxial compressive strength $f_c = 31.0\text{ N/mm}^2$, tensile strength $f_t = 2.70\text{ N/mm}^2$, fracture energy $G_F = 0.095\text{ N/mm}$ and concrete mass density $\rho_c = 2400\text{ kg/m}^3$.

Figure 10.17 shows (a) experimental, and (b) numerically obtained results for the specimen loaded under static loads. It can be appreciated that the numerical model could replicate the failure pattern and crack propagation for the L-specimen quite well. Thus, the same model was then utilized to perform the analysis under higher displacement rates. Similar to the case of the uniaxial tension specimen, the displacement rates considered were 100 mm/s, 300 mm/s, 500 mm/s, 1000 mm/s and 1500 mm/s.

Figure 10.18 shows the failure patterns obtained for the following displacement rates: (a) 100 mm/s, (b) 300 mm/s, (c) 500 mm/s, (d) 1000 mm/s, and (e) 1500 mm/s. It is very interesting to observe how the crack propagation changes with the increasing loading rate. Although in this case the specimen is un-notched, the junction point acts as the critical region due to stress concentration. Therefore, the crack always initializes at the junction



10.18 Failure pattern and crack propagation for the specimen under dynamic loads: (a) quasi-static, (b) 100 mm/s, (c) 300 mm/s, (d) 500 mm/s, (e) 1000 mm/s and (f) 1500 mm/s.

conjugate of the crack observed under the static loading case. At 1000 mm/s (Fig. 10.18e), it becomes vertical and small branching in the end can be seen, which is attributable to the free edge, instead of crack propagation velocity. On further increasing the displacement rate to 1500 mm/s (Fig. 10.18f), the failure first occurs adjacent to the point of loading, and then the crack starts to appear at the junction point. This shows that the displacement rate is so high that it leads to local failure. It is difficult to comment on the propagation of the crack from the junction point, since a large amount of energy is dissipated by the local crack.

In order to verify the reason for change in the crack propagation direction, the analysis for the displacement rate of 500 mm/s was repeated once while considering only rate sensitivity of crack propagation (static analysis) and once only as dynamic analysis without rate sensitivity. The results are summarized in Fig. 10.19. Figure 10.19a shows the failure pattern obtained by performing static analysis with respect to rate sensitivity. The failure pattern remains the same as shown in Fig. 10.17b for the static loading case, without any rate sensitivity, clearly indicating that rate sensitivity has no influence on crack propagation. Figure 10.19b shows the failure pattern obtained by performing dynamic analysis but neglecting rate sensitivity. This figure shows that dynamic analysis (i.e. inertial forces) has a large influence on crack propagation. The crack propagates almost vertically and the failure pattern is very similar to that shown in Fig. 10.18d for 500 mm/s loading rate.

speeds c_p and c_T . The dashed lines extrapolated from the shock measurement points between particle velocities from 450 m/s across 70 m/s down towards 0 m/s end up astonishingly well at the theoretical bulk sound speeds. The reader should note that $(0, c_B)$ is not part of the linear fit through the higher shock intensities, but that it is well matched by it.

From this observation originated the concept of describing weak acoustic excitation to strong shocks in solids by formulating an equation of state for the hydrodynamic portion of the stress tensor, which is described in detail in several books, such as (Meyers 1994) and (Hiermaier 2008). While the pressure term, or the first invariant of the Cauchy stress tensor, describes the compression wave, the shear dominated (or deviatoric) response is independently described using the second and third invariant. This aspect will be further described below.

The problems in statics and moderate dynamics treated in Sections 10.1 and 10.2 deal with situations where concrete is not strongly compacted and most of the energy is dissipated by cracking or quasi-plastic behaviour. Severe density changes additionally occur in shock waves with substantial shock heating. Therefore, the governing Equations [10.10a]–[10.10c] of the so-called hydrocodes, which describe materials under high-rate to shock loading, are derived from the conservation of mass and energy in addition to momentum conservation. In the differential, non-conservative form Equation [10.10a]–[10.10c] the quantity ρ denotes density, v velocities and σ Cauchy stresses. i and j are the spatial indices in Einstein's summation notation.

$$\frac{d\rho}{dt} = -\rho \nabla \cdot v_i \quad [10.10a]$$

$$\frac{dv_i}{dt} = \frac{1}{\rho_0} \nabla \cdot \sigma_{ij} \quad [10.10b]$$

$$\rho \frac{de}{dt} = d_{ij} : \nabla v_i \quad [10.10c]$$

Since all wave lengths, especially the very sharp shock wave portions, are important for the solution of the dynamic material state, explicit time integration is a necessary requisite of hydrocodes. Simple elements with single-point integration are mostly used, together with appropriate shock treatment techniques (Hiermaier 2008).

10.3.2 Hydrocode plasticity models based on tensorial invariants

Concrete models in hydrocodes extend the successful practice of metal plasticity models for high-rate to shock-load cases. The material description

is based on the first, second and third invariants of the stress tensor σ_{ij} (stress deviator tensor S_{ij} or the principal stresses $\sigma_{I,II,III}$). The first invariant I_1 (Equation [10.11]) describes the purely volumetric stresses, the second invariant J_2 (Equation [10.12]) the purely distortional stresses and the third invariant J_3 (Equation [10.13]) the stress triaxiality.

$$I_1 = \sigma_{xx} + \sigma_{yy} + \sigma_{zz} = \sigma_I + \sigma_{II} + \sigma_{III} \quad [10.11]$$

$$\rho = -\frac{1}{3}/1 \quad \sigma_m = \sigma_{oct} = \frac{1}{3}/1 \quad \xi = \frac{1}{\sqrt{3}}/1$$

$$J_2 = \frac{1}{2} S_{ij} S_{ij} = \frac{1}{2} \left(S_x^2 + S_y^2 + S_z^2 + 2(S_{xy}^2 + S_{xz}^2 + S_{yz}^2) \right) \quad [10.12]$$

$$J_2 = \frac{1}{6} \left[(\sigma_x - \sigma_y)^2 + (\sigma_y - \sigma_z)^2 + (\sigma_z - \sigma_x)^2 \right] + \sigma_{xy}^2 + \sigma_{yz}^2 + \sigma_{zx}^2$$

$$\sigma_{eff} = \sqrt{3J_2} \quad \tau_{oct} = \sqrt{\frac{2}{3}J_2} \quad \tau_m = \sqrt{\frac{2}{5}J_2} \quad \rho = \sqrt{2J_2}$$

$$\Delta\sigma = |\sigma_I - \sigma_{III}| = \sqrt{3J_2} \quad (\text{for cylinder tests})$$

$$J_3 = S_1 S_2 S_3 = \det S \quad [10.13]$$

$$\cos 3\theta = \frac{3\sqrt{3}}{2} \frac{J}{J_2^{3/2}} = \frac{27 \det(S)}{2\sigma_{eff}^3}$$

Across the disciplines of civil engineering, continuum mechanics and numerical methods, a number of different notations are derived from these three invariants. I_1 can be written as hydrostatic pressure p (used hereafter), mean stress σ_m , octahedral stress σ_{oct} , or hydrostatic length ξ . Derived from the second invariant J_2 are von Mises stress or effective stress σ_{eff} (used below), octahedral shear stress τ_{oct} , mean shear stress τ_m , deviatoric length ρ and principal stress difference $\Delta\sigma$. The most common property derived from the third invariant J_3 is the Lode angle θ in the deviatoric section.

Dynamic stiffness derived as meso- and macro-scale shock properties

The modified Hopkinson bar experiment (MSHB, see Chapters 6 and 7) represents the highest possible tensile loading (strain rates of up to 200/s for concrete) without prior damage of the specimen in compression. In practical applications, due to the strong wave dispersion in concrete members, high-rate spallation opposite the loading face only occurs if the concrete is charged on the loading side by sharp and short duration waves beyond the compressive strength. Examples are a contact detonation in Plate XXXVIII and Plate XXXXII (see colour section between pages 208 and 209) and

dynamic tensile cracking during ballistic penetration in Fig. 5.1 and Plate VII. The accurate description of the dynamic compression properties is therefore a necessary precondition to propagating correct amplitudes and wave lengths of loading across the member to the opposite spall surface.

The shock compression properties are governed by the first invariant of the stress tensor often described in the form of hydrostatic pressure p . Its dependency on the density and internal energy is commonly called the ‘equation of state’. Holmquist, Johnson and Cook (1993) pioneered combining a multi-linear porous equation of state of concrete with a plasticity model for deviatoric strength. Malvar (1997) deployed a similar approach using the tabular EOS 8 with non-linear compression and compaction in Dyna. However, in both approaches the theoretical treatment of porous compaction was still simplistic and the model calibration suffered from large scattering of concrete shock data (see Fig 10.20, right). Riedel *et al.* (2008), Riedel (2004) and Hartmann (2010) applied the more physical approach of Herrmann’s (1969) p - α equation of state, which treats the porosity α as an additional state variable and links the compaction work with internal energy of the pore-free matrix material. In Equation [10.14] are the material parameters of initial porosity α_{init} , elastic pore crush pressure p_{el} , lockup pressure p_{comp} and exponent N .

$$p = f(\rho\alpha, e) \quad \text{with} \quad \alpha = 1 + (\alpha_{\text{init}} - 1) \left[\frac{p_{\text{comp}} - p}{p_{\text{comp}} - p_{\text{el}}} \right]^N \quad [10.14]$$

Equation-of-state data for concrete from instrumented contact detonations suffered up to the mid-1990s from large scattering because of concrete heterogeneity, as visible in Fig. 10.20 right. Grady (1996) made major improvements by introducing the inverse plate-impact test on mostly unscaled concrete. Combination of this method with mesomechanical analysis (Riedel 2004, 2008), (Gebbeken and Hartmann 2010) reduced the experimental effort and the scattering. Furthermore, it explained the porous compaction as the reason for the drop in the shock-particle-velocity relationship (see Fig 10.20 right), a major dissipation phenomenon in compressive waves between 500 MPa and 5 GPa amplitude. In the mesomechanical simulations the ITZ was shown to have a negligible influence on macroscopic shock properties (Riedel 2004), see Plate XXXIV (see colour section between pages 208 and 209). Gebbeken (2006) found general agreement with equation-of-state measurement using explosive plane wave generators.

Beyond plasticity models, the non-linear volumetric response was also introduced into Bazant’s microplane model using a ‘volumetric-deviatoric split’ to capture shock compression states (Bazant 2000b; Caner and Bazant 2000). However, the works still refer to static high pressures up to 600 MPa rather than shock compression, the difference of which is highlighted in Plate IX of Chapter 5.

Deviatoric limit surfaces

The second invariant J_2 (or the effective stress σ_{eff}) is used in the plasticity-based models to describe strength surfaces. They limit the elastic stresses accumulated from deviatoric strain rates using the shear modulus Holmquist, Johnson and Cook (1993) were the first to propose a pragmatic model including the key phenomena of:

- (1) Porous equation of state to describe shock compression and compaction
- (2) Ultimate strength surface up to high pressures, depending on pressure and strain rate
- (3) Damage evolution based on plastic strains, accounting for increasing ductility under high confinement
- (4) Residual friction resistance of fully failed material under compressive pressures

The pragmatic simplicity (see Equations [10.15] and [10.16]), probably inspired by the outstanding success of the ‘Johnson-Cook Model’ for metals, contributed to the fast spread and implementation into many finite element codes. This wide use quickly demonstrated the ‘JH-model’ to be useful in dynamics, especially when describing penetration load cases into concrete structures. In the sensitivity analysis depicted in Fig. 10.23, discussed in detail later, the four influences (1) – (4) are confirmed again to be of key importance in the simulation of penetration resistance of reinforced concrete targets close to the ballistic limit.

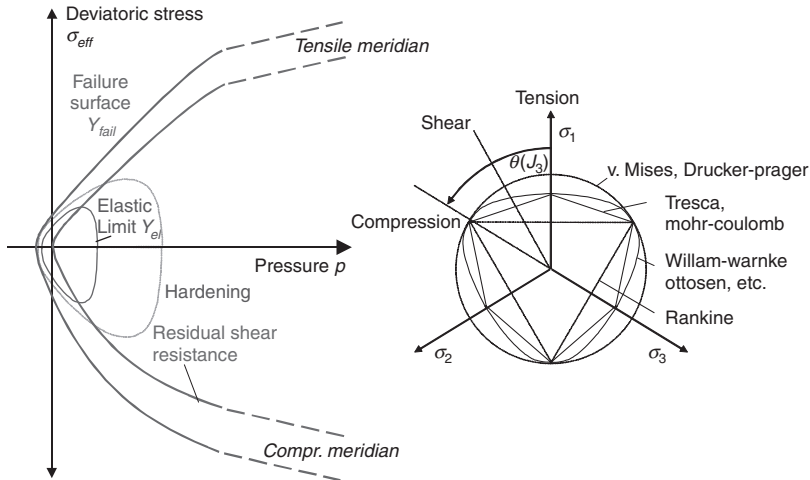
$$f(p, J_2, \dot{\epsilon}) = \sqrt{3J_2} - f_c \left(A(1 - D) + Bp^{*N} \right) \left(1 + C \ln \frac{\dot{\epsilon}}{\dot{\epsilon}_0} \right) = 0 \quad [10.15]$$

$$D = \sum \frac{\Delta \epsilon_p + \Delta \mu_p}{\epsilon_p^f + \mu_p^f} \cdot \epsilon_p^f + \mu_p^f = D_1 \left(p^* - p_{spall}^* \right)^{D_2} \geq EFMIN \quad [10.16a,b]$$

A, B, C, N strength model parameters

ϵ_p, ϵ_p^f	deviatoric plastic strain, deviatoric plastic strain to failure
μ_p, μ_p^f	volumetric plastic strain, volumetric plastic strain to failure
p^*	hydrostatic pressure normalized over uniaxial compressive strength f_c'
$D_1, D_2, EFMIN$	damage model parameters

As shortcomings were noted, in the region of low pressure regime from uniaxial tension, pure shear and uniaxial compression, major compromises have to be taken with form (Equation [10.15]) when fitting to high-pressure



10.21 Left: compressive and tensile meridian of the ultimate strength/failure surface (blue); residual friction surface for failed material (red); initial elastic limit and hardening surface (green); right: deviatoric section of various plasticity models with and without dependence on stress triaxiality J_3 .

triaxial failure stresses (i.e. Plate VI, see colour section between pages 208 and 209). Not described is the further dependence of concrete on the stress triaxiality or third invariant dependence J_3 , resulting in different compressive and tensile meridians, as shown in Fig. 10.21. This property accounts for the fact that the concrete failure stress across the pressure range is sensitive to the combination of the principal stresses. Triaxial compressions are characterized by combinations with $\sigma_I < \sigma_{II} = \sigma_{III}$ (compressive meridian, σ_i denoting tensile principal stresses), $\sigma_I > \sigma_{II} = \sigma_{III}$ (tensile meridian) denote triaxial extensions. Especially in the low pressure regime, this deficiency leads to insufficient modelling of brittleness.

At the Ernst-Mach-Institut and University of Armed Forces of Munich the principal track of Holmquist *et al.* (1993) was continued by Riedel (1999, 2004, 2009a, 'RHT-model'), Gebbeken and Ruppert (2000 'RGGP-model' (RGGP – Ruppert, Gebbeken, Greulich and Pietsch)) and Hartmann *et al.* (2010); Hartmann and Gebbeken (2010, 'HGP-model'. (HGP – Hartmann, Greulich and Pietsch)). They all deal with variations of the limit surfaces as shown in Figure 10.21, left, neglecting detailed stress–strain paths. Damage descriptions are based on accumulated and normalized plastic deviatoric and volumetric strains, similar to Equation [10.16a] and [10.16b] without localization limiters. The RHT model uses, in contrast to the form of the first communication in 1999, one single logarithmic low-rate strength enhancement, separately in tension and compression. The HGP uses a power law

in compression and a double logarithmic law for tension, with high rate enhancement described. This family of still relatively simple plasticity models proved to be useful for many dynamic load cases such as ballistic impact, contact detonations and blast in the strain-rate regime from 1/s to 10⁶/s. The RHT model has been, because of its implementation as a serial model in ANSYS-Autodyn from 2000, the most widely used model within this family (Riedel 2009b) and the most familiar to the author. Therefore, it is used for sensitivity analysis and further discussion of dynamic load cases below.

In the same hydro code have been implemented the DYCAPS (Itoh *et al.* 2000) and CAPROUS (Itoh *et al.* 2011) plasticity models in Japan, which focus initially more on detailed stress–strain paths and dynamic beam bending tests. The recent edition uses a porous equation of state based on confined Hopkinson pressure bar experiments for application in the shock regime. It uses a separate double logarithmic strain rate enhancement factor for low and high rates and no regularization.

Malvar and colleagues (1997) undertook a slightly different track for the ‘K&C Concrete Model’, implementing it into DYNA3D and later LS-Dyna. Their plasticity model also describes the phenomena (1)–(4) reviewed at the beginning of the section. But they formulated limit surface and plastic flow algorithms to replicate in detail stress–strain paths under various (moderate and low) confinements. Furthermore, they included the effect of shear dilation, thus volumetric expansion, upon purely deviatoric stresses. This effect is a noticeable flow effect at low confinements, but at the same time compromises the classic split of volumetric (I_1) and deviatoric (J_2) response, which forms the basis of the theory of hydrocodes (see Section 10.3.2). Moreover, Malvar introduced a localization limiter into the strain-based damage accumulation. Separate double logarithmic strain-rate enhancement factors are used for tension and compression. Implemented in LS-Dyna as model 73R3 for roughly ten years now, it has proved to be suitable for high-rate loading situations as well as for analysis of material experiments, as in Chapter 8. Deficiencies might be suspected for very strong shock propagation problems, since a precision fit of the equation of state to shock experiments is lacking, and the hydrodynamic theory of shock waves in solids is compromised by the shear dilation formulation.

At Gramat Research Center and University of Grenoble the ‘PRM-Model’ (Pontiroli *et al.* 2010) has evolved from the mid-1990s until recently. The strain-based damage descriptions for compression and tension are based on the framework of irreversible thermodynamics with a Hillerborg type regularization method. Single and double power laws are used for low and high rate strength enhancement factors in compression and tension. A modified Krieg plasticity model (Krieg 1978) is used for the high-pressure meridians. A porous equation of state describes non-linear compression properties based on static high-pressure triaxial compression experiments on the

Table 10.1 Overview of rate enhancement description in chosen hydrocode concrete models

	Tension	Compression	High rate enhancement	Localization limiter
JH	Single log		No	No
K&C	Double log	Double log	Yes	G_f/h
RHT 99	Double log	Double log	Yes	No
RHT	Single log	Single log	No	No (optional G_f/h)*
HGP	Power law	Double log	Yes	No
CAPROUS	Double log	Double log	Yes	No
PRM	Power law	Double power law	Yes	G_f/h

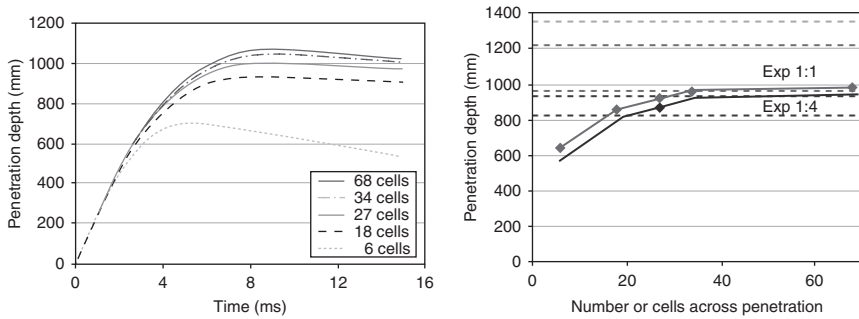
*Clegg *et al.* (2002).

GIGA-press of Grenoble, accounting also for different moisture saturation states. The model is implemented in Abaqus explicit, and applications from low velocity structural dynamics up to high velocity impact and penetration problems have been reported.

Table 10.1 summarizes again the key aspects of the rate enhancement and softening descriptions under tension. Most macro-models for hydrocodes use explicit high rate enhancement in the constitutive model. In contrast to that, the first sections of the chapter highlights that with a suitable modelling approach and with sufficient resolution to represent crack propagation speed and branching, no high rate enhancement is needed. In future, it is to be critically reviewed if the condition of necessary resolution can be satisfied for 3D models of building components. In most design applications of hydrocode models, each cell will contain several cracks, describing a ‘damage zone’. The discussion will continue and has to converge, whether in this case of ‘structural modelling’ the high rate enhancement, caused by inertia around the crack tips, has to be included in the material law or not.

10.3.3 Analysing sensitivities and model complexity

The following example will serve to highlight the importance of chosen concrete modelling aspects in a penetration simulation, where the projectile is stopped closed to the ballistic limited in a highly dynamics tensile membrane mode of the remaining cross-section. The test case has been performed at test site of the Bundeswehr Technical Center WTD 91 in Meppen, Germany and is documented in (Riedel 2004). A penetrator of 426 kg weight (diameter $D = 363$ mm, ogival nose radius $R_{ogive} = 520$ mm, length $L = 1200$ mm, see Fig. 10.23, left) hit at 260m/s in normal direction to a 38 MPa concrete wall of $7.20 \times 7.20 \times 1.60$ m with a weight of about 200 t. The wall contained 36 bars horizontally and vertically with bar diameters $D = 14$ mm of front



10.22 Left: convergence analysis of the penetration simulation shown in Figs 10.28 and 10.29; Right: validation against the range of full (black 810–930 mm) and quarter (grey 960–1220 mm) scale experiments; 1:4 penetration depth is scaled up for easier comparison.

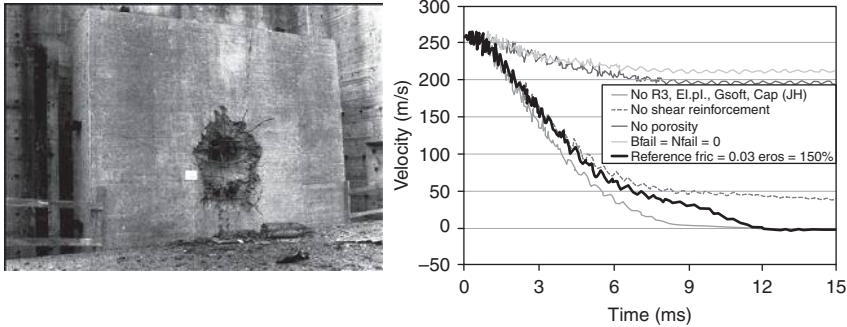
reinforcement. The rear reinforcement contained the double number of bars with $D = 16$ mm. 7×22 bars of shear reinforcement were placed horizontally and vertically. The tests were additionally replicated in scale 1:4 in the laboratories of the Ernst-Mach-Institut, site Efringen-Kirchen.

In Riedel (2004) the test case was modelled using ANSYS-Autodyn, with concrete volume elements and discrete rebar modelling. In 2D axisymmetry, the rebar was simplified as shells with equal overall cross-section and strength, and in 3D the rebar was modelled by discrete beams. In each case they were cinematically coupled to the concrete elements exclusively. The concrete was modelled using the RHT model as presently still implemented in the commercial code. Figure 10.22 shows a convergency study in comparison to the experimental results. The simulations converge very reasonably into the scatter range of the experiments. Despite the lack of regularization, clear convergence is noted, supported by the presence of the rebar close to the rear surface.

Figure 10.23 shows a range of simulations with varied material properties of the modular RHT model. The blue curve denotes the reference curve with the full complexity of the model. The green curves denotes the result without J3 dependency and pre-peak hardening, thus the material properties are very similar to the JH-model. It can be observed that the model of Holmquist (1993) still captures the reference computation quite well.

Dramatic deviations occur if the porosity is disregarded (red curve) or if the fully damaged concrete is modelled without shear resistance under compression (yellow curve). Both cases totally fail to predict the penetration resistance of the target, and the penetrator perforates at 80% of the initial velocity.

Instructive also is the last variation, where the full complexity concrete model is used, but the shear reinforcement is disregarded. It becomes apparent that the shear reinforcement does not play a major role in the initial deceleration and the penetration phase. However, when the penetrator



10.23 Impact configuration after test: penetrator lying undeformed in front of the target.

approaches the rear surface around 6 ms, the target fails to maintain pressure on the penetrator nose and the rear reinforcement fails in membrane deformation.

One numerical artefact needed for body-fixed or Lagrangean computational meshes is the erosion of heavily distorted cells. Plate XXXV (see colour section between pages 208 and 209) shows a parametric study of the influence of the geometric erosion strain. This numerical mechanism is used to disregard highly distorted cells in favour of a stable timestep, once they do not play a role on the target or impactor resistance anymore. It can be seen that for this example and for the chosen discretization minimum 80%, better than 150% erosion strain should be chosen. Further increase will not influence the computational result. It should be noted that the cells with completely damaged concrete have to be maintained in the computation as long as the failed material provides friction resistance to the penetrator nose. Each cell may only be deleted, once it has flown far enough around the penetrator nose, having lost its influence on the penetration resistance.

This example shows that material softening and numerical erosion of distorted elements have to be treated separately in penetration calculations. In some publications a pressure-dependent yield surface with perfectly plastic flow from the yield point is used together with erosion criteria. In this sense, the (necessary) numerical artefact of erosion will act as a material failure criterion. Such a practice will limit the range of predictiveness of the modelling approach when the same parameters are used for different load cases or discretizations.

10.3.4 Model complexity versus range of application

The review of plasticity models and applications cited in Section 10.3.2 may allow some discussion about the context of complexity and applicable range of the models.

Models carefully replicating multi-axial stress-strain paths under various low and intermediate confinements, such as K&C (Malvar 1997), DYCAPS (Itoh 2000) or PRM (PRM – Pontiroli, Rouquand and Mazars; Pontiroli 2010), seem to be specifically strong in replicating dynamic structural loading, such as drop-weight testing of beams or impact at moderate velocities up to a few 100m/s. These models often seem less elaborate in terms of non-linear compression and compaction properties, especially with respect to validation against shock experiments on concrete. The predictive capabilities in dynamic structural loading indicate that the low pressure, multi-axial, plastic flow description and energy balance still dominates the moderate dynamic regime. However, the predictive capabilities might decrease at highest loading rates, when release tensile states result from shock wave loading.

The second class of models, represented by JH (Holmquist 1993), RHT (Riedel 2004, 2009a) and HGP (2010), seems to emphasize more equation-of-state properties and high-pressure strength meridians. They deliberately disregard multi-axial stress-strain paths and focus only on replicating the maximum load-carrying capacity across the pressure- and strain-rate range, together with adequate porous shock compression properties. Their success in simulating ballistics for high to hypervelocity penetration and contact detonations seems to suggest that the momentum conservation – along the failure meridians – and energy balance – governed by plasticity and shock compaction – are the major drivers. The details of the plastic flow path seem to play a minor role in this regime, otherwise these models would not exhibit their known predictive qualities. Also, the lack of regularization for decreasing mesh dependence seems not to be as important as in slower dynamic events, where dissipation through cracking takes a larger portion of the deformation energy.

The microplane model (Bažant 2000b), (Caner 2000) seems to be one of the few models that have bridged the range of smaller scale, multi-axial analysis of material testing, including softening and regularization with non-linear compression properties up to shock loading. However, the initial simplicity of the model, residing in simple traction and friction stress-strain curves cinematically superimposed from multiple microplanes, seems to be compromised for application in the shock regime. The introduction of ‘stress-strain boundaries’ and split in hydrodynamic and deviatoric response in this domain, typical for ‘hydrocodes’ and plasticity models, might show that the task of creating a very simple concrete model, ranging from static or low small-scale material samples up to full-scale three-dimensional building applications in one and the same model, is still an unfulfilled dream.

10.4 Summary

The response of concrete structures between structural dynamics and stress wave loading depends strongly on the loading rate. With an increase of

loading rate there is an increase of resistance, change of failure mode and crack branching phenomena. At low and medium loading rates, to about $1/s$, the influence of strain rate dominates the tensile response of the material. This represents the true rate-dependent material strength and can be attributed to phenomena taking place in the micro-structure of the material, i.e. viscosity and rate-dependent micro-cracking (inertia at the micro-scale). However, at higher loading rates dominates the influence of structural (macro-) inertia forces around the cracks. They cause progressive increase of apparent tensile strength, change of failure mode, and crack branching.

The true material strength can be modelled by the rate sensitive constitutive law of the microplane model. However, the influence of structural inertia on the structural response should automatically result from dynamic analysis, i.e. they should be not a part of the constitutive law, as long as the mesh resolutions allow simulating individual (smeared) cracks and branching. The constitutive law should account properly for the interaction with stresses caused by inertia forces, i.e. the interaction over different directions to be accounted for. In the numerical examples of a CT- and an L-specimen in Section 10.2, a relatively simple modelling approach based on the standard finite elements, a macroscopic constitutive law (microplane), and a smeared crack approach is used. This approach seems to be capable of correctly predicting the rate-dependent resistance, loading-rate dependent failure mode, crack branching, and crack velocity.

Discrete types of models, which are principally similar to the microplane model, account for the interaction between different orientations inside the material, and are capable of predicting the phenomena related to inertia. However, in contrast to the microplane model, which can be used together with standard finite elements, discrete approaches are computationally much more demanding.

The majority of standard macroscopic models based on the theory of tensorial invariants, such as plasticity- or damage-based models have obviously not been developed to account for the influence of local structural inertia between cracks and during crack branching. However, successful application of the plasticity-based K&C and RHT model on a mesoscale have been demonstrated in Chapter 8 and in Riedel (2008), respectively. But it remains to be investigated on a broader scope whether plasticity models might also predict rate-dependent change of failure mode and crack branching.

Building designs are currently modelled for most highly dynamic load cases with macroscopic, invariant based continuum models. For the highest rates of tensile loading, in the order of some $10^2/s$, they need also to account for shock waves with compressive strain rates up to $10^6/s$, because they are the only source of such extremely dynamic tension states in practical applications. To this aim, they have to use explicit time integration and solve the mass and energy conservation equation, as well as the momentum

conservation used in structural dynamics. They also need to represent the equation-of-state properties of concrete with sufficient accuracy, since they represent the dynamic stiffness (i.e. impedance) and thus define the dynamic load amplitude and duration.

The representation of frictional flow of the failed material under dynamic confinement is mandatory in order to capture the penetration resistance. It must be used together with, but clearly separated from, numerical erosion of distorted cells after their load-carrying contribution as long as mesh-based Lagrangean discretizations are used.

Currently, in most macroscopic plasticity models the influence of inertia forces on dynamic strength enhancement is still part of the constitutive law, instead of emerging automatically from dynamic analysis as stated above. Closing the gap between these two modelling domains now seems possible with the microplane model, but still needs to find broader scientific consensus.

10.5 References

- Banthia, N. P., Mindess, S. and Bentur, A. (1987). Impact behaviour of concrete beams, *Materials and Structures/Matériaux et Constructions*, **20**, 293–302.
- Bazant, Z. P. and Oh, B. H. (1983). Crack band theory for fracture of concrete. *RILEM*, **93**(16), 155–177.
- Bazant, Z. P., Adley, M. D., Carol, I., Jirasek, M., Akers, S. A., Rohani, B., Cargile, J. D. and Caner, F. C. (2000a). Large-strain generalization of microplane model for concrete and application. *Journal of Engineering Mechanics, ASCE*, **126**(9), 971–980.
- Bazant, Z. P., Caner, F. C., Carol I., Adley M.D and Akers, S. A. (2000b). Microplane model M4 for concrete I: formulation with work-conjugate deviatoric stress. *Journal of Engineering Mechanics, ASCE*, **126**(9), 944–953.
- Bentur, A., Mindess, S. and Banthia, N. (1987). The behaviour of concrete under impact loading: Experimental procedures and method of analysis, *Materials and Structures / Matériaux et Constructions*, **19**(113).
- Bischoff, P. and Perry, S. (1991). Compressive behaviour of concrete at high strain rates, *Materials and Structures / Matériaux et Constructions*, **24**, 425–450.
- Brandon, D.G. (1987). Dynamic loading and fracture. In T.Z. Blazynski (Ed.), *Materials at high strain rates*. Elsevier, London, 187–218.
- Caner, F. C. and Bazant, Z. P. (2000). Microplane model M4 for concrete II: Algorithm and calibration. *Journal of Engineering Mechanics, ASCE*, **126**(9), 954–961.
- CEB, (1988). *Concrete structures under impact and impulsive loading*, Synthesis Report, Bulletin d'Information No. 187, Lausanne.
- Clegg R., Hayhurst C. and Roberstion I. (2002). *Development and application of a rankine plasticity model for improved prediction of tensile cracking in ceramic and concrete materials under impact*. Dymat Technical Meeting, TP110, Sevilla, Spain.
- Curbach, M. (1987). *Festigkeitssteigerung von Beton bei hohen Belastungsgeschwindigkeiten*. PhD. Thesis, Karlsruhe University, Germany.
- Curbach, M. and Eibl, J. (1990). Crack velocity in concrete. *Engineering Fracture Mechanics*, **35**(1–3), 321–326.

- fib* (2010). New Model Code, Chapter 5, Code-type models for concrete behavior (Draft).
- Freund, L. B. (1972a). Crack propagation in an elastic solid subjected to general loading-I. constant rate of extension. *Journal of Mechanics and Physics of Solids*, **20**, 129–140.
- Freund, L. B. (1972b). Crack propagation in an elastic solid subjected to general loading-II. non-uniform rate of extension. *Journal of Mechanics and Physics of Solids*, **20**, 141–152.
- Gebbeken, N. and Ruppert, M. (2000). *A new concrete material model for high dynamic hydrocode simulations*. Archive of Applied Mechanics ISSN 0939–1533, **70**, 7.
- Gebbeken N. and Hartman Th. (2010). A new methodology for the assessment of the EoS data of concrete, *International Journal of Protective Structures* **1**(3), 299–317.
- Grady D. (1996). *Shock equation of state properties of concrete*, Proc Int Conf Structures under Shock and Impact – SUSI.
- Hartmann Th., Pietzsch A. and Gebbeken N. (2010). A hydrocode material model for concrete, *International Journal of Protective Structures*, **1**(4), 443–468.
- Herrmann W. (1969), Constitutive equation for the dynamic compaction of ductile porous materials, *Journal of Applied Physics*, **40**(6), 2490–2499.
- Hiermaier, S.J. (2008). *Structures under shock and impact, continuum mechanics, discretization and experimental characterization*, Springer ISBN 978-0-387-73862-8.
- Holmquist, T., Johnson, G. and Cook, W. (1993). *A computational constitutive model for concrete subjected to large strain, high strain rates and high pressures*, 14th International Symposium on Ballistics, Quebec, 591–600.
- Hopkinson, B. (1914). *A method of measuring the pressure produced in the detonation of high explosives or by the impact of bullets*, Phil. Trans. Roy. Soc. London. Series A, **213**(10), 437–456.
- Itoh M., Katayarna M., Mitake S., Niwa N., Beppu M. and Ishikawa N. (2000). *Numerical study on impulsive local damage of reinforced concrete structures by a sophisticated constitutive and failure model*, Proc Int Conf Structures under Shock and Impact, Cambridge, 569–578.
- Itoh M., Beppu M. and Katayarna M. (2011). *A dynamic cap model with spall failure for concrete with applications to impact loadings*, Proc 9th Int Conf Shock and Impact Loads and Structures, Fukuoka, Japan, 403–411.
- Kipp, M.E., Grady, D.E. and Chen, E.P. (1980). Strain-rate dependent fracture initiation *International Journal of Fracture*, **16**, 471–478.
- Kolsky, H. (1953). *Stress waves in solids*, Clarendon Press, Oxford.
- Kožar, I. and Ožbolt, J. (2010). Some aspects of load-rate sensitivity in visco-elastic microplane model, *Computers and Concrete*, **7**(4), 317–329.
- Krausz, A. S. and Krausz, K. (1988). *Fracture kinetics of crack growth*. Kluwer, Dordrecht, The Netherlands.
- Krieg R.D. (1978) *A simple constitutive description for soils and crushable foams*, Sandia National Laboratories, SC-DR-72–0833, Albuquerque, New Mexico.
- Larcher, M. (2009). Development of discrete cracks in concrete loaded by shock waves, *International Journal for Impact Engineering*, **36**, 700–710.
- Lu, Y. and Xu, K. (2004), Modelling of dynamic behaviour of concrete materials under blast loading, *International Journal of Solid and Structures*, **41**, 131–143.

- Malvar J., Crawford J., Wesevich J. and Simons D. (1997). A plasticity concrete material model for DYNA3D. *International Journal of Impact Engineering*, **19**, 847–873.
- Mechtcherine, V., Millon, O., Butler, M. and Thoma, K. (2011). Mechanical behavior of strain hardening cement-based composite under impact loading. *Cement and Concrete Composites*, **22**, 1–11.
- Meyers M.A. (1994). *Dynamic behaviour of materials*. John Wiley & Sons, ISBN 0-471-58262-X.
- Mihashi, H. and Wittmann, F.H. (1980). Stochastic approach to study the influence of rate of loading on strength of concrete. *HERON*, **25**(3).
- Ortlepp, S. (2006). *Zur Beurteilung der Festigkeitssteigerung von hochfestem Beton unter hohen Dehnungsgeschwindigkeiten*. Dissertation, Technische Universität Dresden.
- Ožbolt, J., Li, Y. and Kožar, I. (2001). Microplane model for concrete with relaxed kinematic constraint, *International Journal of Solid and Structures*, **38**, 2683–2711.
- Ožbolt J., Pivonka P. and Lackner R. (2002). *Three dimensional FE analyses of fracture of concrete – material models and mesh sensitivity*, Fifth world congress on computational mechanics (WCCM V), Vienna.
- Ožbolt, J. and Reinhardt, H. W. (2005). *Rate dependent fracture of notched plain concrete beams*. Proceedings of the 7th international conference CONCREEP-7, Ed. By Pijaudier-Cabot, Gerard & Acker, 57–62.
- Ožbolt, J., Rah, K. K. and Mestrovic, D. (2006). Influence of loading rate on concrete cone failure, *International Journal of Fracture*, **139**, 239–252.
- Ožbolt, J., Sharma, A. and Reinhardt, H. W. (2011). Dynamic fracture of concrete – compact tension specimen, *International Journal of Solid and Structures*, **48**, 1534–1543.
- Ožbolt, J. and Sharma, A. (2011). Numerical simulation of reinforced concrete beams with different shear reinforcements under dynamic impact loads, *International Journal of Impact Engineering*, **38**, 940–950.
- Ožbolt, J. and Sharma, A. (2012). Numerical simulation of dynamic fracture of concrete through uniaxial tension and L-specimen, *Engineering Fracture Mechanics*, **85**, 88–102.
- Pedersen, R. R. (2009). *Computational modelling of dynamic failure of cementitious materials*, Dissertation, TU Delft, the Netherlands.
- Peroni, M., Solomos, G., Pizzinato, V. and Larcher, M. (2011). Experimental investigation of high strain-rate behaviour of glass, *Applied Mechanics and Materials*, **82**, 63–68.
- Pontiroli Chr., Rouquand A. and Mazars J. (2010). Predicting concrete behaviour from quasi-static to hypervelocity impact, *European Journal of Environmental and Civil Engineering*, **14**(6–7), 703–737.
- Rabczuk, T. and Belytschko, T. (2004). Cracking particles: a simplified meshfree method for arbitrary evolving cracks. *International Journal of Numerical Methods in Engineering*, **61**, 2316–2343.
- Reinhardt, H. W., Ožbolt, J. and Travaš, V. (2010). *Response of concrete members to impact loading, dynamic fracture of concrete – compact tension specimen*, In Oh, B. H., Choi, O. C. and Chung, L. (Eds.), FraMCS-7, Jeju, Korea, May 23–28, 1701–1714.

- Reinhardt, H. W., Körmeling, H. A. and Zielinski, A. J. (1985). The split Hopkinson bar, a versatile tool for the impact testing of concrete, *Materials and Structures*, **19**(109), 55–63.
- Reinhardt, H. W. (1982). Concrete under impact loading, Tensile strength and bond. *Heron*, **27**(3), 1–48.
- Reinhardt, H. W. and Weerheijm, J. (1991). Tensile fracture of concrete at high loading rates taking account of inertia and crack velocity effects. *International Journal Of Fracture*, **51**, 31.
- Riedel W., Thoma K., Hiermaier S. and Schmolinske E. (1999). *Penetration of reinforced concrete by BETA-B-500, Numerical analysis using a new macroscopic concrete model for hydrocodes*. Proc. 9. Int Symp, Interaction of the Effects of Munitions with Structures', Berlin Strausberg, 315–322.
- Riedel W. (2004). *Beton unter dynamischen Lasten: Meso- und makromechanische Modelle und ihre Parameter*, (Ed.), Fraunhofer EMI, Freiburg/Brsg., Fraunhofer IRB, ISBN 3–8167–6340–5.
- Riedel W., Wicklein M. and Thoma K. (2008). Shock properties of conventional and high strength concrete, Experimental and mesomechanical analysis, *International Journal of Impact Engineering*, **35**/3, 155–171.
- Riedel W., Kawai N. and Kondo K. (2009a). Numerical assessment for impact strength measurements in concrete materials, *International Journal of Impact Engineering*, **36**, 283–293.
- Riedel W. (2009b). *10 Years of RHT: A review of concrete modelling and hydrocode applications*, 143–165. In Hiermaier S. (Ed.), *Predictive modeling of dynamic processes – A tribute to professor klaus thoma*, Springer, ISBN 978-1-4419-0726-4.
- Riedel W., Stolz A., Roller Chr., Nöldgen M., Laubach A. and Pattberg G. (2011). *Impact resistant superstructures for power plants, Part I: Box girders and concrete qualities*, Int. Conf. Structural Mechanics in Reactor Technology SMIRT 21, New Delhi, India.
- Schuler, H. (2004). *Experimentelle und numerische Untersuchungen zur Schädigung von stoßbeanspruchtem Beton*. Dissertation, Universität der Bundeswehr München, Gernany.
- Travaš, V., Ožbolt, J. and Kožar, I. (2009). Failure of plain concrete beam at impact load: 3D finite element analysis. *International Journal of Fracture*, **160**, 31–41.
- Winkler B, Hofstetter G and Niederwanger G. (2001). Experimental verification of a constitutive model for concrete cracking. *Proceedings of the Institution of Mechanical Engineers, Part L: Journal of Materials Design and Applications*, **215**, 75–86.
- Weerheijm, J. (1992). *Concrete under impact tensile loading and lateral compression*. Dissertation, TU Delft, the Netherlands.

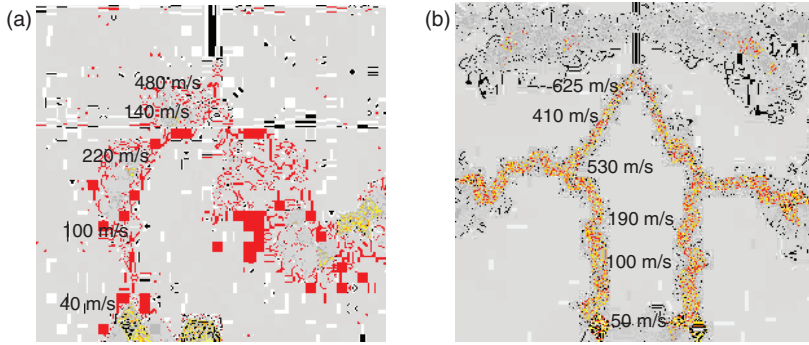


Plate XXX (Chapter 10) Crack velocities for different displacement rates: (a) $\Delta/dt = 1000$ mm/s and (b) $\Delta/dt = 2500$ mm/s.

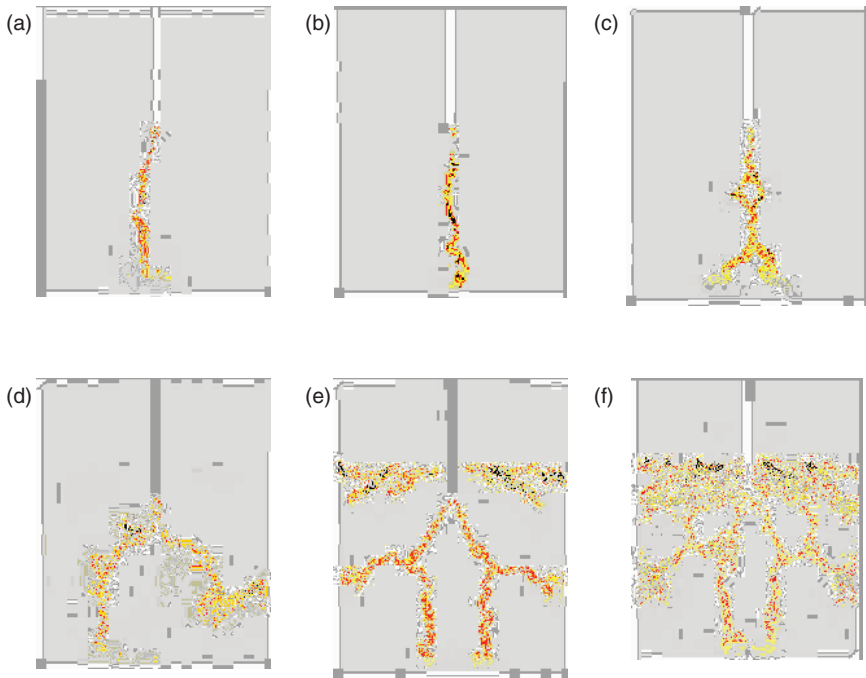


Plate XXXI (Chapter 10) Predicted failure modes: (a) quasi-static analysis (b) $\Delta/dt = 100$ mm/s (c) $\Delta/dt = 500$ mm/s (d) $\Delta/dt = 1000$ mm/s (e) $\Delta/dt = 2500$ mm/s (f) $\Delta/dt = 5000$ mm/s; above 1 m/s failure at the loading points suppressed numerically.

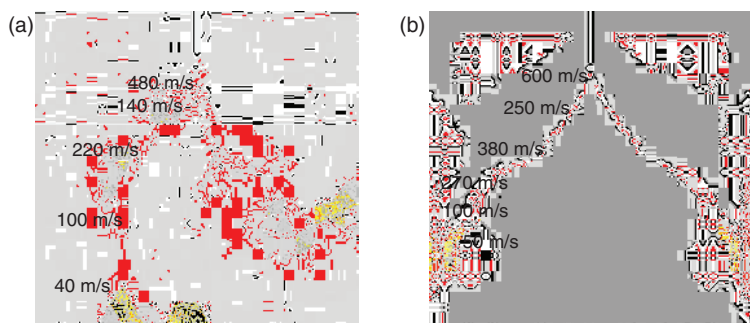


Plate XXXII (Chapter 10) Crack velocities and crack pattern for displacement rate $\Delta/dt = 1000 \text{ mm/s}$ (a) four-node solid elements (tetra-mesh), relatively coarse mesh and (b) eight-node solid elements (hexa-mesh), finer mesh.

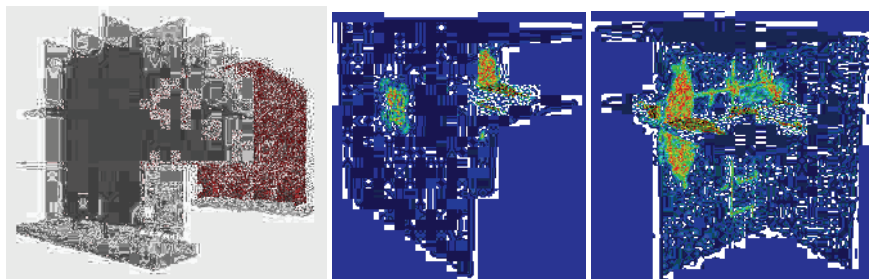


Plate XXXIII (Chapter 10) Damage to four box girder fields and stiffeners ($H \times W \times D = 27 \times 29 \times 20 \text{ m}^3$) of a nuclear power plant protection structure ($70 \times 130 \times 42 \text{ m}^3$) after aircraft impact; resolution with five elements over the thickness; reprinted from Riedel *et al.* (2011) with permission from IASMIT.

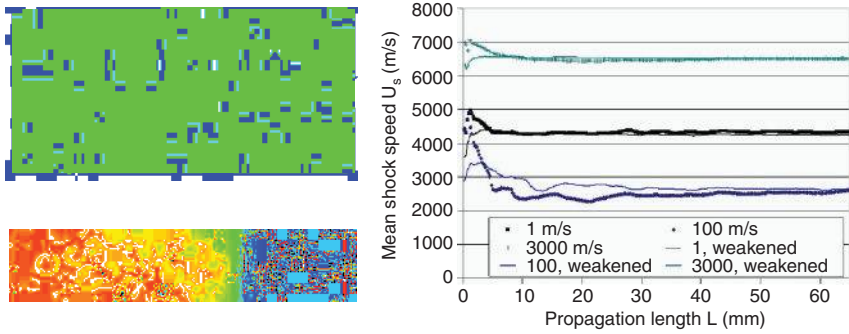


Plate XXXIV (Chapter 10) Left: mesostructural model with ITZ for homogenization simulations of the macroscopic shock propagation speed U_s ; right: the shock velocity U_s converges with and without weakened ITZ toward the same values from acoustic ($u_p = 1$ m/s) to very strong shock excitations with $u_p = 3000$ m/s (Riedel, 2004).

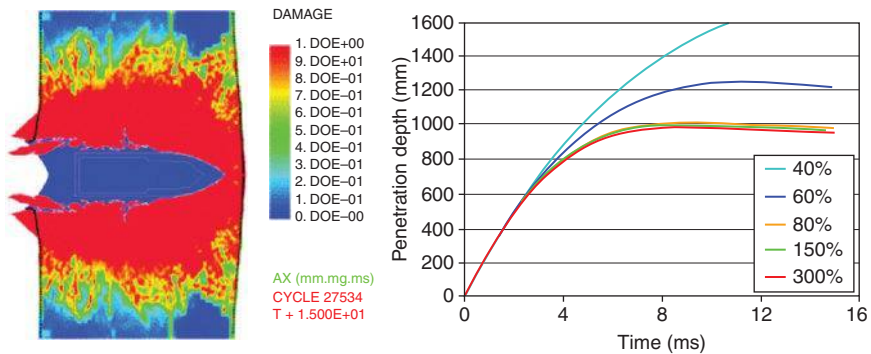


Plate XXXV (Chapter 10) Left: Deformation and damage extension of the projectile stopped close to the ballistic limit; Right: Erosion strains beyond 80% provide for this load case and resolution no additional influence on penetration depth (Riedel, 2004).

Understanding the dynamic response of concrete to loading: practical examples

N. GEBBEKEN, University of the Bundeswehr München,
Germany and T. KRAUTHAMMER,
University of Florida, USA

DOI: 10.1533/9780857097538.2.338

Abstract: This chapter focuses on the influence of the tensile behaviour of concrete on protective structures in practice. Based on the fundamentals given in previous chapters, the actions of impact, penetration and perforation are discussed, followed by the contact detonation. A specific section is devoted to blast design. If a building or a structural element has faced exceptional loads, its residual carrying capacity is of interest. The chapter ends with a description of a number of projects that have been set up.

Key words: protective structures, tensile behaviour, strain rates, blast, impact.

11.1 Introduction

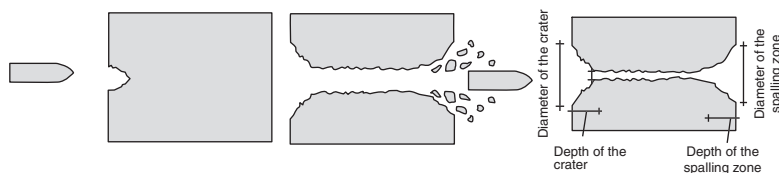
As noted in previous chapters, concrete is advantageous if its compressive strength can be effectively mobilized to balance the stresses in a cross-section. In the case of static loading of concrete, compressive stresses are mainly taken by the concrete, whereas tensile and shear stresses are taken by the reinforcement. For the sake of verification, truss-like models are used (e.g. Eurocode 2). In the case of high dynamic loading, three-dimensional stress states occur and, in addition, the concrete member is too inert to develop truss-like models in macro-mechanics. Thus the behaviour of concrete under high dynamic actions is much more complicated. Even the material properties change – they become strain-rate dependent. This is more beneficial for the tensile strength than for the compressive strength. Consequently, the analysis and simulation methods for high dynamic loading are different, and more complex, than those for static loading. In the following sections we consider impact, penetration, contact detonation and blast actions. (reference to Chapter 5, Introduction to dynamics). The tensile behaviour of the material under these high dynamic loadings is discussed in Chapter 7. In order to design and to verify real structural members or buildings, or to

assess existing structures, practice-oriented methods are desired. They can be found in Guidelines or Codes (e.g. Unified Facilities Criteria (UFC) 3-340-01, UFC 3-340-02, Comité Européen du Béton (CEB 187), or they might be developed as engineering codes (PenSim, XploSim, Dynamic Structural Analysis Suite (DSAS)) that are approved by the authorities. Further guidelines are published by US General Services Administration (GSA), Federal Emergency Management Agency (FEMA), and others. In the following sections, the application of dynamic knowledge in practice is discussed. The physics behind the design of civil structures, such as embassies, airports, or military facilities, is the same. The threats might be defined according to, for example, STANAG 2280 or GSA levels, or they might be defined individually. It is common practice that the especially educated safety engineer designs for these loads, and passes the relevant data (concrete class, member size, reinforcement ratio) to the structural engineer. In this process there is often an interface problem if the structural engineer does not know how to design the structural detailing according to the requirements in high dynamics.^{1,2}

11.2 Impact, penetration and perforation

Impact, penetration and perforation phenomena might occur due to airplane impact, ship collision, missiles, rockets, bullets and fragments amongst others.³ The failure of structures mainly depends on the size and stiffness of the impactor, its velocity, mass, material and the properties of the target, such as type of building, material and size of structural members. It can be seen that impact might affect the entire building or just a localized portion of it. This section focuses on small but fast projectiles in order to show the failure of concrete targets. In this case the structure is only affected at a small localized region (Fig. 11.1). Thus, the global behaviour of the structure can be neglected.

A rigid bullet is assumed as shown in Fig. 11.1. When this projectile impacts a structure it is slowed down, and it might penetrate the concrete member. Depending on the thickness of the structure, the projectile will stop inside or perforate the structural member. The perforation process is schematically shown in Fig. 11.1. The deceleration of the projectile while penetrating is nearly constant.⁴ In the entrance phase of the projectile, the



11.1 Perforation of a concrete plate, process and explanation.

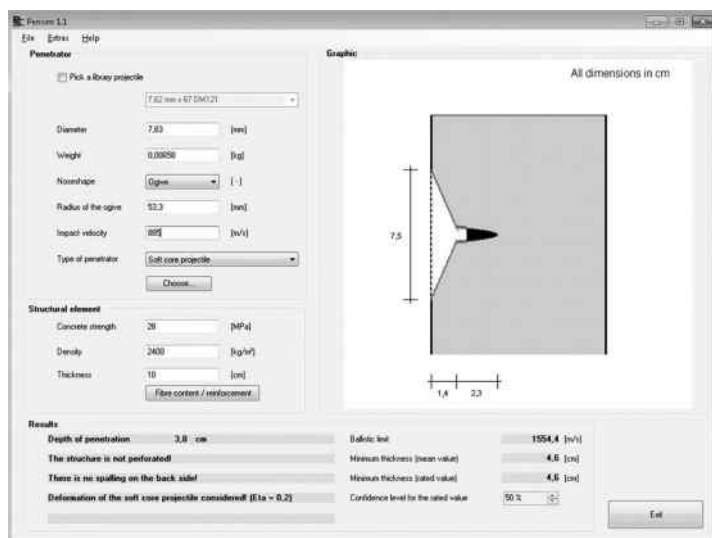
concrete is damaged due to (confined) compression and shear. In the material model, the hydrostatic (Compaction, EoS) and the deviatoric (fracture surface) portions are activated. The pressure in front of the projectile nose can become so high that phase transition occurs. At the rear side (exit side) the failure is initialized mainly by reaching the tensile strength. A secondary effect is the ejection of fragments, which can become impactors themselves.

The problem of projectile penetration has been studied intensively. There is still a lack of perforation tests. In the literature, several formulas for the depth of penetration are available.⁵⁻⁷ These formulas will not be presented here. For further information, please refer to the literature. In addition to the penetration depth of a concrete structure, the sizes of the crater and of the spalling zone are also of interest. While the failure of the penetration channel is mainly affected by the compressive strength and the failure of the micro-pores (compaction), the crater and the spalling region are mainly affected by the mean tensile stress, which is limited by the tensile strength of the concrete. It is necessary to mention that the usual reinforcement ratios do not affect the penetration or perforation behaviour, unless a projectile which is small compared to the reinforcement bar diameter impacts the bar. From a protection viewpoint, the worst situation is when the projectile only penetrates the concrete material. In Section 11.6 a material where the reinforcement is of significant importance is presented.

At the University of the Bundeswehr the software tool PenSim (Penetration Simulation) has been developed, whose objective is twofold: 1. the fast determination of the expected penetration depth, the size of the crater and of the spalling region, and the probable perforation; and 2. the fast dimensioning of a concrete member according to the requirements. The basic requirement is the application for protective structures (perpendicular impact, pure concrete, local failure). In addition, the tool might also be used for vulnerability assessment of concrete structures. PenSim needs several input parameters from both the projectile and the concrete member, as can be seen in Fig. 11.2. The results of PenSim are given as depth of penetration, size of crater and spalling region, possible perforation, residual velocity and ballistic limit (Fig. 11.2).

Whereas for the penetration and perforation analyses PenSim uses well-known formulas to determine the sizes of the crater and of the spalling region, numerical simulations have been carried out based on the material models of Hartmann, Pietzsch and Gebbeken.⁸

Plate XXXVI (see colour section between pages 208 and 209) shows results from these numerical investigations, based on the impact of a rigid projectile on a concrete surface at a velocity of 600 m/s. On the left side of Plate XXXVI the depth of the concrete slab is too small to stop the projectile inside the member. On the right side the penetration is stopped. Thus



11.2 Graphical user interface of PenSim.

the protection requirements are fulfilled. The numerical simulations have been conducted to validate the used formulas, to develop equations for the size of the crater (depth and radius) and the size of the spalling (depth and radius) as functions of several parameters. The numerically determined sizes of the crater and of the spalling region were compared with experiments in order to validate the numerical simulations. Finally, the validated equations were implemented in PenSim.

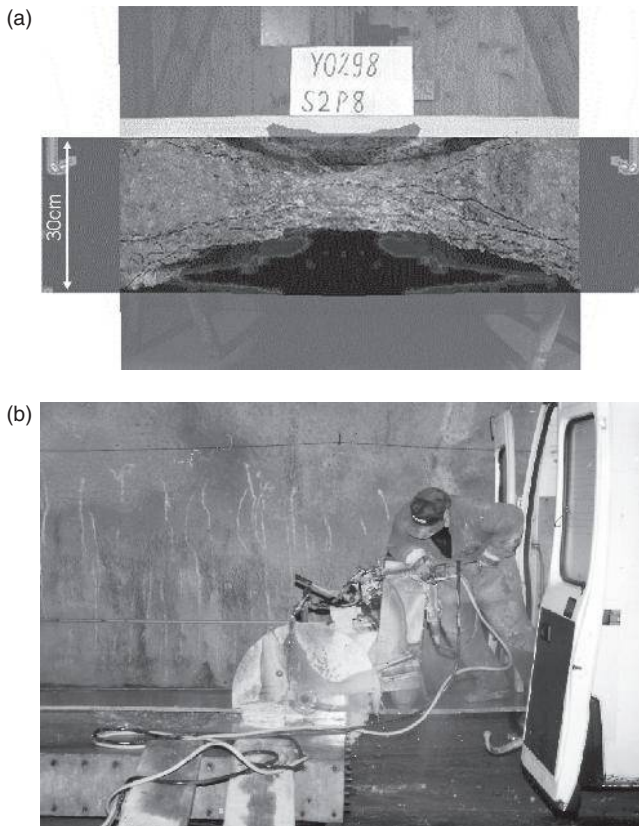
As mentioned before, the region of spalling is influenced by the main tensile stress exceeding the tensile strength. In general, the static tensile strength of concrete is approximately 10% of the compressive strength. Both strength limits depend on the strain rate. Whereas the compressive strength under high strain rates can be twice as much as the static compressive strength, the tensile strength under high strain rates can be six times the static tensile strength. In neglecting this phenomenon, the size of the spalling region is overestimated. From a protection perspective, this is on the safe side, but from an economical point of view it might not be the best solution. What can be done to reduce fragmentation, especially of the spalling side? Influencing the tensile strength by changing cement, aggregate and grading curve, and adding additives is very limited. But fibres might be added. Practical fibre content in terms of volume is limited to 2%. Doing so and applying a homogenization rule in macro-mechanics, the tensile strength of fibre-reinforced concrete is roughly 20% higher than that of the

pure reference concrete.² Due to the fact that published perforation tests are lacking, and that the authors had no resources to carry out such tests, PenSim is prepared to implement fibre-reinforced concrete, although this has not yet been done.

Depending on the requirements of protection, budget and architectural specifications, the safety engineer has a variety of options for design: member thickness, concrete specification, fibre reinforcement, high-strength ‘wallpaper’, etc. This general statement holds also for other scenarios.

11.3 Contact detonation

Contact detonations have something in common with projectile penetrations. Cratering, spalling and perforation are observed (Fig. 11.3). Contact detonations are defined as the detonation of an explosive that is in contact



11.3 Concrete slab (a) contact detonation failure and (b) cross-section of slab after detonation.⁹

with the structure or very nearby. Two types of explosions can be distinguished. On the one hand deflagrations, where the speed of the burning front is slower than the speed of sound. These are, for example, gas explosions. On the other hand detonations, where the burning front in the explosive material is faster than the speed of sound. Contact detonations are the focus hereafter.

The failure behaviour of concrete under far-field detonations (air-blast loading, distance to the charge more than five times the diameter of the charge) is different from contact detonation, and is shown in the following section. The behaviour of concrete in the near-field combines the effects of contact detonation and blast loading.

Figure 11.3⁸ shows some results of a contact detonation experiment with a concrete slab. In Fig. 11.3b, the slab is cut after the experiment. In Fig. 11.3a, the damage can be seen, experimentally and numerically. A series of about 100 experiments was carried out at the Federal Testing Center WTD52, varying the charge mass and concrete-slab depth. In the experiments, the explosive was placed on top of the concrete slab. The lengths of the slab were such that the reflections of the waves at the side surfaces of the plate did not influence the transmission and reflection of the first wave through the thickness. After ignition of the explosive, the detonation front in the explosive reached the concrete surface, inducing a pressure wave into the concrete. When this pressure wave reached the free rear surface of the slab it was reflected, becoming a tensile wave due to the impedance differences. The pressure wave introduced a more or less hydrostatic compression, with pressures that might be up to 300 times the one-dimensional compressive strength of the concrete. When the pressure reached the Hugoniot elastic limit the concrete started to crush, resulting in a crater beneath the explosive. Once the mean tensile stress in the reflected tensile wave exceeded the dynamic tensile strength the concrete failed. As already shown in Section 11.2 the static tensile strength of concrete is approximately only 10% of the static compressive strength. Considering strain-rate effects, the dynamic tensile strength can be up to 50% of the static compressive strength. Therefore, the damage region due to tensile failure is larger than the crater region. This tensile failure is called spalling.

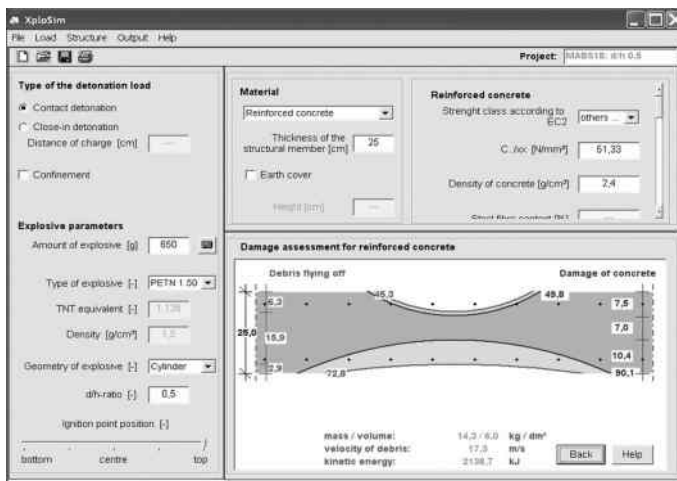
Depending on the size of the charge and the depth of the plate, the depth of the crater and the depth of the spalling region can reach the depth of the plate. If this happens, the plate is perforated.

Physical tests are usually expensive and time consuming. Therefore, numerical simulations are used to complement the tests. Hydrocodes are applied in this research. Especially developed material formulations are required in order to identify the failure behaviour of concrete under contact detonation. The formulations can be achieved based on micromechanics, macro-mechanics or even by modelling discrete cracks with different

geometrical formulations^{1,8-10} (K + C model LS-DYNA). The models use different concepts and material laws to describe the damage to the concrete. The numerical results depend on the numerical model, on the material law chosen, but also on the grid size. The user must know what the damage parameter physically describes; otherwise damage might be misinterpreted (for more detailed information on numerical models see Chapters 9 and 10). On the other hand, it is not uniquely defined what damage is in the physical experiment. As can be seen in Fig. 11.3 some crater material and some spalling material have gone. There are cracks visible, and also fragments that are held by the steel reinforcement or that are still interconnected to the concrete but without bond. Given that concrete normally cracks, it is important to define whether a crack is associated with damage or not. In the present case of contact detonations, the studies reveal that a numerical damage of $D > 0.4$ gives best results. Consequently $D < 0.4$ has been assumed to cause no damage. Figure 11.3a shows a photograph of the cut cross-section of the damaged slab overlaid with an image of the numerical simulation.

Hydrocode simulations take quite some time, which is not acceptable in practice. Therefore, there was a demand for a quick determination of damage due to contact detonations, but also that the dimensioning of concrete structures should be possible.

Therefore, at the University of the Bundeswehr in Munich, the engineering tool XploSim (Explosion Simulation) has been developed (Fig. 11.4). The methodical approach was to use known empirical equations, own test results and an uncounted number of numerical simulations. Based on these



11.4 Graphical user interface of XploSim.

studies, new empirical equations with physically based parameters have been developed.

XploSim requires the following input parameters:

- Distance of charge to the surface/contact detonation
- Amount of explosive/type of explosive
- Geometry of the charge, ignition point location
- Material (concrete, reinforced concrete, steel fibre concrete, steel fibre-reinforced concrete)
- Strength, density of concrete
- Thickness of the plate
- Reinforcement (diameter, distance)
- Sand cover.

The inputting of these parameters is via a guided process using the XploSim graphical user interface (Fig. 11.4). The results are given as an illustration containing the figures for the size of the crater and the size of the spalling zone. In addition, the mass of the fragments and their exit speed are given.

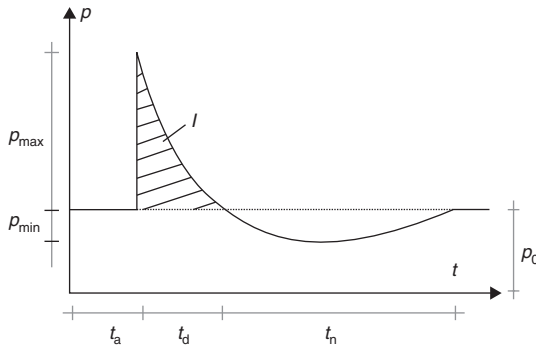
The development of the XploSim equations has been done in the following way.¹¹ First, the material model for concrete RGGP (Ruppert-Gebbeken-Greulich-Pietzsch) was developed. Parallel to the tests, several numerical parameter studies were done. For each run the results were analysed with respect to the output parameters: crater radius and crater depth (Plate XXXVII (see colour section between pages 208 and 209)), spalling radius and spalling depth (Plate XXXVIII) and the size of the perforation (Plate XXXIX). Correlations and dependencies were detected in order to derive the equations that could be implemented into the XploSim computer code.

In addition to the determination of the damage, it is also possible to calculate the required protection parameters for a given load size, and vice versa.

The engineering tools PenSim and XploSim are based on theoretically developed equations, empirically developed formulas, numerous numerical studies and numerous validation tests. Consequently they are very precise in the defined area of application. Depending on the scattering range of material and structural data, the results of the engineering tools must be seen in the natural scattering range.

11.4 Blast

In the following section we will concentrate on far field explosion that generates a blast front.



11.5 Blast wave, pressure–time relation.

11.4.1 Introduction

If the explosive is not close to the structure, an air-blast wave hits the structure entirely. Air-blast waves are pressure waves resulting from detonation or deflagration. The magnitude of the pressure of an air-blast wave that arrives at a certain point depends on the distance to the structure and on the size of the charge. An idealized form of a pressure–time function at a certain distance from the explosive is shown in Fig. 11.5.

The main characteristics of a free-field air-blast wave are as follows:

- The shock wave of the air blast arrives at the point under consideration at **arrival time** t_a .
- The pressure attains its maximum (**peak overpressure** p_{\max}) very quickly (extremely short rise time of nanoseconds). The pressure then starts to decrease until it reaches the **reference pressure** p_0 (in most cases the atmospheric pressure).
- The **duration of the positive phase** t_d is the time taken to reach the reference pressure. After this point the pressure drops below the reference pressure to the **minimal pressure** p_{\min} . The **duration of the negative phase** is denoted as t_n .
- The overpressure impulse (positive impulse) is the integral of the overpressure curve over the positive phase t_d .

The idealized (free air blast) form of the pressure wave in Fig. 11.5 can be significantly altered by the morphology of the medium encountered during its propagation. For instance, the incident peak pressure can be magnified from 2 up to 14 times if the wave is reflected at a rigid obstacle. If the angle of incidence of the blast wave is not known, the minimum magnification factor (coefficient of reflection) is 3. The reflection effects depend on the

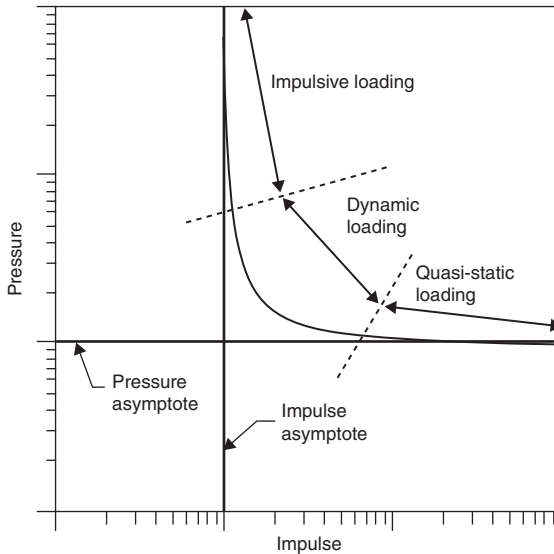
geometry, material, size and angle of incidence. The situation is much more complicated if there are several reflection boundaries, as happens in urban environments or in indoor explosions.¹²

Concrete structures react differently when subjected to blast loads or contact detonations. The pressures in the concrete due to blast are much lower than those due to contact detonations and, in addition, the blast acts on the entire structure. For a structural member, two failure mechanisms can be distinguished: while a strong and short blast wave (big – distributed – charge nearby) results in dynamic shear failure near the support, a weaker but longer blast wave (charge far away) results in a more bending failure. In both cases, the tensile stress and the shear stress are the reason for the failure in the material, and not the hydrostatic pressure. The dynamic shear phenomenon is totally different from the static shear. While in the static case the reinforcement cage mainly carries the shear load, in the dynamic case a cross-section sharply shears off (UFC 3–340).¹³

In the case of blast loadings, entire structures are affected. Depending on the blast characteristics different numerical methods can be chosen. In every case it has to be verified whether classical structural dynamic methods can be applied. For structural members, it is reasonable to use single degree of freedom (SDOF) methods and/or P–I diagrams.

11.4.2 Design of concrete slabs against blast

It is assumed that the blast wave hits the entire slab as a planar wave. The blast wave is represented by the reflected overpressure–time relation, here denoted as blast load. In an ideal situation, the blast load can be calculated by the well-known Kinney formula.¹² It is more realistic to calculate the blast load by using hydrocodes, in order to take the actual situation into account (multiple reflections, no planar wave, etc.). Once the slab is stiff enough, a load-structure interaction need not to be considered. Two different failure modes might occur: flexural failure and dynamic shear failure. If the evenly distributed blast load is very intensive and short in duration, the plate might be too inert to develop flexural yield lines, but simply shears off sharply at the supports. It is also possible that a combined failure mode occurs. There are different methods available to study the behaviour and to carry out the verification. The use of a hydrocode is not recommended for practical use. The CPU time might take several days or weeks, even if parallel computing is used. Therefore, SDOF models can be used to develop characteristic failure curves for uniquely defined structural elements, as discussed by Krauthammer.¹⁴ These curves are plotted in a pressure–impulse diagram. This procedure is favourable for standard elements that are used very frequently. Doing so, the verification can be done for all possible pressure–impulse relations, or in other words, for all possible blast load situations (Fig. 11.6).



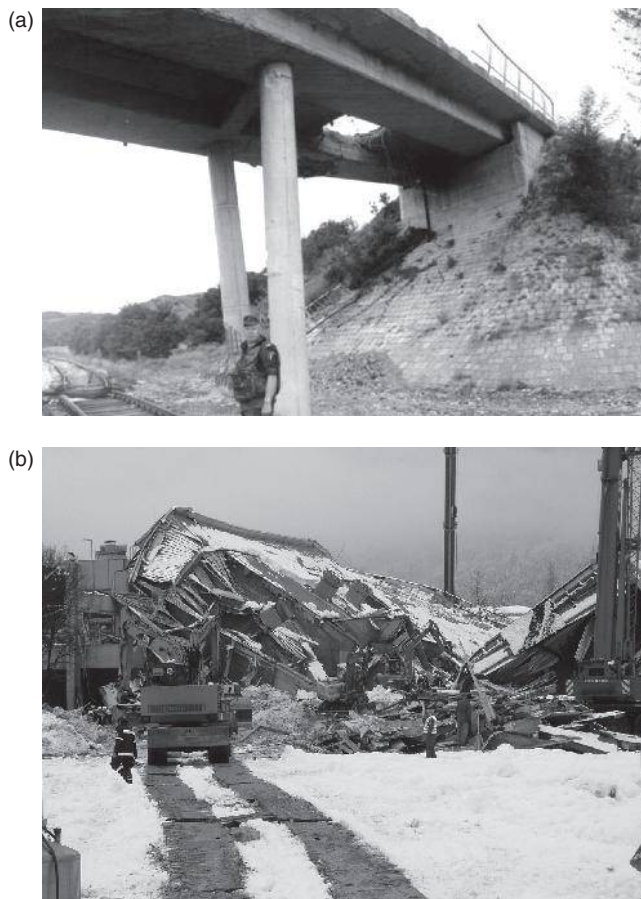
11.6 A typical pressure–impulse diagram, characteristic failure curve.^{14,15,16}

For the design and assessment of entire concrete structures subjected to blast loads, the authors prefer applying the blast load to structural element models of individual components with practical SDOF approaches, as will be shown later herein, before using more advanced finite element codes for more comprehensive analyses (Plate XXXX (see colour section between pages 208 and 209)). SDOF approaches can also be applied theoretically to entire buildings. Doing so, the development of the resistance functions becomes so complicated that it cannot be recommended. For entire buildings the blast load is applied to the structure and modelled numerically using an explicit finite element code that has the capability for verification according to standards.

11.5 Residual load-bearing capacity of damaged structural elements

Extreme loadings, as described in the previous sections, might lead to damaged structural elements or even to the collapse of buildings. Consequently, it is necessary to determine or to assess the residual carrying capacity of these damaged structural elements or structures. The assessment is required by authorities or owners for the sake of rescue, remaining use and reconstruction measures.

Figure 11.7 gives two examples: (a) a damaged concrete bridge due to weapon effects and (b) a collapsed building due to deterioration and heavy snow load.

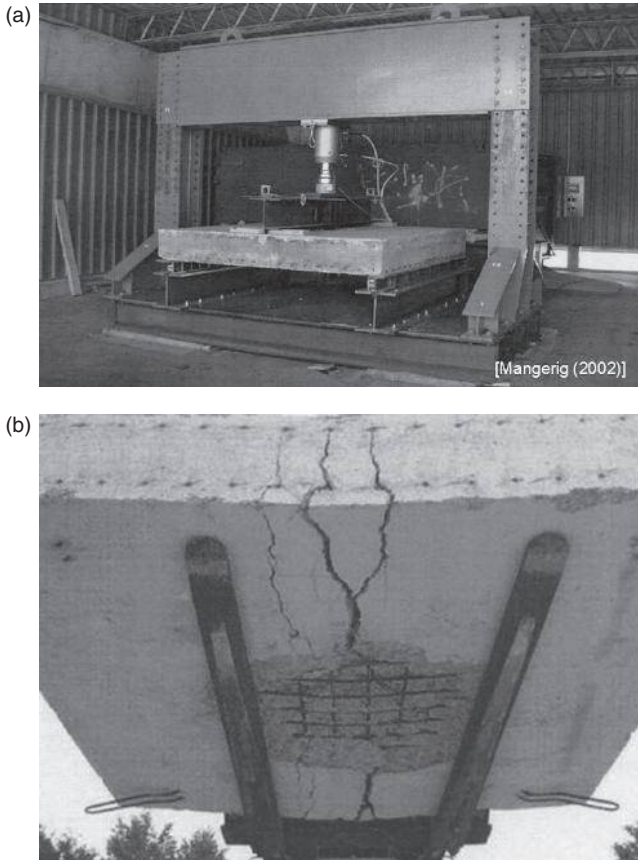


11.7 Damaged structures, residual capacity. (a) What type of vehicles can cross? (b) Rescue assistance, can rescue forces enter?

In both cases, a very special knowledge of the residual load-bearing capacity of materials and structures is required. Additionally, it is recommended that an experienced engineer always takes the lead.

The following example of a damaged reinforced-concrete plate shows the importance of a well-founded knowledge in engineering to assess the residual load-bearing capacity.

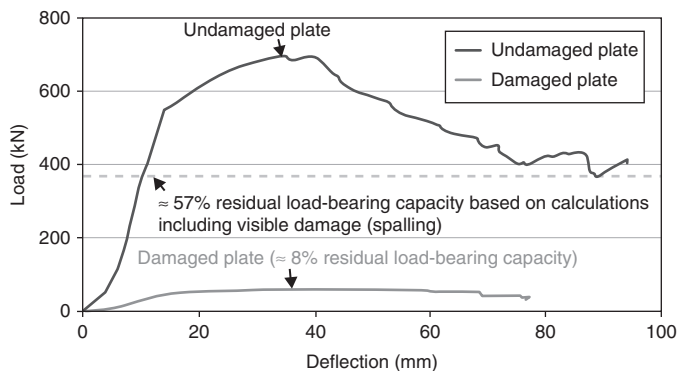
In cooperation with the Federal Testing Center WTD 52 reinforced-concrete plates were subjected to near-field and contact detonations. The plates had sizes of $2\text{ m} \times 2\text{ m} \times$ different depths (Fig. 11.8). The depth of the plate shown in Fig. 11.8 is 0.3 m. The damaged plates were experimentally tested to determine their residual load-bearing capacity.



11.8 Testing of a damaged reinforced-concrete plate. (a) Reinforced-concrete plate in test rig and (b) reinforced-concrete plate after a load carrying capacity test.

Figure 11.8a shows a damaged reinforced-concrete plate in the test rig. The plate was simply supported (free rotation) along the two opposite edges (double T-beams). Between these supported edges, the plate was centrally loaded by a line load (upper double T-beam). In Fig. 11.8b, the plate is shown after the load-bearing test. The spalling at the bottom side results from the detonation impact. The large line cracks are flexural cracks due to the bending failure of the plate.

A visual analysis of the plate after detonation led to the following results with respect to the residual carrying capacity. The spalling area was the largest visible damage. The diameter of the crater on the upper side was 0.85 m, and smaller than the diameter of the spalling area. No damage (cracks) was visible outside the crater and spalling area. The reinforcement in the spalling area could be assumed to be intact. Therefore, it was calculated that



11.9 Concrete slab, experimental load–deflection curves and comparison with an estimated residual load-bearing capacity.

2–0.85 m = 1.15 m of the plate in the compression zone could fully develop the maximum resisting bending moment. So the residual carrying capacity was calculated by the yield line theory to 57% of the carrying capacity of the undamaged plate.

Figure 11.9 shows experimentally determined load–deflection curves. The black solid curve represents the behaviour of the undamaged plate (reference plate). The ultimate load was approximately 700 kN. The expected ultimate load of the damaged plate was approximately 400 kN (57%). Surprisingly, the measured ultimate load of the damaged plate was only 58 kN (8%). In further tests the results were similar. What are the causes of this low residual carrying capacity? There are cracks in the plate induced by the detonation that are not visible from the outside. These cracks led to a reduced concrete strength, and in addition, the bond between the concrete and the reinforcement might be disturbed. Engineers have to keep these effects in mind when assessing the carrying capacity of damaged structural elements which can easily be overestimated. This is a matter of safety and risk.

In a further step the problem was analysed by using different numerical tools. These analyses were based on three major steps:

1. Calculation of the contact detonation by using a hydrocode
2. Remapping of the calculated material damage to a FEM model
3. Calculation of the residual load-bearing capacity

In the first step, the contact detonation and the plate's response behaviour are simulated by using a hydrocode. As one result, amongst others, the material damage to the concrete was determined. In the second step, the damage is mapped from the hydrocode model to a FEM model. This is necessary because hydrocodes are developed for the calculation of wave

propagation phenomena and not for the sake of structural verification. FEM codes, especially those that are able to verify on the basis of standards, are applicable for the calculation of the static residual load-bearing capacity. When the damage values are mapped from the hydrocode model to the FEM model, the influence of the damage on the material parameters, such as strength and stiffness, has to be considered. In the third step, the residual load-bearing capacity can be calculated by the FEM model considering the calculated material damage.

From a practical point of view, this procedure is very time consuming because the hydrocode model has to be generated by very small elements in order to represent the wave propagation precisely. This leads to a huge number of elements, and consequently, based on the CFL (Courant-Friedrichs-Lewy)-criterion, it results in small time steps. Working with hydrocodes requires very special knowledge and experience of the engineer, due to the complexities of the numerical schemes and the non-linear behaviour of the materials. The numerically determined residual load-bearing capacities are also much higher than those experimentally determined. So it can be concluded that the question of what damage is (in the real world and in numerical modelling) cannot be answered yet.

The analytical and numerical calculation of the residual load-bearing capacity of damaged structural elements is an on-going research project of the authors. In a first step, the aim of this research is to investigate the influence of the damage on the bond between concrete and reinforcement and to develop models for the bond behaviour after first damage occurs (Fig. 11.10).

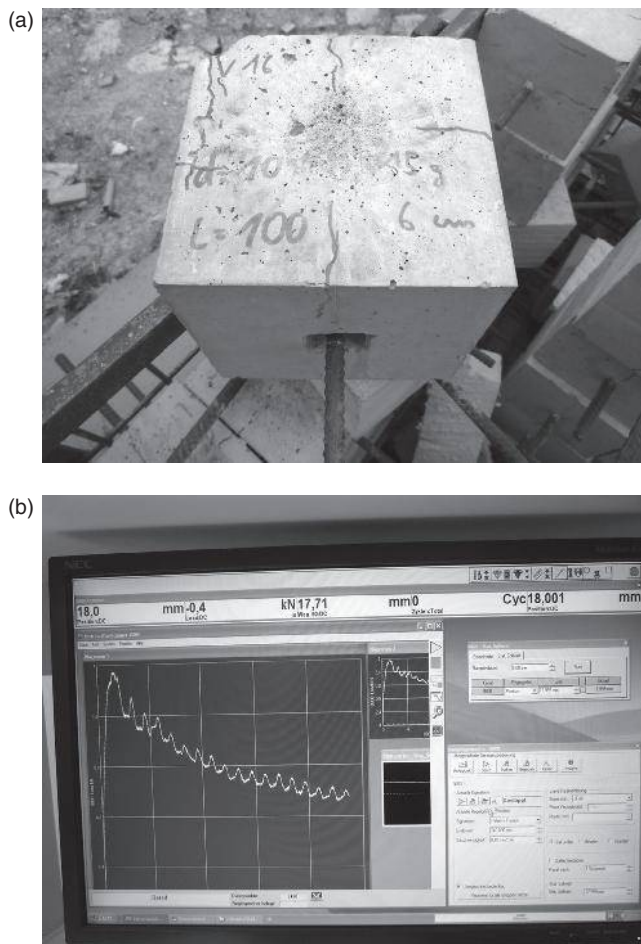
The contact or close-in detonations have been conducted at the WTD52 (Fig. 11.10a). The pull-out tests are carried out at the University of the Bundeswehr in Munich, Institute of Structural Engineering.

11.6 Behaviour of reinforced-concrete beams under localized static and impact loads

This section is aimed at illustrating the contributions of concrete in tension to the behaviour of RC beams subjected to both static and impact loads. To achieve this objective, the behaviour of Beam 1-h that was previously studied by Feldman and Siess^{16,17} as shown in Fig.11.11 is investigated.

1' = 12", and 1'' = 25.4 mm

The material properties on the test data were: concrete uniaxial compressive strength $f'_c = 6150$ psi (42.4 MPa), steel tensile yield stress $f_y = 47.17$ ksi (325.2 MPa), steel compressive yield stress 47.61 ksi (328.26 MPa) and the shear reinforcement yield stress 46.9 ksi (323.4 MPa). Both the static and dynamic tests of this beam were simulated with the computer code DSAS version 3.2.¹⁸ The static tests of all the beams in that series were conducted by applying a concentrated force to the central stub at a

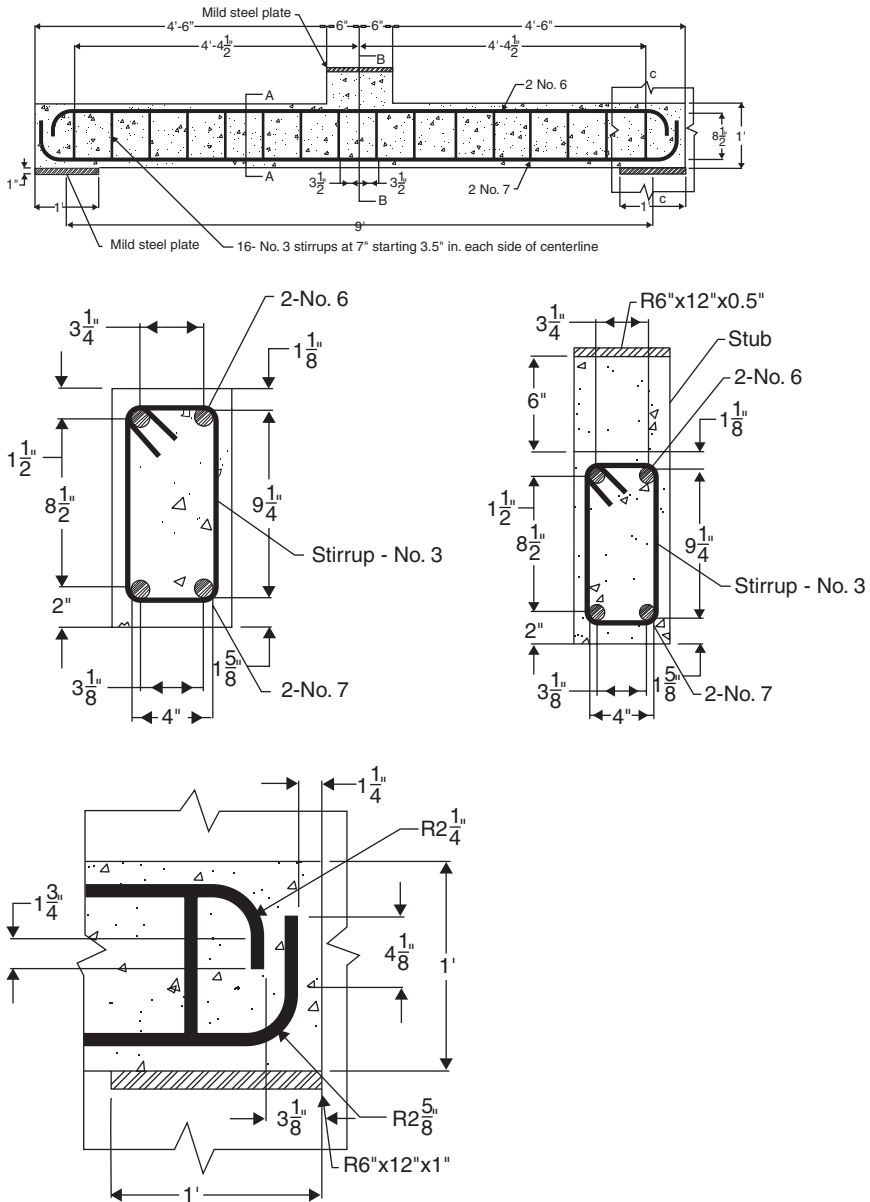


11.10 (a) Concrete cube after close-in detonation and (b) pull-out test after detonation, resulting in bond-slip-behaviour.

rate of between 7 and 9 kip/min (31.1 and 40 kN/min). The impact load on Beam 1-h is shown in Fig. 11.12 and the post-test conditions of the beams are shown in Fig. 11.13.

The comparison between the central displacements for the static test is shown in Fig. 11.14 and for the impact test in Fig. 11.15. It is noted that the simulation seems to capture quite accurately the recorded test data.

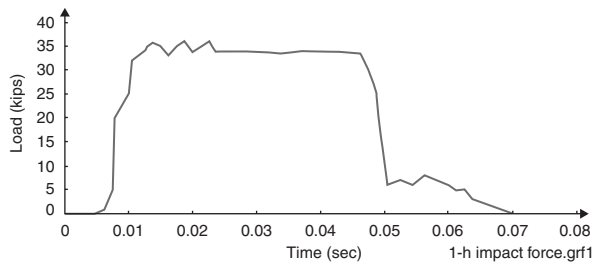
Following the validation process, as described above, a parametric study was conducted in which the same impact case was considered. However, in the parametric study the dynamic concrete compressive strength was kept constant at two levels (DIF (dynamic increase factor) of 1.375 or 2.0), while the dynamic concrete tensile strength was varied. The results for the central



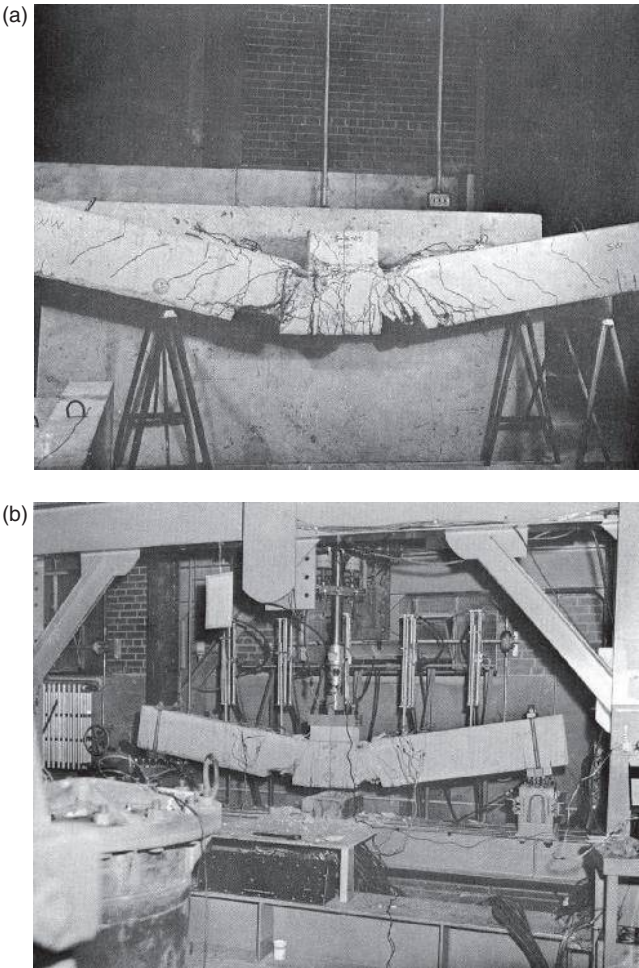
11.11 Details of Beam 1-h.

deflection versus time are shown in Figs 11.16 and 11.17. A corresponding P-I curve for the same beam is shown in Fig. 11.18.

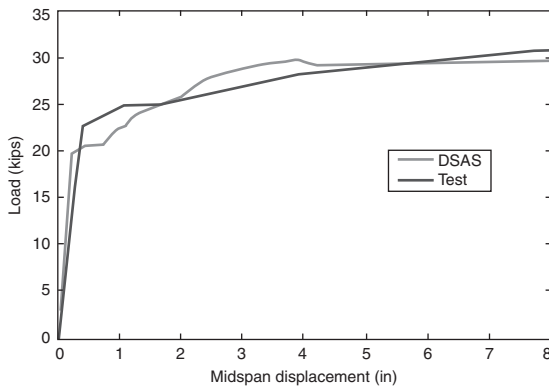
These results demonstrate the effects of concrete tensile strength on the structural behaviour of impact-loaded reinforced-concrete beams. As was



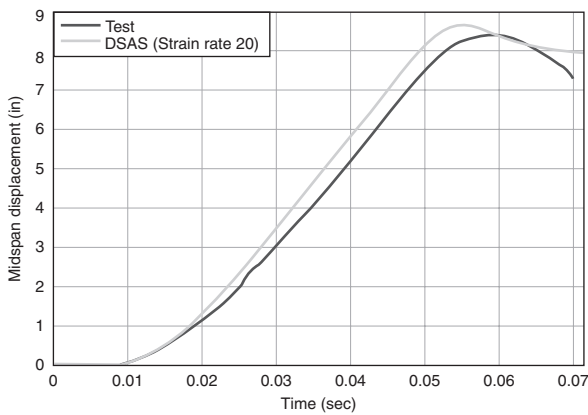
11.12 Dynamic load for Beam 1-h.



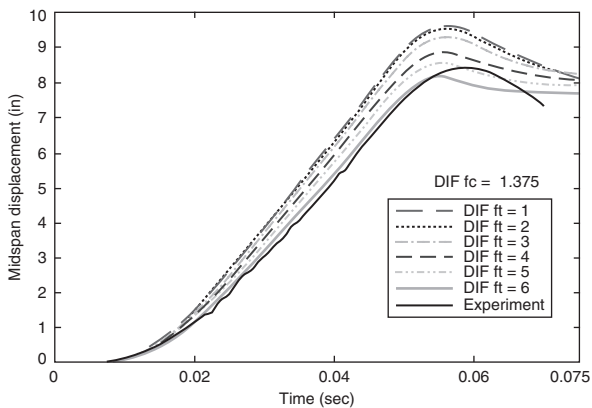
11.13 Beam 1-h after tests: (a) static and (b) impact.¹⁷



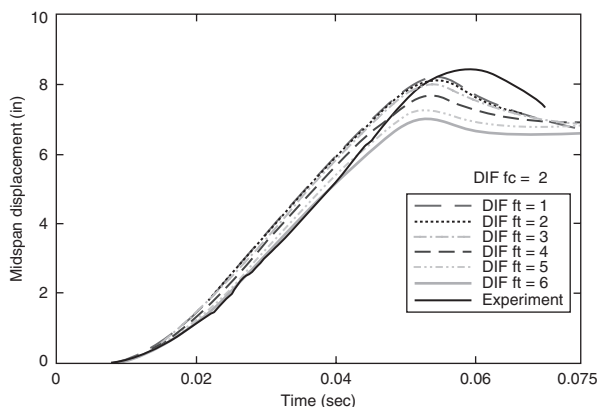
11.14 Test and DSAS simulation for static loading case of Beam 1-h.



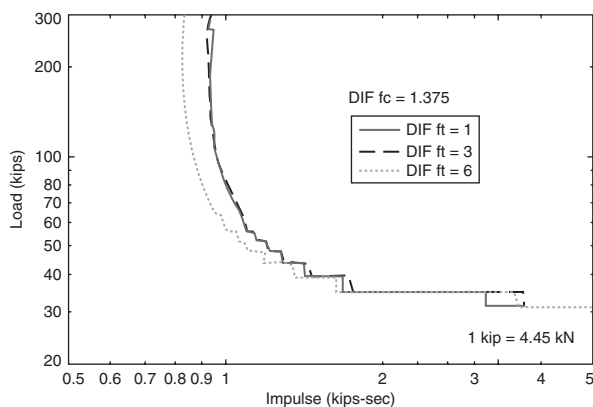
11.15 Test and DSAS simulation for static loading case of Beam 1-h (strain rate 20).



11.16 Central deflection vs time of Beam 1- h for compressive DIF of 1.375 and various tensile DIFs.



11.17 Central deflection vs time of Beam 1-h for compressive DIF of 2.0 and various tensile DIFs.



11.18 P-I curves for Beam 1-h.

noted in Fig. 11.15, the strain rate of about 20 enabled a good comparison between test data and simulation. If one keeps that compressive strength and varies only the tensile strength of the concrete (Fig. 11.16), the peak central deflection increases significantly with lower values of concrete tensile strength. The same general trend is noted if one assumes a higher concrete compressive strength and varies the tensile strength (Fig. 11.17). Finally, one notices an interesting effect of the P-I diagrams for a compressive strength with DIF of 1.375 (Fig. 11.18) in which the quasi-static asymptote is virtually unaffected, while the impulsive asymptote is noticeably affected for higher concrete tensile capacities. Clearly, one must pay careful attention to the tensile strength of concrete when treating structural systems subjected to severe short-duration dynamic loads. It is well known that in the static

domain the concrete below the neutral axis might be ignored because the concrete tensile strength is about 10% of its compressive strength. However, as the strain rate increases, while the concrete compressive strength might approach twice its static strength, the tensile strength might approach about six to eight times static strength. That means that a typical 30 MPa compressive strength concrete (with a 3 MPa tensile strength) might behave as a 60 MPa compressive strength concrete (with an 18–24 MPa tensile strength). It is noted that, at higher strain rates, the tensile strength could be as much as 30–40% of the compressive strength, and that this relative change in material behaviour can significantly affect structural behaviour. After having discussed typical phenomena, real projects that have been executed will be provided.

11.7 Project examples: improving blast resistance

Research and development in engineering is directed towards practical application. Usually actual projects are much more complicated than text book examples. In the following we provide executed projects.

11.7.1 Introduction

The reader can understand that the projects chosen cannot be described in such a way that they are identifiable. Also, giving physical data, geometrical sizes, charge weights or concrete quality is avoided. The examples show the practical importance of the concrete material for protective structures.

11.7.2 Mitigation of explosive effects using sandwich walls

The following project had two objectives: firstly, to assess an existing building and, secondly, if necessary, design it to be blast resistant. For an existing building the threat level had risen and this had led to the assessment that the structure was not strong enough. Therefore, a new design had to be developed without changing the original architectural layout. Sandwich walls can be very efficient in mitigating explosion effects. In the present situation, a close-in explosion and resulting blast had to be considered. Plate XXXXIa (see colour section between pages 208 and 209) shows the basic load-transfer concept. It shows a three-layer wall, comprising a first concrete layer, an interlayer and a second concrete wall. The concrete is a typical ordinary concrete type according to Eurocode 2. The interlayer can be of air, foam, dry sand or anything that results in high impedance. As can be seen in Plate XXXXI the blast wave hits the first concrete wall coming from the

left. This results in a compressive shock wave travelling through the material. At the interface between the first concrete wall and the interlayer, a part of the shock wave is transmitted into the interlayer, depending on the impedance, and a part is reflected as a tensile wave. The ratio of the transmitted and the reflected shock wave depends on the impedance ratio. Impedance is defined as the product of density and wave velocity. Concrete has a density of roughly 2500 kg/m^3 and a longitudinal wave velocity of approximately 3700 m/s , which yields an impedance of 9.25 MPa s/m . This is much larger than the impedance of air (density 1.225 kg/m^3 , wave velocity 340 m/s , impedance 416.5 Pa s/m), and the impedance ratio is approximately 1:22 209 (air : concrete). From this it is seen that air is an ideal interlayer, theoretically. However, due to practical reasons on the construction site (construction technique and process), low density foams or other materials with small impedances were used instead of an air interlayer. Furthermore, a foam interlayer also serves as an impact cover for the second concrete wall if the first one is damaged, as described in the following paragraphs.

A damage plot of a protective sandwich wall is illustrated in Plate XXXXIb. The effect of the impedance at the interface between the first concrete wall and the foam interlayer can be identified. A small part of the blast energy is transmitted through the foam interlayer into the second concrete wall. However, the strain state in the second concrete wall is much smaller than in the first. We observe significant damage indicated by the red colour in Plate XXXXIb, i.e. energy dissipation in the first concrete wall. The reflected tensile wave at the rear face of the first concrete wall results in tensile stresses in the concrete material, which can be much larger than the dynamic ultimate tensile strength of concrete. This leads to scabbing failure on the rear face of the first concrete wall. But the foam interlayer was chosen such that it prevents the concrete fragments from impacting the second concrete wall. Consequently the requirement that the rear wall should stay intact could be fulfilled.

This example shows again that the tensile behaviour of concrete is a significant design parameter.

In the next example, the task was to harden an existing building. The existing concrete walls had to be protected against a contact detonation. The fire control authorities had formulated very strict requirements, due to the available space for the hardening measures. In addition, the protection requirement for the existing wall was the acceptance of certain damage. Therefore, a high-strength, high-ductility concrete was developed and analysed (Plate XXXXII (see colour section between pages 208 and 209)).

The high-strength high-ductility concrete will be described in the following section. The result is shown on the right of Plate XXXXII. The protective concrete wall serves as a victim wall. The interlayer mainly provides distance and the existing wall is damaged acceptably.

11.7.3 Blast walls

We are often asked to design blast walls. They give the subjective feeling of being better protected. In fact give protection from contact detonation, flying fragments, flat trajectory fire, blast in a close range behind the wall, and they act as 'blinds'. If they have to be designed in an urban environmental situation where, in addition, requirements from monument conservation authorities exist, it becomes a real challenge. Even the design of the concrete foundation can become a complicated task if trees have to be preserved, or if supply and waste lines cross the foundation.

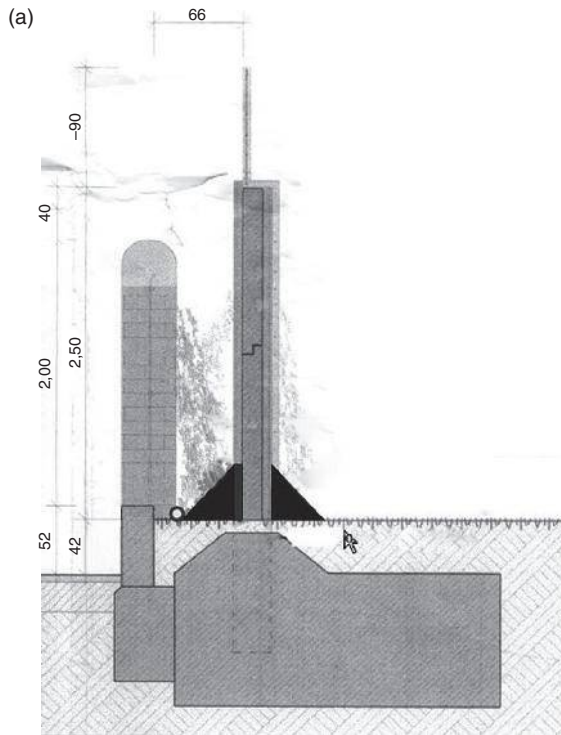
Figure 11.19a shows a cross-sectional view of the situation. Figure 11.19b is a photograph of the wall that has been built. The solution was chosen after several options were studied. The foundations are made of ordinary reinforced concrete carrying the clamped steel posts. The high-strength, high-ductility concrete panels protect from blast, contact detonation and impact. Because of their ductility, they can develop a good flexural behaviour and consequently activate membrane actions.

The high-strength, high-ductility concrete is a product of DUCON, a German company. Its specific features are: three-dimensional fine reinforcement grid, and self-compacting high-strength concrete (Fig. 11.20).

The compression strength goes up to 200 MPa and the tensile strength reaches 75 MPa, which is roughly 40% of the compression strength. Therefore, such materials can be favourably used where high tensile resistance is required.

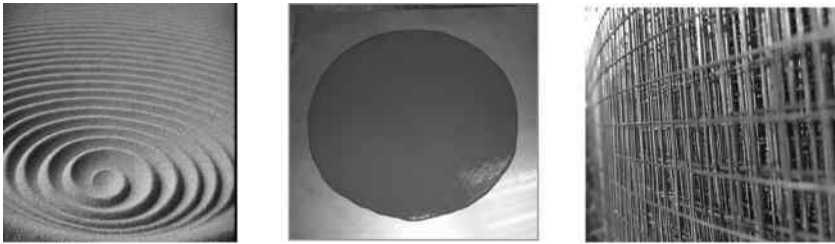
11.7.4 Combined effects

Figure 11.21a gives an overview of a huge state building, which is in fact a multi-purpose building for governmental and private use. The security authorities had defined the threats. It was the task of the authors to provide advice based on numerical studies. Initial general studies provided the overall blast situation, including exterior and interior explosions. Based on these studies, doors, windows, openings and façades were investigated individually. In addition, numerous detonations on the load-bearing structure were investigated numerically. For this aim, relevant portions were cut out of the structure in order to model representative sub-structures. An underground car park subjected to a car bomb (grey circle) is shown in Fig. 11.21b. The upper concrete plate and the concrete walls are not shown in the image. In further steps each significantly affected structural element was analysed individually (see Plate XXXXIII in colour section between pages 208 and 209). In every single project it needs to be discussed whether ordinary concrete should be used or especially designed concrete. From the authors' experiences, it can be said that when using high-strength, high-ductility concrete the structural engineer can save roughly half of the geometrical size of ordinary concrete.

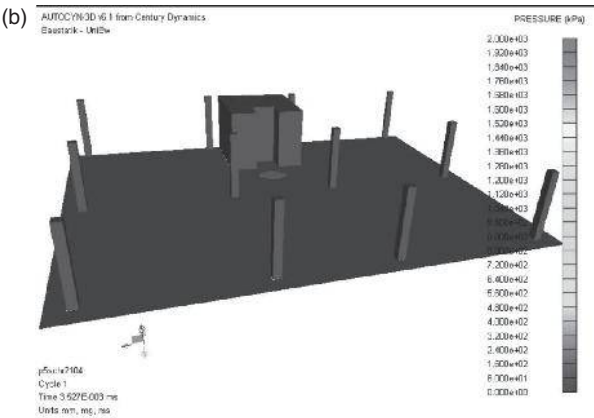
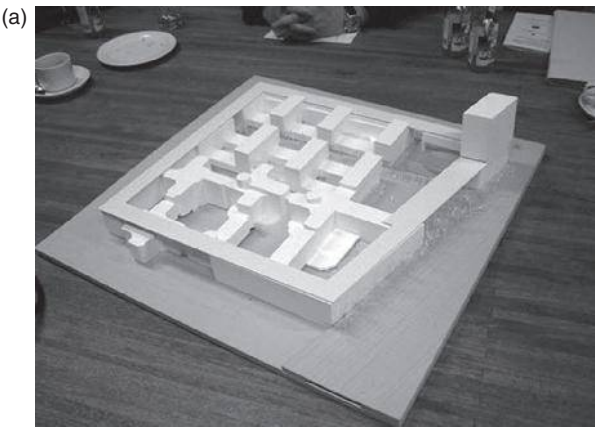


11.19 Blast wall (a) cross-section and (b) blast wall ready (photograph by DUCON).

At the end of the study, the results were discussed with the structural engineer who is normally different from the safety engineer. The consequences for the load-bearing structure were assessed in order to avoid partial or entire collapse. These results were communicated to the architect and to the owner, for final decision.



11.20 DUCON (courtesy of DUCON), sand + self-compacting concrete + MircoMat.



11.21 State building, multiple purpose use, multiple threats.
(a) architectural model and (b) sub-structure modelled numerically.

11.8 Conclusions

Concrete is a very typical construction material when dealing with extraordinary short-duration dynamic loads (e.g., impact, explosion). Ordinary concrete is cheap and has a relatively high compressive strength range. In those regions of the reinforced-concrete structural members where tension and shear predominate, steel bars and/or fibre reinforcement are required to compensate for the concrete lower tensile strength. Impact and contact detonations require relatively large cross-sectional sizes of single layer. Therefore, multiple layer cross-sections are recommended. The disproportionate increase in the tensile and compressive strengths under higher loading rates shows the importance of the concrete tensile strength under such loading conditions. Previously, special concretes have been developed that have better compressive-to-tensile strength ratios. If designed properly, they are very ductile and flexible. From the perspective of the authors there is a high future potential for various types of ultra-high performance concretes (e.g., ultra high performance concrete (UHPC), ultra high strength concrete (UHSC), ultra ultra high strength concrete (UUHSC) and ultra high strength fibre reinforced concrete (UHSFC)). However, the treatment of such innovative materials is beyond the scope of this chapter.

11.9 Acknowledgements

The following research associates and assistants have contributed to this chapter: Dr Serdar Astarlioglu, Dr Torsten Döge, Dr Martin Larcher, Dr Tobias Linse, Achim Pietzsch, Dr Martien Teich and Daniel Koch. Their contribution is gratefully acknowledged. Some of the work presented is based on research granted by the Federal Testing Center WTD52. For its support we are deeply grateful.

11.10 References

1. Riedel, W., Kawai, N. and Kondo, K. 2009. Numerical assessment for impact strength measurements in concrete materials, *International Journal of Impact Engineering*, **36**, 283–293.
2. Gebbeken, N. and Hartmann T. 2008. Modellbildung zur simulation von stahlfaserbeton unter hochdynamischer belastung. Beton- und Stahlbetonbau, **103**, Verlag Ernst & Sohn, ISSN 0005–9900, 398–412.
3. Gebbeken, N., Teich, M. and Linse, T. 2007. *Numerical modeling of high speed impact and penetration into concrete structures*, 7th International Conference on Shock and Impact Loads On Structures (SI07), Beijing (China).
4. Forrestal M. J., Altman B. S., Cargile J. D. and Hanchak S. J. 1994. An empirical equation for penetration depth of ogive-nose projectiles into concrete targets, *International Journal of Impact Engineering*, **15**(4), 395–405.

5. Kennedy, R. P. 1976. A review of procedures for the analysis and design of concrete structures to resist missile impact effects. *Nuclear Engineering and Design*, **37**, 183–203.
6. Li, Q.M., Reid, S.R., Wen, H.M. and Telford, A.R. 2005. Local impact effects of hard missiles on concrete targets. *International Journal of Impact Engineering*, **32**, 224–284.
7. Gebbeken, N. and Linse, T. 2007. *Entwicklung eines engineering tools zur ermittlung der waffenwirkung von penetratoren auf betonartige bauteile*, Forschungsvorhaben: Forschungsauftrag Nr. C/E520/6F005/2F029. Bericht, 5.12.2007, ISSN 1435–3555.
8. Hartmann T., Pietzsch A. and Gebbeken N. 2010. *A hydrocode material model for concrete*. International Journal of Protective Structures, Multi-Science Publishing Co Ltd. UK, ISSN 2041–4196, Volume **1**, Number 4, Dec 2010, 443–468.
9. Larcher, M. 2009. Development of discrete cracks in concrete loaded by shock waves. *International Journal for Impact Engineering*, **36**, 700–710.
10. Holmquist, T., Johnson, G. and Cook, W. 1993. *A computational constitutive model for concrete subjected to large strains, high strain rates, and high pressures*. Proc. 14th International Symposium on Ballistics, Quebec, 591–600.
11. Gebbeken, N., Greulich, S., Pietzsch, A. and Landmann, F. 2004. *The engineering tool XPLOSIM to determine the effects of explosive loadings on reinforced and fibre-reinforced concrete structures*. Proceedings, MABS 2004, Bad Reichenhall, CD 2004.
12. Gebbeken, N. and Döge, T. 2009. *From explosions to the design load*. In: Wu C. and Lok T. (Eds.), *Shock and Impact Loads on Structures*, CI-Premier, Singapore, ISBN 978-981-08-3245-2, 25–36.
13. Gebbeken, N. and Dittrich, G. 2006. Dynamisches abscherversagen von stahlbeton-bauteilen unter detonationsbelastung. Beton- und Stahlbetonbau, ISSN 0005–9900, Heft **7**, 490–498.
14. Krauthammer, T. 2008. *Modern Protective Structures*, CRC Press
15. Shi, Y., Hao, H. and Li, Z.X. 2008. Numerical derivation of pressure–impulse diagrams for prediction of RC column damage to blast loads. *International Journal of Impact Engineering*, Elsevier, **35**(11), 1213–1227.
16. Feldman, A. and Siess, C.P. 1956. *Investigation of resistance and behavior of reinforced concrete members subjected to dynamic loading*, Civil and Engineering Studies, Structural Research Series 125, University of Illinois, Urbana, Illinois, 30 September 1956.
17. Feldman, A. and Siess, C.P. 1958. *Investigation of resistance and behavior of reinforced concrete members subjected to dynamic loading*, Part II, Civil and Engineering Studies, Structural Research Series 165, University of Illinois, Urbana, Illinois, 30 September 1958.
18. Astarlioglu, S. and Krauthammer, T. 2009. *Dynamic Structural Analysis Suite (DSAS)*, User Manual, V. 3, Technical Report CIPPS-TR-003–2009, Center for Infrastructure Protection and Physical Security (CIPPS), December 2009.

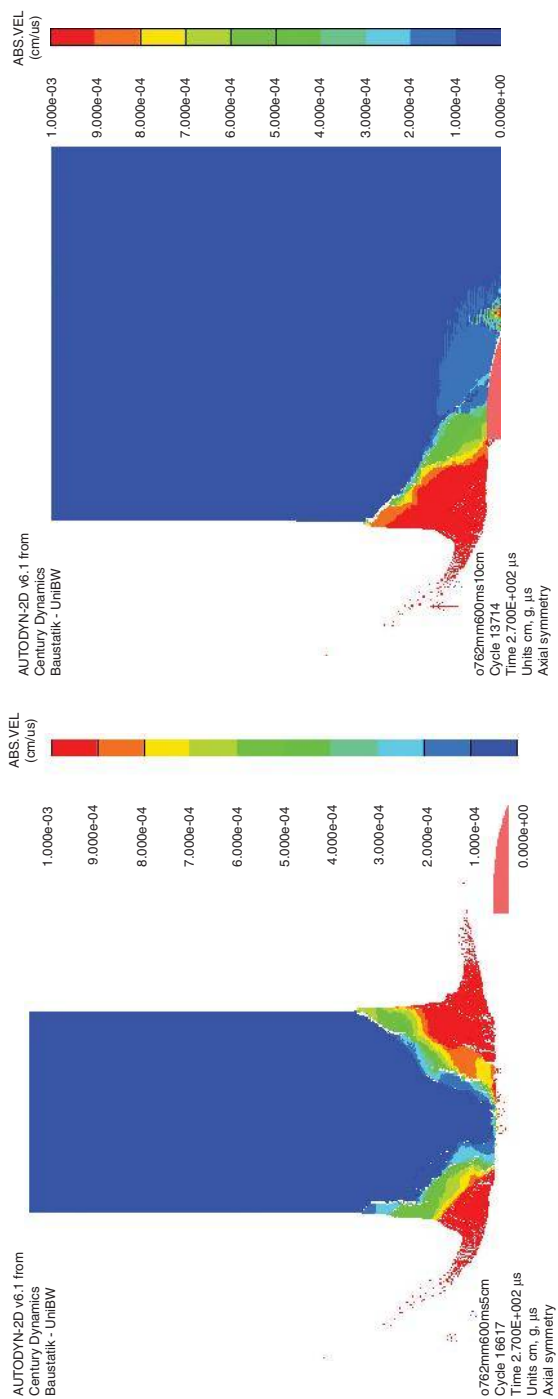


Plate XXXVI (Chapter 11) Projectile impact, concrete slab and numerical simulation (calibre diameter 7.62 mm, impact velocity 600 m/s, left: thickness of the concrete is 5 cm, perforation occurs, right: thickness of the concrete is 10 cm, penetration occurs).

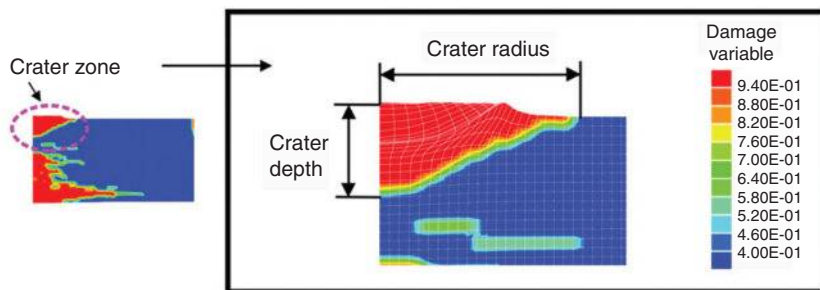


Plate XXXVII (Chapter 11) Contact detonation, determination of the crater radius and the crater depth (2D simulation, axial symmetry).

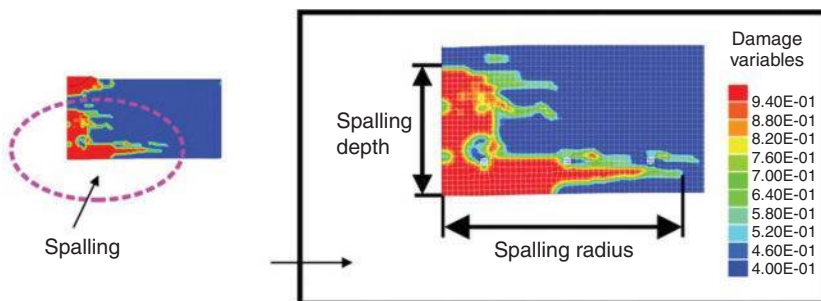


Plate XXXVIII (Chapters 10 and 11) Contact detonation, determination of the spalling radius and the spalling depth (2D simulation, axial symmetry).

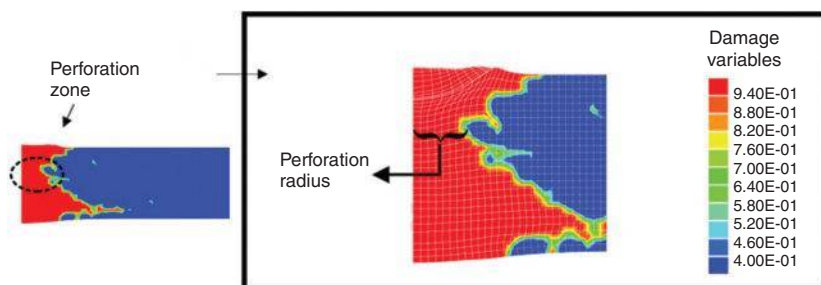
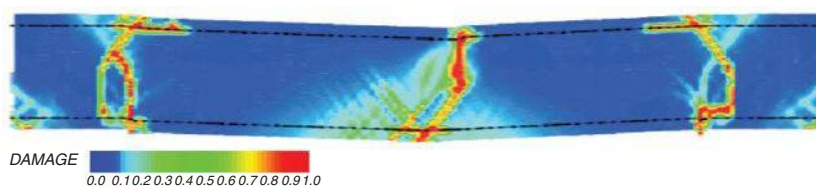
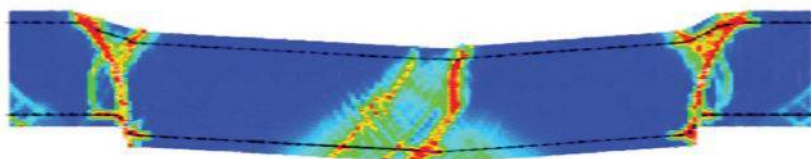


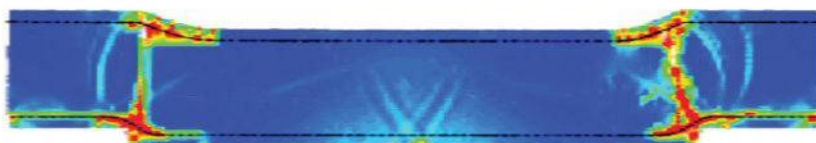
Plate XXXIX (Chapter 11) Contact detonation, determination of the perforation radius (2D simulation, axial symmetry).



(a)



(b)



(c)

Plate XXXX (Chapter 11) Blast load acting on concrete structures, finite element simulation, (a) bending moment failure low charge, (b) bending moment failure high charge, (c) charge as in (b) but higher reinforcement that causes a direct (dynamic) shear failure.¹³

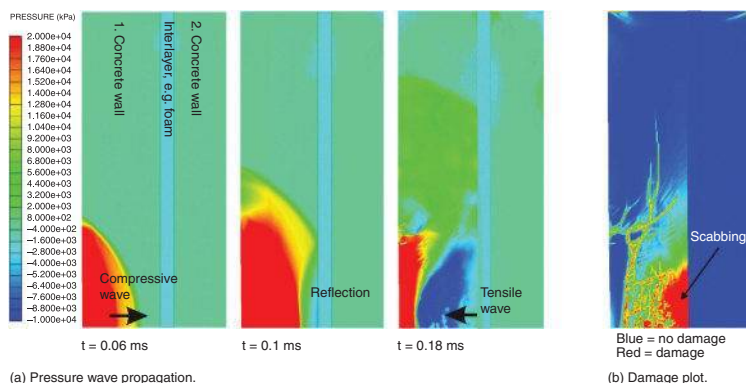


Plate XXXXI (Chapter 11) Principle of wave propagation in a 3-layer concrete sandwich wall after a close-in detonation.

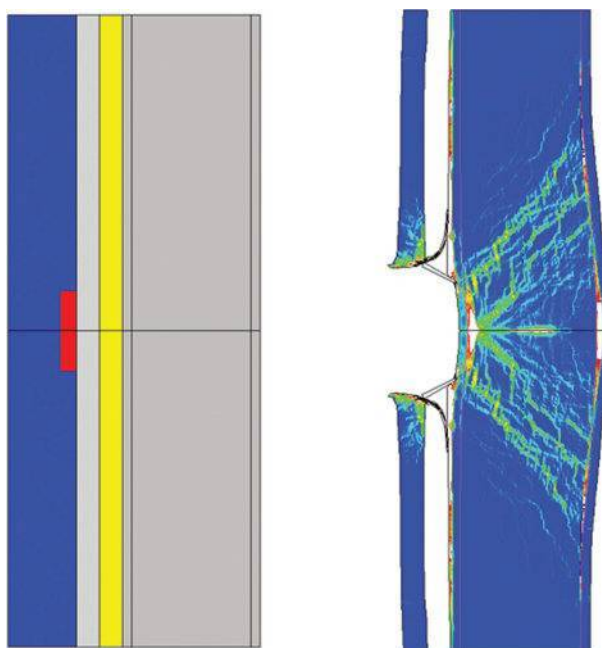


Plate XXXXII (Chapters 10 and 11) 3-layer concrete sandwich wall subjected to contact detonation, left: design with high-strength high-ductility protection wall, right: numerical simulation, result given in effective strain.

- age, 30–1
 - relationship between normalised property and degree of reaction, 31
- aggregate, 8–11
 - distribution effect, 58–9
 - load-deflection curves for two concrete mixes and circular aggregate, 60, 62
 - non-local strain measure for concrete and aggregates, 61, 63
 - roughness effect, 60–1
 - aggregate shape assumed in calculations, 67
 - calculated distribution of non-local strain measure for different aggregate shape, 68, 69
 - calculated load-deflection curves for different aggregate shape, 67, 68
 - shape influence, 283–4
 - circular and polygonal damage profiles, Plate XXV
 - strain measurement of the transmitted tensile wave, 284
 - size, 22–3
 - size and volume effect, 59–60
 - calculated distribution of non-local strain measure for different circular aggregate densities, 66
 - calculated load-deflection curves for different circular aggregate densities, 64, 65
 - stiffness effect, 61
 - FE calculations, 70
 - type, 21–2
- air-blast waves, 346
- aligned meshing, 227
- ANSYS pre-processor, 232
- AUTODYN, 256
- beam size, 65–9
 - calculated and measured size effect in nominal strength vs. beam height for concrete, 76
 - calculated distribution of non-local strain measure above notch from numerical calculations, 76
 - calculated nominal strength vs. normalised beam deflection, 75
 - formation of localised zone directly above notch using DIC, 77
 - width of localised zone in experiments using DIC vs. normalised beam deflection, 78
- blast, 345–8
 - blast load acting on concrete structures, Plate XXXX
 - blast wave, pressure-time relation, 346
 - design of concrete slabs against blast, 347–8
 - improving resistance, 358–62
 - 3-layer concrete sandwich wall subjected to contact detonation, Plate XXXXII
 - blast wall illustration, 361
 - blast walls, 360
 - combined effects, 360–2
 - DUCON sant + self-compacting concrete + MicroMat, 362
 - mitigation of explosive effects using sandwich walls, 358–9
 - state building, multiple purpose use, multiple threats, 362
 - substructuring, Plate XXXXIII

- blast (*cont.*)
 - wave propagation in 3-layer concrete sandwich wall after close-in detonation, Plate XXXXI
 - pressure-impulse diagram, 348
- blast walls, 360
- bleeding, 10
- bond cement matrix, 8–11
- Boolean operation, 233
- bulk viscosity, 281–2, 282–3
 - Fracture planes corresponding to different values of viscosity, Plate XXIII
 - fracture planes corresponding to different values of viscosity, Plate XXIV
 - time-strain measurement, 282, 283
- calcium hydroxide (CH), 4–5
- calcium silicate hydrates (CSH), 4–7
- capillary pressure, 105
- CEB-FIB formula, 201
- CEB-FIP DIF model, 244
- cement matrix, 4–8
 - characteristic of pore size distribution and volume, 10
 - hardened cement paste, 7
 - hydration process, 5
 - microstructure of cement-based materials, 6
 - pores classification, 9
- compact tension specimen (CTS), 312–16
 - crack speed at onset of cracking, 317
 - crack velocities and crack pattern, Plate XXXII
 - crack velocities for different displacement rates, Plate XXX geometry, 313
 - predicted failure modes, Plate XXXI
 - rate-dependent/quasi-static resistance, 314
- composition, 20–3
 - aggregate size, 22–3
 - uniaxial tensile strength, 23
 - aggregate type, 21–2
 - low to high strength concrete, 20–1
 - influence of water cement ratio on tensile strength, 21
 - compressive strength, 46–7
- concrete
 - blast, 345–8
 - blast load acting on concrete structures, Plate XXXX
 - blast wave, pressure-time relation, 346
 - design of concrete slabs against blast, 347–8
 - pressure-impulse diagram, 348
 - bond cement matrix and aggregates, 8–11
 - ITZ, 10
 - shrinkage cracking, 10
 - shrinkage cracks, 12
 - cement matrix, 4–8
 - composition effect modelling on tensile properties, 52–94
 - beams behaviour under 3-point bending, 56–69
 - damage modelling, 54–6
 - elements behaviour under uniaxial tension, 69–86
 - contact detonation, 342–5
 - concrete slab contact detonation failure and slab after detonation, 342
 - crater radius and crater depth determination, Plate XXXVII
 - graphical user interface of XploSim, 344
 - perforation radius determination, Plate XXXIX
 - spalling radius and spalling depth determination, Plate XXXVIII
- damaged structural elements residual load-bearing capacity, 348–52
 - damaged structures residual capacity, 349
 - load-deflection curves vs estimated residual load-bearing capacity, 351
 - testing of a damaged reinforced-concrete plate, 350
- dynamic response modelling with mesoscopic heterogeneity, 218–62

- comprehensive mesoscale continuum model, 231–42
- concrete tensile behaviour in
 - dynamic splitting (Brazilian) tension, 248–54
- mesoscopic structure of concrete, 220–4
- modelling heterogeneity in concrete, 254–9
- pseudo-3D (sandwich) mesoscale model, 242–8
- spalling and fragmentation
 - modelling in concrete structures, 259–61
- types of mesoscale model and their applications, 224–31
- dynamic test devices for tensile
 - properties, 137–78
 - edge-on impact tests, 176–7
 - experimental methods, 138–9
 - tensile strength and fracture
 - energy at high loading rates, 147–74
 - tensile strength and fracture
 - energy at intermediate loading rates, 139–47
 - tensile strength at very high loading rates, 171–6
- factors affecting tensile properties, 19–48
 - age effect, 30–1
 - composition effect, 20–3
 - compressive strength, 46–7
 - crack development at meso-scale, 44–6
 - curing and moisture effect, 23–5
 - cyclic loading effect, 34–8
 - laboratory test implications, 47–8
 - load duration effect, 31–4
 - specimen size, 27–9
 - temperature effect, 25–7
 - type of loading, 38–43
- impact, penetration and perforation, 339–42
 - graphical user interface of PenSim, 341
 - perforation of concrete plate, process and explanation, 339
 - projectile impact, concrete slab and numerical simulation, Plate XXXVI
- improving blast resistance, 358–62
 - 3-layer concrete sandwich wall
 - subjected to contact detonation, Plate XXXXII
 - blast wall illustration, 361
 - blast walls, 360
 - combined effects, 360–2
 - DUCON sant + self-compacting concrete + MicroMat, 362
 - mitigation of explosive effects using sandwich walls, 358–9
 - state building, multiple purpose use, multiple threats, 362
 - substructuring, Plate XXXXIII
 - wave propagation in 3-layer concrete sandwich wall after close-in detonation, Plate XXXXI
- mesoscopic modelling of different
 - moisture conditions and loading rates, 268–89
 - constitutive modelling, 270–4
 - Modified Split Hopkinson Bar test, 284–8
 - Split Hopkinson Bar test, 278–84
- reinforced-concrete beams behaviour
 - under localised static and impact loads, 352–8
- Beam 1-h after tests, 355
- Beam 1-h details, 354
- central deflection vs time of Beam 1-h, 356, 357
- concrete cube after close-in detonation and pullout test after detonation, 353
- dynamic load for Beam 1-h, 355
- P-I curves for Beam 1-h, 358
- test and DSAS simulation for static loading case of Beam 1-h, 356
- test and DSAS simulation for static loading case of Beam 1-h (strain rate 20), 356
- resilient material system, 1–14
- response mechanisms under impulsive tensile loading, 181–215

- concrete (*cont.*)
 - effect of cracking rates on fracture process, 203–14
 - effect of cracking rates on the tensile strength, 183–203
 - strain rate modelling and phenomena, 295–334
 - loading-rate effects, 295–301
 - shock-induced tensile loading, 320–32
 - strain-rate dependent strength measurement, 301–20
 - structure and mechanical properties, 11, 13–14
 - nano-indentation tests on cement paste with unhydrated cement, 13
 - test set-up for ITZ testing, 14
 - structure response modelling to dynamic loading, 125–35
 - blast response, 127–8
 - contact detonation and EFP, 131–3
 - earthquake loading and impact deflection, 127
 - loading regimes, 125–6
 - projectile impact loading, 128–31
 - three geometrical scales, 3
 - understanding the dynamic response to loading, 338–63
- Concrete Damage Model, 237, 256
- concurrent algorithm-based simulation (CAS), 227
- contact detonation, 131–3, 134, 342–5
 - concrete slab contact detonation
 - failure and slab after detonation, 342
 - crater radius and crater depth
 - determination, Plate XXXVII
 - graphical user interface of XploSim, 344
 - initial shock, dispersive release waves and superposition, 133
 - isothermal 1D compression to planar shock state, Plate IX
 - perforation radius determination, Plate XXXIX
 - range of dynamic loading scenarios, 132
 - rear surface of a reinforced concrete plate, Plate VIII
 - spalling radius and spalling depth determination, Plate XXXVIII
- corrosion, 99
- crack branching, 296
- crack density, 192
- crack extension, 184
- Crack Opening Displacement (COD), 196
- crack propagation, 204
- cracking rates
 - effect on concrete tensile strength, 183–203
 - crack-tip velocity of single crack and DIF tensile strength, 188
 - dynamic stress intensity factor on penny-shaped crack, 185
 - effect of transition from moderate to enhanced cracking rates on strength, 184–7
 - loading rate beyond which it becomes rate dependent, 186
 - mechanical response, 183–4
 - mechanical response under high loading rate regimes, 187–9
 - effect on fracture process under moderate and high loading regimes, 203–14
 - crack-tip fracture process, 204
 - data on fracture patterns, 209
 - data on strength and fracture energy, 209
 - definition of fracture energy parameters, 204–5
 - digitised crack pattern and picture of FZ, 208
 - dynamic conditions, 205–7
 - experimental data on dynamic fracture process and fracture energy, 207–14
 - Gf-values from uniaxial tensile tests, 214
 - ratios of FZ width, length of connected microcracks related to static conditions, 212
 - stress, deformation and velocity recordings of the failure zone, 211

- stress deformation curve schematic, 205
- stress displacement and
 - deformation curves, 210
- moisture content on dynamic
 - strength, 198–201
- dynamic stress intensity factor as
 - function of time and strength enhancement factor, 200
- rate effects on strength for dry,
 - normal and wet concrete, 200
- multiple fragmentation due to the
 - limited cracking velocity, 189–98
 - analytical solution and model predictions, 193
- Denoual-Forquin-Hild (DFH)
 - model, 190–2
- DFH fragmentation model
 - predictions in terms of cracking density-vs-strain rate, 198
- DFH model predictions vs
 - experimental data, 196–8
- material parameters identification, 194–6
- optimised specimen geometry used
 - in rocking spalling tests, 196
- post-mortem analysis of two
 - concrete specimens after spalling tests, 190
- quasi-static and dynamic tests
 - results, 197
- strength data and empirical models, 201–3
- DIF experimental data and models, 202
- semi-empirical and physics-based
 - models for concrete tensile strength DIF, 202
- critical defects, 190
- critical stress intensity factor, 206
- cyclic loading, 34–8
 - flexural strength of concrete, 35
 - Goodman diagram for concrete, 36
 - normalised S-N curves of lightweight
 - and normal weight concrete, 38
 - S-N curves for concrete in tension, 37
 - S-N curves for concrete under cyclic
 - tensile and tensile compressive loading, 36
- damage parameter, 55
- deflagrations, 343
- Denoual-Forquin-Hild (DFH) model, 190–2
 - DFH fragmentation model
 - predictions in terms of cracking density-vs-strain rate, 198
 - DFH model predictions vs
 - experimental data, 196–8
- detonations, 343
- diffusivity approach, 107
- direct tensile test
 - high-speed hydraulic press, 140–1
 - schematic diagram, 141
- discrete cracking, 45–6
- discrete element methods (DEM), 224
- discrete fracture models, 112
- displacement-controlled test, 40–3
 - effect of measuring length on stress-displacement, 42
 - load-displacement of concrete in
 - tension, 41
 - load-displacement of concrete in
 - uniaxial tensile cyclic loading, 43
 - uniaxial test experimental result, 43
- disp_notch, 144–5
- distributed cracking, 44–5
 - micro-cracks at the surface of
 - concrete, 45
- ‘dry’ concrete, 199
- dry masonry wall, 116–17
 - deformed configuration of a wet
 - render after different drying periods, Plate II
- dual-permeability models, 111–12
- dual-porosity models, 111
- DUCON, 360
- Ductal, 176, 177
- dynamic bending tests, 207
- dynamic fracture energy
 - spalling, 162–71
 - DIF tensile strength data and mean values fracture energy data, 170
 - EOI experiments performed with
 - Ductal Ultra-High-Strength Concrete, 174–5
 - experiments performed with GEPI
 - facility, 173–4

- dynamic fracture energy (*cont.*)
 - Hopkinson Bar experiments
 - results, 166
 - 74mm MSHB in Delft for high loading rates, 168
 - normal distribution from SHB repetitions with identical input parameters, 165
 - notched specimen and analytically calculated velocity distribution, 164
 - optical extensometer recordings of fragment displacements and relative velocity, 165
 - plate-impact technique, 172
 - reconstructed load-deformation curve, 170
 - recorded and reconstructed strain-time records, 169
 - UHPC concrete, 166
- dynamic fragmentation model, 194
- Dynamic Increase Factor (DIF), 156, 203, 306, 310
- dynamic loading
 - blast response, 127–8
 - concrete structure response
 - modelling, 125–35
 - contact detonation and EFP, 131–3
 - earthquake loading and impact deflection, 127
 - loading regimes, 125–6
 - projectile impact loading, 128–31
- dynamic response modelling
 - concrete with mesoscopic heterogeneity, 218–62
 - comprehensive mesoscale continuum model, 231–42
 - concrete tensile behaviour in dynamic splitting (Brazilian) tension, 248–54
 - mesoscopic structure of concrete, 220–4
 - modelling heterogeneity in concrete, 254–9
 - pseudo-3D (sandwich) mesoscale model, 242–8
 - spalling and fragmentation
 - modelling in concrete structures, 259–61
 - types of mesoscale model and their applications, 224–31
- dynamic splitting (Brazilian) tension
 - concrete tensile behaviour mesoscale modelling, 248–54
 - damage characteristics under different splitting tensile strain rates, Plate XX
 - damage patterns for a target strain rate of 50 s^{-1} with different rise times, Plate XVIII
 - damage patterns for strain rates of 1 s^{-1} and 10 s^{-1} , Plate XIX
 - dynamic splitting simulation, 253
 - limiting strain rate and load rise time for Brazilian test, 250–4
 - numerical studies on Brazilian tests, 249–50
- dynamic stress intensity factor, 184
- dynamic tensile resistance
 - true and apparent, 304–11
 - bar failure modes, 309
 - calculated DIF, 307
 - compressive pulse in a concrete bar, 307–11
 - DIF for concrete strength as a function of strain rate, 310
 - DIF for fracture energy as a function of strain rate, 311
 - numerically vs. experimentally observed apparent strength, 308
 - reaction- and load-time response, 306, 307
 - simple cohesive-elastic FE model, 304–7, 305
- dynamic tensile state, 129
- dynamic viscosity, 272
- edge-on impact (EOI), 138–9, 176–7
 - experiments performed on concrete specimens in LEM3 lab, Plate X
- equivalent strain measure, 55
- ettringite (Aft), 4–5
- Eurocode 2, 40
- explosive formed projectiles (EFP), 131–3
 - initial shock, dispersive release waves and superposition, 133

- isothermal 1D compression to planar shock state, Plate IX
- range of dynamic loading scenarios, 132
- rear surface of a reinforced concrete plate, Plate VIII
- fracture energy
 - high loading rates, 147–74
 - cL derivation and recorded velocity-time signal, 154
 - dynamic loading in the spallation configuration, 151
 - dynamic material properties for different concrete, 156
 - Dynamic Young's Modulus for conventional to UHPC concrete, 155
 - experimental device and data used for spalling tests, 157
 - experimental technique developed in Metz University, 156–62
 - numerical simulations of a spalling test with an elastic model, 159–60
 - quasi-static and dynamic tensile strength of MB50 microconcrete, 162
 - spallation process of concrete due to tensile loading on UHPC, 153
 - spalling, 162–71
 - spalling test, 148–50
 - specimen-geometry for spallation tests, 151
 - test device and methodology used at Ernst Mach Institute, 150–6
 - visualisation of damage in a wet concrete sample, 161
- intermediate loading rates, 139–47
 - direct tensile test through high-speed hydraulic press, 140–1
 - experimental techniques, 139–40
 - gravity driven SHB facility at Delft, 141–6
 - SHB facility at ISPRA, 146–7
- fracture process zone (FPZ), 53, 204, 205, 269, 275–6, 303, 306
- Fracture Zone (FZ), 205
- fractured concrete
 - application to masonry wall, 113–17
 - future trends, 117–18
 - material behaviour interaction, 112–13
 - modelling moisture transport, 110–12
 - conceptual models, 110
- Fuller curve, 232
- Goodman model, 233
- high-performance concrete (HPC), 154
- high-speed hydraulic press, 139
 - direct tensile test, 140–1
 - schematic diagram, 141
- high temperature, 25–6
 - linear relationship between tensile strength and temperature, 27
 - normalised tensile strength as function of temperature, 26
- Hopkinson bar apparatus, 230
- 'hourglass' modes, 238
- hydrated cement paste (hcp), 44, 45
- hydration, 4
- hydrocodes, 343, 351–2
 - dynamic strength and shock waves, 322–3
- plasticity models, 323–9
 - compressive and tensile meridian and plasticity models, 327
 - deviatoric limit surfaces, 326–9
 - dynamic stiffness, 324–5
 - mesostructural model with ITZ
 - for homogenisation and shock velocity converges, Plate XXXIV
 - rate enhancement description, 329
- hypervelocity impact, 134
- impedance, 359
- impulsive tensile loading
 - concrete response mechanisms, 181–215
 - effect of cracking rates on concrete tensile strength, 183–203
 - effect of cracking rates on fracture process, 203–14
- inertia effect, 127, 298
 - global dynamic response of the high-rise building concept 'Security Scraper,' Plate III

- intact concrete
 - application to masonry wall, 113–17
 - future trends, 117–18
 - material behaviour interaction, 112–13
 - modelling moisture transport, 100–10
 - moisture retention, 104–6
 - research, 100–1
 - unsaturated moisture transport, 101–3
- interface transition zone (ITZ), 1, 2, 8, 20, 269, 276, 277
- tensile strength, 285–6
 - FPZs, Plate XXVI
- thickness effect, 62
 - effect of different bond thickness in FE calculations, 72
 - FE-meshes with different bond thickness, 71
- viscosity, 282–3
 - fracture planes corresponding to different values of viscosity, Plate XXIV
 - time-strain measurement, 283
- interlayer water, 7
- Johnson Holmquist (JH) model, 256
- Kinney formula, 347
- L-shaped specimen, 316–20
 - different analyses for loading rate, 320
 - experimental set-up, 318
 - failure pattern and crack propagation, 318, 319
- laboratory test, 47–8
- Lagrange method, 256
- lightweight aggregates (LWA), 22
- Linear Elastic Fracture Mechanics (LEFM), 184
- liquid permeability, 107–8
- load-controlled test, 38–40
 - elastic energy of various concretes, 40
 - load-displacement curve, 39
- load duration, 31–4
 - normalised stress level vs. time to failure, 33
 - normalised stress-strength ratio vs. time to failure, 34
- specimen configuration and test results, 32
- tensile strength of hydrated cement paste, 32
- loading function, 54
- loading-rate effect, 295–301
- modelling frameworks, 297–301
 - material resistance as a function of stress- and strain-rate, 299
- localised zone averaging, 77–84
 - expected value and standard deviation of tensile fracture energy, 86
 - stress-strain curves for various sizes of concrete specimens, 85
- low temperature, 26–7
- LS-DYNA, 260
- macro-cracks, 11
- macroscopic deformation, 126
- masonry wall, 113–17
 - numerical model, 114–15
 - moisture content, liquid and vapour permeability, 115
 - periodic cell of the double-wythe masonry wall, 114
- Matlat, 232
- mercury intrusion porosimetry (MIP), 104
- mesoscopic heterogeneity
 - comprehensive mesoscale continuum model, 231–42
 - aggregate distribution samples, 239
 - compaction curve and strength surfaces of Concrete Damage Model, 235
 - compressive stress-strain curves produced by mesoscale model, 242
 - FE mesh for mesoscale model of concrete, 234
 - FE mesh generation, 232–3
 - generation of coarse aggregates, 231–2
 - material models and other numerical considerations, 233–8

- model validation and influence of
 - non-homogeneity in mortar and aggregates, 238–42
- polygonal aggregates generation and meso-geometry in 2D, 233
- sensitivity to randomness in
 - aggregate arrangement and non-homogeneity, 241
- simulation results under uniaxial tension, Plate XIII
- single-element analysis of axial compressive stress strain curves, 236
- concrete dynamic response
 - modelling, 218–62
- mesoscale modelling in dynamic splitting (Brazilian) tension, 248–54
- damage characteristics under different splitting tensile strain rates, Plate XX
- damage patterns for a target strain rate of 50 s^{-1} with different rise times, Plate XVIII
- damage patterns for strain rates of 1 s^{-1} and 10 s^{-1} , Plate XIX
- dynamic splitting simulation, 253
- limiting strain rate and load rise time for Brazilian test, 250–4
- numerical studies on Brazilian tests, 249–50
- mesoscopic structure of concrete, 220–4
 - comparative simulation of damage patterns, Plate XI
 - concrete mesoscopic geometry, 220
 - four levels of discretisation, 222
- modelling heterogeneity in concrete, 254–9
 - brief overview, 254–6
 - crack patterns variation as degree of heterogeneity increases, 257
 - failure process of heterogeneous specimen under different loading rates, 258
 - failure processes of heterogeneous specimen under different strain rates, 259
 - numerical specimens with increasing degree of heterogeneity, 257
 - probability density functions from Weibull distribution, 255
 - stochastic heterogeneous modelling of concrete, 256–9
- pseudo-3D (sandwich) mesoscale model, 242–8
 - compression DIF from numerical experiments, 245
 - cubic specimen and representative stress distribution, Plate XV
- damaged patterns and 3D
 - homogeneous model, Plate XVI
- mesoscale analysis of strain rate effect in dynamic compression, 244–7
- model configuration, 242–5
- sandwich model (cylinder), Plate XIV
- strain rate limit of concrete in SHPB compression test, 247–8
- stress strain curves inferred from three different wave approaches, 248
- stress time histories in five equally divided strips along loading direction, Plate XVII
- variation of peak stresses in mortar and aggregates, 246
- spalling and fragmentation
 - modelling in concrete structures, 259–61
- modelling of concrete slab
 - fragmentation under blast load, 260
- types of mesoscale model and their applications, 224–31
 - biphasic mesoscale FE model, 228
 - biphasic spherical mesoscale model, 227
 - continuum (Finite Element) model, 226–8
 - direct tension simulation with DEM, 229
 - discrete element and discrete particle methods, 226

- mesoscopic heterogeneity (*cont.*)
 - fracture numerical simulation in spalling tests and velocities of ejection, Plate XII
 - lattice models, 224–6
 - mesoscale models applications in concrete high strain rate analysis, 228–31
- mesoscopic modelling
 - circular and polygonal aggregates, 276
 - concrete moisture conditions and loading rates, 268–89
 - constitutive modelling, 270–4
 - increase of tensile strength as a function of the loading rate, 271
 - macroscopic model parameters used in the SHB and MSHB tests, 275
 - model parameters in the mesoscopic VEPD model, 275
 - rheological representation of the VEPD, 271
- Modified Split Hopkinson Bar test, 284–8
- Split Hopkinson Bar test, 278–84
 - three different realisations of aggregates, 277
- micro-cracks, 10–11, 297, 303
- micro-inertia effect, 300
- micro-scale–discrete modelling, 298
- Modified Split Hopkinson Bar (MSHB), 167, 270, 278, 284–8
 - ITZ tensile strength, 285–6
 - mesostructure with bulk material, aggregate and ITZ, 286
 - saturation level, 287–8
 - dry material, 287, Plate XXVII
 - normal material, 287, Plate XXVIII
 - wet material, 287–8, Plate XXIX
 - two-dimensional model test set-up, 287
- Mohr Coulomb model, 256
- moist curing, 23–5
 - bending strength of concrete in moist and drying condition, 24
 - uniaxial tensile strength, 24
- moisture, 23–5
 - bending strength of concrete in moist and drying condition, 24
 - retention, 104–6
 - idealised cylindrical and real pore network, 106
 - moisture-retention capacity of concrete, 104
 - pore size distribution and moisture-retention curve, 106
 - uniaxial tensile strength, 24
- moisture transport, 106–10
 - modelling in intact and fractured concrete, 98–118
 - application to masonry wall, 113–17
 - degradation of concrete induced by ASR and corrosion, 99
 - future trends, 117–18
 - material behaviour interaction, 112–13
- moving cracks, 189
- network approach, 109–10
 - pore system, 109
- numerical concrete, 224
- obscuration probability, 192
- obscuration zones, 190
- P-I diagrams, 347
- PenSim (Penetration Simulation), 340–1, 345
- 3-point bending, 56–69
 - aggregate distribution effect, 58–9
 - aggregate roughness effect, 60–1
 - aggregate size and volume effect, 59–60
 - aggregate stiffness effect, 61
 - beam size effect, 65–9
 - ITZ thickness effect, 62
 - mesoscopic characteristic length
 - effect, 63, 65
 - calculated distribution of non-local strain measure, 74, 75
 - calculated load-deflection curves, 73, 74
 - numerical implementation, 56–8
 - FE-mesh used for calculations of meso-scale region, 59

- geometry and grading curve for concrete beam, 57
 - material parameters assumed FE calculations, 58
 - poromechanical effective-stress, 113
 - Portland cement, 4
 - power-law
 - dependency, 187
 - function, 193
 - pressure-membrane apparatus (PMA), 104
 - pressure-plate apparatus (PPA), 104
 - PRM-Model, 328
 - pseudo-3D (sandwich) mesoscale model, 242–8
 - compression DIF from numerical experiments, 245
 - cubic specimen and representative stress distribution, Plate XV
 - damaged patterns in pseudo-3D mesoscale model and 3D homogeneous model, Plate XVI
 - mesoscale analysis of strain rate effect in dynamic compression, 244–7
 - model configuration, 242–5
 - sandwich model (cylinder), Plate XIV
 - strain rate limit of concrete in SHPB compression test, 247–8
 - stress strain curves inferred from three different wave approaches, 248
 - stress time histories in five equally divided strips along loading direction, Plate XVII
 - variation of peak stresses in mortar and aggregates, 246
- random particle drop method, 227
 - random sequential addition (RSA) method, 227
 - rate-dependent fracture, 312–20
 - rate-dependent strength, 127–8
 - reinforced concrete frame building loaded by an external blast load, Plate IV
 - Rayleigh wave velocity, 188
 - reinforced-concrete beams
 - behaviour under localised static and impact loads, 352–8
 - Beam 1-h after tests, 355
 - Beam 1-h details, 354
 - central deflection vs time of Beam 1-h, 356, 357
 - concrete cube after close-in detonation and pullout test after detonation, 353
 - dynamic load for Beam 1-h, 355
 - P-I curves for Beam 1-h, 358
 - test and DSAS simulation for static loading case of Beam 1-h, 356
 - test and DSAS simulation for static loading case of Beam 1-h (strain rate 20), 356
 - relative humidity, 103
 - representative elementary volume (REV), 101–2, 194
 - representative volume element (RVE), 52, 53
 - residual tensile strength, 37
 - response mechanisms
 - concrete under impulsive tensile loading, 181–215
 - effect of cracking rates on fracture process under moderate and high loading regimes, 203–14
 - effect of cracking rates on the tensile strength, 183–203
 - RILEM test, 207
 - sandwich walls, 358
 - saturated masonry wall, 115–16
 - deformed configuration of a wet render after 1 day of drying and at equilibrium, Plate I
 - scaling matrix, 273
 - security scraper, 127
 - shock-induced tensile loading, 320–32
 - hydrocode plasticity models, 323–9
 - model complexity vs. range of application, 331–2
 - sensitivity analysis and model complexity, 329–31
 - convergence analysis and validation, 330
 - impact configuration after test, 331
 - vs. moderate loading rates, 320–3

- shock-induced tensile loading (*cont.*)
 - damage to four box girder fields and stiffeners, Plate XXXIII
 - deformation and damage extension of projectile stopped close to the ballistic limit, Plate XXXV
 - hydrocodes for dynamic strength and shock waves, 322–3
- silica fume, 8
- single-degree-of-freedom (SDOF), 128, 347
- smoothed particle hydrodynamics (SPH), 256
- spalling, 148–50, 162–71, 343
 - dynamic tensile test, 150
- specimen size, 27–9
 - measured values of tensile strength and Weibull approximation, 30
 - theoretical prediction of the flexural strength, 29
- Split Hopkinson Bar (SHB), 139, 269–70, 278–84
 - aggregate shape, 283–4
 - bulk and ITZ viscosity, 282–3
 - bulk viscosity, 281–2
 - different aggregate distributions, 280–1
 - fracture planes, Plate XXII
 - tensile strength of the concrete specimen, 281
- facility at ISPRA, 146–7
 - tensile tests performed in the Joint-Research-Centre, 147
- fracture planes corresponding to different values of strength of the ITZ, Plate XXI
- gravity driven facility at Delft, 141–6
 - direct tensile tests performed with hydraulic press, 144
 - displacement time records, 145
 - measurement, set-up and instrumented notched specimen, 142–3
 - specification, 144
 - stress deformation curve, 146
- test set-up two-dimensional model, 279
- time-strain curves, 280
- Split Hopkinson Tensile Bar (SHTB), 141
- splitting test, 28
- standard averaging, 71, 72, 75, 77
 - distribution of non-local softening strain measure, 82, 83
 - expected value and standard deviation of tensile fracture energy, 84
 - stress–strain curves for various sizes of concrete specimens, 81
- Stefan effect, 198–9, 200, 286, 300
- strain
 - loading-rate effects, 295–301
 - modelling and phenomena, 295–334
 - rate dependent strength
 - measurement, 301–20
 - shock-induced tensile loading, 320–32
- strain-rate dependent strength, 301–20
 - rate-dependent fracture modelling phenomena, 312–20
- split Hopkinson bar, 301
- state of equilibrium of forces when concrete softens, 302
- true and apparent dynamic tensile resistance, 304–11
- stress tensor, 55
- stress–strain function, 54
- take-and-place process, 227, 232
- tensile fatigue test, 37
- tensile-fracture process, 184
- tensile strength
 - age effect, 30–1
 - beams behaviour under 3-point bending, 56–69
 - composition effect, 20–3
 - composition effect modelling of concrete, 52–94
 - compressive strength, 46–7
 - conversion factors for Equation for test methods and concrete range of validity, 48
 - concrete, 19–48
 - crack development at meso-scale, 44–6
 - curing and moisture effect, 23–5
 - cyclic loading effect, 34–8
 - damage modelling, 54–6

- dynamic test devices for concrete, 137–78
- edge-on impact tests, 176–7
- elements behaviour under uniaxial tension, 69–86
- experimental methods, 138–9
- fracture energy at high loading rates, 147–74
 - cL derivation and recorded velocity-time signal, 154
 - dynamic loading in the spallation configuration, 151
 - dynamic material properties for different concrete, 156
 - Dynamic Young's Modulus for conventional to UHPC concrete, 155
 - experimental device and data used for spalling tests, 157
 - experimental technique developed in Metz University, 156–62
 - numerical simulations of a spalling test with an elastic model, 159–60
 - quasi-static and dynamic tensile strength of dry and saturated MB50 microconcrete, 162
 - spallation process of concrete due to tensile loading on UHPC, 153
 - spalling, 162–71
 - spalling test, 148–50
 - specimen-geometry for spallation tests, 151
 - test device and methodology used at Ernst Mach Institute, 150–6
 - visualisation of damage in a wet concrete sample, 161
- fracture energy at intermediate loading rates, 139–47
 - direct tensile test through high-speed hydraulic press, 140–1
 - experimental techniques, 139–40
 - gravity driven SHB facility at Delft, 141–6
 - SHB facility at ISPRA, 146–7
- interfacial transition zone (ITZ), 285–6
 - FPZs, Plate XXVI
- laboratory test implications, 47–8
- load duration effect, 31–4
 - specimen size, 27–9
 - temperature effect, 25–7
 - type of loading, 38–43
 - very high loading rates, 171–6
- tension/spall zone, 132
- total mass flux, 103
- triaxial stress, 128–31
 - ballistic impact of a steel projectile, 129
 - compaction and strength measurements of concrete, Plate VI
 - dynamic triaxial compression, 130
 - impact of a kinetic penetrator against a thin concrete slab, Plate V
 - numerical analysis of ballistic impact, 130
 - numerical simulation of a ballistic impact against a mortar matrix, Plate VII
- unaligned meshing, 227–8
- uniaxial tensile test, 28, 29
- uniaxial tension, 69–86
 - localised zone averaging, 77–84
 - material parameters assumed
 - FE calculations of concrete elements, 79
 - numerical implementation, 71
 - concrete specimens of different size, 80
 - standard averaging, 71, 72, 75, 77
 - uniaxial tension test, 79
 - varying characteristic length, 84–6
- uniaxial wave propagation, 302
- unsaturated moisture transport, 101–3
 - mass conservation, 102
- vapour permeability, 108–9
- varying characteristic length, 84–6
 - distribution of non-local softening strain measure, 89, 90, 91, 92
 - expected value and standard deviation of unit fracture energy, 93
 - stress-strain curves for various sizes of concrete specimens, 87, 88

- visco-elastic model, 297
- visco-elastic visco-plastic damage (VEVPD), 269, 276, 283
- visco-plastic model, 273–4
- viscosity, 297
- volumetric-deviatoric split, 325
- wall effect, 28
- wave velocity, 207
- weak aggregate, 61
- weakest-link hypothesis, 191
- Weerheijm model, 203
- Weibull diagram, 194
- Weibull modulus, 194
- Weibull scale parameter, 194
- ‘wet’ concrete, 199
- XploSim, 344–5